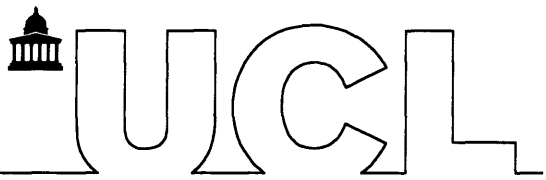

Principles of Two-Phase Flow Microreactors and their Scale-Out

VOLUME I

Carlos Amador Zamarreño

A thesis submitted for the degree of Doctor of Philosophy of

the University of London

University College London

October 2006

ProQuest LLC
789 East Eisenhower Parkway
P.O. Box 1346
Ann Arbor, MI 48106-1346

To my parents Felipe and Carmen

Acknowledgments

I would like to express my gratitude to my principal supervisor *Dr Panagiota Angeli* and my second supervisor *Prof. Asterios Gavriilidis* for their continuous guidance and support throughout this project. Special mention goes to my colleague *Dr Wael Salman* for his valuable advice and help as well as his true friendship. I would also like to thank the EU commission for funding this work within the project *Key Elements for the Application of Microreactors in Multiphasic Catalytic Chemistries (KEMiCC).* The following people are also key contributors to this long journey,

Dr John Shaw and *David Wenn* from Central Research Laboratories for supplying test microreactors and experimental data as well as useful comments in relation to pore stability and mass transfer/chemical reaction in the mesh microreactor. *Dr Michael Abraham* at the Chemistry Department at University College London for the estimation of the partition coefficient of fluorescein diacetate in toluene/water. Master and MEng students *Chinenye Udeh, Somphot Sanguanpiyapan, Olaf Sieker and Alexander Scharf,* whose research projects have contributed to this work. Students and researchers at *Prof. Gavriilidis* group *Dr Enhong Cao, Xiuyan Sun, Dr Monica Zanfir, Dr Kay Kin Yeong* and *Suet-Ping Kee* for their advice and help in the laboratory. *Martin, John, Alan and John L.* at the mechanical workshop, who did a great job bringing designs to life and *Sarah, Martyn and Mark* whose experience and support in electrical and computing stuff is much appreciated.

My flat mates *Jason Lum, Andrea Scuzzarella* and *Stefania Stolfa* as well as my office mates *Dr Wa'el Salman, Luca Cammarata, Dr Talal Al-Wahaibi* and *Nan Shao* for their friendship. I would like to remember *Jason Lum* and *Luca Cammarata* who sadly passed away during their studies and will always be in my memories. All my other friends at UCL, *Max, Gianluca, Ivan, Marta, Sarah, Cristina, Marcello, Giovanna, Karolina, Kit...* which made my years in London a lot more enjoyable.

Dr Parimanan Cherntongchai, for her support, inspiration and true love that extends until today.

My parents *Felipe* and *Carmen,* my brother *José Ángel* and my sister *María Rosa,* for their continuous support and understanding throughout this period.

Principles of Two-Phase Flow Microreactors and their Scale-Out

by

Carlos Amador Zamarreño

Abstract

The main focus of this thesis is to characterise and model a novel multiphase mesh microreactor (continuous-phase microsystem) in relation to hydrodynamics, mass transfer/chemical reaction and scale-out operation. The physical understanding gained by the study of interface stability within the mesh pores and the analysis of single-phase flow distribution is then applied to dispersed-phase microsystems, in particular to the bubble formation in a Taylor flow type microreactor and its influence in the design of two-phase scale-out manifolds.

In the mesh microcontactor, two phases flow in different channels separated by a thin mesh with openings (pores) through which the two phases can come in direct contact allowing mass transfer by diffusion to take place. A resistance network model was developed to optimise the shape of the reaction plate for even flow distribution and minimum sample dispersion. The meniscus shape, position and stability within the mesh pores was modelled and supported by experimental results in single pores and meshes. Different factors that affect meniscus stability in real meshes were identified and modelled. Parametric maps that define the boundaries of the kinetic control regime were developed (i.e. negligible mass transfer resistance) which allow the reaction kinetics to be directly retrieved from the experimental data of conversion vs. time. Flow distribution between parallel channels, required in the scale up operation of manifolds for high throughput, was analysed by means of a resistance network model validated via CFD simulations and experimentation. The model was applied to understand the effect of manufacturing tolerances, channel blockages and additional pressure losses on flow distribution.

The knowledge gained in meniscus stability in single pores and single-phase flow distribution in manifolds was applied to analyse the effect of bubble formation on flow distribution in manifolds during Taylor/bubble flow. Pressure drop during Taylor flow (a function of bubble/liquid slug lengths) and pressure fluctuations during bubble formation were investigated and implemented in the resistance network model. A two-channel manifold structure for water/air and octane/air systems was successfully demonstrated.

Table of Contents

Volume II

List of Figures

List of Tables

List of Acronyms

CFD	Computational Fluid Dynamics.
CpM	Continuous-phase Microsystems.
CRL	Central Research Laboratories.
DpM	Disperse-phase Microsystems.
FFR	Falling Film Reactor.
IMM	Institut für Mikrotechnik Mainz.
RNM	Resistance Network Model.
RTD	Residence Time Distribution.

Chapter 1

Thesis Introduction: Microreaction Technology

"The resourceful professional failing to improve the method changes the moment"

Erdnase – The Expert at the Card Table (1902)

1.1. Capability of Microchemical Systems

At present, precision engineering and semiconductor processing technology allow the construction of micro-engineered devices that have advanced the electronics industry and microanalysis chips for chemical and biochemical applications (Jensen, 2001). However, is there a real need for such devices in the chemical engineering industry?

Mass and heat transfer operations in traditional chemical macrosystems rely on high mass and heat transfer fluxes in order to have a fast and controlled operation. In single-phase operations mixing is used to increase mass/heat transfer rates while in multiphase systems, generally one of the phases is dispersed into the other in small bubbles or droplets that increase the interfacial area and decrease the molecular diffusion distances, increasing the interfacial mass/heat transfer. Generally the optimum size of dispersed bubbles or drops in macrosystems fall within the submilimiter range and the idea of taking the physical system to this scale seems wise for demanding systems. Dispersions created in macrosystems often have a broad drop/bubble size distribution that is difficult to control while in microsystems the volume and specific interfacial area is determined by the channel geometry and surface tension forces, which lead to very narrow size distributions. In macrosystems, mixing processes often feature dead volumes or zones where the mixing is not effective while in microsystems this is barely found as mass/heat transfer by diffusion, heat transfer by conduction and laminar convection found in microflows reach the whole volume of the phases.

Microengineered devices show important advantages compared to traditional macrosystems:

- Increase of mass and heat transfer rates due to thin fluid layers and large specific areas encountered in microsystems. This enhancement of the transport phenomena benefits mass transfer limited reactions as well as highly exothermic or endothermic reactions, which are difficult to control in macrosystems. In this case, a short system response time for efficient control of reaction processes is possible (Ehrfeld, 2003). Furthermore, more extreme temperature and pressure conditions can be applied to reaction processes due to a better control, achieving higher reaction rates. The same benefits are found in mass and heat transfer operations without chemical reaction. Kasagi et al. (2003) designed a micro heat exchanger for electronic equipment cooling applications using bare tubes and found that the core volume is drastically reduced when compared to macro heat exchangers.

- Better heat transfer control achieved in microsystems by removal/delivery of fast heat fluxes has been reported to substantially increase the selectivity of certain reactions (Yoshida et al., 2003).

- A better control of interfacial area in multiphase systems compared to macrosystems, where wider drop/bubble size distributions are found.

- Smaller equipment volume for the same throughput is needed.

- Reactants' availability and cost for analytical studies. Certain reactants and catalysts are very expensive and the use of microreactors reduces costs.

- Safer operation as a result of small reagent volumes.

- On-site on-demand production is more flexible and economical.

- The small characteristic dimensions found in microsystems give rise to hydrodynamics led by laminar flow, mass transfer by diffusion and heat transfer by conduction where *precise modelling equations are available.*

- Construction of microengineeried structures for chemical engineering processes is a well-known science thanks to the silicon microfabrication methods in the microelectronics industry.

- Scale up by numbering up or parallelisation (scale out) ensures that findings from a single microchannel unit apply to the whole scaled out device provided that the process conditions

(temperature, pressure, flow, heat and mass fluxes) in each microchannel are identical. Thus, even flow distribution among all parallel channels and microdevices is required.

- Control loops with physical and chemical sensors, current converters and some type of actuators can be integrated within the microengineered device in a similar way as in electronic microchips. Integration of sensors to monitor temperature and reaction progress via infrared, visible and ultraviolet spectroscopy has been reported by Jensen (2001).

There are also some disadvantages and barriers to the microsystems that need to be considered:

- Material corrosion can lead to channel interconnection/destruction because of the small wall thickness generally available in microchannels. Thus, material selection becomes crucial.

- Scale up is based on numbering up and often it is difficult to ensure even distribution of flow and heat among the parallel channels. The second part of this thesis analyses flow distribution in detail.

- Handling of a solid phase. 50 % of the reactions in the fine chemical and pharmaceutical industries would benefit from microreaction technology. However, the frequent presence of a solid phase (63% of those reactions) still impedes the broad application of this technology (Roberge, 2005).

- There is an important capital expenditure associated with the development of a new technology. Furthermore, microengineered devices are often more expensive to manufacture than conventional equipment.

- Fouling and cleaning of the microdevices. Reactant purity and side reactions must be controlled more closely to avoid channel clogging and mechanical cleaning is not simple.

Fluidic passages are considered *small* when their characteristic dimension is of the order of, or smaller than the Laplace constant $K_{Laplace}$ given by Eq. (1.1), where gravitational effects become less important than surface tension effects, which is the case for most microchemical systems. The Laplace constant $K_{Laplace}$ is obtained from the definition of the Bond number (Bo) when $Bo = 1$ and varies for each liquid-gas system ($K_{Laplace}$ = 2.7 mm for water-air and $K_{Laplace}$ = 1.7 mm for n-octane-air):

$$K_{\text{Laplace}} = \left(\frac{\gamma}{g(\rho_L - \rho_G)} \right)^{1/2} \tag{1.1}$$

where γ is the surface tension, g is the acceleration due to gravity and ρ_L and ρ_G are the densities of the liquid and gas phases respectively. Kew and Cornwell (1997) introduced the Confinement number *Co,* which is the ratio of the bubble departure diameter (equivalent to the Laplace constant in Eq. (1.1)) to the tube hydraulic diameter d_{hyd}. They indicate that the transition from macro- to micro-channels in evaporation takes place at $Co < 0.5$.

$$Co = \left(\frac{\gamma}{g \cdot (\rho_L - \rho_G) d_{hyd}^2} \right)^{1/2} \tag{1.2}$$

Laminar flow requires mixing or transport to surfaces by molecular migration (diffusion or electro-migration). Diffusive transport across streams and absence of turbulent mixing has been demonstrated is these microstructures where diffusion between streams was observed by fluorescent dye, while at the same time 5-μm balls remained within a single stream according to Westwood (1996). Investigations have been carried out in single-phase flow, to confirm that conventional macroscopic fluid flow equations can be applied to liquid flows (Shaw et al., 1996a; Judy et al., 2002).

In laminar flow, the pressure and velocity field can be accurately obtained by solving the Navier-Stokes equations either analytically or numerically. Even though the *Re* number is low, vortices can still be found in specific systems such as Taylor/bubble-train flow (Thulasidas et al., 1997) or static liquid micromixers under certain conditions (Engler et al., 2003). In case of gas flow inside microchannels, rarefaction phenomena may appear at Knudsen numbers ($Kn = \lambda/D_C$,) larger than 0.01, which at standard conditions corresponds to characteristic dimensions smaller than 7 microns (Arkilic et al., 1997). This usually leads to slip condition at the solid walls.

At present a broad range of microdevice manufacturing methods are available and some of them are specifically used in microreaction technology. Improvement of these methods involves the construction of small features with high aspect ratios and precision. The most common methods involve: photolithography and dry (plasma) or wet (chemical) etching, film deposition techniques, LIGA process similar to photolithography but using X-rays rather than UV light and depositing by electroplating the metal mould on the patterned photo-resist, laser machining, ultra-precision machining and electro-discharge machining (EDM) (Gavriilidis et al., 2002;

Ehrfeld et al., 2000). Therefore, a wafer made of silicon, glass or acrylic is patterned with the fluidic channels using one of the above techniques and the channels are sealed using bonding techniques (Madou, 1997). Wafer containing the microfluidic passages can be integrated either horizontally to connect different operation units or vertically in order to obtain three-dimensional units where fluids pass from one layer to another. The latter is necessary when channels are etched all the way through the wafer and there are close loops for some of the flow phases, i.e. in a manifold structure where the flow is split into many channels and then collected back to a main stream.

1.2. Main Applications

Microreaction technology has found applications in chemical synthesis, chemical kinetic studies with a subsequent catalyst and reactant cost reduction and has the potential for process intensification in high throughput production for those processes that are mass or heat transfer limited at macroscale. Highly exothermic reactions such as direct fluorination can be controlled precisely and carried out under more aggressive conditions (Del Mas et al., 2003). Mass transfer limited reactions, especially multiphase systems can be conducted in microfluidic devices achieving mixing times of the order of a microsecond (Nguyen and Wu, 2005; Hessel et al., 2005) while enabling removal of high heat fluxes and narrow distribution of phase properties such as bubble/droplet size. Microreaction technology has found a use in combinatorial chemistry for sequential or parallel screening of catalysts with minimum time and cost (Mies et al., 2003; De Bellefon et al., 2002). On-site on-demand production of high value products is a currently exploited field for microreactors thanks to their small size and portability. The New Jersey Centre for MicroChemical Systems at Stevens institute of Technology is working with FMC inc., one the world's largest producers of hydrogen peroxide, on the on-site and on-demand production, transport and storage of hydrogen peroxide from direct combination of oxygen and hydrogen (New Jersey Centre for MicroChemical Systems, 2006). Processes where final product properties such as uniform particle size or dispersions and purity are very important may benefit from the better control that microreactors offer versus traditional systems. Production of nanoparticles is one of these areas that is being heavily investigated.

However, it should be noted that not all chemical processes will benefit from this emerging technology and each specific chemical process should be carefully analysed in order to judge if microreaction technology delivers overall process advantages.

1.3. Types of Microreactors (Microfluidics)

1.3.1. Single-phase Flow Microengineered Devices

Single-phase fluid flow has been extensively studied in microstructures to assess whether the equations applied in macrosystems are valid in microscale. Discrepancies in friction factor values measured in microsystems compared to those from the macroscale Stokes flow theory are reviewed by Ho and Tai (1998). In incompressible flows, friction factors smaller and larger than those expected from macroflow theory have been reported as well as a frictional factor discrepancy dependence on channel geometry and aspect ratio. Generally, the largest discrepancies were found in channels with hydraulic diameters < 100 μm. Several theories based on electric double layer, electrokinetic retardation of polar liquids and micropolar behaviour of liquids intend to explain a pressure drop increase with respect to macrosystems but no theory is available to explain the decrease in pressure drop that some authors observed (Judy et al., 2002). Judy et al. (2002) conducted extensive pressure drop experiments with different channel sizes, geometries and fluid properties to conclude that Stokes flow theory predicted friction factors well in laminar flow while deviations were within the experimental uncertainties due to the difficulty in working with microengineered devices, which would explain previous discrepancies between theory and experiments. In the case of gas flows, it is accepted that the observed deviations are related to rarefaction phenomena where slip conditions apply at the solid walls (Arkilic and Schmidt, 1997).

1.3.2. Multiphase Flow Microengineered Devices

Multiphase liquid-liquid or gas-liquid systems, either catalytic or non-catalytic, account for a large number of unit operations in chemical processes. Multiple mass transfer operations (distillation, extraction, absorption, etc.), heat transfer operations (condensation, evaporation, heating, etc.) and reaction processes often use multiphase systems.

Two-phase operations may require different approaches in microreactors than those used in conventional systems, in order to achieve desired phase contact conditions that ensure high interfacial area, ease of phase separation and flexibility. In large scale, the two phases are often mixed together to create dispersions, which need to be separated at the end of the operation, usually with the help of a body force such as gravity (decantation, sedimentation), centrifugal force and electrical or electromagnetic forces. In microreactors, where dimensions are small and gravity effects are generally smaller than surface tension forces, some of these approaches are often difficult to implement.

Multiphase microsystems can be classified as *Disperse-phase Microsystems* (DpM) where one phase is dispersed into the other during the mass/heat or reaction operation and *Continuous-phase Microsystems* (CpM) where both phases are brought into contact via an interfacial surface that is stable without convective mixing during the process. The first approach (DpM) generally allows larger interfacial area but the latter one has three important advantages: the phases do not need to be separated at the end of the process, flow distribution of single-phase flows is simpler than flow distribution in disperse-phase flows and there is a more precise control of the interfacial area. The scale out issue in DpM can also be rather complex due to the fact that the bubble or drop formation at different times in parallel channels can give rise to different flow patterns in the parallel channels (Hetsroni et al., 2003). In DpM wetting properties and surface tension forces have been applied to separate phases in microscale as in the distillation system described by Sotowa and Kusakabe (2003).

1.3.2.1. Disperse-Phase Microsystems (DpM) - Bubble Microcolumn Reactor

Different flow patterns have been reported in micro-channels with gas and liquid flowing together (Triplett et al., 1999): bubbly, slug (Taylor or bubble-train), churn, slug-annular and annular. These patterns are consecutively reached both by increasing the gas flow rate and by decreasing the liquid flow rate. For micro-channels with an inner diameter less than 1 mm stratified flow has not been observed, due to the small importance of the gravity force. Other flow patterns have been reported under specific system properties such as *hexagonal flow*, which consists of rigid foam with well packed nearly uniform bubbles, which has been obtained in static micromixers when using high concentration of surfactants (Hessel et al., 1998).

One of the most common DpM is the bubble column reactor where gas bubbles and liquid slugs flow co-currently (Taylor Flow). Taylor or slug flow is one of the most important flow patterns for DpM because of the enhancement of radial mixing due to the vortices found within the liquid slug and low axial dispersion (Salman et al., 2003). The liquid phase is continuous along the whole length of the capillary due to the existence of a thin liquid film surrounding the bubbles, which flows under the effect of gravity and is continuously renewed by the mixing inside the liquid slug. Some authors distinguish Taylor flow as a special case of slug flow where the liquid slugs are completely free of small bubbles (Irandoust and Anderson, 1989).

1.3.2.2. Continuous-Phase Microsystems (CpM) - Falling Film and Mesh Microreactors

The falling film reactor (FFR) developed by Institut für Mikrotechnik Mainz (IMM) and the mesh microcontactor developed by Central Research Laboratories (CRL) are two good examples of CpM. The core of the falling film microreactor shown in Figure 1.1 is a micro-structured reaction plate. At the top of this plate the liquid reactant is divided into many substreams. By means of gravity force, a thin film of a few tens of microns thickness is generated on the plate to contact with the gaseous phase either co-or counter-currently and high specific interfacial areas are achieved (about 20000 m^2/m^3) (Jahnisch et al., 2000).

Figure 1.1. Falling Film Reactor by Institut für Mikrotechnik Mainz (IMM)

These types of microcontactors allow immiscible fluids to come into contact at the required degree of subdivision to promote rapid inter-phase transfer whilst preventing mixture of the phases. A device based on this principle, where overlapping of the channels of the two fluids defines the available interfacial area, was found to have limited stability and small interfacial area (2 %-15 % of the total) (Robins et al., 1997; Bibby et al., 1998; Shaw et al., 1998). Shaw et al. (1996a, 1996b and 1998) and Bibby et al. (1998) performed modelling studies on stability and mass transfer in this type of microcontactor.

The mesh microreactor developed by CRL is an alternative CpM. Two fluids are brought into contact via a mesh structure with openings (pores) that maintain separation of the two thin immiscible fluid phase layers whilst minimising diffusive mass transfer resistance between

phases. This reactor is intended for use in kinetic analysis (sequential catalyst screenings and kinetics retrieval) and high throughput production for both reactive and extraction systems. Figure 1.2 shows an early prototype of the mesh microreactor. The quadrant shape allows large fluid volumes while keeping a small phase height and an even flow distribution during the filling and emptying stages. At the back of the reactor, there is a collecting channel for even flow distribution.

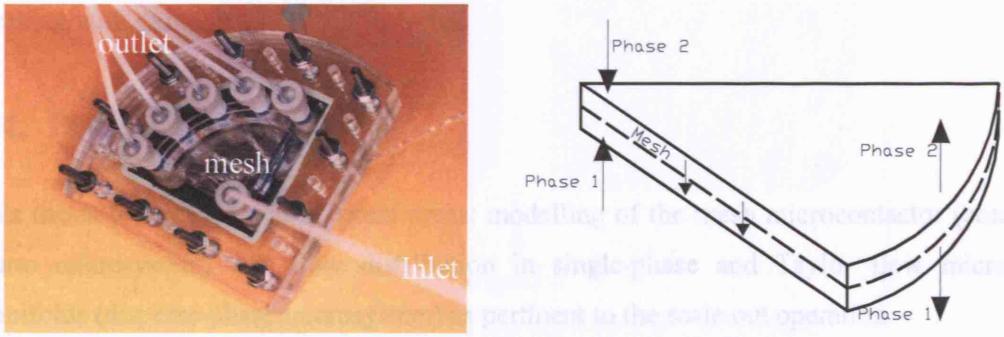

Figure 1.2. Geometry of mesh microreactor for large batch volume and even flow distribution.

A thin mesh (3-10 μm) and small phase heights (~50 to 100 μm) enable fast mass transfer by diffusion so that many multiphase reactions in which one component is transferred between the phases are kinetically controlled. The mesh microreactor can operate in either flow-through or batch modes. In the latter case, the reactor volume needs to be sufficient for sample analysis. When gas-liquid reactions are performed, the gas phase always operates in flow-through mode. The mesh features a dense hexagonal array of pores made of nickel with diameter ranging from 3 to 10 μm and open areas up to 40 % (see Figure 1.3).

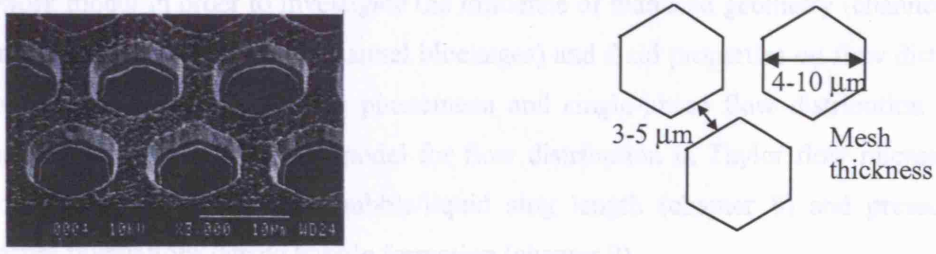

a) b)

Figure 1.3. a) SEM of the mesh structure and b) sketch with the typical dimensions.

Numerical methods are needed for modelling the mesh microreactor, since diffusion between *finite sheets* with chemical reaction (Crank, 1975) has no full analytical solution according to Westwood et al. (1996) and Robins et al. (1997). Results obtained by Backes et al. (1998) for the absorption of dimethylaniline from air to water using a simple plane sheet model, show deviations in the fractional absorption within a factor of 2 from the experimental data. The mesh microreactor is intended to operate under the following conditions: residence times ranging from 60 s to 180 min, temperatures of 0-80 °C (max of 150 °C) and pressures up to 50 bar when working with gases.

1.4. Project Overall Frame

This thesis focuses on two different areas: modelling of the mesh microcontactor (continuous-phase microsystem) and flow distribution in single-phase and Taylor flow microchannel manifolds (disperse-phase microsystem) as pertinent to the scale out operation.

The mesh microreactor is investigated in chapters 2 to 6. Chapter 2 looks into flow distribution of each single phase within the mesh microreactor in order to optimise the plate geometry and increase the capacity for sequential screening of catalysts. Chapters 3 to 5 investigate the meniscus shape, position and stability in the openings of the mesh as a function of wetting properties, pore and mesh geometry and flow conditions. Chapter 6 conducts an analysis of mass transfer and chemical reaction in the mesh microreactor to develop dimensionless parametric maps that indicate the required system properties in order to operate in the kinetic control regime and enable the retrieval of kinetics from conversion versus time experimental data.

Scale out of single-phase flows in microsystems is analysed in chapter 7 via a resistance network model in order to investigate the influence of manifold geometry (channel dimensions, manufacturing tolerances and channel blockages) and fluid properties on flow distribution. The knowledge gained in interfacial phenomena and single-phase flow distribution is applied in chapters 8 and 9 to develop a model for flow distribution in Taylor flow microsystems. This model requires equations for bubble/liquid slug length (chapter 8) and pressure drop and pressure fluctuations during bubble formation (chapter 9).

Figure 1.4 shows a diagram of the research plan during this project and indicates the chapter where a specific topic is analysed in detail.

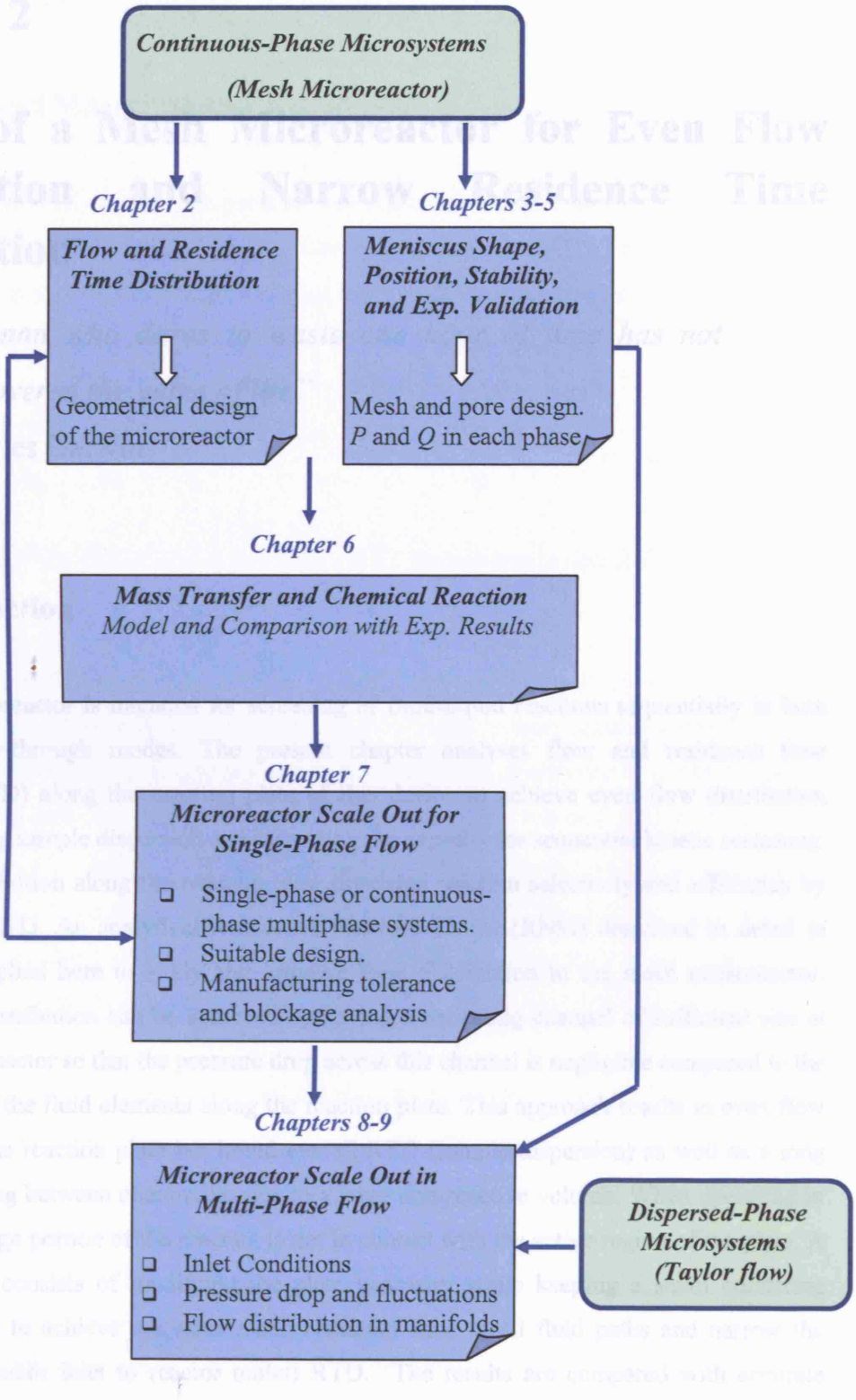

Figure 1.4. Thesis structure.

Chapter 2

Design of a Mesh Microreactor for Even Flow Distribution and Narrow Residence Time Distribution

"A man who dares to waste one hour of time has not discovered the value of life"

Charles Darwin

2.1. Introduction

The mesh microreactor is intended for screening of fluid-liquid reactions sequentially in both batch and flow-through modes. The present chapter analyses flow and residence time distribution (RTD) along the reaction plate of this device to achieve even flow distribution while minimising sample dispersion and increasing the capacity for sequential kinetic screening. Even flow distribution along the reaction plate improves reaction selectivity and efficiency by narrowing the RTD. An analytical Resistance Network Model (RNM) described in detail in Chapter 7 is applied here to study and improve flow distribution in the mesh microreactor. Uniform flow distribution can be achieved by having a collecting channel of sufficient size at the back of the reactor so that the pressure drop across this channel is negligible compared to the pressure drop of the fluid elements along the reaction plate. This approach results in even flow distribution in the reaction plate but broad overall RTD (sample dispersion) as well as a long time for switching between chemistries due to a large non-reactive volume. When operating in batch mode a large portion of the reactant is not in contact with the active region of the plate. A better approach consists of modifying the plate geometry while keeping a small collecting channel in order to achieve the same mean residence time in all fluid paths and narrow the overall (from reactor inlet to reactor outlet) RTD. The results are compared with accurate numerical simulations of the flow field on the reactor plate and particle tracking methodology for obtaining RTD.

2.2. Background

2.2.1. Flow and Mass Transfer Equations

In general, fluid flow inside a reactor presents complicated streamlines so that the three velocity components may depend upon the three co-ordinates and time: $U_x = U_x(x, y, z, t)$, $U_y = U_y(x, y, z, t)$ and $U_z = U_z(x, y, z, t)$. In this general situation there are 9 viscous stress components τ_{ij} which are functions of the velocity gradients as shown by Bird et al., (2002):

$$\tau_{ij} = \mu\left(\frac{\partial U_j}{\partial x_i} + \frac{\partial U_i}{\partial x_j}\right) - \left(\frac{2}{3}\mu - \kappa\right)\left(\frac{\partial U_x}{\partial x} + \frac{\partial U_y}{\partial y} + \frac{\partial U_z}{\partial z}\right)\delta_{ij} \quad i,j = x,y,z$$
$$\boldsymbol{\tau} = \mu\left(\nabla\mathbf{U} + (\nabla\mathbf{U})^{\mathrm{T}}\right) - \left(\frac{2}{3}\mu - \kappa\right)(\nabla\cdot\mathbf{U})\mathbf{I} \quad \text{(vector-tensor notation)} \tag{2.1}$$

where i and j designate directions x, y and z, κ is the dilatational viscosity, $\boldsymbol{\delta}$ is the unit second order tensor of components δ_{ij} (Kronecker delta), $\nabla\mathbf{U}$ is the velocity gradient tensor (dyadic product of two vectors, which is a tensor and is different to the divergence of a vector (scalar), $\nabla\cdot\mathbf{U}$) with components $(\partial/\partial x_i)U_j$, $(\nabla\mathbf{U})^{\mathrm{T}}$ is the transpose of the velocity gradient tensor with components $(\partial/\partial x_j)U_i$ and $\nabla\cdot\mathbf{U}$ is the divergence of the velocity vector. If the fluid is incompressible, $\nabla\cdot\mathbf{U} = 0$ and the term that contains κ is discarded. The dilatational (or volume) viscosity enters into the equations where the flow involves a change in volume. It is zero for monatomic gases at low density and generally neglected for liquids and dense gases.

The tensor component τ_{ij} can be interpreted either as a viscous force that the fluid of lesser x_i exerts on the fluid of greater x_i in the j direction on a unit area perpendicular to the i direction ($\boldsymbol{\tau}_i$ viscous force acting on a perpendicular plane to direction i) or as the flux (flow per unit area) of j-momentum in the positive i direction.

Apart from viscous forces, the fluid also exerts a pressure force that is perpendicular to the surface exposed, $p\boldsymbol{\delta}_i$, where $\boldsymbol{\delta}_i$ is a unit vector in the i-direction and P is the scalar pressure which has one hydrostatic component and another one due to the fluid motion. The components of all the forces per unit area exerted within a fluid (molecular forces), both by the thermodynamic pressure and viscous stresses are expressed in tensor notation by Eq. (2.2),

$$\pi_{ij} = -P\delta_{i,j} + \tau_{ij}$$
$$\boldsymbol{\pi} = -P\boldsymbol{\delta} + \boldsymbol{\tau} \quad \text{(vector-tensor notation)} \tag{2.2}$$

where δ_{ij} is the Kronecker delta (1 if $i = j$ and 0 if $i \neq j$ since pressure is always normal to the surface) and i and j can take x, y and z. π_{xx}, π_{yy} and π_{zz} are the *normal stresses* (pressure P is also a normal stress) and the 6 remaining quantities are called *shear stresses*. The molecular stresses π_{ij} are also second-order tensors over R^3*R^3 as τ_{ij}.

The continuity equation or mass balance for a pure substance is given by Eq. (2.3), where the divergence of the vector $\rho\mathbf{U}$, $\nabla\cdot\rho\mathbf{U}$ is a scalar (gradient).

$$\frac{\partial\rho}{\partial t} = -(\nabla\cdot\rho\mathbf{U})$$
$$(\nabla\cdot\mathbf{U}) = 0 \quad \text{(incompressible fluid, constant } \rho) \tag{2.3}$$

Application of the Newton's second law to a fluid element produces:

$$\frac{\partial(\rho\mathbf{U})}{\partial t} = [\nabla\cdot\boldsymbol{\varphi}] + \rho\mathbf{g} \tag{2.4}$$

where $\mathbf{U}$, $\mathbf{g}$ and ∇ are vectors and $\boldsymbol{\varphi}$ is a tensor R^3*R^3 with components $\phi_{i,j}$ that represent momentum fluxes of any type (convective or molecular $\pi_{i,j}$). The momentum flux tensor $\boldsymbol{\varphi}$ is composed of the convective momentum flux tensor $-\rho\mathbf{UU}$ (dyadic product of $\rho\mathbf{U}$ and $\mathbf{U}$), and the molecular momentum flux tensor $\boldsymbol{\pi}$ given by Eq. (2.2), that is $\boldsymbol{\Phi} = -\rho\mathbf{UU} - p\boldsymbol{\delta} + \boldsymbol{\tau}$. Eq. (2.4) is generally written as:

$$\frac{\partial(\rho\mathbf{U})}{\partial t} = -[\nabla\cdot\rho\mathbf{UU}] - \nabla P + [\nabla\cdot\boldsymbol{\tau}] + \rho\mathbf{g} \tag{2.5}$$

where the divergence of the tensor $\rho\mathbf{UU}$, $\nabla\cdot(\rho\mathbf{UU})$ is a vector. For constant ρ and μ, this expression is simplified to Eq. (2.6).

- $\nabla\cdot\rho\mathbf{UU} = (\rho\mathbf{U}\cdot\nabla)\mathbf{U} + \mathbf{U}(\nabla\cdot\rho\mathbf{U}) = (\rho\mathbf{U}\cdot\nabla)\mathbf{U}$ for an incompressible fluid.

- The sum $\rho\partial(\mathbf{U})/\partial t + (\rho\mathbf{U}\cdot\nabla)\mathbf{U} = \rho D\mathbf{U}/Dt$, where D/Dt is the substantial derivative that represents the change of momentum of the fluid volume from a co-ordinate system moving at the velocity **U**.
- Divergence of the tensor $\boldsymbol{\tau}$, $\nabla\cdot\boldsymbol{\tau} = \mu\nabla\cdot(\nabla\mathbf{U} + (\nabla\mathbf{U})^{\mathrm{T}}) = \mu(\nabla^2\mathbf{U} + \nabla(\nabla\cdot\mathbf{U})) = \mu\nabla^2\mathbf{U}$ from Eq. (2.1) and for an incompressible fluid ($\nabla\cdot\mathbf{U} = \mathbf{0}$) of constant viscosity μ.

$$\rho\frac{D\mathbf{U}}{Dt} = \rho\left(\frac{\partial\mathbf{U}}{\partial t} + (\mathbf{U}\cdot\nabla)\mathbf{U}\right) = -\nabla P + \mu\nabla^2\mathbf{U} + \rho\mathbf{g} \tag{2.6}$$

Eq. (2.6) is made dimensionless by considering the phase height H as characteristic length, the average inlet velocity $U_0 = Q_T/(\pi r^2)$ as characteristic velocity and a reference pressure P_0. Dimensionless variables are defined in Eqs. (2.7)-(2.10). The dimensionless pressure $P^{\#}$ is defined by Eq. (2.10) based on viscosity instead of density (i.e. $P^{\#} = (P-P_0)/\rho U_0^2$), which is a suitable definition for systems with low Reynolds numbers (range of interest in microreactors) where viscous effects are dominant over inertial effects, Bird et al. (2002).

$$x^{\#} = \frac{x}{H};\ y^{\#} = \frac{y}{H};\ z^{\#} = \frac{z}{H};\ \nabla^{\#} = H\nabla;\ \nabla^{\#2} = H^2\nabla^2 \tag{2.7}$$

$$\mathbf{U}^{\#} = \frac{\mathbf{U}}{U_0} \tag{2.8}$$

$$t^{\#} = \frac{tU_0}{H} \tag{2.9}$$

$$P^{\#} = \frac{P - P_0}{\mu U_0 / H} \tag{2.10}$$

Substituting these variables into Eq. (2.6), the dimensionless Eq. (2.11) is obtained where the Reynolds number Re is given by Eq. (2.12) and the Froude number Fr by Eq. (2.13). Therefore, two dimensionless groups define all solutions for a given system geometry. In microsystems operated horizontally, the gravitational term in Eq. (2.11) is negligible.

$$Re\frac{D\mathbf{U}^{\#}}{Dt^{\#}} = Re\frac{\partial\mathbf{U}^{\#}}{\partial t} + Re\left(\mathbf{U}^{\#}\cdot\nabla^{\#}\right)\mathbf{U}^{\#} = -\nabla^{\#}P^{\#} + \nabla^{\#2}\mathbf{U}^{\#} + \frac{Re}{Fr}\frac{\mathbf{g}}{g} \tag{2.11}$$

$$Re = \frac{\rho H U_0}{\mu} \tag{2.12}$$

$$Fr = \frac{U_0^2}{gH} \tag{2.13}$$

2.2.2. Analysis of Tracer Impulse

RTD is generally measured experimentally by injecting a pulse of tracer and analysing its concentration at the reactor outlet. A similar approach can be applied when conducting CFD simulations. In this case, the convection-diffusion for two different components (the liquid and the tracer) is solved together with the continuity and Navier-Stokes equations. A mass balance to the component *i* results in:

$$\frac{\partial c_i}{\partial t} + \nabla \cdot \mathbf{N}_i = \psi_i \qquad \psi_i = 0 \text{ (no reaction)} \tag{2.14}$$

where c_i is the concentration of component *i*, ψ_i is the reaction rate for component *i* and $\mathbf{N}_i$ is the total mass flux of component *i*, defined as:

$$\underbrace{\mathbf{N}_i}_{\text{Total Flux}} = \underbrace{x_i \sum_{j=1}^{n} \mathbf{N}_j}_{\text{Convective Flux}} \underbrace{- c D_i \nabla x_i}_{\text{Diffusion Flux}} \tag{2.15}$$

The convection-diffusion equation is obtained by substituting $\mathbf{N}_i$ in Eq. (2.15) into Eq. (2.14):

$$\frac{\partial c_i}{\partial t} + \mathbf{U}^* \cdot \nabla c_i = D_i \nabla^2 c_i \tag{2.16}$$

Eq. (2.16) is written in dimensionless form for component A (tracer):

$$\frac{D c_A^{\#}}{D t^{\#}} = \frac{1}{Re \cdot Sc} \nabla^{\#2} c_A^{\#} \tag{2.17}$$

where $c^{\#}_A$ is the dimensionless concentration, defined by:

$$c_A^{\#} = \frac{c_A}{c_{A0}} \tag{2.18}$$

and *Sc* is the Schmidt number *Sc* given by:

$$Sc = \frac{\mu}{\rho D_A} \tag{2.19}$$

The dimensionless number *ReSc* is also called Peclet number, *Pe*, defined as the ratio of convective to diffusive flow.

$$Pe = \frac{HU_0}{D_A} \tag{2.20}$$

When the axial dispersion parameter D_e is used, the inverse of the number is called Bodenstain number, $Bod = D_e/HU_0$ and Vessel Dispersion Number, $VDN = D_e/LU_0$ when the characteristic dimension is the length of the reactor *L*.

Numerical methods generally are able to solve the diffusion-convection equation for local values of the Peclet number up to 100-1000. At $Pe > 1000$ in laminar flow regime, mass transfer is basically determined by convection and the resolution of the diffusion-convection equation generally requires extremely fine meshes in order to avoid numerical errors (numerical diffusion), which is a time-consuming procedure and often impracticable (FEMLAB, 2002).

2.2.3. Particle Tracking

A robust approach to obtain RTD is to solve the steady-state flow field inside the reactor via CFD and conduct Lagrangian particle tracking with weightless particles that follow the flow streamlines. This overcomes the numerical diffusion issue generally found when solving the convection-diffusion equation in CFD for flows with tracers at high Peclet numbers (Femlab, 2002). A statistically large number of particles are released at the inlet of the reactor (boundary conditions for particle *i*, $p_{0,i} = (x_{0,i}, y_{0,i}, z_{0,i})$) and the position of a particle at time $t^{\#}$ is obtained by solving the system of equations below. The time that takes a particle to reach the outlet boundary is its residence time:

$$U_z^{\#}(x^{\#}, y^{\#}, z^{\#}) = \frac{dx^{\#}}{dt^{\#}} \tag{2.21}$$

$$U_y^{\#}(x^{\#}, y^{\#}, z^{\#}) = \frac{dy^{\#}}{dt^{\#}} \tag{2.22}$$

$$U_z^{\#}(x^{\#}, y^{\#}, z^{\#}) = \frac{dz^{\#}}{dt^{\#}} \tag{2.23}$$

2.2.4. Residence Time Distribution (RTD)

RTD are generally utilised to analyse axial dispersion. Two different systems may have similar mean residence time but very different axial dispersion which can affect conversion and mainly selectively of the reaction. The RTD is experimentally obtained by injecting a signal of a tracer at a certain time into the reactor and measuring its output concentration at different times. This analysis will show the time that each fluid element remains inside the reactor (Levenspiel 1972). Three types of curves are used: the **E** curve represents the theoretical RTD of the different fluid elements and is normalised according to:

$$\int_0^{\infty} \mathbf{E} \cdot dt = 1$$
$$\int_{t_1}^{\infty} \mathbf{E} \cdot dt = 1 - \int_0^{t_1} \mathbf{E} \cdot dt \tag{2.24}$$

$\mathbf{E}\cdot dt$ is the fraction of fluid whose residence time is between t and $t+dt$. The **C** curve represents the experimental normalised concentration distribution (similarly to Eq.(2.24)) of the tracer at the outlet and the **F** curve represents the accumulated tracer concentration at the reactor outlet at time t and is related to the **C** curve via Eq. (2.25):

$$\mathbf{F} = \int_0^{t} \mathbf{C} \cdot dt \tag{2.25}$$

Two characteristic properties of the RTD, **E** curve, are the mean residence time, t_E, defined by Eq. (2.26) and the amplitude of the distribution or variance (σ_E^2) defined by Eq. (2.27):

$$t_E = \tau = \int_0^\infty t \cdot \mathbf{E} \cdot dt; \qquad t_E = \tau \cong \sum_{i=0}^{i=N} t_i \mathbf{E}_i \cdot \Delta t_i \qquad \text{for } N \text{ discrete values} \quad (2.26)$$

$$\sigma_E^2 = \int_0^\infty t^2 \cdot \mathbf{E} \cdot dt - t_E^2; \qquad \sigma_E^2 \cong \sum_{i=0}^{i=N} t_i^2 \cdot \mathbf{E}_i \cdot \Delta t_i - t_E^2 \qquad \text{for } N \text{ discrete values} \quad (2.27)$$

Similar equations can be written for the **C** curve. In the case of closed systems or recipients (systems without dispersion where tracer follows flow streamlines, (Fogler, 2005), **C** = **E** and $d\mathbf{F}/dt = \mathbf{E}$. Thus, the reactor space time for a constant density fluid is also equal to the mean time of the **C** curve, $\tau = V/Q = t_E = t_C$.

Mean and variance of the RTD using discrete particles are defined as:

$$t_{mean} \cong \frac{\sum_{i=0}^{i=N} t_i}{N_{Particles}} \quad (2.28)$$

$$\sigma_v^2 \cong \frac{\sum_{i=0}^{i=N} (t_i - t_{mean})^2}{N_{Particles}} \quad (2.29)$$

where $N_{Particles}$ is the total number of particles.

2.3. Mesh Microreactor Geometry

The mesh microreactor (see Figure 2.2a for a schematic diagram) features a nickel mesh with a non-active region of 5.6 mm length and 30 μm thickness and an active region (with microfabricated pore openings) of 26.4 mm length and 5 μm thickness (see Figure 2.1). The phase height above the mesh is 100 μm. A collecting channel is placed at the back of the mesh after the active region. The standard plate geometry is a simple 90° quadrant with fixed distance from the inlet to the collecting channel (Wenn et al., 2003).

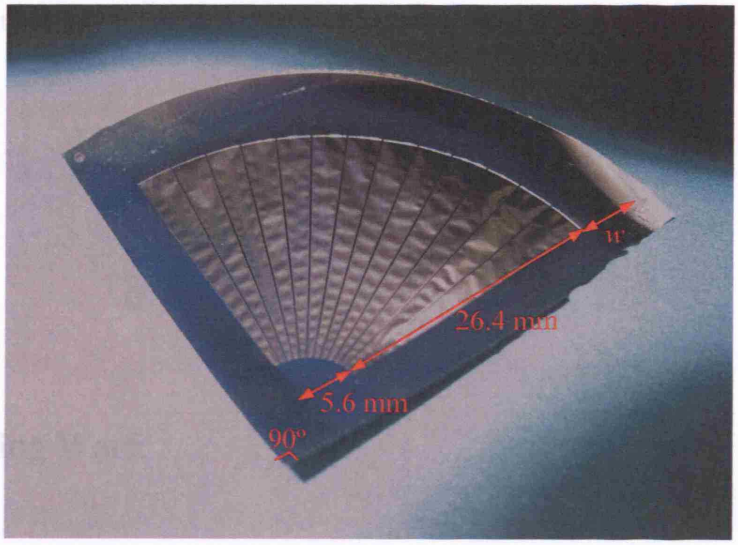

Figure 2.1. Nickel mesh utilised in the mesh microreactor.

Figure 2.2 shows half the mesh microreactor. The other half is simply a mirror image of the one shown in the figure and both of them are clamped together with the mesh in the middle.

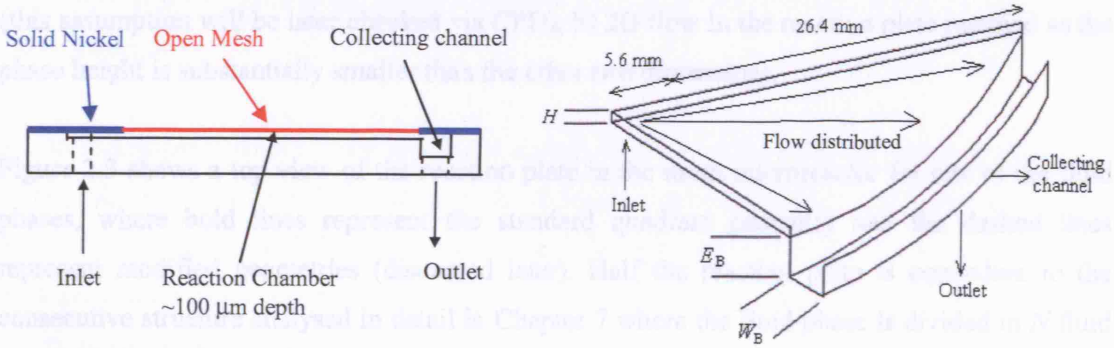

Figure 2.2. Diagram of one half of the mesh microreactor a) side view of fluidic chamber and reactor case b) 3D view of the fluidic chamber including collecting channel.

The initial dimensions of the collecting channel are W_B = 3000 µm and E_B = 1000 µm. All the fluid in the collecting channel leaves through a single 1 mm bore hole located in the middle. It was found that multiple outlets along the collecting channel were impractical, except during priming stage, due to difficulties in balancing the flows in the outlet tubes.

Other dimensionless variables used in the present analysis are defined below.

$$E^{\#} = \frac{E}{H};\ W^{\#} = \frac{W}{H};\ L^{\#} = \frac{L}{H};\ A^{\#} = \frac{A}{H^2} \tag{2.30}$$

$$Q^{\#} = \frac{Q}{U_0 H^2};\ R^{\#} = \frac{RH^3}{\mu} = \frac{\Delta P H^3}{Q\mu} \tag{2.31}$$

2.4. Modelling Work

2.4.1. Simplified Resistance Network Model (RNM)

A simplified methodology based on the analogy between viscous flow and electrical resistance networks is used to analyse flow distribution in the mesh microreactor. The methodology is described in detail in Chapter 7 where basic microchannel manifold geometries are analysed. The RNM can be applied in the mesh microreactor for each of the fluid phases. In this case, it is assumed that half the geometry of the plate resembles a consecutive manifold structure (see Chapter 7). In addition, we assume: a) straight (or known) streamlines along the reaction plate (this assumption will be later checked via CFD), b) 2D flow in the reaction plate justified as the phase height is substantially smaller than the other two dimensions.

Figure 2.3 shows a top view of the reaction plate in the mesh microreactor for one of the fluid phases, where bold lines represent the standard quadrant geometry and the dashed lines represent modified geometries (discussed later). Half the reaction plate is equivalent to the consecutive structure analysed in detail in Chapter 7 where the fluid phase is divided in N fluid paths. In this case, the resistances along the distributing channel are zero ($R_{A,i} = 0$ due to the common inlet point). Eqs. (7.14) and (7.15) define the linear system of equations for the flow in all reaction fluid paths. In the present case the characteristic velocity is independent of the number of fluid paths chosen and $Q^{\#}_{T} \neq N$.

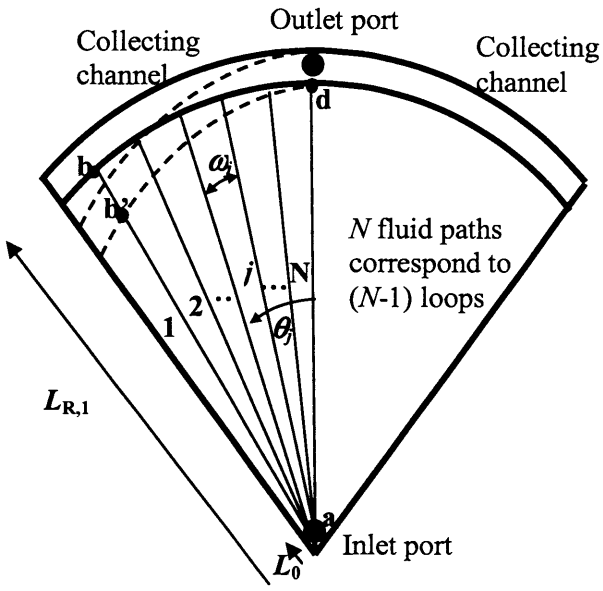

Figure 2.3. Top view of the reaction plate with N fluid paths in half the geometry for application of the RNM.

Two approaches are considered below to achieve even flow and/or residence time distribution in the reaction plate.

a) Reaction plate with a fixed quadrant shape: Because of the quadrant shape of the reactor plate ensuring equal flow distribution in the different fluid path lengths also ensures the same RTD in each path. Considering the closed loop defined by paths **a-b**, **b-d** and **a-d** Figure 2.3, a pressure drop balance results in Eq. (2.32). To have equal flow distribution in each fluid path, the flowrates along paths **a-b** and **a-d** have to be the same, or $\Delta P_{\mathbf{b\text{-}d}} = 0$ which means that the pressure drop across the collecting channel should be negligible:

$$\Delta P_{\mathbf{a-b}} + \Delta P_{\mathbf{b-d}} = \Delta P_{\mathbf{a-d}} \tag{2.32}$$

Velocity and pressure drop along the fluid paths that go from the inlet port to the collecting channel is calculated via Eqs. (2.33) and (2.34), which assume 2D flow between parallel sheets as shown in Figure 2.4 where the phase height H is the characteristic dimension (Papanastasiou et al., 2000).

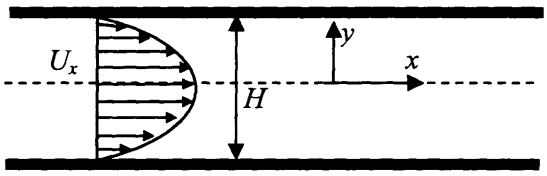

Figure 2.4. 2D flow between parallel sheets.

$$U_x = -\frac{(P_2 - P_1)}{2\mu L}\left(\frac{H^2}{4} - y^2\right) = -\frac{1}{2\mu}\frac{\partial P}{\partial x}\left(\frac{H^2}{4} - y^2\right) = \frac{3}{2}U_{av}\left(1 - \left(\frac{y}{H/2}\right)^2\right) \tag{2.33}$$

$$\frac{\partial P^{\#}}{\partial x^{\#}} = -\frac{12}{W^{\#}}Q^{\#} \tag{2.34}$$

The change in the path width along the fluid paths implies change in the velocity, which needs to be integrated along the path length in order to get the total pressure drop. For a quadrant-type structure, the path width is a function of the distance from the port inlet l and the angle of the fluid path ω, $W^{\#}(l) = \omega(\text{rad})l^{\#}$. Integration of Eq. (2.34) along each fluid path i, from $l^{\#} = L^{\#}{}_0$ (the non-active length immediately after the inlet) to $l^{\#} = L^{\#}{}_{R,i}$ yields Eq. (2.35).

$$\Delta P^{\#}_{R,i} = 12Q^{\#}_{R,i}\int_{L_0}^{L_{R,i}} \frac{1}{W^{\#}(l^{\#})}dl^{\#} = \frac{12Q^{\#}_{R,i}}{\omega(rad)}(\ln(L^{\#}_{R,i}) - \ln(L^{\#}_0)) \tag{2.35}$$

where the subscript "R,i" indicates flow path i in the reaction plate. The pressure drop along each reaction path i is also expressed as $\Delta P^{\#}{}_{R,i} = R^{\#}{}_{R,i}Q^{\#}{}_{R,i}$ where the resistance $R^{\#}{}_{R,i}$ is given by Eq.(2.36),

$$R^{\#}_{R,i} = \frac{12(\ln(L^{\#}_{R,i}) - \ln(L^{\#}_0))}{\omega(rad)} \tag{2.36}$$

The resistance in the collecting channel for calculating the pressure drop as $\Delta P^{\#}{}_{B,i} = R^{\#}{}_{B,i}Q^{\#}{}_{B,i}$ is obtained from Eq. (7.9), where $D^{\#}$ is the dimensionless hydraulic diameter defined by $D^{\#} = 4E^{\#}W^{\#}/(2E^{\#}+2W^{\#})$ for a rectangular channel. Eqs. (7.14) and (7.15) are utilised to solve for the

flow distribution in the mesh microreactor with $R^{\#}_{A,i} = 0$, $R^{\#}_{R,i}$ given by Eq. (2.36) and $R^{\#}_{B,i}$ given by Eq. (7.9). A Matlab script is used to obtain the flow distribution (see Appendix 2A).

b) Modification of the reaction plate geometry: The previous approach would generally require large collecting channels to achieve flow equipartition. A large collecting channel volume though increases the sample dispersion. If a small collecting channel is used instead the flow resistance in it increases and the above approach is not valid. It had previously been found that flow equipartition is still possible even when the pressure drop along the collecting channel becomes substantial, by having varying cross section symmetrical distributing and collecting channels (see Chapter 7). This is not possible with the present mesh microreactor geometry since there is no distributing channel to generate the same pressure drop as in the collecting channel. However, even flow distribution can be achieved by modifying the quadrant shape of the reaction plate as shown for example in Figure 2.3 by the dashed lines (new collecting channel). Thus, **a-b'**< **a-d** and path **a-b'** can have the same flowrate as path **a-d** while having less pressure drop (shorter path).

The RNM yields a simplified solution when flow equipartition is considered (identical $Q^{\#}_{R,i}$ flowrates) together with $R^{\#}_{A,(j+1)} = 0$ and the system of N equations given by Eqs. (7.14) and (7.15) is converted into (N-1) independent equations defined by:

$$jR^{\#}_{B(N-j+1)} - R^{\#}_{R,(j+1)} + R^{\#}_{R,j} = 0 \quad j=1\ldots(N\text{-}1) \tag{2.37}$$

Substituting the value of the resistances $R^{\#}_{B}$ and $R^{\#}_{R}$ in Eq. (2.37) leads to:

$$\frac{32j\lambda_{NC,(N-j+1)}(E^{\#}_{B,(N-j+1)} + W^{\#}_{B,(N-j+1)})^2 L^{\#}_{B,(N-j+1)}}{4E^{\#3}_{B,(N-j+1)} W^{\#3}_{B,(N-j+1)}} - \frac{12\left(\ln(L^{\#}_{R,(j+1)}) - \ln(L^{\#}_{R,j})\right)}{\omega} = 0 \tag{2.38}$$

$$j = 1\ldots(N\text{-}1)$$

where $L^{\#}_{B,(N-j+1)}$ is a function of the unknown $L^{\#}_{R,j}$ given by Eq. (2.39) when a straight collecting sub-path is assumed (see Figure 2.5 where lines represent the centre of the fluid paths):

$$L^{\#}_{B,(N-j+1)} = \sqrt{(L^{\#}_{R,(j+1)} \sin\omega)^2 + (L^{\#}_{R,(j+1)} \cos\omega - L^{\#}_{R,j})^2} \tag{2.39}$$

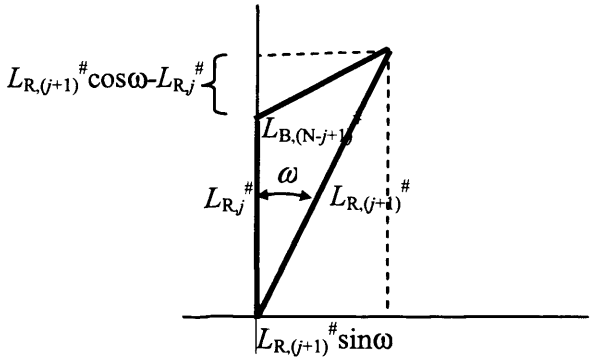

Figure 2.5 Geometry for calculation of the collecting channel path lengths $L_{B,(N-j+1)}$.

Eq.(2.38) represents N-1 equations that can be solved independently since the value of the path length at the middle of the reactor, $L^{\#}_{R,N}$, is known. A nonlinear root finder method is used in order to solve the nonlinear term $L_{R,j}$ by using $L^{\#}_{R,(j+1)}$ as an initial guess. Therefore, the second value calculated for $j = N$-1 is $L^{\#}_{R,j} = L^{\#}_{R,(N-1)}$ and the process is continued until $L^{\#}_{R,1}$ is obtained. A large N value (many fluid paths) is required for better accuracy (see Appendix 2B).

While this approach ensures that the flowrates in the different fluid paths are the same since the path lengths are different the residence times are not the same. Therefore, a quadrant shape geometry for the mesh (active region of the plate) should be adopted ensuring that the mean residence times in all fluid paths in the active region are the same. This, however, means that there would be a large area in the mesh that is non-active that will encourage further dispersion (see Figure 2.6). With this approach the size of the collecting channel (and the dispersion in it) can be reduced but to the expense of increased dispersion in the non-active area of the mesh.

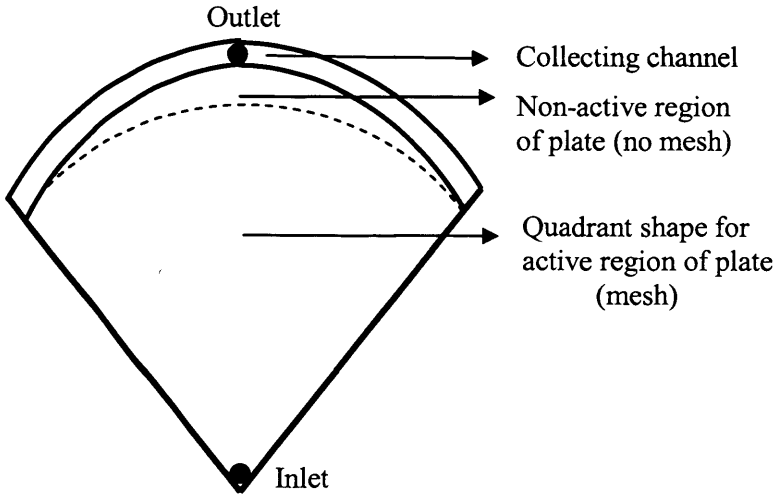

Figure 2.6. Modified plate geometry for flow equipartition.

A better approach is to design the reaction plate for all fluid paths to have the same mean residence time (even average RTD):

$$t^{\#}_{\mathrm{R},i} = \frac{L^{\#}_{\mathrm{R},i} - L^{\#}_{0}}{Q^{\#}_{\mathrm{R},i} / A^{\#}_{\mathrm{R},i}} \tag{2.40}$$

An average fluid path area is obtained by integrating the perpendicular area to the flow $H \cdot \omega \cdot l$ along the fluid path length ($L^{\#}_{\mathrm{R},i}$-$L^{\#}_{0}$):

$$A^{\#}_{\mathrm{R},i} = \frac{\int_{L^{\#}_{0}}^{L^{\#}_{\mathrm{R},i}} \omega l^{\#} dl^{\#}}{L^{\#}_{\mathrm{R},i} - L^{\#}_{0}} = \frac{\omega(L^{\#2}_{\mathrm{R},i} - L^{\#2}_{0})}{2(L^{\#}_{\mathrm{R},i} - L^{\#}_{0})} = \frac{\omega(L^{\#}_{\mathrm{R},i} + L^{\#}_{0})}{2} \tag{2.41}$$

The optimised geometry for the same mean residence time in all fluid paths is found via an iterative procedure. Given a desired mean residence time, $t^{\#}_{\mathrm{R},i} = t^{\#}_{\mathrm{desired}}$ the required initial quadrant radius is obtained by applying Eq. (2.42):

$$L^{\#}_{\mathrm{R},i} = L^{\#}_{0} + \frac{t^{\#}_{\mathrm{R},i} Q^{\#}_{\mathrm{R},i}}{A^{\#}_{\mathrm{R},i}} \tag{2.42}$$

where $A^{\#}_{\mathrm{R},i}$ is given by Eq. (2.41) and flowrates are calculated assuming the same flowrate in all fluid paths (flow equipartition flowrate $Q^{\#}_{\mathrm{EQ}}$) for the first iteration $Q^{\#}_{\mathrm{R},i} = Q^{\#}_{\mathrm{EQ}}$. New flowrates $Q^{\#}_{\mathrm{R},i}$ along each fluid path in this initial quadrant shape are found from Eqs. (7.14) and (7.15) as previously shown. The calculated flowrates $Q^{\#}_{\mathrm{R},i}$ are used to recalculate the fluid path lengths that produce the same desired residence time via Eq. (2.42) which yields a new plate geometry and this process is repeated until new flowrates are within an acceptable tolerance of the previous values (see Appendix 2A).

2.4.2. Fluid Flow Solution via FEMLAB – Velocity Field

The continuity and Navier-Stokes equations, Eqs. (2.3) and (2.11) are solved in steady state for the different geometries of the mesh microreactor via software FEMLAB, which applies the Finite Element Method (FEM). This analysis produces the steady state velocity field in the geometry volume that is used to:

1) Analyse flow distribution.

2) Validate the assumption of nearly straight streamlines in the reaction plate applied in the Resistance Network Model.
3) Conduct particle tracking to retrieve the RTD.

The simulations were carried out on half of one reaction plate since there is symmetry plane along the reactor centre. Figure 2.7 shows half the mesh microreactor for one phase, which features a collecting channel of $W^{\#}_{B} = 10$ and $E^{\#}_{B} = 7$. The phase height $H = 100$ μm is chosen as characteristic dimension so that $H^{\#} = 1$.

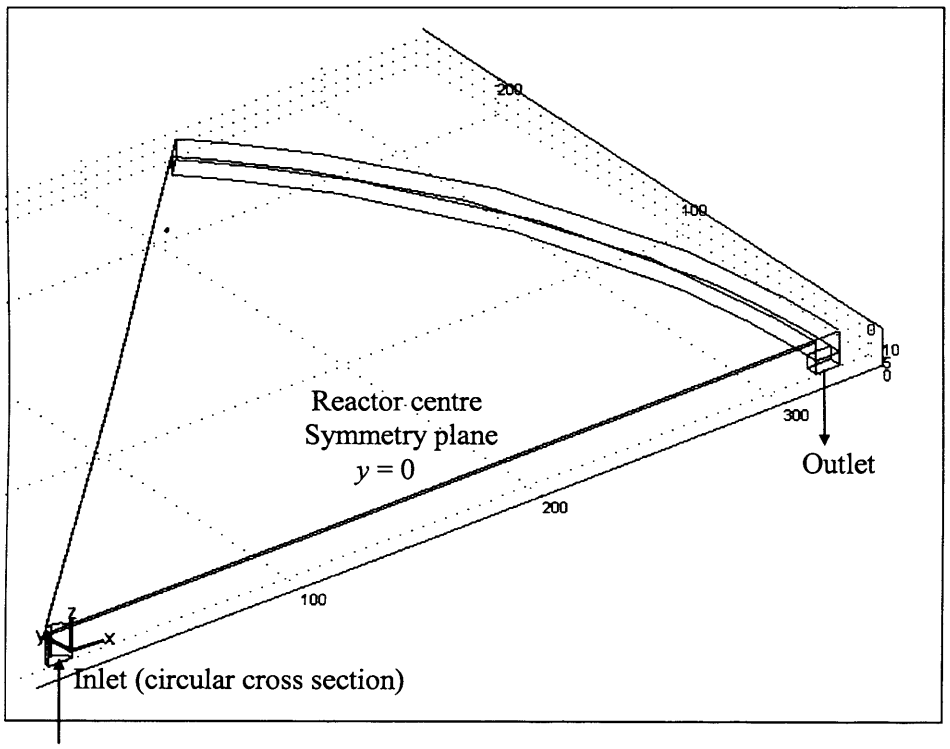

Figure 2.7. Half the geometry of one of the fluid phases in a standard quadrant shaped mesh microreactor. The collecting channel has dimensions $E^{\#}_{B} = 7$ and $W^{\#}_{B} = 10$.

The required steps followed in FEMLAB to set up the simulations are explained in Appendix 2C. The 3D stationary Navier-Stokes application mode is chosen in the model navigator with Lagrange p2-p1 elements.

For those simulations where the geometry is not the standard quadrant shape, the collecting channel curve is interpolated by means of splines, converted into a 2D geometry and imported into Femlab using the script shown in Appendix 2D. During the geometry creation, internal boundaries are deleted in order to improve meshing quality.

The resulting anisotropic mesh contains 20000-22000 elements (see Figure 2.8), for which the flow field solution is independent on mesh size.

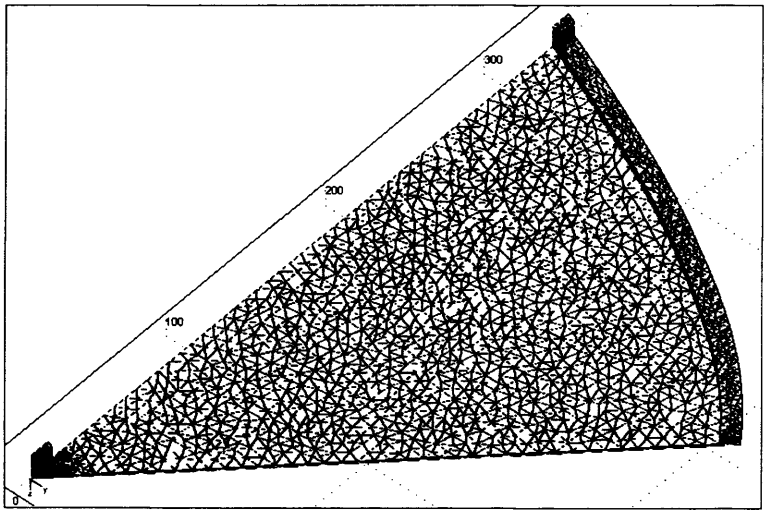

Figure 2.8. Mesh of 20088 second order elements for a mesh microreactor with a collecting channel depth of $E^{\#}_{B} = 4$ and a modified plate geometry.

The boundary conditions according to Figure 2.7 are:

- **Inlet:** Parabolic profile, $U^{\#}_{x} = 0$, $U^{\#}_{y} = 0$ $U^{\#}_{z} = 2U^{\#}_{0}(1-((x^{\#} - x^{\#}_{centre})^2 + ((y^{\#} - y^{\#}_{centre})^2)/r^{\#2})$.
- **Outlet:** Straight-out condition, $P^{\#} = 0$ and $\mathbf{U}^{\#} \cdot \mathbf{t} = 0$.
- **Walls/mesh surface:** No slip, $\mathbf{U}^{\#} = 0$. The mesh surface features pore openings for both fluid phases to come into contact. The boundary condition over each meniscus interface is complex and it is assumed that the pore openings have little effect on the no-slip condition applied. Experimental results shown in section 2.5.3 were carried out substituting the mesh by a flat surface where no-slip condition applies.
- **Symmetry plane:** and $\mathbf{U}^{\#} \cdot \mathbf{n} = 0$ and $\partial \mathbf{U}^{\#} / \partial \mathbf{n} = 0$.

2.4.3. Tracer Injection for RTD in FEMLAB.

The convection-diffusion equation to solve the tracer concentration along the microreactor is decoupled from the fluid flow solution to reduce memory usage. First the steady-state Navier-Stokes equations are solved for certain *Re* as indicated above. Second, the time-dependent convection-diffusion equation is solved independently interpolating the velocity field from the

previous solution. When the cell Peclet number ($Pe_{cell} = Hv_{cell}/D_A$) that defines the ratio of convective to diffusive flow is larger than 1, difficulties in stabilising the numerical solution result in *numerical diffusion* (FEMLAB Reference Manual, 2002). This is due to the dominance of the non-linear advective term in Eq. (2.17) that results in convergence difficulties. Numerical diffusion can be minimised by improving the mesh quality and reducing the size of the mesh elements (reducing the local *Pe*) by refining the mesh utilised for the mass transfer solution (up to 70000 elements were used). FEMLAB has some artificial diffusion techniques, in which a coefficient of artificial diffusion is added to the diffusion term, to deal with local numerical instabilities without the need for a very fine mesh refinement. However, the solution is often inaccurate and solutions obtained in the present study at high *Pe* were inaccurate. A step tracer injection can be simulated via an exponential switch function with time instead of a pulse in order to avoid that the solver uses very small time steps to resolve the discontinuity in time.

2.4.4. RTD via Lagrangian Particle Tracking

Particle tracking quality depends upon quality of the velocity field solution. Also the calculation of the RTD via particle tracking requires special consideration of the boundary condition for the particle release when the velocity profile at the inlet is not flat. If the injection consists of a finite number of particles uniformly distributed at the inlet, the calculated RTD is incorrect. This is illustrated by considering fluid flow between parallel sheets as shown in Figure 2.4 where streamlines are straight and there is an analytical solution for the RTD (see Appendix 2E),

$$\mathbf{E}(t^{\#}/\tau^{\#}) = \frac{2}{6(t^{\#}/\tau^{\#})^3\left[\left(3(t^{\#}/\tau^{\#})-2\right)/\left(3(t^{\#}/\tau^{\#})\right)\right]^{0.5}} \tag{2.43}$$

where the density function $\mathbf{E}(t^{\#}/\tau^{\#})$ fulfils Eq. (2.24). The integral of $E(t^{\#})$ between $t^{\#} = 0.6667$ (residence time of first fluid element coming out) and $t^{\#} = 10$ indicates that 99.82 % of the fluid elements have reached the reactor outlet. Next, a particle RTD curve is obtained by releasing $N_{Particles}$ particles at the inlet of the 2D reactor and measuring the time they take to exit. This boundary condition corresponds to the *injection of a finite volume of tracer with uniform concentration*. The trajectory of the particles is a straight line and the particle velocity is calculated by Eq. (2.33). Finite particles are uniformly distributed along the cross section height H at the reactor inlet (10000 points) and released at time $t^{\#}= 0$. The residence time of each particle is given by $t^{\#} = L^{\#}/U^{\#}_x$ as in this case the streamline length is the same and equal to $L^{\#}$ for all particles. The $\mathbf{E}(t^{\#}/\tau^{\#})$ curve is calculated by Eq. (2.44), where p_i is the number of particles with a residence time $t_i^{\#} < t^{\#} < t_i^{\#} + \Delta t_i^{\#}$:

$$\mathbf{E}_i(t^{\#}/\tau^{\#}) = \frac{p_i}{\left(\Delta t_i^{\#}/\tau^{\#}\right)\cdot N_{\text{Particles}}} \tag{2.44}$$

An integral of this function $E(t^{\#}/\tau^{\#})$ between $t^{\#}/\tau^{\#} = 0.66667$ and $t^{\#}/\tau^{\#} = 10$ indicates that only 96.69 % of the particles have exited the reactor, which is different from the theoretical value of 99.82 % obtained from Eq. (2.43). Figure 2.9 shows that the theoretical $\mathbf{E}(t^{\#})$ curve is different from that obtained releasing particles uniformly distributed at the inlet (see Appendix 2F).

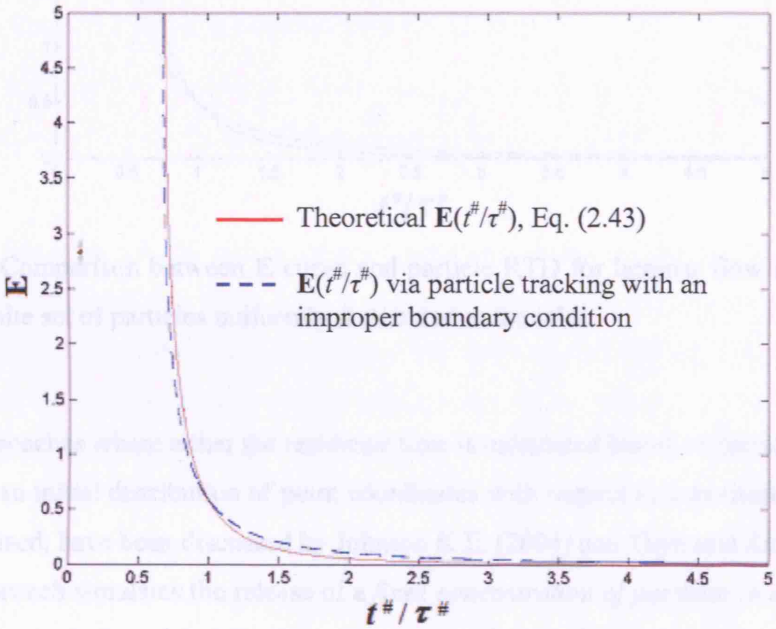

Figure 2.9. Comparison between **E** curve and particle RTD for 2D flow between parallel sheets when releasing a finite set of particles uniformly distributed at the inlet.

The same analysis can be carried out for laminar flow in a circular pipe where the theoretical **E** curve is given by Fogler (2005), $\mathbf{E}(t^{\#}/\tau^{\#}) = 1/(2\,(t^{\#}/\tau^{\#})^{3})$ $((t^{\#}/\tau^{\#}) \geq 0.5$ resulting in Figure 2.10.

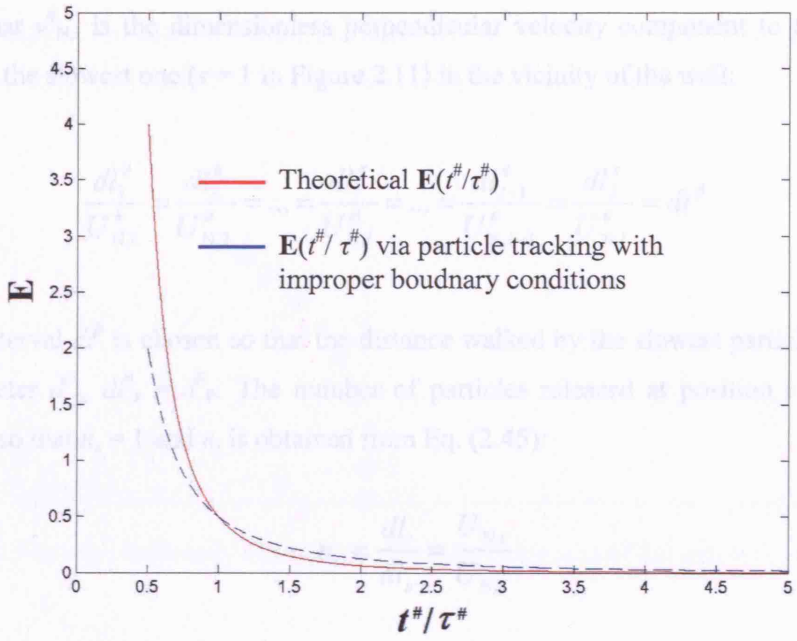

Figure 2.10. Comparison between **E** curve and particle RTD for laminar flow in a pipe when releasing a finite set of particles uniformly distributed at the inlet.

Different approaches where either the residence time is calculated based on particle volume flux weighting or an initial distribution of point coordinates with respect to a momentum or velocity weighting is used, have been discussed by Johnson K.E. (2004) and Thyn and Zitny (2000). The following approach simulates the release of a *fixed concentration of particles in a finite time* (as in a tracer injection). *I* particle injection points are uniformly distributed. More fluid elements and therefore released particles are in the inlet boundary at positions of high velocities after a differential of time as shown in Figure 2.11.

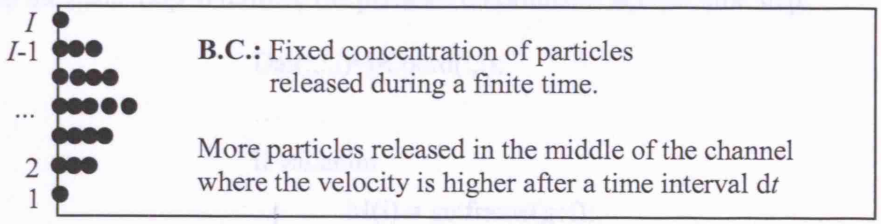

Figure 2.11. Proper boundary condition for particle injection at the reactor inlet for calculation of the RTD.

The distance $l^{\#}$ travelled by particle i in time $dt^{\#}$ is $dl_i^{\#} = v^{\#}_{N,i} dt^{\#}$ and Eq. (2.45) applies. It should be noted that $v^{\#}_{N,i}$ is the dimensionless perpendicular velocity component to the inlet plane. Particle s is the slowest one ($s = 1$ in Figure 2.11) in the vicinity of the wall:

$$\frac{dl_1^{\#}}{U_{N,1}^{\#}} = \frac{dl_2^{\#}}{U_{N,2}^{\#}} = \ldots = \frac{dl_i^{\#}}{U_{N,i}^{\#}} = \ldots = \frac{dl_{I-1}^{\#}}{U_{N,I-1}^{\#}} = \frac{dl_I^{\#}}{U_{N,I}^{\#}} = dt^{\#} \tag{2.45}$$

The time interval $dt^{\#}$ is chosen so that the distance walked by the slowest particle is equivalent to its diameter $d^{\#}_p$, $dl^{\#}_s = d^{\#}_P$. The number of particles released at position i is n_i and it is normalised so that $n_s = 1$ and n_i is obtained from Eq. (2.45):

$$n_i = \frac{dl_i}{dl_s} = \frac{U_{N,i}}{U_{N,s}} \tag{2.46}$$

According to this approach, the total number of particles released is given by Eq. (2.47) and is a function of the velocity profile at the inlet. This approach resembles the continuous nature of the fluid elements. Thus, considering I injection points with n_i particles per injection point ($i = 1 \ldots I$), the $\mathbf{E}(t^{\#}/\bar{t}^{\#})$ curve is exactly coincident with the theoretical curves for both examples shown in Figure 2.9 and Figure 2.10:

$$N_{Particles} = \sum_{i=1}^{n=I} n_i \tag{2.47}$$

In the mesh microreactor, the system of equations given by Eqs. (2.21)-(2.23) is solved via a second order Runge-Kutta scheme implemented in the FEMLAB function postpart.m. Two lines are added to the main loop to retrieve the particles co-ordinates at each time step:

```
Dat(:,:,i)=pCoord(:,:);
...
if val.anim
        M(i) = getframe(gcf);
else
        %3D Array
        M(:,:,i) = Dat(:,:,i) ;
end
```

Particles are released at the beginning of the active region, $R^{\#} = 56$ away from the fluid inlet at different z planes. In each z plane, particles are uniformly distributed along the arc at I_z positions according to Figure 2.12 and the total number of initial positions is $I = \sum I_z$.

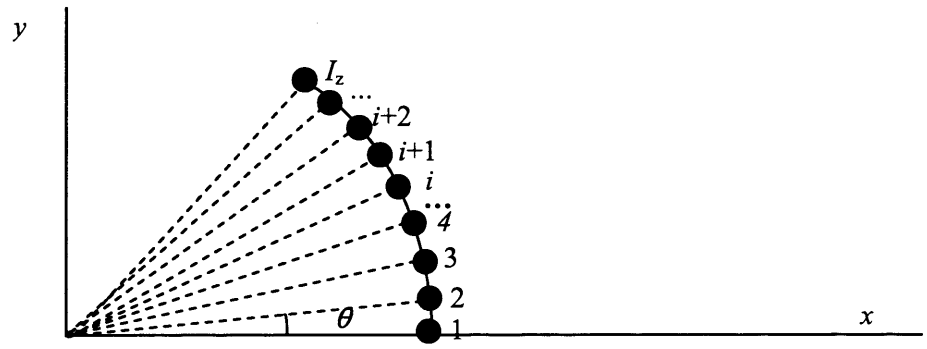

Figure 2.12. Particles uniformly distributed along the beginning of the active region.

The x and y co-ordinates are given by,

$$x_i^{\#} = R^{\#} \cos(\theta \cdot (i-1)) \tag{2.48}$$

$$y_i^{\#} = R^{\#} \sin(\theta \cdot (i-1)) \tag{2.49}$$

where i is the position number in that z plane. Appendix 2G shows the Matlab code to set up the particle positions and run the postpart.m function. Normal velocities to the inlet plane are calculated for all particle positions by the scalar product of the velocity vector and the normal to the inlet plane of components of components for position i given by Eq. (2.50). This allows for calculation of the number of particles released at each position, n_i, according to Eq. (2.46):

$$\begin{aligned} n_{x,i} &= \frac{x_i^{\#}}{\sqrt{x_i^{\#2} + y_i^{\#2}}} \\ n_{y,i} &= \frac{y_i^{\#}}{\sqrt{x_i^{\#2} + y_i^{\#2}}} \end{aligned} \tag{2.50}$$

The **E** curve is calculated via Eq. (2.44) where the number of particles p_i with a residence time $t_i^{\#} < t^{\#} < t_i^{\#} + \Delta t_i^{\#}$ is given by $p_i = \sum n_k = \sum (v^{\#}_{N,k}/v^{\#}_{N,s})$ where k refers to those positions from which the released particles have a residence time within $t_i^{\#}$ and $t_i^{\#}+\Delta t_i^{\#}$ (see Appendix 2H).

2.5. Results and Discussion

2.5.1. Flow and Residence Time Distribution via the RNM

A) Standard Quadrant Shape Mesh Microreactor

Figure 2.13 shows the flow distribution along the different fluid paths in half of the mesh microreactor with standard quadrant geometry (see Figure 2.7) calculated via the RNM considering 200 fluid paths (section 2.4.1). The collecting channel has a width of $W^{\#}_{B} = 10$ and different depths from $E^{\#}_{B} = 1$ to $E^{\#}_{B} = 7$.

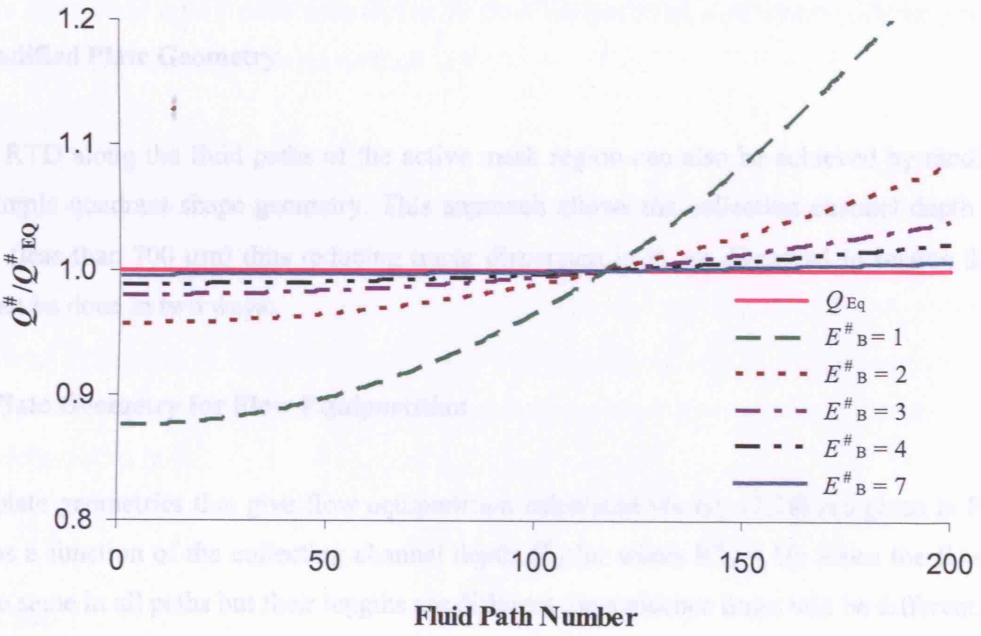

Figure 2.13. Flow distribution in the fluid paths of the mesh microreactor with standard quadrant geometry obtained via the RNM.

A divergence parameter *FD (Flow Distribution)* defined by Eq. (2.51) in which $Q^{\#}_{R,i}$ is the flowrate within each fluid path is given in Table 2.1 for each collecting channel size. For $E^{\#}_{B} < 3$ the flow distribution along the reaction plate becomes substantially uneven with flowrates along the fluid paths deviating from the equipartition flowrates more than 3.9 % (high flowrates at the microreactor centre and lower flowrates towards the side wall).

$$FD(\%) = \max_{j=1}^{N} \left[100 \frac{\left| Q^{\#}_{EQ} - Q^{\#}_{R,j} \right|}{Q^{\#}_{EQ}} \right] \tag{2.51}$$

$E^{\#}_B$ ($W^{\#}_B = 10$)	*FD*, %
7	0.7 %
4	2.2 %
3	3.9 %
2	8.5 %
1	25.6 %

Table 2.1. Flow distribution divergence parameter in a quadrant shape mesh microreactor for different collecting channel depths E_B when the channel width is equal to $W^{\#}_B = 10$.

b) Modified Plate Geometry

Even RTD along the fluid paths of the active mesh region can also be achieved by modifying the simple quadrant shape geometry. This approach allows the collection channel depth to be small (less than 700 μm) thus reducing tracer dispersion in it. As discussed in section 2.4.1b, this can be done in two ways:

b.1) Plate Geometry for Flow Equipartition

Half plate geometries that give flow equipartition calculated via Eq. (2.38) are given in Figure 2.14 as a function of the collecting channel depth $E^{\#}_B$ for width $W^{\#}_B = 10$. Since the flowrates are the same in all paths but their lengths are different the residence times will be different. This is resolved by having an active mesh region (that has pores) with quadrant shape. However, although the collecting channel volume can be reduced, there is an extra non-active volume between the quadrant shape of the active region and the collecting channel that causes extra overall dispersion (see Figure 2.6).

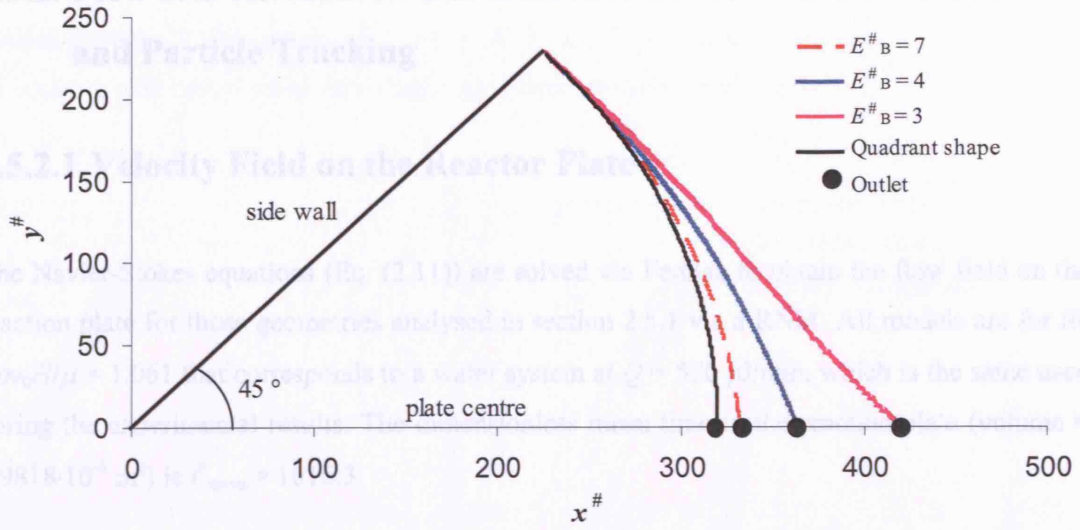

Figure 2.14. Half reactor plate geometries for flow equipartition at different collecting channel depths, $E^{\#}_B$, for collecting channel width $W^{\#}_B = 10$.

b.2) Plate Geometry for Identical Mean Residence Time in Fluid Paths.

Plate designs for the same residence time in all fluid paths are shown in Figure 2.15. In this case even large reductions in the collecting channel depth cause only small changes in the reaction plate geometry. Furthermore, the whole reactor plate is active (pores in the whole area) so no dispersion occurs in it.

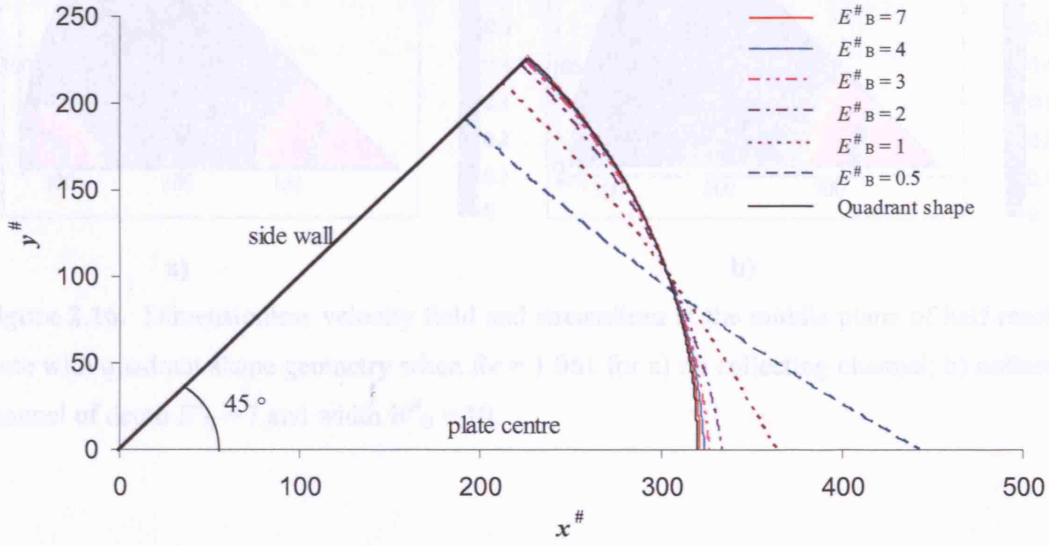

Figure 2.15. Half reactor plate geometries for identical mean residence time in all fluid paths as a function of the collecting channel depth, $E^{\#}_B$, for collecting channel width $W^{\#}_B = 10$.

2.5.2. Flow and Residence Time Distribution via Numerical Simulation and Particle Tracking

2.5.2.1. Velocity Field on the Reactor Plate

The Navier-Stokes equations (Eq. (2.11)) are solved via Femlab to obtain the flow field on the reaction plate for those geometries analysed in section 2.5.1 via a RNM. All models are for $Re = \rho v_0 H/\mu = 1.061$ that corresponds to a water system at $Q = 500$ µl/min. which is the same used during the experimental results. The dimensionless mean time in the reaction plate (volume = $7.9818 \cdot 10^{-8}$ m^3) is $t^{\#}_{mean} = 1016.3$.

Figure 2.16 shows the flow field and streamlines at the middle z-plane of the reaction plate in half the mesh microreactor with the standard quadrant shape for two different collecting channel depths, namely, $E^{\#}_B = 0$ and $E^{\#}_B = 7$. The microreactor with a collecting channel depth of $E^{\#}_B = 7$ produces even flow (similar velocities for same radial positions) while the microreactor without a collecting channel shows uneven flow distribution. The streamlines are straight for the geometry with a collecting channel depth of $E^{\#}_B = 7$.

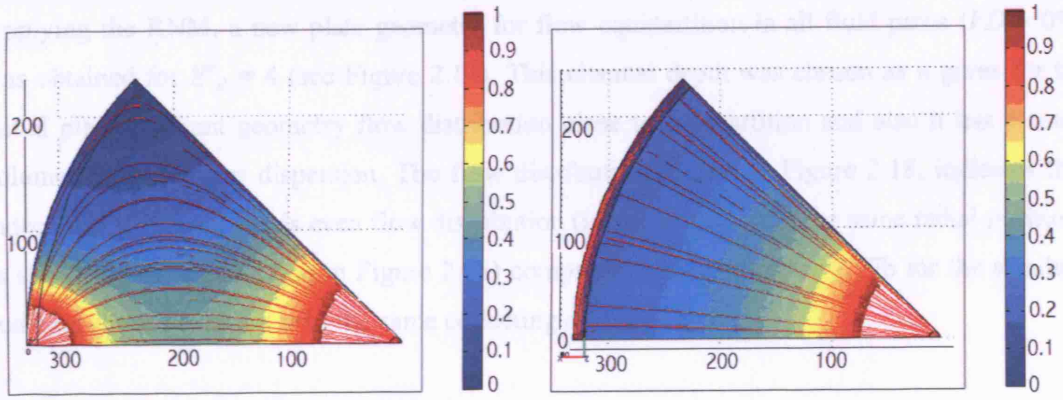

a) b)

Figure 2.16. Dimensionless velocity field and streamlines at the middle plane of half reaction plate with quadrant shape geometry when $Re = 1.061$ for a) no collecting channel; b) collecting channel of depth $E^{\#}_B = 7$ and width $W^{\#}_B = 10$.

Figure 2.17 shows the flow field and streamlines at the middle z-plane of the reaction plate in half the mesh microreactor with the standard quadrant shape for two different collecting channel depths, namely, $E^{\#}_B = 7$ and $E^{\#}_B = 4$. The velocity $U^{\#}$ range included in these plots is smaller

than that used in Figure 2.16. The geometry with $E^{\#}_B = 4$ shows less even flow distribution as indicated by the RNM in Table 2.1, $FD = 0.7\%$ for $E^{\#}_B = 7$ and $FD = 2.2\%$ for $E^{\#}_B = 4$. The streamlines gain curvature as flow distribution becomes less even.

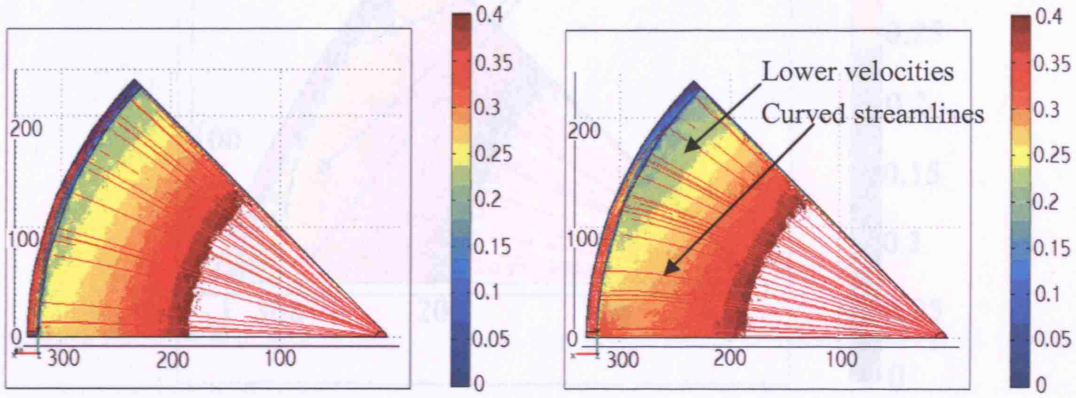

a) b)

Figure 2.17. Dimensionless velocity field and streamlines at the middle plane of half reaction plate with quadrant shape geometry when $Re = 1.061$ for a) collecting channel of depth $E^{\#}_B = 7$; b) collecting channel of depth $E^{\#}_B = 4$ and width $W^{\#}_B = 10$.

Applying the RNM, a new plate geometry for flow equipartition in all fluid paths ($FD = 0\%$) was obtained for $E^{\#}_B = 4$ (see Figure 2.14). This channel depth was chosen as it gives for the initial plate quadrant geometry flow distribution close to equipartition and also it has a small volume which reduces dispersion. The flow distribution, shown in Figure 2.18, indicates that indeed this geometry yields even flow distribution (identical velocities for same radial positions as shown by the dashed line in Figure 2.18) compared to that in Figure 2.17b for the standard quadrant shape geometry with the same collecting channel depth.

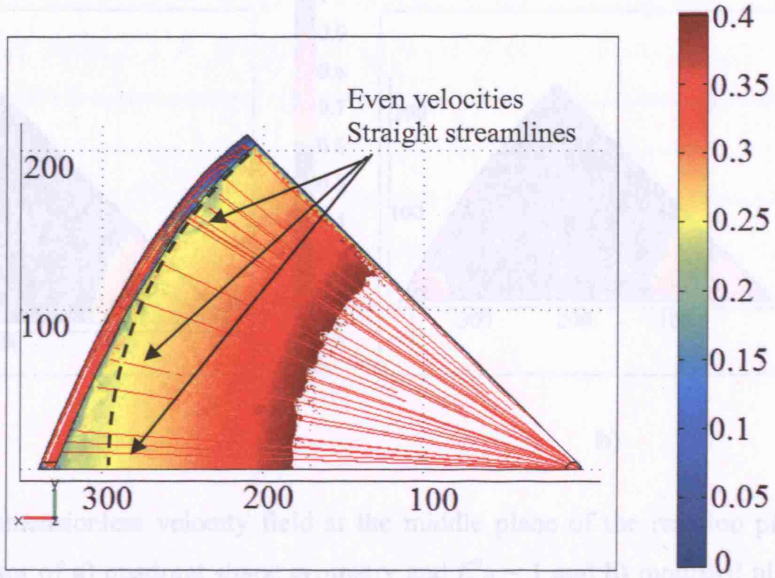

Figure 2.18. Dimensionless velocity field at the middle plane of half reaction plate with a modified plate geometry obtained via the RNM (see Figure 2.14) when Re = 1.061 and the collecting channel has $E^{\#}_{B} = 4$ and $W^{\#}_{B} = 10$.

The CFD results indicate that the assumption of straight streamlines considered in the RNM is acceptable for those geometries designed for even flow distribution along the reaction fluid paths.

To minimise the non-active volume in the plate, the plate geometry was modified using the RNM (section 2.5.1) for even mean residence time in all fluid paths as shown in Figure 2.15. A collecting channel depth of $E^{\#}_{B}$ = 1 is chosen to substantially reduce dispersion in the channel and reactor flushing time. Figure 2.19 compares the dimensionless velocity field in a standard quadrant geometry with $E^{\#}_{B}$ = 1 to the modified plate geometry for even RTD with the same $E^{\#}_{B}$ = 1 (geometry in Figure 2.15). In this case, the streamlines are not straight and the results from the RNM are expected to be less accurate. No quantitative comparison between the standard and the modified geometries can be made based on the velocity field shown in Figure 2.19 and particle tracking is required to obtain the RTD curves.

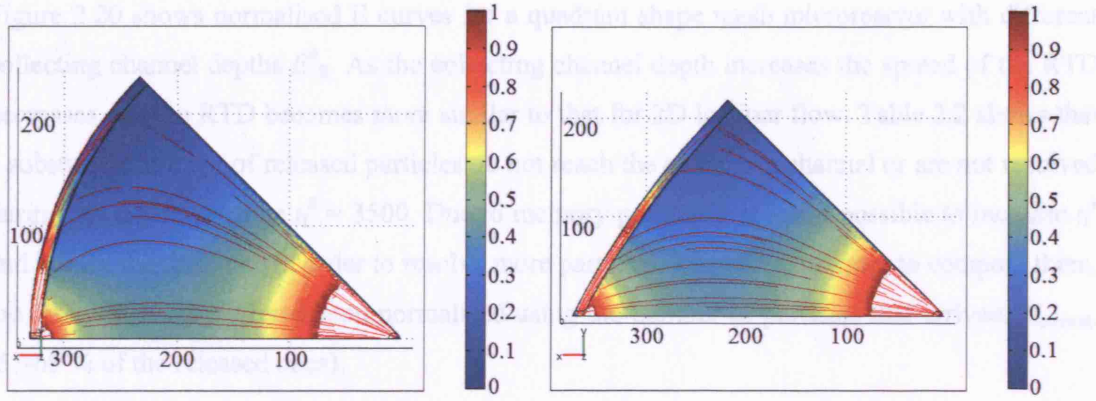

a) **b)**

Figure 2.19. Dimensionless velocity field at the middle plane of the reaction plate in half a mesh microreactor of **a)** quadrant shape geometry and $E^{\#}_{B} = 1$ and **b)** modified plate geometry with $E^{\#}_{B} = 1$. $Re = 1.06$ and $W^{\#}_{B} = 10$.

2.5.2.2. RTD via Lagrangian Particle Tracking

The flow field solutions are utilised to conduct weightless particle tracking and obtain the RTD on the mesh according to the method described in section 2.4.4. Due to the large aspect ratio of the plate geometries, a very small time step is required for accurate particle tracking. As indicated above, $t^{\#}_{mean} = 1016.3$ and $Re = 1.061$ are used for all geometries. Particle tracking is conducted in 5 different geometries using $I_z = 200$, $I_{\perp z} = 15$, $I = 3000$, $\Delta t^{\#} = 2$ and overall (final) solution time $t_f^{\#} = 3500$ (1751 time steps). Table 2.2 shows the initial and boundary conditions utilised for particle tracking in all geometries.

	Quadrant Geometry $E^{\#}_{B} = 7$	**Quadrant Geometry $E^{\#}_{B} = 4$**	**Quadrant Geometry $E^{\#}_{B} = 1$**	**Quadrant Geometry $E^{\#}_{B} = 0$**	**Modified Geometry $E^{\#}_{B} = 1$ (Figure 2.15)**
$I_{arrived}$*	1271	1751	1733	1421	1825
$t^{\#}_{min}/t^{\#}$	0.6357	0.5983	0.457	0.3975	0.551
$N_{Particles}$	194210	207420	196820	131350	136360
$N_{arrived}$	96524	123330	121800	71119	93715

*$I_{arrived}$ indicates the number of injection locations from which released particles arrived to the collecting channel.

Table 2.2. Particle tracking parameters for the different reactor plate geometries analysed.

Figure 2.20 shows normalised E curves for a quadrant shape mesh microreactor with different collecting channel depths $E^{\#}_{B}$. As the collecting channel depth increases the spread of the RTD decreases and the RTD becomes more similar to that for 2D laminar flow. Table 2.2 shows that a substantial amount of released particles do not reach the collecting channel or are not resolved during the simulated time $t_f^{\#} = 3500$. Due to memory problems, it is not possible to increase $t_f^{\#}$ and reduce the time step in order to resolve more particles. Therefore, in order to compare them, the different E curves have been normalised using the number of particles that arrived, $N_{arrived}$, (55-69 % of the released ones).

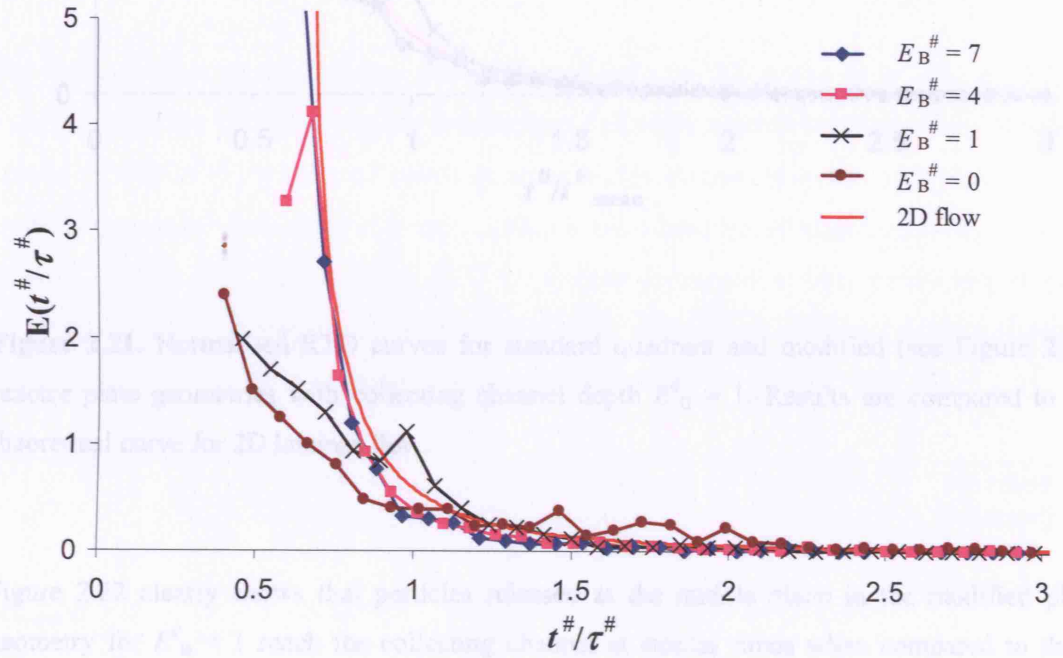

Figure 2.20. Normalised RTD curves for a quadrant shape mesh microreactor with different collecting channel depths, $E^{\#}_{B}$, compared to the theoretical curve for 2D laminar flow.

Figure 2.21 shows RTDs for two plate geometries with the same collecting channel depth $E^{\#}_{B}$ = 1; one is the standard geometry and the other is modified based on the RNM for the same mean residence time in all fluid paths (see Figure 2.15 for $E^{\#}_{B}$ = 1) The modified geometry shows a smaller RTD spread than the quadrant geometry although it does not result in identical mean residence times in all fluid paths (compare to solution for $E^{\#}_{B}$ = 7 in Figure 2.20). This is because the assumption of straight fluid lines in the RNM does not hold entirely as the streamlines are in this case curved.

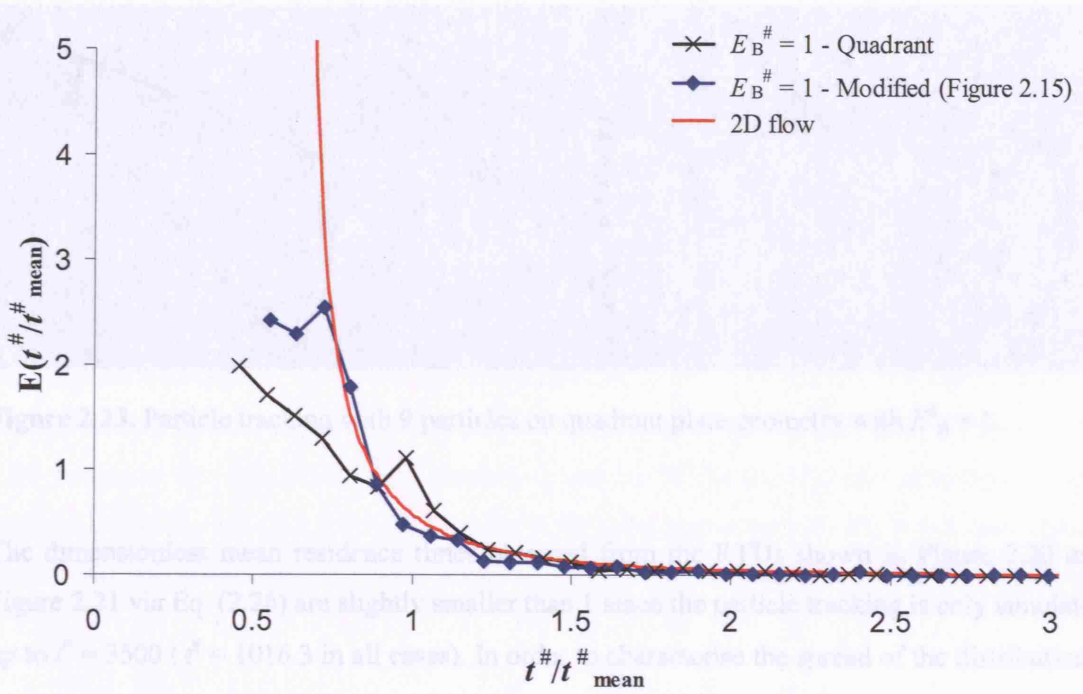

Figure 2.21. Normalised RTD curves for standard quadrant and modified (see Figure 2.15) reactor plate geometries with collecting channel depth $E^{\#}_B$ = 1. Results are compared to the theoretical curve for 2D laminar flow.

Figure 2.22 clearly shows that particles released at the middle plane in the modified plate geometry for $E^{\#}_B$ = 1 reach the collecting channel at similar times when compared to those particles released in the quadrant geometry shown in Figure 2.23.

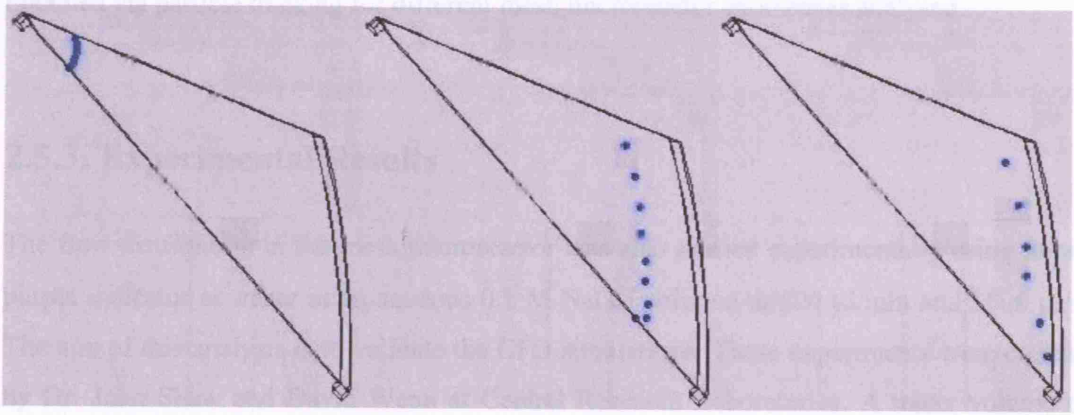

Figure 2.22. Particle tracking with 9 particles on modified plate geometry with $E^{\#}_B$ = 1.

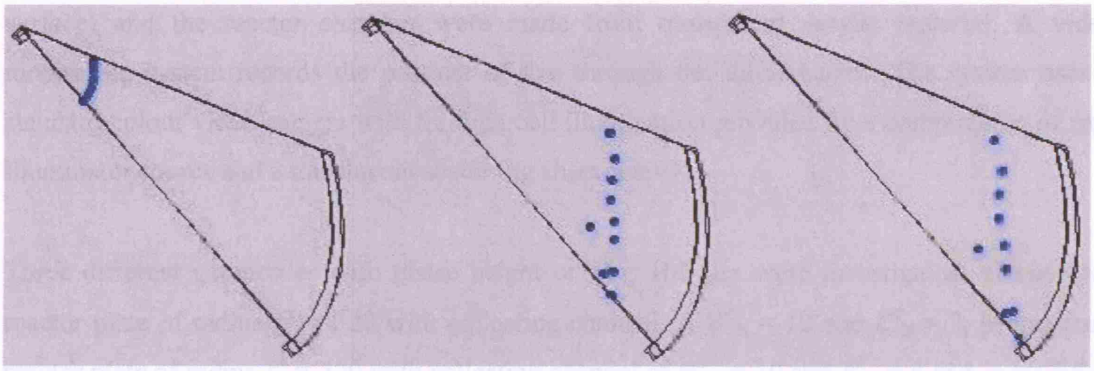

Figure 2.23. Particle tracking with 9 particles on quadrant plate geometry with $E^{\#}_B = 1$.

The dimensionless mean residence times obtained from the RTDs shown in Figure 2.20 and Figure 2.21 via Eq. (2.26) are slightly smaller than 1 since the particle tracking is only simulated up to $t^{\#} = 3500$ ($\tau^{\#} = 1016.3$ in all cases). In order to characterise the spread of the distributions, a spread parameter defined by $S = \sigma_v/t_{mean}$ (%) is calculated for all distributions as shown in Table 2.3 below. The spread of the RTD for a mesh microreactor with a collecting channel depth of $E^{\#}_B = 1$ is considerably improved when the modified reaction plate geometry shown in Figure 2.15 ($S = 35.8$ %) is used, compared to the quadrant shape ($S = 42.6$ %).

	Quadrant Geometry $E^{\#}_B = 7$	**Quadrant Geometry $E^{\#}_B = 4$**	**Quadrant Geometry $E^{\#}_B = 1$**	**Quadrant Geometry $E^{\#}_B = 0$**	**Modified Geometry $E^{\#}_B = 1$ (Figure 2.15)**
$t^{\#}_{mean}/\tau^{\#}$	0.811	0.826	0.844	0.919	0.831
σ_v	0.269	0.304	0.359	0.547	0.297
$\sigma_v/(t^{\#}_{mean}/\tau^{\#})$, %	33.2	36.8	42.6	59.5	35.8

Table 2.3. Mean residence time, standard deviation and spread parameter for the RTD curves obtained via particle tracking for different mesh microreactor geometries analysed.

2.5.3. Experimental Results

The flow distribution in the mesh microreactor was also studied experimentally using m-cresol purple indicator as tracer in an aqueous 0.1 M NaOH solution at 500 µl/min and 1000 µl/min. The aim of this analysis is to validate the CFD simulations. These experiments were conducted by Dr. John Shaw and David Wenn at Central Research Laboratories. A tracer volume of at least 300 µl is required to ensure even concentration across the reactor for certain period of time. For the experimental studies the bottom wall (mesh surface was substituted by a flat

surface) and the reactor chamber were made from transparent acrylic material. A video monitoring system records the passage of dye through the microreactor. The system uses a standard colour video camera with through cell illumination provided by a combination of ring illuminator source and a translucent scattering sheet (paper).

Three different geometries with phase height of H = 100 μm were investigated: a) quadrant reactor plate of radius $L^{\#}$ = 320 with collecting channel of $W^{\#}_B$ = 10 and $E^{\#}_B$ = 7, b) quadrant reactor plate of radius $L^{\#}$ = 320 with collecting channel of $W^{\#}_B$ = 10 and $E^{\#}_B$ = 4 and c) modified plate geometry for flow equipartition with collecting channel of $W^{\#}_B$ = 10 and $E^{\#}_B$ = 4. Figure 2.24 compares dye concentration in models a) and b). While the dye concentration is fairly uniform when $E^{\#}_B$ = 7 (FD = 0.7 % from the RNM), the geometry with $E^{\#}_B$ = 4 shows smaller dye concentration for identical radial positions away from the reactor centre (FD = 2.2 % the RNM).

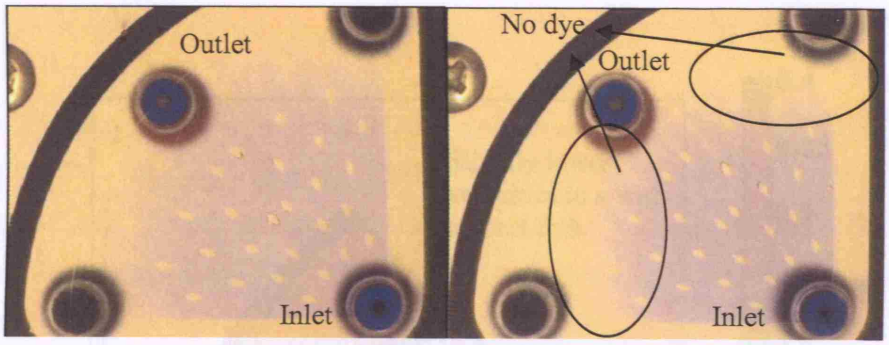

Figure 2.24. Injection of 0.1 NaOH solution with m-cresol dye at Q = 0.5 ml/min (Re = 1.06) into a quadrant shape mesh microreactor for collecting channel with width $W^{\#}_B$ = 10 and depth a) $E^{\#}_B$ = 7 and b) $E^{\#}_B$ = 4.

Figure 2.25 shows a mesh microreactor where the plate geometry has been modified to deliver even flow distribution. This is an intermediate geometry between those geometries presented in Figure 2.14 for $E^{\#}_B$ = 4 and $E^{\#}_B$ = 3. In this geometry the tracer concentration is similar at the same radial positions (dashed line in Figure 2.25). Therefore, if a quadrant active mesh region is implemented, the spread of the mean residence times for all fluid paths in the reaction plate will be small. Considering a perfect rectangular collecting channel of $E^{\#}_B$ = 4 in the experimental device of Figure 2.25, velocities at the reactor centre should be slightly lower than those on the side at the same radial positions according to the RNM and the CFD simulations (see Figure 2.26). Small discrepancies are associated to the exact geometry of the collecting channel.

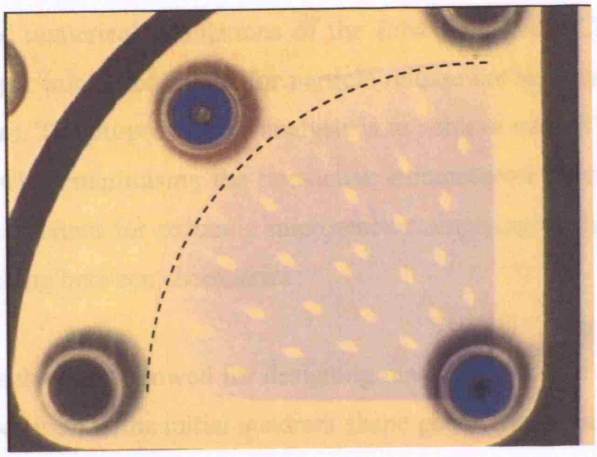

Figure 2.25. Injection of 0.1 NaOH solution with m-cresol dye at Q = 0.5 ml/min (Re=1.06) in a modified reactor plate geometry for even flow distribution for collecting channel with $W^{\#}_{B}$ = 10 and $E^{\#}_{B}$ = 4.

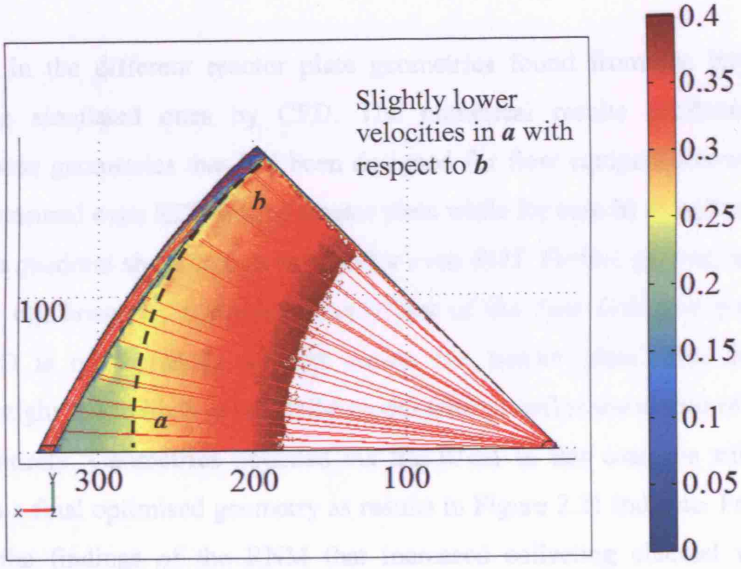

Figure 2.26. Dimensionless velocity field at the middle plane of the reaction plate in half a mesh microreactor with a modified plate geometry identical to that in Figure 2.25. Re = 1.06 and collecting channel of E_B = 400 and W_B = 1000 μm.

2.6. Conclusions

Flow and residence time distributions are investigated on a mesh microreactor with initial quadrant shape geometry. An analytical model based on resistance network model (RNM) is

suggested and the resulting flow and residence time distributions are compared with those obtained from detailed numerical simulations of the flow field using CFD and from particle tracking analysis. Proper initial conditions for particle release are necessary for the calculation of accurate RTD curves. The purpose of the analysis is to achieve even RTD inside the reaction plate (active region) while minimising the non-active microreactor volume. Small non-active reactor volumes are important for reducing microreactor emptying/flushing times and sample dispersion when switching between chemistries.

Three different approaches are followed for designing reactor plates that give uniform RTD. **a)** Design for flow equipartition in the initial quadrant shape geometry by increasing the size of the reactant collecting channel to minimise its resistance (pressure drop). **b)** Design for flow equipartition by modifying (to non-quadrant) the reaction plate geometry; however, a quadrant active region has to be used on a non-quadrant reactor plate for even RTD. **c)** Design for even RTD by modifying the reactor plate geometry. The last approach utilises small collecting channels and the whole reactor plate, thus decreasing non-active areas on the reactor.

The flow fields in the different reactor plate geometries found from the RNM were also compared to the simulated ones by CFD. The numerical results confirmed even flow distribution in those geometries that had been designed for flow equipartition with RNM. For case **a)** this also ensured even RDT on the reactor plate while for case **b)** an active region on the reactor plate with quadrant shape had to be used for even RDT. For the geometries designed for even RTD (case **c)**), however, numerical simulations of the flow field and particle tracking showed the RTD is not perfectly uniform across the reactor plate. This is because the assumption of straight streamlines in the RNM model used to define the shapes of these reactors does not hold entirely. Geometries obtained via the RNM in this case are still a good first approximation to a final optimised geometry as results in Figure 2.21 indicate. Particle tracking also confirmed the findings of the RNM that increased collecting channel volume and/or modified plate geometries can give uniform RTD.

Experimental observations of tracer injection into the mesh microreactor confirmed the findings of the analytical and numerical models.

The above shows that the simple analytical RNM can be applied to design plate type microstructures that give uniform flow and RTD.

Nomenclature

A	Cross section area of the fluid paths.
c	Concentration, kg/m^3.
C	Concentration curve.
H	Characteristic length (H for the mesh microreactor), m.
E	Channel depth, m.
E	**E** curve or RTD curve.
F	Force vector, N.
FD	Divergence parameter, %.
Fr	Froude number.
H	Phase height, m.
I	Injection positions at the inlet, $i = 1 \ldots I$.
I_{arrived}	Initial positions from which released particles reach the collecting channel.
I_z	Injection positions in the z plane.
$I_{\perp z}$	Injection positions in a plane perpendicular to the z plane.
l	length, m.
L	Channel or fluid path length, m.
m	System mass, kg.
n	Interface unit normal vector.
n_i	Number of particles released at position i.
N	Total number of fluid paths.
$\mathbf{N_i}$	Flux vector for component i.
$N_{\text{Particles}}$	Total number of particles released at the inlet.
p	Momentum vector, kgm/s.
P	Pressure, Pa.
P_0	Reference pressure, Pa.
Pe	Peclet number.
Sc	Schmidt number.
Q	Total flowrate between parallel sheet in the x direction.
L	Channel or fluid path length, m.
R	Fluid resistance, Pa·s/m^3
Re	Reynolds number.
S	Spread parameter.
t	Residence time, s.
t	Interface unit tangent vector.

U_0	Characteristic velocity, m/s.
U_x	Velocity in the x direction (similar for components y and z).
U_{mean}	Average velocity in the cross section (Q/(2RW)).
U_N	Normal velocity component to the inlet plane.
VDN	Vessel dispersion number.
W	Channel/path width.
x	x co-ordinate.
y	y co-ordinate.
z	z co-ordinate.
x_i, x_j	Co-ordinates x, y and z.

Greek Letters

$\delta_{i,j}$	Kronecker delta.
$\phi_{i,j}$	j-momentum in the positive i direction, Pa.
κ	Dilatational viscosity, Pa·s.
μ	Fluid viscosity, Pa·s.
$\pi_{i,j}$	Pressure plus viscous fluid stresses, N/m^2.
ρ	Fluid density, kg/m^3.
τ	Space time defined as Volume/flowrate = V/Q.
$\tau_{i,j}$	Viscous stresses. Flux (flow per unit area) of j-momentum in the positive i direction, Pa.
ω	Fluid path angle.
ψ_i	Reaction rate for component i.

Subscripts

A	Distributing channel.
B	Collecting channel.
CV	Control volume.
EQ	Equipartition.
f	Final.
max	Maximum.
mean	Mean or average.
min	Minimum.
N	Normal or perpendicular.

P	Particle.
R	Reaction channel/path.
s	Position of the slowest particle at the injection point.
S	Close system.

Superscripts

#	Dimensionless variable.

Chapter 3

A Systematic Methodology for Determination of Meniscus Shape, Position and Stability in Circular and Polygonal, Uniform and Tapered Cross Section Pores

"When it is not in our power to follow what is true, we ought to follow what is most probable"

Rene Descartes

3.1. Introduction

Multiphase operations in microscale systems may require different approaches to those applied in conventional macrosystems to ensure high interfacial area, ease of phase separation and efficient mass transfer. Since separation by gravity in these scales is difficult, alternative ways have been used to bring in contact different phases without inter-dispersing them. One device used for liquid/liquid solvent extraction employed partial overlapping of open channels to define the liquid/liquid interface (Shaw et al., 1998). However, the contactor had limited stability and interfacial area (2-15 % of total area). These were improved by separating the phases through a mesh with openings of 5-10 μm diameter, open areas up to 40 % and thickness 5 μm (Wenn et al., 2003). TeGrotenhuis et al. (1998) used a 25-μm kapton mesh with 25 μm openings and small open area. The contactor performed at least as well as commercial membranes during extraction experiments. A similar contacting principle, using 100 μm microfabricated holes was utilised by Cypes and Engstrom (2003) for stripping applications. An order of magnitude higher overall mass transfer capacity was observed as compared to a conventional packed column. A slightly different configuration was suggested by Maruyama et al. (2004). The microfluidic device had intermittent partition walls in the centre of the confluent microchannels, thus creating vertical openings, which stabilised the liquid/liquid interface. The partition walls induced slight turbulence that promoted mixing and mass transfer. In all the above devices the fluid layers are kept thin for efficient mass transfer. This however can lead to significant pressure drop within each phase giving rise to varying pressure difference between

phases along the microcontactor. In the mesh-type microcontactors, the mesh should be thin enough to reduce species diffusion time in the pores and have large open area to increase interfacial mass transfer. At the same time it should have structural stability. The pore geometry, pressure difference between phases, interfacial tension and contact angle determine the shape of interfacial area available for mass transfer and the position of the interfacial meniscus within the pore, which in turn affect mass transfer resistance (Prasad et al., 1990). To avoid one phase dispersing into the other (*breakthrough*), the meniscus should remain within the pores (*meniscus stability*) for the range of pressure differences existing between the two phases during operation and modified along the mesh due to pressure drop.

Thus, in traditional membrane contactors with long, tortuous pores and irregular cross-section, diffusion distances are long and it is difficult to assure that a certain phase fills all the pores. This reduces both performance and reproducibility and mass transfer rates (Yang and Cussler, 1986; Prasad and Sirkar, 1987; Prasad et al., 1990). In contrast microfabricated meshes have regular pore cross section that allows improved control of the position and area of the interfacial meniscus as a function of pressure difference between the phases. This leads to substantial reproducibility of the process and enhance mass transfer (Turner et al., 2000; Kuiper et al., 2002) provided that short diffusion distances are present in the bulk phases.

In the present work, aspects of interfacial area, meniscus position and stability, as pertinent to mesh microcontactors, are investigated. More specifically a systematic methodology for prediction of *breakthrough* and *critical filling* pressures in regular straight pores with either circular or polygonal and constant or tapered cross-sections is presented. The results indicate that breakthrough pressures are always positive in static systems. Criteria and equations to calculate the meniscus area and its position within the pores are also given. The potential effect of line tension on the increase/decrease of the breakthrough pressure is introduced and experiments are conducted in single capillaries to validate the results.

3.2. Background

3.2.1. Critical Entry/Filling and Breakthrough Pressures

There has been extensive theoretical and experimental work on *critical entry* (or displacement) and *breakthrough* pressure difference in displacement of oil in reservoirs (Mason and Morrow, 1994; Patzek and Member, 2000) and membrane contactors. Models based on cylindrical capillaries have been applied to estimate these pressures for membranes although only a few

synthetic membranes have regular pores. Thus, the Laplace Equation for cylindrical capillaries in the absence of gravity has been applied to estimate without distinction critical entry and breakthrough pressures using the actual contact angle of the fluid-liquid interface at the solid wall, θ (Vaidya et al., 1994a; Kim and Harriot, 1986):

$$P_{NW} - P_W = \Delta P = \frac{2\gamma\cos\theta}{r} \tag{3.1}$$

Where r is the pore radius and γ is the surface tension. Positive breakthrough pressures (P_W-P_{NW}) of wetting phases in membranes have been reported (Byoung-sik and Harriot, 1984; Prasad et al., 1990; Vaidya et al., 1994b) which seemingly contradict the prediction of the Laplace equation. Vaidya et al. (1994a) considered positive breakthrough pressures in an amphiphilic polymer membrane when operating in both hydrophobic and hydrophilic modes as extremely surprising explaining this behavior as a result of restructuring effects at the membrane surface. Prasad et al. (1990) reported positive breakthrough pressure for aqueous and organic phases filling the pores in hydrophobic and hydrophilic membranes respectively, so that a restructuring phenomenon as that described by Vaidya et al. (1994b) could not explain this behavior. This is due to the fact that the solid wall inclination change at the pore ends (for regular pore membranes) or at pore interior (for tortuous pore membranes) is not accounted for. This effect is already described by Adam (1948) for a liquid that penetrates a porous solid and reaches a constriction. In this case, the meniscus remains pinned to the constriction coping with an increase in capillary pressure by changing its curvature from the value that corresponds to the incoming solid wall inclination to that found after the constriction. The above indicates that one needs to use with care the Laplace equation.

In this work, where regular straight pores are considered, the term *critical entry pressure* of one phase refers to the pressure difference necessary for this phase to enter a pore. Even more important than critical entry pressure for the present work is the critical filling pressure of one phase ΔP_C, defined as the pressure difference necessary to completely fill the pores with that phase. Critical entry and filling pressures are identical for constant cross section pores but they differ for tapered pores when the wetting phase is on the small pore opening side (see section 3.4.2). The *breakthrough pressure* refers to the pressure difference necessary to cause the breakthrough of one phase into the other. Thus, there are two critical filling pressures defined as critical filling pressure of the wetting phase $\Delta P_{C,W}$ and of the non-wetting phase $\Delta P_{C,NW}$,

$$\Delta P_{C,W} = (P_W\text{-}P_{NW})_{C,W} \tag{3.2}$$

$$\Delta P_{C,NW} = (P_{NW}\text{-}P_W)_{C,NW} \tag{3.3}$$

and two breakthrough pressures $\Delta P_{B,W}$ and $\Delta P_{B,NW}$ for the wetting and non-wetting phases respectively.

$$\Delta P_{B,W} = (P_W\text{-}P_{NW})_{B,W} \tag{3.4}$$

$$\Delta P_{B,NW} = (P_{NW}\text{-}P_W)_{B,NW} \tag{3.5}$$

In microreaction technology, the pressure difference range that the interfacial meniscus in the pores can cope with without breakthrough (*stability range*) is of interest. *This is the sum of the breakthrough pressures of the non-wetting and wetting phases,* ($\Delta P_{B,NW} + \Delta P_{B,W}$). In meshes there is one value for the critical filling pressure for all pores. In contrast, in membranes featuring irregular and tortuous pores a wide distribution of critical filling pressures is present. Different models for non-cylindrical pores have been developed to estimate the critical entry and breakthrough pressures in which the Laplace equation is modified to account for a change in the apparent contact angle and the radius of the meniscus as a function of pore geometry (Purcell, 1949; Crisp and Thorpe, 1948; Kim and Harriot, 1986; Mason and Morrow, 1994).

3.2.2. Parameters Affecting Contact Angle

Various phenomena can affect the value of the equilibrium contact angle. Based on the thermodynamic theory of capillarity, first developed by Gibbs (Gibbs, 1961), the following Laplace-Young Eq. (3.16) and (3.17) respectively are defined,

$$\Delta P = P_{NW} - P_W = \gamma \cdot \left(\frac{1}{R_1} + \frac{1}{R_2} \right) = \gamma\kappa \tag{3.6}$$

$$\cos\theta_Y = \frac{\gamma_{F\text{-}S} - \gamma_{L\text{-}S}}{\gamma} \tag{3.7}$$

where ΔP_{NW} is the pressure difference across a fluid-liquid curved interface at each point, γ is the interfacial tension of the fluid-liquid interface, R_1 and R_2 are the two principal radii of curvature for each point at the interface, κ is the surface curvature at the specific point, θ_Y is the Young's contact angle (macroscopic) of the three-phase contact line, $\gamma_{F\text{-}S}$ is the surface tension of the fluid-solid interface and $\gamma_{L\text{-}S}$ is the surface tension of the liquid-solid interface. The Gibbs

approximation works well for many systems but fails to explain such phenomena as contact angle hysteresis, capillary condensation and dependence of contact angle on surface heterogeneity, roughness and contortion of the solid/liquid/fluid three-phase contact line. Boruvka and Neumann (1976) generalized the classical theory of capillarity by applying the concept of dividing lines and points in conjunction with the concept of dividing surfaces that had already been used by Gibbs and suggested the following generalized Young's equation,

$$\cos\theta = \frac{\gamma_{F\text{-}S} - \gamma_{L\text{-}S}}{\gamma} - \frac{\sigma}{\gamma}\kappa_{gS} = \cos\theta_Y - \frac{\sigma}{\gamma}\kappa_{gS} \tag{3.8}$$

where σ is the line tension defined as the free energy per unit length of the three-phase contact line (linear analogue of the surface/interfacial tension) and κ_{gS} is the local geodesic curvature of the three-phase contact line on the plane of the solid surface. Eq. (3.8) indicates that wetting phenomena are strongly dependent on the system scale because of κ_{gS}. An important case for the present work, where the geodesic curvature is simple to calculate is that of an axisymmetric pore that produces menisci with a circular three-phase contact line as shown in Figure 3.1. In this case Eq. (3.8) simplifies to Eq. (3.9) as derived independently by Lin and Li (1994).

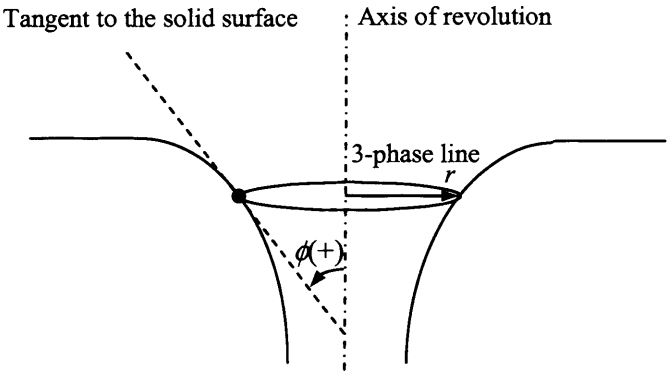

Figure 3.1. Geometric characteristics of a general axisymmetric pore.

$$\cos\theta = \cos\theta_Y - \frac{\sigma}{\gamma}\frac{\cos(90°-\phi)}{r} \tag{3.9}$$

Eq. (3.9) shows the effect of the solid wall inclination on the contact angle. ϕ is defined as the angle of the tangent to the solid wall at the point of contact of the three phase contact line with the meniscus axis (ϕ(-) clockwise, ϕ(+) counter clockwise as shown in Figure 3.1).

There is no agreement on the sign of line tension while its magnitude was found to vary between 10^{-6} J/m to 10^{-12} J/m with the largest discrepancy seen in experimental (Gaydos and Neumann, 1987; Duncan et al., 1994; Gu et al., 1996, Jensen and Li, 1999; Pompe and Herminghaus, 2000; Asekomhe and Elliott, 2003; Checco et al., 2003) rather than theoretical studies (Harkins, 1937; Rowlinson and Widom, 1984; Marmur, 1997; Solomentsev and White, 1999, Checco et al., 2003 for magnitude discrepancy; Li and Steigmann, 1995; Li and Steigmann, 1996; Rusanov, 1999 for sign discrepancy).

Surface roughness and heterogeneity magnify the effect of the line tension term by additional corrugation of the three-phase contact line (increase of local curvature $1/r$ in Eq. (3.9)) and therefore the effect of the solid wall inclination on macroscopic contact angle (Yost et al., 1995; Marmur, 1998; Rusanov, 1999; Lin and Li, 1993; Lin and Li, 1995; Swain and Lipowsky, 1998; Cubaud and Fermigier, 2004). Thus, line tension is important in micron size drops/menisci or in larger size drops/menisci with local micron size radii of curvature in the contact line due to roughness or heterogeneity of the solid surface (Marmur, 1998). Wenzel equation is generally used to quantify the effect of surface roughness on macroscopic contact angle (Wenzel, 1936):

$$\cos\theta = \xi_S \cos\theta_Y \tag{3.10}$$

where ξ_S is the solid roughness, which is the ratio of the real to the projected surface area. In a rough surface, the actual local contact angle with the actual solid surface is the microscopic contact angle. Marmur (1998) modified the Young's equation in order to estimate the contact angle including the effect of surface roughness within the line tension term that explains large measured values of the line tension when Eq. (3.9) is applied on non-ideal surfaces:

$$\cos\theta = \frac{\xi_S(R)\cos\theta_Y(X) - \dfrac{k\sigma}{X\gamma} - \dfrac{d\sigma}{\gamma dX}}{1 + dy_S(X)/dX \cdot dy_{LG}(X)/dX} \tag{3.11}$$

where ξ_S is the local solid roughness evaluated at the three-phase contact line position X, k is 0 for a 2D interface and 1 for an axisymmetric one, y_S and y_{LG} are the solid and liquid/gas interface profiles. Eq. (3.11) is an implicit equation since dy_{LG}/dX and σ are a function of the macroscopic contact angle θ. For a smooth surface ($dy_S/dX = 0$, $\xi_S = 1$), Eq. (3.11) reduces to:

$$\cos\theta = \cos\theta_Y - \frac{1}{\gamma}\left(\frac{k\sigma}{X} + \frac{d\sigma}{dX}\right) \tag{3.12}$$

which in turn reduces to Eq. (3.9) with $\phi = 90°$ if an axisymmetric system ($k = 1$) and a constant line tension σ are considered. Rusanov (2004) also includes the line roughness ξ_1 in his generalised expression for contact angle. The effect of surface heterogeneity on contact angle was analysed by Cassie and Baxter (1944):

$$\cos\theta = f_{A,1}\cos\theta_{1Y} + f_{A,2}\cos\theta_{2Y} \tag{3.13}$$

where $f_{A,1}$ and $f_{A,2}$ are the fractional surface areas of each component of the composite surface and θ_{1Y} and θ_{2Y} are the interface contact angles with each of the components. Lin and Li (1995) combined Eq. (3.9) for a sessile drop ($\phi = 90°$) with the Cassie equation considering a local radius of curvature of the contact line on each component of the surface (r_1 and r_2). The corrugated contact line produces a positive radius of curvature r_1 and a negative one r_2.

$$\cos\theta = f_{A,1}\left(\cos\theta_{1Y} - \frac{\sigma_1}{\gamma r_1}\right) + f_{A,2}\left(\cos\theta_{2Y} + \frac{\sigma_2}{\gamma r_2}\right) \tag{3.14}$$

The contact angle measured for a liquid advancing *slowly* across a surface, θ_A, exceeds that of the liquid receding on the surface, θ_R, and all intermediate contact angles correspond to metastable equilibrium states (Volpe et al., 2002). This phenomenon is called contact angle hysteresis, and is in general attributed to surface roughness and heterogeneity, solution impurities, swelling, rearrangement or alteration of the surface by the solvent (Adamson and Gast, 1997). The difference between receding and advancing contact angles can be very large in some systems (Shouxiang et al., 1996; He B. et al., 2004). The validity of Young's equation under gravity has also been a matter of controversy (Ward and Sasges 1998a and 1998b; Ward et al. 2000; Blokius 2000), although in general it is considered that it still holds under a gravity field (Roura and Fort 2004).

It should be noted that when the solid walls are tapered then the contact angle that defines the meniscus curvature in the absence of gravity is determined by the *apparent contact angle*, θ_{App} (Adam 1948). For two-dimensional or axisymmetric menisci the apparent contact angle at a given point is defined as the angle that the fluid-liquid meniscus forms (measured on the side of the wetting phase if not stated differently) with a line that crosses the given point and is perpendicular to the plane that contains the three-phase meniscus contact line (see section 3.4.1).

3.2.3. Effect of Wettability on Mass Transfer Resistance

Large-scale membrane contactors (instead of micro-fabricated meshes) have become common in large-scale industrial operations such as removal or dissolution of gases in water (Wiesler, 1996) or degasification of boiler feed water to avoid boiler corrosion using microporous hydrophobic membranes (Wiesler, 2003). In general, the aqueous fluid that flows on one side of the hydrophobic membrane comes into direct contact with the gas phase, which is set at a vacuum to avoid dispersing of one phase into the other. By adjusting the partial pressure of the gas (either by changing the total gas pressure or altering the gas concentration), a selective removal or dissolution process is accomplished. The overall mass transfer coefficient of the molecules that must diffuse is composed of the three individual mass transfer coefficients, liquid-phase, membrane and gas-phase mass transfer coefficients:

$$\frac{1}{k_{ov}} = \frac{1}{k_L} + \frac{1}{k_{mem}} + \frac{1}{k_G} \tag{3.15}$$

Since the diffusivity of the molecules in a liquid phase is 4-5 orders of magnitude larger than that in gases, filling the pores with the gas phase improves mass transfer between both phases. Yang and Cussler (1986) verified experimentally that the liquid phase is the dominant resistance to mass transfer for oxygen in water, being the membrane and gas resistances negligible.

Defining m_i as the solute distribution coefficient (concentration in organic/concentration in aqueous/polar organic phase), Prasad and Sirkar (1987) indicate that for similar membrane features, hydrophobic membranes yield a higher mass transfer coefficient k_{ov} if $m_i > 1$ and hydrophilic membranes produce a higher k_{ov} when $m_i < 1$. Prasad et al. (1990) reported mass transfer and breakthrough pressure results in hydrophobic and hydrophilic membranes with organic and aqueous/polar organic phases filling the pores with four different configurations: hydrophilic-organic, hydrophilic-aqueous, hydrophobic-organic and hydrophobic-aqueous. They recommend organic in pore for $m_i > 1$ and aqueous/polar organic in pore for $m_i < 1$. These results indicate the importance of controlling which phase fills the pores, which is achieved by setting the pressure difference between the phases. Prasad et al (1990) considers the following factors for selecting a suitable membrane: chemical/pH stability of membrane (higher in hydrophobic membranes), coupling requirements for enzyme immobilisation in extractive membrane reactors (hydrophilic membranes needed), pore size of membrane (small pore size results in low mass transfer coefficient but high breakthrough pressure), fouling from the process stream and precipitation in the pore liquid causing pore plugging.

3.3. Definition of the Problem

A typical mesh microcontactor can be represented as shown in Figure 3.2 where a liquid phase comes into direct contact with a fluid phase via the pores of the mesh. The wetting phase, *W*, is the phase that has an actual contact angle $\theta \leq 90°$ with the solid wall of the pore while the other one is the non-wetting phase, *NW*. In practice, these phases will most probably be partially wetting or not wetting, unless $\theta = 0°$ or $\theta = 180°$ respectively. Figure 3.2 shows the wetting phase filling the pores of the mesh although as it will be shown in section 3.4.2 the non-wetting phase can also stably fill the pores.

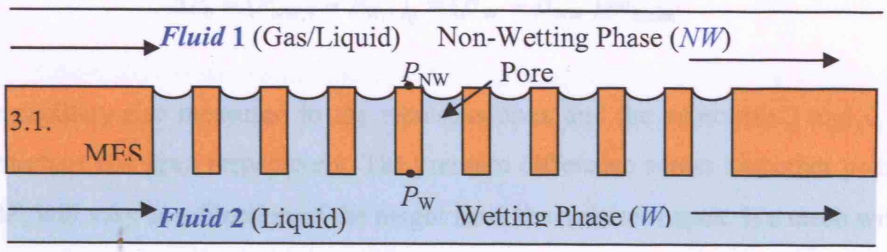

Figure 3.2. Schematic diagram of a mesh microcontactor.

A pore in the mesh can be considered as a capillary and the interface inside each pore can be modelled using the concept of capillary rise (Adamson and Gast, 1997). Figure 3.3 shows the classical capillary rise effect on the left and the corresponding situation in a cylindrical pore of a mesh on the right.

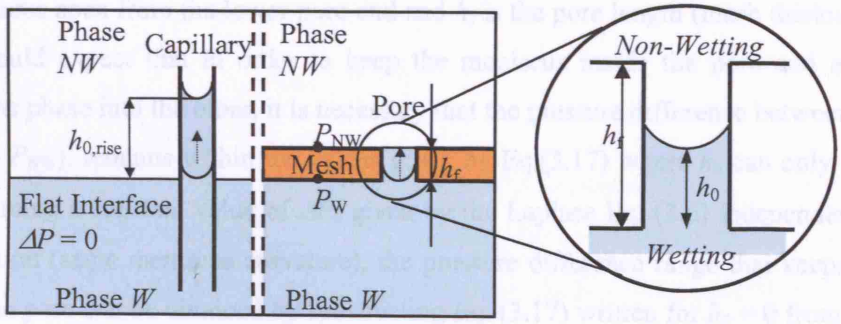

Figure 3.3. Capillary rise, a) single capillary on the left and b) pore of a mesh microcontactor.

If a capillary is introduced in a two-phase system the interface inside the capillary becomes curved and its shape depends on the contact angle of the phases with the solid wall, θ, the capillary geometry and gravity. Initially, the interface is not in equilibrium since the pressure in each side of the interface is the same and it is known that the pressure difference across a curved interface in equilibrium is given by the Laplace Eq. (3.6), which applies for *each point at the interface* (Adamson and Gast, 1997). As a consequence, the meniscus rises inside the capillary until this pressure difference is satisfied. The meniscus apex reaches the equilibrium height $h_{0,\text{rise}}$ with respect to the "flat interface" and the pressure difference across the meniscus apex, ΔP_0, found by Eq. (3.6), is also given by Eq. (3.16).

$$\Delta P_0 = \left(P_{\text{NW,I}} - P_{\text{W,I}}\right)_0 = (\rho_{\text{W}} - \rho_{\text{NW}})gh_{0,.\text{rise}} \tag{3.16}$$

$h_{0,\text{rise}}$ is the capillary rise measured to the meniscus apex and the subscripts I and 0 refer to meniscus interface and apex respectively. The pressure difference across any other point of the interface, ΔP, will vary as a function of the height from the meniscus apex. If a mesh with pores separates the two phases (right side in Figure 3.3), the pressure in each phase can be independently modified. The two phases are only in contact via the menisci inside the pores, which are assumed to be identical to each other. Pressure changes in one of the phases (P_{NW} or P_{W}) will move the meniscus in the direction that makes the pressure difference across the meniscus equal to that given by the Laplace equation, Eq. (3.6). In particular, the pressure difference across the meniscus apex is:

$$\Delta P_0 = \left(P_{\text{NW,I}} - P_{\text{W,I}}\right)_0 = (P_{\text{NW}} - P_{\text{W}}) + (\rho_{\text{W}} - \rho_{\text{NW}})gh_0 + \rho_{\text{NW}}\, gh_{\text{f}} \tag{3.17}$$

where P_{NW} and P_{W} are the pressures in each phase at the mesh surface (see Figure 3.3), h_0 is the height of the meniscus apex from the lower pore end and h_{f} is the pore length (mesh thickness). Therefore, one would expect that in order to keep the meniscus inside the pore and avoid breakthrough of one phase into the other, it is necessary that the pressure difference between the two phases, $(P_{\text{W}} - P_{\text{NW}})$, remains within the values given by Eq.(3.17) where h_0 can only vary from 0 to h_{f}. Assuming a constant value of ΔP_0 given by the Laplace Eq. (3.6) independent of the meniscus position (same meniscus curvature), the pressure difference range that keeps the meniscus within the pore can be obtained by substracting Eq. (3.17) written for $h_0 = 0$ from that written for $h_0 = h_{\text{f}}$.

$$(P_{\text{NW}} - P_{\text{W}})_{\text{W end}} - (P_{\text{NW}} - P_{\text{W}})_{\text{NW end}} = (\rho_{\text{W}} - \rho_{\text{NW}})gh_{\text{f}} \tag{3.18}$$

Considering pore lengths of $h_f = 200$ μm in a water-air system, the available range of pressure difference across the phases to avoid breakthrough is only 2 Pa. However, as it will be shown in the next section, ΔP_0 can vary inside the pores within a much larger range due to contact angle hysteresis and change of the solid wall inclination angle at the pore ends, which influences both apparent contact angle and actual contact angle via an effect on line tension. The meniscus shape, area and its stability range are analysed below.

3.4. Stability Model in Axisymmetric Cylindrical and Tapered Pores

3.4.1. Meniscus Shape and Area in Cylindrical and Tapered Pores

The pressure difference across the meniscus and the pore geometry define the meniscus shape and therefore the contact area between phases. Pressure difference at any point of the meniscus surface, $\Delta P = P_{NW,I} - P_{W,I}$ can be expressed as a function of the pressure difference across the meniscus apex plus a hydrostatic term,

$$\Delta P = \Delta P_0 \pm (\rho_W - \rho_{NW}) \cdot g \cdot y \tag{3.19}$$

where y is the height from the meniscus apex to the point considered (+ for concave and – for convex meniscus). In order to find ΔP from Eq. (3.6) it is necessary to know the two radii of curvature R_1 and R_2 that describe the curved surface at any point. A cylindrical or tapered pore with circular cross section (conical) is represented in Figure 3.4 where r_l and r_s are the radii of the large and small pore openings respectively and ϕ_{Int} is the solid wall inclination at the three-phase contact line in the interior of the pore. The apparent contact angle is defined in general by Eq. (3.20).

$$\theta_{App} = \theta + \phi \tag{3.20}$$

When the wetting phase is at the large pore opening side, the apparent contact angle of the meniscus at the interior of the pore is $\theta_{App,Int} = \theta - |\phi_{Int}|$ and when the wetting phase is at the small pore opening side it is $\theta_{App,Int} = \theta + |\phi_{Int}|$. Spontaneous capillary rise (negative critical filling pressure) occurs when $\theta_{App,Int} < 90°$. This implies that a non-wetting phase ($\theta > 90°$) may spontaneously rise in a tapered capillary from large to small pore opening, while a wetting phase ($\theta < 90°$) may not rise from small to large opening depending on ϕ_{Int}. Therefore, we define as an *apparent wetting phase (W)* that with $\theta_{App,Int} < 90°$ and an *apparent non-wetting phase*

(NW) that with $\theta_{App,Int} > 90°$. Unless otherwise stated, in the present work, the contact angle θ refers to the *apparent wetting phase* and this phase is considered to be underneath the mesh in both configurations shown in Figure 3.4 although a parallel analysis applies when the *apparent non-wetting phase* is underneath the mesh. The pore radius at any point is given by Eq. (3.21) depending on whether the lower pore end has the large or small opening respectively.

$$\begin{aligned} r &= r_l + h\tan\phi_{Int} \qquad (\phi_{Int}\text{ negative}) \\ r &= r_s + h\tan\phi_{Int} \qquad (\phi_{Int}\text{ positive}) \end{aligned} \tag{3.21}$$

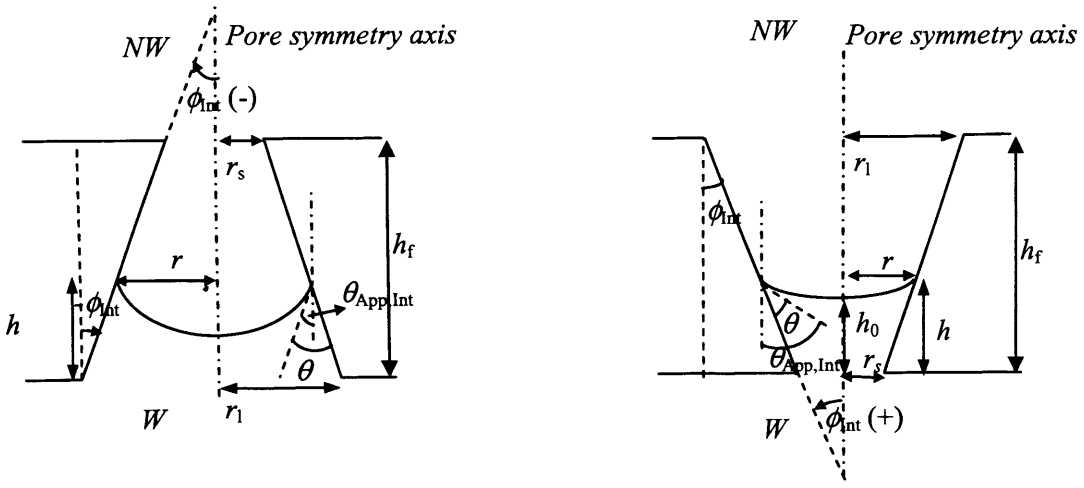

Figure 3.4. Geometrical characteristics of tapered pores.

The meniscus profile in an axisymmetric pore under gravity influence can be found numerically following the process described in Appendix 3A and results are shown in Figure 3.5 as a function of the Bond number, *Bo*, for a cylindrical pore (ϕ_{Int} = 0°, and according to Eq. (3.9) there is no line tension effect) with contact angle θ= 0°. The *Bo* is given by

$$Bo = \frac{(\rho_W - \rho_{NW})gr_s^2}{\gamma} \tag{3.22}$$

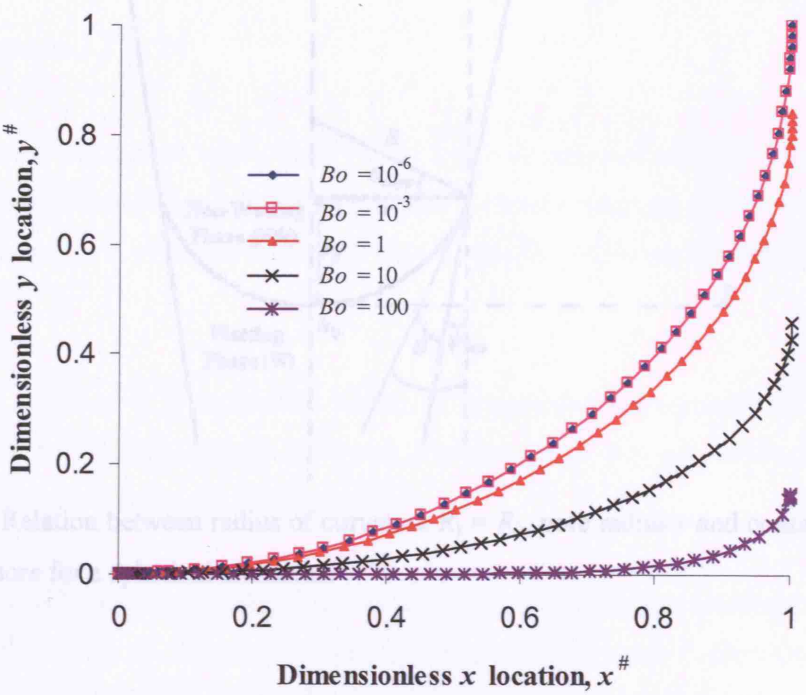

Figure 3.5. Meniscus profiles in a cylindrical pore for different *Bo* numbers at zero contact angle.

As Figure 3.5 shows, spherical profiles are obtained for $Bo << 1$, as expected. For a fluid-liquid system with low interfacial tension and large density difference, γ= 0.001 N/m and $(\rho_{NW} - \rho_W)$ = 5000 kg/m^3, in pores with diameters smaller than d = 90 μm, $Bo < 0.1$ and the meniscus shape is very close to spherical. For fluid pairs with larger interfacial tension or smaller density difference even larger pores would give spherical menisci. This same analysis can be applied to find the meniscus profile at the pore mouth at any apparent contact angle given by Eq. (3.21). Therefore, at low *Bo* the system is not influenced by gravity and since $\Delta P = \Delta P_0$ at every point of the meniscus (see Eq. (3.19)) a constant curvature describes the whole meniscus, which in cylindrical or tapered pores results in a spherical cap meniscus ($R_1 = R_2 = R = r/\cos\theta_{App}$). For a tapered pore, Laplace Eq. (3.6) in dimensionless form becomes,

$$\Delta P^{\#} = P_{NW}^{\#} - P_W^{\#} = \frac{r_s \Delta P}{\gamma} = \frac{2\cos\theta_{App}}{r^{\#}} \tag{3.23}$$

where $\Delta P^{\#}$ is the dimensionless pressure difference and $r^{\#} = r/r_s$ is the dimensionless pore radius at a given location inside the pore.

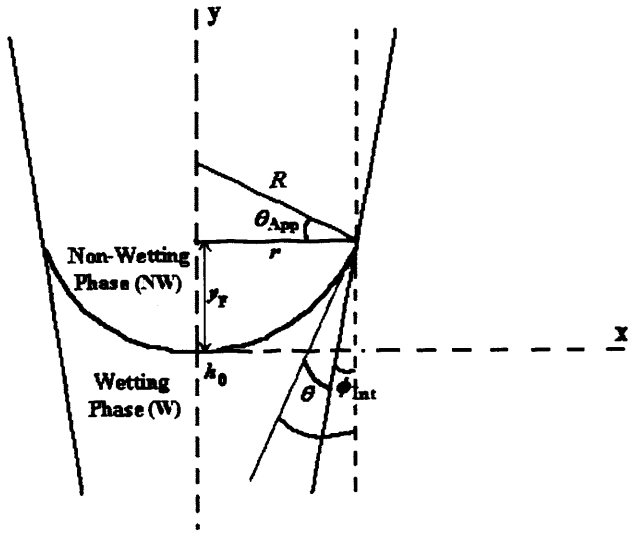

Figure 3.6. Relation between radius of curvature $R_1 = R_2$, pore radius r and contact angle θ in a cylindrical pore for a spherical meniscus.

The meniscus area, A, can be calculated from Eq. (3.24), which is applicable to any surface generated by the revolution of a 2D profile (Bronshtein and Semendyayev, 1997). This equation can also be used when the meniscus is not spherical due to gravity. For a spherical meniscus where the apex is at ($y = 0$, $x = 0$), $y = R-(R^2-x^2)^{1/2}$. The limits in Eq. (3.24) are $y_0 = 0$ and $y_F = R - (R^2 - r^2)^{1/2}$. Taking into account that $\cos\theta_{App} = r/R$ and $(\cos^2\theta_{App} + \sin^2\theta_{App}) = 1$, Eq. (3.24) results in Eq. (3.25), where $A^{\#} = A/r_s^2$.

$$A = 2 \cdot \pi \cdot \int_{y_0}^{y_F} x \cdot \sqrt{1 + (dx/dy)^2}\, dy \tag{3.24}$$

$$A^{\#} = 2\pi \frac{r^{\#2}}{\cos^2 \theta_{App}} \left(1 - \sin \theta_{App}\right) \tag{3.25}$$

Eq. (3.25) can be written as a function of the pressure difference across the interface, $\Delta P^{\#}$, obtaining Eq. (3.26), where the limits of $\Delta P^{\#}$ are given by $-\Delta P^{\#}_{B,W} \leq \Delta P^{\#} \leq \Delta P^{\#}_{B,NW}$.

$$A^{\#} = \frac{8\pi}{\Delta P^{\#2}} \cdot \left(1 - \sqrt{1 - \left(r^{\#} \Delta P^{\#} / 2\right)^2}\right) \tag{3.26}$$

3.4.2. Meniscus Position and Stability Range in Cylindrical and Tapered Pores

The meniscus is considered stable when for the available range of pressure difference between the two phases the meniscus remains in the pore without breakthrough of one phase into the other. In the study of meniscus stability within a pore the following considerations are taken into account:

a) Pores are supposed to have uniform surface roughness and heterogeneity so that the actual contact angle is uniform along the pore wall. For non-planar surfaces, wetting properties are poorly understood (Wapner and Hoffman, 2002).

b) The effect of gravity on static pressure variation along the pore and meniscus shape is neglected although Eq. (3.17) could be applied to take it into account. A spherical cap meniscus is assumed although the concepts discussed below can be applied to a non-spherical cap meniscus (see Appendix 3A for calculating the pressure difference ΔP across a meniscus under the effect of gravity).

c) Dynamic effects on breakthrough pressures both inside and outside the pore are neglected since they are generally small compared to surface tension forces.

d) For meshes with perfectly flat surfaces, at the non-wetting pore end the solid wall inclination changes from ϕ_{Int} to $\phi_{max} = 90°$ while at the wetting pore end it changes from ϕ_{Int} to $\phi_{min} = -90°$ This implies that at the pore ends, while the pore radius remains constant an extra change of the apparent contact angle θ_{App} is allowed (*edge effect*), $\pm 90° + |\phi_{Int}|$ (+ meniscus at small pore opening and – meniscus at large pore opening) when the apparent wetting phase is at the large pore opening and $\pm 90° - |\phi_{Int}|$ when this phase is at the small pore opening (+ meniscus at large pore opening and – meniscus at small pore opening). According to Adam (1948) this phenomenon occurs independently of the geometry of the corners at micro-scale (sharp, gradual or imperfect corners). However, smoothness of the pore ends may affect contact angle hysteresis. When pore ends are significantly rounded a similar approach to that presented by Purcell (1949) can be applied to calculate breakthrough pressures (see Appendix 3B).

e) There are two mechanisms by which one phase can break through into the other,

1. *Breakthrough by spreading,* when the apparent contact angle becomes equal to the sum of advancing contact angle and maximum solid wall inclination,

$$\theta_{App,max} = \theta_A + \phi_{max} < 180^\circ \tag{3.27}$$

The wetting phase breaks through into the non-wetting phase by spreading out horizontally along the mesh.

2. *Breakthrough by maximum curvature*, when

$$\theta_{App,max} = \theta_A + \phi_{max} \geq 180^\circ \tag{3.28}$$

The meniscus at the non-wetting pore opening will reach its maximum curvature of hemispherical shape (θ_{App} = 180°), which can accommodate the largest pressure difference between the two phases. Beyond this point, the wetting phase breaks through by bubble/droplet formation. Breakthrough by maximum curvature is the common mechanism of breakthrough of a non-wetting phase in a wetting phase since a hemispherical meniscus (θ_{App} = 0°) is reached in all cases apart from those which do not satisfy Eq. (3.29) (e.g. for a "flat mesh" when $\theta_R > 90^\circ$, which is possible for an apparent wetting phase if ϕ_{Int} negative). The condition for *breakthrough by maximum curvature* of the non-wetting phase is,

$$\theta_{App,min} = \theta_R + \phi_{min} \leq 0^\circ \tag{3.29}$$

Based on the above discussion, the meniscus position can be determined knowing pore geometry (ϕ_{Int}) and contact angle hysteresis (θ_A and θ_R) as shown in Table 3.1.

Condition	Meniscus Position
$\max(0^\circ, \theta_R - 90^\circ) < \theta_{App} < \theta_R + \phi_{Int}$	Wetting pore end
$\theta_R + \phi_{Int} < \theta_{App} < \theta_A + \phi_{Int}$	Any part of the pore
$\theta_A + \phi_{Int} < \theta_{App} < \min(180^\circ, \theta_A + 90^\circ)$	Non-wetting pore end

Table 3.1. Meniscus position as a function of apparent contact angle θ_{App}.

Eq. (3.23) can be used with the values of θ_{App} of Table 3.2 to calculate the critical filling and breakthrough pressures of each phase ($r^{\#}$ takes the values of $r^{\#}_s$ and $r^{\#}_1$ for tapered pores). The results are summarised in Table 3.2 for meshes with perfectly flat meshes ($\phi_{max} = -\phi_{min} = 90°$).

Critical Filling/Breakthrough pressure	Phase at large opening (See Figure 3.4)	Radius $r^{\#}$	θ_{App}	ϕ_{Int} [3] sign
$\Delta P^{\#}_{C,NW}$ [1]	W	$r^{\#}_s$	$\max(0°, \theta_R + \phi_{Int})$	-
$-(\Delta P^{\#}_{C,W})$	W	$r^{\#}_1$	$\theta_A + \phi_{Int}$	-
$\Delta P^{\#}_{C,NW}$	NW	$r^{\#}_s$	$\theta_R + \phi_{Int}$	+
$-(\Delta P^{\#}_{C,W})$	NW	$r^{\#}_1$	$\theta_A + \phi_{Int}$	+
$\Delta P^{\#}_{B,NW}$	W	$(A^{(2)} \geq 0)\ r^{\#}_s$	$\max(0°, \theta_R + \phi_{Int})$	-
		$(A^{(2)} < 0)\ r^{\#}_1$	$\max(0°, \theta_R - 90°)$ [4]	
$-(\Delta P^{\#}_{B,W})$	W	$r^{\#}_s$	$\min(180°, \theta_A + 90°)$	-
$\Delta P^{\#}_{B,NW}$	NW	$r^{\#}_s$	$\max(0°, \theta_R - 90°)$	+
$-(\Delta P^{\#}_{B,W})$	NW	$r^{\#}_1$	$\min(180°, \theta_A + 90°)$	+

(1) When $\theta_{App} = \theta_R + \phi_{Int} \leq 0°$, filling of the pores is immediately followed by breakthrough of the NW phase. If $\theta_{App} > 0°$ pore filling is immediately followed by breakthrough only if $\Delta P^{\#}_{C,NW} \geq \Delta P^{\#}_{B,NW}$, i.e. $A \geq 0$.

(2) $A = 2\cos(\max(0°, \theta_R + \phi_{Int}))/r^{\#}_s - 2\cos(\max(0°, \theta_R - 90°))/r^{\#}_1$.

(3) ϕ_{Int} sign indicates if the values of ϕ_{Int} are negative (-) or positive (+).

(4) θ_R can be larger than 90° even with $\theta_{App} < 90°$ (apparent wetting phase).

Table 3.2. Values of the radius and apparent contact angle used in Eq. (3.23) to calculate critical filling/breakthrough pressures in a circular cross section pore.

The negative sign in $-(\Delta P^{\#}_{B,W})$ and $-(\Delta P^{\#}_{C,W})$ is because these are defined by Eq. (3.2) and (3.4) while Eq. (3.23) gives the value of a pressure difference $P^{\#}_{NW} - P^{\#}_{W}$. The sign of ϕ_{Int} is defined according to Figure 3.4. For the case of the W phase at the large pore opening $\Delta P^{\#}_{C,NW}$ is calculated at $\theta_{App} = 0$ if $\theta_R \leq |\phi_{Int}|$ and at $\theta_{App} = \theta_R + \phi_{Int}$ if $\theta_R > |\phi_{Int}|$. Also in this case the available pressure difference range at the large pore opening is completely contained within that at the small pore opening when $A > 0$ (see Table 3.2) in which case $\Delta P^{\#}_{B,NW} = \Delta P^{\#}_{C,NW}$. The critical filling pressure of a phase, depends on the side where it is placed, because of the different apparent contact angle but not the radius. When the wetting phase is at the large pore opening (Figure 3.4a), the meniscus is unstable in the pore interior. This is due to an overlap between the ranges of pressure difference that the meniscus can cope with at each pore end

(*pressure difference overlap*). As soon as the meniscus enters the pore it moves spontaneously to the other end. Hence the critical filling pressure is always determined by the pore radius of meniscus entry. When the non-wetting phase is at the large pore opening (Figure 3.4b), the meniscus is stable in the pore interior. Thus, the critical filling pressure is determined by the radius of the pore opening opposite the meniscus entry. This is so because when the *W* phase is at the large pore opening there is a negative pressure difference change when the meniscus moves from one pore end to the other, being a geometry-driven spontaneous motion. However, when the *W* phase is at the small pore opening, an increase in the pressure difference of the phase moving inside the pore is required to take the meniscus from one pore end to the other.

According to Table 3.2, breakthrough pressures are always positive if $\phi_{max} \geq 90°$ and $\phi_{min} \leq -90°$ while critical filling pressure can be negative for wetting phase in flat meshes ($\phi_{max} = 90°$ and $\phi_{min} = -90°$). Mason and Marrow (1994) made the same observation for the displacement pressure in a solid ring or doughnut shape pore. Figure 3.7 represents a pore with the meniscus at the breakthrough positions, showing also the corresponding θ_{App}'s. Meniscus positions inside the pore in this case are unstable as discussed above.

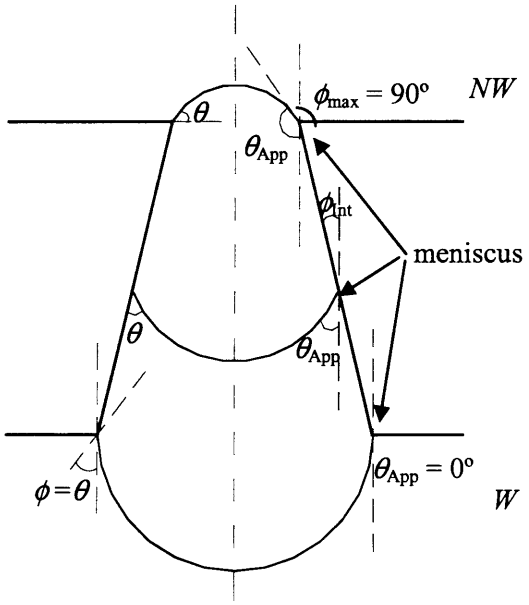

Figure 3.7. Meniscus breakthrough positions and shapes along with corresponding apparent contact angle changes. Note that the contact angle θ is constant.

According to Eq. (3.9) the contribution of the line tension to the contact angle θ depends on solid wall inclination angle ϕ at the pore ends (no contribution at $\phi = 0°$ and maximum

contribution at ϕ = 90°). In addition, imperfections at the pore ends can increase the local curvature of the three-phase contact line and accentuate the line tension effect modifying the contact angle and its hysteresis. A positive line tension σ results in an increase in θ as ϕ increases and a decrease in θ as ϕ decreases, which leads to an increase in the maximum and a decrease in the minimum apparent contact angle. This results in a larger available range of pressure difference for breakthrough. Conversely, a negative line tension σ results in a decrease of the available range of pressure difference for breakthrough. This effect of the line tension on breakthrough has not been examined yet. It is worth noting that no line tension effect exists when ϕ = 0° or $r \rightarrow \infty$, corresponding to the interior of vertical wall pores or large menisci.

Illustrating Examples

i) Cylindrical pore (ϕ_{Int} = 0°)

A cylindrical pore and a fluid pair with θ_A = 60°, θ_R = 30° is considered. Figure 3.8 shows the dimensionless meniscus area and position versus the dimensionless pressure difference between the phases considering that the apparent contact angle can change from 0° at the wetting pore end to θ_A + 90°= 150° at the non-wetting pore end (see Table 3.1). At contact angles $\theta_R < \theta < \theta_A$, the meniscus is located at any part within the pore, at $\theta_{App} < \theta_R$ the meniscus is pinned at the wetting end and at $\theta_{App} > \theta_A$ at the non-wetting end. As the apparent contact angle gets closer to 0° at the wetting end, small changes in the pressure difference modify the meniscus area significantly.

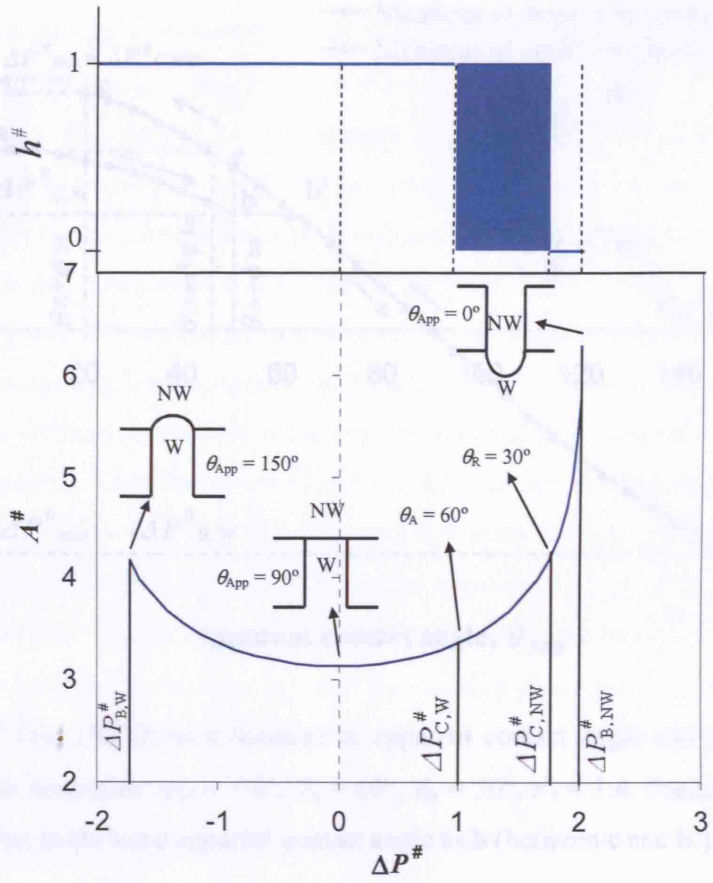

Figure 3.8. Dimensionless meniscus height $h^{\#}$ and area $A^{\#}$ area given as a function of the pressure difference across the meniscus $\Delta P^{\#} = P^{\#}_{NW}$-$P^{\#}_{W}$. Breakthrough and critical filling pressures are also indicated.

ii) Tapered pores

Tapered pores with ϕ_{Int} = -10° and ϕ_{Int} = 10° are considered next as those represented by Figure 3.4a (wetting phase on the large pore side) and Figure 3.4b (wetting phase on the small pore side) respectively. The properties of the system are: θ_A = 60°, θ_R = 30°, $r^{\#}_s$ = 1 and $r^{\#}_l$ = 1.4 ($h^{\#}_f$ = 2.27). The change in the dimensionless pressure difference between the two phases as a function of the apparent contact angle is shown in Figure 3.9 for ϕ_{Int} = -10° and in Figure 3.10 for ϕ_{Int} = 10°.

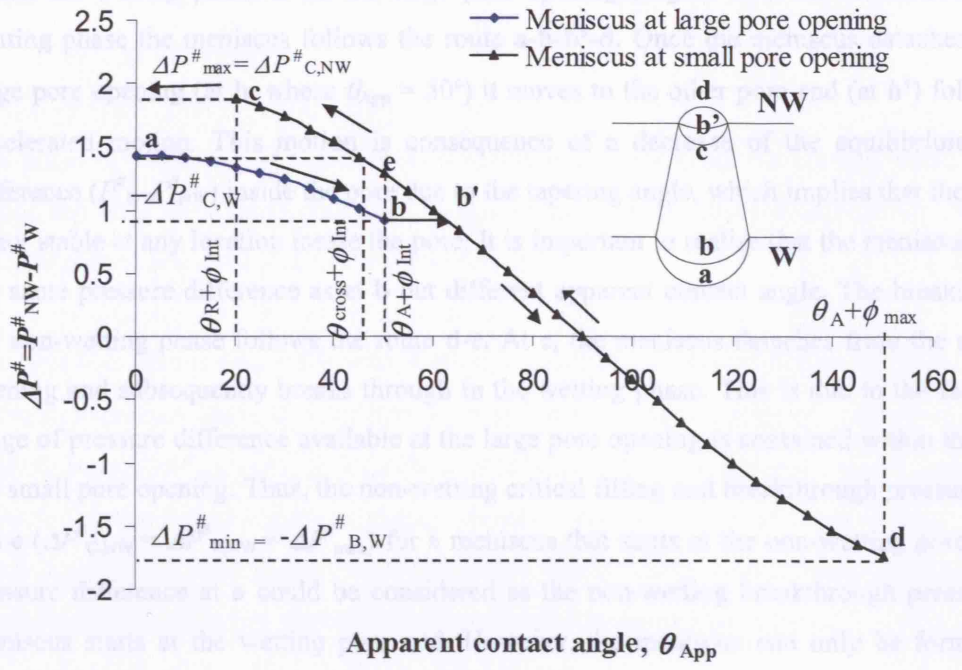

Figure 3.9. $\Delta P^{\#}$ (Eq. (3.23)) as a function of apparent contact angle and pore position in a tapered pore with properties: ϕ_{Int} = -10°, θ_A = 60°, θ_R = 30°, $r^{\#}_1$ = 1.4. Position **e** occurs at the small pore opening at the same apparent contact angle as **b** (between **c** and **b'**).

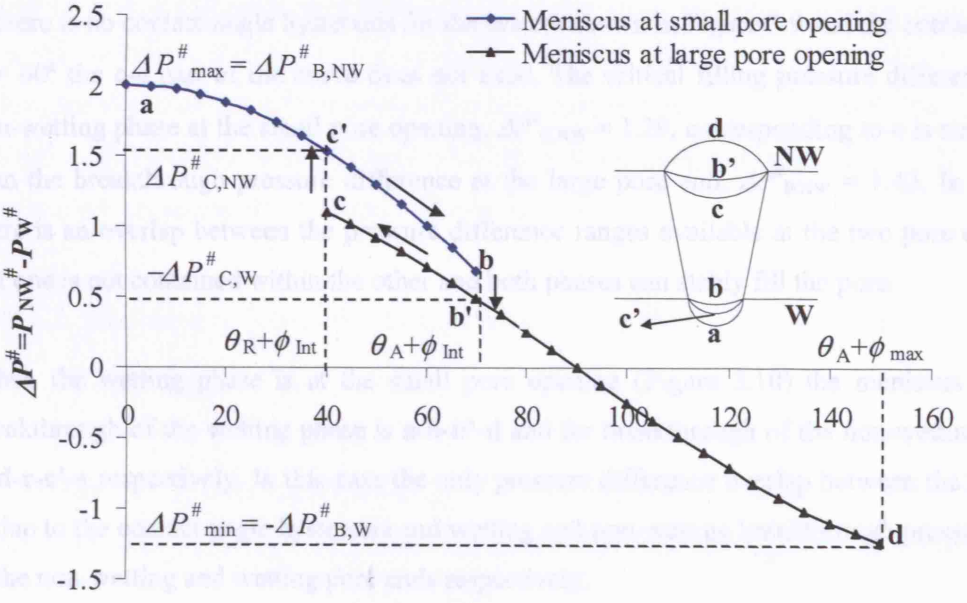

Figure 3.10. $\Delta P^{\#}$ (Eq. (3.23)) as a function of apparent contact angle and pore position in a tapered pore with properties: ϕ_{Int} = 10°, θ_A = 60°, θ_R = 30°, $r^{\#}_1$ = 1.4.

When the wetting phase is on the large pore opening (Figure 3.9), for breakthrough of the wetting phase the meniscus follows the route **a-b-b'-d.** Once the meniscus detaches from the large pore opening (at **b,** where $\theta_{App} = 50°$) it moves to the other pore end (at **b'**) following an accelerated motion. This motion is consequence of a decrease of the equilibrium pressure difference ($P^{\#}_{W}$-$P^{\#}_{NW}$) inside the pore due to the tapering angle, which implies that the meniscus is not stable at any location inside the pore. It is important to realise that the meniscus at **b'** has the same pressure difference as at **b** but different apparent contact angle. The breakthrough of the non-wetting phase follows the route **d-c.** At **c**, the meniscus detaches from the small pore opening and subsequently breaks through in the wetting phase. This is due to the fact that the range of pressure difference available at the large pore opening is contained within the range at the small pore opening. Thus, the non-wetting critical filling and breakthrough pressures are the same ($\Delta P^{\#}_{C,NW} = \Delta P^{\#}_{B,NW} = \Delta P^{\#}_{max}$) for a meniscus that starts at the non-wetting pore end. The pressure difference at **a** could be considered as the non-wetting breakthrough pressure if the meniscus starts at the wetting pore end. However, the meniscus can only be formed at the wetting pore end by priming the mesh with the non-wetting phase and only if ($\theta_A + \phi_{Int}$) > 90°, since a negative pressure difference ($P^{\#}_{NW}$-$P^{\#}_{W}$) is required to drain out the non-wetting phase through the pores. If it is desirable to fill the pores with a non-wetting phase (e.g. for reducing mass transfer resistances) it is more suitable to place the wetting phase on the side of the small opening.

If there is no contact angle hysteresis for the system shown in Figure 3.9 and the contact angle is $\theta = 60°$ the **c-e** part of the curve does not exist. The critical filling pressure difference of the non-wetting phase at the small pore opening, $\Delta P^{\#}_{C,NW} = 1.29$, corresponding to **e** is now smaller than the breakthrough pressure difference at the large pore end, $\Delta P^{\#}_{B,NW} = 1.43$. In this case, there is an overlap between the pressure difference ranges available at the two pore ends (**e-b**) but one is not contained within the other and both phases can stably fill the pore.

When the wetting phase is at the small pore opening (Figure 3.10) the meniscus route for breakthrough of the wetting phase is **a-b-b'-d** and for breakthrough of the non-wetting phase it is **d-c-c'-a** respectively. In this case the only pressure difference overlap between the pore ends is due to the contact angle hysteresis and wetting and non-wetting breakthrough pressures occur at the non-wetting and wetting pore ends respectively.

The available range of pressure difference for stable menisci in both systems shown in Figure 3.9 and Figure 3.10 are very similar, ($\Delta P^{\#}_{B,NW} + \Delta P^{\#}_{B,W}$)= 3.161 and 3.237 respectively. However, the individual values of $\Delta P^{\#}_{B,NW}$ and $\Delta P^{\#}_{B,W}$ are evidently different.

3.4.3. Wetting Conditions for Maximum Stability against Breakthrough

The following analysis helps to decide in which side of the mesh the wetting phase should be placed and what the wetting properties for maximum meniscus stability should be. This enables the selection of suitable mesh materials or coatings.

For cylindrical pores ($\phi_{Int} = 0°$) with limiting solid wall inclination angles $-90° \leq \phi \leq 90°$ (*flat meshes*), a contact angle $\theta = 90°$ (or $\theta_A = 90°$ if hysteresis is present) produces the largest stability range ($\Delta P^{\#}_{max} - \Delta P^{\#}_{min}$) = ($\Delta P^{\#}_{B,NW} + \Delta P^{\#}_{B,W}$) = 4, since the ϕ change at each pore end leads to hemispherical meniscus shapes (*breakthrough by maximum curvature* at both pore ends). Any other contact angle θ leads to smaller stability range since at one of the pore ends the hemispherical shape is not reached and *breakthrough by spreading* occurs.

For tapered pores, the stability range also depends on the wall inclination and the sizes of the two pore openings. As seen in the previous section, when the wetting *W* phase is at the large pore opening, the available pressure difference ranges at both pore ends overlap. This pressure range overlap is also a function of the wetting conditions, θ, for a specific pore geometry and at certain contact angle θ_{cross}, the pressure difference range at the large pore end is completely contained within the pressure difference range at the small pore end (see Figure 3.9). In this case, for maximum stability it is desirable to have the meniscus at the small pore opening. Below, the available range of pressure difference in tapered pores is considered when there is no contact angle hysteresis, although hysteresis can be easily included by substituting $\theta = \theta_A$ if the meniscus advances and $\theta = \theta_R$ if the meniscus recedes.

3.4.3.1. Apparent Non-Wetting Phase ($\theta \leq 90° - |\phi_{Int}|$) at the Large Pore Opening

In this case, $\Delta P^{\#}_{max} = \Delta P^{\#}_{B,NW}$ and $\Delta P^{\#}_{min} = -\Delta P^{\#}_{B,W}$ are always reached at the small and large pore openings respectively. Using Table 3.2 the stability range ($\Delta P^{\#}_{max} - \Delta P^{\#}_{min}$) is calculated ($r^{\#}_s = 1$).

$$\left(\Delta P^{\#}_{max} - \Delta P^{\#}_{min}\right) = \frac{2}{r_s^{\#}} - \frac{2\cos(\theta + 90°)}{r_l^{\#}} = 2\left(\frac{1}{r_s^{\#}} - \frac{\cos(\theta + 90°)}{r_l^{\#}}\right) \tag{3.30}$$

3.4.3.2. Apparent wetting phase ($\theta \leq 90° + |\phi_{Int}|$) at large pore Opening

For certain pore geometries (ϕ_{Int}) and wetting properties (θ), the *apparent* wetting phase may always be on the large pore opening irrespective of which side the *real* wetting phase is placed. For example for $\theta = 80°$ and $\phi_{Int} = 20°$, $\theta_{App,int} = (\theta + \phi_{Int}) = 60°$ when placing the wetting phase on the large pore opening and $\theta_{App,int} = (\theta + \phi_{Int}) = 100°$ when placing the non-wetting phase on this side in which case it becomes the apparent wetting phase ($\theta_{App,int} = (\theta + \phi_{Int}) = 80°$ now when θ refers to the apparent wetting phase, $\theta = 100°$). In tapered pores in *flat meshes*, a contact angle of $\theta = 90°$, still produces hemispherical cap menisci at both pore ends ($\theta_{App} = 0°$ and $\theta_{App} = 180°$).

In this case, $\Delta P^{\#}_{max} = \Delta P^{\#}_{B,NW}$ is reached at either the small or large pore opening depending on the values of θ and ϕ_{Int}. $\Delta P^{\#}_{min} = -\Delta P^{\#}_{B,W}$ is always reached at the small pore opening. Using Table 3.2, the stability range ($\Delta P^{\#}_{max} - \Delta P^{\#}_{min}$) is calculated for three cases,

$$\left(\Delta P^{\#}_{max} - \Delta P^{\#}_{min}\right) = \max\left[2\cos(0), \frac{2}{r_1^{\#}}\cos(0)\right] - 2\cos(\theta + 90°) \qquad 0 < \theta \leq |\phi_{Int}| \tag{3.31}$$

$$\left(\Delta P^{\#}_{max} - \Delta P^{\#}_{min}\right) = \max\left[2\cos(\theta + \phi_{Int}), \frac{2}{r_1^{\#}}\cos(0)\right] - 2\cos(\theta + 90°) \qquad |\phi_{Int}| < \theta \leq 90° \tag{3.32}$$

$$\left(\Delta P^{\#}_{max} - \Delta P^{\#}_{min}\right) = \max\left[2\cos(\theta + \phi_{Int}), \frac{2}{r_1^{\#}}\cos(\theta - 90°)\right] - 2\cos(180°) \qquad 90° < \theta \leq 90° + |\phi_{Int}| \tag{3.33}$$

The first term in the max bracket represents the maximum value of $\Delta P^{\#}$ achievable at the small pore opening and the second the maximum value of $\Delta P^{\#}$ at the large pore opening. In certain cases, breakthrough can occur at both of these $\Delta P^{\#}$ values depending on the initial conditions as described earlier, but for the purpose of maximum stability calculations, the maximum of these two values is considered as $\Delta P^{\#}_{B,NW}$. The second right hand term in these equations represents the breakthrough pressure of the wetting phase, which always takes place at the small pore opening.

It can be seen in Eq. (3.31) that for $0 < \theta \leq |\phi_{Int}|$ both $\Delta P^{\#}_{max}$ and $\Delta P^{\#}_{min}$ are reached at the small pore end. Equating both terms inside the max brackets of Eq. (3.32) and (3.33), θ_{cross} is found.

$$\theta_{cross} = \arccos\left(\frac{1}{r_1^{\#}}\right) - \phi_{Int} \qquad \theta_{cross} \leq 90^{o} \tag{3.34}$$

$$\theta_{cross} = 180^{o} + \arctan\left[\frac{r_1^{\#}}{1/\cos\phi_{Int} + r_1^{\#}\tan\phi_{Int}}\right] \qquad 90^{o} < \theta_{cross} < 90^{o} + |\phi_{Int}| \tag{3.35}$$

At contact angles $\theta > \theta_{cross}$, $\Delta P^{\#}_{max}$ is reached at the large pore opening while at $\theta < \theta_{cross}$, $\Delta P^{\#}_{max}$ is reached at the small pore opening. In the latter case, maximum stability between the phases is obtained by pinning the meniscus at the small pore opening. θ_{cross} is always smaller than $90^{o}+|\phi_{Int}|$ because at larger contact angles than $90^{o}+|\phi_{Int}|$ the apparent wetting phase becomes the one at the small pore opening and the analysis of section 3.4.3.1 applies ($\Delta P^{\#}_{max}$ always takes place at the large pore opening if hysteresis is not considered). A mesh with $r^{\#}_{s}$ = 1, $h^{\#}_{f}$ = 10 and ϕ_{Int} = -10° ($r^{\#}_{1}$ = 2.76) and the wetting phase at the large pore opening is considered for illustration of the overlapping of the pressure difference at the two pore openings. Figure 3.11 represents the maximum and minimum values of $\Delta P^{\#}$ versus θ that are reached at both pore openings of this system. The ■ area represents the pressure difference range defined by the maximum and minimum values at the small pore opening and the □ area represents the equivalent range at the large pore opening. From Eq. (3.34) θ_{cross} = 78.8°. When θ < 78.8°, the pressure difference range available at the large pore opening (□ area) is contained within the pressure difference range available at the small pore opening (■ area). These ranges overlap only partly for θ > 78.8°.

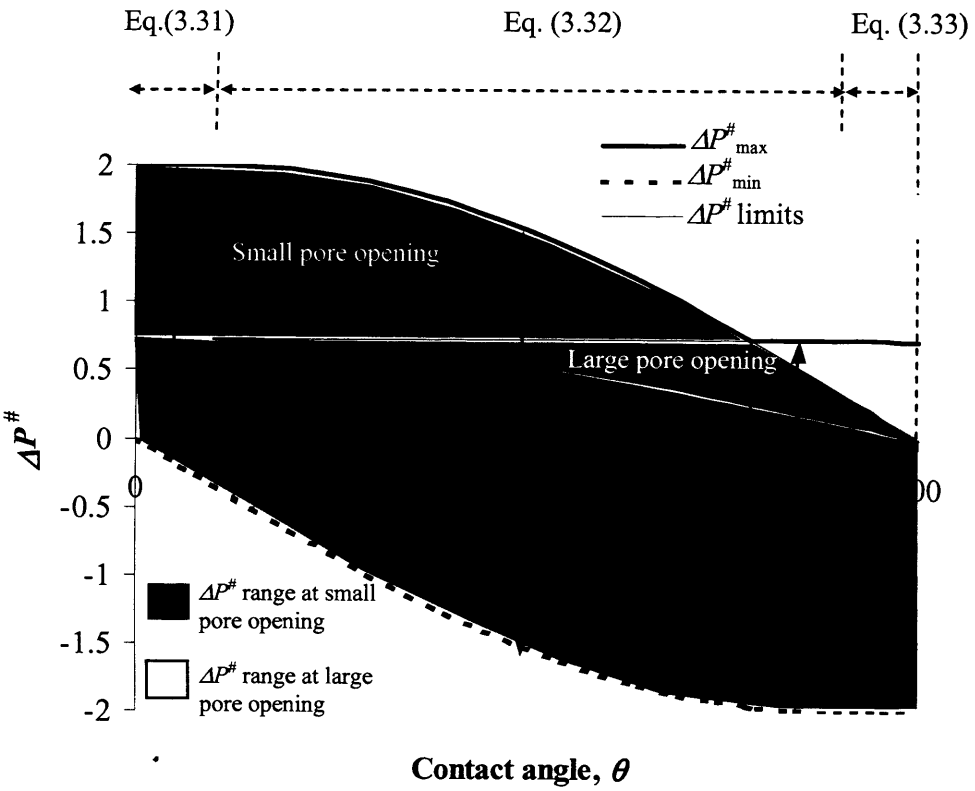

Figure 3.11. Pressure difference range at each pore end for $\phi_{Int} = -10°$, $r^{\#}_{s} = 1$ and $r^{\#}_{l} = 2.76$. The double-sided arrows (**a**, **b** and **c**) indicate maximum stability range for a specific contact angle.

From Figure 3.11 it is difficult to establish which contact angle θ produces the maximum stability range, ($\Delta P^{\#}_{max}$ - $\Delta P^{\#}_{min}$). This is calculated from Eqs. (3.31)-(3.33) by using either the first (if $\theta \leq \theta_{cross}$) or second (if $\theta > \theta_{cross}$) term inside the max brackets. The results can be seen in Figure 3.12. The dashed line at $\theta > \theta_{cross}$ shows the available pressure difference range at the small pore opening, which does not give the maximum stability range (e.g. **e** in Figure 3.12). The dashed line at $\theta < \theta_{cross}$ indicates the pressure difference range given by the maximum $\Delta P^{\#}$ at the large pore opening minus the minimum $\Delta P^{\#}$ at the small pore opening, $\Delta P^{\#}_{min}$ (e.g. **d** in Figure 3.12).

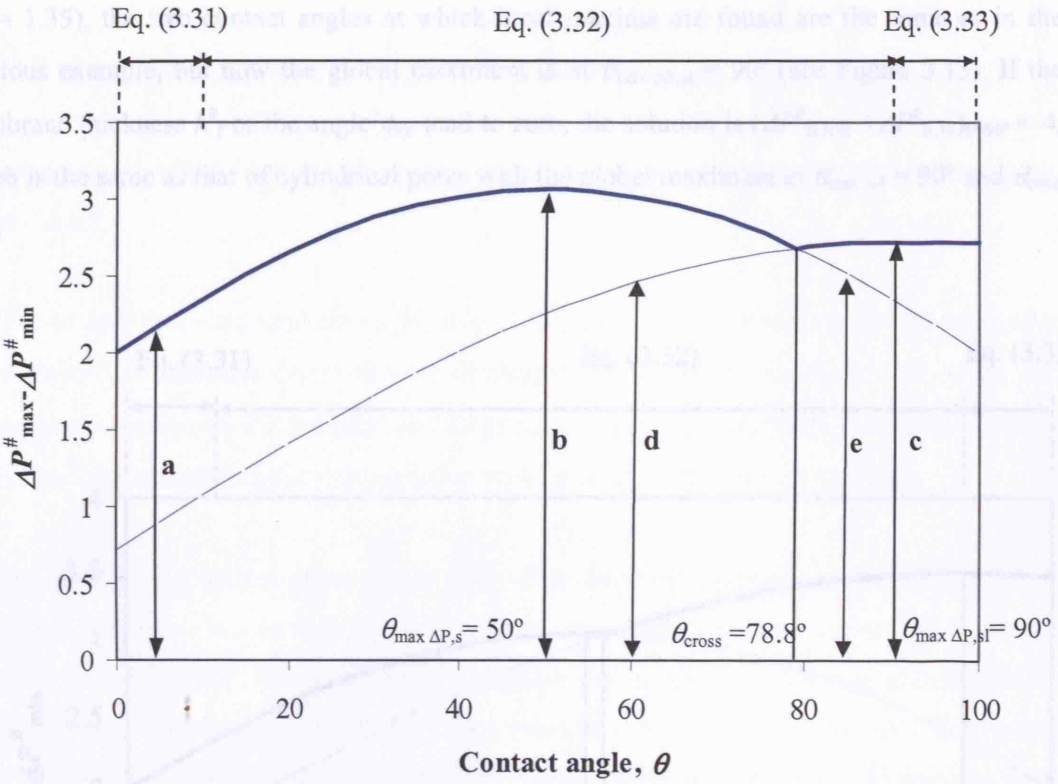

Figure 3.12. Line (——) indicates the maximum stability range, ($\Delta P^{\#}_{max}$-$\Delta P^{\#}_{min}$), as a function of contact angle θ for a mesh with properties ϕ_{Int} = -10°, $h^{\#}_{f}$ = 10, $r^{\#}_{1}$ = 2.76. The dashed line (– – –) indicates a) available pressure difference at the small pore opening for $\theta > \theta_{cross}$ and b) pressure difference range considering the maximum $\Delta P^{\#}$ at the large pore opening and the minimum $\Delta P^{\#}$ at the small pore opening.

Figure 3.12 shows two local maxima, one at 90° (at **c**) when both pore openings contribute to the pressure difference range and the other at 50° (at **b**) for which only the small pore contributes to the available range. These positions are also shown in Figure 3.11 for clarification. The values of θ at the two local maxima are found by differentiating ($\Delta P^{\#}_{max}$ - $\Delta P^{\#}_{min}$) with respect to the contact angle, $d(\Delta P^{\#}_{max} - \Delta P^{\#}_{min})/d\theta = 0$, yielding,

$$\theta_{max\ \Delta P,s} = \arctan\left(\frac{1-\sin\phi_{Int}}{\cos\phi_{Int}}\right) \quad for\ \theta < \theta_{cross}$$
$$\theta_{max\ \Delta P,sl} = 90° \quad for\ \theta \geq \theta_{cross} \tag{3.36}$$

In this example the global maximum is reached at $\theta = 50°$. If the thickness of the mesh is $h^{\#}_{f} = 2$ ($r^{\#}_{1} = 1.35$), the two contact angles at which local maxima are found are the same as in the previous example, but now the global maximum is at $\theta_{\max\ \Delta P,sl} = 90°$ (see Figure 3.13). If the membrane thickness $h^{\#}_{f}$ or the angle ϕ_{Int} tend to zero, the solution is $(\Delta P^{\#}_{B,NW} + \Delta P^{\#}_{B,W})_{\theta=90°} = 4$, which is the same as that of cylindrical pores with the global maximum at $\theta_{\max\ \Delta P} = 90°$ and $\theta_{cross} = 0°$.

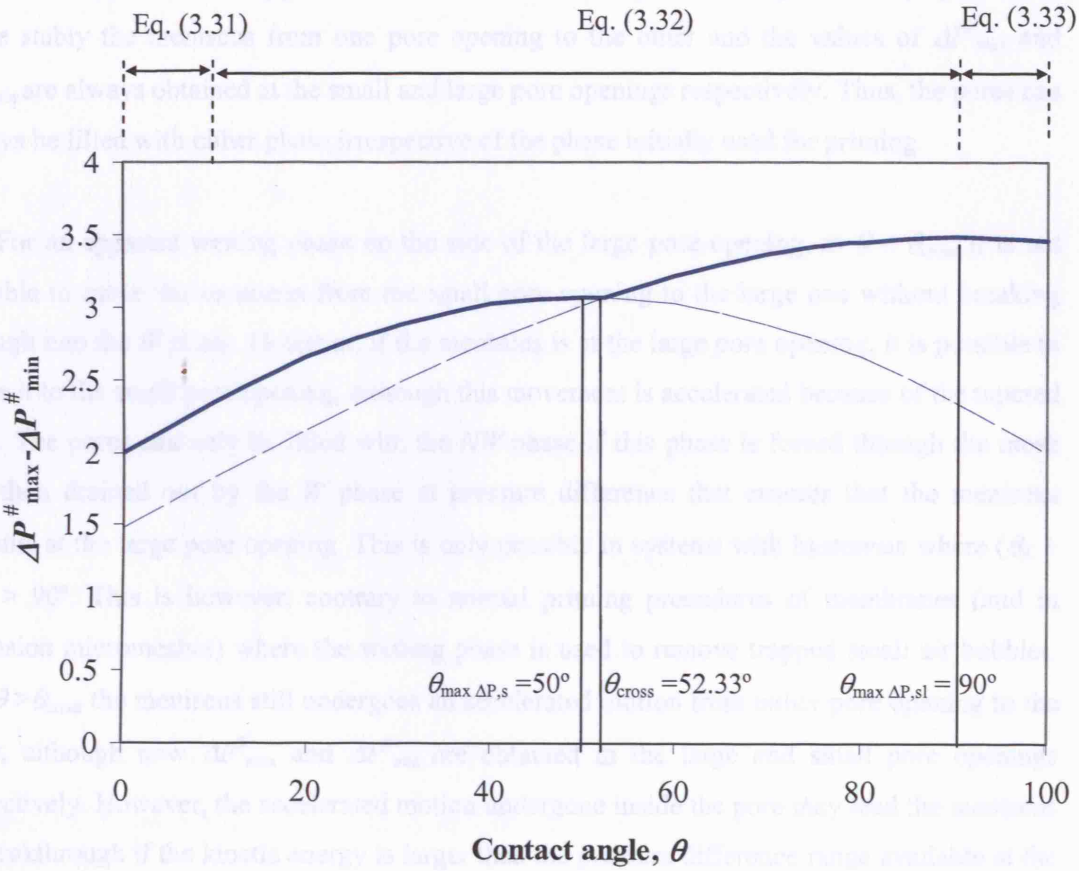

Figure 3.13. Maximum stability range, $(\Delta P^{\#}_{max} - \Delta P^{\#}_{min})$, as a function of contact angle θ for a mesh with properties $\phi_{Int} = -10°$, $h^{\#}_{f} = 2$, $r^{\#}_{1} = 1.35$.

A value of $\theta_{cross} > 90°$ implies that the global maximum of the stability range always is obtained at the small pore opening, since the value of $\theta_{\max\ \Delta P,sl}$ is always 90°, and occurs when,

$$r_1^{\#} \geq \frac{1}{\cos(90° + \phi_{Int})} \qquad (3.37)$$

Obtained from Eq. (3.34) or equivalently when,

$$h_f^{\#} \geq -\frac{1-\cos(90^\circ+\phi_{Int})}{\cos(90^\circ+\phi_{Int})\tan\phi_{Int}} \tag{3.38}$$

Summarising the effect of phase placement on breakthrough characteristics, the following can be concluded:

A. For an apparent wetting phase on the side of the small pore opening it is always possible to move stably the meniscus from one pore opening to the other and the values of $\Delta P^{\#}_{max}$ and $\Delta P^{\#}_{min}$ are always obtained at the small and large pore openings respectively. Thus, the pores can always be filled with either phase irrespective of the phase initially used for priming.

B. For an apparent wetting phase on the side of the large pore opening, at $\theta < \theta_{cross}$ it is not possible to move the meniscus from the small pore opening to the large one without breaking through into the W phase. However, if the meniscus is at the large pore opening, it is possible to move it to the small pore opening, although this movement is accelerated because of the tapered pore. The pores can only be filled with the NW phase if this phase is forced through the mesh and then drained out by the W phase at pressure difference that ensures that the meniscus remains at the large pore opening. This is only possible in systems with hysteresis where (θ_A + ϕ_{Int}) > 90°. This is however, contrary to normal priming procedures of membranes (and in extension micromeshes) where the wetting phase is used to remove trapped small air bubbles. For $\theta > \theta_{cross}$ the meniscus still undergoes an accelerated motion from either pore opening to the other, although now $\Delta P^{\#}_{max}$ and $\Delta P^{\#}_{min}$ are obtained in the large and small pore openings respectively. However, the accelerated motion undergone inside the pore may lead the meniscus to breakthrough if the kinetic energy is larger than the pressure difference range available at the pore end.

3.5. Stability Model in Polygonal Pores

Polygonal pores are also considered in this work since many microfabricated meshes feature non-cylindrical openings. In particular hexagonal pores are very common since they emulate the honeycomb structure that allows great strength and large open area (Yang et al., 1999; Turner et al., 2000). The following analysis attempts to identify the suitability of these pore geometries in relation to meniscus stability and contact area.

3.5.1. Meniscus Shape and Area in Polygonal Pores

In polygonal pores two different types of menisci, *main terminal meniscus* (MTM) and *arc menisci* (AM), can appear as shown in Figure 3.14 where β is the half angle of the polygonal cross section corner given by Eq. (3.39), p_S is the perimeter of the meniscus in contact with the inner pore wall and p_L is the perimeter of the meniscus that is not in contact with the inner pore wall.

$$\beta = \pi / 2\left(\frac{n-2}{n}\right) \tag{3.39}$$

where n is the number of the polygonal pore sides.

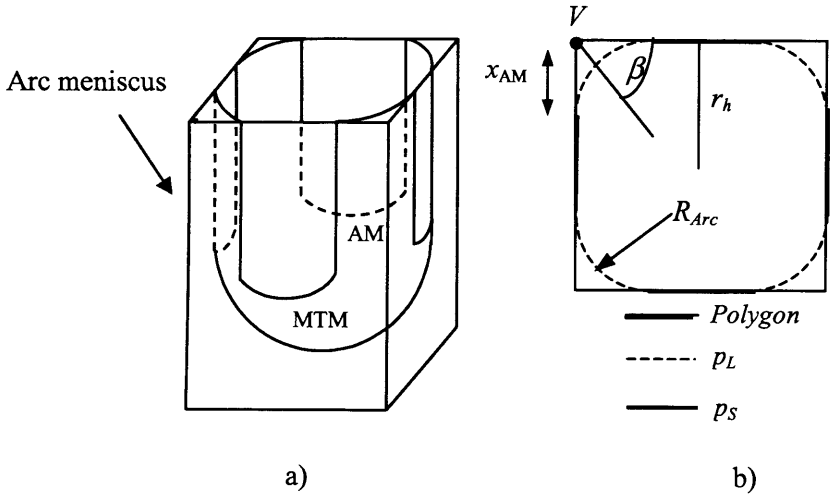

Figure 3.14. Types of menisci inside a square pore, a) 3D representation, b) top view of pore.

The MTM is always present and is the region that fills the tubular space of the pore. In the absence of gravity and for contact angles satisfying the Concus-Finn condition (Concus and Finn, 1969, 1974),

$$\theta < (90° - \beta_{corner}) \tag{3.40}$$

development of capillary underpressure at the corners gives rise to spontaneous redistribution of fluid along the interior of the pore corners (Finn, 1999; Weislogel and Lichter, 1998), generating the AM that can be represented as an arc of a circle (with radius R_{Arc}) in each corner of the cross section of the meniscus interface within the pore (see Figure 3.14). It is worth

noting that in tapered pores $\beta_{corner} \neq \beta$. In tapered pores ($\phi_{Int} \neq 0$) with regular polygonal cross sections, β_{corner} is half the interior angle that two adjacent faces form, which is defined by Eq. (3.41) as deduced in Appendix 3C.

$$\beta_{corner} = \frac{1}{2}\arccos\left[(\cos\beta)^2 \cos(2\phi_{Int}) - (\sin\beta)^2\right] \tag{3.41}$$

which reduces to Eq. (3.42) (see also Appendix 3D for a different approach).

$$\beta_{corner} = \arccos[\cos\beta \cos\phi_{Int}] \tag{3.42}$$

If the system has contact angle hysteresis, the smallest attainable contact angle (θ_R) is used to determine whether or not arc menisci can be formed (Shouxiang et al., 1996). Therefore, the formation of AM is a function of wettability properties, the number of sides of the polygonal pore and the interior solid wall inclination ϕ_{Int}.

At $\theta < 90°-\beta_{corner}$, as the corner vertex is approached, there is no solution for a constant curvature meniscus that satisfies the contact angle boundary condition $\mathbf{k}\cdot\mathbf{n} = \cos\theta$ along the three phase contact line, where $\mathbf{k}$ is a vector normal to the interface and $\mathbf{n}$ is a vector normal to the solid pore wall. In this situation, the curvature of the meniscus increases as the corner vertex is approached, generating a pressure gradient in the wetting phase that gives rise to a spontaneous and permanent fluid flow in the vicinity of the corner, forming AM. In the absence of gravity, arc menisci rise indefinitely although the velocity decreases as the wetted length increases due to an increase in the frictional losses (Weislogel and Lichter, 1998). Concus and Finn (1969) reported simple experimental evidence of this phenomenon by partially immersing two microscope slides at an angle of 10° inside water and oil and recording the liquid rise at the corner. Dong and Chatzis (1995) introduced a slug of wetting liquid into one end of a dry square capillary tube that was then closed. The wetting liquid is observed to imbibe only along the corners of the tube due to the capillary underpressure that eventually leads to the formation of an isolated bubble. This type of spontaneous fluid flow is of great importance in microgravity environment for spacecrafts for the design of fuel containers that can guarantee outflow on demand, since a small change in contact angle or corner geometry can lead to very large shifts of the fluid mass (Langbein 1990). Concus et al. (2000) reported experiments carried out in the Interface Configuration Experiment on board the NASA USML-2 Space Shuttle flight that further support their previous analysis. Contact angle hysteresis (for the case when $\theta_R < (90°-\beta) < \theta_A$) was found not to prevent the predicted behavior by the Concus-Finn condition, but only to

noticeably impede it while the equilibrium contact angle by Young-Laplace theory would define whether AM form. Concus and Finn (1996) have extended this condition for the case when the contact angle of the wetting phase is different at each side of the wedge.

The condition given by Eq. (3.40) indicates that the contact angle below which arc menisci appear decreases as $|\phi_{Int}|$ increases, and for $|\phi_{Int}| \rightarrow 90°$, $\beta_{corner} \rightarrow 90°$ and arc menisci are never formed ($\theta < 0°$ not possible). For a tapering angle $\phi_{Int} = 0°$, $\beta_{corner} = \beta$, and the condition reduces to $\theta < 90° - \beta$. For example, for an interior solid wall inclination $\phi_{Int} = 30°$ in a square cross section pore, arc menisci form for $\theta \leq 37.76°$, while for $\phi_{Int} = 0°$ arc menisci form for $\theta \leq 45°$. When the number of sides inside the polygon tends to infinite, the polygonal tapered pore approaches the case of the circular cross section capillary with $\beta \rightarrow 90°$ ($\beta_{corner} \rightarrow 90°$ and $\theta < 0°$ for AM), for which arc menisci are never formed irrespective of the interior solid wall inclination ϕ_{Int}.

The AM have an infinite radius of curvature in the direction of the corner edges (same direction as pore axis only if $\phi_{Int} = 0°$) and therefore their curvature is equal to $\kappa_{AMs} = 1/R_{Arc} + 1/\infty$, where R_{Arc} is defined in a plane perpendicular to the side pore edge (same plane where β_{corner} is defined). For negligible gravity the MTM mean curvature is equal to the AM curvature and the Mayer-Stowe and Princen (MS-P) Method (Mayer and Stowe 1965, 1966, 2005; Princen 1968, 1969) can be applied to calculate the mean curvature κ of complex menisci in uniform cross section (non-tapered) pores (Mason and Morrow 1994). The mean curvature of the main terminal meniscus is taken equal to that of the arc menisci, which only have one radius of curvature, $\kappa = \kappa_{AMs}$. A force balance or a thermodynamic approach can be applied to solve for the mean curvature (Princen, 1968; Pellicer et al., 1995; Lago and Araujo, 2001). Below, carrying out a work balance to displace the meniscus by dx and neglecting line tension effects, Eq. (3.43) is obtained,

$$\Delta P A' dx = (\gamma_{NW\text{-}S} p_{NW\text{-}S} - \gamma_{W\text{-}S} p_{W\text{-}S} + \gamma p_L) dx \tag{3.43}$$

where A' is the main terminal meniscus area projected in a plane perpendicular to the meniscus (pressure force is perpendicular to the interface and radial components of the pressure force are counteracted), $p_{NW\text{-}S}$ and $p_{W\text{-}S}$ are the projected contact perimeters of the non-wetting and wetting phases respectively with the pore solid walls, which are identical in this case ($p_{NW\text{-}S} = p_{W\text{-}S} = p_S$, See Figure 3.14b) and p_L is the projected meniscus liquid perimeter, (see Figure 3.14b). Line tension effects are neglected in this analysis since non-axisymmetric menisci result in complex curvatures of the three-phase contact line (see Figure 3.15). This type of analysis is

exact in the absence of gravity for capillaries of uniform cross section (Mason and Morrow, 1994).

Although the balance in Eq. (3.43) applies to the MTM, the pressure difference across the interface ΔP is the same at the AM, which only have one radius of curvature. The surface tensions of the wetting and non-wetting phases, $\gamma_{W\text{-}S}$ and $\gamma_{NW\text{-}S}$ respectively, are related to the interfacial tension of the system by Young's equation, Eq. (3.7), taking F = NW and L = W. Eq. (3.43) is reduced to Eq. (3.44) where p' is calculated at any height of the pore by $p' = p_S \cos\theta_{App} + p_L$ and $r_{h,s}$ is the distance from the centre of the polygonal tube to the middle of any side at the small pore opening (characteristic dimension) and $\kappa^{\#} = \kappa r_{h,s} = r_{h,s}/R_{Arc}$ (see Figure 3.14b).

$$\Delta P^{\#} = \kappa^{\#} = \frac{r_{h,s} p'}{A'} \tag{3.44}$$

Considering the geometric relationships in an n-side polygonal pore and employing the MS-P method (see Eq. (3.44)), similarly to Mason and Morrow (1984), the capillary pressure across the meniscus for regular polygonal pores of uniform cross section ($\phi_{Int} = 0$) when $\theta_R < (90° - \beta_{corner})$ is obtained.

$$\Delta P^{\#} = \frac{\Delta \mathrm{Pr}_{h,s}}{\gamma} = \kappa^{\#} = \frac{1}{r_h^{\#}}\left[\cos\theta_{MTM} + \left[\frac{\pi/2 - (\theta_{AM} + \beta) + (\cos\theta_{AM} - \cos\theta_{MTM})^2 \cot\beta - (\cos\theta_{AM} - 2\cos\theta_{MTM})\sin\theta_{AM}}{\tan(\pi/2 - \beta)}\right]^{1/2}\right] \tag{3.45}$$

Eq. (3.45) considers the general case when the contact angle along the AM contact line, θ_{AM} and the contact angle along the MTM contact line, θ_{MTM} are different (e.g. imbibition of the wetting phase once AM have been formed) and reduces to the equation given by Mason and Marrow (1984) when $\theta_{AM} = \theta_{MTM}$.

At $\theta \geq (90° - \beta_{corner})$, AM do not exist and the MTM meniscus is spherical. By applying a force balance to the meniscus in equilibrium (pressure force = surface tension force), the pressure difference across the interface for either non-tapered or tapered polygonal pores is obtained (see Pellicer et al., 1995 for a discussion on the force balance and thermodynamic approaches).

$$\Delta P^{\#} = \frac{\Delta P \cdot r_{h,s}}{\gamma} = \kappa^{\#} = \frac{2\cos\theta_{App}}{r_h^{\#}} = \frac{2}{R^{\#}} \tag{3.46}$$

Mason and Morrow (1991) also applied the MS-P method to irregular triangular pores with uniform cross section in which the capillary pressure is characterised by the radius of the inscribed circle r_h and a shape factor defined as the ratio of the pore cross-sectional area to the square of the pore perimeter. Princen (1992) further extended the previous analysis to consider irregular triangular cross section pores with curved sides.

It must be noted that since $\theta_{App} = \theta + \phi_{Int}$ is the angle that defines the meniscus curvature and it is based on the in-circle radius r_h according to Eq. (3.46), it corresponds to the lower point of the three-phase contact line (centre of polygon side), at which the interior solid wall inclination with respect to the pore axis is ϕ_{Int}. The interior solid wall inclination with respect to the pore axis along other points of the three-phase contact line is different from ϕ_{Int} and at the pore corners it is given by,

$$\phi_{Int,corner} = \arctan(\tan\phi_{Int} / \sin\beta) \tag{3.47}$$

The meniscus shape in a polygonal non-tapered pore at contact angles $\theta \geq (90° - \beta_{corner})$ is found by cutting a sphere of radius $R = r_h/\cos\theta$ with the polygonal domain that contains it, as Figure 3.15 shows for a hexagonal pore ($\phi_{Int} = 0°$), $\theta = 45°$ and $r_h = 5.20$ μm.

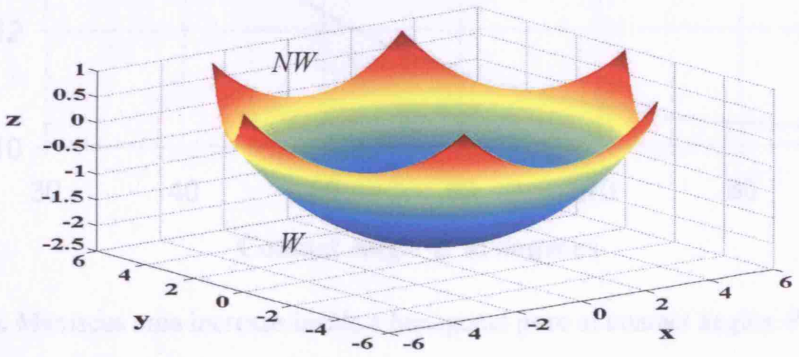

Figure 3.15. Meniscus in a hexagonal non-tapered pore with $r_h = 5.20$ μm and $\theta = 45°$.

The meniscus area is found in this case (non-tapered polygonal pore at $\theta \geq (90° - \beta_{corner})$) by the surface integral of a sphere contained within the polygonal domain (see Appendix 3E for a detailed calculation in a hexagonal pore),

$$\mathbf{A} = \iint_{Domain} \sqrt{1+\left(\frac{\partial z}{\partial x}\right)^2+\left(\frac{\partial z}{\partial y}\right)^2}\,\mathbf{n}\,dxdy = \iint_{Domain} \frac{R}{\sqrt{R^2-y^2-x^2}}\,\mathbf{n}dxdy \qquad (3.48)$$

As an example, the meniscus area increase as a function of θ can be calculated from Eqs. (3.25) and (3.48) for non-tapered hexagonal pores ($\theta \geq 90°-\beta_{corner} = 30°$) as compared to a cylindrical pore with the same radius r_h. An increase in interfacial area up to 19 % is observed (see Figure 3.16). In slightly tapered pores, similar results are expected when using the $\theta_{App,Int} = \theta + \phi_{Int}$, since the r_h variation along the three phase contact line is insignificant. In this case, $\theta_{App,Int} = \theta + \phi_{Int}$ is used in Figure 3.16.

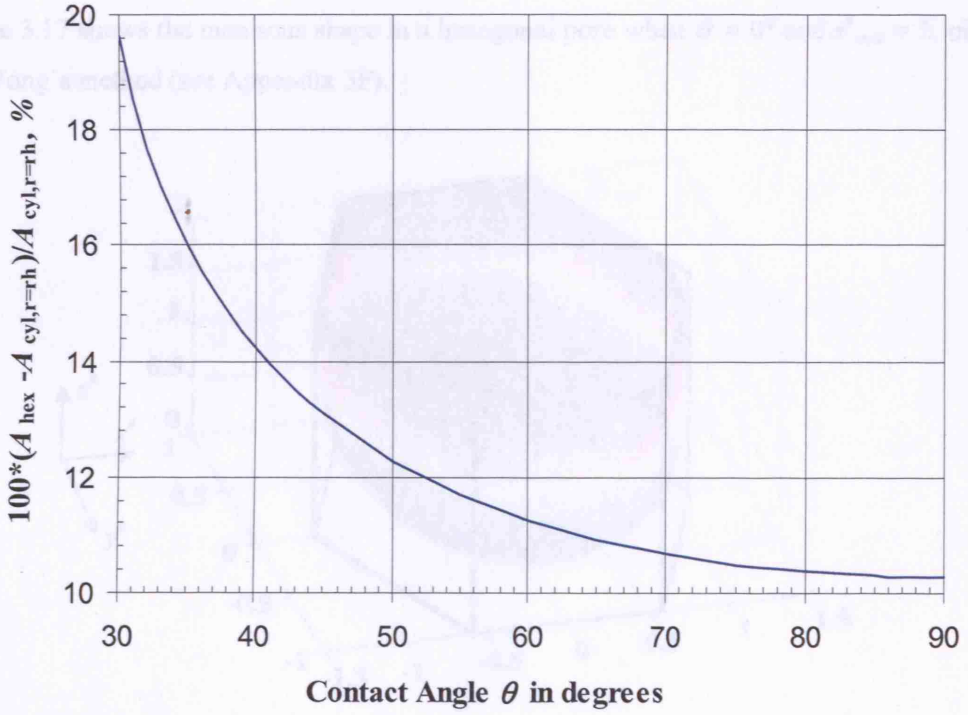

Figure 3.16. Meniscus area increase inside a hexagonal pore at contact angles $\theta \geq (90°-\beta) = 30°$ as compared to a cylindrical pore with the same radius r_h.

At contact angles $\theta \leq (90°- \beta_{corner})$ AM are formed, which decrease the mean curvature of the MTM although the contact area between phases can increase as AM extend along the pore length. Computation of the meniscus shape at $\theta \leq (90°- \beta_{corner})$ requires a three-dimensional analysis, as the geometry is not axisymmetric. The common boundary condition of a constant contact angle along the contact line between the meniscus and the pore wall makes the solution complex, since the location of the contact line is not known in advance, becoming a free-

boundary problem (Orr et al., 1977). This can be avoided using the augmented Young-Laplace equation as shown by Wong et al. (1992) for polygonal pores of uniform cross section. The augmented Young-Laplace equation incorporates thin-film forces (i.e. conjoining/ disjoining pressure) that repel the meniscus at small distances from the capillary wall,

$$\nabla \cdot \mathbf{n} + \Pi^{\#}(h^{\#}) = \kappa^{\#} \tag{3.49}$$

where $\Pi^{\#} = r_h \Pi/\gamma$ is the dimensionless conjoining/disjoining pressure isotherm and $h^{\#}$ is the dimensionless location of the meniscus measured normal to the wall. Therefore, a thin film is assumed to separate the meniscus from the capillary walls and the solution with a contact line along the capillary wall is retrieved when the film thickness tends to zero (Wong et al., 1992). Figure 3.17 shows the meniscus shape in a hexagonal pore when $\theta = 0°$ and $z^{\#}_{max} = 2$, obtained via Wong's method (see Appendix 3F).

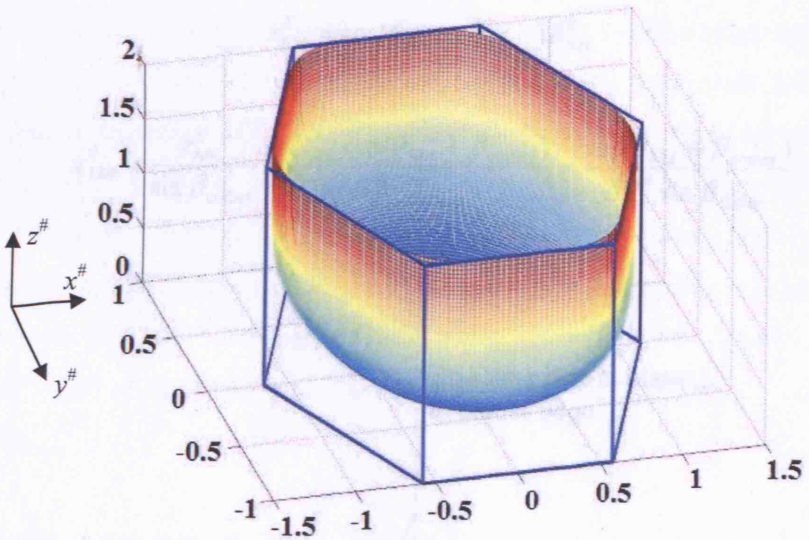

Figure 3.17. Hexagonal meniscus, $\theta = 0°$, $z^{\#}_{max} = 2$.

The meniscus area when AM are present can be approximated, considering separately the contributions from the MTM and the AM. The AM area is taken as the product of the meniscus arc length and the AM length from the lower point of the meniscus contact line with the pore wall (at $r^{\#} = r/r_h = 1$) to the top of the pore, $l^{\#} = l/r_h$, to obtain Eq. (3.50), where $1/R^{\#}_{Arc} = \kappa^{\#} = \Delta P^{\#}$ is the capillary pressure. Eq. (3.50) uses the contact angle of the AM, θ_{AM} and the capillary pressure $\Delta P^{\#}$, which limit values are a function of the available solid wall inclinations at the point of contact of the three phase contact line, ϕ. If contact angle hysteresis is present, the

contact angle along the AM, θ_{AM}, can have a different value from that along the three-phase contact line of the MTM, θ_{MTM}, although $\theta_R \leq \theta_{AM} \leq \theta_A$. In case of tapered pores ($\phi_{Int} \neq 0$), it should be noted that although the pore cross-section changes, the AM have the same radius of curvature R_{Arc} (and same arc length) at different pore heights since a constant curvature exists along the meniscus in the absence of gravity. In this case R_{Arc} is found in a plane perpendicular to the side pore edge, the same plane where β_{corner} and θ_{AM} are defined.

$$A_{AM}^{\#} = 2nl^{\#}(\pi/2 - (\theta_{AM} + \beta_{corner}))R_{Arc}^{\#} = \frac{2nl^{\#}(\pi/2 - (\theta_{AM} + \beta_{corner}))}{\Delta P^{\#}} \tag{3.50}$$

A pore corner with an AM can be considered as a 2D tapered pore with an interior solid wall inclination equal to β_{corner} and a symmetry axis coincident with the corner bisecting line. It can easily be seen that,

$$r_{AM}^{\#} = \cos(\theta_{AM} + \beta_{corner})R_{Arc}^{\#} \tag{3.51}$$

$$x_{AM}^{\#} = \frac{r_{AM}^{\#}}{\sin\beta_{corner}} = \frac{R_{Arc}^{\#}\cos(\theta_{AM} + \beta_{corner})}{\sin\beta_{corner}} = \frac{\cos(\theta_{AM} + \beta_{corner})}{\Delta P^{\#}\sin\beta_{corner}} \tag{3.52}$$

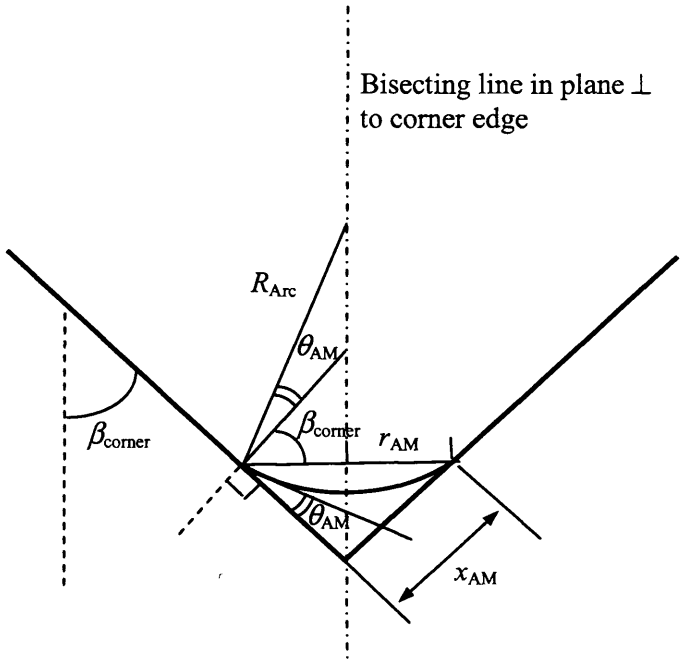

Figure 3.18. Important dimensions of an arc meniscus (AM) in a polygonal tapered cross-section pore. These dimensions are in a perpendicular plane to the arc meniscus and not in a perpendicular plane to the pore axis when $\phi_{Int} \neq 0$.

In the field of oil recovery that deals with networks of connected pores, the displacement of the wetting phase by movement of the MTM is called *primary drainage* while the filling of the pore with the wetting phase as capillary pressure $\Delta P^{\#}$ decreases is referred to as *imbibition* (Patzek, 2000). The imbibition process in an isolated pore can take place by pore filling with the MTM (*piston-drive imbibition*) or by pore filling with the AM (*snap-off*). A snap-off mechanism is the progressive pore filling with the wetting phase via an increase of the AM volume as capillary pressure decreases, until all AM fuse together trapping portions of the non-wetting phase. In regular polygonal pores for $\theta < (90°-\beta_{corner})$, the snap-off takes place when the adjacent AM meet, which happens when,

$$x_{AM}^{\#}\frac{\cos\phi_{Int}}{\cos\phi_{Int,corner}}=\frac{r_h^{\#}}{\tan\beta}=D/2 \tag{3.53}$$

where D is the length of a side in a polygonal pore measured in a plane perpendicular to the pore axis. It must be noted that $r^{\#}_h$ depends on the meniscus location along the pore. However, in an operating mesh all pores have a MTM, and the pore filling via the AM will take place only until the pressure difference $\Delta P^{\#}$ necessary to displace the MTM is reached, $\Delta P^{\#}_{Imb}$ (piston-drive imbibition capillary pressure). When the MTM is not present (e.g. interconnected pores that have been completely drained) AM pore filling takes place, even when $\Delta P^{\#} < \Delta P^{\#}_{Imb}$ until they fuse together (*snap-off*), forming a new MTM that is not in equilibrium. For example, a square cross section pore ($\beta = 45°$) with $\phi_{Int} = 0°$ and $\theta = \theta_{AM} = \theta_{MTM} = 30°$, requires a critical filling pressure, $\Delta P^{\#}_{C,NW} = 1.70$ (Eq.(3.45)) and a snap-off pressure of $\Delta P^{\#}_{Snap\text{-}off} = 0.366$ (Eqs. (3.52) and (3.53)).

The MTM area, is approximated by Eq. (3.25) assuming a spherical MTM with $r^{\#} = r_h^{\#}$ and θ_{App} = acos($\kappa^{\#}/2$), i.e. the apparent contact angle is not the real one but the one that a spherical meniscus would have in order to produce the same curvature as that of the main terminal meniscus in the polygonal pore. However, the value of $\kappa^{\#} = \Delta P^{\#}$ is calculated via Eq. (3.45) using the real values of θ_{MTM} and θ_{AM} and correcting the result to account for ϕ_{Int} when $\phi_{Int} \neq 0$. As θ approaches $(90°-\beta_{corner})$, the AM become smaller ($A_{AM} \rightarrow 0$) for the same capillary pressure $\Delta P^{\#}$ and this approximated solution gives the same area as that of a meniscus in a circular cross section pore of radius r_h so that the extra meniscus area due to the curved contact line (see Figure 3.16 for a hexagonal pore) is neglected. A more accurate solution could be obtained by Eq.(3.48) and measuring the length of the AM from the highest point of the meniscus contact line, but at the expense of more complex calculations.

For a given fluid-liquid-solid system (specific contact angle) the total area of the AM, A_{AM}, increases as the number of sides of the polygon decreases even though their number decreases. This increase is more substantial at larger contact angles. Figure 3.19 shows the dimensionless area per dimensionless length of the AM, $A^{\#}_{AM}/l^{\#}$ as a function of θ_{AM} and n for a non-tapered pore ($\phi_{Int} = 0°$) obtained from Eq. (3.50) and a system where $\Delta P^{\#} = \Delta P^{\#}_{C,NW}$ and $\theta_{MTM} = \theta_{AM}$. It is shown that this area increases as both θ_{AM} and n decrease. The total area of the AM can be substantial compared to the area of a cylindrical pore meniscus (similar to MTM), which varies from $A^{\#} = 3.14$ to $A^{\#} = 6.28$ when θ changes from 90° to 0°. For a system with $\theta_{MTM} = \theta_{AM} = 20°$ and AM length $l^{\#} = 20$, the AM area for $n = 6$ and $n = 3$ is $20 \cdot A^{\#}_{AM}/l^{\#} = 22.44$ and 49.08 respectively (see Figure 3.19) compared to the MTM area (Eq. (3.25)) that is $A^{\#}_{MTM} = 4.62$ and 4.13 respectively.

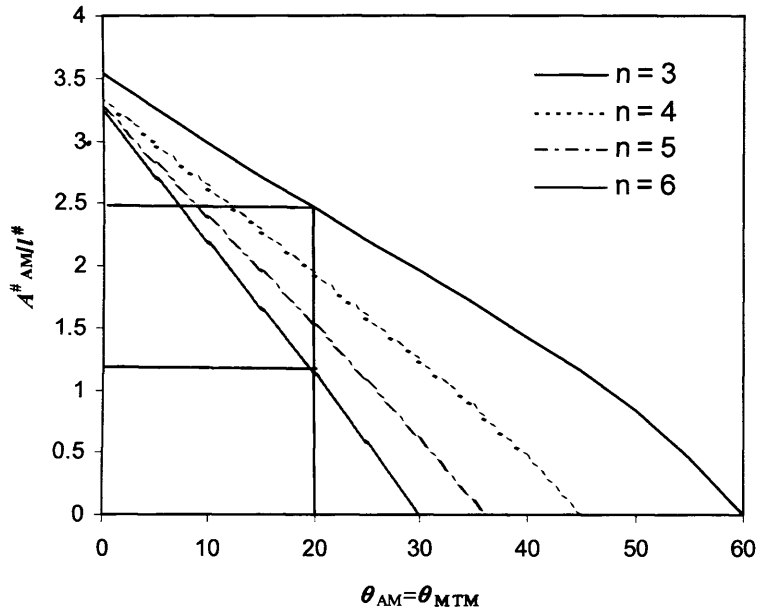

Figure 3.19. Dimensionless AM area per dimensionless AM length $A^{\#}_{AM}/l^{\#}$ as a function of contact angle θ_{AM} and number of sides n of the polygonal pore (Eq. (3.50)).

It must be noted that the change in AM area as θ_{App} changes at the pore ends does not correspond to the change in AM area shown in Figure 3.19 for different contact angles θ.

3.5.2. Meniscus Position and Stability in Polygonal Pores

The same considerations noted in section 4.2 are applied for polygonal cross section pores. Meniscus position is determined according to Table 3.1 although when hysteresis is present the

contact angle that determines if the meniscus advances or recedes is $\theta_{MTM} = \theta_A$ or $\theta_{MTM} = \theta_R$ ($\theta_{App} = \theta_{MTM} + \phi$), which can be different from θ_{AM}. For tapered polygonal pores, which can be obtained by anisotropic etching, a similar analysis to that shown in section 4.3 for circular pores can be applied.

Effect of the Solid Wall Inclination at the Pore Ends and in Tapered Pores

In the absence of AM, ($\theta \geq 90°-\beta_{corner}$), $\theta = \theta_{MTM}$ and the meniscus is perfectly spherical inside both tapered and non-tapered pores and the pressure difference $\Delta P^{\#}$ is calculated by Eq. (3.23) with $\theta_{App} = \theta + \phi_{Int}$ and $r^{\#} = r_h^{\#}$. As the three-phase contact line location is difficult to determine, it is not clear how the meniscus curvature and the three-phase contact line change at the pore openings with applied pressure. For example, since the height of the three-phase contact line is not uniform, in the hexagonal pore shown in Figure 3.15, when the meniscus advances 6 points reach the pore end before the rest of the contact line. The solid wall inclination experienced by the various points of the three-phase contact line when applying pressure to the wetting phase will be different. Therefore, the interface is not spherical. When the meniscus recedes towards the wetting phase a similar phenomenon occurs but now the lower points of the meniscus contact line reach the pore end first. Because of this, no simple method exists to our knowledge for calculating capillary pressure in a non-spherical meniscus at the pore ends of a polygonal capillary. The assumption of a spherical meniscus at the pore ends is considered in the procedure presented in Table 3.3 for calculating pressure difference $\Delta P^{\#}$ in the absence of AM.

ϕ	Procedure
$\phi_{min} \leq \phi \leq \phi_{max}$	Eq. (3.23) is used with $r^{\#} = r_h^{\#}$. The values of θ_{App} and $r_h^{\#}$ to calculate $\Delta P^{\#}_{C,W}$, $\Delta P^{\#}_{C,NW}$, $\Delta P^{\#}_{B,W}$ and $\Delta P^{\#}_{B,NW}$ are given by Table 3.2 where $r_s^{\#} = r^{\#}_{h,s}$ and $r^{\#}_l = r^{\#}_{h,l}$.

Table 3.3. Procedure to calculate pressure difference in both tapered and non-tapered polygonal pores in the absence of AM ($\theta_R \geq 90°-\beta_{corner}$).

In the presence of AM ($\theta < 90°-\beta_{corner}$), analyses carried out applying the MS-P method for calculation of capillary pressure are only exact for uniform cross-section pores ($\phi_{Int} = 0°$) and do not take into consideration the solid wall inclination change found at the pore ends or in tapered pores. Analyses for uniform cross-section pores have often been used in systems with non-uniform cross sections considering only the smallest pore radius (Man and Jing, 2001), which is

only correct for zero contact angle. It is important to note that the effect of solid wall inclination change on pressure difference is generally more significant than the effect of different polygonal cross-section (different n). In a polygonal pore of uniform cross section, at $\theta = 0°$ $\Delta P^{\#}$ changes from 1.778 to 2 as n increases from 3 to infinite, while a 90° change of ϕ at the pore ends leads to $\Delta P^{\#} = 0$.

To calculate the capillary pressure at solid wall inclination $\phi \neq 0$ when AM are present ($\theta_{MTM} = \theta_R < 90°-\beta_{corner}$), an approximate method is presented Table 3.4, which is similar to that proposed by Mason and Morrow (1994) for converging-diverging pores which in turn is based on a combination of Purcell (1949) and MS-P methods. When the MTM meniscus reaches the non-wetting pore end ($\phi > \phi_{Int}$), AM vanish and similarly to the case $\theta \geq 90°-\beta_{corner}$, a spherical meniscus is considered.

ϕ	Procedure
$\phi_{min} \leq \phi \leq \phi_{Int}$ **Meniscus at W pore end or inside pore**	A) Calculate $\Delta P^{\#}$ for a uniform cross section pore ($\phi_{Int} = 0$) and $r^{\#}_{h}$ at the meniscus location. 1. No hysteresis ($\theta_{MTM} = \theta_{AM} = \theta$). Eq. (3.45) is used to calculate $\Delta P^{\#}$. 2. Hysteresis. a) For filling with the *NW* phase (drainage, $\theta_{MTM} = \theta_{AM} = \theta_R$). Eq. (3.45) is used to calculate $\Delta P^{\#}$. b) For filling with the *W* phase (imbibition, $\theta_{MTM} = \theta_A \neq \theta_{AM}$). Eq. (3.45) and (3.54) are solved simultaneously. B) Calculate $r^{\#}_{h,Cyl}$. The dimensionless pore radius of an equivalent cylindrical capillary, $r^{\#}_{h,Cyl}$ is calculated by Eq. (3.23) using the previous calculated value of $\Delta P^{\#}$ and $\theta_{App} = (\theta_{MTM} + \theta_{AM})/2$. C) Calculate $\Delta P^{\#}$ for $\phi \neq 0$. The value of $r^{\#}_{h,Cyl}$ is employed in Eq. (3.23) to calculate $\Delta P^{\#}$ using $\theta_{App} = \theta_{MTM} + \phi$ given in Table 3.2 when $\theta_{MTM} = \theta_{AM}$ and $\theta_{App} = (\theta_{MTM} + \theta_{AM})/2 + \phi$ when $\theta_{MTM} \neq \theta_{AM}$ (relevant for calculation of $\Delta P^{\#}_{C,W}$).
$\phi_{Int} < \phi \leq \phi_{max}$ **Meniscus at NW pore end**	D) In this case (relevant for calculation of $\Delta P^{\#}_{B,W}$) AM vanish and Eq. (3.23) is used with θ_{App} obtained from Table 3.2

Table 3.4. Procedure to calculate pressure difference in both tapered and non-tapered ($\phi_{Int} \neq 0$) polygonal pores in the presence of AM ($\theta_R < 90°-\beta_{corner}$).

In uniform cross-section pores, the change in the solid wall inclination at the wetting pore end can also be considered using Eq. (3.45) with $\theta_{MTM} = \theta_R+\phi = 0°$ and $\theta_{AM} = \theta_R$ since the solid wall inclination change does not affect the contact angle along the AM. Byoung-Sik and Harriot (1986) also indicated that the toroid model by Purcell (1949) could be applied to calculate critical entry pressure in fiber-like pores with other cross section than circular by using a Laplace constant factor between 1 and 2.

Critical Filling and Breakthrough Pressure in Systems without Contact Angle Hysteresis

For negligible gravity, the dimensionless pressure difference ($\Delta P^{\#} = \kappa^{\#} = \Delta P r_h/\gamma$) is constant throughout the interface. In this case, $\Delta P^{\#}$ is calculated by the procedure shown in Table 3.3 or Table 3.4 in the absence or in the presence of AM respectively.

Critical Filling and Breakthrough Pressure in Systems with Contact Angle Hysteresis

When AM are not formed ($\theta_R \geq 90°-\beta_{corner}$), $\Delta P^{\#}$ is calculated via the procedure in Table 3.3. When AM are present ($\theta_R < 90°-\beta_{corner}$), $\Delta P^{\#}_{C,NW}$, $\Delta P^{\#}_{B,NW}$ and $\Delta P^{\#}_{B,W}$ values are calculated using Eq. (3.45) as shown in Table 3.4. During pore imbibition (filling with the wetting phase) the contact angle along the AM and MTM contact lines can be different. The MTM starts filling the pore via a piston-driven imbibition mechanism when $\theta_{MTM} = \theta_A$ even if $\theta_{AM} \neq \theta_A$. Hence, $\Delta P^{\#}_{C,W}$ cannot be calculated utilizing Eq. (3.45) because it contains two unknowns, $\Delta P^{\#} = -\Delta P^{\#}_{C,W}$ and θ_{AM}, and an additional equation is required. During the imbibition process the AM three-phase contact line location, $x^{\#}_{AM}$, remains constant while θ_{AM} increases until $\theta_{MTM} = \theta_A$ when the meniscus fills the pore. The AM location (see Figure 3.18) is determined via Eq. (3.52) using the drainage pressure difference, which is $\Delta P^{\#}_{C,NW} < \Delta P^{\#}_{D} < \Delta P^{\#}_{B,NW}$ ($r^{\#}_h$ at the MTM location is used), and $\theta_{AM} = \theta_R$, obtaining $x^{\#}_{AM,D}$. Eq. (3.54) relating $\Delta P^{\#} = (-\Delta P^{\#}_{C,W})$, and θ_{AM} (obtained from Eq. (3.52)) is employed along with Eq. (3.45) to calculate $-\Delta P^{\#}_{C,W}$ and θ_{AM} via an iterative procedure,

$$\Delta P^{\#} = (-\Delta P^{\#}_{C,W}) = \frac{\cos(\theta_{AM} + \beta_{corner})}{x^{\#}_{AM,D} \sin \beta_{corner}} \tag{3.54}$$

Illustrating Examples

As an example, consider a square pore ($\beta = 45°$) of uniform cross section ($\phi_{Int} = 0°$, $r^{\#}_h = 1$) for a system with $\theta_R = 10°$ and $\theta_A = 90°$. Since the cross section is uniform, $\Delta P^{\#}_{C,NW}$ is found from Eq.

(3.45) using $\theta_{MTM} = \theta_{AM} = \theta_R$ to be $\Delta P^{\#}_{C,NW} = 1.869$. $\Delta P^{\#}_{B,NW}$ is obtained from Table 3.4 following steps A2a-B-C. **Step A2a:** $\Delta P^{\#} = \Delta P^{\#}_{C,NW} = 1.869$, **step B:** $r^{\#}_{h,Cyl} = 2\cos(10°)/1.869 = 1.054$ and **step C:** $\Delta P^{\#}_{B,NW} = 2\cos(0°)/1.054 = 1.898$ (if Eq. (3.45) is used to estimate $\Delta P^{\#}_{B,NW}$, with $\theta_{MTM} = 0°$ and $\theta_{AM} = \theta_R$ a similar value is obtained, $\Delta P^{\#}_{B,NW} = 1.887$). In order to calculate $\Delta P^{\#}_{C,W}$ the drainage pressure difference $\Delta P^{\#}_{D}$ needs to be known. For the meniscus to move to the wetting pore end without breakthrough, the drainage pressure difference $\Delta P^{\#}_{D}$ must be between 1.869 and 1.898. Considering $\Delta P^{\#}_{D} = 1.869$ and $\theta_{AM} = \theta_R$ Eq. (3.52) yields $x^{\#}_{AM,D} = 0.434$. Solving Eqs. (3.45) and (3.54) simultaneously for $\theta_{MTM} = \theta_A$ it is found that $-\Delta P^{\#} = \Delta P^{\#}_{C,W} = -0.6727$, which indicates that the imbibition process is spontaneous, and $\theta_{AM} = 33.1°$. If AM are not present initially (e.g. when filling empty pores with the wetting phase), the value of $(-\Delta P^{\#}_{C,W})$ when $\theta_A = 90°$ would be $(-\Delta P^{\#}_{C,W}) = 0$, which is obtained from Eq. (3.23) with $\theta_{App} = 90°$ and $r^{\#} = 1$. This indicates that the wetting phase of a system with contact angle hysteresis is "more wetting" if AM are present in the pore. In addition, the pore filling can be spontaneous even when $\theta_A \geq 90°$ as indicated by the negative $\Delta P^{\#}_{C,W}$. $(-\Delta P^{\#}_{B,W})$ is obtained via step D in Table 3.4 using $\theta_{App} = \min(180°, \theta_A + 90°)$ $\Delta P^{\#}_{B,W} = 2$. According to Eq. (3.50), the AM area when the meniscus is at the W pore end can vary from $A^{\#}/l^{\#} = 2n(\pi/2-(10+45)\pi/180)/1.898 = 2.575$ to $A^{\#}/l^{\#} = 2n(\pi/2-(33.1+45)\pi/180)/0.6727 = 2.470$. This decrease of the AM area as they remain pinned is accompanied by an increase of θ_{AM} from 10° to 33.1° and an increase of the wetting phase volume (commonly called saturation) in the corners.

The same system is considered within a tapered square pore with $\phi_{Int} = 20°$, $r^{\#}_{h,s} = 1$ and $r^{\#}_{h,l} = 2$ (see Figure 3.4b). The breakthrough and critical filling pressures $\Delta P^{\#}_{C,NW}$ and $\Delta P^{\#}_{B,NW}$ are calculated using the pore radius of an equivalent cylindrical pore calculated previously (steps A2a-B) using the radius at the small pore end $r_{h,s}$. **Step C** gives $\Delta P^{\#}_{C,NW} = 2\cos(10°+20°)/1.054 = 1.643$ and $\Delta P^{\#}_{B,NW} = 2\cos(0°)/1.054 = 1.898$. To calculate $\Delta P^{\#}_{C,W}$, the procedure **A2b-BC** in Table 3.4 is applied. Considering $\Delta P^{\#}_{D} = 1.643$ and $\theta_{AM} = \theta_R$ Eq. (3.52) yields $x^{\#}_{AM,D} = 0.4937$. **Step A2b**: for $\phi_{Int} = 0$, $r^{\#}_{h} = 2$ and $\theta_{MTM} = \theta_A = 90°$, Eq. (3.45) and (3.54) yield $\Delta P^{\#} = 0.3925$ and $\theta_{AM} = 29.1°$. **Step B**: $r^{\#}_{h,l,Cyl} = 2\cos((29.1°+90°)/2)/0.3925 = 2.58$. **Step C:** $\theta_{App} = (90+29.1)/2 + \phi_{Int} = 79.5°$ and Eq. (3.23) yields $\Delta P^{\#}_{C,W} = -2\cos(79.5°)/2.58 = -0.140$. The negative $\Delta P^{\#}_{C,W}$ value indicates that the pore filling with the wetting phase still occurs spontaneously. Eq. (3.50) can also be used in this case to calculate the AM area considering that β_{corner} is given by Eq. (3.41), $\beta_{corner} = 48.4° \neq \beta$.

Figure 3.20 shows the dimensionless pressure difference across the meniscus as a function of the contact angle and number of sides of the polygonal pore. Contact angle hysteresis can also

apply to the meniscus stability range definition in polygonal pores in the same way as in circular ones.

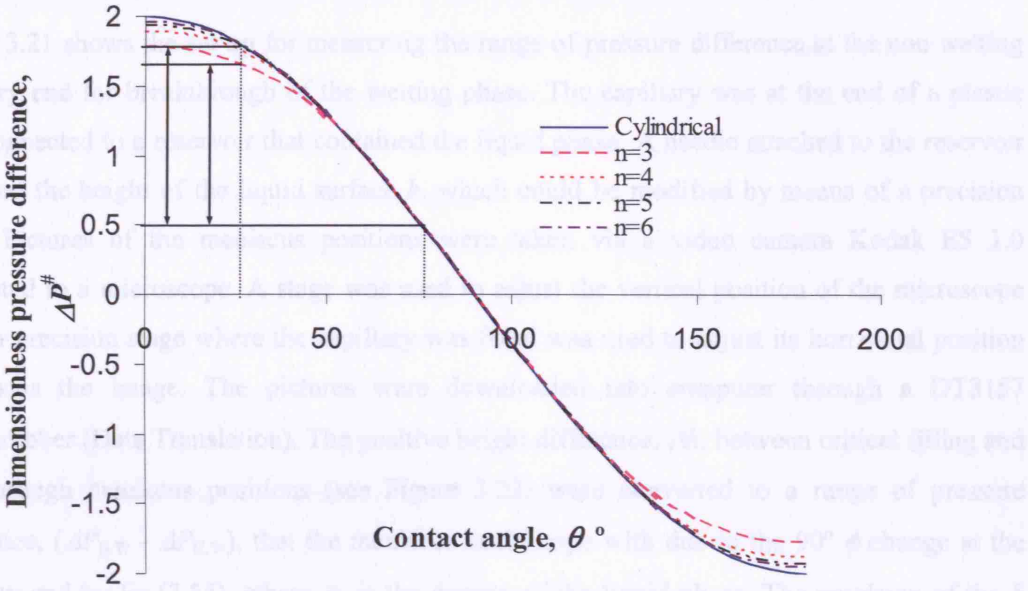

Figure 3.20. Pressure difference as a function of contact angle in cylindrical and polygonal (n = 3, 4, 5 and 6) pores.

AM rise inside the pore reaching the non-wetting pore end. However, they do not give rise to breakthrough of the wetting phase because the solid wall inclination change at the non-wetting pore end from ϕ_{Int} to ϕ_{max} keep the AM from breaking through into the non-wetting phase.

3.6. Experimental Results

Experimental work was carried out in cylindrical and square (polygonal) capillaries to investigate **a)** if the assumption of a solid wall inclination change ϕ up to ϕ_{max} = 90° at the pore ends needs to be considered in practice to calculate breakthrough pressures in both types of capillaries, **b)** if there is an effect of line tension at the pore end as ϕ changes that influences the breakthrough pressure, **c)** if the assumption of a spherical meniscus to calculate $\Delta P_{B,W}$ according to Table 3.3 is realistic and **d)** if the AM can induce the breakthrough of the wetting phase independently of the MTM. Air (ρ = 1.19 kg/m^3) was used as non-wetting phase while two different liquids were used as wetting phases: octane (γ = 21.49 mN/m, ρ = 703 kg/m^3) and ethanol GPA (γ = 22.15 mN/m, ρ = 789 kg/m^3). The surface tension was measured at T = 23.3 °C via the plate method. Three cylindrical glass capillaries (diameters d = 99, 282 and 556 μm)

and three square glass capillaries (inner side length $2r_h$ = 50, 200 and 500 μm) were used. The capillaries had a constant cross section $\phi_{int} = 0°$.

Figure 3.21 shows the set up for measuring the range of pressure difference at the non-wetting capillary end for breakthrough of the wetting phase. The capillary was at the end of a plastic tube connected to a reservoir that contained the liquid phase. A needle attached to the reservoir indicated the height of the liquid surface h, which could be modified by means of a precision stage. Pictures of the meniscus positions were taken via a video camera Kodak ES 1.0 connected to a microscope. A stage was used to adjust the vertical position of the microscope while a precision stage where the capillary was fixed was used to adjust its horizontal position and focus the image. The pictures were downloaded into computer through a DT3157 framegrabber (Data Translation). The positive height difference, Δh, between critical filling and breakthrough meniscus positions (see Figure 3.22) were converted to a range of pressure difference, ($\Delta P_{B,W}$ - $\Delta P_{C,W}$), that the meniscus could cope with due to the 90° ϕ change at the capillary end by Eq.(3.55), where ρ_L is the density of the liquid phase. The precision of the h measurement was ± 0.25 mm, giving a height difference Δh precision of ±0.5 mm. For the experiments with the 556 μm and 500 μm capillaries this resulted in errors smaller than 2 % while with the other capillaries the errors were smaller than 1 %. Evaporation effect on wetting behaviour was neglected because a constant pressure is used for each meniscus position.

$$\Delta P_{B,W} - \Delta P_{C,W} = (P_W - P_{NW})_{B,W} - (P_W - P_{NW})_{C,W} = (\rho_L - \rho_{Air})g\Delta h \qquad (3.55)$$

For the small capillaries (cylindrical 99 μm and square 50 and 200 μm) the pressure difference range was higher and a pressure transducer (Autotrans 860 series, 4 pressure ranges from 0-0.5 psi up to 0-4 psi) in conjunction with pressurisation of the reservoir with air were used for the measurements.

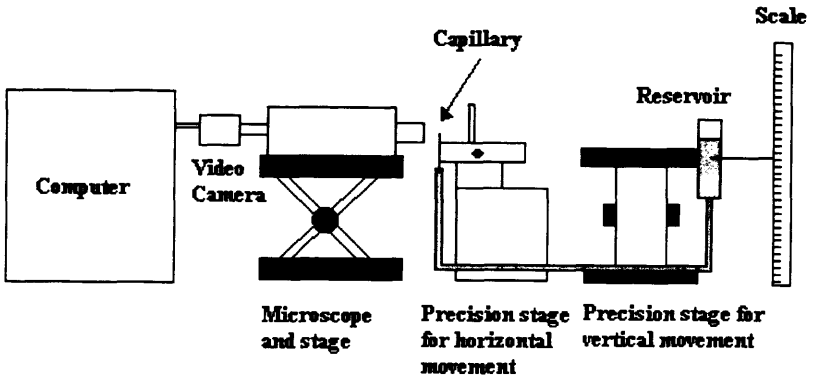

Figure 3.21. Experimental set up to measure pressure difference range at the *NW* capillary end.

The advancing and receding contact angles were measured inside the 556 μm diameter cylindrical capillaries by determining the liquid rise in the capillary using a micrometer with precision ± 10 μm. Therefore, the effect of surface roughness and heterogeneities on contact angle is contained in the measured values. The capillary rise from a flat liquid/air interface was $h_{0,\text{rise}} = 2.190$ cm and $h_{0,\text{rise}} = 1.980$ cm for the octane-air and ethanol-air systems respectively for receding contact angles so that the measurement error is negligible. The capillary rise of the ethanol-air system for advancing contact angle was $h_{0,\text{rise}} = 1.920$ cm, while in the octane-air system hysteresis was negligible and the advancing contact angle was equal to the receding one. The Bond numbers (see Eq. (3.22)) were: octane-air: $Bo_{\text{O-A}} = 0.02476$ and ethanol-air: $Bo_{\text{E-A}} = 0.02696$. Since $Bo \ll 1$ Eq. (3.56) was used to find the contact angle values. The exact solution given in Appendix 3A can be used to find an accurate value of the contact angle when gravity is important. All the contact angles are shown in Table 3.5. Since the contact angles are measured inside the capillaries, their values are for zero line tension ($\phi_{\text{Int}} = 0°$).

$$h_{0,\text{rise}} = \frac{2\gamma\cos\theta}{rg\Delta\rho} \tag{3.56}$$

Figure 3.22 shows the critical filling and breakthrough positions for the ethanol-air meniscus inside a cylindrical capillary ($d = 556$ μm). As can be seen, the apparent contact angle at the breakthrough position is larger than 90° (105°-115°), resulting in a positive breakthrough pressure $\Delta P_{\text{B,W}}$.

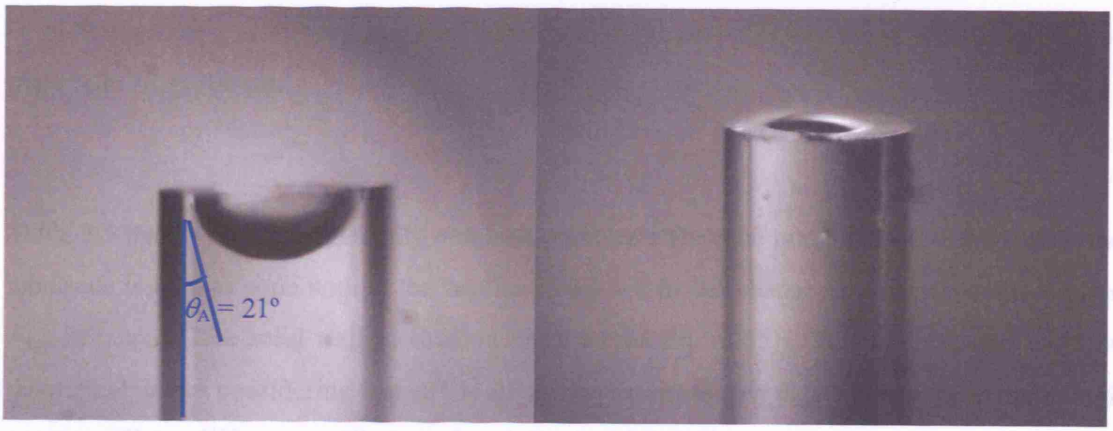

Figure 3.22. Meniscus position at a) critical filling pressure $\Delta P_{\text{C,W}}$ and b) at imminent breakthrough, $\Delta P_{\text{B,W}}$. Ethanol-air system in a cylindrical capillary of diameter $d = 556$ μm.

Figure 3.23 shows the same positions in a 500-μm square capillary for the ethanol-air system. AM are present since the contact angle θ is smaller than $(90°-\beta) = 45°$. While the MTM is inside the capillary, the arc menisci are retained at the pore ends irrespective of the MTM position, without causing early breakthrough of the wetting phase (see Figure 3.23a). Breakthrough only occurs when the MTM reaches the pore end and the solid wall inclination angle ϕ changes along the whole contact line. Figure 3.23b also shows a meniscus with an apparent contact angle θ_{App} larger than 90° (100°-110°) in the square capillary, which considering that $\theta_A = 21°$ for the ethanol-air system indicates that a change in the solid wall inclination ϕ up to $\phi_{max} = 90°$ must be considered.

Figure 3.23. Meniscus position at a) critical filling pressure, $\Delta P_{C,W}$ and b) imminent breakthrough, $\Delta P_{B,W}$, with a non-spherical meniscus. Ethanol-air system in a square capillary of inner side $2r_h = 500$ μm.

Table 3.5 shows the experimentally obtained pressure difference range ($\Delta P_{B,W}$ - $\Delta P_{C,W}$) that the meniscus is able to cope with at the capillary end due to the change in apparent contact angle θ_{App} because of the solid wall inclination change (see Eq. (3.55)). This is compared with the theoretical values considering that $\Delta P^{\#} = \Delta P\gamma/r$ and assuming $\phi = \phi_{max} = 90°$ at the breakthrough position. Three different capillaries of each kind and 3 different runs for each condition were used. The standard deviation of the measured pressure difference in each capillary was smaller than 2 % in all cases. Only average values are presented.

For the octane-air system in the square capillaries, $(\Delta P^{\#}_{B,W})_{O\text{-}A} = 0.4158$ was found from Eq. (3.23) using $\theta_{App} = \theta + 90°$ (**step D** in Table 3.4). $(\Delta P^{\#}_{C,W})_{O\text{-}A} = -1.869$ was found via Eq. (3.45)

with $\theta_{MTM} = \theta_{AM} = 12°$. Thus, the pressure difference that the meniscus can cope with at the *NW* capillary end is $(\Delta P^{\#}_{B,W}-\Delta P^{\#}_{C,W})_{O\text{-}A} = 2.2848$. For the ethanol-air system $(\Delta P^{\#}_{B,W})_{E\text{-}A} = 0.71674$ found via Eq. (3.23) using $\theta_{App} = \theta_A + 90°$ and $(\Delta P^{\#}_{C,W})_{E\text{-}A} = -1.8036$ as calculated previously. Thus, the pressure difference that the meniscus can cope with is $(\Delta P^{\#}_{B,W}-\Delta P^{\#}_{C,W})_{E\text{-}A} = 2.5203$. For cylindrical capillaries $\Delta P^{\#}_{B,W}$ are calculated as described in Table 3.2 to be $(\Delta P^{\#}_{B,W})_{E\text{-}A} = 0.7167$ and $(\Delta P^{\#}_{B,W})_{O\text{-}A} = 0.4158$.

Table 3.5 also shows the range of pressure difference that the meniscus can cope with due to contact angle hysteresis ΔP_{Hys}, which in a uniform cross-section pore corresponds to $\Delta P^{\#}_{Hys} = (\Delta P^{\#}_{C,NW} + \Delta P^{\#}_{C,W})$. For the ethanol-air system in the square capillaries it was found that $\Delta P^{\#}_{C,W} = -1.8036$ and $\theta_{AM} = 15.8°$ solving simultaneously Eq. (3.45) and (3.54) with $\theta_{MTM} = 21°$ and $x^{\#}_{AM,D} = 0.3832$. From Eq. (3.45) with $\theta_{MTM} = \theta_{AM} = \theta_R = 15°$, $\Delta P^{\#}_{C,NW} = 1.8455$. For the cylindrical capillaries $\Delta P^{\#}_{C,W}$ and $\Delta P^{\#}_{C,NW}$ can be calculated easily from Table 3.2: $(\Delta P^{\#}_{C,W})_{E\text{-}A} = -1.8672$, $(\Delta P^{\#}_{C,NW})_{E\text{-}A} = 1.9319$, $(-\Delta P^{\#}_{C,W})_{O\text{-}A} = (\Delta P^{\#}_{C,NW})_{O\text{-}A} = 1.9135$.

System	θ_R, °	θ_A, °	$\Delta P_{Hys.}$, Pa	$(\Delta P_{B,W}-\Delta P_{C,W})_{Exp}$ Pa	$(\Delta P_{B,W}-\Delta P_{C,W})_{Theo}$ Pa	ϕ_{max} ± 2 °
O-A 556C	12	12	0	179	183	88
O-A 282C	12	12	0	342	362	86
O-A 99C	12	12	0	873	1030	80
O-A 500S	12	12	0	189	196	88
O-A 200S	12	12	0	491	491	90
O-A 50S	12	12	0	1861	1964	86
E-A 556C	15	21	5.2	214	206	93
E-A 282C	15	21	10.2	407	406	90
E-A 99C	15	21	29	957	1156	77
E-A 500S	15	21	3.7	209	223	85
E-A 200S	15	21	9.3	567	557	91
E-A 50S	15	21	37.0	1668	2228	71

O = Octane, A = Air, E = Ethanol, C = Cylindrical capillary, S = Square capillary, *T* = ideal (90 ° ϕ change), Exp = Experimental ; Theo = Theoretical.

Table 3.5. Comparison of experimental pressure difference range $(\Delta P_{B,W}-\Delta P_{C,W})$ with theoretical predictions accounting for solid wall inclination ϕ change at the capillary end.

The last column in Table 3.5 shows the *apparent* maximum solid wall inclination (ϕ_{max}) utilised in the theoretical calculation to match exactly the experimental values $(\Delta P_{B,W} - \Delta P_{C,W})_{Exp}$. In cylindrical capillaries of diameters larger than 100 μm there is good agreement of ($\Delta P_{B,W}$ - $\Delta P_{C,W}$) between experimental and theoretical values using ϕ_{max} = 90°. Interestingly, the theoretical predictions of ($\Delta P_{B,W}$ - $\Delta P_{C,W}$) assuming a spherical meniscus to calculate $\Delta P_{B,W}$, are close to experimental results for square capillaries. This indicates that the above assumption does not introduce significant error. The ϕ_{max} shown in Table 3.5 is close to the value of 90° given by the theory presented earlier for capillary hydraulic diameters larger than or equal to 200 μm.

However, in the cylindrical capillaries of d = 99 μm and square capillaries of $2r_h$ = 50 μm the measured ϕ_{max} at the pore end is in all cases smaller than 90°, which may indicate that line tension effect (negative) becomes important at small capillary diameters. Therefore, the advancing contact angle decreases as ϕ increases at the capillary end towards ϕ_{max}, reducing the meniscus stability range. Using the values for cylindrical capillaries of d = 99 μm given in Table 3.5, an apparent line tension can be estimated from Eq. (3.9) assuming that the *apparent* decrease in maximum solid wall inclination ϕ_{max} is in fact a decrease of the actual advancing contact angle when ϕ_{max} = 90°. The values obtained for octane-air and ethanol air systems are σ = $-2.3 \cdot 10^{-8}$ N and $\sigma = -6.2 \cdot 10^{-8}$ N respectively. Although theoretical values of line tension are expected to be 1-2 orders of magnitude larger than these (Marmur, 1997; Checco et al., 2003), experimental values (*apparent line tension*) up to 10^{-6} N have been measured (Gaydos and Neumann, 1987; Duncan et al., 1994; Gu et al., 1996) and were attributed to the magnifying effect of surface roughness (Li, 1996; Marmur, 1998). Small discrepancies in ϕ_{max} in capillaries larger than 200 μm, generally resulting in a smaller stability range at the capillary end than the theoretical one, can be attributed to perturbations in the system like vibrations and pressure air fluctuations that affect more the largest diameter capillaries (smaller capillary pressures) as well as surface irregularities at the capillary ends (e.g. imperfect cutting as seen in the square cross section capillaries).

3.7. Conclusions

The interfacial area in polygonal pores can increase substantially when AM are present at contact angles that satisfy the Concus-Finn condition $\theta < (90° - \beta_{corner})$, since their length can reach the pore height. According to Eq. (3.50), for a specific fluid-gas-solid system the AM area increases as the number of sides of the polygon decreases. It has been shown (see Appendix 3C)

that in tapered polygonal pores, β_{corner}, which determines the existence of AM, is not equal to half the angle of the polygonal cross section but a function of β and solid wall inclination of the pore interior $\phi_{Int.}$ As $|\phi_{Int}|$ increases (β_{corner}- β) increases in a way that the contact angle at which AM appear decreases, with limiting case when $|\phi_{Int}| = 90°$ ($\beta_{corner} = 90°$) for which AM are never formed irrespective of the number of sides of the polygonal pores.

The model for determining meniscus position and stability predicts that in axisymmetric (cylindrical and tapered) pores the range of pressure differences across the phases that do not cause breakthrough consists of three contributions: contact angle hysteresis, the ability of the meniscus to change its apparent contact angle, $\theta_{App} = \theta + \phi$, at the capillary ends due to the solid wall inclination change (up to ϕ_{max} at the *NW* pore end and ϕ_{min} at the *W* pore end) and line tension effect on contact angle as ϕ changes. The former two increase the pressure difference range between the two phases that result in stable meniscus while the latter can either increase or decrease it depending on its sign. The available range of pressure difference can be found from the methodology presented in Section 4.2. The solid wall inclination of the pore interior, ϕ_{Int} does not influence the apparent contact angle at which breakthrough takes place but it determines the apparent contact angle for filling the pore with a specific phase. Critical filling and breakthrough pressures are clearly distinguished in the present work and Table 3.2 summarises the value of the capillary radius and apparent contact angle for their calculation using Eq. (3.23).

When the wetting phase in on the side of the large pore opening (see Figure 3.4a), there is an overlap of the pressure difference range available at each pore end in a way that the meniscus can be at either pore end for the same pressure difference. This pressure difference overlap gives rise to an accelerated motion of the meniscus from one pore end to the other in either direction. When this overlap is complete (the pressure difference range at the large pore opening is contained within the range at the small pore opening) the critical filling and breakthrough pressures of the non-wetting phase are the same and filling of the pores with the non-wetting phase is only possible if $\theta_A + \phi_{Int} > 90°$ and the mesh is primed with the non-wetting phase, which is not the standard procedure. For this system, it is preferable to place the wetting phase on the side of the small pore openings. Section 3.4.3 presents an analysis for calculating the wetting conditions for maximum meniscus stability range, which helps to decide mesh material and placement of the phases. Irrespective of wetting conditions, placement of the apparent wetting phase on the small pore opening always allows filling of the pore with either of the phases as a function of capillary pressure as $\Delta P^{\#}_{max}$ and $\Delta P^{\#}_{min}$ values are reached at the small and large pore openings respectively.

Meniscus stability and position in polygonal pores is analysed in a similar way to that in axisymmetric pores. The same three contributions (contact angle hysteresis, solid wall inclination change at the pore ends and line tension effect) determine meniscus stability. The meniscus curvature reduces when AM are present at $\theta < (90^\circ - \beta_{corner})$. Reduced curvature results in reduced pressure difference between the two phases that decreases as the number of sides of the pore decreases. This also translates in a reduced available range of pressure difference that the meniscus can cope with without breakthrough. The Mayer-Stowe and Princen method is used to calculate pressure difference when AM are present in polygonal pores of uniform cross section. A method to account for the change in the solid wall inclination at the pore ends and for tapered pores is also presented.

In the methodology presented (dynamic effects as the meniscus moves from one pore end to the other and flow effects on meniscus deformation are neglected) the breakthrough pressure of either wetting or non-wetting phases, $\Delta P_{B,W} = (P_W - P_{NW})_{max}$ and $\Delta P_{B,NW} = (P_{NW} - P_W)_{max}$ respectively is always positive ($\Delta P_B \geq 0$) in *flat meshes* ($\phi_{max} = 90^\circ$ $\phi_{min} = -90^\circ$), even for wetting phases with small θ, which agrees with reported experimental data (Vaidya et al., 1994b, Prasad et al., 1990). Breakthrough pressure can only be negative if there are imperfections at the mesh surface (membranes with irregular and tortuous pores) or for pore designs with $\phi_{max} < 90^\circ$ or $\phi_{min} > -90^\circ$. Rounded pore ends with large R_{Cor} (see Appendix 3B) or line tension effects on meniscus stability still result in positive breakthrough pressures. However, negative breakthrough pressures found in local pores cannot give rise to continuous breakthrough since a positive pressure difference is required thereafter to displace the non-wetting phase outside the pores. Negative breakthrough pressures have been reported experimentally (Kim and Harriot, 1986), which could be due to flow or gravity effects.

Wetting phase breakthrough experiments were carried out in cylindrical and square cross-section glass capillaries for two different systems, namely octane-air and ethanol-air. The breakthrough results obtained in the cylindrical capillaries confirmed that the meniscus apparent contact angle at the pore end changed about 90° for large diameter capillaries ($d \geq 200$ μm), which corresponds to the solid wall inclination change. However, in the small capillaries ($d = 99$ μm) the change in the apparent contact angle at the pore end was smaller than 90°, which is attributed to a substantial effect of negative line tension ($\sigma \sim -10^{-8}$ N) reducing the meniscus stability range. Although according to theoretical models, line tension effect is generally 1-2 orders of magnitude smaller than 10^{-8} N, surface roughness can magnify its effect resulting in a larger apparent line tension. The experiments in the square capillaries show that the same concepts can be applied to polygonal capillaries even though the menisci formed in them have

three-phase contact lines of non-uniform height. The assumption of a spherical meniscus to calculate $\Delta P_{B,W}$ according to Table 3.3 turned out to be practical. A similar negative line tension effect is present in the small square capillaries ($2r_h$ = 50 μm). Experiments also show that AM are retained at the pore ends due to the solid wall inclination change without causing early breakthrough. In the square capillaries, the measured value of ϕ_{max} was slightly smaller that the theoretical value of $\phi_{max} = 90°$ perhaps because the finishing of the pore ends was not as smooth as in the cylindrical capillaries.

Nomenclature

A	Meniscus interfacial area, m^2.
A'	Main terminal meniscus area projected in a perpendicular plane, m^2.
$A^{\#}$	Dimensionless area, A/r_s^2.
AM	Arc menisci, which appear at $\theta < (90^o - \beta_{corner})$.
Bo	Dimensionless Bond number.
d	Pore diameter, m.
D	Length of a side in a polygonal pore measured in a plane perpendicular to the pore axis.
$f_{A,1}, f_{A,2}$	Fractional surface area of components 1 and 2 in a composite surface.
g	Acceleration of gravity, m/s^2.
h	Height from lower pore end to three phase contact line.
h_0	Height of the meniscus apex from the lower pore end, m.
$h_{0,rise}$	Height of the meniscus apex over a flat surface with $\Delta P = 0$ or capillary rise, m.
h_f	Pore (capillary) length or thickness of the mesh with openings, m.
k	Mass transfer coefficient, m/s.
$\mathbf{k}$	Normal unit vector to a meniscus projected area differential in a perperdicular plane to the meniscus.
l	Approximated length of the arc menisci from the lower point of the meniscus contact line, m.
L	Length of the dividing line, m.
MTM	Main terminal meniscus.
m_i	Solute distribution coefficient for component i.
n	Number of sides of the polygonal pore or capillary.
$\mathbf{n}$	Normal unit vector to a meniscus area differential.
NW	Non-wetting phase.
$p_{NW\text{-}S}$	Contact perimeter of the non-wetting phase with the solid wall, m.
p'	Efficient meniscus perimeter, $p' = p_S \cos\theta + p_L$
p_L	Contact perimeter of the fluid-fluid arc menisci, m.
p_S	Contact perimeter of the no-wetting and wetting phase with the pore solid wall, m.
$p_{W\text{-}S}$	Contact perimeter of the wetting phase with the solid wall, m.
P	Pressure, Pa.
$P^{\#}$	Dimensionless pressure, $Pr_{h,s}/\gamma$.
r	Capillary or pore radius, m.

$r^{\#}$	Dimensionless pore radius, $r/r_{h,s}$.
r_{AM}	Distance from the contact line of the AM at the polygon side to the bisecting line of the internal corner of the pore (defined by β_{corner}) measured in a perpendicular plane to the AM.
r_h	In-circle radius of the polygonal pore, m.
r_{hCyl}	Pore radius of a cylindrical capillary equivalent to the polygonal one in capillary pressure when $\phi = 0°$.
R	Radius of curvature of a spherical meniscus, m.
R_1, R_2	Radii of curvature at each point of an interfacial meniscus, m.
R_{Arc}	Radius of curvature of the arc menisci, m.
S	Arc length, m.
$\mathbf{t}$	Tangent vector.
U	Internal energy, J.
W	Wetting phase.
x, y, z	Spatial variables, m.
y_S, y_L	Solid and liquid interface fun
x_{AM}	AM location distance measured from the vertex to the AM contact line in a perpendicular plane to the AM or corner edge.

Greek Letters

α	Angle o f the tangent to the meniscus profile with the x-axis, °.
β	Half angle of the polygonal cross section corner on a plane normal to the pore axis, °.
β_{corner}	Half angle of the corner on a plane normal to the pore edge (angle between two adjacent faces of the tapered pore). This is the value applied to the Concus-Finn condition (Concus and Finn, 1968).
γ	Surface (or interfacial) tension, N/m.
ΔP	Pressure difference P_{NW} - P_W across the meniscus at a given point, Pa.
ΔP_0	Pressure difference across the interfacial meniscus at the meniscus apex, Pa.
ΔP_{Hys}	Range of pressure difference that the meniscus can cope with due to contact angle hysteresis, Pa.
θ	Contact angle (macroscopic) of the apparent wetting phase, °. For systems with contact angle hysteresis it can take any value between advancing θ_A and *receding θ_R contact angles.*
θ_Y	Young's contact angle, °.

θ_{App}	Apparent contact angle of the apparent wetting phase, °.
θ_{cross}	Contact angle in a tapered pore at which ΔP_{max} is encountered at both large and small pore openings (see Figure 3.9).
ϕ	Solid wall inclination at the three-phase contact line.
ϕ_{Int}	Solid wall inclination of the inner wall of the pore. This corresponds to the solid wall inclination with respect to the pore axis at the lower point of the three-phase contact line (pore side centre).
$\phi_{Int,corner}$	Inclination angle of the interior corner edge.
κ	Mean meniscus curvature, m^{-1}.
κ_{gS}	Geodesic curvature of the three-phase contact line on the plane of the solid surface , m^{-1}.
$\boldsymbol{\kappa}$	Vector curvature of the three-phase contact line, m^{-1}.
Π	Conjoining/disjoining pressure isotherm.
ρ	Density, kg/m^3.
σ	Line tension, J/m.
ξ_S	Solid roughness. Ratio of real to projected area.

Subscripts

A	Advancing.
App	Apparent.
AM	Arc menisci.
B	Breakthrough property.
C	Critical filling.
Cor	Corner.
Cyl	Cylindrical pore.
D	Drainage.
E-A	Ethanol-air system.
F	Fluid phase.
G	Gas phase.
Hex	Hexagonal pore.
Hys	Hysteresis.
I	Property evaluated at the meniscus.
Imb	Imbibition.
Int	Interior of the pore.
l	Large

L	Liquid phase.
MTM	Main terminal meniscus.
max	Maximum property.
mem	Membrane property.
min	Minimum property.
NW	(Apparent) non-wetting phase.
NW end	When the meniscus is at the non-wetting pore end.
ov	Overall property.
O-A	Octane-air system.
R	Receding.
s	Small.
S	Solid phase.
W	(Apparent) wetting phase.
W end	When the meniscus is at the wetting pore end.
Y	Relative to Young's equation.
0	Property evaluated at the apex of the meniscus.

Superscripts

#	Dimensionless variable.

Chapter 4

Meniscus Stability Issues in Mesh Microcontactor: Support, Edge, Foreign Particle and Priming Effects

"For those who believe, no explanation is necessary. For those who do not, none will suffice"

Joseph Dunninger

4.1. Introduction

A simple systematic methodology presented in Chapter 3 for meniscus stability in single pores is validated in meshes with regular pores. Under constant system properties and identical dimensions in all pores, the single-pore model should predict the results accurately, as found with meshes having large pore openings without built-in supports. Different potential issues with a negative effect on meniscus stability have been identified and modelled. These include pressure drop along the phases, support/foreign particle effects, defective pores produced during the mesh manufacture, priming operation with wetting phase, inertial and flow effects and line tension effect. Pressure drop along the fluid phases modifies the pressure difference across the phases, whose variation should be no larger than the available range of pressure difference in static conditions. An analysis based on fluid flow between parallel plates is presented, which can be applied to calculate the maximum allowable pore size of the mesh for a given system as well as different design parameters in the micro-contactor if the pore size is known. A 2D model was implemented, which quantitatively estimates the breakthrough pressure reduction due to mesh supports, foreign particles and sealing objects in contact with the active region of the mesh. Supports/particles of the same order of magnitude as the pore size may cause a very substantial reduction of the breakthrough pressure. The Gauss equation is utilised to calculate the mean curvature of menisci inside typical defective pores caused during the mesh manufacture. The priming stage was found to be a crucial stage for removal of trapped bubbles/droplets of non-wetting phase for which a pressure difference condition is suggested. Experimental work was conducted with different meshes (in pore size and material) in order to

validate the model for a single pore as well as the models for support/foreign particle effect on breakthrough pressure reduction, priming stage and defective pores.

4.2. Background

Single and multiphase microcontactors have been successfully used for various applications (Hessel et al., 2005). For two-phase processes it may be desirable to maximise the area of contact between the phases but also facilitate phase separation at the end of the process. Systems where the phases come into direct contact usually ensure high interfacial area but phase separation would be required at the end. An alternative approach is to bring the two phases into contact via a pore containing material such as a mesh with regular pores through which mass transfer by diffusion occurs (TeGrotenhuis et al., 1998; Wenn et al., 2003, Cypes and Engstrom, 2003). In a mesh microcontactor, conditions should be ensured so that the interfacial meniscus remains within the pores of the mesh and no dispersion (or *breakthrough*) of one phase into the other occurs in a similar way as in conventional membrane contactors (Reed et al., 1995). The meniscus stability, position and shape within a single pore of a mesh were analysed in detail in Chapter 3. The pressure stability range enables the maximum allowable pressure drop in each phase to be calculated either for co-current or counter-current fluid flow. The meniscus shape defines the area available for interfacial mass transfer and the volume of each phase. The meniscus position in the pore also affects the volume of the phases as well as mass transfer resistance within the pores; it is preferable to fill the pores with the phase that produces the highest mass transfer fluxes (Prasad et al, 1990).

According to the model presented in Chapter 3 the stability range in a single straight pore (uniform or tapered cross section) is mainly determined by the change of the solid wall inclination at the point of contact of the three-phase contact line at the pore ends, ϕ, and the contact angle hysteresis. The solid wall inclination ϕ changes from ϕ_{Int} to ϕ_{max} = 90° at the *NW* pore end and from ϕ_{Int} to ϕ_{min} = -90° at the *W* pore end (see Figure 3.4). Breakthrough pressure values can be calculated via Eq. (4.1) and Table 3.2 in Chapter 3 for a circular uniform/non-uniform (tapered) cross section pore where or a 2D pore (see Chapter 3),

$$\Delta P = P_{NW} - P_{W} = \frac{f_L \gamma \cos(\theta_{App})}{d_{Eff}/2} \tag{4.1}$$

where f_L is a pore geometry factor in the Laplace equation (i.e. 2 for axisymmetric pores and 1 for 2D pores), d_{Eff} is the diameter/width of the three-phase contact line and $\theta_{App} = \theta + \phi$ is the apparent contact angle that determines the meniscus curvature.

Line tension effects (Boruvka and Neumann, 1977) may come into play at the pore ends where the solid wall inclination at the point of contact with the three-phase contact line ϕ changes and the real contact angle is modified as shown by Eq. (3.8). A positive value of the line tension would increase the stability pressure difference range while a negative line tension would result in a decrease of this range (see Chapter 3).

4.3. Breakthrough Pressure in a Mesh in Static Conditions

The breakthrough pressure of the non-wetting and wetting phases in a mesh are defined according to Eq. (4.2), considering that the properties of each pore, *i*, can be different.

$$(\Delta P_{B,NW})_{mesh} = \min_{i=1}^{n}[(\Delta P_{B,NW})_i] \qquad (\Delta P_{B,W})_{mesh} = \min_{i=1}^{n}[(\Delta P_{B,W})_i] \tag{4.2}$$

The sum of these two values gives the mesh stability range, which can also be defined as the overlap of the stability range in all pores (see Eq. (4.3)).

$$(\Delta P_{B,NW} + \Delta P_{B,W})_{mesh} = \min_{i=1}^{n}[(\Delta P_{B,NW})_i] + \min_{i=1}^{n}[(\Delta P_{B,W})_i] = \bigcap_{i=1}^{i=n}[(\Delta P_{B,NW} + \Delta P_{B,W})_i] \tag{4.3}$$

It is possible to have different surface tension and advancing and receding contact angles in each pore because of the presence of impurities as well as mass transfer and reaction that can modify the solute concentration along the microntactor (Vaidya et al., 1994). In addition, pores along the mesh can have different geometry and/or size. These result in different breakthrough pressures in each pore of the mesh, which can lead to decreased stability of the mesh compared to a single pore.

4.4. Influence of ΔP along the Mesh on Pore Filling and Meniscus Breakthrough

Once the mesh stability range is known, the range of pressure difference across the phases as a result of pressure drop during flow needs to be estimated in order to assess mesh operability.

Therefore, under flow conditions, the stability range may be defined as the stability range in static conditions minus the pressure difference variation across the phases due to pressure drop. In cases where the pores need to be filled with a specific phase (e.g. wetting phase *W*) because of mass transfer considerations, the absolute value of the pressure difference variation between the phases $|\Delta P_x - \Delta P_{x=0}|$ due to flow should be no larger than the available range of pressure difference at the filling pore end,

$$|\Delta P_x - \Delta P_{x=0}| \leq |\Delta P_{B,W} + \Delta P_{CE,NW}| \quad \text{(Filling with } W \text{ phase)} \tag{4.4}$$

It is also required that the individual values ΔP_x fall within the available range of pressure differences at the pore end. For example, for a system with the *W* phase at the large pore opening and $A < 0$ (see Table 4.2), $\Delta P_{x=0}$ must fall within the limits defined by Eq. (4.5) and (4.6) if $(\Delta P_x - \Delta P_{x=0}) \geq 0$ or Eq. (4.7) and (4.8) if $(\Delta P_x - \Delta P_{x=0}) < 0$ for filling with the *NW* (Eq. (4.5) and (4.7)) and *W* (Eq. (4.6) and (4.8)) phases.

$$\Delta P_{B,NW} - (\Delta P_x - \Delta P_{x=0}) > \Delta P_{x=0} > -\Delta P_{C,W} \quad \text{if } (\Delta P_x - \Delta P_{x=0}) \geq 0 \text{ for filling with } NW \text{ phase} \tag{4.5}$$

$$-\Delta P_{B,W} < \Delta P_{x=0} < \Delta P_{C,NW} - (\Delta P_x - \Delta P_{x=0}) \quad \text{if } (\Delta P_x - \Delta P_{x=0}) \geq 0 \text{ for filling with } W \text{ phase} \tag{4.6}$$

$$\Delta P_{B,NW} > \Delta P_{x=0} > -\Delta P_{C,W} - (\Delta P_x - \Delta P_{x=0}) \quad \text{if } (\Delta P_x - \Delta P_{x=0}) < 0 \text{ for filling with } NW \text{ phase} \tag{4.7}$$

$$-\Delta P_{B,W} - (\Delta P_x - \Delta P_{x=0}) < \Delta P_{x=0} < \Delta P_{C,NW} \quad \text{if } (\Delta P_x - \Delta P_{x=0}) < 0 \text{ for filling with } W \text{ phase} \tag{4.8}$$

If there is no restriction as to what phase should fill the pores, $\Delta P_{B,NW}$ replaces $\Delta P_{CE,NW}$ in Eq. (4.4).

Next, a model is presented, which can be used to estimate allowable values for mesh pore size, fluid layer height, length and inclination based on frictional pressure losses in each phase. Capillary condensation, which can trap the non-wetting phase and increase mass transfer resistances within the pores, relative diameter variations due to manufacturing tolerances, efficient mesh cleaning and influence of small particles dictate the use of large pores. On the other hand, small pores are beneficial in terms of meniscus stability. Hence, an optimum value of the pore size exists.

Generally, with mesh microcontactors, the phases flow in plates rather than channels. Equal flow distribution across the plates can be achieved by having distributing and collecting

chambers of size larger than the main plate (Wenn et al., 2003). As the phase height H is much smaller than the reactor length or width, the flow of each phase can be considered as two-dimensional (see Figure 4.1).

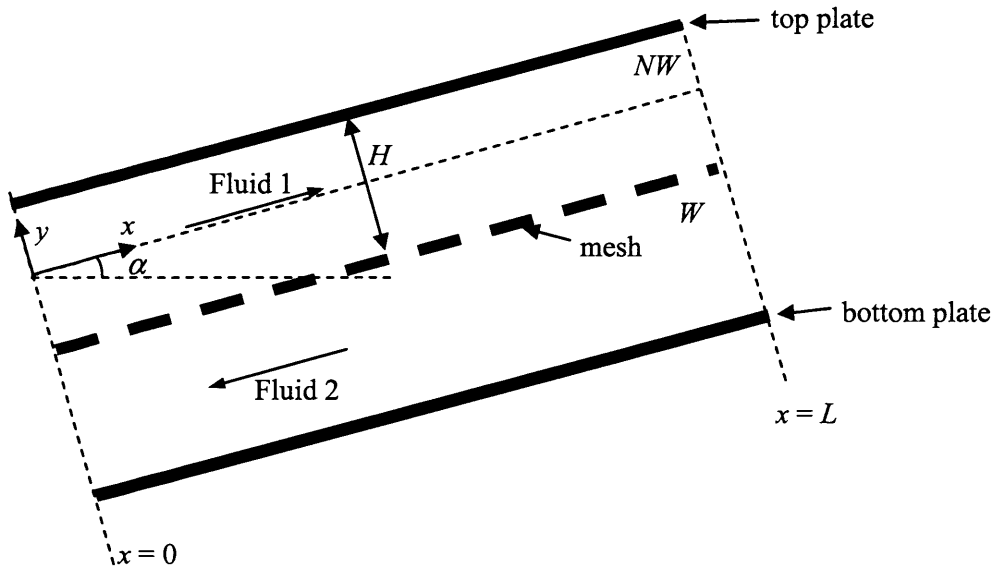

Figure 4.1. Flow between parallel plates.

For the very low *Re* numbers encountered in microcontactors, frictional losses are generally more significant than inertial or additional pressure losses due to entrance/exit, bends and merging/splitting effects and 2D flow between parallel sheets is used to estimate the pressure drop along the fluid phases (Papanastasiou et al., 2000),

$$\frac{dP}{dx} = -\frac{12U_{av}\mu}{H^2} - \rho g \frac{\partial h}{\partial x} \quad \rightarrow \quad \frac{dP}{dx} = -\frac{12U_{av}\mu}{H^2} - \rho g \sin\alpha \tag{4.9}$$

where $U_{av} = Q/(2HW)$ is the average velocity of the fluid phase, μ is the viscosity of the fluid phase, α is the angle between the x axis and the horizontal and the negative sign in the gravity term is used because α is considered positive when an increase of x results in an increase in height. No pressure variation in the cross section within each fluid phase is considered. The variation in the static pressure due to gravity can be substantial along the x direction for mesh stability when the pore size is relatively large (d > 50-100μm). Eq. (4.9) becomes dimensionless using the following dimensionless variables, where the characteristic properties are based on the wetting phase,

$$P^{\#}=\frac{P}{\mu_W U_{av,W}/r_s},\ U^{\#}=\frac{U}{U_{\mathrm{Av,W}}}\ x^{\#}=\frac{x}{r_s},H^{\#}=\frac{H}{r_s}\ r^{\#}=\frac{r}{r_s} \tag{4.10}$$

where r_s is the pore radius at the small pore opening, μ_W is the viscosity of the wetting phase and $U_{av,W}$ is the average/characteristic velocity of the wetting phase. Using these dimensionless variables the pressure drop along the mesh in the two phases is given by Eq. (4.11). The Bo_W and Ca_W numbers are defined by Eqs. (4.13) and (4.14).

Wetting phase (W)
$$\frac{dP_W^{\#}}{dx^{\#}}=-\frac{12U_W^{\#}}{H_W^{\#2}}-\frac{Bo_W}{Ca_W}\sin\alpha \tag{4.11}$$

Non-Wetting phase (NW)
$$\frac{dP_{NW}^{\#}}{dx^{\#}}=\pm\frac{12U_{NW}^{\#}}{H_{NW}^{\#2}}\left(\frac{\mu_{NW}}{\mu_W}\right)-\frac{Bo_W}{Ca_W}\left(\frac{\rho_{NW}}{\rho_W}\right)\sin\alpha \tag{4.12}$$

$$Bo_W=\frac{\rho_W g r_s^2}{\gamma} \tag{4.13}$$

$$Ca_W=\frac{\mu_W U_{av,W}}{\gamma} \tag{4.14}$$

The negative sign of the first term in the right hand side of Eq. (4.12) indicates that the non-wetting phase flows in the same direction as the wetting phase and the positive sign indicates counter-current flow. For rectangular plates where the velocities $U^{\#}_W$ and $U^{\#}_{NW}$ are independent of $x^{\#}$, integrating Eq. (4.11) and (4.12) from 0 to $L^{\#}$ for the wetting and non-wetting phases respectively, the pressure difference across the phases can be calculated, considering that the wetting phase flows in the positive x direction.

$$P_{NW,L}^{\#}-P_{W,L}^{\#}=\left(P_{NW,0}^{\#}-P_{W,0}^{\#}\right)+L^{\#}\left[\pm\frac{12U_{NW}^{\#}}{H_{NW}^{\#2}}\left(\frac{\mu_{NW}}{\mu_W}\right)+\frac{12U_W^{\#}}{H_W^{\#2}}-\frac{Bo_W}{Ca_W}\sin\alpha\left(\frac{\rho_{NW}}{\rho_W}-1\right)\right] \tag{4.15}$$

This equation is further simplified to Eq. (4.16), which shows that counter-current flow (sign +) yields a larger variation in the pressure difference between the two phases along the mesh,

$$\Delta P_{\mathrm{L}}^{\#} - \Delta P_{x=0}^{\#} = L^{\#}\left[\frac{12U_{\mathrm{W}}^{\#}}{H_{\mathrm{W}}^{\#2}}(1 \pm Rt) - \frac{Bo_{\mathrm{W}}}{Ca_{\mathrm{W}}}\sin\alpha\left(\frac{\rho_{\mathrm{NW}}}{\rho_{\mathrm{W}}} - 1\right)\right] \tag{4.16}$$

$$Rt = \frac{U_{\mathrm{NW}}\mu_{\mathrm{NW}}H_{\mathrm{W}}^{2}}{U_{\mathrm{W}}\mu_{\mathrm{W}}H_{\mathrm{NW}}^{2}} \tag{4.17}$$

where Rt is a dimensionless number defining the relative importance of frictional pressure drop in the NW phase with respect to the W phase. Considering cylindrical pores (f_{L} =2), the Laplace pressure difference across an interface (see Eq. (4.1)) in dimensionless form becomes,

$$\Delta P^{\#} = P_{\mathrm{NW}}^{\#} - P_{\mathrm{W}}^{\#} = 2\frac{\cos\theta_{\mathrm{App}}}{r^{\#}Ca_{\mathrm{W}}} \tag{4.18}$$

The design and physical parameters for filling all the pores with the, e.g. wetting phase, should be such that the variation of the pressure difference between the phases $\Delta P^{\#}$ along the mesh is less than the available range of pressure difference at the NW pore end (see Eq. (4.4)). If the W phase is at the large pore opening $\Delta P^{\#}_{\mathrm{CE,NW}} = \Delta P^{\#}_{\mathrm{C,NW}}$ but when the W phase is at the small pore opening, $\Delta P^{\#}_{\mathrm{CE,NW}} \neq \Delta P^{\#}_{\mathrm{C,NW}}$. Substituting Eq. (4.16) and (4.18) into Eq. (4.4) and utilising Table 3.2, the condition for operation with the pores filled with the wetting phase when this phase is placed at the large pore opening becomes,

$$\left|L^{\#}\left[\frac{12Ca_{\mathrm{W}}U_{\mathrm{W}}^{\#}}{H_{\mathrm{W}}^{\#2}}(1 \pm Rt) - Bo_{\mathrm{W}}\sin\alpha\left(\frac{\rho_{\mathrm{NW}}}{\rho_{\mathrm{W}}} - 1\right)\right]\right| < \left|-2\left(\frac{\cos(\min[180^{\circ}, \theta_{\mathrm{A}} + \phi_{\max}])}{r^{\#}} - \frac{\cos(\max[0, \theta_{\mathrm{R}} + \phi_{\mathrm{Int}}])}{r^{\#}}\right)\right| \tag{4.19}$$

Where $r^{\#}$ is defined at the meniscus location (NW pore end in this case). Appendix 4A illustrates the use of Eq. (4.19). In general, for liquid/liquid co-current flow, it is possible to use larger pores as compared to counter-current flow, although the latter is generally preferable for mass transfer operations.

4.5. Meniscus Stability Issues in Meshes

Below, several issues related to interfacial meniscus stability in meshes are analysed. These have mainly been identified during our experimental program where unexpected behaviour was observed under certain conditions.

4.5.1. Support/Edge/Foreign Particle Effect on Meniscus Stability

Microfabricated meshes often have supports, usually built-in, to improve the structural rigidity and in certain cases to provide the spacing necessary between the mesh capping plates (Wenn et al., 2003). It has been experimentally observed that these supports can result in a decrease of the meniscus stability (see subsequent Results section). A similar effect is obtained a) at the edges of the mesh, where gaskets or O-rings are used for sealing, b) on the mesh itself because of small foreign particles resting on it.

A 3D analysis of the meniscus stability in the presence of supports or small particles would require complex non-axisymmetric calculations since the location of the three phase contact line is not known a priori (Wong et al., 1992) and the geometry is unbounded. Furthermore a 3D analysis would depend on many geometrical factors and the solution would be restricted to specific geometries. Here, a simplified 2D analysis is conducted in order to gain insight on the support/edge/foreign particle effect on meniscus stability. The results can be used to estimate the effect in 3D systems considering that the factor f_L in the Laplace equation is between 1 and 2 (Byoung-Sik and Harriott, 1984).

Figure 4.2 represents a 2D mesh with an extension that can be either a (built-in) support or a gasket or O-ring. The contact angle on the support, θ_S, can either be the same as in the pores or different. Figure 4.3 represents a similar case for a spherical particle resting on the mesh. The meniscus accommodates an increase of pressure in the wetting phase by changing its curvature. During this change of curvature, one end of the meniscus remains pinned to the pore mouth (point 1) changing its apparent contact angle, $\theta_{App} = \theta + \phi - \varphi$, and the other rises along the support/particle while keeping a constant contact angle θ_S (advancing). φ is the angle between the symmetry axis of the meniscus and the symmetry axis of the pore (or the angle between the horizontal and the meniscus contact line). It increases as the meniscus rises along the support/particle. The solid wall inclination ϕ, varies from ϕ_{Int} to 90° at the pore end (the sign of ϕ_{Int} is defined according to Figure 3.4) and from $\phi_{S,Int}$ to 90° at the end of the support, while for a spherical particle on the mesh ϕ_S changes gradually from -90° to 90° at the top of the particle and back to -90°.

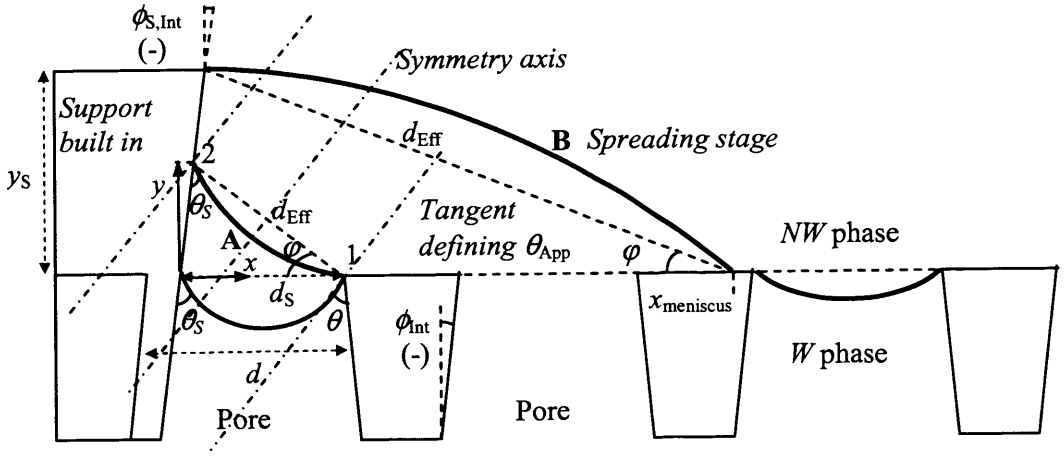

Figure 4.2. Meniscus breakthrough at the pore mouth and subsequent spreading in case of a built-in support.

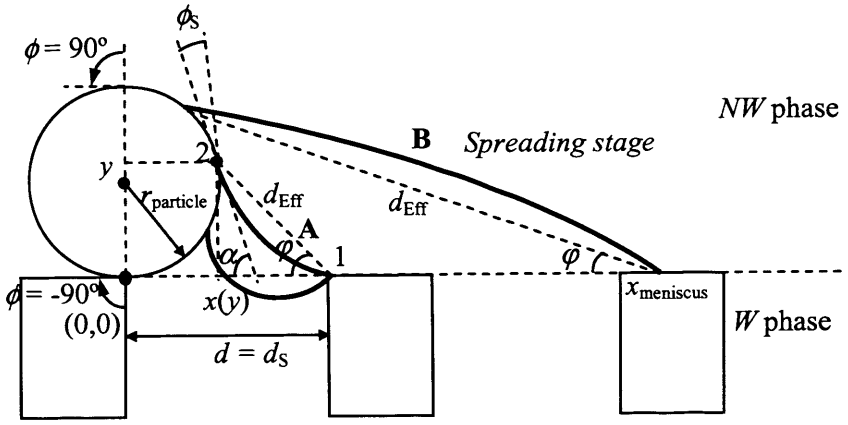

Figure 4.3. Meniscus breakthrough at the pore mouth and subsequent spreading due to the presence of a spherical particle resting on the mesh with $d = d_S$.

The overall meniscus breakthrough process at the support/particle consists generally of two stages. The first stage is the *meniscus breakthrough at the pore* (meniscus position A in Figure 4.2 and Figure 4.3), where the meniscus rises until it breaks through at the pore mouth (point 1) in response to an increase of the pressure difference P_W-P_{NW}. The breakthrough will occur either when the meniscus reaches the *maximum curvature* $(1/R)_{max}$ or when it achieves *maximum contortion* ($\phi = \phi_{max}$); whichever is encountered first. The second stage is the *meniscus spreading along the mesh* (position B in Figure 4.2 and Figure 4.3), where the meniscus advances over the mesh while it continues to rise on the support/particle. For particles, the solid

wall inclination changes during the meniscus rise, while for supports the inclination only changes at the support top. During this stage, the meniscus merges with other menisci as it advances along the mesh. The mesh breakthrough pressure can correspond to either of these two stages depending on the support/particle geometry, size and wetting characteristics. Meniscus breakthrough may also take place first at the support top in whose case the spreading stage is different. Below, the two stages of meniscus breakthrough are analysed.

4.5.1.1. Stage 1: Meniscus Breakthrough at the Pore

The meniscus rises on the support/particle if a) there is an increase in pressure difference between the phases, b) the support/particle is more wetting than the pores and c) there is a favourable combination of contraction/expansion at the support/particle vicinity. Considering that the support/particle may contact many pores, as a conservative approach, the pore diameter where the support /particle is, d_S, is taken equal to the pore diameter, d. The apparent contact angle that determines the meniscus curvature at any equilibrium stage is measured with respect to a line parallel to the meniscus symmetry axis that passes by the three-phase contact line (points 1 and 2 at pore mouth and support/particle respectively). This angle must be the same at both points 1 and 2 (see Eq. (4.20)).

$$\theta_{App} = \underbrace{\theta_S + \varphi + \phi_S}_{\text{at } \mathbf{2}} = \underbrace{\theta + \phi - \varphi}_{\text{at } \mathbf{1}} \quad \text{(see Figure 4.2 and Figure 4.3)} \tag{4.20}$$

The value of φ can be written by Eq. (4.21).

$$\varphi = \frac{\theta - \theta_S + \phi - \phi_S}{2} \tag{4.21}$$

To generalise the equations and according to the sign convention used, the $x(y)$ functions defining the shape of the support and of a spherical particle with its base at the (x,y) point (0,0) are given by Eqs. (4.22) and (4.23) respectively.

$$x(y) = -y \tan \phi_{S,Int} \tag{4.22}$$

$$x(y) = \sqrt{r_{particle}^2 - (y - r_{particle})^2} \tag{4.23}$$

The solid wall inclination along the straight support, ϕ_S, is given by Eq. (4.24) while for any other geometrical shape it is best described by Eq. (4.25), where α= arctan ($\partial y/\partial x$) is defined by Eq. (4.26) in the case of a spherical particle.

$$\begin{aligned} &\phi_S = \phi_{S,Int} && \text{for } y < y_S \\ &\phi_{S,Int} < \phi_S < \phi_{S,max} \ (90^\circ \text{ generally}) && \text{for } y = y_S \end{aligned} \tag{4.24}$$

$$\phi_S = \pm 90^\circ + \alpha \qquad (- \text{ if } \alpha > 0 \text{ and } + \text{ if } \alpha < 0) \tag{4.25}$$

$$\alpha = \arctan\left(\frac{\partial y}{\partial x}\right) = \arctan\left(\frac{-\sqrt{r_{particle}^2 - (y - r_{particle})^2}}{y - r_{particle}}\right) \tag{4.26}$$

The effective width of the meniscus contact line is defined by Eq. (4.27) and the angle φ is given by Eq. (4.28).

$$d_{Eff} = \sqrt{(d_S - x(y))^2 + y^2} = \frac{y}{\sin\varphi} \tag{4.27}$$

$$\begin{aligned} &\varphi = \arctan\left(\frac{y}{d_S - x(y)}\right) && \text{if } d_S\text{-}x(y) > 0 \\ &\varphi = 180 + \arctan\left(\frac{y}{d_S - x(y)}\right) && \text{if } d_S\text{-}x(y) < 0 \end{aligned} \tag{4.28}$$

For a straight support the meniscus height can be expressed combining Eq. (4.22) and (4.28),

$$y = \frac{d_S \tan\varphi}{1 - \tan\phi_{S,Int} \tan\varphi} \tag{4.29}$$

The pressure difference across the meniscus depicted in Figure 4.2 and Figure 4.3 is given by the Laplace Eq. (4.1) with a Laplace factor f_L = 1 using the effective diameter of the three phase contact line d_{Eff} and the apparent contact angle for the given position θ_{App}. Although this model is precise for f_L = 1, 3D geometries should result in Laplace factors f_L between 1 (2D case) and 2 (3D spherical menisci).

The calculation of the breakthrough pressure (maximum pressure difference) for one phase dispersing into the other can be carried out analytically for straight supports or by calculating the pressure difference at different meniscus equilibrium positions according to the procedure presented in Table 4.1.

A.	Calculation of θ_{App}.
	1. For each y, $x(y)$ is obtained via Eq. (4.22) for a support or Eq. (4.23) for a spherical particle.
	2. The solid wall inclination along the support is obtained via Eq. (4.24) for a support or Eq. (4.25) for a spherical particle, in which case α is calculated via Eq. (4.26).
	3. The angle of change of the meniscus symmetry axis, φ is obtained via Eq. (4.28).
	4. ϕ is obtained via Eq. (4.20) once ϕ_S is known. Values of $\phi < \phi_{Int}$ are not allowed and breakthrough at the pore mouth (point 1 at Figure 4.2 and Figure 4.3) takes place when ϕ becomes ϕ_{max}.
	5. The apparent contact angle θ_{App} is found by Eq. (4.20). For a straight support when the meniscus reaches the support top, the breakthrough pressure is always found at $\theta_{App} \leq 180°$.
B.	Calculation of the effective meniscus radius $r_{Eff} = d_{Eff}/2$ via Eq. (4.27).
C.	Calculation of the pressure difference ΔP by substituting the values of θ_{App} and d_{Eff} in Eq. (4.1).

Table 4.1. Procedure for calculation of pressure difference at different meniscus equilibrium positions during the *meniscus breakthrough at the pore* stage in the presence of a support/particle according to Eq. (4.1).

In spherical particles, the equilibrium positions to be used are best selected by equidistributing points along the circle arc length in order to ensure small steps in pressure difference increase. For $\phi_S = \phi_{S,max}$ and $\phi < \phi_{max}$, breakthrough takes place first at the support top. It is important to note that $\phi_{S,max}$ in spherical particles is 180° although in the present analysis $\phi_{S,max}$ is considered to be 90° since the breakthrough pressure is generally found before the meniscus reaches the top of the particle ($\phi_{S,max}$ = 90°). The procedure presented in Table 4.1 can also be applied to calculate the breakthrough pressure of the non-wetting phase (P_{NW}-P_W) at the wetting pore end using (180°-θ) and (180°-θ_S) as contact angles instead of θ and θ_S respectively.

However, in most cases it is only required to know the breakthrough pressure (maximum pressure difference) for one phase dispersing into the other, which for straight supports can be

calculated analytically from two characteristic curves ΔP vs. y. For spherical particles the analysis is only for one particle size and therefore only the first ΔP vs. y curve is considered since changing the size of the particles implies an overall change of the y-ΔP profile.

1) The first ΔP vs. y curve (obtained as described in Table 4.1 considers a support of infinite length, $y_S = \infty$. This results in a constant solid wall inclination $\phi_S = \phi_{S,Int}$ and an apparent contact angle $\theta_{App} = \theta_S + \phi_{S,Int} + \varphi$ (see Eq. (4.20)). When meniscus height y approaches infinite, $(P_{NW}$-$P_W) = 0$ although the meniscus generally will break through at the pore earlier. There are two characteristic points in this curve:

a) Height, $y_{\phi max}$, at which the meniscus breaks through by *maximum contortion* at the non-wetting pore end (point 1 in Figure 4.2 and Figure 4.3) when the maximum solid wall inclination is reached, $\phi = \phi_{max} = 90°$. At this point, $\phi = 90°$, the angle φ is found by Eq. (4.30) for a support/particle and $y_{\phi max}$ is found by substituting $\varphi_{\phi max}$ in Eq. (4.29) obtaining Eq. (4.31) for a straight support. For a spherical particle, Eq. (4.28) is non-linear in $y_{\phi max}$, and a numerical iterative method must be applied.

$$\varphi_{\phi max} = \frac{\theta - \theta_S + \phi_{max} - \phi_{S,Int}}{2} \tag{4.30}$$

$$y_{\phi max} = \frac{d_S \tan \varphi_{\phi max}}{1 - \tan \phi_{S,Int} \tan \varphi_{\phi max}} \tag{4.31}$$

For a mesh with built-in uniform cross-section supports ($\phi_{S,Int} = 0$) of the same material as the mesh ($\theta = \theta_S$) and uniform cross section 2D pores, the value $\varphi_{\phi max} = 45°$ ($y_{\phi max} = d_S = d$) gives rise to breakthrough by *maximum contortion* at point 1 (commencement of *spreading* stage). This is an interesting result that indicates that all supports of height larger than the pore diameter, $y_S > d$, undergo the same breakthrough pressure reduction. If the supports have higher wettability than the mesh pores ($\theta_S < \theta$), the breakthrough takes place at larger $\varphi_{\phi max}$.

b) Height, $y_{\Delta P max}$, at which the maximum pressure difference of the meniscus at the non-wetting pore end $(P_W$-$P_{NW})_{max}$ is reached independently of the value of ϕ (*breakthrough at the pore by maximum curvature*). This height can be either larger or smaller than $y_{\phi max}$ and it is found by equating the first derivative of the Laplace pressure difference given by Eq. (4.1) to zero, using as apparent contact angle, $\theta_{App} = \theta_S + \phi_S + \varphi$ and $d_{Eff} = d_S \tan\varphi / (\sin\varphi(1 - \tan\phi_{S,Int} \tan\varphi))$ for the case of a straight support (see Eq. (4.27) and (4.29)),

$$\frac{d\Delta P}{d\varphi} = \frac{2\gamma \sec\phi_{S,Int} \sin\left(\theta_S + 2(\varphi + \phi_{S,Int})\right)}{d_S} = 0 \tag{4.32}$$

$$\varphi_{\Delta P\max} = \frac{1}{2}\left(\pi - \theta_S - 2\phi_{S,Int}\right) \tag{4.33}$$

For a straight support $y_{\Delta P\max}$ is calculated analytically from Eq. (4.29):

$$y_{\Delta P\max} = \frac{d_S \tan\varphi_{\Delta P\max}}{1 - \tan\phi_{S,Int} \tan\varphi_{\Delta P\max}} \tag{4.34}$$

Eqs. (4.31) and (4.34) indicate that in a typical case of straight supports or sealing gaskets made from the same material as the mesh ($\theta = \theta_S$), the meniscus breaks through by *maximum contortion* for a wetting phase ($y_{\phi\max} = d_S < y_{\Delta P\max}$, if $\theta < 90°$) and by *maximum curvature* for a non-wetting phase ($y_{\Delta P\max} < y_{\phi\max} = d_S$, if $\theta > 90°$). Thus, when using a mesh with built-in supports of height $y_S > d_S$, the maximum achievable pressure difference of a wetting phase, $(P_W\text{-}P_{NW})_{max}$ is always reduced by the same amount when compared to meshes without supports and the breakthrough takes place at $y = d_S$. For a non-wetting phase it always takes place at a height smaller than d_S at which the meniscus acquires a shape of maximum curvature, not necessarily with $\theta_{App} = 180°$ since the meniscus effective radius varies along the support (Purcell, 1948).

2) The second characteristic ΔP vs. y curve (obtained as described in Table 4.1) considers a support with height y_S smaller than $y_{\phi\max}$, and represents the maximum pressure difference $(P_W\text{-}P_{NW})_{max}$ for the meniscus to break through by *maximum contortion* at either point 1 or 2 (see Figure 4.2 and Figure 4.3) when $y = y_S$. The condition that determines at what point the breakthrough takes place first is given by:

$$\begin{aligned} &(\phi - \phi_S) - (\phi_{\max} - \phi_{S,\max}) > 0 && \text{Breakthrough at 1 (pore mouth)} \\ &(\phi - \phi_S) - (\phi_{\max} - \phi_{S,\max}) < 0 && \text{Breakthrough at 2 (support top)} \end{aligned} \tag{4.35}$$

From Eq. (4.21), $(\phi\text{-}\phi_S) = \theta_S - \theta + 2\varphi_S$ where φ_S is the angle of the meniscus symmetry axis at $y = y_S$. Considering this, the previous conditions become,

$$\varphi_S > \frac{\theta - \theta_S + \phi_{\max} - \phi_{S,\max}}{2} \quad \text{Breakthrough at pore mouth} \tag{4.36}$$

$$\varphi_S < \frac{\theta - \theta_S + \phi_{max} - \phi_{S,max}}{2} \quad \text{Breakthrough at support top}$$

Depending on the location of the breakthrough, θ_{App} is calculated with the corresponding maximum solid wall inclination (see Eq. (4.20)). If the apparent contact angle of the meniscus θ_{App} reaches the value 180° (hemispherical shape of maximum curvature for a fixed meniscus diameter d_{Eff}) before either of the solid wall inclinations ϕ or ϕ_S reaches their maximum values ϕ_{max} or $\phi_{S,max}$, $\theta_{App} = 180°$ is employed in Eq. (4.1) to calculate the maximum pressure difference. This occurs when:

$$\begin{aligned} &\varphi_S < \theta + \phi_{max} - 180° \quad \text{when breakthrough is at pore mouth} \\ &\varphi_S > 180° - \theta_S - \phi_{S,max} \quad \text{when breakthrough is at support top} \end{aligned} \tag{4.37}$$

For the case when $\phi_{max} = \phi_{S,max} = 90°$ (flat meshes), the first condition in Eq. (4.37), applicable for breakthrough at the pore mouth, indicates that a hemispherical shape can only be reached at contact angles $\theta > 90°$. However, in systems with breakthrough at the support top the hemispherical shape can be reached for any support wettability.

These two ΔP vs. y curves for infinite and finite support height intersect at $y_{\phi max}$. In any support with $y_S > y_{\phi max}$ the meniscus breaks through by *maximum contortion* when $\phi = \phi_{max}$ at the pore end (point 1) before reaching the top of the support. For a system with a specific support height y_S, the pressure difference at $y_{\Delta P max}$ can be either a local or a global maximum. Given the support height y_S and the characteristic values $y_{\phi max}$ and $y_{\Delta P max}$, the global maximum pressure difference during the *meniscus breakthrough at the pore* stage is calculated according to Table 4.2,

1.	$y_S < \min(y_{\phi max}, y_{\Delta P max})$, the maximum pressure difference is reached as the meniscus is pinned at points 1 and 2 ($y = y_S$) and is calculated via Table 4.1 using y_S and $\theta_{App,max}$ at the breakthrough point, 1 or 2 according to condition given by Eq. (4.35), $\theta_{App} = (\theta + \phi_{max} - \varphi)$ for breakthrough at the pore end, $\theta_{App} = (\theta_S + \phi_{S,max} + \varphi)$ for breakthrough at the support top or $\theta_{App} = 180°$ if Eq. (4.37) is satisfied.
2.	$y_{\phi max} < y_S < y_{\Delta P max}$, the maximum pressure difference $(P_W\text{-}P_{NW})_{max} = -\Delta P$ is obtained via Table 4.1 using $y_{\phi max}$ and $\theta_{App} = (\theta + \phi_{max} - \varphi)$.
3.	$y_{\Delta P max} < y_S < y_{\phi max}$, the maximum pressure difference is the maximum of the values calculated at $y_{\Delta P max}$ and y_S. In the latter, Eqs. (4.35) and (4.37) are used to find the maximum apparent contact angle.
4.	$y_S > \max(y_{\Delta P max}, y_{\phi max})$, in this case, $\min(y_{\Delta P max}, y_{\phi max})$ always determines the height at which the global maximum pressure difference $(P_W\text{-}P_{NW})_{max}$ takes place.

Table 4.2. Procedure for calculation of maximum pressure difference during the meniscus breakthrough at the pore stage for straight supports of height y_S.

Below, an example that illustrates the calculation of the maximum pressure difference during the *meniscus breakthrough at the pore* stage for the wetting phase is presented. Two additional examples for breakthrough of the non-wetting phase are presented in Appendix 4B.

Example 1: A mesh with cylindrical pores ($\phi_{int} = 0$), built-in supports, $\theta = \theta_S = 30°$ and $d_S = d$ is considered. Figure 4.4 shows the two characteristic curves ΔP vs. y for $y = y_S$ and $y_S = \infty$, for this system. According to Eqs. (4.36) and (4.37), the meniscus always breaks through first at the pore mouth (point 1 in Figure 4.2) irrespective of the support height and θ_{App} never reaches 180°. $\varphi_{\phi max} = 45°$ ($y_{\phi max}/r = 2$) and $\varphi_{\Delta P max} = 75° > \varphi_{\phi max}$ and breakthrough at the pore mouth occurs before reaching $y_{\Delta P max} = 7.46$. The portion of the ΔP vs. y curve for $y_S = \infty$, on the right hand side of point **e** is unattainable. Therefore, for supports with $y_S/r > 2$, the maximum pressure difference at the pore mouth is found using $y_{\phi max}/r = 2$ in Table 4.1 (point **e** in Figure 4.4) with $\theta_{App} = \theta + \phi_{max} - \varphi_{\phi max} = 30°+90°-45° = 75°$, resulting in $(P_W\text{-}P_{NW})_{max} r/\gamma = -0.183$. If the support height y_S is shorter than $y_{\phi max}/r = 2$, e.g. $y_S/r = 1$, the meniscus reaches the support top and copes with a pressure difference change by changing its curvature until it breaks through at the pore end, following the **a-b-c** pressure difference path in Figure 4.4. At $y_S/r = 1$, $\varphi = 26.6°$ (Eq. (4.28)). The maximum pressure difference in this situation (meniscus reaches the top of the support) is given by the Laplace equation using the maximum apparent contact angle at point 1 (Figure 4.2) where the meniscus first breaks through, $\theta_{App,max} = \theta + \phi_{max} - \varphi = 30°+90°-26.6° =$

93.4°, which results in $(P_W\text{-}P_{NW})_{max}r/\gamma = 0.0535$. In the pores away from the supports, the maximum pressure difference the meniscus can cope without breakthrough is $(P_W\text{-}P_{NW})_{max}r/\gamma = -\cos 120° = 0.5$, represented by a horizontal line in Figure 4.4.

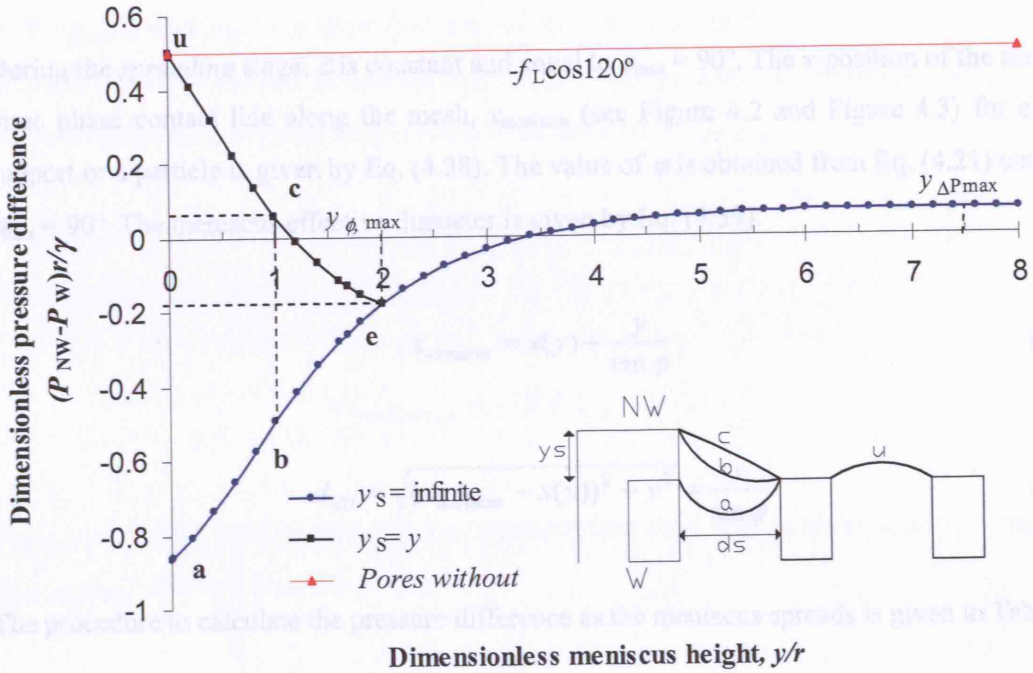

Figure 4.4. Dimensionless pressure difference $(P_W\text{-}P_{NW})r/\gamma$ as a function of the dimensionless meniscus height y/r, during the *meniscus breakthrough at the pore* stage. Cylindrical pores ($\phi_{Int} = 0$), $\phi_{S,Int} = 0$, $\theta = \theta_S = 30°$ and $d_S/r = 2$.

4.5.1.2. Stage 2: Meniscus Spreading along the Mesh

After the meniscus breaks at the pore mouth, it spreads along the mesh as shown by position **B** in Figure 4.2 and Figure 4.3. When the meniscus breakthrough takes place first at the support top (see Eq. (4.36)), the *spreading* stage also occurs along the top of the support. In this case the maximum pressure difference is always found just before the breakthrough takes place. When the meniscus starts spreading at the support top the value of the apparent contact angle $\theta_{App} = \theta_S+\phi_S+\varphi$ (see Eq. (4.20)) decreases (due to the reduction of φ) while the effective diameter of the meniscus d_{Eff} increases resulting in a reduction of the pressure difference according to Eq. (4.1). The maximum pressure difference found as the meniscus spreads may be either smaller or larger than the maximum value during the *meniscus breakthrough at the pore*

stage and therefore spreading proceeds either spontaneously or an increase of ΔP between the phases is required. In the latter case, the breakthrough pressure is defined within the *spreading* stage. During the *spreading* stage, *slow motion* is assumed so that the equilibrium contact angle (or the advancing contact angle) is used rather than the dynamic one, which is a function of the meniscus motion rate (Rose and Heins, 1962).

During the *spreading* stage, ϕ is constant and equal to $\phi_{max} = 90°$. The x-position of the meniscus three phase contact line along the mesh, $x_{meniscus}$ (see Figure 4.2 and Figure 4.3) for either a support or a particle is given by Eq. (4.38). The value of φ is obtained from Eq. (4.21) using $\phi = \phi_{max} = 90°$. The meniscus effective diameter is given by Eq. (4.39).

$$x_{meniscus} = x(y) + \frac{y}{\tan\varphi} \tag{4.38}$$

$$d_{Eff} = \sqrt{(x_{meniscus} - x(y))^2 + y^2} = \frac{y}{\sin\varphi} \tag{4.39}$$

The procedure to calculate the pressure difference as the meniscus spreads is given in Table 4.3.

A.	Calculation of θ_{App}.
	1. For each y, $x(y)$ is obtained via Eq. (4.22) for a support or Eq. (4.23) for a spherical particle.
	2. The solid wall inclination along the support is obtained via Eq. (4.24) for a support or Eq. (4.25) for a spherical particle, in which case α is calculated via Eq. (4.26). When $y = y_S$ for the case of a support, ϕ_S values between $\phi_{S,Int}$ and $\phi_{S,max}$ are possible.
	3. The angle of change of the meniscus symmetry axis, φ is obtained via Eq. (4.21) using $\phi = \phi_{max} = 90°$.
	4. The apparent contact angle θ_{App} is found by Eq. (4.20), $\theta_{App} = \theta + \phi_{max} - \varphi$ (only dependent on φ).
B.	Calculation of the effective meniscus radius $r_{Eff} = d_{Eff}/2$ via Eq. (4.39); the required $x_{meniscus}$ is obtained from Eq. (4.38).
C.	Calculation of the pressure difference ΔP by substituting the values of θ_{App} and d_{Eff} in Eq. (4.1).

Table 4.3. Procedure for calculation of pressure difference at different meniscus equilibrium positions during the *spreading stage* in the presence of a support/particle according to Eq. (4.1).

As the meniscus rises during the *spreading* stage at the straight support (perpendicular or inclined to the mesh), θ_{App} remains constant while d_{Eff} increases. This results in a monotonic

pressure difference decrease or increase depending on whether the meniscus curvature is convex or concave respectively. This curve is a ΔP vs. y curve for $y_S = \infty$ hence, a local maximum of pressure difference cannot be found before the meniscus reaches the support top, $y = y_S$. The value of φ, at which there is a local maximum of pressure difference for straight supports, is given by Eq. (4.41). This is obtained by differentiating the Laplace Eq. (4.1) where $y = y_S$, $\theta_{App} = \theta + \phi_{max} - \varphi$ and $d_{Eff} = y_S/\sin\varphi$ (see Eq. (4.40)). It is important to note that $\varphi_{spread,\Delta Pmax}$ is independent of the support inclination angle $\phi_{S,Int}$. A similar analysis can be applied to spherical particles although there is no simple linear expression for $\varphi_{spread,\Delta Pmax}$.

$$\frac{\partial \Delta P}{\partial \varphi} = -\frac{2\gamma\cos(\theta - 2\varphi + \phi_{max})}{y_S} = 0 \tag{4.40}$$

$$\varphi_{spread,\Delta Pmax} = \frac{1}{2}(\theta + \phi_{max} - \pi/2) = \frac{\theta}{2} \tag{4.41}$$

$\varphi_{spread,\Delta Pmax}$ is then used to calculate the corresponding solid wall inclination at the support top $\phi_{S,spread,\Delta Pmax}$ obtained from Eq. (4.21).

$$\phi_{S,spread,\Delta Pmax} = \frac{\pi}{2} - \theta_S \tag{4.42}$$

The maximum pressure difference during the *spreading* stage is then calculated by following steps **A4** to **C** in Table 4.3. Eq. (4.42) indicates that $\phi_{S,spread,\Delta Pmax}$ cannot be larger than 90° which means that the maximum pressure difference is always reached before the meniscus breaks at the support top. When the angle calculated by Eq. (4.41) is larger than the maximum obtainable value of φ, φ_{max} (see Eq. (4.43)), the equation is not applicable and there is no local maximum of pressure difference during the *spreading* stage.

$$\begin{aligned} &\varphi_{max} = \varphi_S,\ \varphi_S \text{ obtained from Eq. (4.28) for } y = y_S. && (y_S \le y_{\phi max}) \\ &\varphi_{max} = \varphi_{\phi max},\ \varphi_{\phi max} \text{ obtained from Eq. (4.30).} && (y_S > y_{\phi max}) \end{aligned} \tag{4.43}$$

In order to determine the mesh breakthrough pressure, the maximum pressure difference obtained at the *meniscus breakthrough at the pore* stage (according to Table 4.1) and at the *spreading* stage (in the case $\varphi_{spread,\Delta Pmax} < \varphi_{max}$) need to be calculated. The maximum of these two values is the mesh breakthrough pressure. When $\varphi_{spread,\Delta Pmax} > \varphi_{max}$, there is no local maximum during the *spreading* stage and the mesh breakthrough pressure is always found

during the *meniscus breakthrough at the pore* stage. Assuming gravity effects on the meniscus shape are neglected, φ becomes zero as the meniscus spreading ($x_{meniscus}$) approaches infinity. ϕ_S for infinite spreading is calculated from Eq. (4.20) to obtain,

$$\phi_{S,\infty} = \phi_{max} + \theta - \theta_S \tag{4.44}$$

In a spherical particle this angle will also determine the meniscus position on the particle. For illustration purposes the following examples are presented,

Example 1: Straight supports or edges. A system with straight perpendicular supports ($\phi_{S,Int}$ = 0) and properties θ = 30°, θ_S = 30°, ϕ_{Int} = 0°, ϕ_{max} = 90° and $\phi_{S,max}$ = 90° is considered. Five different support heights are analysed, namely, y_S/r = 0.2, 1, 2, 4 and 10. Figure 4.5 shows dimensionless pressure difference versus dimensionless height of the meniscus at the support, during the two-stage breakthrough process obtained via Table 4.1 and Table 4.3. The change in pressure difference during the first stage is given by a path following the ΔP vs y curve for y_S = ∞ until $y/r = y_S/r$ and then vertically to the ΔP vs y curve for $y_S = y$ (e.g. path **a-b-c** for y_S/r = 1; path **a-e** for y_S/r = 4). For $y_S \leq y_{\phi max}$ the *spreading* stage commences when the meniscus is already at the support top. The pressure difference path continues along the solid vertical line, whose maximum pressure difference is found at $\varphi_{spread,\Delta Pmax}$ given by Eq. (4.41) if $\varphi_{spread,\Delta Pmax} \leq \varphi_{max}$ (e.g. path **c-d** for y_S/r = 1) or at φ_S if $\varphi_{spread,\Delta Pmax} > \varphi_{max}$ (e.g. point **i** for y_S/r = 0.2). For $y_S > y_{\phi max}$ the *spreading* stage commences before the meniscus reaches the top of the support, following the monotonic ΔP vs y curve for y_S = ∞ (e.g. path **e-f** for y_S/r = 4). At $y = y_S$, shown by the vertical line from this curve, the meniscus will break through at the top of the support and the pressure difference path is up to the mesh breakthrough point (e.g. path **f-g** for y_S/r = 4). The dimensionless breakthrough pressure difference at **g** can be easily calculated, $\Delta P_{B,W} r/\gamma$= 0.0335 by applying Eq. (4.41) to obtain $\varphi_{spread,\Delta Pmax}$ = 15°. Eq. (4.20) and (4.39) are then used to obtain θ_{App} = 105° and $d_{Eff}/r = (y_S/r)/\sin\varphi_{spread,\Delta Pmax}$ = 15.46. Beyond the mesh breakthrough point, the meniscus equilibrium pressure difference drops to zero at infinite spreading. In all these cases apart from the one with y_S/r = 0.2 ($\varphi_{spread,\Delta Pmax} > \varphi_{max}$ = arctan(0.2/2) = 5.7° according to Eq. (4.43)), mesh breakthrough occurs during the *spreading* stage.

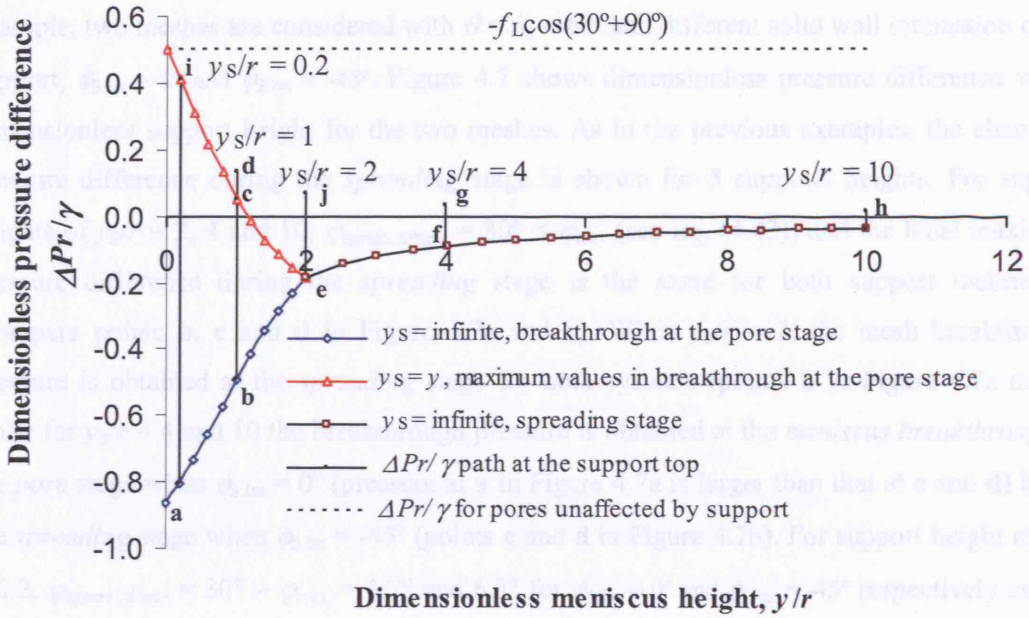

Figure 4.5. Dimensionless pressure difference $\Delta Pr/\gamma$ versus dimensionless meniscus height y/r during the *meniscus breakthrough at the pore* and *spreading* stages in a system with straight support. θ_S = 30°, $\phi_{S,Int}$ = 0°, θ = 30°, ϕ_{max} = 90° and ϕ_{Int} = 0°. Points **i**, **d**, **j**, **g** and **h** represent mesh breakthrough at y_S/r = 0.2, 1, 2, 4 and 10 respectively. Vertical lines indicate the $\Delta Pr/\gamma$ path after the support top is reached (only larger pressure difference than those before reaching the support top are shown), either during the *breakthrough at the pore stage* (on the left of **e** and up to the $y_S = y$) or during the *spreading* stage (above the $y_S = y$ curve).

Figure 4.6 represents two of the mesh breakthrough paths shown in Figure 4.5.

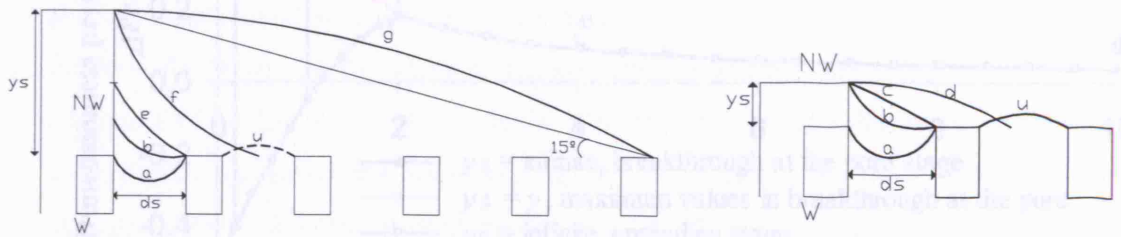

b)

Figure 4.6. Representation of mesh breakthrough paths in a system with straight support. θ_S = 30°, $\phi_{S,Int}$ = 0°, θ = 30°, ϕ_{max} = 90° and ϕ_{Int} = 0° for two different support heights, a) y_S/r = 4 and b) y_S/r = 1.

Example 2: Effect of Solid Wall Inclination in a Wetting Support/Mesh System. In this example, two meshes are considered with $\theta = \theta_S = 60°$ and different solid wall inclination of the support, $\phi_{S,Int} = 0°$ and $\phi_{S,Int} = -45°$. Figure 4.7 shows dimensionless pressure difference versus dimensionless support height for the two meshes. As in the previous examples, the change in pressure difference during the *spreading* stage is shown for 5 supports heights. For support heights of $y_S/r = 2$, 4 and 10, $\varphi_{spread,\Delta Pmax} = 30° < \varphi_{max}$ (see Eq. (4.43)) and the local maximum pressure difference during the *spreading* stage is the same for both support inclinations (compare points **b**, **c** and **d** in Figure 4.7a and b). When $y_S/r = 2$, the mesh breakthrough pressure is obtained at the *spreading* stage for both systems (points **b** in Figure 4.7a and b) while for $y_S/r = 4$ and 10 the breakthrough pressure is obtained at the *meniscus breakthrough at the pore* stage when $\phi_{S,Int} = 0°$ (pressure at **a** in Figure 4.7a is larger than that at **c** and **d**) but at the *spreading* stage when $\phi_{S,Int} = -45°$ (points **c** and **d** in Figure 4.7b). For support height of $y_S/r = 0.2$, $\varphi_{spread,\Delta Pmax} = 30° > \varphi_{max} = 5.7°$ and 6.3° for $\phi_{S,Int} = 0°$ and $\phi_{S,Int} = -45°$ respectively and no local ΔP maximum is reached during the *spreading* stage. Hence, mesh breakthrough always occurs during the *meniscus breakthrough at the pore* stage (points **e** in Figure 4.7a and b). For support height of $y_S/r = 1$, $\varphi_{max} = 26.6° < \varphi_{spread,\Delta Pmax} = 30°$ when $\phi_{S,Int} = 0°$ (meniscus breakthrough at the pore) and $\varphi_{max} = 45° > \varphi_{spread,\Delta Pmax} = 30°$ when $\phi_{S,Int} = -45°$ (meniscus breakthrough during the spreading stage).

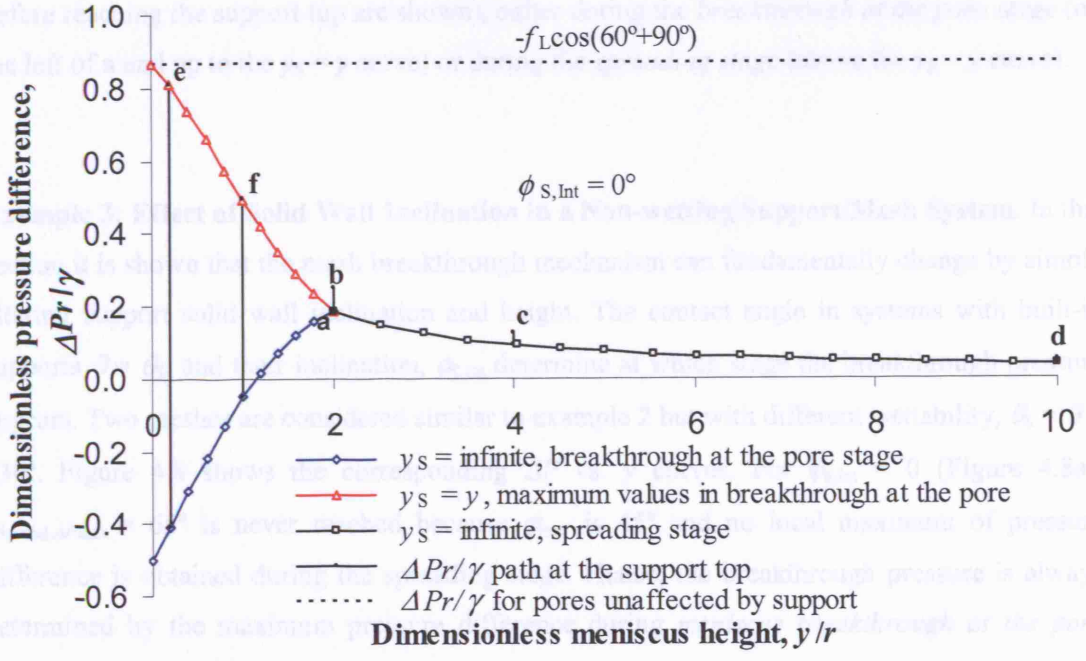

a)

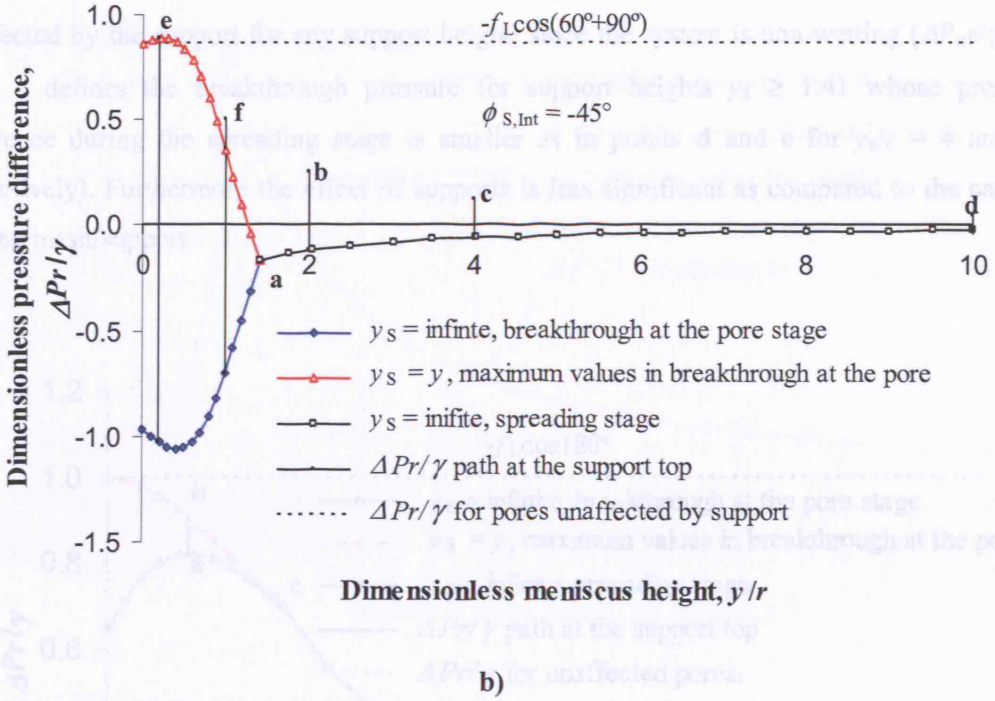

b)

Figure 4.7. Dimensionless pressure difference $\Delta Pr/\gamma = (P_W - P_{NW})r/\gamma$ versus dimensionless meniscus height y/r during the *meniscus breakthrough at the pore* and *spreading* stages in a system with two different support inclinations a) $\phi_{S,Int} = 0°$ and b) $\phi_{S,Int} = -45°$. $\theta_S = \theta = 60°$ and $\phi_{max} = 90°$. Different support heights, y/r = 0.2, 1, 2, 4 and 10 are represented. Vertical lines indicate $\Delta Pr/\gamma$ path after the support top is reached (only larger pressure difference than those before reaching the support top are shown), either during the *breakthrough at the pore stage* (on the left of **a** and up to the $y_S = y$ curve) or during the *spreading stage* (above the $y_S = y$ curve).

Example 3: Effect of Solid Wall Inclination in a Non-wetting Support/Mesh System. In this section it is shown that the mesh breakthrough mechanism can fundamentally change by simply altering support solid wall inclination and height. The contact angle in systems with built-in supports $\theta = \theta_S$, and their inclination, $\phi_{S,Int}$ determine at which stage the breakthrough pressure appears. Two meshes are considered similar to example 2 but with different wettability, $\theta_S = \theta = 130°$. Figure 4.8 shows the corresponding ΔP vs. y curves. For $\phi_{S,Int} = 0$ (Figure 4.8a), $\varphi_{spread,\Delta Pmax} = 65°$ is never reached because φ_{max} is 45° and no local maximum of pressure difference is obtained during the spreading stage. Hence, the breakthrough pressure is always determined by the maximum pressure difference during *meniscus breakthrough at the pore* stage (point **a** at $y_{\Delta Pmax}/r = 0.9326$ for meniscus heights $y_S/r \geq 1.39$). For $\phi_{S,Int} = -45°$ (Figure 4.8b), φ_{max} is 67° and although a local maximum exists during spreading (above point **b**), this is very small and indistinguishable from the ΔP vs. y for $y_S = y$ *spreading* curve. In this case, a

negative support inclination results in a breakthrough pressure even higher than that in pores unaffected by the support for any support height, since the system is non-wetting ($\Delta P_B r/\gamma > 1$; point **c** defines the breakthrough pressure for support heights $y_S \geq 1.41$ whose pressure difference during the spreading stage is smaller as in points **d** and **e** for $y_S/r = 4$ and 10 respectively). Furthermore the effect of supports is less significant as compared to the case of wetting mesh/support.

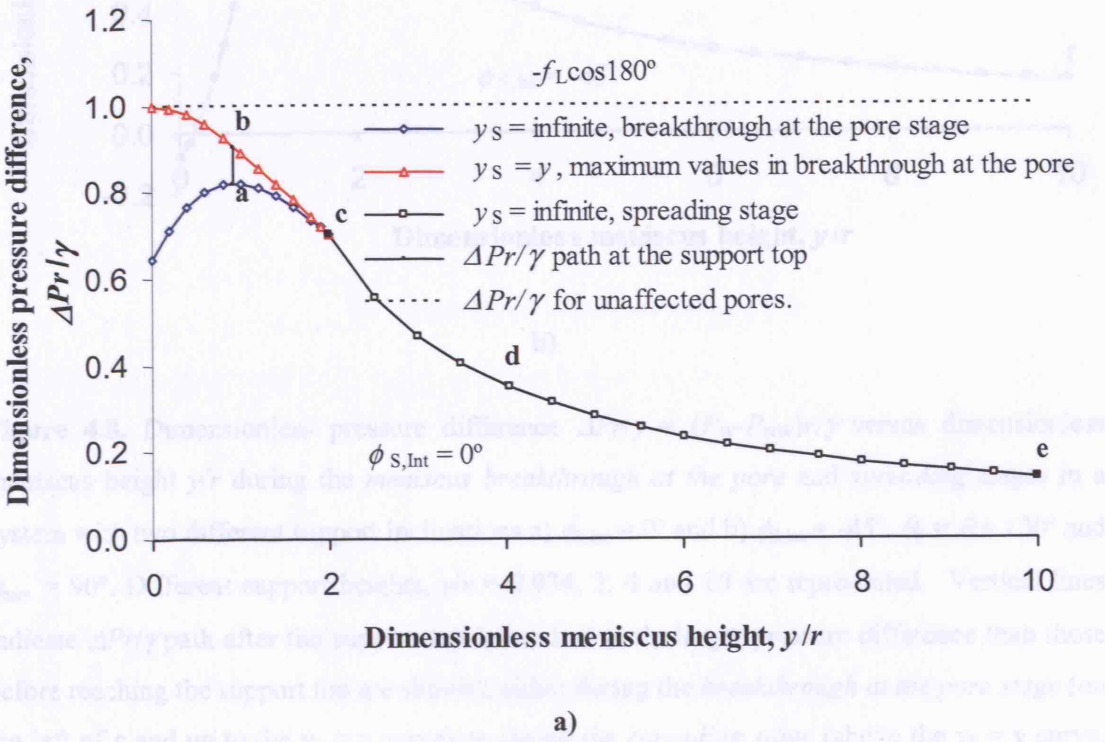

a)

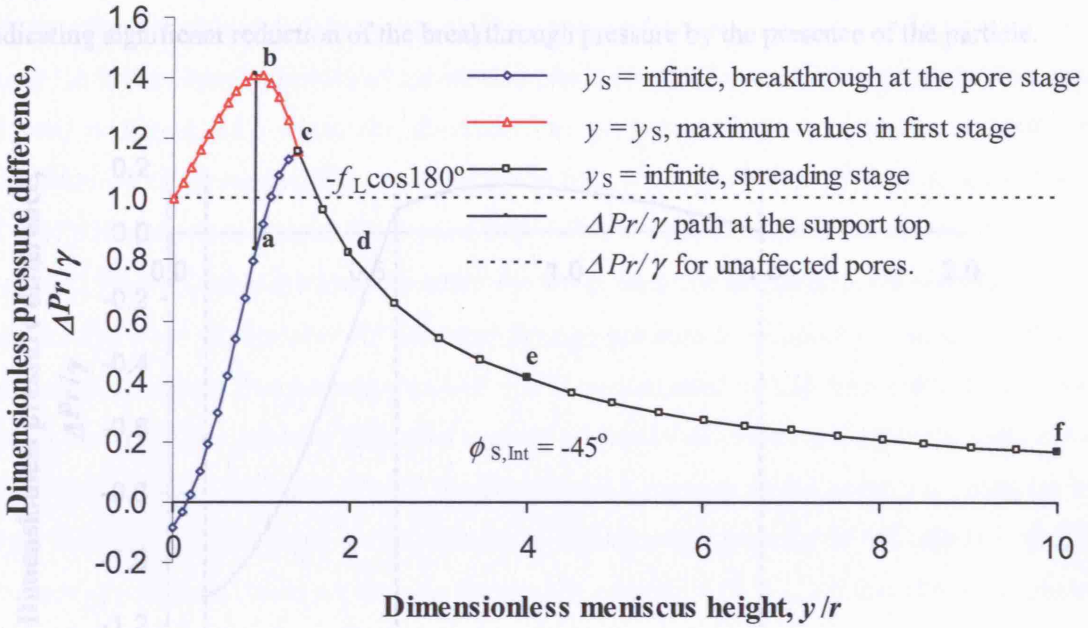

b)

Figure 4.8. Dimensionless pressure difference $\Delta Pr/\gamma = (P_W - P_{NW})r/\gamma$ versus dimensionless meniscus height y/r during the *meniscus breakthrough at the pore* and *spreading* stages in a system with two different support inclinations a) $\phi_{S,Int} = 0°$ and b) $\phi_{S,Int} = -45°$. $\theta_S = \theta = 130°$ and $\phi_{max} = 90°$. Different support heights, y/r = 0.934, 2, 4 and 10 are represented. Vertical lines indicate $\Delta Pr/\gamma$ path after the support top is reached (only larger pressure difference than those before reaching the support top are shown), either during the *breakthrough at the pore stage* (on the left of **c** and up to the $y_S = y$ curve) or during the *spreading stage* (above the $y_S = y$ curve, not present in these cases).

Example 4: Spherical Particles Resting on the Mesh. Breakthrough Determination Procedure. Figure 4.9 shows the dimensionless equilibrium pressure difference and the meniscus spread along the mesh as the meniscus height increases. A spherical particle is considered to rest on a pore of a mesh with properties $d_{particle} = d$, $\theta = 30°$, $\theta_S = 90°$, $\phi_{Int} = 0°$, $\phi_{max} = 90°$. Three regions can be identified: region 1, if ϕ obtained by Table 4.1 *is* $\phi < \phi_{Int}$ the meniscus cannot be in equilibrium while pinned at the pore mouth and hence no physically realistic result is possible. Region 2 represents the *meniscus breakthrough at the pore* stage (calculated by applying Table 4.1). Region 3 is the *spreading* stage (pressure difference is calculated from Table 4.3) at which the absolute pressure difference maximum is found; at the last point of region 3, the meniscus spreading becomes infinite for $\phi_{S,\infty} = 60°$ (see Eq. (4.44))

and y_∞/r = 1.50 (see (4.25) and (4.26)). The meniscus breaks through at $\Delta Pr/\gamma$ = 0.144, indicating significant reduction of the breakthrough pressure by the presence of the particle.

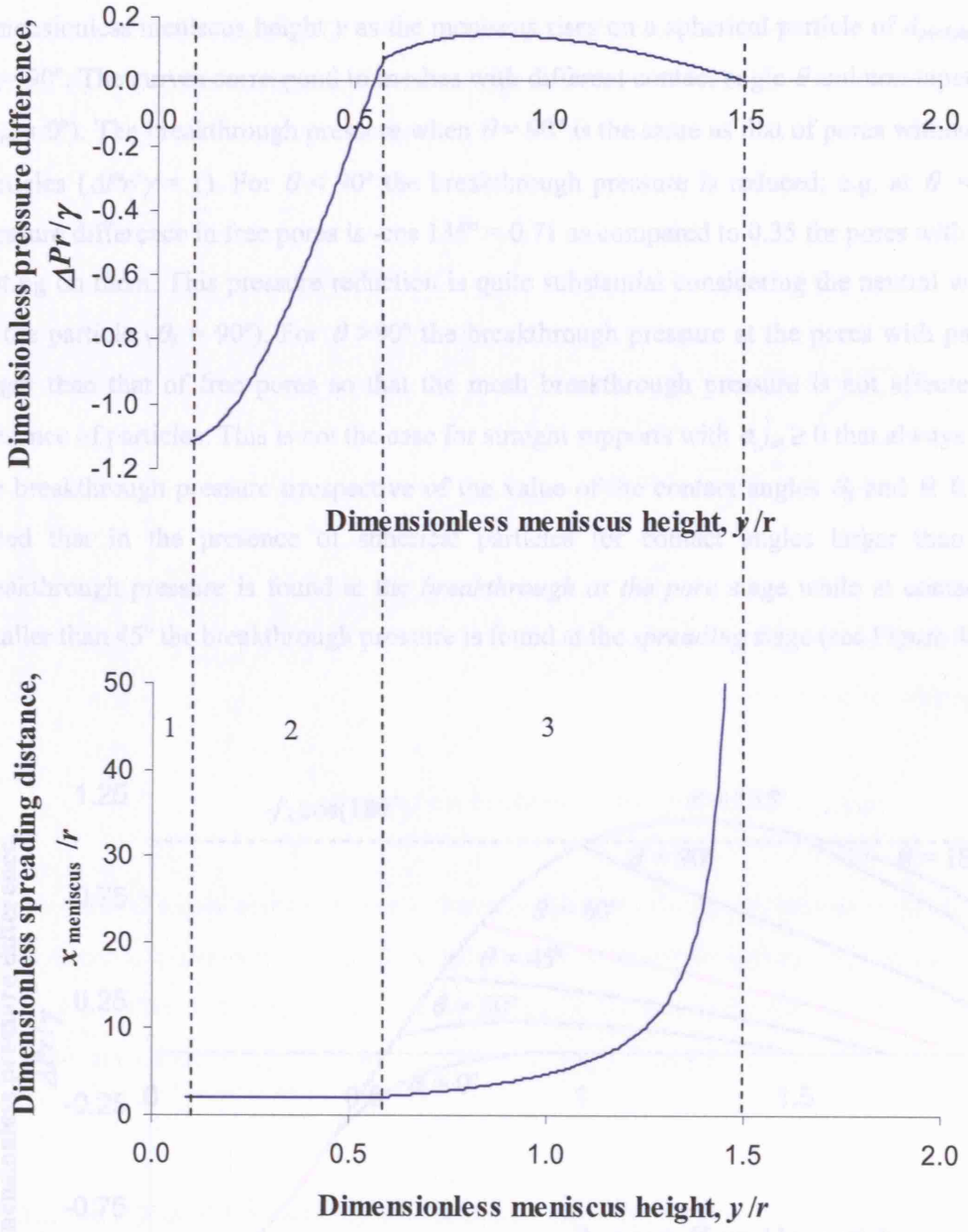

Figure 4.9. Dimensionless pressure difference $\Delta Pr/\gamma = (P_W - P_{NW})r/\gamma$ and dimensionless spreading distance $x_{meniscus}/r$ (see Figure 4.3) versus dimensionless meniscus height y/r during the *meniscus breakthrough at the pore* and *spreading* stages in a system with a spherical particle resting on the mesh. $d_{particle} = d$, $\theta_S = 90°$, $\phi_{Int} = 0°$, $\theta = 30°$ and $\phi_{max} = 90°$. Region 1: $\phi < \phi_{Int}$, Region 2: stage of breakthrough at the pore, Region 3: Spreading stage.

Example 5: Effect of Mesh Wettability on Breakthrough Pressure for Particle/Mesh System. Small particles that may rest on the mesh surface will in general affect to a larger extent the breakthrough pressure of the wetting phase ($\theta < 90°$) compared to supports. This can be seen in Figure 4.10 where the dimensionless pressure difference is plotted against the dimensionless meniscus height y as the meniscus rises on a spherical particle of $d_{particle} = d$ and $\theta_S = 90°$. The curves correspond to meshes with different contact angle θ and non-tapered pores ($\phi_{Int} = 0°$). The breakthrough pressure when $\theta = 90°$ is the same as that of pores without foreign particles ($\Delta Pr/\gamma = 1$). For $\theta < 90°$ the breakthrough pressure is reduced; e.g. at $\theta = 45°$ the pressure difference in free pores is -cos 135° = 0.71 as compared to 0.35 for pores with particles resting on them. This pressure reduction is quite substantial considering the neutral wettability of the particle ($\theta_S = 90°$). For $\theta > 90°$ the breakthrough pressure at the pores with particles is larger than that of free pores so that the mesh breakthrough pressure is not affected by the presence of particles. This is not the case for straight supports with $\phi_{S,Int} \geq 0$ that always decrease the breakthrough pressure irrespective of the value of the contact angles θ_S and θ. It must be noted that in the presence of spherical particles for contact angles larger than 45° the breakthrough pressure is found at the *breakthrough at the pore* stage while at contact angles smaller than 45° the breakthrough pressure is found at the *spreading* stage (see Figure 4.10).

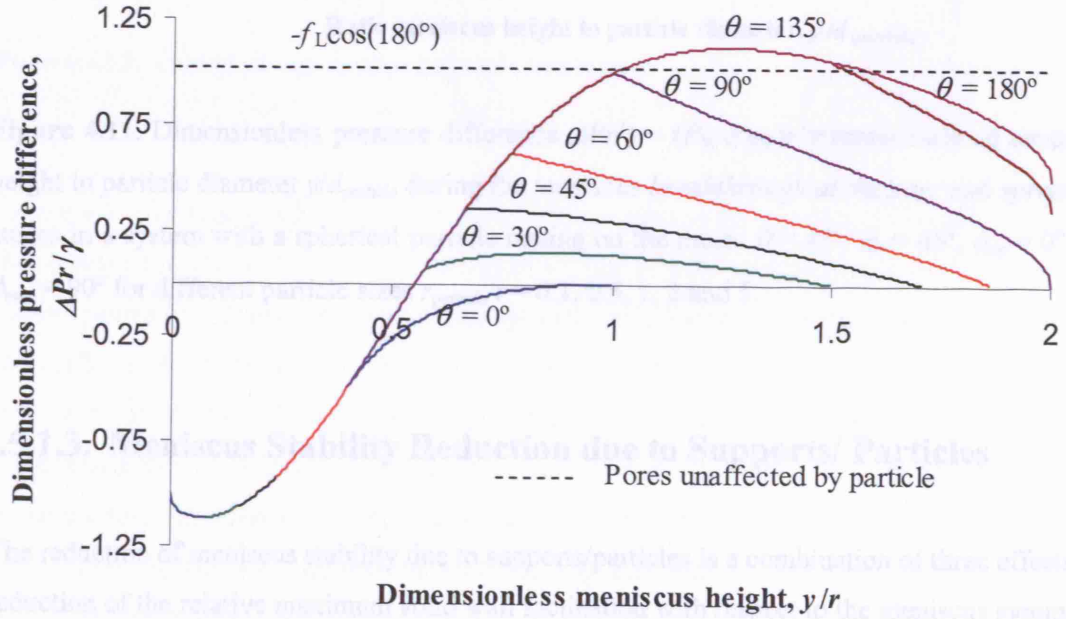

Figure 4.10. Dimensionless pressure difference $\Delta Pr/\gamma = (P_W - P_{NW})r/\gamma$ versus dimensionless meniscus height y/r during the *meniscus breakthrough at the pore* and *spreading* stages in a system with a spherical particle resting on the mesh. $d_{particle} = d$, $\theta_S = 90°$, $\phi_{Int} = 0°$, $\phi_{max} = 90°$ and 7 different meniscus contact angles at the pore, $\theta = 0°$, 30°, 45°, 60, 90°, 135° and 180°.

Example 6: Effect of Particle Size on Breakthrough Pressure for Particle/Mesh System. For wetting pores and particles if the particle size is larger than the pore diameter, the effect on pressure difference reduction is magnified as can be seen in Figure 4.11 where the horizontal line defines the pressure difference for the free pores. By comparing Figure 4.10 (for $\theta = 45°$) and Figure 4.11 (for $r_{particle}/r = 1$) it can be seen that reducing the wettability of the particle ($\theta_S = 90°$ vs. $\theta_S = 45°$) also reduces the breakthrough pressure difference ($\Delta Pr/\gamma$ decreases from 0.35 to 0.18).

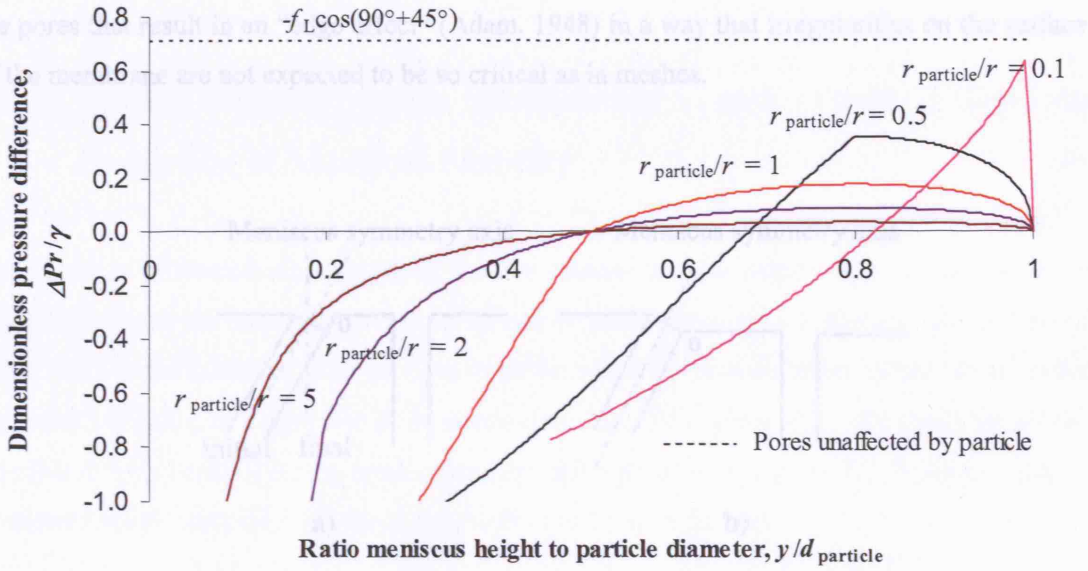

Figure 4.11. Dimensionless pressure difference $\Delta Pr/\gamma = (P_W - P_{NW})r/\gamma$ versus ratio of meniscus height to particle diameter $y/d_{particle}$ during the *meniscus breakthrough at the pore* and *spreading* stages in a system with a spherical particle resting on the mesh. $\theta = 45°$, $\theta_S = 45°$, $\phi_{Int} = 0°$ and $\phi_{max} = 90°$ for different particle sizes $r_{particle}/r = 0.1$, 0.5, 1, 2 and 5.

4.5.1.3. Meniscus Stability Reduction due to Supports/ Particles

The reduction of meniscus stability due to supports/particles is a combination of three effects: a) reduction of the relative maximum solid wall inclination with respect to the meniscus symmetry axis (ϕ_{max}-φ) at the pore mouth, b) increase of the effective diameter of the pore, and in some cases c) increase of the wettability (if $\theta_S > \theta$). The inclination of the supports influences the value of φ during the *breakthrough at the pore stage* so that the reduction in the breakthrough pressure during this stage in a inclined support with $\phi_{S,Int} = -45°$ is substantially larger than that

in a perpendicular support with $\phi_{S,Int} = 0°$ for a wetting system and viceversa for a non wetting system. Several pore imperfections commonly found in conventional membranes can be analysed in a similar way. For example, an inclined pore as that shown in Figure 4.12a results in a reduction of stability due to a larger effective pore diameter than that of a straight pore since the maximum wall inclination of the meniscus at **o** continues to be 90° with respect to the final symmetry axis of the meniscus ($\varphi_{final} = 0$). However, if the inclined pore is in a step (see Figure 4.12b), the maximum solid wall inclination of the meniscus at **o** is less than 90° with respect to the meniscus symmetry axis ($\varphi_{final} > 0$), giving rise to a large decrease on meniscus breakthrough pressure. Conventional membranes with tortuous pores have constrictions along the pores that result in an "edge effect" (Adam, 1948) in a way that irregularities on the surface of the membrane are not expected to be so critical as in meshes.

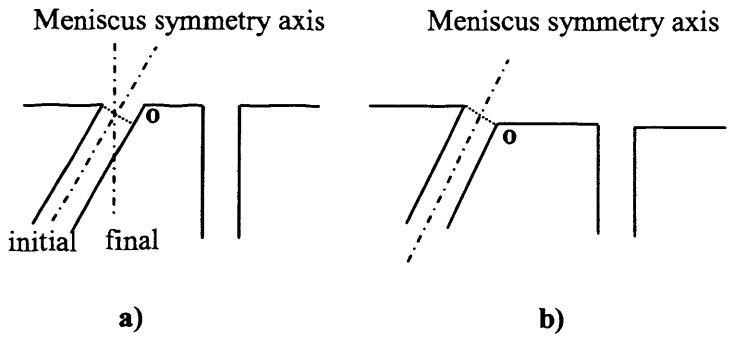

Figure 4.12. Imperfections in conventional membranes.

Figure 4.7 and Figure 4.11 show that although the maximum pressure difference during the *breakthrough at the pore stage* may be negative, the mesh breakthrough pressure difference is always positive no matter how wetting the phase is as long as the mesh surface is far from the top wall of the microreactor and a static pressure model applies. In order to enable the displacement of a two-phase flat interface (reached at an infinite spreading), a positive pressure difference needs to be applied. Vaidya et al. (1994) and Prasad et al. (1990) reported positive experimentally measured breakthrough pressures for wetting systems. However, several phenomena neglected in the present analysis, may give rise to breakthrough at negative ΔP, such flow of the phases, gravity and capillary displacement. Flow of the fluid phases and gravity may give rise to drop formation even at negative pressure differences. A continuous phase displacement, or mesh breakthrough, can also occur if one phase displaces the other by capillarity (Figure 4.13), in which the *NW* phase is being displaced by the *W* phase at a negative pressure. This situation is likely to appear in mesh microcontactors when the phase height is of

comparable size to the pore openings and support/edge effects are present. The wetting phase can reach the top wall of the microcontactor giving rise to a continuous capillary spreading.

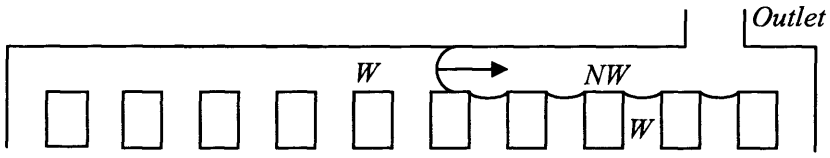

Figure 4.13. Capillary breakthrough at negative pressure difference.

4.5.2. Defects during Mesh Manufacture and Their Effect on Reduction of Meniscus Stability

The pressure difference range between the two phases that the interfacial meniscus can cope with depends on the meniscus curvature. If two or more pores are joined together because of some fault in the manufacturing process, then the effective pore diameter of the joined pores increases, resulting in a decrease in meniscus curvature for a given θ_{App}. The geometry of the possible defects depends on the mesh microfabrication process. Appendix 4C shows an analysis on breakthrough pressure reduction due to defective pores in the mesh.

4.5.3. Priming Stage of the Mesh

For proper priming of a mesh microcontactor it is most suitable to use the wetting phase. During this stage, all bubbles/drops of the non-wetting phase are removed from the mesh surface on the side of the wetting phase for which certain pressure difference is required. It was experimentally observed during the present work that when these non-wetting drops/bubbles are left on the mesh surface, the breakthrough pressure of the non-wetting phase can substantially decrease. This is because the diameter of these non-wetting bubbles/drops is usually larger that the pore diameter leading to a decrease of the Laplace pressure difference across the interface, which is a function of the meniscus size. Trapping of the non-wetting phase inside the mesh pores can also affect mass transfer performance of the microcontactor.

Figure 4.14 shows a suggested process for the bubble/droplet formation of the *NW* phase during the priming stage with the *W* phase.

a) Breakthrough of the wetting phase into the non-wetting phase during the priming procedure first at specific parts of the mesh, such as defective or larger pores, supports/seals or parts of the mesh that are first reached by the wetting phase as shown in Figure 4.14**a**.

b) After the *W* phase has broken through some pores, then during the spreading stage it will also cover pores that still have *NW* phase inside and will trap it. It is possible then that at these pores the *W* phase may flow backwards and form drops/bubbles of the *NW* phase in the *W* phase side of the mesh (Figure 4.14**b-c**). Contact angle, pressure difference across the phases during priming, which determines the speed of the process, support/edge/particle effects or pore uniformity determine the type and size of bubbles/drops formed. During this process either small bubbles that are partially inside the pores or larger bubbles completely outside the mesh can form. Small bubbles can be partially inside the pores as their increased curvature means that their pressure is higher than that of the surrounding fluid and stop the backward flow of the *W* phase. Another case in which formed drops/bubbles can be partly inside the pores is when the *W* phase breaks through certain points at which the breakthrough pressure is considerable lower than that of normal pores (supports, foreign particles or defective pores). In this case, the *W* phase is able to break through locations of reduced breakthrough pressure but is unable to break through the normal pores forming bubbles that are trapped inside the pores. For those cases with non-preferential breakthrough locations, formation of free drops/bubbles at the *W* phase is likely to take place since the *W* phase breaks through with the same ease in both directions of the pores.

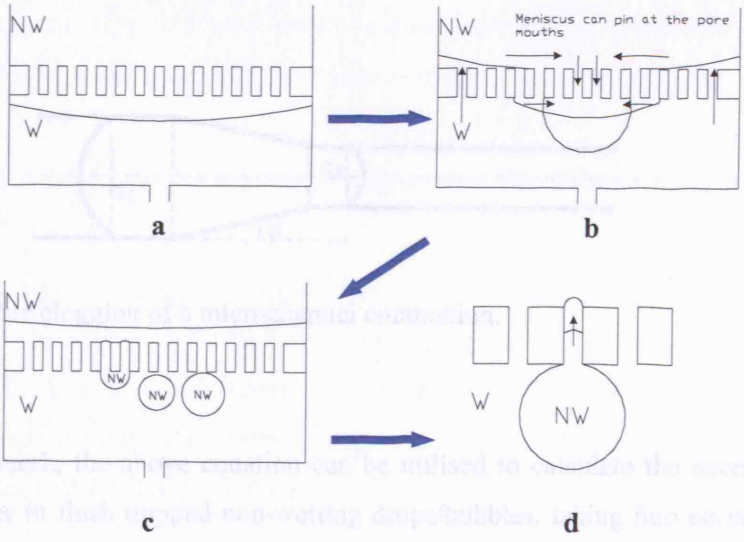

Figure 4.14. Bubble/drop formation during priming with the wetting phase.

The non-wetting phase bubbles/drops must be removed from the wetting phase side of the mesh (see Figure 4.14d). The required pressure difference for pushing out the trapped drops/bubbles is determined by the curvature of the drop/bubble interface in contact with the channel. Jensen et al. (2003) analysed the required external pressure (*clogging pressure*) for pushing a bubble in quasi-static motion through a tapered contraction of a hydrophobic channel. They found that the total energy of the microchannel system can either increase or decrease as the bubble passes from the wide part of the channel to the narrow part. Those cases where the total energy of the system is lower in the narrow part of the channels were analysed in terms of clogging pressure distinguishing between non-clogging (β) and clogging systems (α). Non-clogging systems are classified in 4 categories depending on the final position at which the bubble clogs the channel (position at which clogging pressure becomes positive). Even when the total energy of the system decreases as the bubble goes through the contraction, there is only one case at which this process may be spontaneous (negative clogging pressure) which corresponds to small bubbles that are completely contained within the tapered section. Eq. (4.45) gives the equilibrium pressure difference for each position of the two bubble contact lines. The largest value of this pressure difference as the bubbles moves from the wide to the narrow part of the channel is the clogging pressure. Contact angle hysteresis increases the clogging pressure since the bubble will move when $\theta = \theta_A$ at the bubble rear and $\theta = \theta_R$ at the bubble front.

$$\Delta P_{\text{clogging}} = 2\gamma\left(\frac{\cos(\theta + |\phi(x_R)|)}{r(x_R)} - \frac{\cos(\theta - |\phi(x_L)|)}{r(x_L)}\right) \tag{4.45}$$

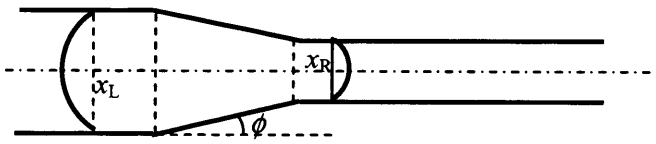

Figure 4.15. Bubble clogging of a microchannel contraction.

In the case of a mesh, the above equation can be utilised to calculate the necessary pressure difference in order to flush trapped non-wetting drops/bubbles, taking into account that a) the lower part of the pore can be considered as a sudden contraction ($-90° < \phi(x_L) < \phi_{Int}$) while the upper as a sudden expansion ($\phi_{Int} < \phi(x_L) < 90°$). Free drops/bubbles do not penetrate into the pore until the pressure difference is that given by Eq. (4.45), where $\cos(\theta - |\phi(x_L)|)/r(x_L) = 1/R_{Drop/Bubble}$ (curvature of the free drop/bubble), $r(x_R) = r$ and $\phi(x_R) = \phi_{Int}$. The maximum

curvature determining the clogging pressure is reached when $(\theta + \phi(x_R)) = 0°$ (hemispherical meniscus). If the drops/bubbles are large in comparison with the pore diameter and volume, the second right hand side term in Eq. (4.45) can be neglected (bubble/drop curvature negligible, $1/R_{Drop/Bubble} \rightarrow 0$) and the clogging pressure is equal to the breakthrough pressure of the wetting phase, $\Delta P_{B,W}$. As the drop/bubble size of the formed bubbles is not known, a conservative approach is to use a pressure difference during priming given by Eq. (4.46). However it is not easy to apply in practise this pressure difference since the rest of the mesh pores are open for the wetting liquid to flow through, and the pressure difference between the bubble/drop ends will only be determined by the pressure drop through the pores. This leads to higher pressure differences between wetting and non-wetting phases than expected in order to remove the trapped drops/bubbles.

$$|(P_W - P_{NW})_{priming}| > |(P_{NW} - P_W)_{max}| = \Delta P_{B,NW} \tag{4.46}$$

Once the microcontactor is primed with the wetting phase, this is drained from the non-wetting phase by decreasing the pressure difference (P_W-P_{NW}) to a negative value, displacing the wetting phase until the menisci form inside the pores. As the wetting phase retreats it is possible that a thin film forms on the non-wetting part of the mesh which becomes unstable and may result in droplets that can cover one or more pores. If these are not drained and remain during the normal operation of the microcontractor they may lead to a smaller breakthrough pressure difference of the wetting phase. These drops can be dried with a stream of air before the non-wetting phase is introduced. Furthermore, inside wall edges, wetting phase may also accumulate that will promote earlier breakthrough in the pores very near them.

4.5.4. Inertial and Flow Effects on Meniscus Stability

Flow of the two phases in the microcontactor above and below the mesh will affect not only the pressure that each phase has at a particular point along the mesh (see section 4.4) but will also create extra normal and tangential stresses that can affect the meniscus shape (see Chapter 5) at the pore end. In addition, sudden pressure changes can affect the meniscus movement inside the pores and reduce the breakthrough pressure.

4.6. Experimental Work on Breakthrough Pressures

The reduction in breakthrough pressure in meshes where supports/seals and/or deposited particles (contamination) are present compared to single pores was investigated experimentally

for a number of different microfabricated meshes. Priming was also studied and helped to identify and solve the problems discussed in section 4.5.3.

Two liquids with different surface tension and contact angle in the different mesh materials employed were chosen as the wetting phase; n-octane (Fluka nº 74823, purum > 95 %, GC) with properties γ= 21.49 mN/m, ρ = 703 kg/m^3 and water (HPLC grade) with γ= 72.26 mN/m and ρ = 1000 kg/m^3. Atmospheric air was used as non-wetting phase in the experiments where the wetting phase liquid is pressurised/vacuumed, while zero grade air (ρ = 1.19 kg/m^3) was used in *reversed systems*, in which the gas phase is the one pressurised/vacuumed. Zero grade air was also used to pressurise/vacuum the liquid phase. The four types of meshes studied are described below:

Microfabricated Nickel Meshes from: The mesh was made from nickel with a nominal hexagonal pore diameter d_N = 5 µm and pore centre separation 3-4 µm. The mesh was made by nickel electrodeposition at Central Research Laboratories (CRL). This mesh has two regions; a) the active region, which contains the pores and has a mesh thickness of e = 5 µm and b) the built-in support/edge region with thickness e = 30 µm above or below the active region level. Figure 4.16a shows one of these meshes as used in a microcontactor and Figure 4.16b shows the experimental prototypes used in the current breakthrough experiments, of which the first two have the edges above and the other two have the edges below.

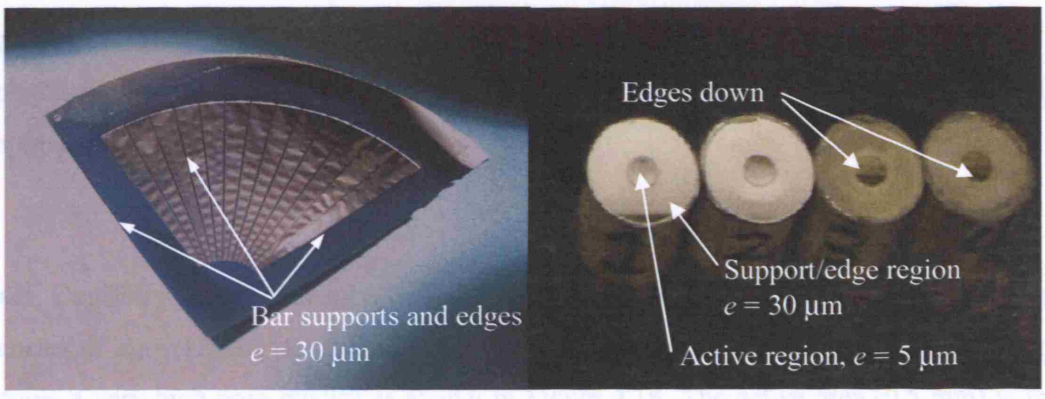

Figure 4.16. Nickel Mesh developed by Central Research Laboratories (CRL) utilised in a) a real microcontactor system (Wenn et al., 2003) and b) the present study.

Figure 4.17 shows SEM pictures of both sides of the CRL mesh with d_N = 5 μm; the opposite side to the supports with large pore openings, d_l= 5.5 ± 0.1 μm (Figure 4.17a) and the same side as the supports with small pore openings d_s = 3 ± 0.1 μm (Figure 4.17b). The magnification used provided a pixel size of 0.1 μm. This results in an interior solid wall inclination of ϕ_{Int} = ±19.6° (+ for *W* phase on the side of the small pore opening and – for *W* phase on the side of the large pore opening). For the current experiments (see Figure 4.16b) the mesh prototypes were mounted with the supports both up (in the air phase or liquid phase in *reversed systems*) and down (in the wetting liquid phase or gas phase in *reversed systems*). Mesh thickness was measured with a confocal microscope obtaining e = 3.5 μm for the active region and e = 30 μm for the support region.

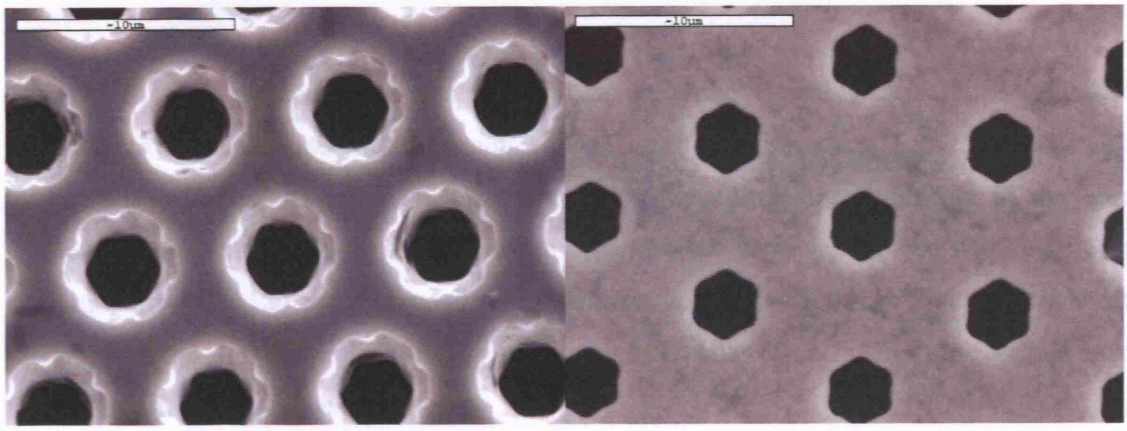

a) b)

Figure 4.17. SEM image of both sides of a nickel mesh with built-in supports up, a) side opposite to the built-in supports with pore radius $r_{h,l} \approx 5.5/2$ μm and b) side of the built-in supports with a pore radius $r_{h,s} \approx 3/2$ μm.

Glass Capillary Plate: The glass plates contained pores with a nominal cylindrical pore diameter of d_N = 12±0.5 μm and thickness of e = 500 μm (Hamamatsu)**.** The capillary plate features a very high pore quality as shown in Figure 4.18. The active area (0.5 mm) is in the middle of the plate (5 mm diameter size), which means that its connection and sealing with the gasket takes place at the non-active area of the plate. In addition there are no built-in supports across the active area and the transition from the non-active to the active region is continuous, so that no edge/support effects are present in this mesh.

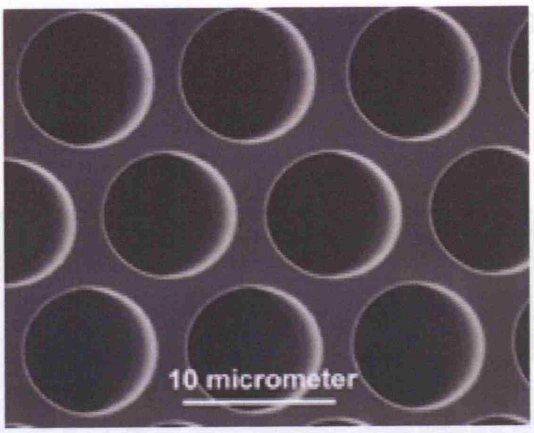

Figure 4.18. Glass capillary plate made by Hamamatzsu, d_N = 12 μm.

Stainless Steel Mesh: This mesh was produced via a photo-chemical isotropic etching process and made from stainless steel with a nominal cylindrical pore diameter of d_N = 75 μm and mesh thickness e = 50 μm (InterNet Incorporated). However, direct measurements of the pore diameter with a scanning electron microscope show that the pores are tapered with large pore openings up to d_l =130 μm and small pore openings up to d_s = 100 μm. Pixel size in these pictures was 0.5 μm. The tapered pores are a result of a photo-chemical isotropic etching used for the manufacturing process.

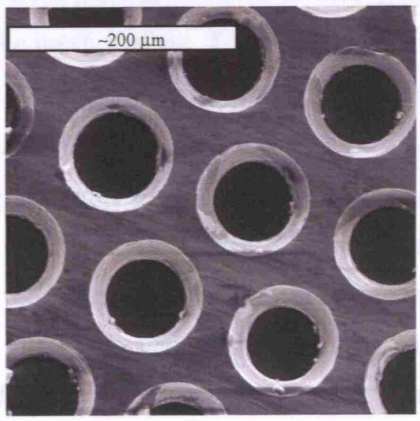

Figure 4.19. SEM image of the stainless steel mesh that allows measurements of both pore openings in the tapered pores, d_s = 93 μm and $d_l \approx$ 123 μm on this picture.

Acrylic mesh: This mesh was made in-house by drilling and polishing in an acrylic sheet with nominal cylindrical pore diameter of d = 400 microns (see Figure 4.20). In total, 19 pores were

made and their relatively large size allows the exact pore where breakthrough first takes place to be identified. These pores can also easily be cleaned from particles of comparable size to the pores that can affect breakthrough pressures.

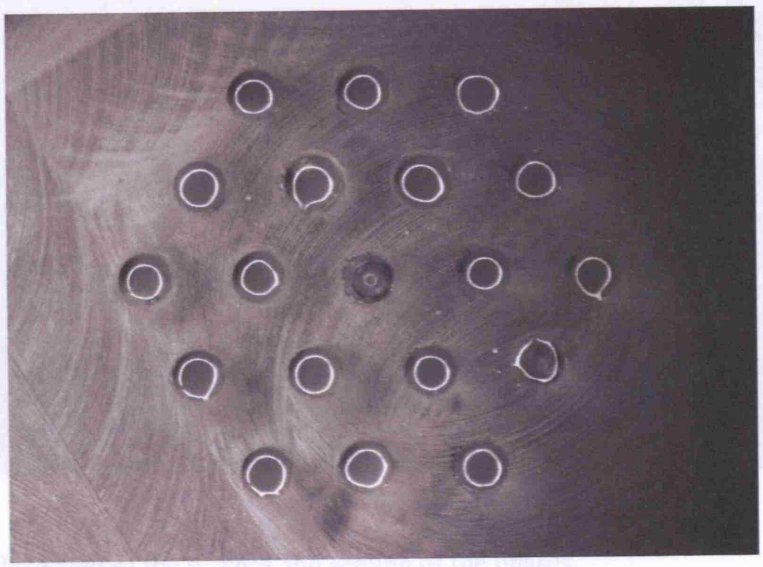

Figure 4.20. Optical image of the acrylic mesh, whose pores are filled with water, that features openings of diameter d_l = 470 μm on the air side and d_s = 400 μm on the liquid side.

Figure 4.21 shows all the different meshes mounted in their respective cases used to bring the liquid phase in contact with the mesh surface. The cases for the acrylic and glass meshes were made from acrylic, while the cases for the stainless steel meshes were glass tubes (glass has small θ for both octane/air and water/air system). These tubes were attached to the stainless steel mesh with highly hydrophilic glue to avoid an appreciable edge support/effect during gas breakthrough. Generally, the liquid phase (pressurised/vacuumed phase) was underneath the mesh and the gas phase was atmospheric air. However, some experiments (*reversed systems*) were carried out having the gas phase underneath (pressurised/vacuumed zero grade air) in order to analyse the effect of phase placement on breakthrough and also allow breakthrough pictures to be taken from above the mesh. Since the experiments aimed at understanding the stability issues under static conditions, the fluid chambers on the liquid side are designed with large phase height for simplicity. All the meshes were ultrasonically cleaned in distilled water and acetone and dried with nitrogen before experiments were performed.

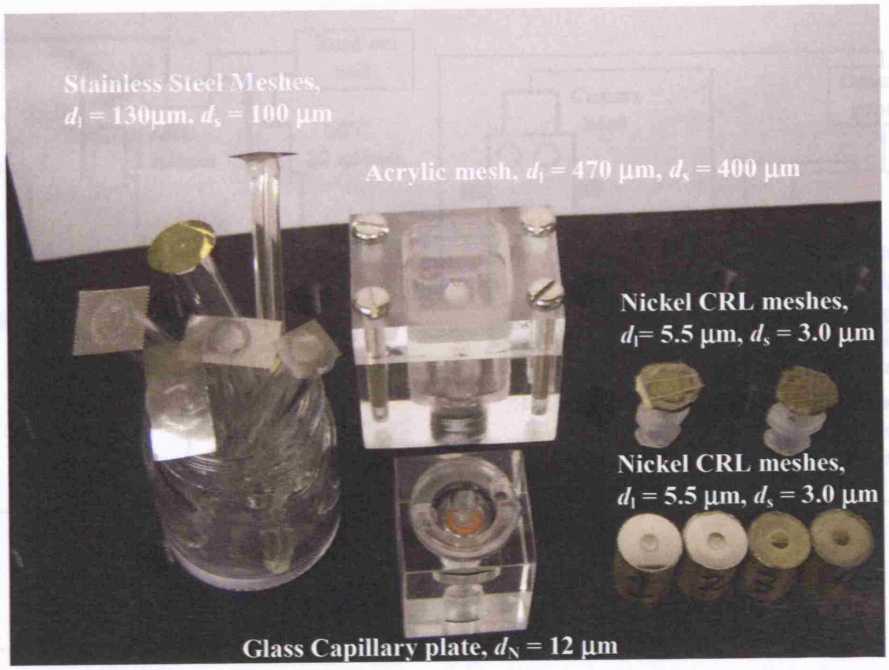

Figure 4.21. Placement of the meshes and sealing of the phases.

The experimental set-up shown in Figure 4.22 was used to study breakthrough pressure by visualising the meshes during the experiments. The liquid phase is contained in a 3-valve glass bottle. Its pressure is increased by means of compressed zero grade air, until it breaks through to the gas phase. A micrometering valve connected to the 3-valve glass bottle relieves the pressure of the liquid phase after the breakthrough occurs. The compressed air flowrate is precisely controlled using a Bronkhorst EL-FLOW F-110C mass flow controller (MFC) for flows between 0.01-1 ml/min gas and a Chell Mk4607 mass flow controller for flows between 1-20 ml/min. The micrometering valve in the liquid bottle can also be connected to a venturi type system to generate vacuum in the liquid phase, necessary for studying breakthrough of the gas phase. The liquid phase is connected to the mesh via tubing that has a large diameter of 6 mm to avoid any capillary effects on the pressure readings. The mesh is placed underneath a microscope connected to a high-resolution video camera CCD Kodak ES 1.0 for visualisation of the breakthrough. A pressure transducer measures the pressure inside the glass bottle and the values are logged into a PC. Measure Foundry from Data Translation is the data acquisition software utilised.

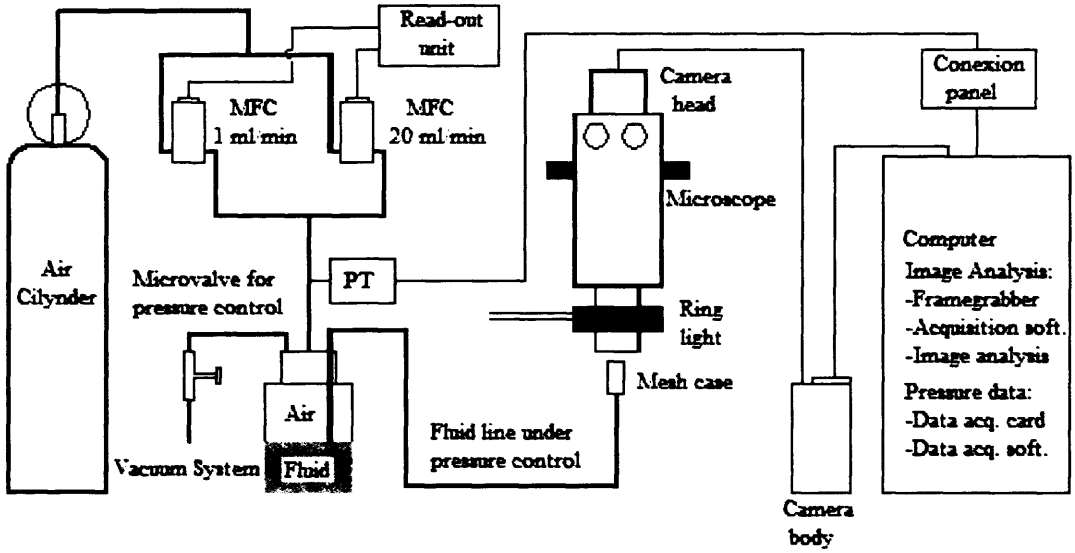

Figure 4.22. Experimental set up for breakthrough pressure measurements.

In most experiments liquid is placed inside the reservoir bottle while tube is used to connect its exit to the mesh under investigation. This connecting tube has a large diameter of 6 mm to avoid any capillary effects on the pressure readings. In a typical run, the micrometering valve on the bottle is closed and the air flowrate switched on to displace the liquid from the glass bottle to the mesh. The pressure reading at which the liquid reaches the mesh is taken as the zero pressure. Breakthrough of the wetting liquid phase is induced for priming the mesh microcontactor. The air flow is then stopped and the liquid pressure is relieved via the micrometering valve in the bottle. A nitrogen stream is passed over the top surface of the mesh to dry it completely from any liquid phase that may have wetted it in the priming stage. When the mesh surface is dry, the micrometering valve is closed and the air flowrate is switched on again and set at a low value, producing a small temporary pressure variation (1-5 Pa/s) until breakthrough of the wetting phase occurs, at which the pressure reading is taken. After breakthrough the air flow is stopped and the micrometering valve is opened to relieve the pressure at the glass bottle and connected to the vacuum system to measure the breakthrough pressure of the gas phase into the liquid below the mesh. The micrometering valve aperture and the water flowrate of the venturi vacuum system are set up so that the pressure in the glass bottle decreases slowly (1-5 Pa/s). The pressure transducer features four pressure ranges from 0-0.5 psi up to 0-4 psi, which cover all the ranges measured in the present work apart from the gas breakthrough measurements in the water-air systems with the nickel meshes. In this case, a 1 bar pressure gauge was used. In the *reversed systems*, the gas phase was placed inside the glass bottle and the liquid phase above the mesh in the form of a large drop.

4.7. Results and Discussion

Table 4.4 presents the breakthrough pressure difference results of the gas and liquid phases in the different meshes investigated. These are compared with the theoretical predictions given by Eq. (4.1) together with Table 3.2 for single pores. Maximum error in theoretical breakthrough pressure estimation is 3 % for CRL meshes (small pore opening d_S = 3 μm, 0.1 μm pixel size).

	Mesh	Sup./Edges	System	θ	ϕ_{Int}	d_l, μm	d_s, μm	$\Delta P_{B,L}$, Pa	$\Delta P_{B,L}$, Pa Eq. (4.1)	$\Delta P_{B,G}$, Pa	$\Delta P_{B,G}$, Pa Eq. (4.1)
1	Nickel	Nickel-L	Wa-A	70°	20°	5.5 A	3 Wa	5861-8207	49383	42500-43107	96347
2	Nickel	Nickel-G	Wa-A	70°	-20	5.5 Wa	3 A	6072	90536	46213-49660	52553
3	Nickel	ballotini-G	Wa-A	70°	20°	5.5 A	3 Wa	962	Particle		
4	Nickel	Nickel-G	O-A	0°	-20°	5.5 O	3 A	0	0	27938-26426	28653
5	Nickel	Nickel-L	O-A	0°	20°	5.5 A	3 O	0	0	27277-22095	28653
6	Glass	No	Wa-A	20°	0°	12.50	12.50	3637	7909	18487-15394	23123
7	S. Steel	Glue/glass-L	Wa-A	66°	16°	130 A	100 Wa	1864	2031	2615	2890
8	S. Steel	Glue/glass-L	Wa-A	66°	-16°	130 Wa	100 A	2795	2641	2104	2234
9	S. Steel	Glue/glass-G	Wa-A	66°	-16°	130 Wa	100 A	391	Glass Sup.	2104	2234
10	S. Steel	Glue/glass-L	O-A	0°	16°	130 A	100 O	0	0	880	860
11	S. Steel	Glue/glass-L	O-A	0°	16°	130 O	100 A	0	0	865	860
12	S. Steel	Glue/glass-L	Wa-A	45°	-	250	250	Expe.		Expe.	
13	S. Steel	Glue/glass-L	O-A	0°	-	250	250	0	0	358	344
14	Acrylic	No	Wa-A	75°	0-7°	470 A	400 Wa	593	594	637	723
15	Acrylic	No	O-A	0°	0.7°	470 A	400 O	34	0	209	215

Sup./Edges = Indicates if the mesh set-up has supports or edges, material and the phase where they are.
G = Gas phase; *L* = Liquid phase; Wa = water; A = air; O = octane; BL/BG = Liquid/Gas breakthrough

Table 4.4. Summary of the experimental breakthrough pressure results in different meshes and comparison with theoretical values for singles pores (Eq. (4.1)).

Equilibrium contact angles from literature were used for the calculation of the theoretical breakthrough values although certain hysteresis may be present in the water-air system (θ_A - θ_R

= 20°-30°), which would increase the breakthrough pressure of the wetting phase. However, since contact angle hysteresis is dependent on surface roughness and heterogeneity, which may be slightly different at each pore, the equilibrium contact angle instead of the advancing and receding contact angles was used to estimate the apparent contact angle and the mesh breakthrough pressures.

Breakthrough pressure values for the gas and liquid phases are in all cases positive even for the breakthrough of the wetting phase. The octane-air systems have a very low contact angle in all mesh surface materials and the effect of supports or edges in some meshes (e.g. nickel meshes) may result in a negative maximum pressure difference for the *breakthrough at the pore stage* for the octane phase. However as shown in section 4.5.1 the pressure difference required for the *spreading* stage (for continuous breakthrough) is always positive if capillary spreading does not occur (see Figure 4.13). This was clearly observed with the nickel meshes when the octane first broke at the edges and spread when the pressure difference P_W-P_{NW} was slightly larger than 0.

In general, theoretical results for meshes with relatively large pores are close to the experimental values (steel and acrylic meshes, **cases 7-8, 10-15**). However, theoretical values are higher than the experimental ones for meshes with small pores (glass and nickel meshes, **cases 1-6**). In **case 8** the experimental breakthrough pressure of the liquid phase $\Delta P_{B,L}$ = 2795 Pa was slightly higher than the expected theoretical value $\Delta P_{B,L}$ = 2641 Pa indicating that the advancing contact angle at all non-wetting pore ends was slightly larger than the equilibrium one θ = 66°. Some of these differences are expected due to support or edge effects. However in other cases, such as the nickel mesh for the water/air system with supports on the side of the gas phase (**case 2**) or glass mesh (**case 6**) the low experimental breakthrough pressure difference of the water phase cannot be explained a priori. In addition, microscope observations did not show any defective meshes in these two cases as those presented in section 4.5.2 although only part of the surface of the meshes was checked. However, the match between experimental and theoretical breakthrough pressures for the non-wetting gas phase implies that no defective pores are present as explained below. Furthermore, the largest pore size in the glass mesh (12.5 μm) was used for the theoretical calculation of breakthrough pressures.

By using octane, which has a small contact angle in all mesh surfaces ($\theta \approx 0°$), the presence of defective joined pores in a mesh can be checked, confirming that the size of the pore openings corresponds to those measured via scanning electron microscopy. For octane contact angle ~0°, the breakthrough pressure of the gas phase in octane-air systems should always be defined by the radius of the small pore opening (see Table 3.2), while supports/edges/particles have also no

effect (contact angle of the non-wetting phase is $\theta = 180°$). As can be seen from **cases 4-5** and **10-11** in Table 4.4, the theoretical breakthrough pressures correspond to the small pore openings of 3 and 100 μm for the nickel and stainless steel meshes respectively. The experimental results also agree very well with the theoretical predictions. These results indicate that the air breakthrough pressure is independent of the mesh side the wetting phase is placed on. It also confirms that at these meshes there are no defective pores and the pore openings have the dimensions measured via SEM for a few pores.

Although critical filling pressures were not measured, Figure 4.23 shows the stainless steel mesh pores (d_S = 100 μm) filled with air (Figure 4.23a) and water (Figure 4.23b) respectively. By modifying the pressure difference across the phases, it is possible, therefore, to fill the pores with the non-wetting phase (air) without breakthrough of that phase.

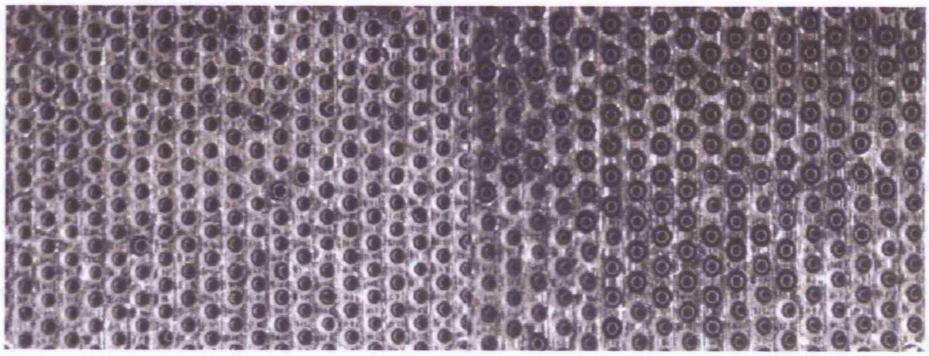

a) **b)**

Figure 4.23. Filling of the pores of the stainless steel mesh (d_s = 100 μm) by the air and water phases respectively.

Ballotini particles with 90 μm diameter were placed on top of the nickel meshes to simulate the effect of foreign particles on breakthrough pressure reduction. Breakthrough results were compared to those obtained from the 2D model for spherical particles modifying the Laplace factor f_L. The particles were placed on the mesh side that is free of supports (d_l = 5.5 μm) and in contact with air. The breakthrough pressure of water was in this case very reproducible and equal to ΔP = +962 Pa (**case 3** in Table 4.4), which was substantially smaller than that measured in the same mesh without particles as shown in **case 1** (ΔP = 5861-8207 Pa) and much smaller than the theoretical value expected ΔP = 49383 Pa. The contact angle of water in glass ballotini particles was θ_S = 44° (Hapgood et al., 2002). According to the results obtained from the 2D model in the presence of particles (see section 4.5.1) the meniscus breaks through at the pore mouth when x = 5 μm and y = 0.27 μm at a negative pressure difference of P_W-P_{NW} = -4.65·10^5

Pa, which is much smaller than the pressure difference at which the meniscus reaches the pore mouth (ΔP = 0 Pa, since $\theta_{App} = \theta + \phi_{Int}$ = 70°+20° = 90°). Therefore the meniscus breaks through at the pore mouth and starts spreading as soon as it reaches the top of the pore. The experimental value of breakthrough pressure ΔP = 962 Pa agrees well with the theoretical one considering the particle effect (see section 4.5.1) for f_L = 1.43 in the Laplace Eq.(4.1) (see Figure 4.24), which is reasonable as it is between the value for a 2D system, f_L = 1, and the value for an axisymmetric meniscus f_L = 2. Figure 4.24 shows the results from the 2D model for Laplace factors f_L = 1.43 and f_L = 2. In a real 3D system, f_L changes as the meniscus rises on the particle/support from 2 (value for meniscus inside the pore) to a smaller value as the meniscus rises on the particle and the geometry changes so that not the whole real pressure difference curve can be represented by a constant f_L. Furthermore, f_L is expected to be dependent on the geometry and size of the support/particles, and to be smaller for large supports/particles.

Wang et al. (2002) found that the contact angle of water microdroplets (0.111-0.203 μm radius) on pure nickel was 20° while for macrodroplets it was 70°. Although Wang et al. (2002) do not refer to line tension effects, their data can be used to estimate an apparent line tension value σ from Eq. (3.9), considering that ϕ = 90° (drop on a surface) and therefore cos(90°-ϕ) = 1. For θ = 20° and θ_Y = 70°, the average line tension value calculated from Eq. (3.9) when d = 0.157 μm is $\sigma_{Water\text{-}air\text{-}nickel} = -6.78 \cdot 10^{-9}$ N, which is of the same order of magnitude as that found by theoretical analysis (Marmur, 1997; Checco and Guenoun, 2003). The maximum effect of line tension on contact angle (at ϕ = 90° and ϕ = -90°) on the nickel meshes for d_s = 3μm, results in contact angles of θ = 66.1° and θ = 73.8° at ϕ = 90° and ϕ = -90° respectively, which are not very different from the value θ_Y = 70° and therefore line tension can be neglected.

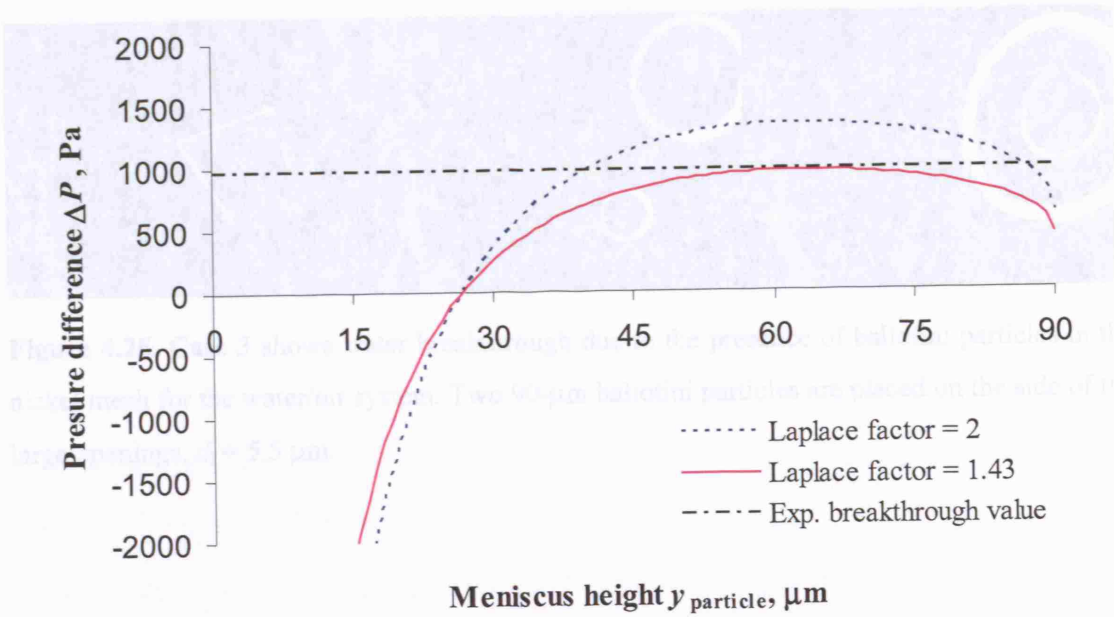

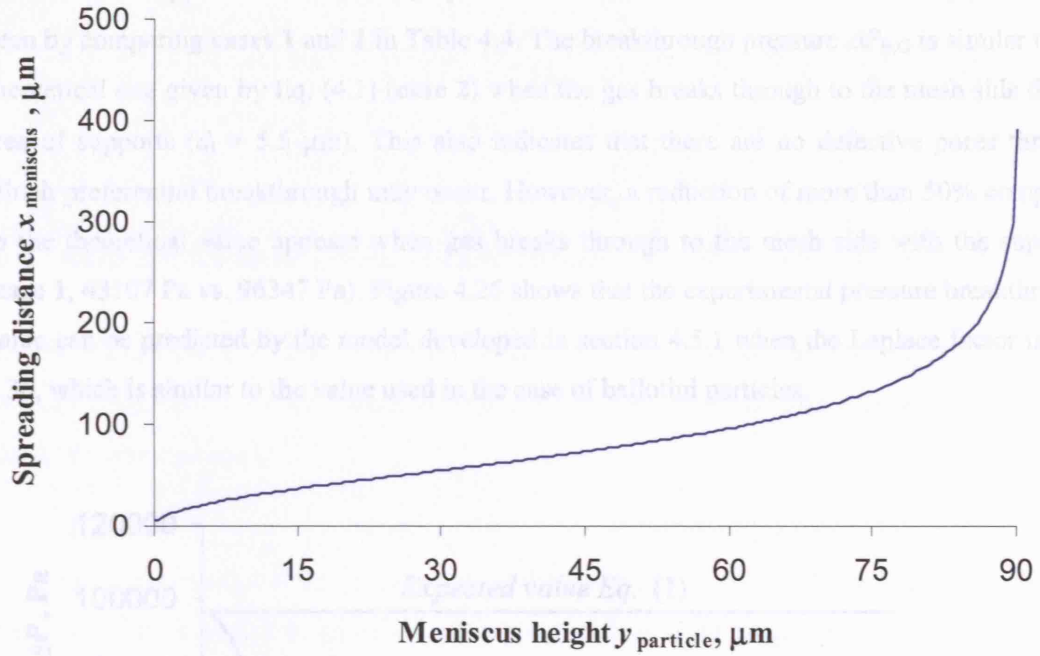

Figure 4.24. 2D model prediction of breakthrough pressure at the nickel mesh pores affected by a 90-μm Ballotini particle. $\phi_{Int} = 20°$, $\theta = 70°$ and $\theta_S = 44°$.

Figure 4.25 shows three consecutive images taken during water breakthrough in a nickel mesh with ballotini particles. The images clearly indicate that breakthrough happens first at the location of the particles.

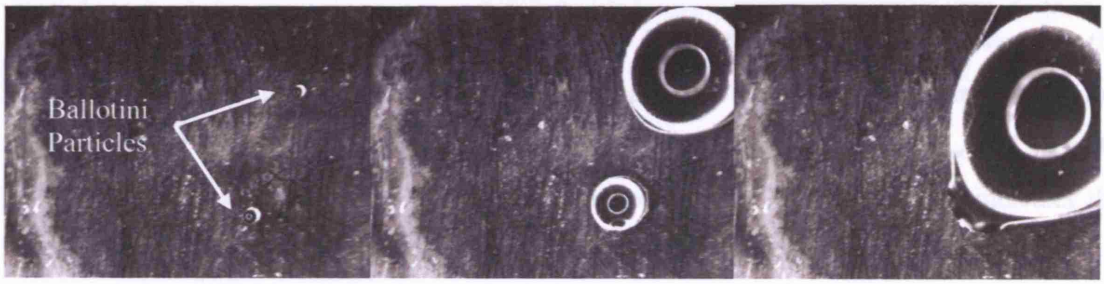

Figure 4.25. Case 3 shows water breakthrough due to the presence of ballotini particles in the nickel mesh for the water/air system. Two 90-μm ballotini particles are placed on the side of the large openings, $d_1 = 5.5$ μm.

The effect of supports on breakthrough pressure in nickel meshes in the air-water system can be seen by comparing **cases 1** and **2** in Table 4.4. The breakthrough pressure $\Delta P_{B,G}$ is similar to the theoretical one given by Eq. (4.1) (**case 2**) when the gas breaks through to the mesh side that is free of supports (d_1 = 5.5 μm). This also indicates that there are no defective pores through which preferential breakthrough may occur. However, a reduction of more than 50% compared to the theoretical value appears when gas breaks through to the mesh side with the supports (**case 1**, 43107 Pa vs. 96347 Pa). Figure 4.26 shows that the experimental pressure breakthrough value can be predicted by the model developed in section 4.5.1 when the Laplace factor is f_L = 1.36, which is similar to the value used in the case of ballotini particles.

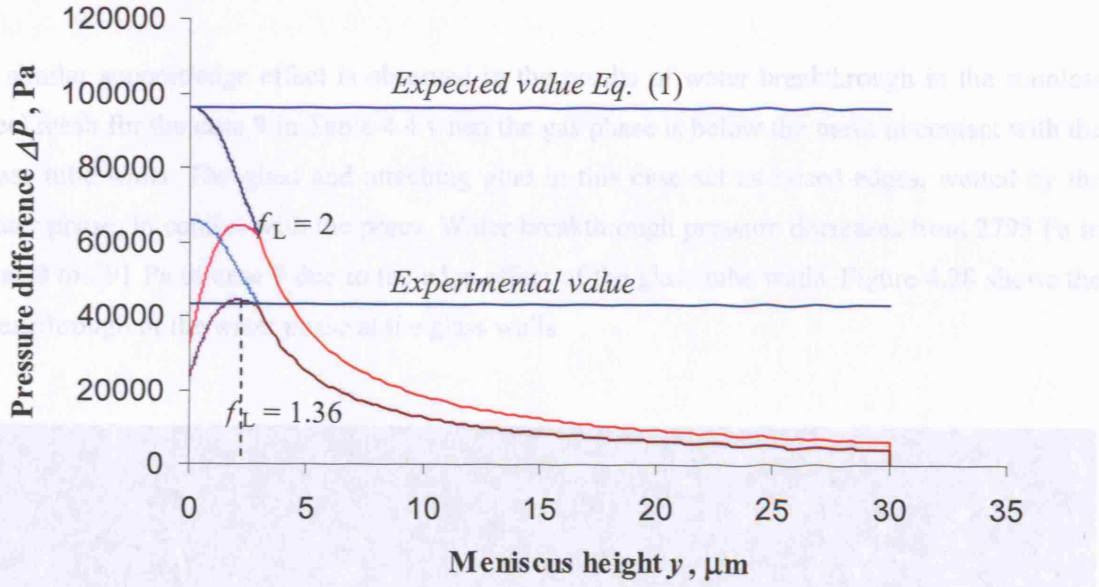

Figure 4.26. Experimental value and prediction (f_L = 1.36) of the breakthrough pressure for the system water-air in the nickel meshes when the gas breaks through to the side with 30-μm supports where the pore diameter is d_s = 3 μm. System properties ϕ_{Int} = 20°, $\phi_{S,Int}$ = 0°, θ= 70° and θ_S = 70°. Theoretical curves were obtained as in Figure 4.7. Line (------) indicates the meniscus height at which the maximum pressure difference is found (experimental value).

Figure 4.27 shows consecutive images of gas breakthrough in the nickel mesh for the water-air system (**case 1**). Breakthrough takes place at the 30 μm supports, which are located at the periphery of the active mesh area.

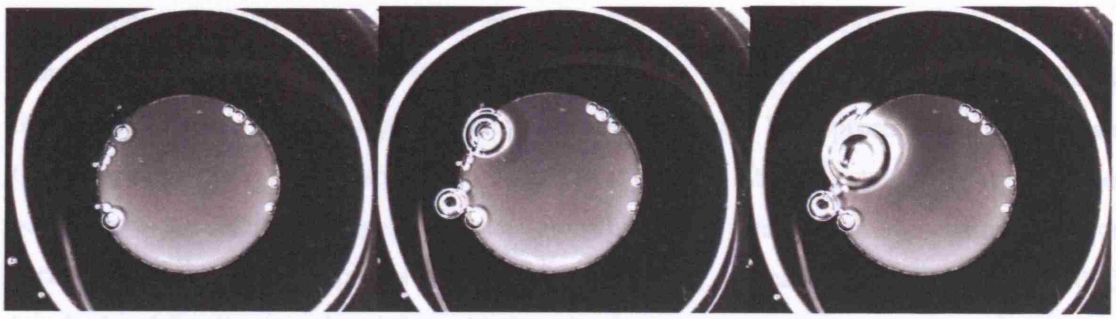

Figure 4.27. Case 1 for the water-air system in the nickel mesh with the gas phase breaking through preferentially at the 30-μm supports/edges. The gas phase was placed underneath the mesh (*reversed system*).

A similar support/edge effect is observed in the results of water breakthrough in the stainless steel mesh for the **case 9** in Table 4.4 when the gas phase is below the mesh in contact with the glass tube walls. The glass and attaching glue in this case act as raised edges, wetted by the water phase, in contact with the pores. Water breakthrough pressure decreases from 2795 Pa in **case 8** to 391 Pa in **case 9** due to the edge effect of the glass tube walls. Figure 4.28 shows the breakthrough of the water phase at the glass walls.

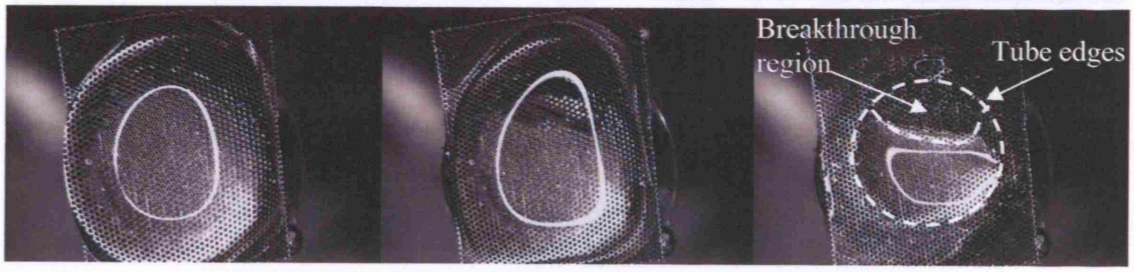

Figure 4.28. Case 9 that corresponds to the *Reverse System* water/air in a stainless steel mesh (d_s = 100 μm and d_l = 130 μm), in which a breakthrough of the water phase (above the mesh) is observed at low pressure difference due to the edge effect caused by the glass-tube walls that act as wetting supports.

The breakthrough pressure values of the water phase in the nickel and glass meshes (**cases 1, 2** and **6**) are those that show the largest reduction compared with the theoretical values even when supports are not present (**cases 1** and **6**). It is believed that this is caused by foreign particles deposited on the meshes. As mentioned in section 4.5.1, particles can reduce substantially the breakthrough pressure of both phases, particularly the wetting one. It is likely that both

hydrophobic and hydrophilic particles may be present in the same environment. The size of atmospheric dust particles varies from submicron size up to 20 μm (Lide, 1995) which implies that their effect on breakthrough pressure reduction will only be appreciable in those meshes that have small pores (nickel and glass) but not in the others (stainless steel and acrylic), whose pores have considerably larger diameter. For the nickel mesh with the water-air system corresponding to **case 1** (supports on the liquid phase side), a breakthrough pressure of 8200 Pa is calculated for the water breakthrough when foreign particles of $d_{particle}$ = 11 μm, θ_S = 45° and f_L = 1.5 are considered, which matches the upper experimental limit value in **case 1** (8207 Pa). The lower experimental value of 6000 Pa in **case 1** would be predicted if foreign particles with $d_{particle}$ = 15 μm are considered. These particle sizes seem realistic as shown by the SEM pictures in Figure 4.29. These pictures were obtained for meshes one day after the cleaning procedure was performed.

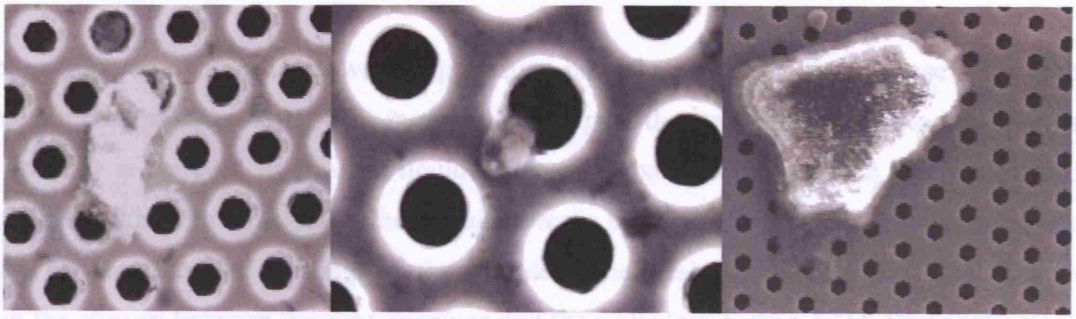

a) b) c)

Figure 4.29. Foreign particles resting on the nickel mesh. The pore diameter is 5.5 μm in (a) and (b) and 3 μm in (c).

The priming stage of the nickel mesh with the liquid was important in order to ensure that no bubbles remained trapped in the liquid side of the mesh, which would affect the reproducibility of the gas breakthrough results. Some measurements of gas breakthrough pressure in **cases 1,2,4,5** were actually substantially lower and less reproducible than those shown in Table 4.4 due to initial priming issues. Bubbles remaining in the liquid side of the mesh were observed during the priming stage of the acrylic mesh as explained in section 4.5.3. Figure 4.30 shows the priming stage of the octane-air system in the acrylic mesh, where a bubble remains within the liquid phase after the liquid has broken through the mesh. Smaller bubbles were observed in the same mesh for the water-air system and depending on the pressure difference during the priming stage, some bubbles were partially inside the pores.

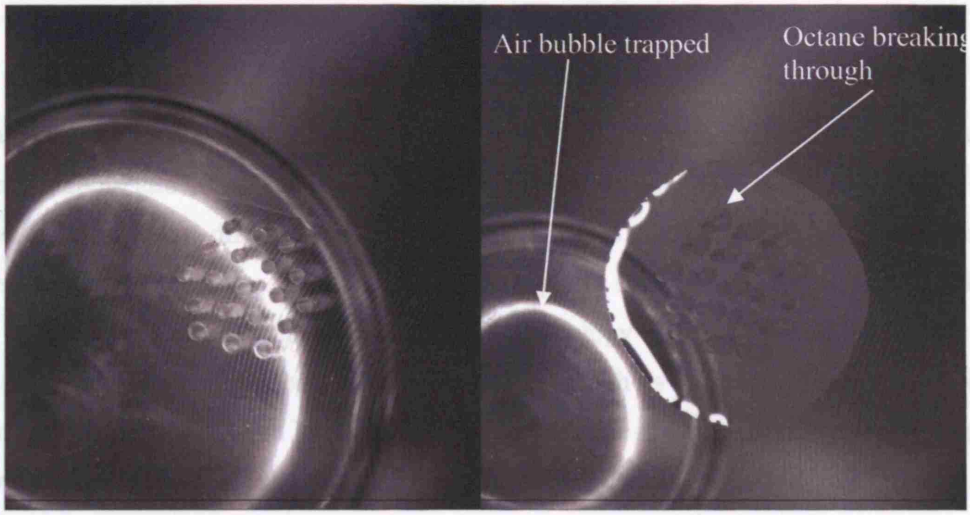

Figure 4.30. Bubble forming during priming stage in octane-air system in the acrylic mesh.

Another important phenomenon was the premature breakthrough of the liquid phase in the cases where after the priming stage of the mesh with the liquid, the mesh side in contact with gas was not dried. It is believed that as the liquid is reversing back to the pores at the last stage of priming, the thin film of liquid in the gas side breaks up to small droplets. These droplets can remain between the pore openings on the air side of the mesh, while there may also be liquid left in the corners between the pore openings and the walls (see Figure 4.31). During the liquid breakthrough experiments, when the liquid phase reaches the top of the pores, the menisci may contact the liquid left behind in the air phase generating a premature breakthrough.

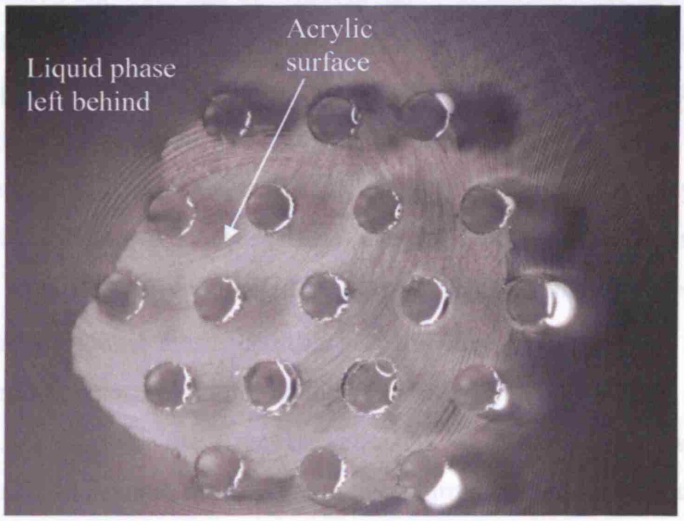

Figure 4.31. Liquid left behind during the drainage stage in the acrylic mesh. Liquid phase is underneath the mesh and gas phase above the mesh (picture).

4.8. Conclusions

Interfacial meniscus breakthrough pressure was studied in two-phase microcontactors where the two phases come into contact via the pores of a microfabricated mesh. Breakthrough pressure is defined as the pressure difference between the two phases at which one phase will break and disperse into the other phase. Breakthrough of one phase into the other should be avoided for stable operation of such systems. A systematic methodology that had been developed for single pores (see Chapter 3) was extended to include effects such as presence of supports/edges and foreign particles. The effect on breakthrough pressure of the pressure drop of the phases as they flow on either side of the mesh as well as the way priming is carried out were also studied.

A different pressure drop in each phase in co-current flow as well as combination of high and low pressures in counter-current systems results in different pressure difference between the two phases across the meniscus. It is possible therefore that breakthrough pressure can be reached at one part of the mesh but not at the others. An analysis was carried out that considers fluid flow between parallel plates and allows the calculation of the maximum pore size in the mesh that does not lead to breakthrough for a given contactor size and fluid system or of the reactor geometry (in particular length) for a specific fluid system and mesh.

A 2D, two-stage model was developed to describe and estimate the breakthrough pressure reduction in meshes compared to single pores due to the presence of mesh supports (built-in generally), foreign particles (dust) or sealing objects that rest on the active region of the mesh. According to the model, the first stage of breakthrough is at the pore end and the second stage is after the meniscus has left the pore and is spreading on the mesh. A maximum pressure difference can appear in either of these two stages which is the necessary *breakthrough pressure*. This static pressure model predicts positive breakthrough pressure in all cases as was also found experimentally. Real 3D systems can be analysed in the same way by using a factor in the Laplace equation between 1 (2D systems) and 2 (3D axisymmetric systems). The results of the model were experimentally validated by the use of 30-μm built-in supports and ballotini particles of 90 μm in a nickel mesh. Built-in perpendicular supports, $\phi_{S,Int} = 0°$, significantly reduce the breakthrough pressure of both wetting (partially) and non-wetting phases (see Figure 4.7a and Figure 4.8a) although the effect decreases as the contact angle increases (the phase becomes less wetting). In general, the maximum breakthrough pressure appears in the *spreading* stage for wetting and/or short support height while it appears at the *meniscus breakthrough at the pore* stage for non-wetting high supports. A negative support inclination (Fig. 3.4a) generally decreases further the breakthrough pressure for wetting systems (Figure 4.7b) and

increases it for non-wetting systems (Figure 4.8b) while a positive inclination (Fig. 3.4b) has the opposite effect. The effect of spherical particles is similar to supports with negative inclination and they have a larger impact on the breakthrough pressure of wetting phases than perpendicular straight supports. An important result, not previously reported to the best of the authors' knowledge, is that particles of the same order of magnitude as the pores reduce significantly the breakthrough pressure. This implies that for meshes with pore sizes of the same order of magnitude as common dust particles (1-20 μm) the single-pore model (see Chapter 3) largely overpredicts the breakthrough pressure difference especially for the wetting phase. This is likely to be the main reason why experimental breakthrough pressures in meshes with small pores (nickel and glass meshes) were substantially smaller than predictions from the single-pore model. The single-pore model was still able to predict satisfactorily the experimental breakthrough pressures in meshes (acrylic and stainless steel) with large pores and no support/edge effects present.

It was found that line tension effects could not be responsible for this reduction in the breakthrough pressure. It was also demonstrated that it is possible to fill the pores of the mesh with either the wetting or the non-wetting phase by controlling the critical filling pressure of that phase.

The priming stage of a micromesh contactor must be carried out properly as a phase remaining on the opposite side of the mesh can greatly affect breakthrough pressure of that phase. Priming usually happens with the wetting phase. To ensure that all drops/bubbles of the non-wetting phase are removed from the wetting phase side of the mesh a pressure difference between the phases given by Eq. (4.46) should be applied for priming. Once both sides of the mesh are primed with the partially wetting phase, this phase is drained from the non-wetting phase by decreasing the pressure difference to a negative value. At this stage droplets of the wetting phase occupying the mesh spaces between adjacent pores or several pores at once are generally formed and were also observed experimentally. These drops need to be removed (dried) as they can decrease the breakthrough pressure of the wetting phase if they remain on the non-wetting side of the mesh.

Based on the above it is suggested that mesh microcontactors prior to use should be thoroughly cleaned to eliminate any dirt particles. The priming stage that follows has to be carried out at the pressure difference given by Eq. (4.46) followed by a pressure difference reduction so that the wetting phases retreats into the pores. Air should then be passed over the non-wetting side of the mesh to remove any wetting phase left from the last priming stage. If supports/seals/edges are in contact with the active region of the mesh, it is better to place them on the side of the phase used

to fill the pores, generally the wetting phase, since built-in supports also affect to a smaller extent the breakthrough of the non-wetting phase.

The problems induced by particles resting on the mesh is more significant in meshes with regular pores rather than membranes with tortuous pores, in which the solid wall inclination changes along the pore and not just at the pore end. Regular pores are more reproducible compared to membranes in terms of breakthrough pressure but are affected more by supports and/or foreign particles resting on them.

Nomenclature

A'	Meniscus projected area, m^2.
D	Pressure difference decrease percentage.
d	Pore diameter and diameter in general, m.
d_S	Diameter of the opening defined between the inner pore wall and the support, particle of sealing object.
f	Ratio of pore diameter to distance between centres of two adjacent holes.
f_L	Factor in the Laplace equation. 1 for 2D systems and 2 for axisymmetric spherical menisci.
g	Acceleration of gravity, m^2/s.
h	Height, m.
H	Phase height, m.
L	Plate length, m.
Q	Flowrate, m^3/s.
P	Pressure, Pa.
p	Distance between centres of two adjacent holes, m.
p'	Perimeter of the (defective) pore openings.
r	Pore radius of radius in general, m.
r_h	Radius of the inscribed circle to a regular polygonal pore, m.
R	Radius of curvature of the meniscus, m.
U	Velocity, m/s.
x	Axis co-ordinate, m.
$x_{meniscus}$	x co-ordinate defining the spreading of the meniscus front.
y	Axis co-ordinate defining the height of the meniscus at the support/particle, m.
y_S	Support height, m.
W	Plate width, m.
Re	Reynolds number.
Rt	Ration number that indicates the relative importance of frictional pressure drop in the non-wetting phase with respect to the wetting phase.

Greek Letters

α	Angle of the tangent to a point with the x axis.
β	Half the angle of the corner in a regular polygonal pore.
γ	Surface tension, N/m.

φ	Angle Between symmetry axis of the meniscus and the symmetry axis of the pore or angle between the horizontal plane and the plane of the meniscus three-phase contact line.
ΔP	Laplace pressure difference, Pa.
θ	Contact angle, rad.
κ	Meniscus mean curvature, m^{-1}.
ϕ	Solid wall inclination at the point of contact of the three phase contact line, rad.
σ	Line tension, N or J/m.
μ	Viscosity, *sPa.*
ρ	Phase density, kg/m^3.

Subscripts

A	Advancing.
App	Apparent.
Arc	Arc menisci or wedges.
av	Average value.
B	Breakthrough.
C	Critical filling.
CE	Critical entry.
Eff	Effective.
Int	Interior of the pore, e.g. ϕ_{Int} is the solid wall inclination of the interior of the pore.
l	Large or property of the large pore opening.
max	Maximum.
max, ϕ	Value of property when the ϕ is maximum.
ΔP_{max}	Value of property when the meniscus Laplace pressure difference is maximum as the meniscus rises an infinite support.
spread,ΔP_{max}	Value of property when the meniscus Laplace pressure difference is maximum during the spreading stage.
min	Minimum.
mesh	Property of the mesh as a whole.
N	Nominal value.
NW	Non-partially wetting phase.
Particle	Property of the particle.
R	Receding.

s	Small or property of the small pore opening.
S	Support/particle/sealing object.
W	Partially wetting phase.
Y	Property obtained from the Young equation.

Superscripts

#	Dimensionless numbers

Chapter 5

Flow Effect on Meniscus Shape and Breakthrough Pressure

"We are just an advanced breed of monkeys on a minor planet of a very average star. But we can understand the Universe. That makes us something very special."

Stephen Hawking

5.1. Introduction

In the previous chapters, a simple methodology to calculate meniscus shape, position and stability in the mesh microcontactor was developed and implemented, which can be applied to either circular or polygonal pores. No flow effects on meniscus deformation or dynamic effects inside the pore as the meniscus moves from one pore opening to the other were considered, since their influence on breakthrough pressure is generally negligible for very small pores as those present in the mesh microreactor. This is due to the large surface tension forces in pores of 5 μm diameter and to the relatively small meniscus height when compared to the phase height (appr. 100 μm in CRL mesh microcontactor). Considering a parabolic velocity profile for each of the phases, a very low velocity is expected close to the mesh, which leads to small normal stresses on the menisci.

However, in systems with low surface tension forces, high velocities and/or small ratio of phase to meniscus height, flow and dynamic effects may become substantial. Considering flow effects on meniscus breakthrough pressure can also be of interest to other types of systems such as bubble formation in microchannels for multiphase manifolds where Taylor bubbles are formed in parallel channels connected to the same gas and liquid distribution channels. In this chapter a theoretical analysis is presented that enables the estimation of the system design and operation parameters for breakthrough of one phase into the other under flow conditions. It also defines the limits below which a simple Laplace static pressure model is sufficient to describe the stability range of pressure difference that the meniscus can cope with, without breakthrough of one phase into the other. The meniscus is assumed to break through when its apparent contact

angle with the pore wall reaches the value $\theta_{App,max} = \theta_A + \phi_{max}$ at the back/front of the 2D meniscus (*breakthrough by maximum contortion*) or when the maximum meniscus curvature is reached (*breakthrough by maximum curvature*) as explained in Chapter 3. It must be noted that for flow conditions maximum curvature does not correspond to a semicircular meniscus (hemispherical meniscus in a cylindrical pore).

5.2. Background

In conventional membranes with small size and tortuous pores menisci are usually found inside the pores at some constriction and not at the pore mouth where fluid flow would affect their shape and breakthrough pressure. This may explain the lack of research into this area. In the literature the effect of flow is usually considered for bubble formation and deformation.

The process of bubble formation from orifices submerged in a cross-flowing liquid is relevant to the present work. Bubble formation research is generally focused on determining bubble detachment criteria (Kumar and Kuloor, 1970) and bubble formation frequency (Iguchi et al. 1998), which allow for the estimation of bubble volume and length (in constrained spaces). Bubble formation occurs via either a single-stage or a multi-stage process. In the latter, the bubble undergoes a lift-off stage in which a neck is formed (Clift et al., 1978). This differs from the present work where the minimum pressure required for breakthrough of one phase into the other and the apparent contact angle under flow conditions need to be calculated.

For a cross-flow system in the micro-scale range, the bubble detachment occurs when buoyancy and liquid drag forces overcome those due to surface tension as shown by Rayner and Trägårdh (2002) when modelling membrane emulsification in cross-flow. Liquid and gas inertia forces (Bhumia et al., 2000) and dynamic surface tension force (Rayner and Trägårdh, 2002) are also considered depending on system geometry and parameters. The required pressure difference to start the bubble formation process is generally approximated to $\Delta P = 4\gamma/d$ (Di Marco et al., 2003; Rayner and Trägårdh, 2002; Clift et al., 1978), which corresponds to the breakthrough pressure of a non-wetting gas phase in a static system (see Chapter 3). In a mesh/membrane microreactor, the breakthrough pressure or maximum pressure difference is found before the meniscus develops a neck. A macroscopic balance of the drag, gravity and interfacial forces has also been applied to waves in two-phase flows in order to predict droplet entrainment rate. Holowach et al. (2002) followed this approach to obtain droplet entrainment rate in heated annular flow assuming waves of sinusoidal shape.

Chebbi (2003) analysed the deformation of 2D advancing gas-liquid interfaces in pre-wetted and dry capillaries neglecting inertial and gravitational forces and solved the one-dimensional flow field around the bubble to obtain the pressure over the interface. Viscous normal stresses over the interface were not considered. Shen and Udell (1985) obtained the interface shape of an inviscid bubble at low Re in a 2D axisymmetric system by solving the flow field around the bubble and balancing interfacial tension forces with viscous and pressure forces via an iterative process. Giavedoni and Saita (1997) and (1999) extended this analysis to consider inertial effects $Re >> 1$ using a Galerkin finite element approach that solves flow field and interface position simultaneously using a parameterisation of the free surface by means of spines (FIDAP, 2002). The Volume of Fluid (VOF) method is generally used in problems with surface merging and breaking while the Finite Element Method (FEM) in conjunction with a surface tracking technique, such as the spine method, is generally preferred in problems with simple surface deformation (Ashgriz, 2005). The latter approach is applied in the present work to analyse the flow effect on meniscus shape and breakthrough pressure.

The shape of the interfacial meniscus under flow conditions is initially unknown. It is found by balancing the surface tension (or interfacial tension) forces against the normal stresses (viscous and pressure forces). The inertial forces are contained in the pressure field. The steady-state vector momentum equation in fluid is given by Eq. (5.1) (see Chapter 2). The ratio *Re/Fr* is equivalent to the ratio *Ca/Bo* (generally used for two-phase flow) and its importance is generally negligible in microscale.

$$Re(\mathbf{U}^{\#} \cdot \nabla^{\#})\mathbf{U}^{\#} = -\nabla^{\#} P^{\#} + \nabla^{\#2}\mathbf{U}^{\#} + \frac{Re}{Fr}\mathbf{g}^{\#} \tag{5.1}$$

In general the fluid flow presents complicated streamlines where the three velocity components may depend upon the three spatial co-ordinates and time: $U_x = U_x(x, y, z, t)$, $U_y = U_y(x, y, z, t)$ and $U_z = U_z(x, y, z, t)$. In this general situation there are 9 stress components τ_{ij}, where i and j represent any of the spatial co-ordinates x, y and z (see Chapter 2.2.1 and Eq. (2.1)).

Figure 5.1 shows the viscous stresses and pressure exerted on three planes perpendicular to the three spatial co-ordinate axes, whose combination represents all the planes in which a force can be exerted. Thus, $\boldsymbol{\tau}_x$,$\boldsymbol{\tau}_y$ and $\boldsymbol{\tau}_z$ are three *reference stresses* (vectors). The cube is made of faces that have unit area and its centre is at the position x, y, z. At certain time $t = t$ the cube is sliced by those three perpendicular planes in a way that the fluid in one half of the cube is removed obtaining a free surface on which pressure and viscous forces act, which represent the force that the liquid was exerting. The pressure force is *perpendicular* to the surface exposed (opposite

direction to the outward unit vector) and for the *yz*-plane it is $-P\boldsymbol{\delta}_x$, where $\boldsymbol{\delta}_x$ is a unit vector in the *x*-direction and *P* is the scalar pressure which has a static and a dynamic (due to the flow) component. For the *xz* and *xy* planes the components of the pressure force are $-P\boldsymbol{\delta}_y$ and $-P\,\boldsymbol{\delta}_z$ respectively. The viscous forces are a result of the velocity gradients (different velocity of the molecules in adjacent positions of the fluid) that result in momentum transfer from the fluid molecules at high velocity towards those molecules at lower velocity and can have any direction with respect to the three perpendicular planes to the co-ordinates producing 9 components. For instance, the viscous surface stress $\boldsymbol{\tau}_x$ (acting on a plane perpendicular to the *x* axis or *yz* plane) is the vector $\tau_{xx}\mathbf{i} + \tau_{xy}\mathbf{j} + \tau_{xz}\mathbf{k}$, i.e. τ_{xy} represents the *y*-component of the viscous stress acting on a surface oriented in the positive *x*-direction. A surface stress at a given point is a more complex quantity than a scalar or a vector and it can only be defined when the surface passing through the point is defined. The convention is that the surface stress acting on a surface (e.g. bounding surface of a fluid element) is positive in the direction of the outward vector to the surface (opposite direction to the pressure force). Another way to think of the 9 stress components is to consider that there are three velocity components (U_x, U_y and U_z), whose gradients can take place in any of the three co-ordinate systems, giving a total of 9 different stresses.

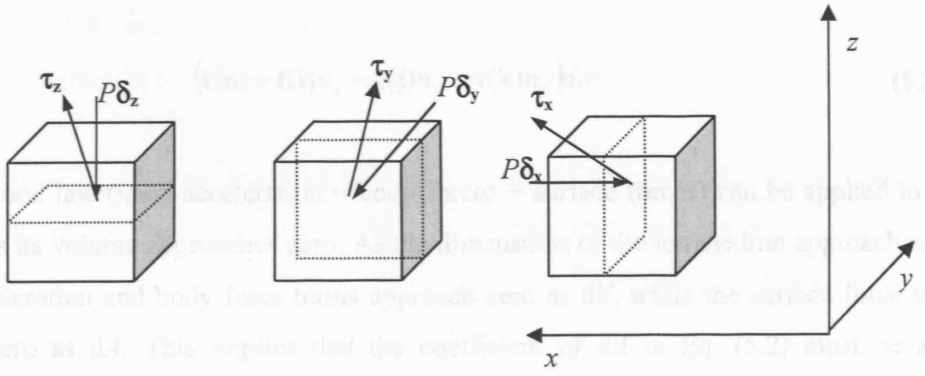

Figure 5.1. Pressure and viscous forces acting on perpendicular planes to the three spatial co-ordinates.

The orientation of a given surface is defined by its unit normal **n,** which is the vector $n_x\mathbf{i} + n_y\mathbf{j} + n_z\mathbf{k}$ and the forces on this surface $\mathbf{n}dA$ are equivalent to the forces exerted on three reference surfaces oriented in the *x*, *y* and *z*-directions with values $-n_x dA\mathbf{i}$, $-n_y dA\mathbf{j}$ and $-n_z dA\mathbf{k}$. Figure 5.2 shows a tetrahedron with three orthogonal faces with normal vectors –**i**, -**j** and –**k** and a slanted face with normal **n** (Leal, 1992). Considering δA the area of the slanted face, the area of each of the three orthogonal faces is given by $n_x\delta A$, $n_y\delta A$ and $n_z\delta A$ respectively.

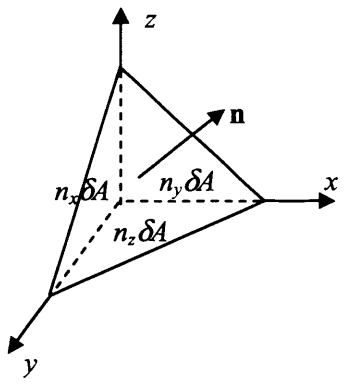

Figure 5.2. Elemental volume with a tetrahedron shape that features three orthogonal faces with normal vectors –**i**, -**j** and –**k**.

The sum of the surface forces acting on the 4 faces of the tetrahedron is given by Eq. (5.2), where **t(n)** is the stress vector acting on the surface with outward vector in the **n** direction and **t(i)**, **t(j)** and **t(k)** are the stress vectors acting on the faces perpendicular to the **i**, **j** and **k** directions.

$$\left(\mathbf{t(n)} - \mathbf{t(i)}n_x - \mathbf{t(j)}n_y - \mathbf{t(k)}n_z\right)dA \tag{5.2}$$

Newton's second law (mass·acceleration = body forces + surface forces) can be applied to the tetrahedron as its volume approaches zero. As the dimensions of the tetrahedron approach zero, the mass·acceleration and body force terms approach zero as dV, while the surface force term approaches zero as dA. This implies that the coefficient of dA in Eq. (5.2) must be zero obtaining Eq. (5.3).

$$\mathbf{t(n)} = \mathbf{t(i)}n_x + \mathbf{t(j)}n_y + \mathbf{t(k)}n_z \tag{5.3}$$

The surface stresses over the three orthogonal faces of the tetrahedron are vectors, each of them with components **i**, **j** and **k**. For a fluid they can be written as a function of the reference viscous surface stresses and pressure: $\mathbf{t(i)} = (\tau_{xx}\mathbf{i} + \tau_{xy}\mathbf{j} + \tau_{xz}\mathbf{k} - P\mathbf{i})$, $\mathbf{t(j)} = (\tau_{yx}\mathbf{i} + \tau_{yy}\mathbf{j} + \tau_{yz}\mathbf{k} - P\mathbf{j})$ and $\mathbf{t(k)} = (\tau_{zx}\mathbf{i} + \tau_{zy}\mathbf{j} + \tau_{zz}\mathbf{k} - P\mathbf{k})$, obtaining Eq. (5.4). These forces exerted on each of the three oriented areas are not multiplied by the normal vectors **i**, **j** and **k**, which would produce the normal forces to those surfaces.

$$\begin{aligned}\mathbf{t}(\mathbf{n}) = &(n_x\tau_{xx} + n_y\tau_{yx} + n_z\tau_{zx} - n_xP)\mathbf{i} + \\ &(n_x\tau_{xy} + n_y\tau_{yy} + n_z\tau_{zy} - n_yP)\mathbf{j} + \\ &(n_x\tau_{xz} + n_y\tau_{yz} + n_z\tau_{zz} - n_zP)\mathbf{k} = \mathbf{n}\cdot\mathbf{T} = \mathbf{n}\cdot(-P\mathbf{I} + \boldsymbol{\tau})\end{aligned} \tag{5.4}$$

In this analysis the second order tensors are represented by their square matrixes, considering that the definition is given by Eq. (5.5), where $\mathbf{e}_1$, $\mathbf{e}_2$ and $\mathbf{e}_3$ represent the three unit vectors in the three spatial coordinates, $\mathbf{e}_1 = \mathbf{i}$, $\mathbf{e}_2 = \mathbf{j}$ and $\mathbf{e}_3 = \mathbf{k}$.

$$\mathbf{T} = (\mathbf{e}_1, \mathbf{e}_2, \mathbf{e}_3)\begin{bmatrix}\tau_{1,1} - P & \tau_{1,2} & \tau_{1,3} \\ \tau_{2,1} & \tau_{2,2} - P & \tau_{2,3} \\ \tau_{3,1} & \tau_{3,2} & \tau_{3,3} - P\end{bmatrix}\begin{pmatrix}\mathbf{e}_1 \\ \mathbf{e}_2 \\ \mathbf{e}_3\end{pmatrix} = \sum_{i=1}^{3}\sum_{j=1}^{3}(\tau_{i,j} - P\delta_{i,j})\mathbf{e}_i\mathbf{e}_j \tag{5.5}$$

In brief,

$$\mathbf{T} = -P\mathbf{I} + \boldsymbol{\tau} \rightarrow T_{i,j} = -P\delta_{i,j} + \tau_{i,j} \tag{5.6}$$

The stress tensor **T** of the surface forces is a combination of pressure and viscous forces. **I** is the unit tensor (ones along its diagonal), $\boldsymbol{\tau}$ is the viscous stress tensor and $\delta_{i,j}$ is the Kronecker delta.

For incompressible Newtonian fluids as well as for most of compressible fluids (apart from fluids where density changes are induced either over extremely small distances or over very short time scales), the second term in Eq. (2.1) is zero and the viscous stress tensor becomes symmetric ($\tau_{i,j} = \tau_{j,i}$):

$$\boldsymbol{\tau} = \mu\left(\nabla\mathbf{U} + (\nabla\mathbf{U})^{\mathrm{T}}\right) \qquad \tau_{ij} = \mu\left(\frac{\partial U_j}{\partial x_i} + \frac{\partial U_i}{\partial x_j}\right) \tag{5.7}$$

The boundary condition defining the shape of a two-phase interface can be obtained via a force balance of a fluid F1-fluid F2 interface differential as shown in Figure 5.3, which leads to Eq. (5.8) (Papanastasiou et al., 1999).

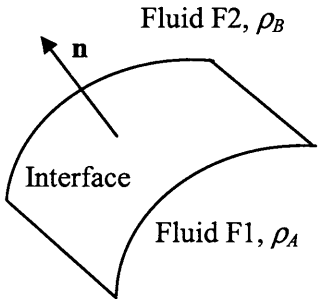

Figure 5.3. Fluid-fluid interface on which a force balance can be applied.

$$\mathbf{n}\cdot(\mathbf{T}_{F2}-\mathbf{T}_{F1})+\nabla_{II}\gamma-\gamma\mathbf{n}(\nabla\cdot\mathbf{n})+\rho_S(\mathbf{F}_g-\mathbf{a})=0 \tag{5.8}$$

where $\mathbf{n}$ is the outwardly directed unit normal, $\mathbf{T}_{F1}$ and $\mathbf{T}_{F2}$ are the stress tensors of fluids F1 and F2 respectively, γ is the surface (or interfacial) tension, $\nabla\cdot\mathbf{n}$ is the mean interface curvature at the point, ρ_S is the surface density, $\mathbf{F}_g$ is the body force per unit mass and $\mathbf{a}$ is the acceleration vector. The gradient operator ∇_{II} is defined in terms of local normal and tangent coordinates $(\mathbf{n},\mathbf{t})$:

$$\nabla_{II}=\mathbf{t}\frac{\partial}{\partial t}+\mathbf{n}\frac{\partial}{\partial n} \tag{5.9}$$

Contaminants at the vicinity of alternating curvature and non-isothermal interfaces can give rise to surface tension gradients (Marangoni effects) that give rise to *shear stress discontinuities*, able to initiate flow in thin films. In the present analysis a zero surface tension gradient is assumed, which together with a negligible surface density ρ_S simplifies Eq. (5.8) to:

$$\mathbf{n}\cdot(\mathbf{T}_{F2}-\mathbf{T}_{F1})-\gamma\mathbf{n}(\nabla\cdot\mathbf{n})=0 \tag{5.10}$$

The two components of the vector Eq. (5.10), obtained by multiplying the equation with $\mathbf{n}$ and $\mathbf{t}$ vectors respectively, represent the *normal stress interface condition* (Eq. (5.11)), in which $n_x^2+n_y^2+n_z^2 = 1$ for the pressure of the fluid phase F2 and the *tangential stress interface condition* (Eq. (5.12)). The mean curvature $\nabla\cdot\mathbf{n}$ in Eq. (5.11) allows for normal stress discontinuities due to the effect of surface tension γ. The normal and tangential viscous stresses for a specific phase (F1 or F2) are given by Eqs. (5.13) and (5.14).

$$(P_{F1} - P_{F2}) + (\tau_{F2,nn} - \tau_{F1,nn}) = \gamma(\nabla \cdot \mathbf{n}) \tag{5.11}$$

$$(\tau_{F2,nt} - \tau_{F1,nt}) = 0 \tag{5.12}$$

$$\begin{aligned} -P_F + \tau_{nn} = \mathbf{t(n)} \cdot \mathbf{n} = \mathbf{n} \cdot \mathbf{T} \cdot \mathbf{n} = (n_x^2 \tau_{xx} + n_y n_x \tau_{yx} + n_z n_x \tau_{zx}) + \\ (n_x n_y \tau_{xy} + n_y^2 \tau_{yy} + n_z n_y \tau_{zy}) + \\ (n_x n_z \tau_{xz} + n_y n_z \tau_{yz} + n_z^2 \tau_{zz}) - P_F \end{aligned} \tag{5.13}$$

$$\begin{aligned} \tau_{nt} = \mathbf{t(n)} \cdot \mathbf{t} = \mathbf{n} \cdot \mathbf{T} \cdot \mathbf{t} = (n_x t_x \tau_{xx} + n_y t_x \tau_{yx} + n_z t_x \tau_{zx}) + \\ (n_x t_y \tau_{xy} + n_y t_y \tau_{yy} + n_z t_y \tau_{zy}) + \\ (n_x t_z \tau_{xz} + n_y t_z \tau_{yz} + n_z t_z \tau_{zz}) \end{aligned} \tag{5.14}$$

Eqs. (5.11) and (5.12) contain the special case of a free surface, when $\tau_{F1,ij} = 0$ (no motion of phase F1), which is the case analysed in the present work in which the fluid equations need to be solved only in the liquid domain.

5.3. Definition of the Problem

The case analysed in the present work for mesh microreactors consists of a gas/liquid steady state system in which the gas phase (*non-wetting*) fills the pores of the mesh and the meniscus is at the liquid pore end (phase F2). The contact angle is measured with respect to the liquid phase. This situation is generally desirable in gas/liquid systems where the diffusivity of reactants/products in the gas phase (filling the pores) is 4-5 orders of magnitude larger than that in the liquid phase, while at the same time, gas densities are only 3 orders of magnitude smaller than liquid densities at low/moderate pressures. This results in larger mass fluxes when the pores are filled with the gas phase. When the liquid phase is static, the pressure difference across the meniscus at the wetting pore end is given by the Laplace equation,

$$\Delta P = P_G - P_L = \gamma\left(\frac{1}{R_1} + \frac{1}{R_2}\right) = f_L \gamma \frac{\cos\theta_{App}}{r} \tag{5.15}$$

where the Laplace factor is $f_L = 1$ for a 2D system, $f_L = 2$ for a 2D axisymmetric system (cylindrical pore) and takes values between 1 and 2 (not necessarily constant) in other geometries (e.g. polygonal pores), γ is the surface tension of the system, r is the pore radius (or half the width of the pore in a 2D system) and $\theta_{App} = \theta + \phi$ is the apparent contact angle:

$$\theta_{App} = \theta + \phi \tag{5.16}$$

where θ is the contact angle that can take any value between the advancing and receding contact angles and ϕ is the solid wall inclination at the point of contact of the meniscus three-phase contact line, which varies from $\phi = \phi_{Int}$ (solid wall inclination of pore inner wall) to $\phi = \phi_{min} = -90°$ at the liquid pore end. Therefore, the pore is filled with the gas phase when a pressure difference ΔP is applied with values between the critical filling and breakthrough pressure values, $\Delta P_{C,G} = f_L \gamma \cos(\theta_R + \phi_{Int})/r \leq \Delta P \leq \Delta P_{B,G} = f_L \gamma \cos(\max[(\theta_R + \phi_{min}),0])/r$ (see Chapter 3). When $\theta_R < 90°$, the gas breaks through into the liquid phase for $\theta_{App} = 0°$. This corresponds to a hemispherical meniscus, which is the shape of maximum curvature under static conditions (*breakthrough by maximum curvature*). If $\theta_R > 90°$, the gas phase breaks through into the liquid phase at $\theta_{App} = \theta_R - 90°$ by spreading out sideways before the meniscus reaches a shape of maximum curvature (*breakthrough by maximum contortion - spreading*).

Under flow conditions, Laplace Eq. (5.15) is not applicable since fluid stresses on the meniscus surface must be accounted for. Under the influence of fluid surface stresses, the meniscus can become asymmetric with respect to the pore axis giving rise to different apparent contact angles along the three-phase contact line. In a simplified 2D system, there are different apparent contact angles at the front and back of the meniscus, $\theta_{App,front}$ and $\theta_{App,back}$ respectively (see Figure 5.5). The meniscus shape of maximum curvature corresponds to the meniscus shape at imminent gas breakthrough (at maximum P_G before breakthrough for given liquid flow conditions and system geometry) in a system where the apparent contact angle θ_{App} is allowed to take any value (down to –90°). This shape under flow conditions is not a hemisphere and because of asymmetry, the maximum curvature shape does not have a constant curvature. The contact angles $\theta_{App,front}$ and $\theta_{App,back}$ at which the maximum curvature shape is reached are not equal to 0°. However, before reaching the maximum curvature shape, the apparent contact angle at the back of the meniscus may reach the minimum attainable apparent contact angle given by $\theta_{App} = \theta_R + \phi_{min} = \theta_R - 90°$ ($\phi = \phi_{min} = -90°$) resulting in *breakthrough by maximum contortion*. Since $\theta_{App,back}$ and the meniscus shape of maximum curvature depend on flow conditions, the effect of flow parameters on them and consequently on gas breakthrough pressure difference is analysed below.

The local curvature of the meniscus is determined by the difference in normal stresses (pressure and viscous stresses) between the gas and liquid phases. It must be noted that when the meniscus is at the liquid pore end, under flow conditions the liquid pressure and normal viscous stresses (0 for a flat meniscus) intrinsically change as the meniscus grows (liquid pressure

decreases via Venturi effect and normal viscous stresses increase as U increases). Since the key variables that need to be estimated are the available range of pressure difference (externally controlled independently of meniscus growth, e.g. due to external control of gas/liquid pressure, pressure drop or system perturbations) that the meniscus is able to cope with before it breaks through at either pore end (meniscus stability) and/or before the pore is filled with the undesired phase, the breakthrough pressure difference under flow conditions is defined as,

$$\Delta P_B^{Flow} = (P_{G,max} - P_L^*)_B \tag{5.17}$$

where $P_{G,max}$ is the gas pressure at the imminent breakthrough position and $P_L^* = (P^{\#}_{L,} - \tau^{\#}_{nn})_{Flat}$ is the liquid normal stresses at the middle point of the meniscus (normal stresses can vary along the meniscus) for a flat meniscus under the same flow conditions when the meniscus is at the imminent breakthrough position (in a flat meniscus normal viscous stresses on the surface are zero but pressure is not exactly the same as that when the meniscus is substituted by wall where a no-slip condition applies). In cases when the meniscus cannot be flat, zero height is taken at the centre. This definition of breakthrough pressure is equivalent to the available range of pressure difference to take the meniscus from a flat shape to the breakthrough shape. Figure 5.4 illustrates this concept for static and flow systems respectively in which flat and imminent breakthrough meniscus positions are shown.

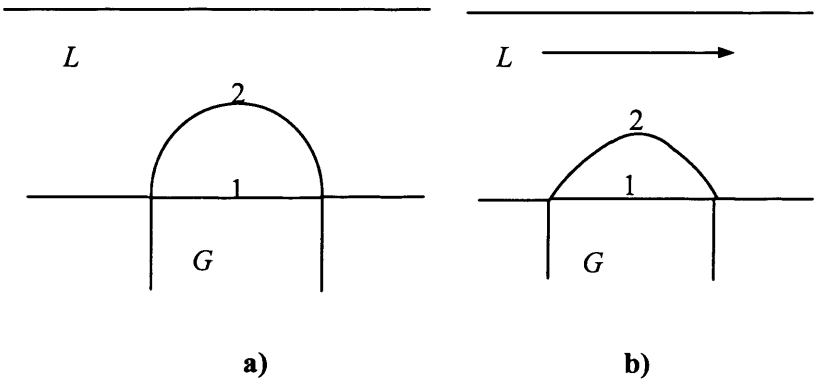

Figure 5.4. Comparison between flat (1) and breakthrough (2) meniscus shapes under a) static and b) flow (inertial) conditions.

In both systems, the gas pressure, which is uniform along the meniscus, is increased while moving from position 1 to position 2. At the meniscus centre, the normal stress difference at position 2 is larger in the flow system since the local curvature is larger (Figure 5.4b). However,

the external gas pressure change required to go from position 1 to position 2 may be smaller in the flow system than in the static one due to the intrinsic liquid pressure reduction via Ventury effect as the meniscus grows (e.g. $(P_{G2}\text{-}P_{G1})^{Static} > (P_{G2}\text{-}P_{G1})^{Flow}$). Considering no external change in P_L* (method followed in simulation and experiments) and $P_{G1} = P_L$* ($\Delta P = 0$ in a flat meniscus), Eq. (5.17) results in Eq. (5.18),

$$\Delta P_{B,G} = P_{G,B,G} - P_G\,(Flat\ meniscus) \tag{5.18}$$

where $P_{G,B,G}$ is the pressure of the gas phase for breakthrough of the gas phase. Similarly, the total available range of pressure difference when P_L* does not change is,

$$\Delta P_T = \Delta P_{B,G} + \Delta P_{B,L} + (\rho_L - \rho_G)gh_{pore} = P_{G,B,G} - P_{G,B,L} \tag{5.19}$$

where $P_{G,B,L}$ is the gas pressure for breakthrough of the liquid phase. Figure 5.5 shows the geometry considered in the present work. The complexity of free surface boundary problems lies on the fact that the final location of the interface and the velocity-pressure fields are coupled. The 2D system shown in Figure 5.5 is chosen for simplicity since the *breakthrough by maximum contortion* is defined by only one apparent contact angle at the back of the meniscus, $\theta_{App,back}$ (a 2D axisymmetric geometry is not possible). The 3D equivalent geometry corresponds to a pore slit that occupies all the width of a plate with width >> height (see experimental section for the actual experimental device used).

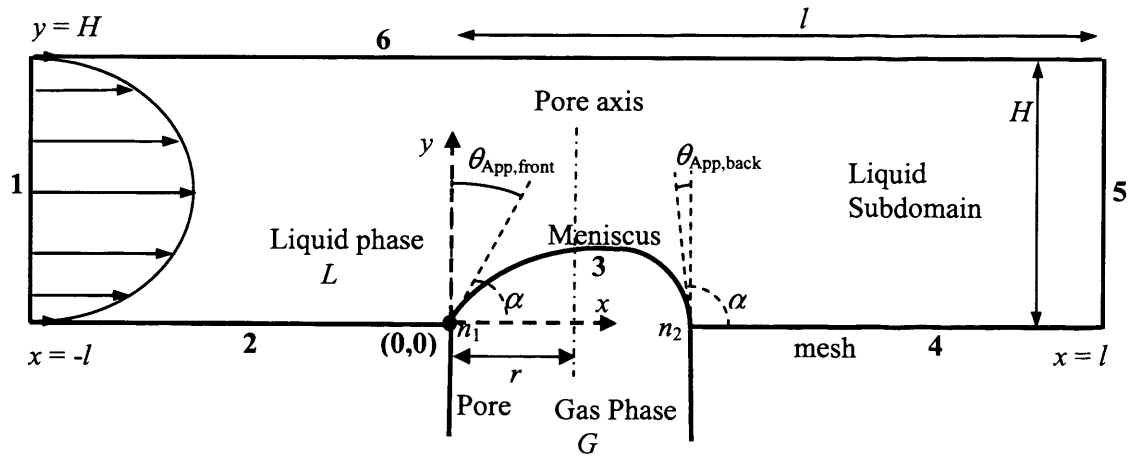

Figure 5.5. Meniscus deformation as a result of the viscous and pressure forces.

5.4. Modelling Work

5.4.1. Full Mathematical Model

The angle α in Figure 5.5 is the angle of the tangent at each point of the 2D meniscus profile with the x-axis. Defining the apparent contact angle θ_{App} on the side of the liquid, at $x = 0$, $\theta_{App,front}(x = 0) = \pi/2-\alpha$ and at $x = x_f$, $\theta_{App,back}(x = x_f) = \alpha - \pi/2$. The meniscus is a free static surface in which the normal and tangential viscous stresses exerted from the gas side are zero, $\tau_{G,nt} = \tau_{G,nn} = 0$, further simplifying Eqs. (5.11) and (5.12). For a 2D profile the local mean curvature at a specific point is simply defined by one radius of curvature, $(\nabla \cdot \mathbf{n}) = 1/R$, which can be written as (Adamson and Gast, 1997),

$$\frac{1}{R} = -\frac{\partial^2 y/\partial x^2}{\left(1+(\partial y/\partial x)^2\right)^{3/2}} \tag{5.20}$$

or via Eq. (5.21) using the angle α as,

$$\frac{1}{R} = -\cos\alpha \frac{\partial \alpha}{\partial x} = -\frac{\partial \sin\alpha}{\partial x} \tag{5.21}$$

The normal stress interface condition (Eq. (5.11)) is simplified to Eq. (5.22) where τ_{nn} are the normal surface stresses exerted by the liquid phase over the meniscus, which are given by Eq. (5.23), obtained via Eqs. (5.7) and (5.13).

$$(P_G - P_L) + \tau_{nn} = \gamma \frac{1}{R} \tag{5.22}$$

$$\tau_{nn} = (n_x^2 \tau_{xx} + n_y n_x \tau_{yx}) + (n_x n_y \tau_{xy} + n_y^2 \tau_{yy}) = 2\mu\left(n_x^2 \frac{\partial U_x}{\partial x} + n_y n_x \left(\frac{\partial U_x}{\partial y} + \frac{\partial U_y}{\partial x} \right) + n_y^2 \frac{\partial U_y}{\partial y} \right) \tag{5.23}$$

When gravity is important, the gas pressure can be written as $P_G = P_{G0}-\rho_G g y$ and the liquid pressure as $P_L = P_{L0}-\rho_L g y$. If the gravity term for the liquid pressure is considered in the Navier-Stokes equations within the liquid phase, Eq. (5.22) becomes,

$$(P_{G,0}-P_L)-\rho_G g y+2\mu\left(n_x^2\frac{\partial U_x}{\partial x}+n_y n_x\left(\frac{\partial U_x}{\partial y}+\frac{\partial U_y}{\partial x}\right)+n_y^2\frac{\partial U_y}{\partial y}\right)=-\gamma\frac{\left(\partial^2 y/\partial x^2\right)}{\left(1+\left(\partial y/\partial x\right)^2\right)^{3/2}}=-\gamma\cos\alpha\frac{\partial\alpha}{\partial x} \quad (5.24)$$

The *tangential stress interface condition* given by Eq. (5.12) is reduced to Eq. (5.25) within the liquid phase. Therefore, the bubble is only deformed due to an asymmetric distribution of normal stresses along the x direction (pressure and normal viscous stresses to the meniscus). This condition is generally no applicable to liquid-liquid systems in which $\tau_{G,nt} \neq 0$.

$$\tau_{nt}=0 \quad (5.25)$$

The steady-state Navier-Stokes equation and the normal stress condition are made dimensionless using the definitions given below, where the pore width r is the characteristic length, the mean liquid velocity at the mesh microreactor inlet $U_0 = Q/H$ is the characteristic velocity, where Q is the flowrate per width ($m^3/(s.m)$). The definition of the dimensionless pressure and viscous stresses considers the viscosity, which is more suitable than density in the case of laminar flows where viscous forces are substantial (Bird et al., 2000).

$$x^{\#}=\frac{x}{r} \qquad y^{\#}=\frac{y}{r} \quad (5.26)$$

$$\mathbf{U}^{\#}=\frac{\mathbf{U}}{U_0} \quad (5.27)$$

$$P^{\#}=\frac{P-P_0}{\mu U_0/r} \quad (5.28)$$

$$\tau^{\#}=\frac{\tau-\tau_0}{\mu U_0/r} \quad (5.29)$$

$$\nabla^{\#}=r\nabla \quad (5.30)$$

$$\nabla^{\#2}=r^2\nabla^2 \quad (5.31)$$

The dimensionless Navier Stokes and continuity equations are given by Eq. (5.32) and (5.33) respectively and are solved within the liquid domain shown in Figure 5.5 (components x and y

for a 2D system). Although the ratio *Ca/Bo* may not be close to zero, its effect on fluid flow is generally negligible in microscale analysis when the flow occurs in the horizontal plane (integral of the gravity force along the phase height is generally negligible).

$$Re(\mathbf{U}^{\#}\cdot\nabla^{\#})\mathbf{U}^{\#}=\frac{\mathrm{Re}_{\mathrm{stan}}}{H^{\#}}(\mathbf{U}^{\#}\cdot\nabla^{\#})\mathbf{U}^{\#}=-\nabla^{\#}P^{\#}+\nabla^{\#2}\mathbf{U}^{\#}+\frac{Ca}{Bo_{\mathrm{L}}}\mathbf{g}^{\#} \qquad (5.32)$$

(Ca is marked 0)

$$\nabla^{\#}\cdot\mathbf{U}^{\#}=0 \qquad (5.33)$$

The dimensionless normal stress and tangential stress conditions are given by Eqs. (5.34) and (5.35).

$$Ca\left[(P^{\#}_{\mathrm{G},0}-P^{\#}_{L})+\tau^{\#}_{nn}\right]-Bo_{\mathrm{G}}y^{\#}=-\frac{\left(\partial^2 y^{\#}/\partial x^{\#2}\right)}{\left(1+\left(\partial y^{\#}/\partial x^{\#}\right)^2\right)^{3/2}}$$

$$Ca\left[(P^{\#}_{\mathrm{G},0}-P^{\#}_{L})+2\left(n_x^2\frac{\partial U^{\#}_x}{\partial x^{\#}}+n_y n_x\left(\frac{\partial U^{\#}_x}{\partial y^{\#}}+\frac{\partial U^{\#}_y}{\partial x^{\#}}\right)+n_y^2\frac{\partial U^{\#}_y}{\partial y^{\#}}\right)\right]-Bo_{\mathrm{G}}y^{\#}=-\frac{\left(\partial^2 y^{\#}/\partial x^{\#2}\right)}{\left(1+\left(\partial y^{\#}/\partial x^{\#}\right)^2\right)^{3/2}} \qquad (5.34)$$

$$\tau^{\#}_{nt}=0 \qquad (5.35)$$

Therefore, 7 dimensionless numbers appear in the equations; *Re*, *Ca*, Bo_L, Bo_G given by Eqs. (5.36)-(5.39), the system geometry defined by $H^{\#}$ and $l^{\#}$ (see Figure 5.5) and the system property $P^{\#}_{\mathrm{G},0}$ (considering $P_{\mathrm{L},x=l}=0$), yield all solutions to the problem as long as a parabolic velocity profile is developed in front of the meniscus. Large values of $H^{\#}$ imply a small effect of the fluid on meniscus deformation for given values of *Re*, *Ca* and *Bo* since the velocity in the vicinity of the meniscus will be insignificant:

$$Re=\frac{\rho_l U_0 r}{\mu_l}=\frac{Re_{\mathrm{stan}}}{H^{\#}} \qquad (5.36)$$

$$Ca=\frac{\mu U_0}{\gamma} \qquad (5.37)$$

$$Bo_{\mathrm{L}}=\frac{\rho_{\mathrm{L}} g r^2}{\gamma} \qquad (5.38)$$

$$Bo_G = -\frac{\rho_G g r^2}{\gamma} \tag{5.39}$$

The Re number defined with the pore width r is equivalent to the standard Re_{stan} (defined with the phase height H) divided by $H^{\#}$:

$$Re = \frac{Re_{stan}}{H^{\#}} \tag{5.40}$$

When inertial forces are dominant, the Weber number We ($We >> 1$), which is the ratio of inertial to surface tension forces as defined by Eq.(5.41), instead of the Ca determines the effect of flow on the meniscus.

$$We = \frac{\rho U_0^2 r}{\gamma} = ReCa = \frac{Re_{stan}}{H^{\#}} Ca \tag{5.41}$$

The second order non-linear dimensionless normal stress condition (Eq. (5.34)) can be written using the parameter arc length $S^{\#}$, as a system of 3 ODEs considering Eq. (5.21) for the curvature and taking into account that $dS^{\#} = dx^{\#}/\cos\alpha$, obtaining Eqs. (5.42)-(5.44), which are easily solved if the viscous normal stresses to the surface are known

$$Ca\left[(P^{\#}_{G,0} - P^{\#}_L) + 2\left(n_x^2 \frac{\partial U_x^{\#}}{\partial x^{\#}} + n_y n_x \left(\frac{\partial U_x^{\#}}{\partial y^{\#}} + \frac{\partial U_y^{\#}}{\partial x^{\#}}\right) + n_y^2 \frac{\partial U_y^{\#}}{\partial y^{\#}}\right)\right] - Bo_G y^{\#} = -\frac{\partial \alpha}{\partial S^{\#}} \tag{5.42}$$

$$\frac{dy^{\#}}{dS^{\#}} = \sin\alpha \tag{5.43}$$

$$\frac{dx^{\#}}{dS^{\#}} = \cos\alpha \tag{5.44}$$

Gravity is generally neglected in mesh microreactors where the phase height is around 50-500 μm and pore sizes 5-100 μm. Thus, terms containing the Bo number are generally insignificant. Considering this assumption, all solutions for a given system are determined by a set of Re, Ca, $H^{\#}$, $P^{\#}_{G,0}$ and $l^{\#}$. Using the same dimensionless variables, Eq. (5.15) for gravity-free static two-dimensional menisci becomes,

$$P_G^{\#} - P_L^{\#} = \frac{1}{R^{\#}Ca} = \frac{\cos\theta_{App}}{r^{\#}Ca} \tag{5.45}$$

The pressure difference range available to the meniscus at the wetting pore end (gas filling the pores) is an important system property dependent on flow conditions. This available range of pressure difference is defined as the gas breakthrough pressure (difference) at which the meniscus breaks into the liquid phase minus the liquid critical entry pressure (difference) at which the meniscus detaches from the liquid pore end. In static conditions, this range is given by Eq. (5.46) and $f_L = 1$ for a 2D system.

$$(P_G^{\#} - P_L^{\#})_{B,G} - (P_G^{\#} - P_L^{\#})_{C,G} = \frac{f_L}{Ca}\left(\frac{\cos(\max[0, \theta_R - 90]) - \cos\theta_A}{r^{\#}}\right) \tag{5.46}$$

5.4.2. Solution of Equations

Eqs. (5.32)-(5.34) or alternatively Eqs. (5.32), (5.33) and (5.42)-(5.44) are solved in the liquid subdomain defined in Figure 5.5. The equations are solved simultaneously since the final meniscus profile is part of the solution. Values of $H^{\#}$ and $l^{\#}$ define the system geometry but in a simplified analysis where one isolated pore is considered, $H^{\#}$ is the only geometrical parameter that affects the solution provided that a parabolic velocity profile is developed in the liquid in front of the meniscus. By assuming an already developed parabolic profile at the liquid inlet, the channel length before the meniscus does not need to be long. Properties of the system determine the values of *Re*, *Ca* and $P^{\#}_{G,0}$. The boundary conditions for the geometry shown in Figure 5.5 are,

Boundary 1: Inlet condition, liquid parabolic velocity profile between parallel sheets,

$$U_x^{\#} = \frac{3}{2}U_{mean}^{\#}\left(1 - \left(\frac{y^{\#} - H^{\#}/2}{H^{\#}/2}\right)^2\right) \quad U_y^{\#} = 0 \tag{5.47}$$

Boundaries 2, 4 and 6: No-slip condition.

$$\mathbf{U}^{\#} = 0 \tag{5.48}$$

Boundary 3: Normal stress and tangential stress interface conditions defined by Eq. (5.34) and (5.35). It must be noted that the position of the three phase contact line, end points n_1 and n_2 in

Figure 5.5 that correspond to the pore end, is fixed during the solution process and only the rest of the points of the meniscus profile are allowed to move. This is a valid boundary condition while the apparent contact angle at the front and back of the meniscus is smaller than the advancing contact angle, ($\theta_{App,front}$, $\theta_{App,back}$) $< \theta_A$, otherwise the meniscus will partially go into the pore. However, this condition applies in most of the situations due to the fact that the meniscus apparent contact angle θ_{App} changes as the solid wall inclination changes from ϕ_{Int} to $\phi_{max} = 90°$, before breakthrough takes place by maximum contortion. Furthermore, the meniscus reaches the pore end at the receding contact angle $\theta_R < \theta_A$.

Boundary 5: Straight-out conditions,

$$P^{\#}_{x=l} = 0 \tag{5.49}$$

$$\mathbf{U}^{\#} \cdot \mathbf{t} = 0 \tag{5.50}$$

The simultaneous solution of this system of equations (Eq. (5.32)-(5.35) and (5.47)-(5.50)) yields the velocity/pressure field ($U_x^{\#}$,$U_y^{\#}$) and $P_L^{\#}$ and the meniscus shape $x^{\#}$,$y^{\#}$, considering that the reference pressure at the exit of the liquid domain is $P^{\#}_L = 0$.

Initially, an iterative solution approach was used. The flow field around a rigid meniscus was solved by Femlab and a new meniscus shape was calculated in Matlab by solving the normal stress condition independently. This required fitting the meniscus shape via cubic spline interpolation which produced curves continuous in the second derivative (Farin 1992; Piegl and Tiller, 1997) and enabled the calculation of local curvature. This approach was time consuming and presented convergence issues due to steep jumps in the values of the normal stresses. Smoother results were obtained by manually fitting the shape to second/third order Bezier curves (Rogers and Adams, 1990) but an algorithm was not available to improve precision and efficiency. Eventually, the commercial software FIDAP 8.7.0 was employed to solve the set of equations and obtain the meniscus shape for different dimensionless numbers and geometries. In FIDAP, the continuum equations and boundary conditions over the meniscus are discretised via a Galerkin Finite Element method producing a set of non-linear algebraic equations that are solved using a coupled Newton-based solver. There are two main issues when dealing with free surfaces that are related to a) numerical stability and correct set up of the boundary and end conditions and b) re-meshing of the computational fluid domain subsequent to the movement of the boundary. Gambit 2.1 is used to mesh the solution domain in the liquid. Two different areas

of the grid can be distinguished: an area with *fixed elements* that is utilized in the region far from the meniscus and an area of *moving elements* in the vicinity of the meniscus, which is likely to be invaded by the meniscus (see Figure 5.7). The moving nodes along the free surface and in its vicinity are free to move along lines called *spines* (FIDAP, 2002), which are fixed straight lines passing through the meniscus free surface nodes and determine a direction for the free surface to move. The direction of the spines is determined by the configuration of the initial mesh. The moving free surface node positions are solved simultaneously with the velocity-pressure field within the liquid domain thus improving convergence. There are other available methods for the iterative update of the nodes in the region near the free surface, such us mapping. In the mapped approach, the nodes in the moving elements area are free to be remapped using the new free surface boundary, whose nodes move in either selected direction (spine, normal or another user-defined direction). The spines approach is more restrictive than the mapped one regarding the new nodal positions although it only requires one mapped mesh for the entire solution process, resulting in a more time-efficient approach. In addition, the spine method is the only approach that can be used with Newton-based solvers and requires quadrilateral elements via a mapped meshing process (not pave process, Gambit, 2005). A severe deformation of the free surface can lead to mesh destruction if the free surface reaches points where two spines intersect (see Figure 5.6). The spine orientation via the meshing process must be carefully chosen as a function of the type and geometry of the problem.

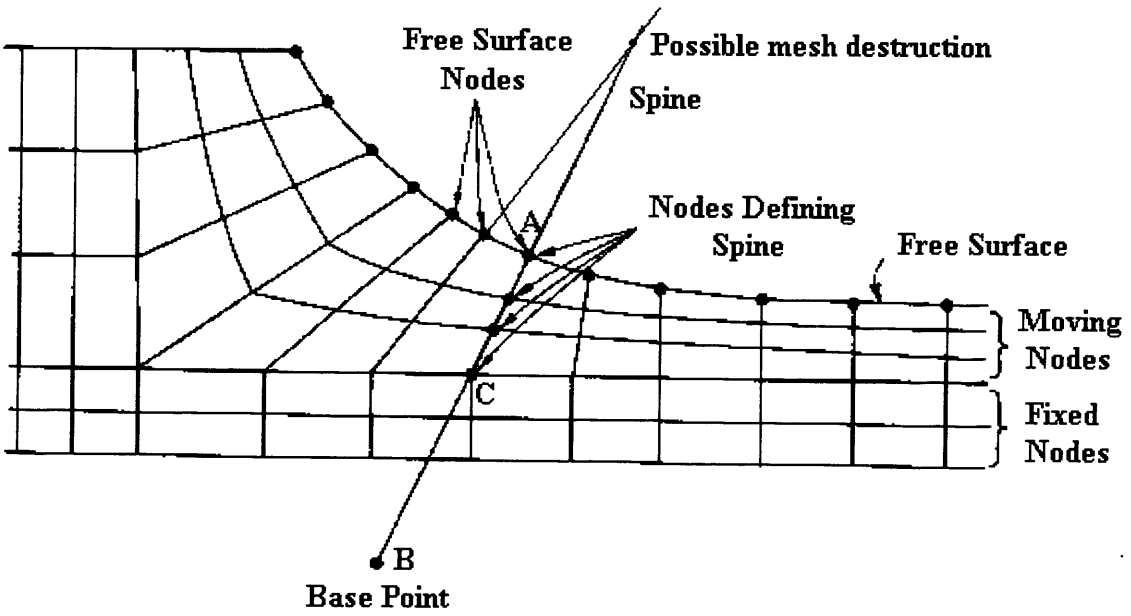

Figure 5.6. Spine orientation in a free surface and potential mesh destruction under severe interface deformation (FIDAP, 2002).

Figure 5.7 shows the initial mesh (fixed and moving elements) that determines the spine orientation for the geometry $H^{\#} = H/r = 2$. During each iteration, the moving nodes move along the spines fulfilling the normal and tangential stress interface conditions. The spherical region containing the moving elements defines a spine orientation that improves the meniscus solution at the pore ends when compared to a uniform mapped rectangular mesh. Accurate values of the apparent contact angles at the front and back of the meniscus can thus be obtained for different deformed interface shapes.

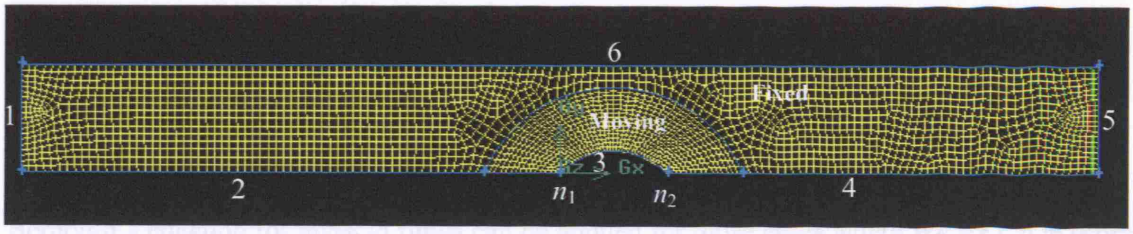

Figure 5.7. Initial mesh of the liquid domain. Fixed and moving elements in the grid are shown.

Steady state simulations are carried out at different pressures of the gas phase, $P^{\#}_G$, starting from the $P^{\#}_G$ that gives a flat meniscus to that required for breakthrough by maximum meniscus curvature. The solution is generally reached in few iterations although it is dependent on meniscus deformation from the initial state and *Re* (high *Re* leads to stability problems). An initial meniscus shape based on a static circular meniscus of radius of curvature $R^{\#}$ obtained from Eq. (5.45), $R^{\#} = 1/(Ca(P^{\#}_L - P^{\#}_G))$, is utilised to improve the convergence of the steady state solution. $P^{\#}_L$ is calculated as the average value of the normal stresses in the fluid phase between $x^{\#} = 0$ and $x^{\#} = 2$ ($x = d$) in a channel of the same length without the pore (see Figure 5.8).

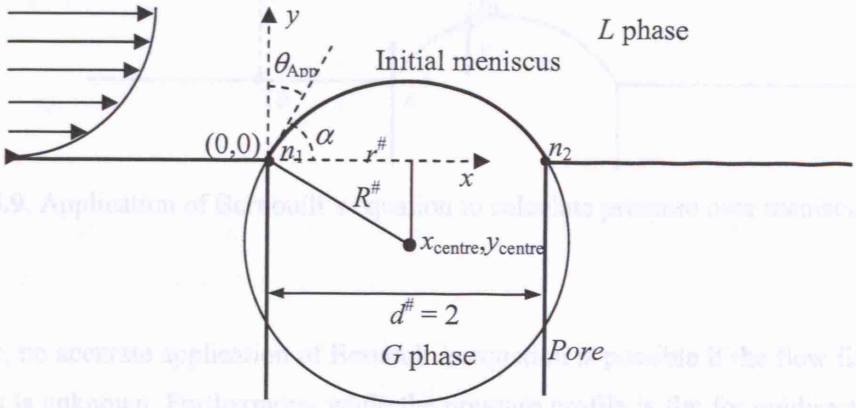

Figure 5.8. Initial meniscus shape to improve solution convergence.

For those cases (high *Ca* or *We* numbers) in which there are still convergence problems, an initial shape for the steady state simulation is used from a previous solution with slightly different $\Delta P^{\#}$. It is also useful to solve the transient equations for the previous meniscus until the change of the meniscus shape with time becomes small, using this shape for the final steady state simulation. When the pressure difference overcomes the breakthrough pressure by maximum curvature (any θ_{App} is allowed) there is no equilibrium meniscus shape and the steady state equations do not yield any solution. The transient equations can then be solved in order to check the breakthrough pressure has been overcome. The implementation of the problem in FIDAP is summarized in Appendix 5A.

5.4.3. Simplified Mathematical Model (*We* >> *Ca*)

Bernoulli's equation for inviscid fluids can be applied for those cases where *We* >> *Ca* in order to obtain a simplified solution of the meniscus shape and breakthrough pressure. Eqs. (5.42)-(5.44) under negligible viscous stresses and gravity are reduced to Eq. (5.51) in which $(P^{\#}_{G}-P^{\#}_{L,1}) = \Delta P^{\#}$ (externally controllable pressure difference as defined in Eq. (5.17)). The term $P^{\#}_{L,1}-P^{\#}_{L,2a}$ ($P^{\#}_{L,1a} = P^{\#}_{L,1}$) indicates the pressure reduction over the meniscus as this grows (see Figure 5.9), which can be estimated from Bernoulli's equation:

$$\Delta P = \gamma\frac{1}{R} \rightarrow P^{\#}_{G} - (P^{\#}_{L,1} - (P^{\#}_{L,1} - P^{\#}_{L,2a})) = -\frac{1}{Ca}\frac{\dfrac{d^2y}{dx^2}}{\left(1+\left(\dfrac{dy}{dx}\right)^2\right)^{3/2}} \qquad (5.51)$$

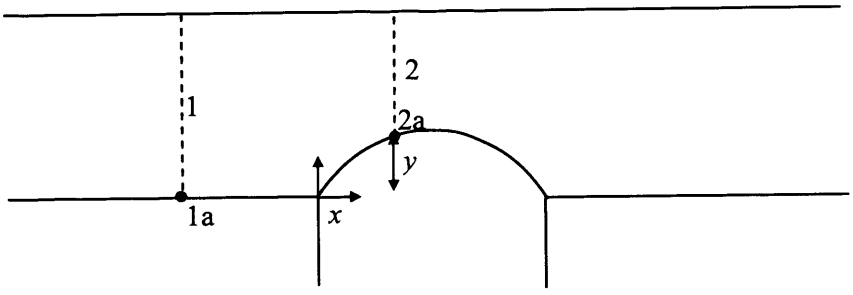

Figure 5.9. Application of Bernoulli's equation to calculate pressure over meniscus.

However, no accurate application of Bernoulli's equation is possible if the flow field around the meniscus is unknown. Furthermore, while the pressure profile is flat for unidirectional flows as 2D laminar flow, the curved streamlines around the meniscus produce a pressure gradient in the

radial direction (Massey and Ward-Smith, 1998). Bernoulli's equation can be applied to either a streamline in the vicinity of the meniscus (points 1a and 2a) or the whole cross sections 1 and 2 in Figure 5.9 using average fluid properties. In the former case, $U_{1a} = 0$ and neglecting gravity and using the previously defined dimensionless variables, the pressure reduction over 2a due to the velocity increase is given by Eq. (5.52) in which $P^{\#}_{L,1a} = P^{\#}_{L,1}$ (constant pressure in the cross section). However, velocity at point 2a $U_{2a}{}^{\#}$ is unknown and cannot be expressed as a function of the average velocity in section 1, $U_{av,1} = U_0$ (characteristic velocity).

$$P^{\#}_{L,1} - P^{\#}_{L,2a} = \frac{Re}{2} U^{\#}_{2a} \tag{5.52}$$

When applying Bernoulli's equation to the whole cross section, the kinetic energy correction factor f_{KE}, defined by Eq. (5.54), where U_{av} is the average velocity in the considered cross section, must be taken into account because of the non-flat velocity profile in sections 1 and 2. This factor is $f_{KE} = 1.543$ in section 1 (2D laminar flow) according to Eqs. (5.54) and (5.55) but unknown and x,y dependable in section 2 over the meniscus.

$$f_{KE} = \frac{2KE}{U^2_{av}} \tag{5.53}$$

$$KE = \text{Kinetic energy per mass} = \frac{\text{Total kinetic energy rate}}{\text{Total mass rate}} = \frac{\int \frac{\rho U^3}{2} dA}{\int \rho U dA} = \tag{5.54}$$

$$KE = \frac{\int_0^{H/2} \left(1.5U_0 \left(1 - \left(\frac{r}{H/2} \right)^2 \right) \right)^3 2dr}{\int_0^{H/2} 1.5U_0 \left(1 - \left(\frac{r}{H/2} \right)^2 \right) 2dr} = 0.7714U_0^2 \rightarrow f_{KE} = \frac{2KE}{U_0^2} = 1.543 \tag{5.55}$$

Assuming the same correction factor for section 2, and considering that $U_2 = U_0 H/(H-y)$, the average pressure reduction between section 1 and 2 is,

$$P^{\#}_{L,1} - P^{\#}_{L,2} = \frac{f_{KE} Re}{2} \left(\left(\frac{H^{\#}}{H^{\#} - y^{\#}} \right)^2 - 1 \right) \tag{5.56}$$

However, the required pressure reduction that determines the meniscus shape in Eq. (5.51) is $P^{\#}_{L,1}$-$P^{\#}_{L,2a}$ where $P^{\#}_{L2a}$ is always smaller than $P^{\#}_{L2}$ due to the pressure gradient perpendicular to the curved convex streamlines in the vicinity of the meniscus (similar to Coanda effect, Massey and Ward-Smith, 1998). Thus, an effective kinetic energy correction factor larger than f_{KE} = 1.54 should be used. Eq. (5.56) with a suitable effective $f_{KE,eff}$ larger than 1.54 is substituted in Eq. (5.51) to produce Eq. (5.57).

$$(P_G^{\#} - P_{L,1}^{\#}) + \frac{f_{KE,eff}\, ReCa}{2}\left(\left(\frac{H^{\#}}{H^{\#} - y^{\#}}\right)^2 - 1\right) = -\frac{\dfrac{d^2y}{dx^2}}{\left(1+\left(\dfrac{dy}{dx}\right)^2\right)^{3/2}} \qquad (5.57)$$

Eq. (5.57) is a second order non-linear differential equation that is solved in Mathematica (see Appendix 5B) using the initial conditions $y(x = 0) = 0$ and $dy/dx(x = 0) = \tan(\pi/2\text{-}\theta)$. As $We >> Ca$, $ReCa$ is substituted by We into Eq. (5.57), which assumes that the pressure reduction as the meniscus grows is only a function of the meniscus y co-ordinate and therefore generates symmetrical shapes. This meniscus symmetry is expected when $We >> Ca$ (see Figure 5.31) for the Re range under consideration where streamlines follow the meniscus contour smoothly even at large meniscus curvatures and Re as shown in Figure 5.10. This curvature of the streamlines defines a larger pressure reduction in the vicinity of the meniscus than far from it.

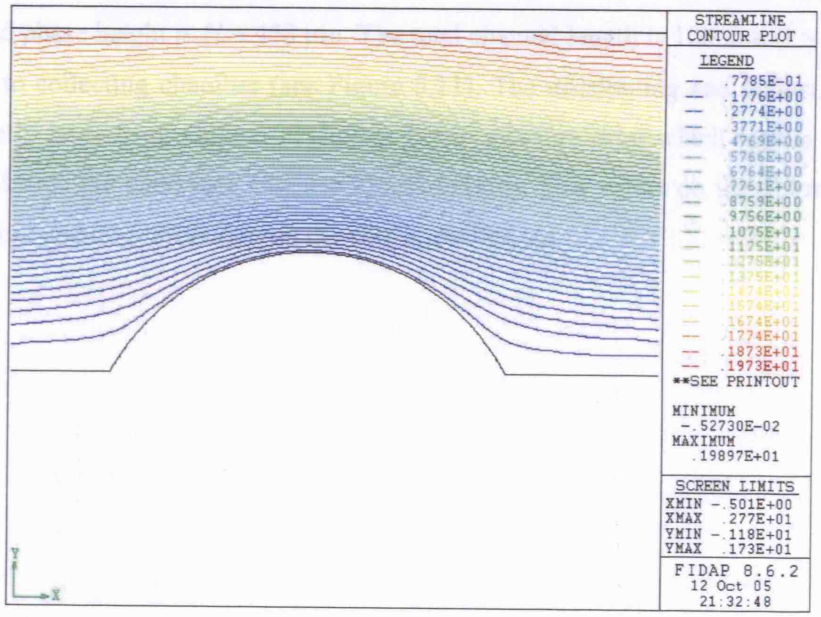

Figure 5.10. Streamlines in liquid phase for $H^{\#} = 2$, $Ca = 0.001$, $Re = 100$ ($We = 0.1$, $We >> Ca$) and $\Delta P^{\#}_{rel} = 85$ % ($\Delta P^{\#}_{rel,B,G,max} = 86.8$ %).

5.5. Experimental Work

The influence of flow conditions on the stability pressure range of the interfacial menisci formed in the openings of a porous mesh separating two phases is investigated experimentally in a water/air/acrylic system. This system was chosen as it is easy to handle and has a large surface tension that results in a significant Laplace pressure difference for a slit of half a millimetre. Experimental results for several (*Ca*, *Re*) pairs at a given system geometry (i.e. $H^{\#}$ = 2) are required in order to validate the numerical model presented (validity of assumptions and proper implementation). Different *Ca* and *Re* numbers can be obtained simply by modifying the water flowrate.

The wetting phase (*W*) is distilled water, whose properties are γ= 72.26 mN/m (measured by the plate method at 23 °C), ρ = 1000 kg/m^3, μ = 0.00095 Pa·s (Perry and Green, 1997). The non-wetting phase is pressurised zero grade air with ρ = 1.19 kg/m^3. The equilibrium contact angle of the system water/air on acrylic surface is θ = 75° (O'Brien and Ryge, 1965) although hysteresis is present with an advancing contact angle of $\theta_A \approx$ 90°-100° and a receding contact angle of θ_R = 30-40° (estimated via image analysis of moving drops).

Figure 5.11 shows the design of the 2D flow test unit where water and air are brought into contact via a slit that generates a two dimensional meniscus that can be compared with the results obtained from the model (see Figure 5.5). The liquid channel width is W = 16 mm and the machined phase height is H = 458 μm. The total channel length is 100 mm (l = 50 mm) from distributing to collecting chamber (see Figure 5.11). The distributing and collecting chambers are sufficiently large to produce a negligible liquid pressure drop which results in even flow distribution inside the plate (see Chapter 7) and uniform flow effect on the 2D meniscus. The slit width (pore opening) measured on the side is d = 466 μm.

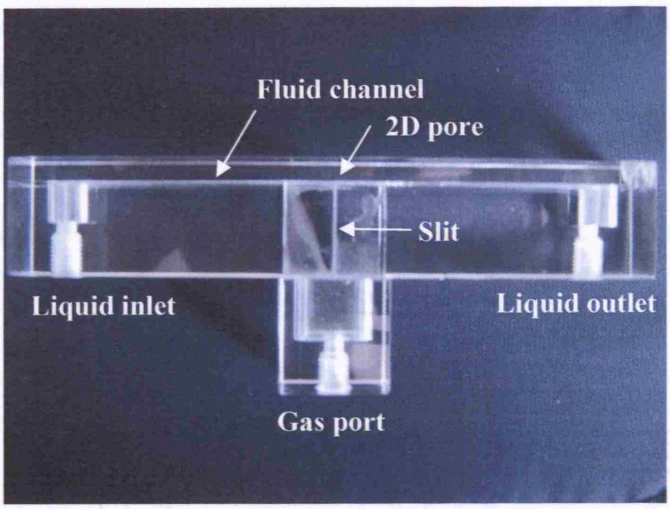

Top view

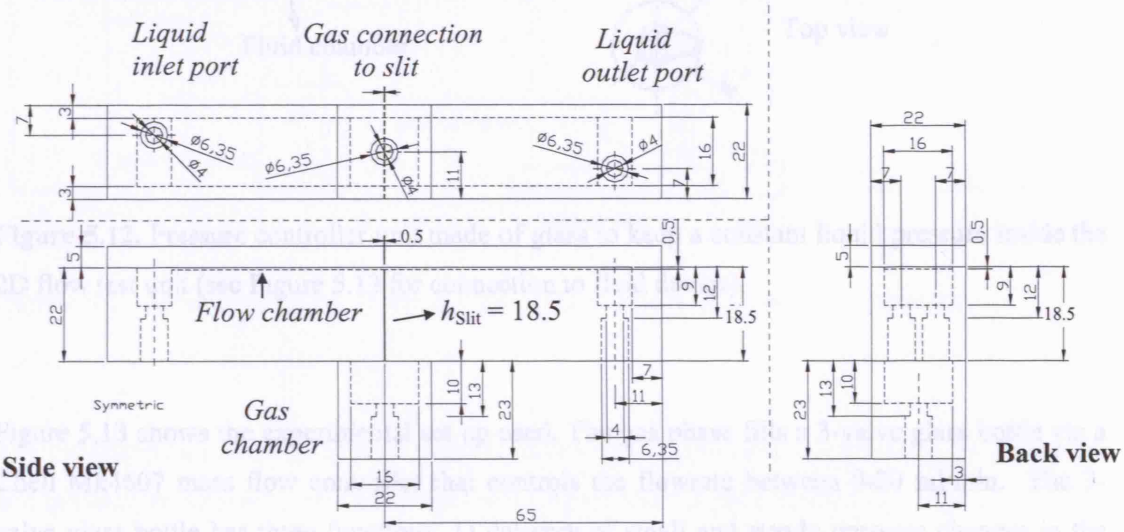

Figure 5.11. 2D flow test unit to analyse the influence of flow conditions on breakthrough pressure.

The glass device shown in Figure 5.12 is directly connected to the liquid outlet port of the 2D flow test unit (see Figure 5.11) and is designed to keep a constant hydrostatic liquid pressure at the slit, which corresponds to 98 mm of water (961.4 Pa) on the side of the liquid phase and 98-h_{Slit} = 80 mm of water (784.8 Pa) on the side of the gas phase. This is achieved by 1) keeping a constant liquid level and therefore a constant hydrostatic pressure term at the slit, 2) avoiding flexible connections such as flexible tubing, which is subject to vibrations that generate pressure fluctuations and 3) avoiding narrow passages for the liquid phase in its way from the collecting

chamber to the water beaker, which can encourage the trapping of air bubbles after air breakthrough that would give rise to large pressure variations at the slit.

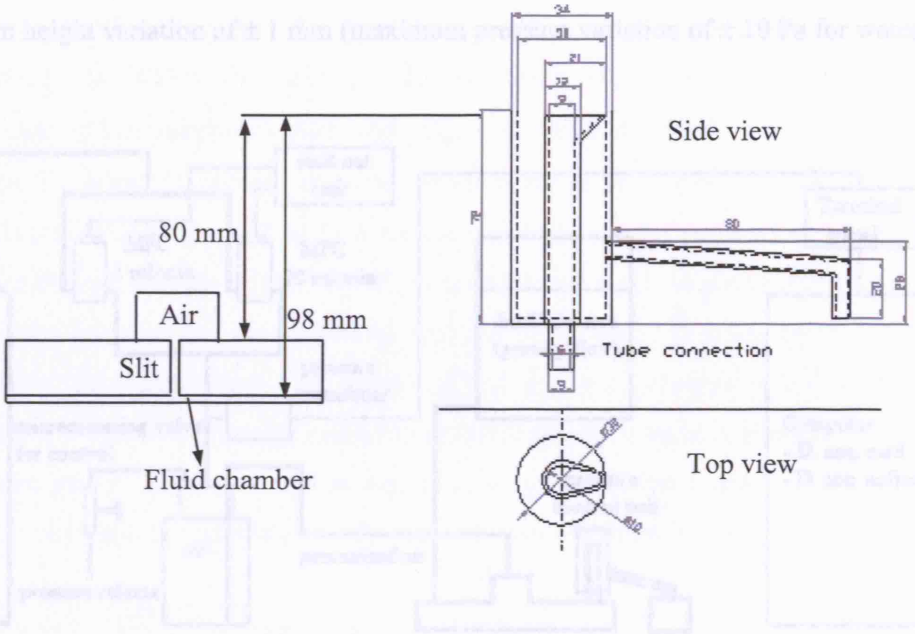

Figure 5.12. Pressure controller unit made of glass to keep a constant liquid pressure inside the 2D flow test unit (see Figure 5.13 for connection to fluid device).

Figure 5.13 shows the experimental set up used. The gas phase fills a 3-valve glass bottle via a Chell Mk4607 mass flow controller that controls the flowrate between 0-20 ml/min. The 3-valve glass bottle has three functions, 1) delivery of small and steady pressure changes in the gas phase, 2) attenuation of pressure fluctuations, and 3) air release via a micrometering valve connection that is used partially open in order to generate very low gas pressure increase in the test unit while it is also used to cause liquid breakthrough into the gas phase to calculate ΔP_{BL}. The air is supplied from the glass bottle into the gas chamber of the test unit via 1.6 mm i.d. tube connected through a port. A pressure transducer measures the air pressure inside the glass bottle (same as that inside the test unit) logging the data into a PC. The liquid phase is supplied to the test unit plate from a water container by means of gravity. The flowrate is controlled via a combination of liquid height above the test unit and valve aperture in the water container. In order to achieve water flowrates of up to 300 ml/min a large 6-mm i.d. tube connection is employed; as a result all pressure drop in the liquid phase is produced inside the acrylic test unit only. Gravity flow was chosen after carrying out experiments with different pumps that resulted in an anomalously large breakthrough pressure reduction as a function of liquid flowrate due to the pressure fluctuations generated by the pumps (of comparable magnitude to the Laplace

pressures in the slit). In contrast, using gravity flow at similar conditions, a much smaller breakthrough pressure reduction for the same flowrates was measured. In order to keep a constant flowrate for each run, a large cross-section water container is required (diameter of 25 cm). The water container volume was controlled within ± 50 ml in all cases, resulting in a maximum height variation of ± 1 mm (maximum pressure variation of ± 10 Pa for water).

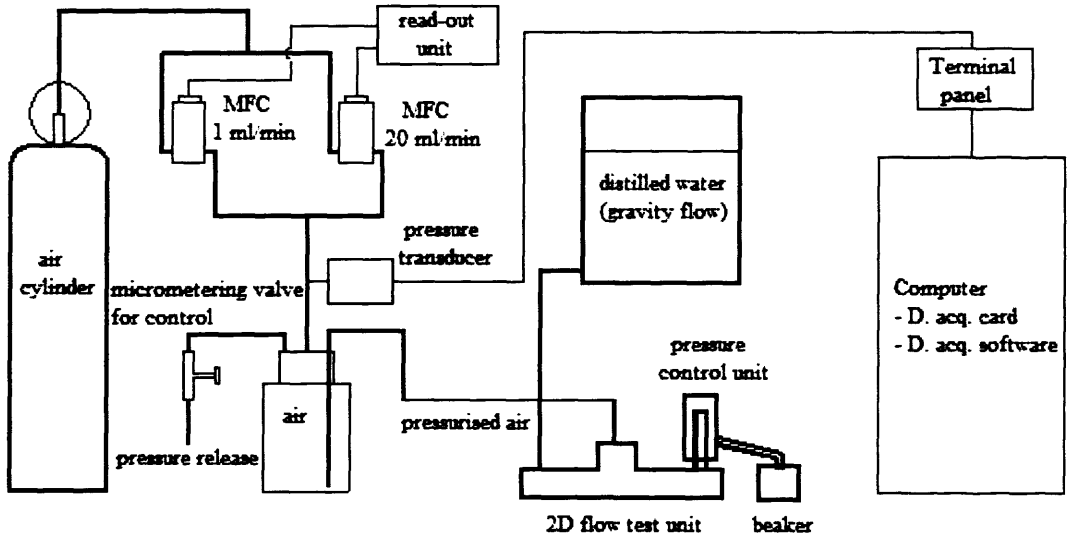

Figure 5.13. Experimental set up for analysis of flow effect on breakthrough pressure.

The reduction in gas breakthrough pressure difference due to flow is calculated by Eq. (5.58) and is based on measuring the gas pressure for liquid and for gas breakthrough, $P_{G,B,L}$ and $P_{G,B,G}$ respectively. The value of $\Delta P_{B,L}$ is assumed to be unaffected by flow conditions while $\Delta P_{B,G}^{Flow}$ is obtained from Eq. (5.19) where $h_{pore} = h_{slit}$.

$$RED = \frac{\Delta P_{B,G}^{Static} - \Delta P_{B,G}^{Flow}}{\Delta P_{B,G}^{Static}} 100 \qquad (5.58)$$

5.6. Results and Discussion

5.6.1. Theoretical Results

Simulations were carried out for values of $H^{\#}$ = 2, 4 and 10, Re_{stan} from 0 to 1000 (Re_{stan} = 0 corresponds to creeping flow without any inertial effects), Ca ranging from 0.001 to 0.5 and $P^{\#}_{G}$

changes from the value that produces a flat meniscus ($P_G^{\#} = (P^{\#}_L - \tau^{\#}_{nn})_{mean}$) to the value $P^{\#}_G$ that results in breakthrough under flow conditions in a system where any apparent contact angle θ_{App} is allowed and breakthrough happens by *maximum curvature*. Contact angles at the back and front of the meniscus are obtained at different values of $P^{\#}_G$ calculating $dy(x)/dx$ at both points where the contact line is pinned. Therefore these results apply to systems with any contact angle characteristics in which *breakthrough by maximum contortion* may occur instead of breakthrough by maximum curvature when $\theta_{App} = \theta_R + \phi_{min}$. It should be noted that under flow conditions the apparent contact angle at which a meniscus copes with the maximum gas pressure is not equal to $\theta_{App} = 0°$ and the meniscus curvature is not constant along the meniscus. All simulations are carried out for $l^{\#} = 5H^{\#}$. In principle the liquid pressure at $x^{\#} = 0$ is the liquid pressure drop between the channel outlet and the pore, which is given by Eq. (5.59) for a unidirectional 2D laminar flow. For instance, $P^{\#}_L(x^{\#} = 1) = 27$ when $H^{\#} = 2$, $l^{\#} = 5H^{\#} = 10$ and $P^{\#}_L(\text{outlet}) = 0$. However, the slip condition on the meniscus results in non-unidirectional flow with curved streamlines in that region that induce a cross-sectional pressure gradient (Massey 1998). The exact solution yields a slightly different pressure drop than that given by:

$$\Delta P_L^{\#} = 12\frac{l^{\#}}{H^{\#2}} \tag{5.59}$$

Table 5.1 shows the results for geometry $H^{\#} = 2$ ($l^{\#} = 5$) in which the meniscus can occupy a large portion of the channel cross section. In this case, the meniscus is greatly affected by both viscous and inertial forces, which are generated as the meniscus grows and the liquid phase velocity is increased due to the cross-section channel reduction. The maximum gas pressure $P^{\#}_{G,max}$ is obtained via an iterative process with an error of 0.5% for any *Ca* number. Eq. (5.60) defines the pressure difference under flow conditions relative to the gas breakthrough pressure of a meniscus of maximum curvature ($\theta_{App} = 0°$) in static conditions. The breakthrough pressure under flow conditions is obtained from Eq. (5.18). Thus, $\Delta P^{\#}_{rel,B,G,max} = \Delta P^{\#}_{B,G,max}/\Delta P^{\#}_{B,G,max}{}^{Static}$ indicates the gas breakthrough pressure under flow conditions when any apparent contact angle at the back and front of the meniscus is allowed (subscript max) relative to the maximum gas breakthrough pressure in static conditions (*breakthrough by maximum curvature*).

$$\Delta P_{rel}^{\#} = 100\frac{\Delta P^{\#}}{\Delta P_{B,G,max}^{\#Static}} \tag{5.60}$$

	$Re = 0$ ($Re_{stan} = 0$)				$Re = 10$ ($Re_{stan} = 20$)				$Re = 100$ ($Re_{stan} = 200$)		
Ca	0.001	0.01	0.1	0.25	0.001	0.01	0.02	0.1	0.001	0.01	0.02
$We = CaRe$	0	0	0	0	0.01	0.1	0.2	1	0.1	1	2
$\Delta P^{\#\ Static}_{B,G,max}$ $\theta_{App} = 0°$	1000	100	10	4	1000	100	50	10	1000	100	50
$P^{*\#}_{L,mean}$	25.67	25.67	25.67	25.67	28.01	28.01	28.01	28.01	33.01	33.01	33.01
$P^{\#}_{G,max}$	1035	148.5	40	30.55	1016.5	116.0	66.5	32.9	901	61.5	37.3
$\Delta P^{(1)}_{rel,BG,max}$ %	100.9	122.8	143.3	120.8	98.8	88.0	77.0	48.9	86.8	28.5	8.4
Dominant[2] Forces	STF	VF	VF	VF	STF	VF/IF	VF/IF	VF/IF	STF/IF	IF	IF

(1) Subscript max indicates that any θ_{App} is allowed during the gas breakthrough process.

(2) STF = Surface Tension Force (Ca << 1, We << 1, ≈ static stability), VF = Viscous forces (Ca (O(1)) >> We) and IF = Inertial Forces (We (O(1)) >> Ca).

Table 5.1. Gas breakthrough pressure results under flow conditions for $H^{\#} = 2$. Any apparent contact angle is allowed at the back and front of the meniscus. Dominant force is also shown.

Results for geometries $H^{\#} = 4$ ($l^{\#} = 20$) and $H^{\#} = 10$ ($l^{\#} = 50$) are shown in Table 5.2 and Table 5.3 respectively.

	$Re = 0.25$ ($Re_{stan} = 1$)			$Re = 25$ ($Re_{stan} = 100$)					$Re = 100$ ($Re_{stan} = 400$)		
Ca	0.001	0.01	0.1	0.001	0.01	0.02	0.05	0.1	0.001	0.01	0.02
$We = CaRe$	0.00025	0.0025	0.025	0.025	0.25	0.5	1.25	2.5	0.1	1	2
$\Delta P^{\#\ Static}_{B,G,max}$ $\theta_{App} = 0°$	1000	100	10	1000	100	50	20	10	1000	100	50
$P^{*\#}_{L,mean}$	14.12	14.12	14.12	16.02	16.02	16.02	16.02	16.02	17.41	17.41	17.41
$P^{\#}_{G,max}$	1015	114.5	24.25	1000.5	101.0	52.5	25.25	18.25	963	75.5	35.75
$\Delta P^{(1)}_{rel,B,G,max}$ %	100.1	100.4	101.3	98.4	85.0	73.0	46.1	22.3	94.6	58.1	36.7
Dominant[2] Forces	STF	STF/VF	VF[3]	STF	IF	IF	IF	IF	STF/ IF	IF	IF

(1) Subscript max indicates that any θ_{App} is allowed during the gas breakthrough process.

(2) STF = Surface Tension Force (Ca << 1, We << 1, ≈ static stability), VF = Viscous forces (Ca (O(1)) >> We) and IF = Inertial Forces (We (O(1)) >> Ca).

Table 5.2. Gas breakthrough pressure results under flow conditions for $H^{\#} = 4$. Any apparent contact angle is allowed at the back and front of the meniscus. Dominant force is also shown.

	$Re = 5$ ($Re_{stan} = 50$)			$Re = 10$ ($Re_{stan} = 100$)			$Re = 100$ ($Re_{stan} = 1000$)		
Ca	0.01	0.1	0.5	0.01	0.1	0.2	0.01	0.1	0.2
$We = CaRe$	0.05	0.5	2.5	0.1	1	2	1	10	20
$\Delta P^{\#\,Static}_{B,G,max}$ $\theta_{App} = 0°$	100	10	2	100	10	5	100	10	5
$P^{*\#}_{L,mean}$	6.11	6.11	6.11	6.26	6.26	6.26	6.95	6.95	6.95
$P^{\#}_{G,max}$	105.0	15.05	7.40	104	14.45	9.7	93.25	10.25	7.7
$\Delta P^{(1)}_{rel,B,G,max}$ %	98.9	89.4	64.5	97.7	81.9	68.9	86.3	33.0	15.0
Dominant Forces[(2)]	STF	VF	VF	STF	IF	IF	IF	IF	IF

(1) Subscript max indicates that any θ_{App} is allowed during the gas breakthrough process.

(2) STF = Surface Tension Force ($Ca \ll 1$, $We \ll 1$, ≈ static stability), VF = Viscous forces (Ca (O(1)) >> We) and IF = Inertial Forces (We (O(1)) >> Ca)

Table 5.3. Gas breakthrough pressure results under flow conditions for $H^{\#} = 10$. Any apparent contact angle is allowed at the back and front of the meniscus. Dominant force is also shown.

Figure 5.14 to Figure 5.16 summarise the results shown in Table 5.1 to Table 5.3 where maximum relative breakthrough pressure under flow conditions, $\Delta P^{\#}_{rel,B,G,max}$ defined in Eq. (5.60) is given as a function of Ca and Re.

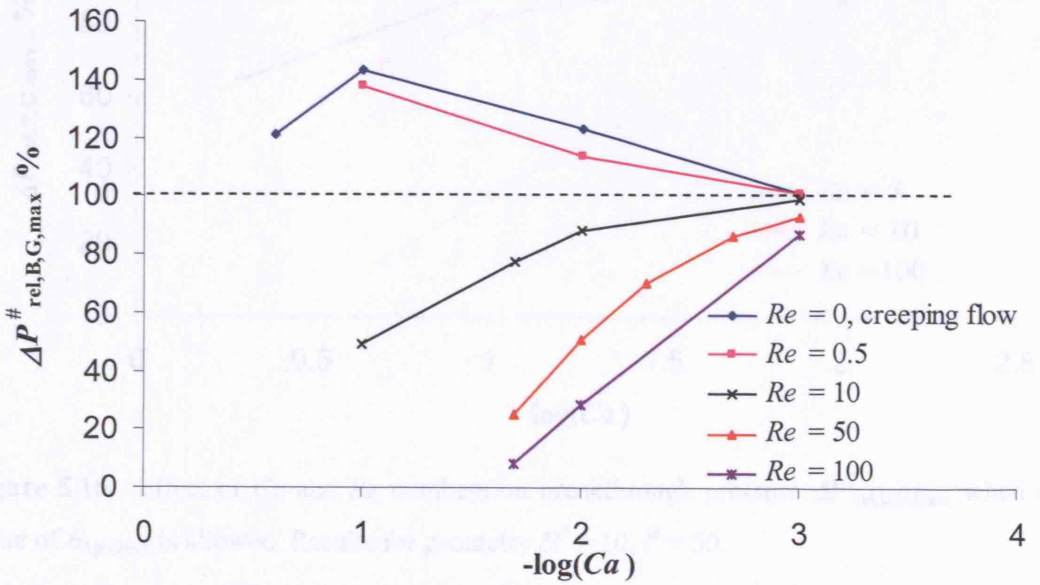

Figure 5.14. Effect of Ca and Re numbers on breakthrough pressure $\Delta P^{\#}_{rel,B,G,max}$ when any value of $\theta_{App,back}$ is allowed. Results for geometry $H^{\#} = 2$, $l^{\#} = 10$.

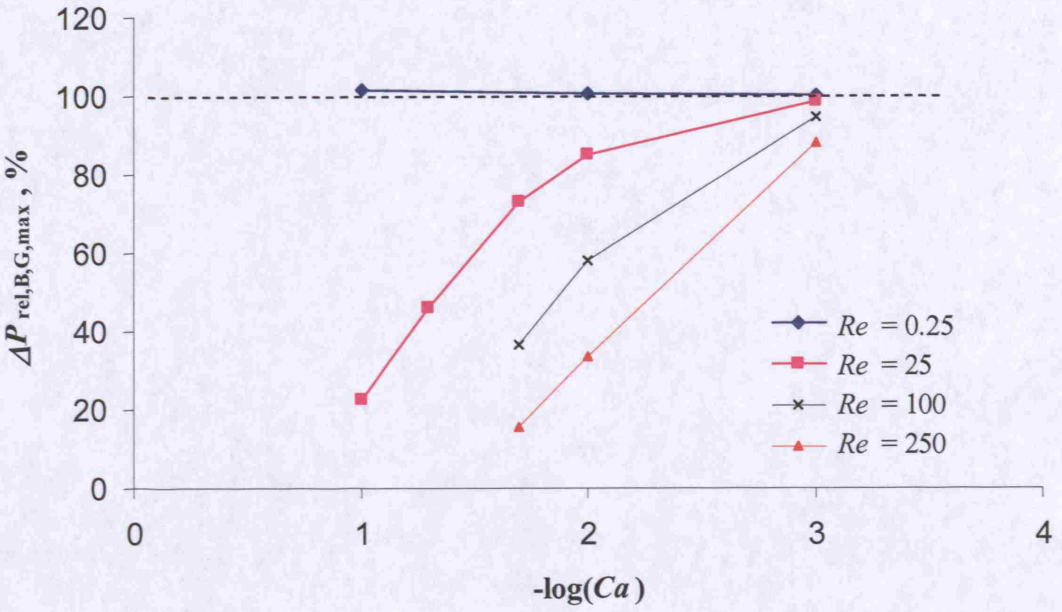

Figure 5.15. Effect of *Ca* and *Re* numbers on breakthrough pressure $\Delta P^{\#}_{rel,B,G,max}$, when any value of $\theta_{App,back}$ is allowed. Results for geometry $H^{\#} = 4$, $l^{\#} = 20$.

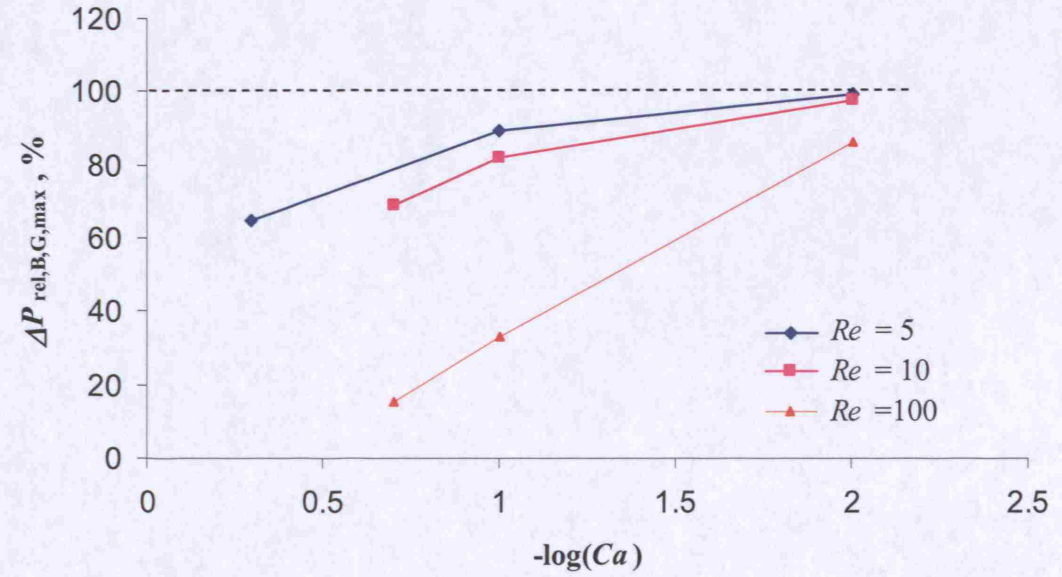

Figure 5.16. Effect of *Ca* and *Re* numbers on breakthrough pressure $\Delta P^{\#}_{rel,B,G,max}$, when any value of $\theta_{App,back}$ is allowed. Results for geometry $H^{\#} = 10$, $l^{\#} = 50$.

Three forces define the shape and breakthrough pressure of the meniscus under flow conditions: surface tension forces (STF) at low *Ca* and *We*, viscous forces (VF) at high *Ca* and inertial

forces (IF) at high *We*. STF tend to preserve the meniscus shape as a circular arc, while VF in the form of normal viscous stresses tend to push the meniscus back into the pore and IF tend to extract the meniscus out of the pore as it grows via pressure reduction in the liquid above it (Venturi effect). The effect of flow conditions on meniscus shape is governed by *Ca* at high viscous forces (*Re* << 1) and by *We* = *CaRe* when inertial forces become larger than viscous ones (*Re* >> 1) (FIDAP, 2002). A high *Re* does not necessarily imply a substantial effect on meniscus shape and breakthrough pressure if *We* is small. The results from geometry $H^{\#} = 2$ presented in Figure 5.14 show these features. In particular, the breakthrough pressure increases in relation to static conditions at low *Re* when *Ca* is high (low *We*), similar results to static conditions are observed at low *Ca* and the breakthrough pressure decreases substantially for high *Ca* and *Re*, i.e. high *We*. These results are important for Taylor bubble formation from side junctions (typically $H^{\#} = 2$) into the main flow channel as the required pressure fluctuation to form one bubble becomes largest at low *We* and high *Ca* (low flowrates), yielding flow distribution problems in scale-out manifolds for Taylor flow (see Chapter 9). As $H^{\#}$ increases, the effect of velocity over the meniscus decreases since a parabolic profile results in low velocities in the vicinity of the wall.

Therefore, since *Ca* and *We* determine the effect of viscous and inertial forces on meniscus shape and breakthrough pressure, most results shown in Figure 5.14-Figure 5.16 where *We* >> *Ca* (apart from *Re* = 0 and *Re* = 0.5 in geometries $H^{\#} = 2$) are mainly a function of *We*. The values of $\Delta P_{rel,B,G,max}$ are therefore plotted as a function of *We* in Figure 5.17 for the three different geometries considered. It can also be seen from this figure that the inertial force effect on breakthrough pressure reduction decreases as $H^{\#}$ increases. The present micromesh reactor has a geometry with $H^{\#}$ = 20-40 for which inertial effects will be negligible until *We* becomes larger than 1. Furthermore, *We* = *CaRe*, where *Re* is defined with the pore radius *r* so that the required value of $Re_{stan} = H^{\#}Re$ for *We* > 1 will generally be too large (for *We* = 1, $H^{\#}$ = 30 and *Ca* = 0.02, *Re* = 50 and Re_{stan} = 1500, which is too high for flow in microstructures).

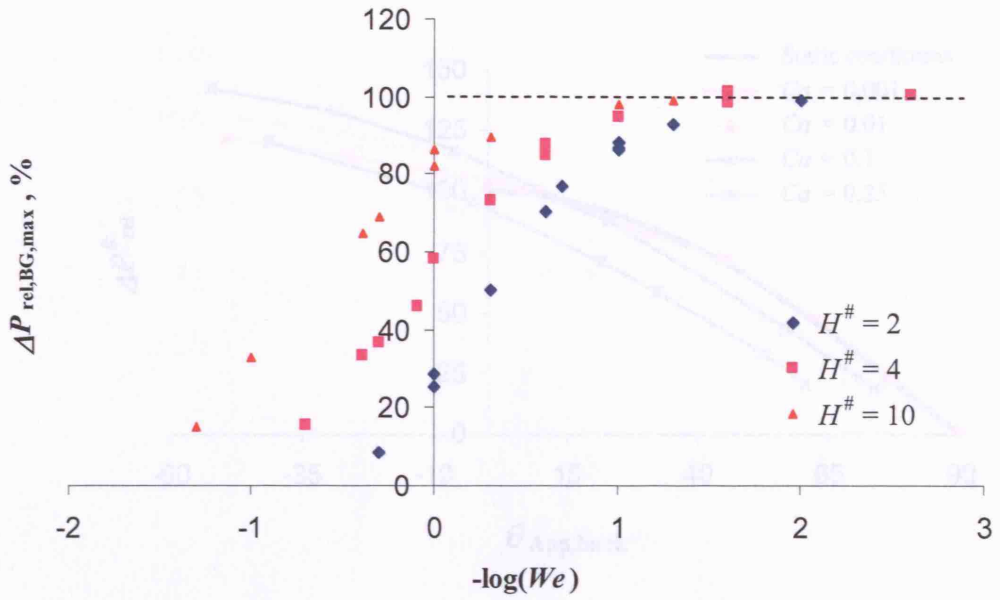

Figure 5.17. Relative meniscus breakthrough pressure $\Delta P^{\#}_{rel,B,G,max}$ as a function of *We* and $H^{\#}$ for those cases when *We* >> *Ca* (or *Re* >>1).

In geometry $H^{\#}$ = 2, the condition defined by *Ca* = 0.1 and *Re* = 10 has the same *We* as the condition defined by *Ca* = 0.01 and *Re* = 100, *We* = 1, although the breakthrough pressure reduction is larger in the latter case with the smaller *Ca*. In the other two geometries this effect of *Ca* for a fixed *We* is opposite, i.e. breakthrough pressure reduction is higher at higher *Re* because viscous forces do not become important within the range of *Ca* analysed (the upper value of *Ca* is limited when the liquid pressure drop along the meniscus becomes comparable to the breakthrough pressure in static conditions at which point the meniscus is highly asymmetrically deformed).

The results above refer to the case of gas breakthrough when any θ_{App} is allowed and can be directly applied to those systems where breakthrough happens at an angle $\theta_{App} > \theta_R + \phi_{min}$ (wetting liquids generally). However, the breakthrough of the gas phase can occur earlier if the apparent contact angle at the back of the meniscus reaches the value $\theta_{App} = \theta_R + \phi_{min}$ (*breakthrough by maximum contortion*). Figure 5.18 to Figure 5.28 show the relative meniscus pressure difference $\Delta P^{\#}_{rel}$ (see Eq. (5.60)) as a function of the apparent contact angle at the back of the meniscus $\theta_{App,back}$ for different *Ca*, *Re* and $H^{\#}$. These results can be applied to calculate the breakthrough pressure by maximum contortion ($\theta_{App,back} = \theta_R + \phi_{min}$). The range of $\theta_{App,back}$ in Figure 5.18-Figure 5.28 is different at different *Ca*, which determines meniscus deformation.

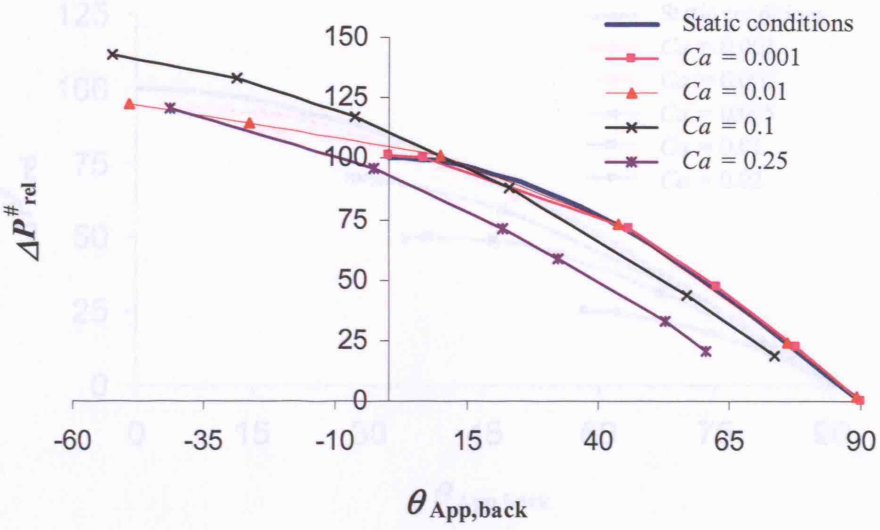

Figure 5.18. Meniscus relative pressure difference $\Delta P^{\#}_{rel}$ as a function of apparent contact angle at the back of the meniscus $\theta_{App,back}$ and Ca. $Re = 0$ ($Re_{stan} = 0$), $H^{\#} = 2$.

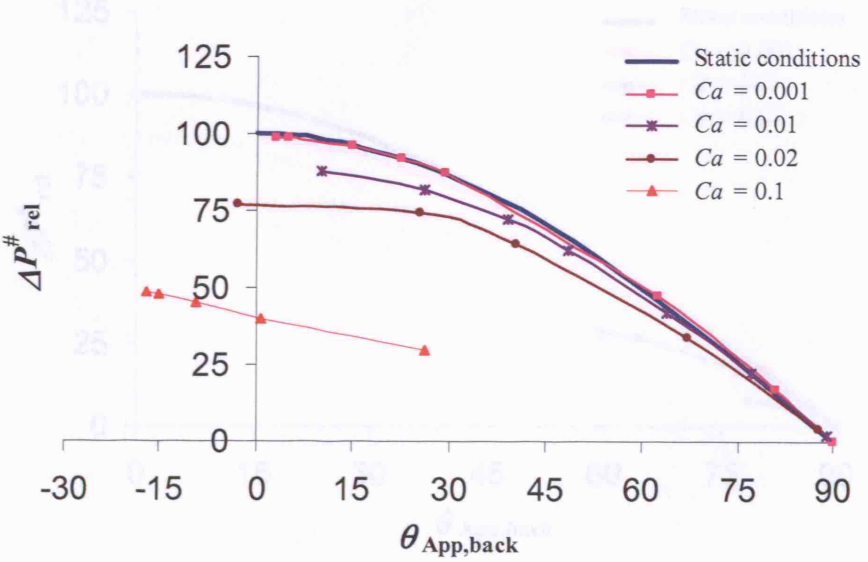

Figure 5.19. Meniscus relative pressure difference $\Delta P^{\#}_{rel}$ as a function of apparent contact angle at the back of the meniscus $\theta_{App,back}$ and Ca. $Re = 10$ ($Re_{stan} = 20$), $H^{\#} = 2$.

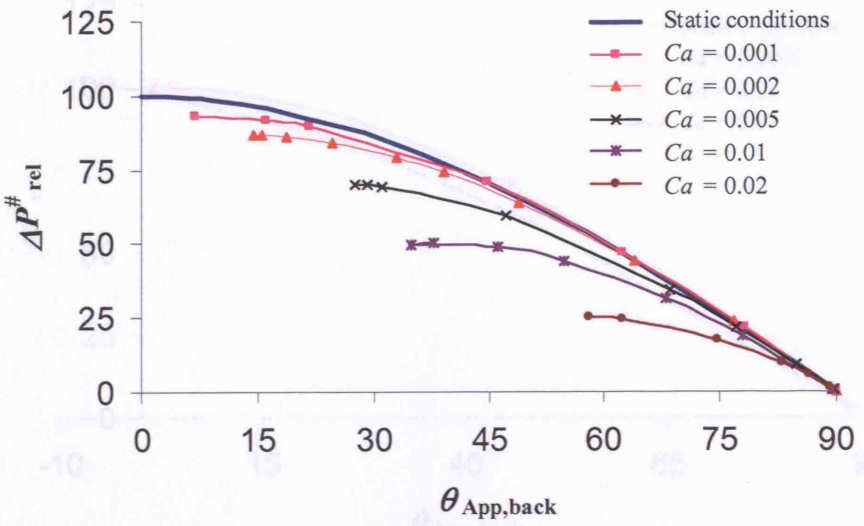

Figure 5.20. Meniscus relative pressure difference $\Delta P^{\#}_{rel}$ as a function of apparent contact angle at the back of the meniscus $\theta_{App,back}$ and Ca. Re = 50 (Re_{stan} = 100), $H^{\#}$ = 2.

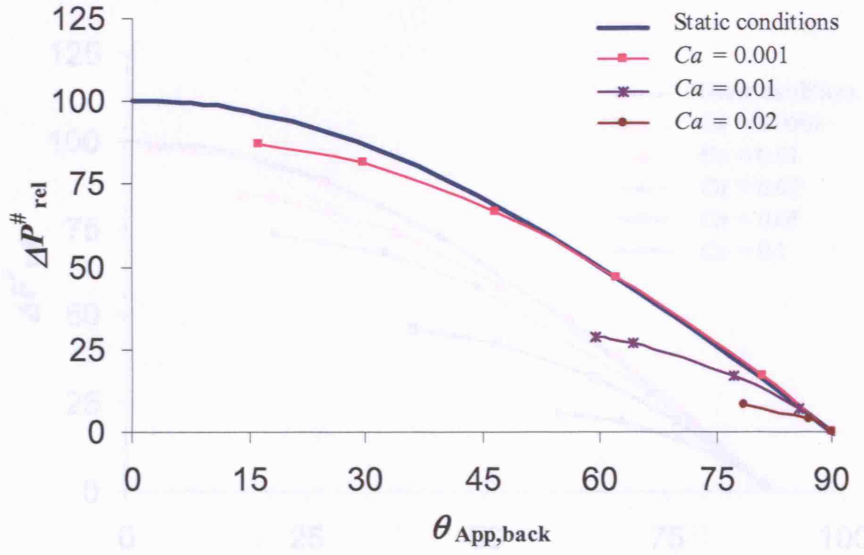

Figure 5.21. Meniscus relative pressure difference $\Delta P^{\#}_{rel}$ as a function of apparent contact angle at the back of the meniscus $\theta_{App,back}$ and Ca. Re = 100 (Re_{stan} = 200), $H^{\#}$ = 2.

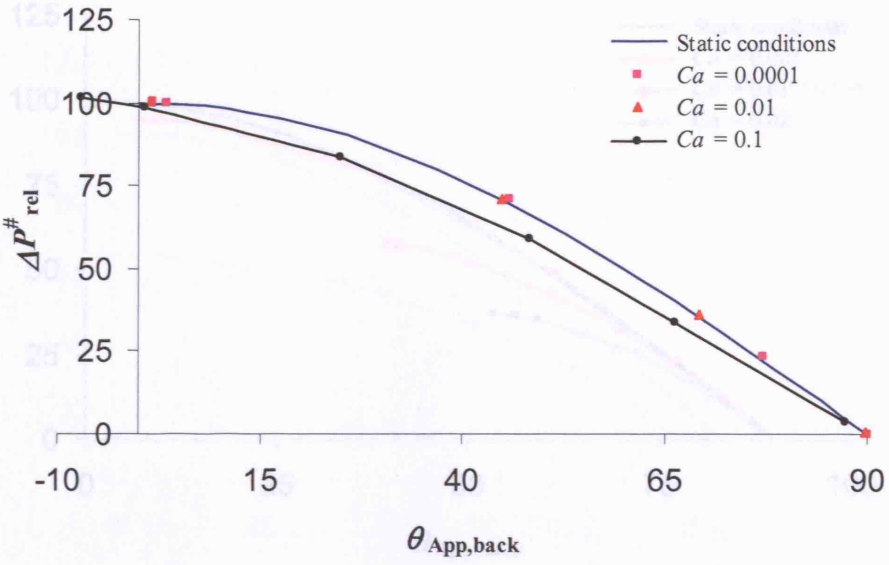

Figure 5.22. Meniscus relative pressure difference $\Delta P^{\#}_{rel}$ as a function of apparent contact angle at the back of the meniscus $\theta_{App,back}$ and Ca. $Re = 0.25$ ($Re_{stan} = 1$), $H^{\#} = 4$.

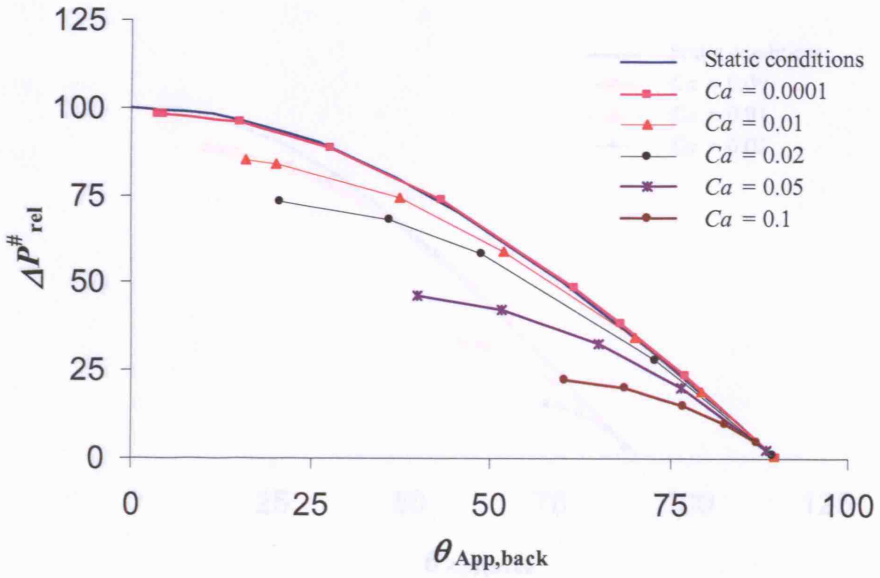

Figure 5.23. Meniscus relative pressure difference $\Delta P^{\#}_{rel}$ as a function of apparent contact angle at the back of the meniscus $\theta_{App,back}$ and Ca. $Re = 25$ ($Re_{stan} = 100$), $H^{\#} = 4$.

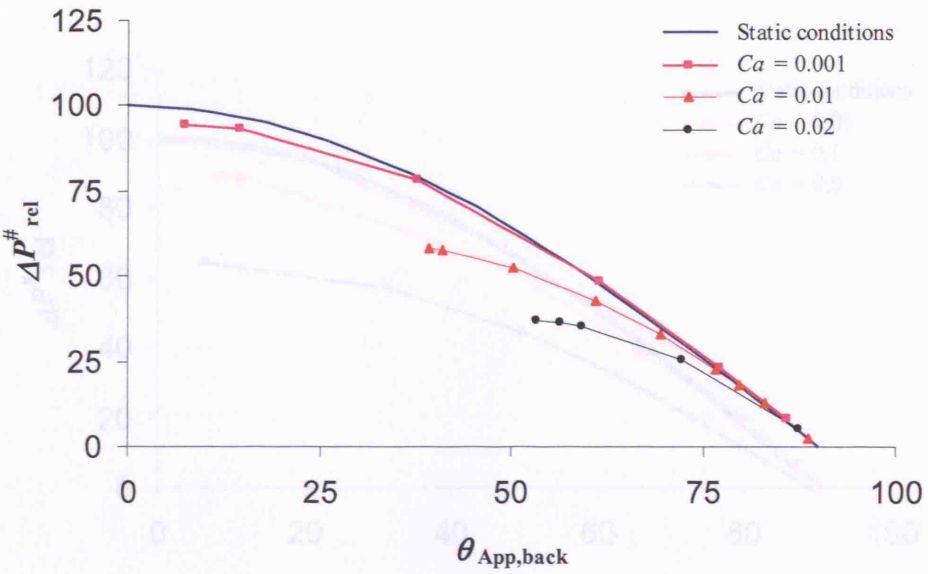

Figure 5.24. Meniscus relative pressure difference $\Delta P^{\#}_{rel}$ as a function of apparent contact angle at the back of the meniscus $\theta_{App,back}$ and Ca. Re = 100 (Re_{stan} = 400), $H^{\#}$ = 4.

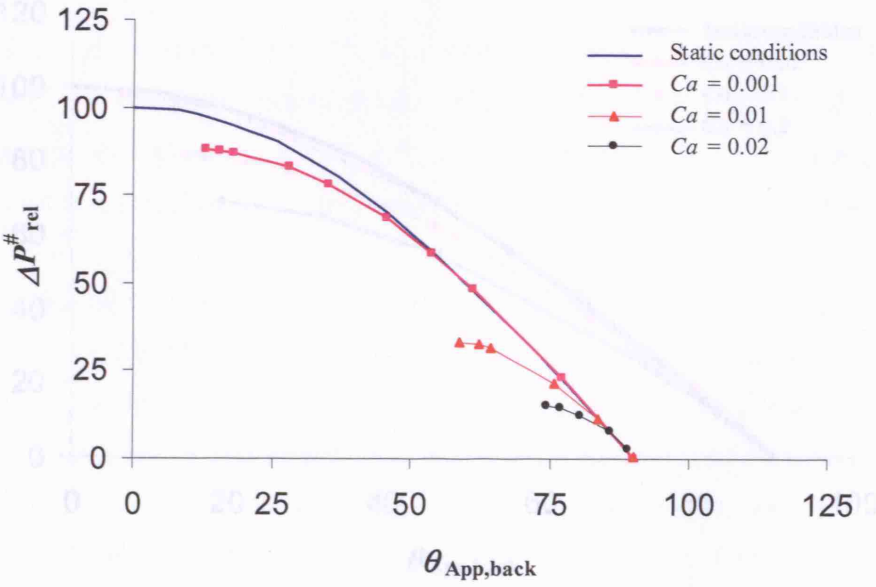

Figure 5.25. Meniscus relative pressure difference $\Delta P^{\#}_{rel}$ as a function of apparent contact angle at the back of the meniscus $\theta_{App,back}$ and Ca. Re = 250 (Re_{stan} = 1000), $H^{\#}$ = 4.

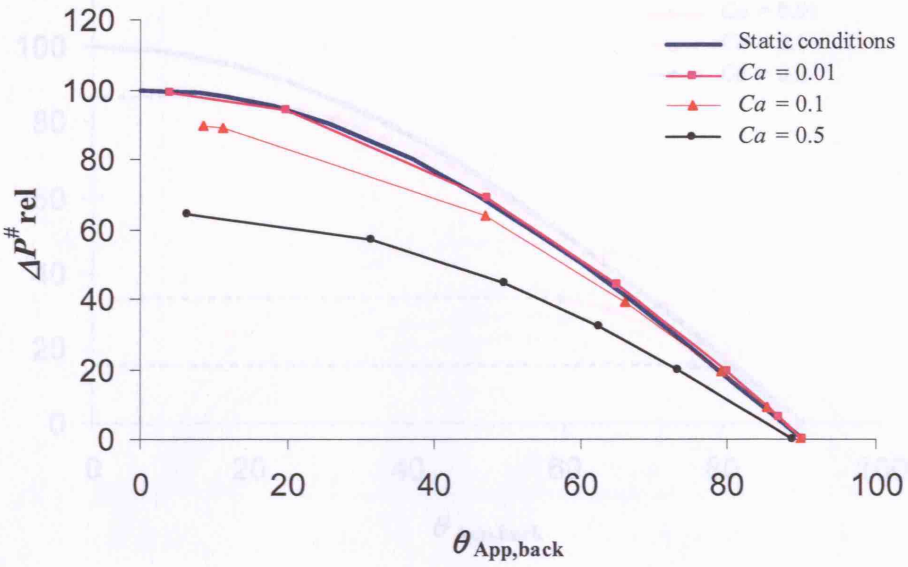

Figure 5.26. Meniscus relative pressure difference $\Delta P^{\#}_{rel}$ as a function of apparent contact angle at the back of the meniscus $\theta_{App,back}$ and Ca. $Re = 5$ ($Re_{stan} = 50$), $H^{\#} = 10$.

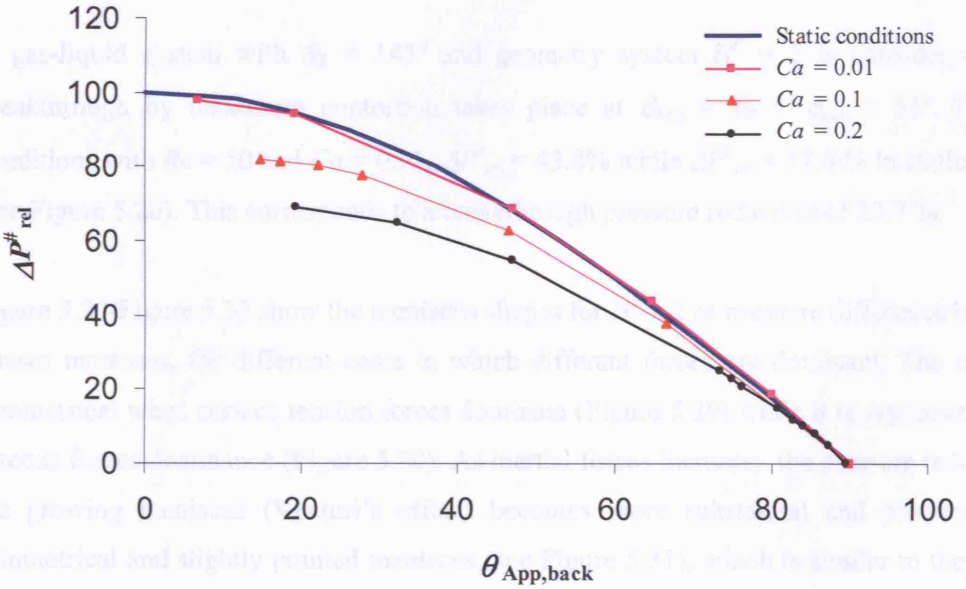

Figure 5.27. Meniscus relative pressure difference $\Delta P^{\#}_{rel}$ as a function of apparent contact angle at the back of the meniscus $\theta_{App,back}$ and Ca. $Re = 10$ ($Re_{stan} = 100$), $H^{\#} = 10$.

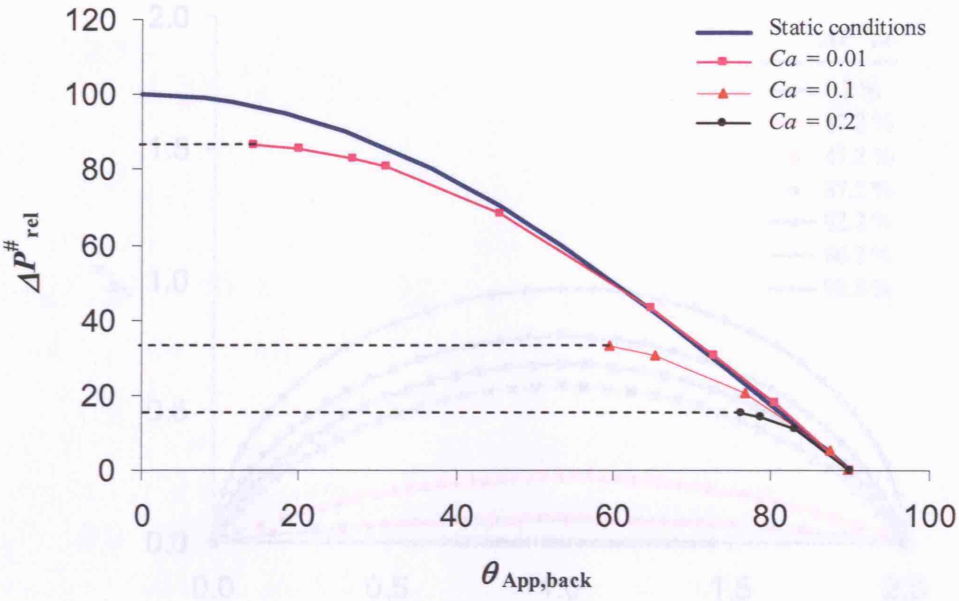

Figure 5.28. Meniscus relative pressure difference $\Delta P^{\#}_{rel}$ as a function of apparent contact angle at the back of the meniscus $\theta_{App,back}$ and Ca. Re = 100 (Re_{stan} = 1000), $H^{\#}$ = 10.

Calculation of breakthrough pressure for breakthrough by maximum contortion

A gas-liquid system with θ_R = 145° and geometry system $H^{\#}$ = 2 is considered. The gas breakthrough by maximum contortion takes place at θ_{App} = θ_R + ϕ_{min} = 55°. Under flow conditions with Re = 50 and Ca = 0.01, $\Delta P^{\#}_{rel}$ = 43.8% while $\Delta P^{\#}_{rel}$ = 57.4 % in static conditions (see Figure 5.20). This corresponds to a breakthrough pressure reduction of 23.7 %.

Figure 5.29-Figure 5.32 show the meniscus shapes for $H^{\#}$ = 2 as pressure difference between the phases increases, for different cases in which different forces are dominant. The meniscus is symmetrical when surface tension forces dominate (Figure 5.29) while it is asymmetrical under viscous forces dominance (Figure 5.30). As inertial forces increase, the pressure reduction over the growing meniscus (Venturi's effect) becomes more substantial and produces a more symmetrical and slightly pointed meniscus (see Figure 5.31), which is similar to the sinusoidal waves assumed in two-phase pipe flow to model droplet entrainment (Holowach et al. 2002).

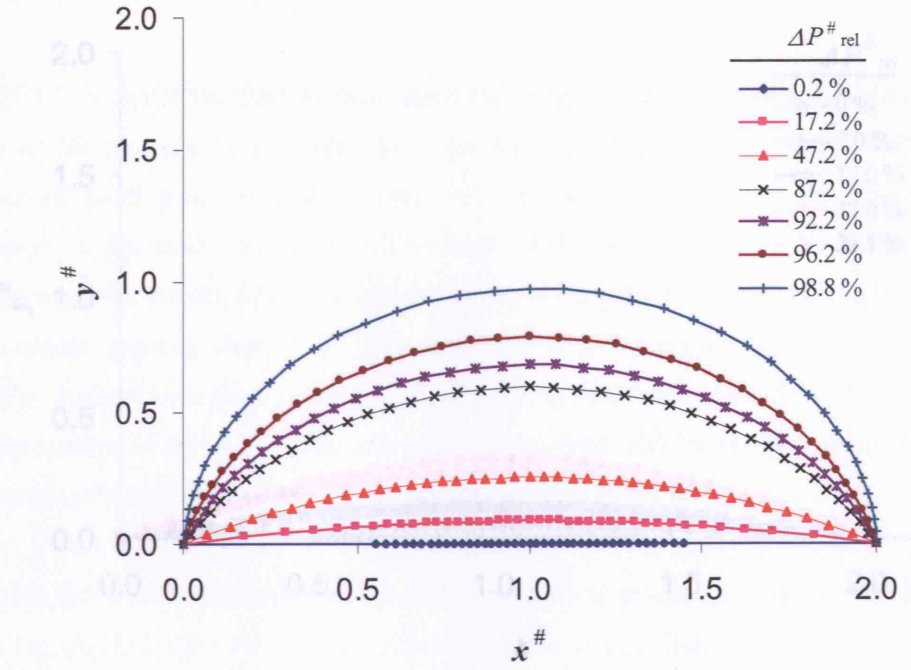

Figure 5.29. Meniscus shapes under STF dominance. Re = 10 (Re_{stan} = 20), Ca = 0.001 (We = 0.01), $H^{\#}$ = 2.

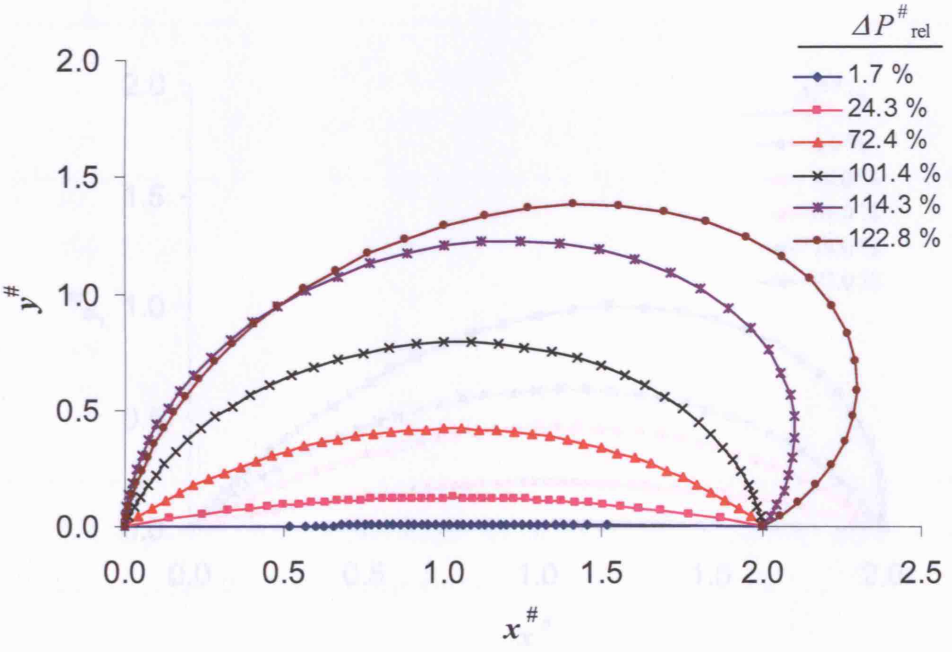

Figure 5.30. Meniscus shapes under VF dominance. Re = 0 (Re_{stan} = 0), Ca = 0.01 (We = 0), $H^{\#}$ = 2.

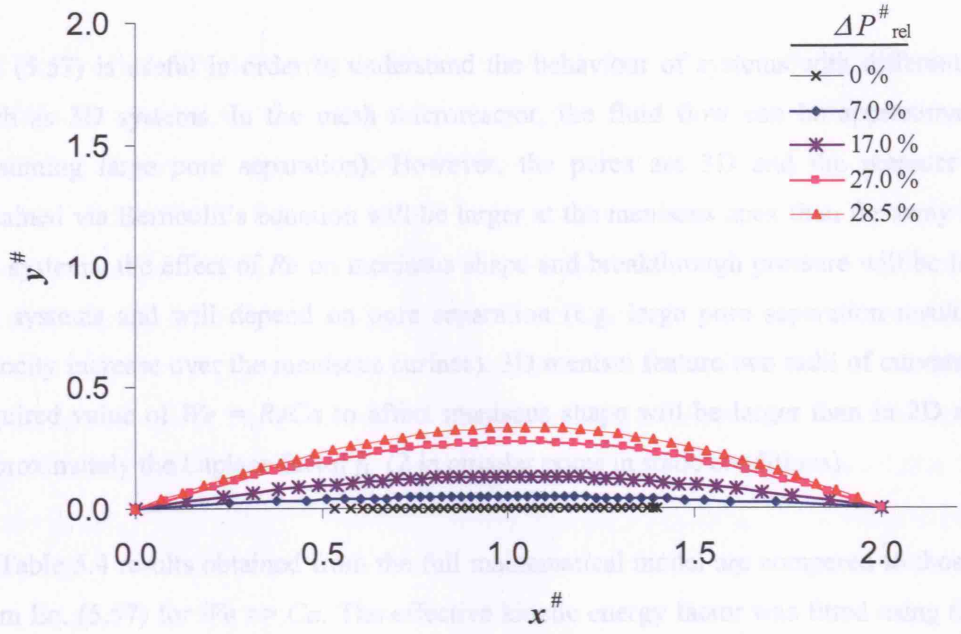

Figure 5.31. Meniscus shapes under IF dominance. $Re = 100$ ($Re_{stan} = 200$), $Ca = 0.01$ ($We = 1$), $H^{\#} = 2$.

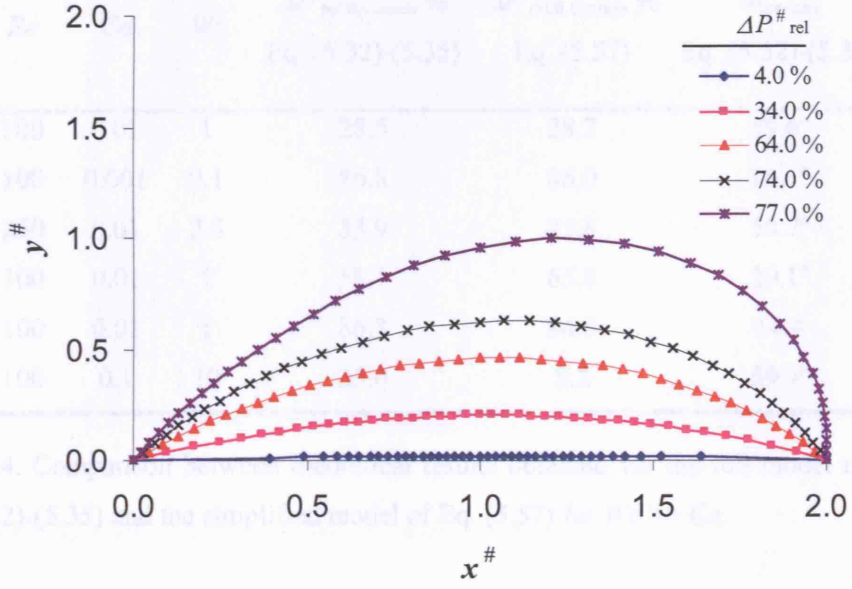

Figure 5.32. Meniscus shapes under IF/VF dominance. $Re = 10$ ($Re_{stan} = 20$), $Ca = 0.02$ ($We = 0.2$), $H^{\#} = 2$.

5.6.2. Results - Simplified Model

Eq. (5.57) is useful in order to understand the behaviour of systems with different geometry such as 3D systems. In the mesh microreactor, the fluid flow can be approximated to 2D (assuming large pore separation). However, the pores are 3D and the pressure reduction obtained via Bernoulli's equation will be larger at the meniscus apex than far away from it. In 3D systems, the effect of *Re* on meniscus shape and breakthrough pressure will be less than in 2D systems and will depend on pore separation (e.g. large pore separation results in small velocity increase over the meniscus surface). 3D menisci feature two radii of curvature and the required value of $We = ReCa$ to affect meniscus shape will be larger than in 2D systems by approximately the Laplace factor f_L (2 in circular pores in static conditions).

In Table 5.4 results obtained from the full mathematical model are compared to those obtained from Eq. (5.57) for $We >> Ca$. The effective kinetic energy factor was fitted using the data for $H^{\#} = 2$, to obtain $f_{KE,eff} = 1.86$. The breakthrough pressure values are the maximum pressure difference at which a meniscus solution (Eq. (5.57)) passing by $(y,x) = (0,0)$ exists. The deviation between the two models increases as $H^{\#}$ increases indicating that the effective kinetic energy factor $f_{KE,eff}$ changes.

$H^{\#}$	*Re*	*Ca*	*We*	$\Delta P^{\#}_{rel,B,G,max}$, % Eq. (5.32)-(5.35)	$\Delta P^{\#}_{rel,B,G,max}$, % Eq. (5.57)	$\theta_{App,max}$ Eq. (5.32)-(5.35)	$\theta_{App,max}$ Eq. (5.57)
2	100	0.01	1	28.5	28.7	59.6°	53.1°
2	100	0.001	0.1	86.8	86.0	16.1°	15°
4	250	0.01	2.5	33.9	25.8	58.7°	51.7°
4	100	0.01	1	58.1	65.8	39.1°	26.3°
10	100	0.01	1	86.3	84.6	14.4	11.3
10	100	0.1	10	33.0	8.2	59.4°	64.8°

Table 5.4. Comparison between theoretical results obtained via the full model represented by Eqs. (5.32)-(5.35) and the simplified model of Eq. (5.57) for $We >> Ca$.

5.6.3. Experimental Results

Bubbles trapped within the plate, which are generally difficult to flush out using gravity flow, can affect pressure at the slit due to additional pressure losses. Because of this, the breakthrough of the liquid phase is analysed previous to the breakthrough of the gas phase. Assuming a constant width at both sides of the slit and considering that $\theta_A = 90°$, static breakthrough pressures would be $\Delta P_{B,G}^{Static} = \gamma\cos(0°)/r = -\gamma\cos(\theta_A+90°)/r = -\Delta P_{B,L}^{Static}$. Experimental results are shown in Table 5.5, with *Re* ranging from 0 to 177 and *Ca* ranging from 0.0013 to 0.01. The absolute values of $P_{G,B,G}$ and $P_{G,B,L}$ allow estimation of many parameters. In static conditions, the liquid pressure at the slit prior to the liquid breakthrough corresponds to 80 mm of water, $P_{L,B,L}$ = 785 Pa (see Figure 5.12), while the gas pressure is $P_{G,B,L}$ = 509 pa (see Table 5.5), which results in $\Delta P_{B,L}^{Static} = \Delta P_{B,L}^{Flow}$ = 276 Pa. Applying Eq. (5.19), $\Delta P_{B,G}^{Static}$ is found to be $\Delta P_{B,G}^{Static}$ = 286 Pa.

$\Delta P_{B,G}^{Static}$ = 286 Pa and $\Delta P_{B,L}^{Static}$ = 276 Pa are slightly smaller than the value expected for a measured average radius of r = 233 μm ($\Delta P_{B,G}^{Static} = \Delta P_{B,L}^{Static}$ = 310.1 Pa). This could be due to irregularities in the geometry of the test unit and particularly the slit. As can be seen in Figure 5.33 the corners of the slit are not uniform and symmetrical along the length.

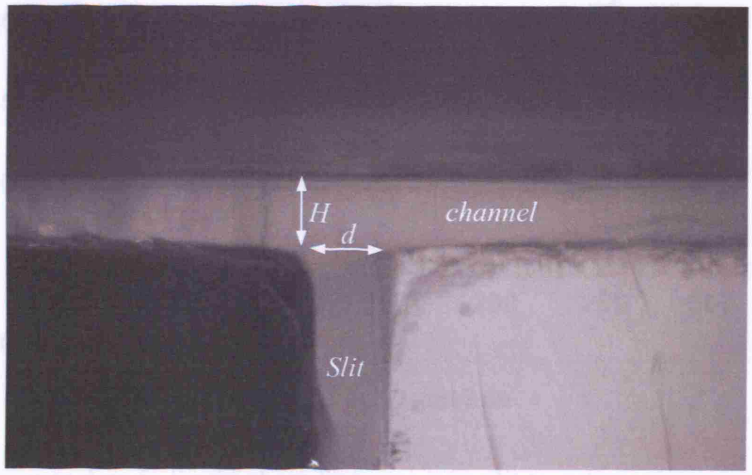

Figure 5.33. Side view of channel and slit in the 2D flow test unit.

Figure 5.34 shows the pressure drop of the liquid phase due to flow between the slit and the liquid outlet and is obtained from the values of gas pressure for liquid breakthrough, $P_{G,B,L}$, that are shown in Table 5.5 and provides another estimation of the channel height (measured as H =

458 μm). For flow between parallel plates, frictional pressure drop varies linearly with velocity ($\Delta P^{\#} = 12l^{\#}/H^{\#2}$). However, the slope of the experimentally measured liquid pressure drop against flowrate increases from $d\Delta P/dQ$ = 9 Pa/(ml/min) at low flowrate to $d\Delta P/dQ$ = 19.7 Pa/(ml/min) at high flowrate as shown in Figure 5.34. This is probably a result of the increase of additional pressure losses due to bends, trapped bubbles and port connections as liquid flowrate (velocity) increases. Error bars are negligible (± 18 Pa) although additional errors due to trapped bubbles are not captured in the results. Considering exclusively frictional pressure losses inside the plate, an average value of H can be estimated from Eq. (5.59) as shown by Eq. (5.61). This results in H = 404 μm for $\Delta P/Q$ = 9 Pa/(ml/min) that corresponds to $Q \rightarrow 0$ (no additional pressure losses). The value of H = 404 μm is lower than H = 458 μm although the slope of the first experimental points in Figure 5.34 is slightly lower than 9 Pa/(ml/min):

$$H = \left(\frac{12l\mu}{w\Delta P / Q} \right)^{1/3} \tag{5.61}$$

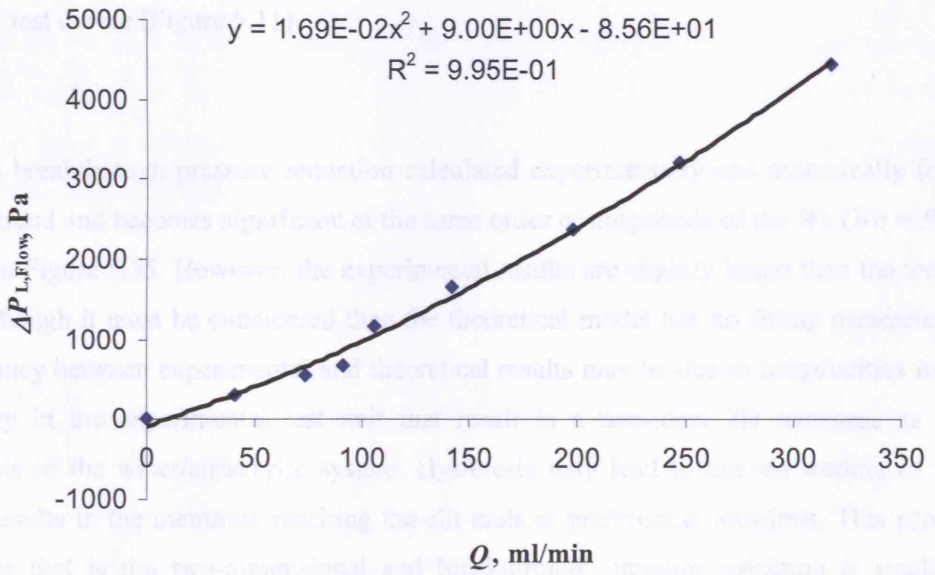

Figure 5.34. Pressure drop in liquid phase from gas inlet slit to outlet.

The experimental values of gas breakthrough pressure reduction given in Table 5.5 are obtained from Eq. (5.58), where $\Delta P_{B,G}^{Flow}$ is calculated by Eq. (5.19). For example, when Re = 58.4, $\Delta P_{B,G}^{Flow}$ = 696 Pa – 276 Pa - $\rho_L g h_{Slit}$ = 243 Pa (see Eq. (5.19)) and according to Eq. (5.58), RED_{Exp} = 15.0 %.

The breakthrough pressure reduction is calculated differently for the numerical results. According to Eq. (5.45) $\Delta P^{\#}_{B,G}{}^{Static} = \cos 0°/Ca = 1/Ca$ while $\Delta P_{B,G}{}^{\#Flow} = (P_{G,B,G}{}^{\#} - P_L{}^{\#*})$ with $P_L{}^{\#*} \approx 27$ in all cases (calculated via Eq. (5.59)) and $P_{G,B,G}{}^{\#}$ calculated via FIDAP 8.6 as the maximum gas pressure where the meniscus is stable. Thus, for $Re = 58.4$, $\Delta P^{\#}_{B,G}{}^{Static} = 1/Ca = 303.3$, $\Delta P_{B,G}{}^{\#Flow} = 262.5$ and $RED_{Model} = 22.35$ % versus 15.26 % measured experimentally.

				EXPERIMENTAL				NUMERICAL	
Q, ml/min	Re	$1/Ca$	We	$P_{G,B,G}$	$P_{G,B,L}$	$P_{G,B,G} - P_{G,B,L}$ Pa	RED_{Exp} %	$P_{G,B,G}{}^{\#}$	RED_{Model} %
0.0	0.0	∞	0.000	1248	509	739	0.0	∞	0.0
40.7	22.7	780.6	0.029	1531	801	730	3.0	777.0	3.9
73.4	41.0	432.6	0.095	1771	1067	704	12.0	406.0	12.4
90.3	50.4	351.9	0.143	1892	1170	721	6.0		
104.8	58.4	303.3	0.193	2364	1668	696	15.0	262.5	22.3
141.3	78.8	224.9	0.350	2828	2166	661	27.0	172.5	35.3
198.6	110.8	160.0	0.692	3480	2871	610	45.0	100.5	54.1
247.8	138.2	128.2	1.078	4279	3712	567	60.1	69.2	67.1
317.5	177.1	100.1	1.770	5499	4949	550	66.1	48.5	78.5

Table 5.5. Experimental results on breakthrough pressure reduction under flow conditions in the flow test device (Figure 5.11).

The gas breakthrough pressure reduction calculated experimentally and numerically follows a similar trend and becomes significant at the same order of magnitude of the We ($We = ReCa$) as shown in Figure 5.35. However, the experimental results are slightly larger than the theoretical ones although it must be considered than the theoretical model has no fitting parameters. This discrepancy between experimental and theoretical results may be due to irregularities in the slit geometry in the experimental test unit that result in a non-ideal 2D meniscus as well as hysteresis of the water/air/acrylic system. Hysteresis may lead to uneven wetting of the slit, which results in the meniscus reaching the slit ends at preferential locations. This produces a meniscus that is not two-dimensional and breakthrough pressure reduction is smaller than expected (Laplace factor increases as meniscus becomes more three-dimensional). Error bars are obtained considering the maximum/minimum pressure transducer readings for three repetition runs and its precision (± 9 Pa). Further experimental validation of the flow effect on meniscus breakthrough pressure is presented in Chapter 9 in which pressure fluctuations during Taylor bubble formation in cross flow are measured at different gas and liquid flowrates.

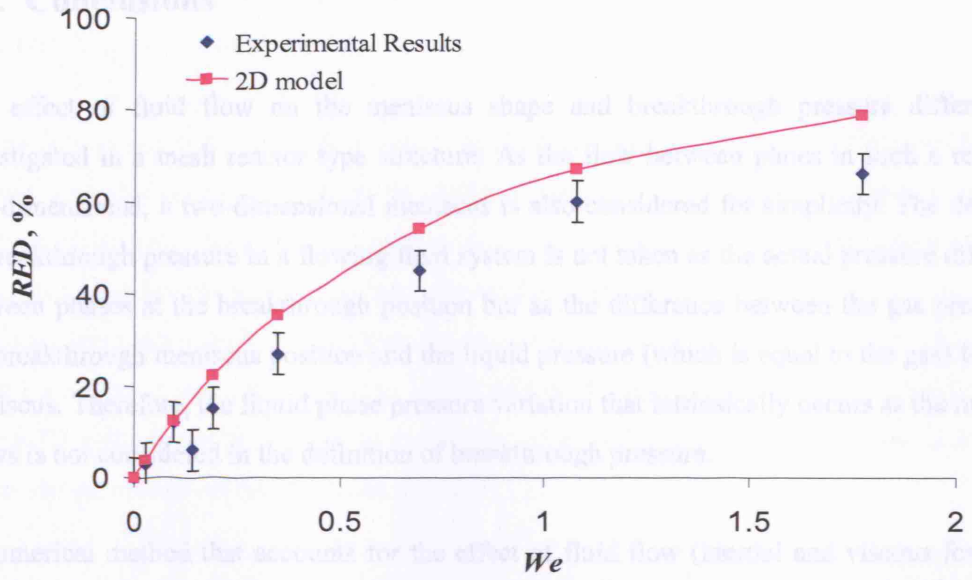

Figure 5.35. Breakthrough pressure reduction *RED* (see Eq. (5.58)) in the flow test device as a function of *We* for a constant ratio $Re/Ca = 17723$.

Because $We >> Ca$ it is not expected that the meniscus will become asymmetric as the results from the model show in Figure 5.36. The imminent breakthrough positions shown in Figure 5.36 correspond to stable shapes at maximum $P_{G,max}$. Once $P_{G,max}$ is reached the meniscus grows until bubble formation takes place.

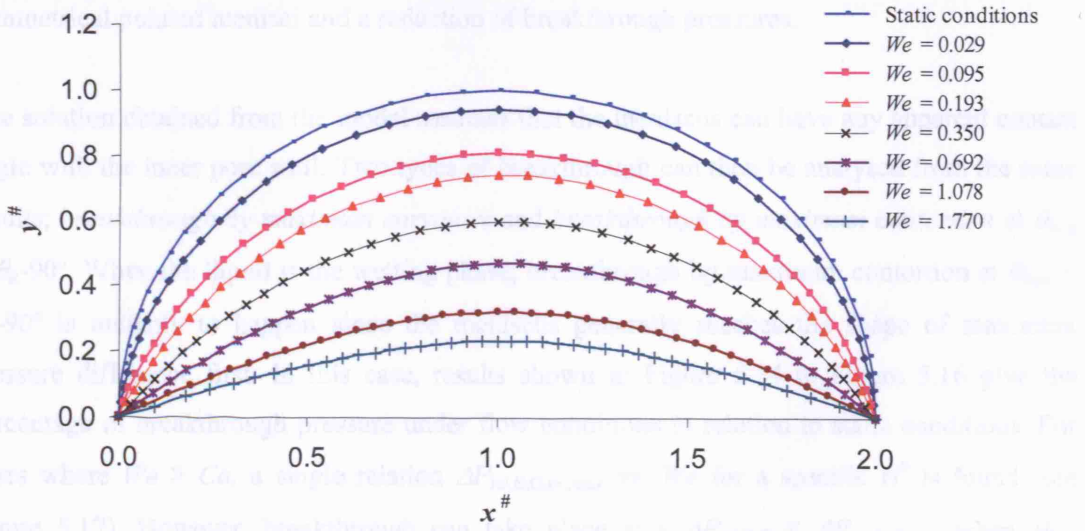

Figure 5.36. Meniscus shapes of maximum gas pressure $P_G^{\#}$ (imminent gas breakthrough) obtained from 2D model. Ratio Re/Ca is constant and equal to $Re/Ca = 17723$.

5.7. Conclusions

The effect of fluid flow on the meniscus shape and breakthrough pressure difference is investigated in a mesh reactor type structure. As the flow between plates in such a reactor is two-dimensional, a two-dimensional meniscus is also considered for simplicity. The definition of breakthrough pressure in a flowing fluid system is not taken as the actual pressure difference between phases at the breakthrough position but as the difference between the gas pressure at the breakthrough meniscus position and the liquid pressure (which is equal to the gas) for a flat meniscus. Therefore, the liquid phase pressure variation that intrinsically occurs as the meniscus grows is not considered in the definition of breakthrough pressure.

A numerical method that accounts for the effect of fluid flow (inertial and viscous forces) on meniscus shape and breakthrough pressure (surface tension forces) is implemented. The method consists of solving the flow field around the meniscus to obtain pressure and viscous stresses on the meniscus, which coupled with the normal stress condition on the interface, produce the meniscus shape. In the absence of gravity and for an isolated pore, three dimensionless numbers define the system behaviour, namely, *Re*, *Ca* (or *We*) and $H^{\#}$. At low *Re* and *Ca*, surface tension forces dominate and the solution is that given by the Laplace equation for static conditions. At low *Re* and high *Ca* (*We* << *Ca*) viscous forces become dominant which push the meniscus inside the pore as it grows resulting in asymmetric shapes and an increase of breakthrough pressure. At high *Re* and low *Ca* (*We* >> *Ca*) inertial forces become dominant, which cause a pressure reduction in the liquid phase above the meniscus as the meniscus grows giving rise to symmetrical pointed menisci and a reduction of breakthrough pressures.

The solution obtained from the model assumes that the meniscus can have any apparent contact angle with the inner pore wall. Two types of breakthrough can then be analysed from the same results; *breakthrough by maximum curvature* and *breakthrough by maximum contortion* at $\theta_{App} = \theta_R$-90°. When the liquid is the wetting phase, breakthrough by maximum contortion at $\theta_{App} = \theta_R$-90° is unlikely to happen since the meniscus generally reaches the shape of maximum pressure difference first. In this case, results shown in Figure 5.14 to Figure 5.16 give the percentage of breakthrough pressure under flow conditions in relation to static conditions. For cases where *We* > *Ca,* a single relation $\Delta P_{rel,B,G,rel,max}$ vs. *We* for a specific $H^{\#}$ is found (see Figure 5.17). However, breakthrough can take place at a $\Delta P_{rel,B,G} < \Delta P_{rel,B,G,max}$ when θ_{App} reaches the value θ_R-90° (*breakthrough by maximum contortion*). Fluid flow can highly affect the value of the meniscus apparent contact angle at the back and front of the meniscus and give rise to breakthrough by maximum contortion at reduced pressure difference (see Figure 5.18 to

Figure 5.28). This is more likely to happen for non-wetting liquids or wetting liquids under high *Ca* where high meniscus deformation occurs.

Bernoulli's equation for inviscid fluids is applied to cases where $We >> Ca$ (dominance of inertial over viscous forces) in order to obtain an approximate pressure over the meniscus as a function of height. This is not as accurate as the full model since the kinetic energy factor is dependent on the unknown velocity/pressure profile over the meniscus and the pressure over the meniscus is expected to be higher than the cross-section average value. However, the solution provides a simple way for estimating breakthrough pressure reduction under flow conditions and in 3D systems can be utilised to analyse the effect of geometrical parameters such as pore shape and separation on breakthrough pressure.

A structure that brings into contact a flowing liquid (water) and a gas (air) via a single 2D pore (slit) is designed to validate the model. The liquid plate is rectangular with two large distributing and collecting chambers that ensure even flow distribution inside the plate with a two-dimensional velocity profile neglecting side wall effects (plate width >> plate height). The hydrostatic pressure inside the plate is kept constant by a special outlet design, which allows precise measurement of the gas pressure during liquid and gas breakthroughs respectively. Pressure drop in the liquid phase is used to confirm the plate height measurement. Breakthrough pressure results under flow conditions follow the same trend as those obtained from the 2D model with consistently slightly smaller values. This small and consistent difference between experimental and theoretical results could be due to geometrical errors in plate height and slit width in the structure when trying to simulate a 2D geometry in a real 3D system.

Nomenclature

Bo	Bond number.
Ca	Capillary number.
d	Pore diameter and diameter in general, m.
f_L	Factor in the Laplace equation. 1 for 2D systems and 2 for axisymmetric spherical menisci.
f_{KE}	Kinetic energy correction factor.
g	Acceleration due to gravity, m2/s.
h_{Slit}	Slit height, m.
H	Phase height, m.
KE	Kinetic energy per mass, J/kg.
L	Plate length, m.
$\mathbf{n}$	Unit normal to a surface.
Q	Flowrate, m^3/s.
P	Pressure, Pa.
P_L*	Liquid normal stresses at the middle point of a flat meniscus, N/m^2.
r	Pore radius of radius in general, m.
R	Radius of curvature of the meniscus, m.
$\mathbf{t}$	Unit tangential to a surface.
$\mathbf{t(n)}$	Stress vector acting on a surface with normal $\mathbf{n}$, N/m^2.
$\mathbf{T}$	Stress tensor, N/m^2.
U	Velocity, m/s.
x	Axis co-ordinate, m.
y	Axis co-ordinate, m.
Re	Reynolds number defined with the pore radius.
Re_{stan}	Reynolds number defined with the phase height (standard definition).
RED	Gas breakthrough pressure reduction due to flow conditions, %.
W	Channel width, m.
We	Weber number, $ReCa$.

Greek Letters

α	Angle of the tangent to a point of the meniscus with the x-axis.
γ	Surface tension, N/m.
ΔP	Pressure difference, Pa.

ΔP_{rel}	Pressure difference across the phases under flow conditions relative to the maximum ($\theta_{App} = 0°$) gas breakthrough pressure in static conditions, %.
$\Delta P_{rel,B,G,max}$	Maximum (any θ_{App} allowed) gas breakthrough pressure under flow conditions relative to the maximum breakthrough pressure in static conditions, %.
θ	Contact angle, rad.
ϕ	Solid wall inclination at the point of contact of the three phase contact line, rad.
μ	Viscosity, *sPa*.
ρ	Phase density, kg/m^3.
ρ_S	Surface density, kg/m^2.
$\tau_{i,j}$	*j*-component of the viscous stress acting on a surface oriented in the positive *i*-direction

Subscripts

A	Advancing.
App	Apparent.
av	Average value.
B	Breakthrough.
C	Critical filling.
CE	Critical entry.
Eff	Effective.
Exp	Experimental.
Flat	Flat meniscus.
G	Gas.
Int	Interior of the pore, e.g. ϕ_{Int} is the solid wall inclination of the interior of the pore.
L	Liquid.
max	Maximum.
min	Minimum.
NW	Non-partially wetting phase.
R	Receding.
rel	Property under flow conditions relative to static conditions.
W	Partially wetting phase.

Superscripts

Static	Static conditions.
#	Dimensionless numbers.

Principles of Two-Phase Flow Microreactors and their Scale-Out

VOLUME II

Carlos Amador Zamarreño

A thesis submitted for the degree of Doctor of Philosophy of

the University of London

University College London

October 2006

Table of Contents

Volume II

Chapter 6

Mass Transfer/Homogenous Chemical Reaction in a Novel Mesh Microreactor

"The best way to make your dreams come true is to wake up"

Paul Valéry

6.1. Introduction

A novel two-phase microreactor that keeps the phases separate and offers increased stability and open interfacial area (up to ~45 %) has been developed by CRL, Turner et al. (2000), (see also Chapter 1). One of the purposes of the system is to accomplish kinetic studies of two-phase, fluid-liquid reactions. It has a mesh structure separating planar chambers where the fluids may contact at the mesh pores. Mesh to wall distances can be set, generally to 80-140 μm, providing chamber volumes of ~100 μl. The 90° quadrant shape allows even flow of immiscible fluids into and out of the reactor with relatively low dispersion (see Chapter 2). The mesh features a dense hexagonal array of 3-10 μm pores made of nickel and has a thickness of 3-5 μm, which minimises diffusive mass transfer resistance while maintaining fluid phase separation.

In this chapter, a modelling analysis of coupled mass transfer and chemical reaction in the mesh microreactor is presented, which is used to define the conditions necessary for kinetic control (allowing recovery of reaction rates) in terms of a parametric map. In the mesh microcontactor two phases, 1 and 2, are separated by a mesh with pores, which allow contact between the phases for interfacial mass transfer. Reactant B in the gas/liquid Phase 1 diffuses into the static liquid Phase 2 where it reacts with component A. The system was modelled for two different cases, namely, constant interfacial concentration of B in Phase 2 and constant concentration of component A in the liquid Phase 2.

Dimensionless parametric maps are developed, which allow the selection of parameters (and especially initial concentrations) in order to ensure kinetic control in the mesh microreactor. Under this regime, the mesh microreactor is ideal for kinetic studies. The dimensionless parametric maps are obtained for a 1D geometry and the 2D axisymmetric geometry that Central Research Laboratories (CRL) currently uses in the mesh microreactor. For the

modelling, finite element simulations were used together with analytical solutions for limiting cases (kinetic and pseudo-kinetic limits). The initial parametric map is for a second order and irreversible reaction with 1:1 stoichiometry but an extended analysis to take into account different reaction orders, stoichiometry and reversible reactions is also presented.

Fast reactions are also studied and relevant expressions on conversion are presented. Compared with experimental data the results of this model will indicate whether a mesh microreactor is under mass transfer control (no kinetic resistances). In case of fast reaction, the reactor can be used to estimate the diffusivity of reactant A.

The models are compared with experimental data available from CRL on fluorescein diacetate hydrolysis and on pyrogallol oxidation. The comparisons indicate that under these operation conditions both reactions are mass transfer limited. Using the parametric maps, initial concentration values of both components were suggested that would bring the system under kinetic control.

6.2. Background

Carslaw and Jaeger (1986) discussed multiple analytical solutions of the transient conductive heat transfer equation in systems with different geometry (co-ordinates), infinite, semi-infinite and finite media, whose solutions are also applicable for the transient diffusive mass transfer equation substituting the temperature T by the concentration c. For a finite medium such as the mesh microcontactor, the analytical mass transfer solution within one phase is generally given as a Fourier series. However, in the case of two finite phases where one component diffuses from one phase to the other, there is no analytical solution for the concentration profile of this diffusant inside both phases and numerical methods are needed. If a chemical reaction takes place together with mass transfer by diffusion, numerical methods are also required. Only in the simple case of absorption of a diffusant into an absorbent and first order chemical reaction of the diffusant with respect to its concentration there is an analytical solution given by Danckwerts (1951). However this case is not very relevant for the two reactive systems analysed in this chapter.

6.3. Definition of the Problem and Model Geometry

Figure 6.1a shows the hexagonal distribution of the hexagonal pores in the mesh, which resembles a honeycomb to maximise open area and mesh strength. The dashed line encloses the

unit cell that is repeated over the whole mesh. Its boundaries are symmetry planes for concentration profiles developed for a reactor with static fluid phases and considering negligible wall effects. In order to reduce computation time and number of parameters, the analysis considers only the dashed region and is based on approximating the 3D geometry to the 2D axisymmetric geometry given in Figure 6.1b (plant view) and Figure 6.2 (side view). Actually, the small hexagonal pores tend to be almost circular so that this approximation is minor.

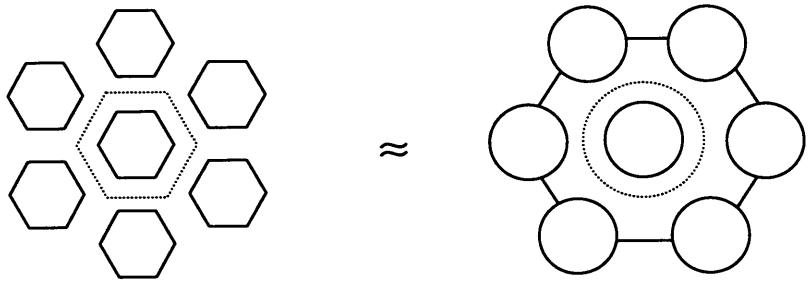

a) b)

Figure 6.1. Symmetrical zone to simulate, a) real geometry, b) approximated geometry.

For the present analysis, the wetting phase is considered to be below the mesh and fills the pores with a flat meniscus. It was found that the differences in the meniscus area between flat and curved shapes had a very small effect on the mass transfer rate (carried out via Femlab simulations), and a flat meniscus was chosen to simplify the simulations. Furthermore, the solution for a meniscus at the bottom of the pore is contained as a solution of the current system in the limit of mesh open area of 100 %.

The system analysed is the absorption of a gaseous or liquid species B contained in phase 1 into a static liquid phase that contains A. Both substances react in this phase according to an irreversible reaction:

$$aA + bB \rightarrow pAB \quad r_A = r_B\left(\frac{a}{b}\right) = -k_A \cdot c_A^{\alpha} \cdot c_B^{\beta} \tag{6.1}$$

As the study analyses the influence of geometric parameters and diffusion/reaction rates on the reactor performance, the kinetics have been simplified. Although initial studies are carried out with reaction orders $\alpha = 1$ and $\beta = 1$ and stoichiometry 1:1, extensions to reversible reactions, different stoichiometries and reaction orders are also presented in this chapter. The concentration profile of AB is not analysed, since the reaction is irreversible.

Two reaction systems were considered (Case 1 and Case 2), in each of which the concentration of one component was kept constant. Subscripts 1 and 2 referring to phases are not used for component *A*, which always remains in Phase 2. The systems were modelled using Finite Element simulations (Femlab) for the approximated geometry shown in Figure 6.2 in order to establish the conditions under which the microreactor operates within the kinetic control regime (flat concentration profiles within the phase for all reactants) defined by analytical solutions.

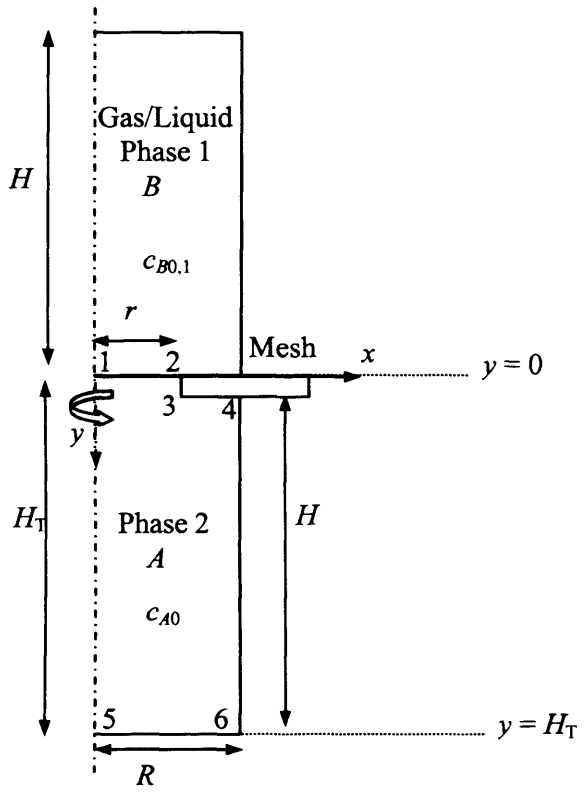

Figure 6.2. 2D axisymmetric geometry considered for the fluid/liquid system.

6.4. Kinetic Control for Homogeneous Catalysis. Case 1: Constant Interfacial Concentration of Difussant *B*

Interfacial concentration of *B* in Phase 2, $c_{Bint,2}$, is assumed constant during the reaction and given by the gas solubility or partition coefficient $P = c_{Bint,1}/c_{Bint,2}$. Phase 1 is therefore not considered in the following analysis. The assumption is correct when the gaseous Phase 1 flows fast enough to keep the Phase 2 interface saturated of component *B*, $c_{Bint,2} = c_{B0,1}/P$. For diffusion distances in both phases of the same order of magnitude, the assumption of a constant interfacial concentration also applies when Phase 1 is a still liquid phase and *B* is in excess (i.e. $Co = (\nu_2 c_{A0})/(\nu_1 c_{B0,1}) < 0.01$) as long as mass transfer resistance in Phase 1 appears later than in

Phase 2 (either large diffusivity of B in Phase 1, or low diffusivity but high partition coefficient, P) where Eq. (6.2) gives the initial interfacial concentration of B, $c_{B\text{int},2}$ when considering that component is already uniformly distributed among the phases 1 and 2 (flat concentration profiles):

$$c_{B\,\text{int},2} = \frac{c_{B0,1} v_1}{(v_2 + v_1 P)} \tag{6.2}$$

6.4.1. Dimensionless Analysis: Second-Order and Irreversible Reaction

The basic parametric map is carried out for an irreversible reaction as Eq. (6.1) with reaction orders $\alpha = 1$, $\beta = 1$ and stoichiometry 1:1. The differential equations that define the diffusion/reaction problem in two dimensions are,

$$\frac{\partial c_A}{\partial t} = D_A \cdot \left(\frac{\partial^2 c_A}{\partial x^2} + \frac{\partial^2 c_A}{\partial y^2} \right) - k_A \cdot c_A \cdot c_B \tag{6.3}$$

$$\frac{\partial c_B}{\partial t} = D_B \cdot \left(\frac{\partial^2 c_B}{\partial x^2} + \frac{\partial^2 c_B}{\partial y^2} \right) - k_A \cdot c_A \cdot c_B \tag{6.4}$$

where k_A is the reaction rate and D_A and D_B are the diffusivities of components A and B respectively. To transform these two expressions into dimensionless equations, different characteristic dimensions can be used, obtaining different equations that describe the same problem. In the present analysis the characteristic time is $t_C = H_T^2/D_{B,2}$ ($D_{B,2}$ is the diffusivity of the diffusant in phase 2), the characteristic length l_C is the whole diffusion length $l_C = H_T$, the characteristic concentration of component A is its initial concentration in phase 2 $c_{A,C} = c_{A0}$ and the characteristic concentration of component B is its constant interfacial concentration in phase 2 $c_{B,2,C} = c_{B\text{int},2}$, which were chosen to simplify the above equations and obtain meaningful dimensionless numbers. For the dimensionless time in Eq. (6.5) (Fourier number), the diffusivity of the substance that is absorbed into the liquid phase is chosen.

$$t^{\#} = \frac{t \cdot D_{B,2}}{H_T^2} \tag{6.5}$$

$$x^{\#} = \frac{x}{H_T}; \quad y^{\#} = \frac{y}{H_T} \tag{6.6}$$

$$c_{B,2}^{\#} = \frac{c_{B,2}}{c_{B\,\mathrm{int},2}}; \quad c_A^{\#} = \frac{c_A}{c_{A0}} \tag{6.7}$$

Substituting the variables t, c_A, $c_{B,2}$, x and y from Eqs. (6.5) to (6.7) into the two differential Eqs. (6.3) and (6.4), Eqs. (6.8) and (6.9) for substances A and B respectively are obtained,

$$\frac{D_{B,2} \cdot c_{A0}}{H_T^2} \cdot \frac{\partial c_A^{\#}}{\partial t^{\#}} = \frac{D_A \cdot c_{A0}}{H_T^2} \left(\frac{\partial^2 c_A^{\#}}{\partial x^{\#2}} + \frac{\partial^2 c_A^{\#}}{\partial y^{\#2}} \right) - k_A \cdot c_{A0} \cdot c_{B\,\mathrm{int},2} \cdot c_A^{\#} \cdot c_{B,2}^{\#} \tag{6.8}$$

$$\frac{D_{B,2} \cdot c_{B\,\mathrm{int},2}}{H_T^2} \cdot \frac{\partial c_{B,2}^{\#}}{\partial t^{\#}} = \frac{D_{B,2} \cdot c_{B\,\mathrm{int},2}}{H_T^2} \left(\frac{\partial^2 c_{B,2}^{\#}}{\partial x^{\#2}} + \frac{\partial^2 c_{B,2}^{\#}}{\partial y^{\#2}} \right) - k_A \cdot c_{A0} \cdot c_{B\,\mathrm{int},2} \cdot c_A^{\#} \cdot c_{B,2}^{\#} \tag{6.9}$$

Dividing these equations by $D_{B,2} \cdot c_{A0}/H_T^2$ and $D_{B,2} \cdot c_{B\mathrm{int},2}/H_T^2$ respectively, the following expressions are found,

$$\frac{\partial c_A^{\#}}{\partial t^{\#}} = \left(\frac{D_A}{D_{B,2}} \right) \cdot \left(\frac{\partial^2 c_A^{\#}}{\partial x^{\#2}} + \frac{\partial^2 c_A^{\#}}{\partial y^{\#2}} \right) - \left(\frac{k_A H_T^2 \cdot c_{B\,\mathrm{int},2}}{D_{B,2}} \right) \cdot c_A^{\#} \cdot c_{B,2}^{\#} \tag{6.10}$$

$$\frac{\partial c_{B,2}^{\#}}{\partial t^{\#}} = \left(\frac{\partial^2 c_{B,2}^{\#}}{\partial x^{\#2}} + \frac{\partial^2 c_{B,2}^{\#}}{\partial y^{\#2}} \right) - \left(\frac{k_A H_T^2 \cdot c_{B\,\mathrm{int},2}}{D_{B,2}} \right) \cdot \left(\frac{c_{A0}}{c_{B\,\mathrm{int},2}} \right) \cdot c_A^{\#} \cdot c_{B,2}^{\#} \tag{6.11}$$

where three dimensionless numbers appear, the ratio of diffusivities T, the ratio of interfacial concentration of B to initial concentration of A, C, and the Damköhler number, Da, that is the ratio of reaction rate to diffusion rate,

$$T = \frac{D_A}{D_{B,2}} \tag{6.12}$$

$$C = \frac{c_{A0}}{c_{B\,\mathrm{int},2}} \tag{6.13}$$

$$Da = \frac{k_A H_T^2 \cdot c_{B\,\mathrm{int},2}}{D_{B,2}} \tag{6.14}$$

Applying these definitions, Eqs. (6.10) and (6.11) produce Eqs. (6.15) and (6.16).

$$\frac{\partial c_A^{\#}}{\partial t^{\#}} = T \cdot \left(\frac{\partial^2 c_A^{\#}}{\partial x^{\#2}} + \frac{\partial^2 c_A^{\#}}{\partial y^{\#2}} \right) - Da \cdot c_A^{\#} \cdot c_{B,2}^{\#} \tag{6.15}$$

$$\frac{\partial c_{B,2}^{\#}}{\partial t^{\#}} = \left(\frac{\partial^2 c_{B,2}^{\#}}{\partial x^{\#2}} + \frac{\partial^2 c_{B,2}^{\#}}{\partial y^{\#2}} \right) - Da \cdot C \cdot c_A^{\#} \cdot c_{B,2}^{\#} \tag{6.16}$$

Considering the 2D axisymmetric geometry given in Figure 6.2, three geometrical dimensionless numbers appear in the boundary conditions, the ratio of diffusion distance in the x-axis to diffusion distance in the y-axis, G_{Rh} and the ratios of diffusion distances in the y-axis G_h and in the x-axis G_r:

$$G_{Rh} = \frac{R}{H_T};\ G_h = \frac{H}{H_T};\ G_r = \frac{r}{R} \tag{6.17}$$

where H is the channel height, r is the pore radius and R is half the pitch or separation between pore centres. Thus, 9 parameters are reduced to 6 dimensionless parameters according to Buckingham Π theorem. The main objective of this dimensionless parametric study is to calculate the values of the model parameters under which there is complete kinetic control. This is necessary because the rector is intended to be used for kinetic studies. The mass transfer resistance can be on the part of substance A, substance B or both. Thus, in the kinetic control zone, both concentration profiles should be flat. According to Eqs. (6.15) and (6.16) the values of T and Da determine whether there is mass transfer resistance on behalf of A while for B this is determined by the product DaC. Small values of Da with respect to T (dimensionless diffusivity of A) in the case of A and a small value of DaC with respect to 1 (dimensionless diffusivity of B) in the case of B ensure that the kinetic rate is slow in comparison with the mass transfer rate for A and B respectively, obtaining flat concentration profiles for both substances. In the limit when Da and DaC tend to zero complete kinetic control exists. This limit can be found analytically. However, as initially there is no component B in the liquid Phase 2, there will be an interval of time where its concentration profile develops until it becomes flat.

The current CRL mesh microreactor geometry is defined by R = 3.5 μm, r = 2 μm, H = 100 μm and H_T = 105 μm. These values give the following dimensionless geometric parameters: G_{Rh} = 0.03333, G_h = 0.95238 and G_r = 0.57143. Initially, the number G_r is not modified as the ratio of pitch of the mesh to radius of the pores is kept constant. Parameter G_h will be important if the mesh thickness is large and G_r is small. G_{Rh} will be important at low values of G_h and G_r.

The value of the dimensionless numbers Da, T, C, G_{Rh}, G_h and G_r under which the system is kinetically controlled are analysed. Set of these numbers where concentration profiles of both components A and B along the liquid phase become flat will be presented in a parametric map, which relates Da, C and T for each specific geometry. T is assumed to take values from 0.1 to 10 since the liquid diffusivity of most components are of the order of magnitude 10^{-9} or 10^{-10}. m^2/s. Therefore, for each T there is a limiting Da, above which the concentration profile of A is not flat anymore while for the substance B, there is always a small enough value of C that eliminates its mass resistance. Da decreases with diffusion distance H_T or interfacial concentration of B decreases.

Figure 6.3 shows the conversion of A X_A versus dimensionless time $t^{\#}$ (see Eq. (6.5)) at different concentration ratios C obtained via Femlab while the other parameters are kept constant to T = 0.1, Da = 0.001 and G_{Rh} = 0.0333, G_h = 0.9524 and G_r = 0.5714 (CRL geometry). As $Da << T$ the concentration profile of A is flat and all mass transfer resistance is due to B. By decreasing C (i.e. decreasing DaC) the actual conversion of A gets closer to the kinetic conversion limit. Concentration profiles are obtained in Femlab by solving Eqs. (6.15) and (6.16) and they are integrated according to Eq. (6.18) in order to get the mass of component A inside the liquid phase at any time.

$$m\left(t^{\#}\right)=\int_{x^{\#}-dom}\int_{y^{\#}-dom}c^{\#}\left(t^{\#},x^{\#},y^{\#}\right)dx^{\#}dy^{\#} \tag{6.18}$$

Eq. (6.19) gives the conversion of substance A after time $t^{\#}$.

$$X_A\left(t^{\#}\right)=\frac{m_A\left(t^{\#}=0\right)-m_A\left(t^{\#}\right)}{m_A\left(t^{\#}=0\right)} \tag{6.19}$$

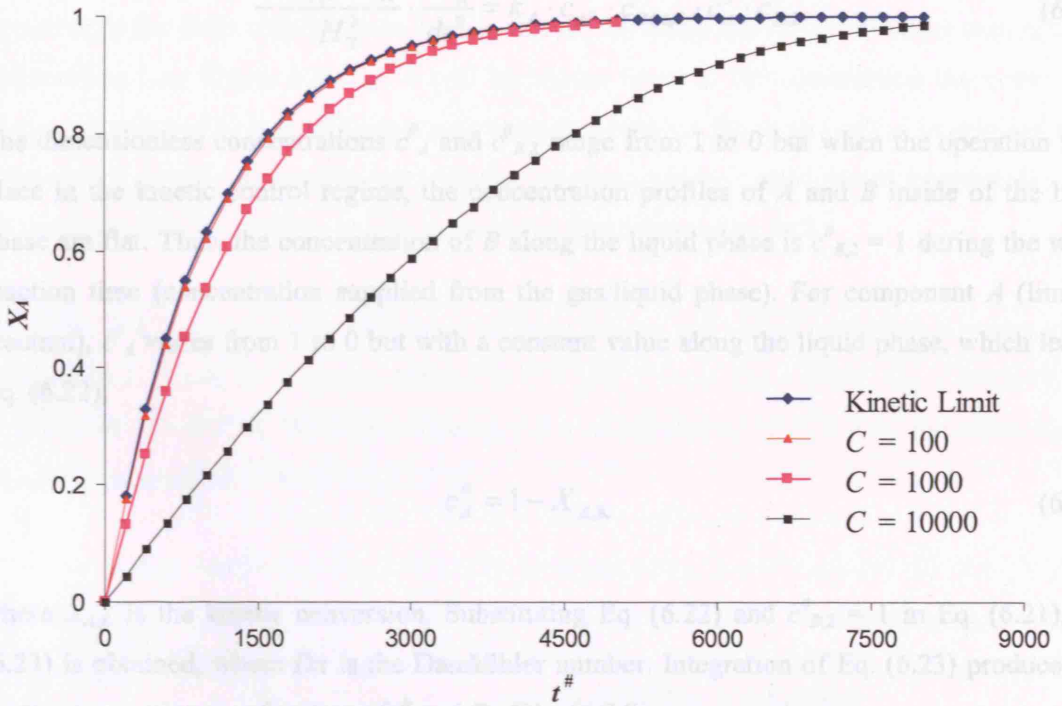

Figure 6.3. Conversion of component *A* X_A vs. dimensionless time $t^{\#}$ obtained via Femlab as a function of *C*. Results are compared to the kinetic conversion (flat concentration profiles). T = 0.1, Da = 0.001, G_{Rh} = 0.0333, G_h = 0.9524 and G_r = 0.5714 (CRL geometry).

The kinetic limit in Figure 6.3 is the conversion curve for total kinetic control and it will be called *kinetic conversion of A*, $X_{A,K}$. The equations for this limiting solution are explained in the next section. Theoretically full kinetic control occurs when *C* and *Da* tend to zero, thus it is necessary to define kinetic control with certain tolerance.

6.4.2. Kinetic Conversion of *A*, $X_{A,K}$

The dimensionless kinetic equation for a second-order and irreversible reaction is,

$$-r_A = \frac{-dc_A}{dt} = k_A \cdot c_A \cdot c_{B,2} \tag{6.20}$$

Eq. (6.20) is made dimensionless using the previously defined dimensionless variables given in Eqs. (6.5) and (6.7) to obtain:

$$-\frac{D_{B,2}\cdot c_{A0}}{H_T^2}\cdot\frac{dc_A^{\#}}{dt^{\#}} = k_A\cdot c_{A0}\cdot c_{B\,\mathrm{int},2}\cdot c_A^{\#}\cdot c_{B,2}^{\#} \tag{6.21}$$

The dimensionless concentrations $c^{\#}_A$ and $c^{\#}_{B,2}$ range from 1 to 0 but when the operation takes place in the kinetic control regime, the concentration profiles of A and B inside of the liquid phase are flat. Thus, the concentration of B along the liquid phase is $c^{\#}_{B,2} = 1$ during the whole reaction time (concentration supplied from the gas/liquid phase). For component A (limiting reactant), $c^{\#}_A$ varies from 1 to 0 but with a constant value along the liquid phase, which lead to Eq. (6.22),

$$c_A^{\#} = 1 - X_{A,\mathrm{K}} \tag{6.22}$$

where $X_{A,\mathrm{K}}$ is the kinetic conversion. Substituting Eq. (6.22) and $c^{\#}_{B,2} = 1$ in Eq. (6.21), Eq. (6.23) is obtained, where Da is the Damköhler number. Integration of Eq. (6.23) produces the kinetic conversion as a function of $t^{\#}$ and Da (Eq. (6.24)).

$$\frac{dX_{A,\mathrm{K}}}{dt^{\#}} = \frac{k_A\cdot c_{B\,\mathrm{int},2}\cdot H_T^2}{D_{B,2}}\cdot(1-X_{A,\mathrm{K}}) = Da\cdot(1-X_{A,\mathrm{K}}) \tag{6.23}$$

$$X_{A,\mathrm{K}} = 1 - e^{-Da\cdot t^{\#}} \tag{6.24}$$

This equation defines the kinetic limit shown in Figure 6.3. The rest of the curves are obtained for different values of C where mass transfer resistance of B has different importance. At C = 10000 the mass transfer resistance is still quite important. However, the curve at C = 100 is very close to the kinetic conversion and it may be said that for this set of dimensionless numbers, T, Da, G_{Rh}, G_h and G_r, C = 100 brings the system under kinetic control regime. Thus, when operating with this set of parameters, values of C smaller than 100 result in complete kinetic control.

However, as the kinetic limit is an asymptotic solution when Da and C tend to zero, certain tolerance must be included to define *kinetic control regime*. In this work *total kinetic control is considered to take place when the actual conversion is 1 % within the kinetic conversion when this is 10 %*. Instead of using 1 % within the kinetic conversion, other percentages can also be used, 2 % and 5 %, if a larger error in the retrieval of the reaction rate value is allowed. A conversion of 10 % was chosen for a number of reasons. During experimental studies this

conversion is achieved in a shorter time than a larger conversion. Furthermore, at lower conversions the difference between the kinetic and the actual conversion is larger than at higher conversions (see Figure 6.3). As it will be shown later, at 10% conversion the error in the recovered value of k_A is practically the same as that between the values of the kinetic and actual conversions. Finally, reversible and complex reactions can be considered as irreversible at low conversions, and the analysis can be extended to those systems as well.

In Figure 6.4, the percentage difference between kinetic and actual conversions versus kinetic conversion is shown for a system defined by $C = 100$, $T = 0.1$, $Da = 0.001$, $G_{Rh} = 0.03333$, $G_h = 0.9524$ and $G_r = 0.5714$. While the difference at a conversion of 10 % is 4 %, the difference at a kinetic conversion of 90 % is only 0.5 %.

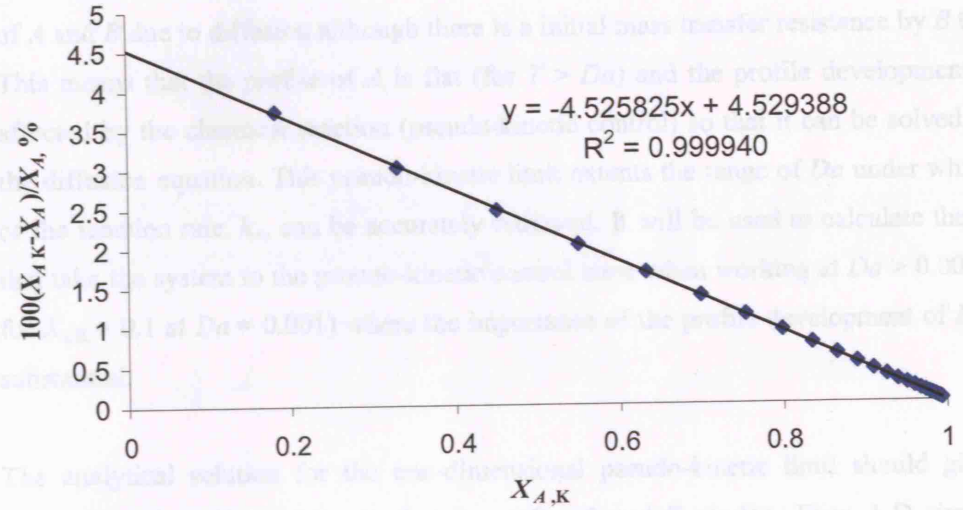

Figure 6.4. Difference between kinetic and actual conversions as a function of the kinetic conversion $X_{A,K}$ for $C = 100$, $T = 0.1$, $Da = 0.001$, $G_{Rh} = 0.03333$, $G_h = 0.9524$ and $G_r = 0.5714$.

As an example with the data shown in Figure 6.3, the time at which 10 % of the kinetic conversion takes place is given by Eq. (6.25),

$$t^{\#} = \frac{-\ln(1-0.1)}{Da} = 105.36 \tag{6.25}$$

Conversions at this time for different values of C, $C = 1$, $C = 100$ and $C = 10000$ are 9.95, 9.57 and 2.39 respectively. By linear interpolation between the points at $C = 1$ and $C = 100$, the

limiting value of C at which the actual conversion is 9.9 % (that is 1 % within the kinetic one) is found to be C = 14.4 (limiting value for kinetic control).

6.4.3. Pseudo-kinetic Conversion: Concentration Profile for Absorbed Component *B* in the Liquid Phase (Phase 2)

Initially there is no component B in the liquid phase 2 or the concentration is smaller than the interfacial concentration available from the fluid phase 1. In this case, certain time is required for the profile of B in the liquid to become flat ($t^{\#} \approx 2$ for $c_{B0,2} = 0$), even when C tends to zero, Carslaw and Jaeger (1986). As Da increases, this time becomes comparable to the total reaction time ($t^{\#} = 10.54$ for $X_{A,K} = 0.1$ at $Da = 0.01$), however, under certain values of C and T it can still be assumed that the fluxes consumed by the chemical reaction are much smaller than the fluxes of A and B due to diffusion although there is a initial mass transfer resistance by B to overcome. This means that the profile of A is flat (for $T > Da$) and the profile development of B is not affected by the chemical reaction (pseudo-kinetic control) so that it can be solved by applying the diffusion equation. This pseudo-kinetic limit extents the range of Da under which the value of the reaction rate, k_A, can be accurately retrieved. It will be used to calculate the values of C that take the system to the pseudo-kinetic control zone when working at $Da > 0.001$ ($t^{\#} = 105.4$ for $X_{A,K} = 0.1$ at $Da = 0.001$) where the importance of the profile development of B starts being substantial.

The analytical solution for the one-dimensional pseudo-kinetic limit should give the same solution as the 1-D Femlab simulations at $C = 0$ and $T >> Da$. Thus, 1-D simulations at a specific value of T and Da are carried out and compare to the pseudo-kinetic limit in order to obtain the values of C for which the actual conversion (at $X_{A,PK} = 10$ %) is 1, 2 or 5 % within the pseudo-kinetic one due to the mass transfer resistances. The diffusion of B into the liquid phase when it is not affected by the chemical reaction is given by Eq. (6.26) that provides the concentration profile of B, $c_{B,2}(y, t)$.

$$\frac{\partial c_{B,2}}{\partial t} = D_{B,2} \cdot \frac{\partial^2 c_{B,2}}{\partial y^2} \tag{6.26}$$

Initial and boundary conditions for the 1-D solution according to Figure 6.1 are given by:

I $$c_{B,2}(y,0) = 0 \tag{6.27}$$

II $$c_{B,2}(0,t) = c_{B\text{int},2} \tag{6.28}$$

III $$\frac{\partial c_{B,2}(H_T,t)}{\partial y} = 0 \tag{6.29}$$

The third boundary condition implies that there is no flux of B at the bottom of the reactor. The solution for this equation is given by Crank (1975) for the case of sorption and desorption by a membrane in the region $-H_T < y < H_T$ where there is an initial uniform concentration and the surfaces are kept at a constant concentration (see Eq. (6.30)). This solution fulfils the initial and boundary conditions aforementioned in the region $0 < y < H_T$ as the plane $y = 0$ is symmetric and equivalent to an impermeable surface (zero flux).

$$\frac{c_{B,2} - c_{B0,2}}{c_{B\text{int},2} - c_{B0,2}} = 1 - \frac{4}{\pi}\sum_{n=0}^{\infty}\left[\frac{(-1)^n}{2n+1}\exp\left\{\frac{-D_{B,2}(2n+1)^2\pi^2 t}{4H_T^2}\right\}\cos\left(\frac{(2n+1)\pi y}{2H_T}\right)\right] \tag{6.30}$$

Considering that $c_{B0,1} = 0$ in the liquid phase and Eq. (6.30) for the concentration profile of B is made dimensionless using the dimensionless variables given in Eqs. (6.5)-(6.7).

$$c_{B,2}^{\#} = 1 - \frac{4}{\pi}\sum_{n=0}^{\infty}\left[\frac{(-1)^n}{2n+1}\exp\left\{\frac{-(2n+1)^2\pi^2 t^{\#}}{4}\right\}\cos\left(\frac{(2n+1)\pi y^{\#}}{2}\right)\right] \tag{6.31}$$

Figure 6.5 shows the development of the concentration profile of B, where full development is achieved for $t^{\#} > 2$. Therefore, this method will be more suitable when the global process time is comparable to 2. Even when the global time ($t^{\#} = 1.38$ for $X_{A,PK} = 0.1$ at $Da = 0.1$) is of the same order of magnitude as the time for the B concentration profile to develop ($t^{\#} \approx 2$), it is possible that the reaction process does not affect the profile development when C is small enough (B in excess). It is important to note that Eq. (6.30) can also be used when the initial concentration of B in Phase 2 is not zero, resulting in different solutions for the pseudo-kinetic limit (different importance of the development of the B concentration profile). In this case, an additional dimensionless number is considered, $C_B = c_{B0,2}/c_{B\text{int},2}$ (analysis in this chapter is for $C_B = 0$).

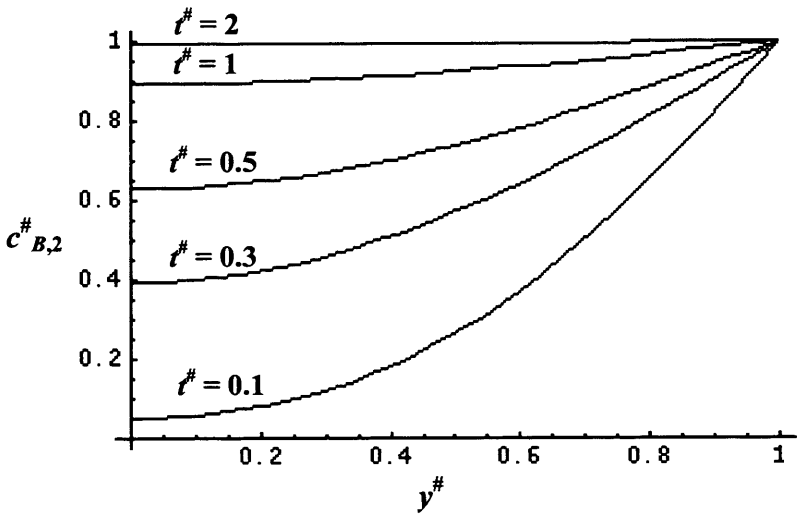

Figure 6.5. Profile development of component *B* as it absorbs into the liquid phase 1.

Now, the application of Eq. (6.21) considers that the concentration of *B* is not constant along the whole liquid phase, which leads to Eq. (6.32). This equation is integrated over the whole length of the liquid phase as shown by Eq. (6.33). Eq. (6.31) is used to solve the integral of $c^{\#}_{B,2}$ with respect to time to obtain Eq. (6.34).

$$\frac{dX_{A,\mathrm{PK}}}{dt^{\#}} = Da \cdot (1 - X_{A,\mathrm{PK}}) \cdot c^{\#}_{B,2}(y^{\#}, t^{\#}) \tag{6.32}$$

$$\int_{X_{A,\mathrm{PK}}=0}^{X_{A,\mathrm{PK}}} \frac{dX_{A,\mathrm{PK}}}{(1 - X_{A,\mathrm{PK}})} = \frac{Da}{(y^{\#}_{\mathrm{Final}} - y^{\#}_{\mathrm{Initial}})} \int_{t^{\#}=0}^{t^{\#}} \int_{y^{\#}=0}^{y^{\#}=1} c^{\#}_{B,2} dy^{\#} dt^{\#} \tag{6.33}$$

$$\int_{y^{\#}=0}^{y^{\#}=1} c^{\#}_{B,2} dy^{\#} = 1 - \frac{4}{\pi} \sum_{n=0}^{\infty} \left[\frac{2(-1)^n}{\pi(2n+1)^2} \exp\left\{ \frac{-(2n+1)^2 \pi^2 t^{\#}}{4} \right\} \sin\left(\frac{(2n+1)\pi}{2} \right) \right] \tag{6.34}$$

Substituting Eq. (6.34) into Eq. (6.33) and integrating both sides with respect to conversion and dimensionless time respectively, Eq. (6.35) for the pseudo-kinetic conversion of component *A*, $X_{A,\mathrm{PK}}$ is obtained.

$$X_{A,\mathrm{PK}} = 1 - \exp\left\{ -Da \cdot \left(t^{\#} - \frac{4}{\pi} \sum_{n=0}^{\infty} \left[\frac{1}{(2n+1)^2 \pi} \cdot 2(-1)^n \cdot \left(\frac{4}{(2n+1)^2 \pi^2} - \frac{4}{(2n+1)^2 \pi^2} \exp\left\{ -\frac{(2n+1)^2 \pi^2 t^{\#}}{4} \right\} \right) \sin\left(\frac{(2n+1)\pi}{2} \right) \right] \right) \right\} \tag{6.35}$$

Figure 6.6 shows conversion versus time results for a system with G_{Rh} = 0.03333, G_h = 0.9524 and G_r = 0.5714, T = 0.1 and Da = 1. As C tends to zero, the results approach the pseudo-kinetic limit although they never reach it due to the fact that the analytical pseudo-kinetic limit is based on a 1-D mass transfer solution and the analysed geometry is 2-D axisymmetric. Furthermore, in this case $Da > T$ (1 vs. 0.1) and there is partial mass transfer resistance on the side of A. It will be shown that the pseudo-kinetic limit gives the same solution as the 1-D Femlab simulations when $C = 0$ and $T > Da$.

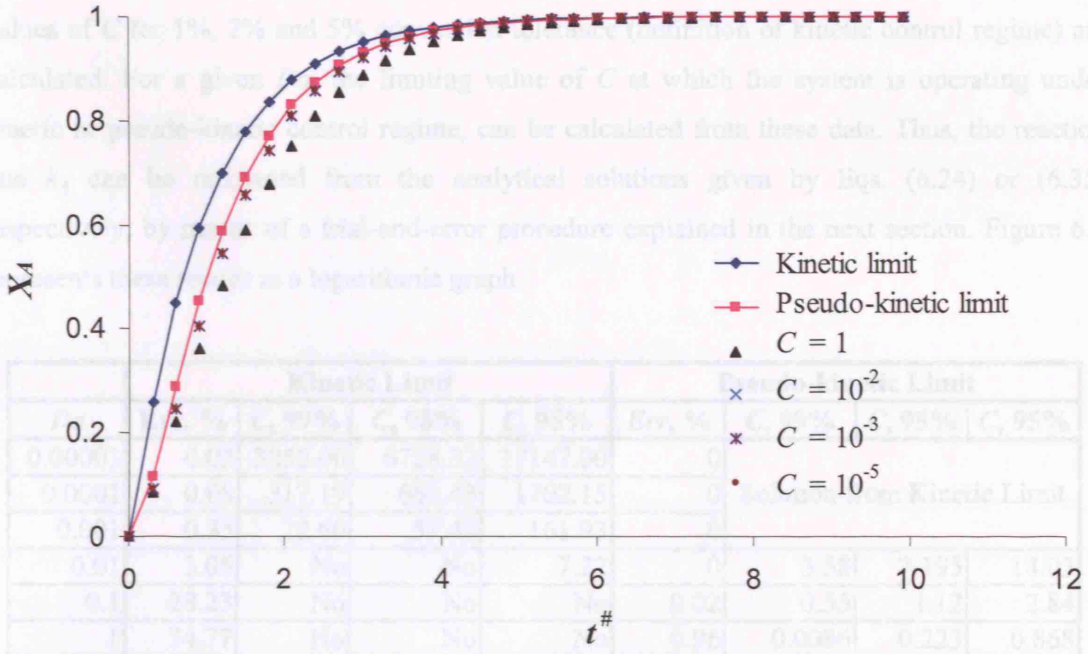

Figure 6.6. Conversion of component A vs. dimensionless time $t^{\#}$ obtained via Femlab as a function of C. Results are compared to the kinetic and pseudo-kinetic limits. T = 0.1, Da = 1, G_{Rh} = 0.0333, G_h = 0.9524 and G_r = 0.5714 (CRL geometry).

Data for T = 0.1, Da = 0.1 and CRL geometry, show that the limit from Femlab at $C \rightarrow 0$ is X_A = 0.8584 when $t^{\#}$ = 20. The kinetic limit is $X_{A,K}$ = 0.8647 and the pseudo-kinetic limit is $X_{A,PK}$ = 0.8601, slightly different from 0.8584 due to the 2-D effect.

6.4.4. Simulations Results vs. Kinetic and Pseudo-kinetic Limits

6.4.4.1.1D Geometry

Unlike the kinetic limit, the pseudo-kinetic limit depends on the geometry so that the first dimensionless map is made for a 1D geometry, which is equivalent to a 2D axisymmetric geometry with $G_r = 1$, where the 1D mass transfer solution used in the pseudo-kinetic limit is accurate. Table 6.1 shows results for *Da* and *C* when $T = 1$. At each value of *Da*, three different values of *C* for 1%, 2% and 5% conversion tolerance (definition of kinetic control regime) are calculated. For a given *Da*, the limiting value of *C* at which the system is operating under kinetic or pseudo-kinetic control regime, can be calculated from these data. Thus, the reaction rate k_A can be recovered from the analytical solutions given by Eqs. (6.24) or (6.35) respectively, by means of a trial-and-error procedure explained in the next section. Figure 6.7 represents these results in a logarithmic graph.

	Kinetic Limit				Pseudo-kinetic Limit			
Da	**Err. %**	***C*, 99%**	***C*, 98%**	***C*, 95%**	***Err*, %**	***C*, 99%**	***C*, 98%**	***C*, 95%**
0.00001	0.05	3255.00	6728.32	17147.00	0	Solution from Kinetic Limit		
0.0001	0.08	317.19	663.43	1702.15	0			
0.001	0.35	22.60	57.43	161.93	0			
0.01	3.05	No	No	7.22	0	3.58	7.195	18.03
0.1	28.23	No	No	No	0.02	0.55	1.12	2.84
1	74.77	No	No	No	0.96	0.0086	0.223	0.868
10		No	No	No	6.69	No	No	No

Table 6.1. One-dimensional results of *Da* and *C* for the dimensionless parametric map at $T = 1$. Case 1.

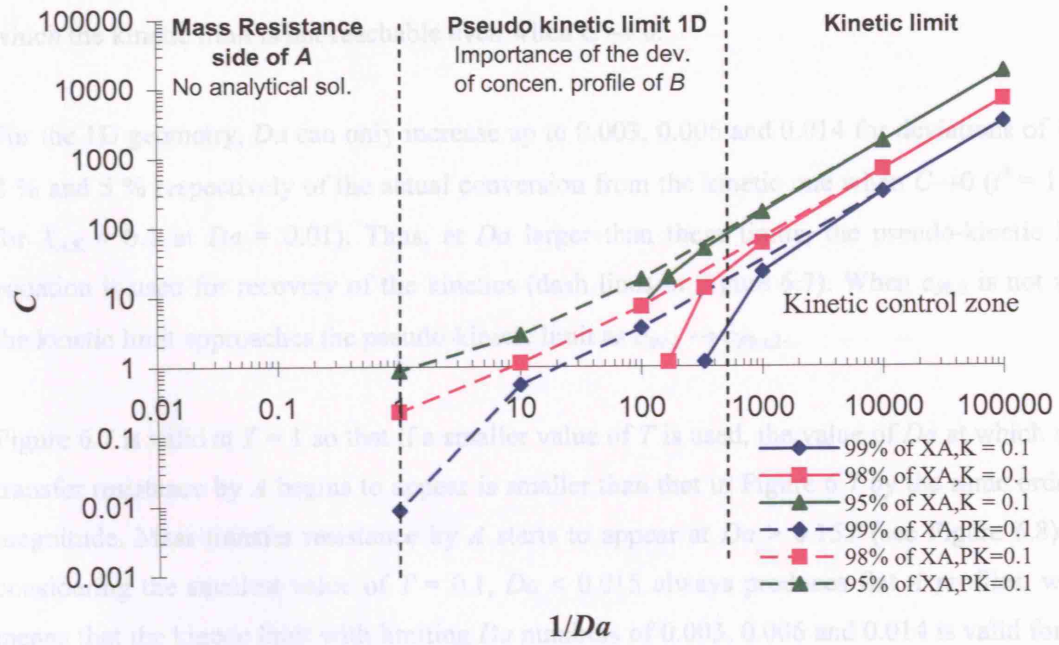

Figure 6.7. 1D dimensionless parametric map of C vs. $1/Da$ at $T = 1$. Case 1.

The residual errors presented in Table 6.1 are the difference between the accurate conversion values calculated via Femlab simulations and those given by the kinetic and pseudo-kinetic limits (analytical solutions), when C tends to zero and $X_{A,K} = X_{A,PK} = 0.1$. One component of the error is related to the lineal interpolation, and is generally small (~0.05 % as shown in Table 6.1 for the lowest Da). For the pseudo-kinetic limit the interpolation error has not been considered but it is approximately of the same magnitude as for the kinetic limit. The other component of the error increases as Da increases, as a result of the development of the B concentration profile in the kinetic limit (for $Da > 0.001$) and as result of the appearance of mass transfer resistance by A (at $Da > 0.1$) in the pseudo-kinetic limit (see zones in Figure 6.7). The point at $1/Da = 1$ on the curve for 99 % of $X_{A,PK}$ is slightly lower than the previous slope because the error due to the mass transfer resistance by A is already very close to 1.

Figure 6.7 also shows that at small values of Da, the product DaC remains constant to 0.0326, 0.0673 and 0.1715 for 1%, 2% and 5% differences between the actual conversion and the kinetic one. However as Da increases, which decreases the dimensionless time for the same conversion according to Eq. (6.24), the product DaC using the kinetic limit decreases. This corresponds to cases where the global reaction time is of the same order as the time that takes B to develop its concentration profile in Phase 2 until it becomes flat, which occurs at $t^{\#} \approx 2$. Therefore, as the global reaction time becomes of the same order as the diffusion time of B, the

value of C to reach the kinetic limit decreased more rapidly until a limiting value is found for which the kinetic limit is not reachable even when $C \rightarrow 0$.

For the 1D geometry, Da can only increase up to 0.003, 0.006 and 0.014 for deviations of 1 %, 2 % and 5 % respectively of the actual conversion from the kinetic one when $C \rightarrow 0$ ($t^{\#} = 10.54$ for $X_{A,K} = 0.1$ at $Da = 0.01$). Thus, at Da larger than these limits, the pseudo-kinetic limit equation is used for recovery of the kinetics (dash lines in Figure 6.7). When $c_{B0,2}$ is not zero, the kinetic limit approaches the pseudo-kinetic limit as $c_{B0,2} \rightarrow c_{BInt,2}$.

Figure 6.7 is valid at $T = 1$ so that if a smaller value of T is used, the value of Da at which mass transfer resistance by A begins to appear is smaller than that in Figure 6.7 by the same order of magnitude. Mass transfer resistance by A starts to appear at $Da > 0.15T$ (see Figure 6.8) and considering the smallest value of $T = 0.1$, $Da < 0.015$ always produces flat A profiles, which means that the kinetic limit with limiting Da numbers of 0.003, 0.006 and 0.014 is valid for any T between 0.1 and 10 but the pseudo-kinetic limit is trimmed by one order of magnitude for $T = 0.1$ and extended by one order of magnitude for $T = 10$. Figure 6.8 shows the start of mass transfer resistance by A at $Da = 0.10T$ (residual error = 0.02 %) and Figure 6.9 shows the increase in this resistance when $Da = 1T$. The residual error, $err = 0.96\%$, is still smaller than the available conversion tolerances 1%, 2% and 5 %. Thus, at $T = 10$ all data presented in Figure 6.7 is valid and it can be also extrapolated up to $1/Da = 0.1$. However at $T = 0.1$, only the data ranging from $1/Da = 10^5$ to $1/Da = 10$ should be used as the residual error due to mass transfer resistance by A in the pseudo-kinetic limit appears one order of magnitude before.

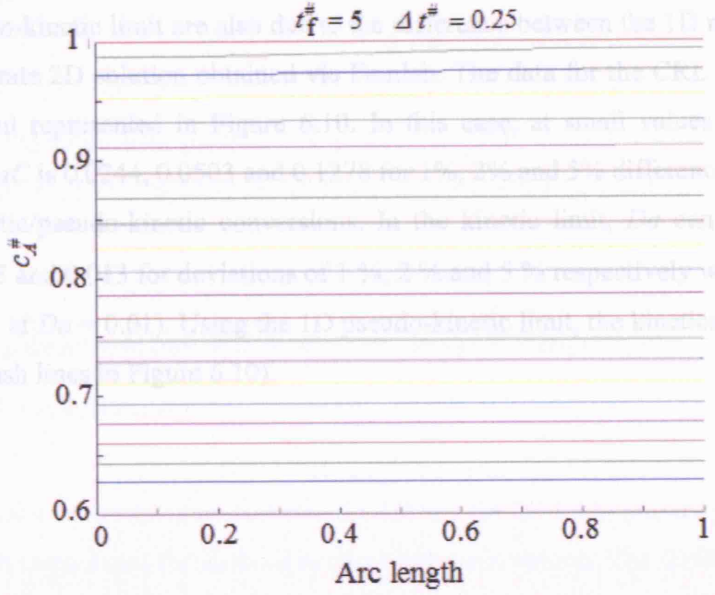

Figure 6.8. Concentration profile of A. $Da = 0.1$, $T = 1$ and $C = 0$.

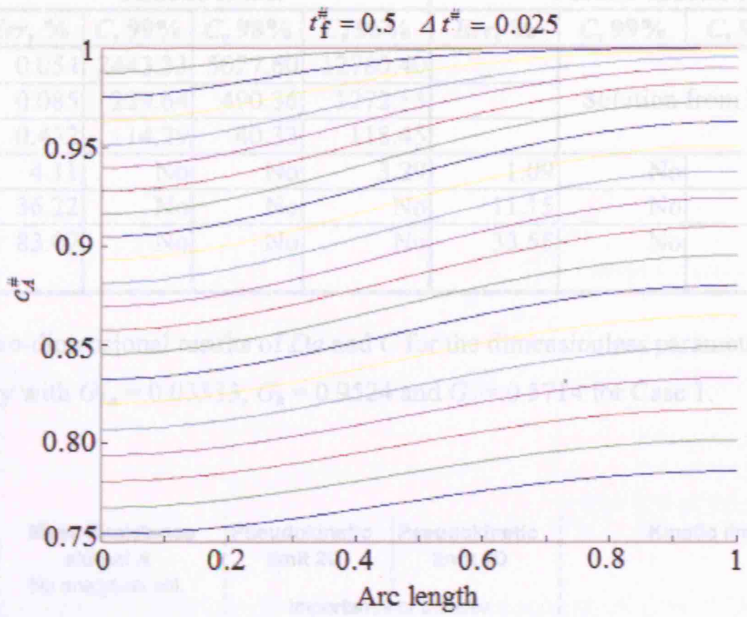

Figure 6.9. Concentration profile of *A*. $Da = 1$, $T = 1$ and $C = 0$.

6.4.4.2. 2D Axisymmetric Geometry

The geometry currently used by CRL is approximated to the 2D axisymmetric geometry defined by $G_{Rh} = 0.03333$, $G_h = 0.9524$ and $G_r = 0.5714$. In this case, the kinetic limit is still suitable for $Da < 0.001$ although the analytical 1-D pseudo-kinetic limit is not an accurate limit for the Femlab simulations between $Da = 0.001$ and $Da = 0.1$ when $G_r \neq 1$. Therefore residual errors for the pseudo-kinetic limit are also due to the difference between the 1D mass transfer solution and the accurate 2D solution obtained via Femlab. The data for the CRL geometry is given in Table 6.2 and represented in Figure 6.10. In this case, at small values of *Da*, the constant product of *DaC* is 0.0244, 0.0503 and 0.1278 for 1%, 2% and 5% differences between the actual and the kinetic/pseudo-kinetic conversions. In the kinetic limit, *Da* can only increase up to 0.0025, 0.005 and 0.013 for deviations of 1 %, 2 % and 5 % respectively when $C \rightarrow 0$ ($t^{\#} = 10.54$ for $X_{A.K} = 0.1$ at $Da = 0.01$). Using the 1D pseudo-kinetic limit, the kinetics can be retrieved at a larger *Da* (dash lines in Figure 6.10).

	Kinetic Limit				Pseudo-kinetic Limit			
Da	*Err*, %	*C*, 99%	*C*, 98%	*C*, 95%	*Err*, %	*C*, 99%	*C*, 98%	*C*, 95%
0.00001	0.054	2443.33	5027.60	12780.40		Solution from Kinetic Limit		
0.0001	0.085	229.64	490.36	1272.53				
0.001	0.452	14.29	40.33	118.45				
0.01	4.11	No	No	3.29	1.09	No	3.26	14.43
0.1	36.22	No	No	No	11.15	No	No	No
1	83.07	No	No	No	33.55	No	No	No

Table 6.2. Two-dimensional results of *Da* and *C* for the dimensionless parametric map at $T = 1$. CRL geometry with $G_{Rh} = 0.03333$, $G_h = 0.9524$ and $G_r = 0.5714$ for Case 1.

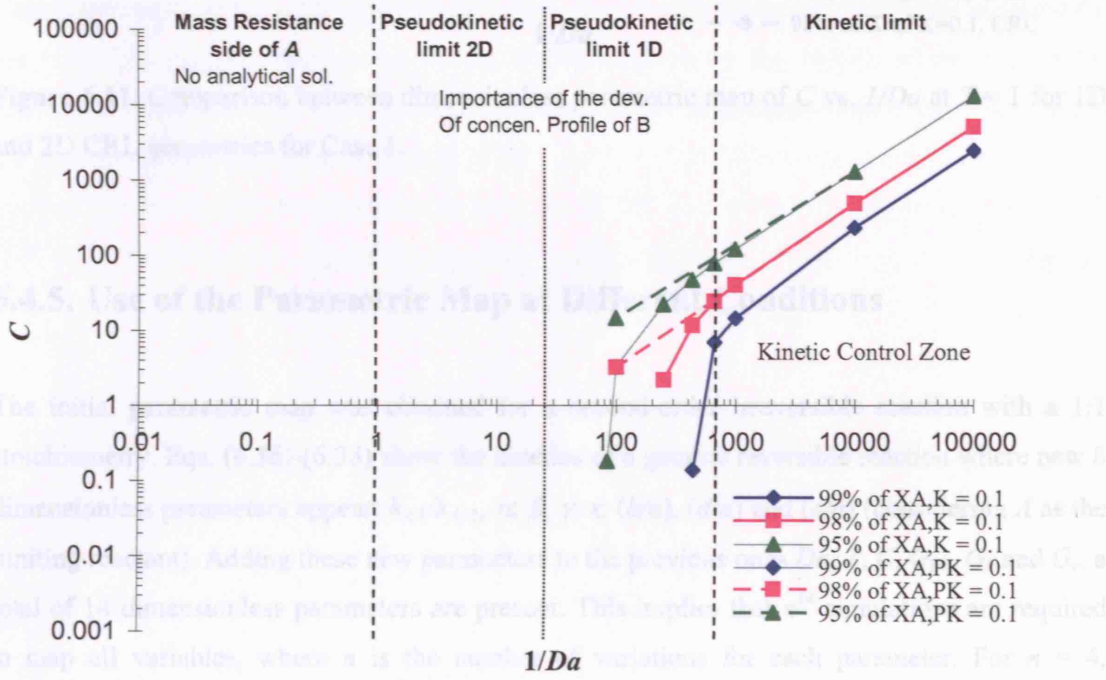

Figure 6.10. Dimensionless parametric map of *C* vs. *1/Da* at $T = 1$. Two-dimensional results for CRL geometry with = 0.03333, $G_h = 0.9524$ and $G_r = 0.5714$ for Case 1.

6.4.4.3. Dimensionless Parametric Map Comparison between 1D and 2D Geometries.

Figure 6.11 shows a comparison between the 1D and the 2D CRL geometry for a difference of 2 % between the actual and the kinetic/pseudo-kinetic conversion. The difference between curves is small and indicates that an interpolation could be used for different intermediate geometries.

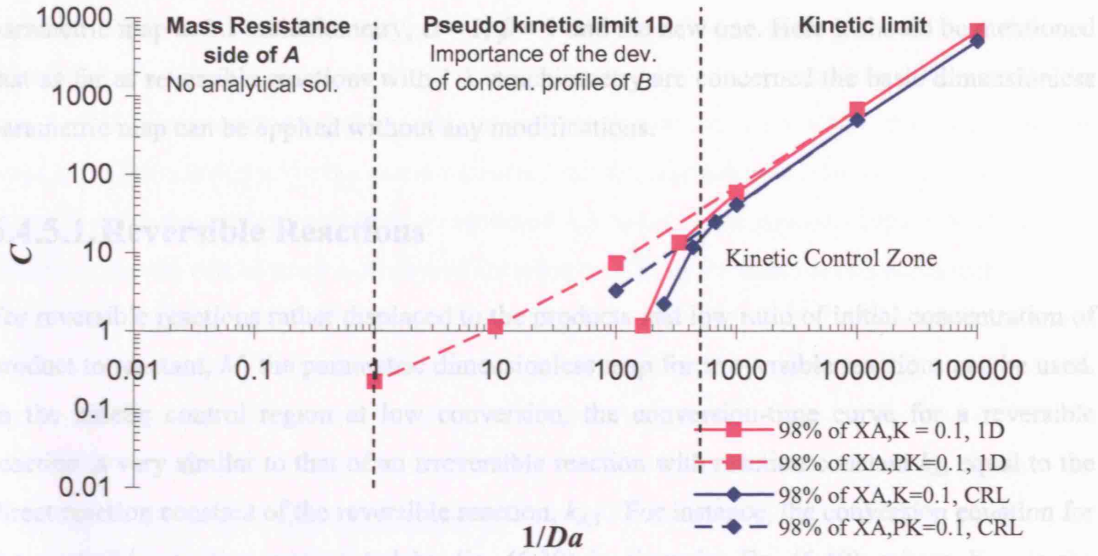

Figure 6.11. Comparison between dimensionless parametric map of C vs. $1/Da$ at $T = 1$ for 1D and 2D CRL geometries for Case 1.

6.4.5. Use of the Parametric Map at Different Conditions

The initial parametric map was obtained for a second-order irreversible reaction with a 1:1 stoichiometry. Eqs. (6.36)-(6.38) show the kinetics of a general reversible reaction where new 8 dimensionless parameters appear: $k_{A,1}/k_{A,-1}$, α, β, γ, κ, (b/a), (d/a) and (e/a) (considering A as the limiting reactant). Adding these new parameters to the previous ones Da, T, C, G_{Rh}, G_h and G_r, a total of 14 dimensionless parameters are present. This implies that n^{14} simulations are required to map all variables, where n is the number of variations for each parameter. For $n = 4$, 268435456 simulations would be necessary to define all possible combinations, which would be extremely time consuming. Accordingly, it is important to derive correlations that would allow the use of the basic parametric map under different kinetics.

$$aA + bB \leftrightarrow dD + eE \tag{6.36}$$

$$r_A = k_{A,-1} \cdot c_D^{\gamma} \cdot c_E^{\kappa} - k_{A,1} \cdot c_A^{\alpha} \cdot c_{B,2}^{\beta} \tag{6.37}$$

$$r_B = \left(\frac{b}{a}\right) \cdot r_A; \quad r_D = -\left(\frac{d}{a}\right) \cdot r_A; \quad r_E = -\left(\frac{e}{a}\right) \cdot r_A \tag{6.38}$$

1D simulations were performed in order to get a simple relationship between the previous parametric map at 1:1 stoichiometry, $\alpha = 1$, $\beta = 1$ and the new one. Here it should be mentioned that as far as reversible reactions with 1:1 stoichiometry are concerned the basic dimensionless parametric map can be applied without any modifications.

6.4.5.1. Reversible Reactions

For reversible reactions rather displaced to the products and low ratio of initial concentration of product to reactant, M, the parametric dimensionless map for irreversible reactions can be used. In the kinetic control region at low conversion, the conversion-time curve for a reversible reaction is very similar to that of an irreversible reaction with reaction constant k_A, equal to the direct reaction constant of the reversible reaction, $k_{A,1}$. For instance, the conversion equation for the reversible reaction represented by Eq. (6.39) is given by Eq. (6.40), where $X_{A,eq}$ is the equilibrium conversion of A. Figure 6.12 represents conversion versus time at $k_{A,1} = 1\ s^{-1}$ when the equilibrium conversion is 100% and 80 %.

$$A \leftrightarrow B \quad r_A = k_{A,-1} \cdot c_{B,2} - k_{A,1} \cdot c_A \tag{6.39}$$

$$X_A = X_{A,eq} \cdot \left(1 - e^{\frac{M+1}{M+X_{A,eq}} \cdot k_{A,1} \cdot t}\right) \tag{6.40}$$

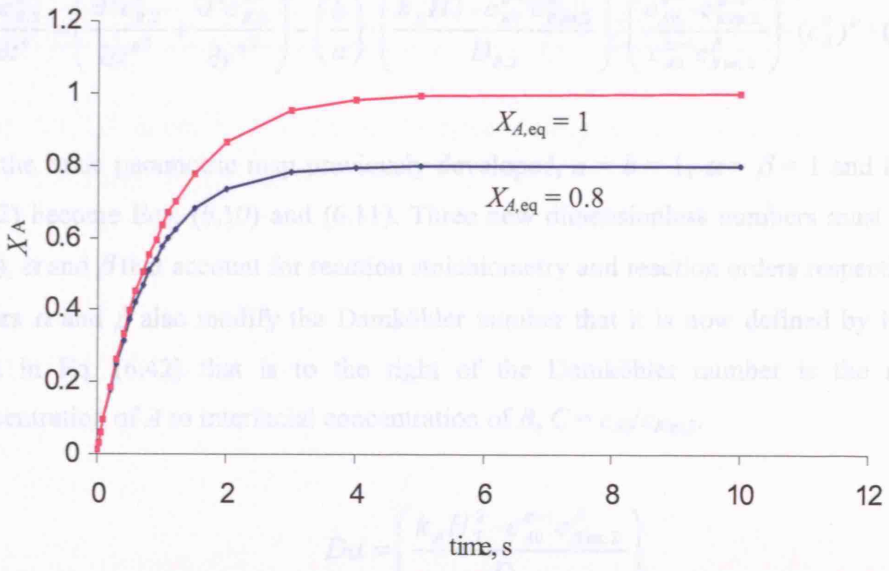

Figure 6.12. Conversion-time for $X_{A,eq}$ = 100 % and $X_{A,eq}$ = 80%. Reaction $A \leftrightarrow B$.

Clearly, the conversions are practically the same up to $X_A = 0.4$. At $X_A = 0.1$ the actual values at $t = 0.1$ are 0.0952 and 0.0940 respectively, which are very close to each other. If the initial ratio M is not zero, this difference can be larger, i.e. for $M = 0.5$, the conversion values are 0.0952 and 0.0872. However the usual case is not to have product at the reaction start and it is also what has been considered in the pseudo-kinetic limit and Femlab simulations so far. As a result, the trial-and-error method explained in section 6.4.3 to move the reaction system to the kinetic control zone can still be used with reversible reactions, using its direct reaction constant $k_{A,1}$ and finding the limiting value of the ratio C from Figure 6.7 or Figure 6.10. Once it is known that the reactor is operating in the kinetic control regime, both reaction constants, $k_{A,1}$ and $k_{A,-1}$ can be recovered adjusting the experimental data to its kinetic equation.

6.4.5.2. Order and Stoichiometry

The above considerations for reversible reactions mean that 5 dimensionless parameters (γ, κ, d/a, e/a and $k_{A,-1}$) do not need to be taken into account and stoichiometry and reaction order are studied for irreversible reactions. Considering Eq. (6.36) for the irreversible reaction, Eqs. (6.3) and (6.4) that define the system are transformed into the dimensionless Eqs. (6.41) and (6.42) using the characteristic dimensions given by Eqs. (6.5)-(6.7).

$$\frac{\partial c_A^{\#}}{\partial t^{\#}} = \left(\frac{D_A}{D_{B,2}}\right)\cdot\left(\frac{\partial^2 c_A^{\#}}{\partial x^{\#2}} + \frac{\partial^2 c_A^{\#}}{\partial y^{\#2}}\right) - \left(\frac{k_A H_T^2 \cdot c_{A0}^{\alpha-1} \cdot c_{B\,\mathrm{int},2}^{\beta}}{D_{B,2}}\right)\cdot (c_A^{\#})^{\alpha} \cdot (c_{B,2}^{\#})^{\beta} \qquad (6.41)$$

$$\frac{\partial c_{B,2}^{\#}}{\partial t^{\#}} = \left(\frac{\partial^2 c_{B,2}^{\#}}{\partial x^{\#2}} + \frac{\partial^2 c_{B,2}^{\#}}{\partial y^{\#2}}\right) - \left(\frac{b}{a}\right)\cdot\left(\frac{k_A H_T^2 \cdot c_{A0}^{\alpha-1} c_{B\,\mathrm{int},2}^{\beta}}{D_{B,2}}\right)\cdot\left(\frac{c_{A0}^{\alpha} \cdot c_{B\,\mathrm{int},2}^{\beta-1}}{c_{A0}^{\alpha-1} c_{B\,\mathrm{int},2}^{\beta}}\right)\cdot (c_A^{\#})^{\alpha} \cdot (c_{B,2}^{\#})^{\beta} \qquad (6.42)$$

For the basic parametric map previously developed, $a = b = 1$, $\alpha = \beta = 1$ and Eqs. (6.41) and (6.42) become Eqs. (6.10) and (6.11). Three new dimensionless numbers must be considered, (b/a), α and β that account for reaction stoichiometry and reaction orders respectively. Reaction orders α and β also modify the Damköhler number that it is now defined by Eq. (6.43). The term in Eq. (6.42) that is to the right of the Damköhler number is the ratio of initial concentration of A to interfacial concentration of B, $C = c_{A0}/c_{B\mathrm{int},2}$.

$$Da = \left(\frac{k_A H_T^2 \cdot c_{A0}^{\alpha-1} c_{B\,\mathrm{int},2}^{\beta}}{D_{B,2}}\right) \qquad (6.43)$$

Therefore, in the following analysis, the ratio C necessary to move a reaction system with varying stoichiometry and reaction order to the kinetic control regime is obtained where Da is calculated via Eq. (6.43).

6.4.5.2.1. Stoichiometry

Stoichiometry does not modify the kinetic and pseudo-kinetic limits as these limits are based on the limiting reactant conversion (component A) and $c^{\#}_{B,2}$ is constant to 1 in the kinetic limit and defined by the mass transfer equation in the pseudo-kinetic limit. Next, a simple case given by Eq. (6.44) is analysed. Although the a:b stoichiometry is 1:0.5 the reaction is not considered to be an elemental reaction (where stoichiometry defines reaction mechanism and therefore reaction orders) so that the only effect analysed is due to stoichiometry. Table 6.3 and Figure 6.13 show results for the parametric map with $T = 1$.

$$A + 0.5B \rightarrow AB \quad r_A = -k_A \cdot c_A \cdot c_B \quad r_B = (1/2) \cdot r_A \tag{6.44}$$

	Kinetic limit				Pseudo-kinetic Limit			
Da	***Err. %***	***C*, 99%**	***C*, 98%**	***C*, 95%**	***Err*, %**	***C*, 99%**	***C*, 98%**	***C*, 95%**
0.00001	0.05	6456.17	13244.79	33610.63	0	Solution from Kinetic Limit		
0.0001	0.08	627.86	1337.63	3466.96	0			
0.001	0.35	45.91	116.69	329.02	0			
0.01	3.05	No	No	14.55	0	7.13	14.52	36.7
0.1	28.23	No	No	No	0.02	1.03	2.19	5.53
1	74.77	No	No	No	0.96	0.016	0.446	1.736
10					6.69	No	No	No

Table 6.3. 1D results of Da and C for the dimensionless parametric map at $T = 1$, stoichiometry 1:0.5, $\alpha = 1$ and $\beta = 1$. Case 1.

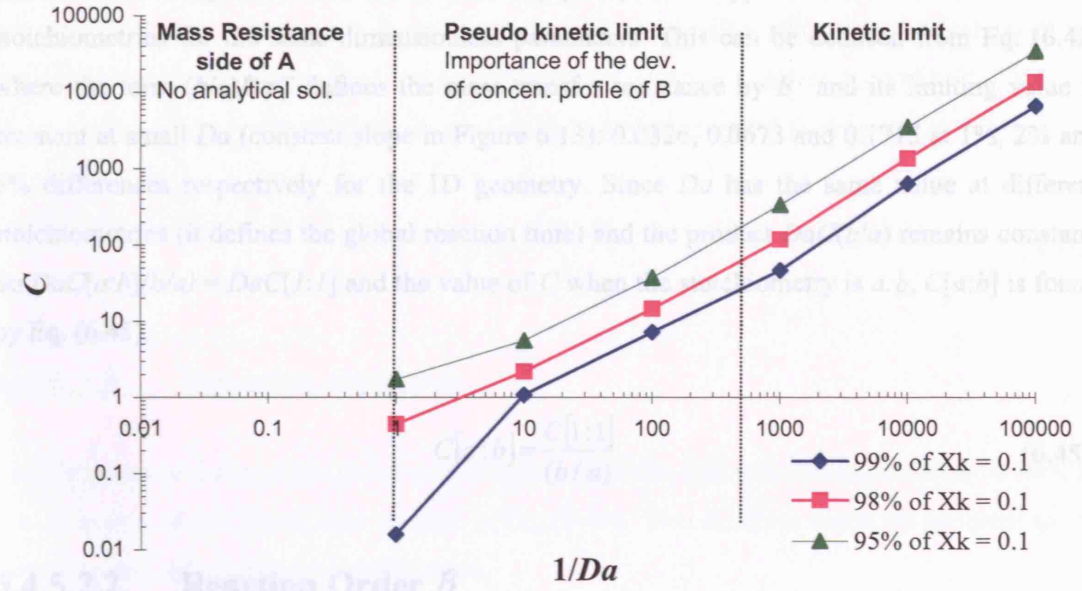

Figure 6.13. 1D dimensionless parametric map of C vs. $1/Da$. T = 1, stoichiometry 1:0.5, $\alpha = 1$ and $\beta = 1$. Case 1.

As the kinetic and pseudo-kinetic limits do not change, the residual errors between the Femlab simulations and the analytical solutions in Table 6.3 are the same as previously. Similar results to those shown in Table 6.3 are obtained by multiplying the ratio C for a stoichiometry 1:1 by 2 since now the reaction rate for B is half the previous one. Table 6.4 compares the results shown in Table 6.3 and those estimated by multiplying the ratio C at 1:1 by 2.

	C 99 %	C, 99% Estimated	Error %	C 98 %	C, 98% Estimated	Error %	C 95 %	C 95% Estimated	Error %
Kinetic Limit	6456.2	6510.0	-0.8	13244.8	13456.6	-1.6	33610.6	34294.0	-2.0
	627.9	634.4	-1.0	1337.6	1326.9	0.8	3467.0	3404.3	1.8
	45.9	45.2	1.5	116.7	114.9	1.6	329.0	323.9	1.6
Pseudo-kinetic Limit	7.13	7.16	-0.4	14.52	14.39	0.9	36.7	36.1	1.7
	1.07	1.10	-2.6	2.19	2.24	-2.3	5.53	5.68	-2.7
	0.016	0.017	-8.9	0.446	0.446	0.0	1.74	1.74	0.0

Table 6.4. Comparison between the C values obtained via simulations and those calculated as $2 \cdot C(1{:}1)$ for a reaction with $(a/b) = 2$. Case 1.

The results are very similar and indicate that Eq. (6.45) can be applied to calculate C at different stoichiometries for the same dimensionless parameters. This can be deduced from Eq. (6.42) where the term $(b/a)DaC$ defines the mass transfer resistance by B and its limiting value is constant at small Da (constant slope in Figure 6.13): 0.0326, 0.0673 and 0.1715 at 1%, 2% and 5% differences respectively for the 1D geometry. Since Da has the same value at different stoichiometries (it defines the global reaction time) and the product $DaC(b/a)$ remains constant. So $DaC[a:b](b/a) = DaC[1:1]$ and the value of C when the stoichiometry is $a:b$, $C[a:b]$ is found by Eq. (6.45).

$$C[a:b]=\frac{C[1:1]}{(b/a)} \tag{6.45}$$

6.4.5.2.2. Reaction Order β

The reaction order β does not modify the kinetic limit since $c^{\#}_{B,2} = 1$ but it modifies the pseudo-kinetic limit where C changes with height inside the liquid phase. In this case, a new pseudo-kinetic limit is obtained via Femlab simulations. The next analysis, therefore, only applies to the kinetic zone and it is important to consider than when the values of β and α change, the definition of the Damköhler number also changes according to Eq. (6.43). Two different values of β, $\beta = 2$ and $\beta = 3$ are tried to find some relationship between the C values at $\beta = 1$ and those for different β, while keeping the stoichiometry constant to 1:1 and the order $\alpha = 1$. Results are shown in Table 6.5 and are compared with results estimated by dividing the C values at $\beta = 1$ (see Table 6.1) by the new value of β.

	Reaction order, $\alpha = 1$, $\beta = 2$ and Stoichiometry 1:1								
Da	***C* 99%**	***C*, 99% Estimated**	**Error %**	***C* 98%**	***C*, 98% Estimated**	**Error %**	***C* 95%**	***C*, 95% Estimated**	**Error %**
0.00001	1666.9	1627.5	2.36	3496.9	3364.2	3.80	8987.0	8573.5	4.60
0.001	9.25	11.30	-22.16	27.58	28.72	-4.13	82.56	80.97	1.93
	Reaction order, $\alpha = 1$, $\beta = 3$ and Stoichiometry 1:1								
Da	***C* 99%**	***C*, 99% Estimated**	**Error %**	***C* 98%**	***C*, 98% Estimated**	**Error %**	***C* 95%**	**C, 95% Estimated**	**Error, %**
0.00001	1079.8	1085.0	-0.5	2332.5	2242.8	3.8	6090.5	5715.7	6.2

Table 6.5. Comparison between the C values obtained via simulations and with those obtained by dividing C at $\beta = 1$ by the new β. Case 1.

The error is slightly larger than that from Eq. (6.45) for different stoichiometry although considering that the experiments should be carried out at a smaller value than the limiting C, the error will not significantly affect the precision of the reaction constant k_A retrieved. Thus Eq. (6.46) can be applied in the kinetic zone to calculate the parameter C at different β.

$$C[\beta] = \frac{C[\beta = 1]}{\beta} \tag{6.46}$$

6.4.5.2.3. Reaction Order α

The variation of the reaction order α modifies the kinetic and pseudo-kinetic limits as well as the definition of the Damköhler number in Eq. (6.43). Two different cases are analysed in the kinetic region, using the new kinetic limits.

I. Stoichiometry 1:1, $\beta = 1$ and $\alpha = 2$.

II. Stoichiometry 1:1, $\beta = 1$ and $\alpha = 3$.

The kinetic limits for these cases are given by Eqs. (6.47) and (6.48) and were checked via Femlab simulations with $C \rightarrow 0$.

Case **I**

$$X_{A,K} = \frac{Da \cdot t^{\#}}{1 + Da \cdot t^{\#}} \tag{6.47}$$

Case **II**

$$X_{A,K} = \frac{(2 + 4Da \cdot t^{\#}) - \sqrt{(2 + 4Da \cdot t^{\#})^2 - 8Da \cdot t^{\#} \cdot (1 + 2Da \cdot t^{\#})}}{2 + 4Da \cdot t^{\#}} \tag{6.48}$$

Table 6.6 shows the results for C at Da = 0.00001. The results are not related with the values of C at 1:1, $\alpha = 1$ and $\beta = 1$ although the order of magnitude is similar. In this case the ratio C increases as the reaction order α increases.

	$\alpha = 1$			$\alpha = 2$			$\alpha = 3$		
Da	***C*, 99%**	***C*, 98%**	***C*, 95%**	***C*, 99%**	***C*, 99%**	***C*, 99%**	***C*, 99%**	***C*, 99%**	***C*, 99%**
0.00001	3255.0	6728.3	17147	3447.9	7396.2	19241.0	4294.7	8644.7	21694.8

Table 6.6. 1D results of C for Da = 0.00001 as a function of the reaction order $\alpha = 1$, 2 and 3. Case 1.

6.4.5.2.4. Combination of Stoichiometry and Reaction Order

Two cases shown in Eqs. (6.49) and (6.50) are considered. The expected C values are estimated by combining Eqs. (6.45) and (6.46). Good agreement with Femlab simulations was found. Table 6.7 shows that the estimation error increases as difference between the actual and the kinetic limit conversion increases.

$$\text{Elemental}\quad A+2B \Rightarrow AB \quad r_A = -k_A c_A c_{B,2}^2 \qquad \text{Rule}: C = \frac{C[1:1,\beta=1]}{(b/a)\cdot\beta} = \frac{C[1:1,\beta=1]}{4} \tag{6.49}$$

$$\text{No Elemental}\quad A+2B \Rightarrow AB \quad r_A = -k_A c_A c_{B,2}^3 \qquad \text{Rule}: C = \frac{C[1:1,\beta=1]}{(b/a)\cdot\beta} = \frac{C[1:1,\beta=1]}{6} \tag{6.50}$$

	Stoichiometry 1:2, α = 1 and β = 2								
Da	***C*, 99%**	***C*** **Estimated**	**Error %**	***C*, 98%**	***C*, 98%** **Estimated**	**Error %**	***C*, 95%**	***C*, 95%** **Estimated**	**Error %**
0.00001	819.95	813.8	0.76	1735.92	1682.1	3.10	4483.80	4286.8	4.39
	Stoichiometry 1:2, α = 1 and β = 3								
Da	***C*, 99%**	***C*, 99%** **Estimated**	**Error %**	***C*, 98%**	***C*, 98%** **Estimated**	**Error %**	***C*, 95%**	***C*, 95%** **Estimated**	**Error %**
0.00001	538.90	542.5	-0.7	1149.60	1121.4	2.5	2981.69	2857.8	4.2

Table 6.7. Comparison of 1D results of C (obtained via Femlab or estimated via Eqs. (6.45) and (6.46)) for Da = 0.00001 in two different cases a) stoichiometry 1:2, α = 1 and β = 2 and b) Stoichiometry 1:2, α = 1 and β = 3. Case 1.

6.4.6. Recovery of the Kinetics from Experimental Data

A trial-and-error method is used to extract the reaction rate k_A and the values of the reaction orders α and β, from the dimensionless parametric maps. In the reaction rate k_A is known, a trial-and-error procedure is not necessary in order to know if a system operates under kinetic control.

First, a reaction order α is assumed because the form of the kinetic conversion equation only depends on it. The reaction order β is chosen in a conservative way to make Da small so that the limiting C to operate in the kinetic control regime is larger. The reaction rate k_A is also assumed, which allows Da to be calculated and combined with the parametric map to give the limiting

value of C. Experiments are carried out with this C to obtain a (X_A vs. $t^{\#}$) graph. If the form of the actual conversion curve (X_A vs. $t^{\#}$) is the same as that from the kinetic conversion equation ($X_{A,K}$ vs. $t^{\#}$) (o pseudo-kinetic conversion), the value of α assumed is correct. If the experimental conversions are lower than those obtained using the kinetic (or pseudo-kinetic) equation with the assumed values of α, β and Da, the system is under kinetic control. If not then another higher reaction rate must be chosen to recalculate Da and the limiting C. To calculate the values of k_A and β, another run of experiments at different interfacial concentration of B $c_{B\text{int},2}$ but identical initial concentration of A c_{A0} is needed. As the reaction constant k_A is independent of concentrations, Eq. (6.51) can be used to calculate the reaction order β. The reaction rate k_A can be found from one of the two Da at different interfacial concentration of B using the value of β calculated.

$$\beta = \frac{\log[(Da)_{C1}/(Da)_{C2}]}{\log[(c_{B\text{int},2})_{C1}/(c_{B\text{int},2})_{C2}]} \tag{6.51}$$

Another issue to be considered is to know what kinetics are too fast for the mesh microreactor to operate under kinetic control due to the appearance of mass transfer resistance. From the parametric map, it is possible to define what is the faster reaction rate for a specific kinetics in a given mesh microreactor geometry in order to operate under kinetic control. That is, if the reaction is very fast, Da is large and even if C tends to zero the kinetic control regime cannot be reached, because mass transfer resistance by A has developed. The value of Da for a specific kinetic can only be reduced by decreasing the height of the channel, H_T and the interfacial concentration of B, $c_{B,\text{int},2}$, which depends on the solubility and the partial pressure of the gas phase (there is a limiting pressure that the reaction can be accomplished). The *pseudo-kinetic limit* explained in section 6.4.3 allows the recovery of k_A values via a trial-and-error method when operating at high Damkhöler numbers ($Da > 0.001$).

6.4.7. Error Estimation for the Recovered Value of k_A

The maximum error of the recovered value of k_A needs to be estimated, considering that when working in the kinetic control regime of the parametric map, the actual conversion can still be 1, 2 and 5 % different from the kinetic conversion, when the kinetic conversion is 0.1 (10%). Eq. (6.24) represents the kinetic conversion for a second order irreversible reaction. The recovered value of k_A will be the kinetic value, $k_{A,K}$, multiplied by the error, according to Eq. (6.52),

$$k_A = k_{A,K} \cdot \frac{(100 - err)}{100} \tag{6.52}$$

where *err* is the percentage error. Assuming that the actual and kinetic conversion curves have a similar form given by Eq. (6.24), Eq. (6.53) is written.

$$\frac{X_{A,K} - 1}{X_A - 1} = \frac{e^{-Da \cdot t^{\#}}}{e^{-Da \cdot \frac{(100-err)}{100} \cdot t^{\#}}} \tag{6.53}$$

where $X_{A,K}$ is the kinetic conversion (equal to 0.1), X_A is the actual conversion used for the definition of total kinetic control, 0.099, 0.098 or 0.095 according to the percentage error chosen in the conversion (1, 2 or 5 %). The product $Dat^{\#}$, can be expressed by Eq. (6.54).

$$Dat^{\#} = -\ln(1 - X_{A,K}) \tag{6.54}$$

Substituting Eq. (6.54) into Eq. (6.53) and taking natural logarithms at both sides, Eq. (6.55) is obtained, which gives the percentage error for the estimated value of k_A.

$$err = 100 \cdot \frac{\ln\left((X_{A,K} - 1)/(X_A - 1)\right)}{\ln\left(1 - X_{A,K}\right)} \tag{6.55}$$

This maximum error is 1.05%, 2.06% and 5.26% for conversion differences of 1%, 2% and 5% when $X_{A,K}$ = 0.1 and it does not depend on *Da*. For the case of the pseudo-kinetic limit and following a similar analysis, the same Eq. (6.55) for *err* is obtained.

6.5. Kinetic Control for Homogeneous Catalysis. Case 2: Constant Concentration of Component A in Phase 2

6.5.1. Dimensionless Analysis: Irreversible Reaction

In this case, where both phases are still, *A* is the component in excess with respect to the initial concentration of *B* in the liquid Phase 1 ($Co = (\nu_2 c_{A0})/(\nu_1 c_{B0,1}) > 100$) and conversion of *B* depends on consumption of *B* while *A* remains constant (no mass transfer resistance by *A*). The same characteristic dimensions and dimensionless variables apply. As $c_{Bint,2}$ changes with time, its maximum value (assuming complete distribution between phases), given by Eq. (6.56), is

used as characteristic concentration for substance B, $c_{Bint,2,max}$, so that Da and C are solved for this value. The dimensionless equations that define the system in this case are Eqs. (6.57) for Phase 1 and Eqs. (6.58) and (6.59) for Phase 2. The reaction rate of B in Phase 2 is defined as $-r_B = k_B c_A^{\alpha} c_{B,2}^{\beta}$ since B is the limiting reactant. Therefore, now Da is based on k_B rather than k_A. T_B is the ratio of diffusivity of B in Phase 1 to that in Phase 2.

$$c_{B\,\mathrm{int},2} = \frac{c_{B0,1} v_1}{(v_2 + v_1 P)} \tag{6.56}$$

$$\frac{\partial c^{\#}_{B,1}}{\partial t^{\#}} = T_B \left(\frac{\partial^2 c^{\#}_{B,1}}{\partial x^{\#2}} + \frac{\partial^2 c^{\#}_{B,1}}{\partial y^{\#2}} \right) \tag{6.57}$$

$$\frac{\partial c^{\#}_{A}}{\partial t^{\#}} = T \left(\frac{\partial^2 c^{\#}_{A}}{\partial x^{\#2}} + \frac{\partial^2 c^{\#}_{A}}{\partial y^{\#2}} \right) - Da \left(\frac{a}{b} \right) \left(c^{\#}_{A} \right)^{\alpha} \left(c^{\#}_{B,2} \right)^{\beta} \tag{6.58}$$

$$\frac{\partial c^{\#}_{B,2}}{\partial t^{\#}} = \left(\frac{\partial^2 c^{\#}_{B,2}}{\partial x^{\#2}} + \frac{\partial^2 c^{\#}_{B,2}}{\partial y^{\#2}} \right) - DaC (c^{\#}_{A})^{\alpha} (c^{\#}_{B,2})^{\beta} \tag{6.59}$$

The initial conditions are $c^{\#}_{B0,1} = (v_2+v_1P)/v_1$ 1, $c^{\#}_{A0} = 1$ in Phase and $c^{\#}_{B0,2} = 0$ in Phase 2. Again no perpendicular flux exists at the symmetry planes and solid wall boundaries, while at the interface the ratio of concentrations of B in the two phases is constant and equal to P and the flux leaving Phase 1 is equal to that entering Phase 2, Eq. (6.60).

$$(\mathrm{Flux})_1 = (\mathrm{Flux})_2 \text{ on the interface} \Rightarrow \left(T_B \nabla c^{\#}_{B} \right)_1 = \left(\nabla c^{\#}_{B} \right)_2 \tag{6.60}$$

6.5.2. Kinetic Conversion of B, $X_{B,K}$

As in the previous case, a kinetic conversion limit is required. Assuming that there is no mass transfer resistance by B in both phases, Eq. (6.61) gives the variation of the interfacial concentration of B in Phase 2 with the global conversion (based on the initial concentration of B in Phase 1).

$$c_{B\,\mathrm{int},2} = \frac{c_{B0,1} v_1 (1 - X_{B,K})}{(v_2 + v_1 P)} \tag{6.61}$$

The initial amount of moles of B, $m_{B0,1}$, is $c_{B0,1}v_1$ and the amount of moles at any time, m_B, is, $c_{B0,1}v_1(1\text{-}X_{B,K})$. For a system with reaction orders $\alpha = 1$ and $\beta = 1$, the decrease on moles of B is $-dm_B/dt = k_B c_A c_{Bint,2} v_2$. After substituting in this expression the values for m_B and $c_{Bint,2}$ and making it dimensionless, Eq. (6.62) is obtained, for constant c_A. This represents the kinetic limit to compare with the simulations that consider mass transfer together with chemical reaction. Eq. (6.62) is similar to Eq. (6.24) although now $DaCv_2/(v_2+v_1P)$, rather than Da, defines the global reaction time with respect to the conversion of B.

$$X_{B,K} = 1 - \exp\left(-\frac{DaCv_2 t^{\#}}{(v_2 + v_1 P)}\right) \tag{6.62}$$

6.5.3. Simulations Results vs. Kinetic limit for a 2D CRL Geometry

Figure 6.14 shows the dimensionless parametric map in Case 2 for the 2D CRL geometry and kinetic limit, obtained after following the same procedure as in Case 1. The part of the curve where the slope is constant corresponds to a constant value of DaC: 0.0248, 0.0495 and 0.1237 for 1%, 2% and 5% differences from the kinetic conversion. The limiting DaC starts decreasing at $DaCv_2/(v_2+v_1P)$~0.001 where the time for B to establish its concentration profile becomes comparable to the global reaction time and mass transfer resistance by B is substantial. In Figure 6.14, $DaCv_2/(v_2+v_1P)$ can only increase up to 0.0036, 0.0072 and 0.018 for deviations of 1 %, 2 % and 5 % respectively of the actual from the kinetic conversion when $P \to 0$ ($v_2/(v_2+v_1P) = 1$).

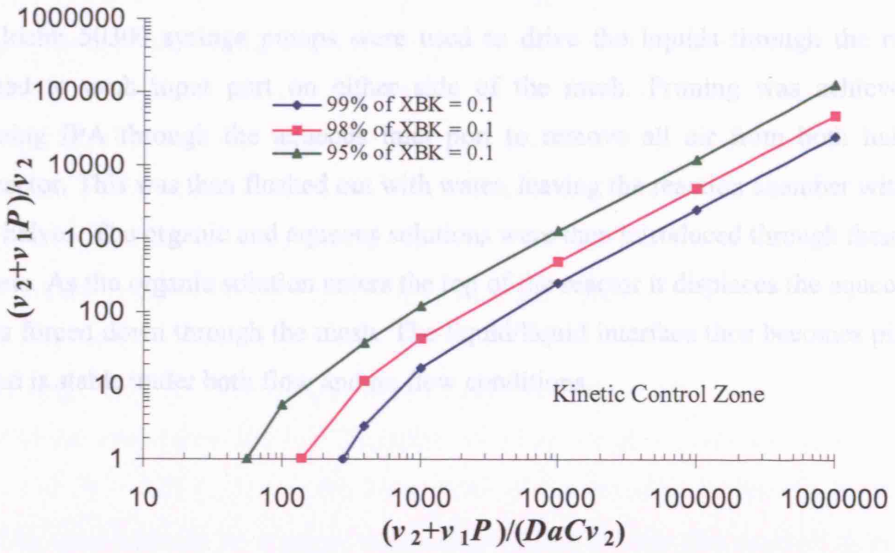

Figure 6.14. 2D dimensionless parametric map at $T = 1$. CRL geometry with = 0.03333, $G_h = 0.9524$ and $G_r = 0.5714$ for Case 2.

Mass transfer resistance by A appears at Da larger than $0.15T$, which is beyond the limits of the parametric map. The minimum value for T is 0.1 and the limiting DaC is 0.025 (for 1% difference from the kinetic conversion), however as A is in excess, $Co \geq 100$, which implies a limiting Da of the order of or smaller than 0.00025, that is always smaller than $0.15T$. Mass transfer resistance by B in Phase 1 appears after the mass transfer resistance by B in Phase 2 if $T_B > 1$ and $P > 1$. Even if $T_B = 0.1$ and $P > 10$ the mass transfer resistance by B in Phase 2 appears before in Phase 1.

If the reaction has stoichiometry different than 1:1, the limiting values do not change because stoichiometry only affects component A, Eq. (6.58). Different reaction orders α can be considered in a similar way as reaction order β in Case 1 (in Case 2 $c^{\#}_A = 1$) and Da changes with the reaction orders (see Eq. (6.43)). However the reaction order α does not modify the parametric map in Figure 6.14, as α can only affect the mass transfer resistance by A (power of $c^{\#}_A$). To analyse different reaction orders β, a new kinetic limit, similar to Eq. (6.62), is needed.

6.6. Experimental Results for Parametric Map in Case 2

Experimental results on the hydrolysis of fluorescein diacetate, FDA ($C_{25}H_{17}ClO_7$), (liquid-liquid reaction), obtained in the mesh microreactor by CRL (sections 6.6.1 and 6.6.2), were compared with the parametric maps to establish whether reaction kinetics could be extracted.

6.6.1. Experimental Set-up

Two Kloehn 50300 syringe pumps were used to drive the liquids through the reactor, one connected to each input port on either side of the mesh. Priming was achieved by first introducing IPA through the aqueous inlet port to remove all air from both halves of the microreactor. This was then flushed out with water, leaving the reaction chamber with the water in both halves. The organic and aqueous solutions were then introduced through their respective inlet ports. As the organic solution enters the top of the reactor it displaces the aqueous solution which is forced down through the mesh. The liquid/liquid interface then becomes pinned at the mesh and is stable under both flow and no flow conditions.

6.6.2. Materials and Methods

For the reaction experiments, a 300 μM fluorescein diacetate solution in toluene (Phase 1) was used as the organic phase while the aqueous phase (Phase 2) was 0.1 M NaOH. The parametric map for Case 2 can be used where reactant A (NaOH) is in excess. When in contact with an alkaline aqueous solution, the fluorescein diacetate undergoes a hydrolysis reaction and fluorescein is produced in the aqueous solution. Measuring the fluorescence or light absorption of the aqueous sample at the relevant wavelength produces a measure of the extent of the reaction.

To perform a reaction, the microreactor was primed and the required temperature was set on the control box. After the temperature had stabilised, fresh reagents were flushed through the device and all flow was halted for the required hold time, before extracting the product. To ensure that all product was collected, allowing for mixing with unreacted aqueous solution in the tubing, a total of 1 mL of solution was extracted. Thus the resulting extracted sample had a known dilution of 10%, assuming a reactor volume of 100 μL. The absorption of the sample at 491 nm was then measured on a UV/vis Spectrophotometer (Cecil CE7200).

6.6.3. Analysis of Experimental Results with Dimensionless Parametric Map

Diffusivity of FDA in toluene and water were estimated using the Wilke-Chang method (Sinnott, 1993) obtaining $D_{B,1} = 1.01 \cdot 10^{-9}$ m^2/s and $D_{B,2} = 3.93 \cdot 10^{-10}$ m^2/s respectively, that give $T_B = 2.57$, Reid et al. (1998). The partition coefficient of FDA in toluene/water, P, was also estimated by the solvation descriptor method to be $P = 5248$ (Abraham et al., 2002). This large value for P together with the value of T_B ensures that the mass transfer resistance by B appears first in Phase 2. The conversion times for the hydrolysis of FDA were non-dimensionalised by Eq. (6.5) using the above value for $D_{B,2}$ and $H_T = 105 \cdot 10^{-6}$ m. The results at 20 °C shown in Figure 6.15 are fitted to Eq. (6.62) assuming that the reaction is in kinetic control and $\beta = 1$, obtaining the value $(\nu_2+\nu_1 P)/(DaC\nu_2) = 23810$. For $P = 5248$, the ratio $(\nu_2+\nu_1 P)/\nu_2$ is 5165.2 which is larger than the limiting one from Figure 6.14 (about 600 for a tolerance of 1 % and about 3000 for a tolerance of 5 %). Therefore, although the global reaction times are very large (64 hours at $X_B = 0.283$), due to the large value of the partition coefficient P, the system is affected by mass transfer. At a higher temperature (40°C) the reaction constant k_B increases and the system will not be closer to the kinetic limit. To bring the system under kinetic control, DaC

would have to be reduced, either by decreasing the diffusion distance H_T, or the concentration of A (while keeping an excess of A, Co >100), or by increasing the diffusivity of B in Phase 2, $D_{B,2}$.

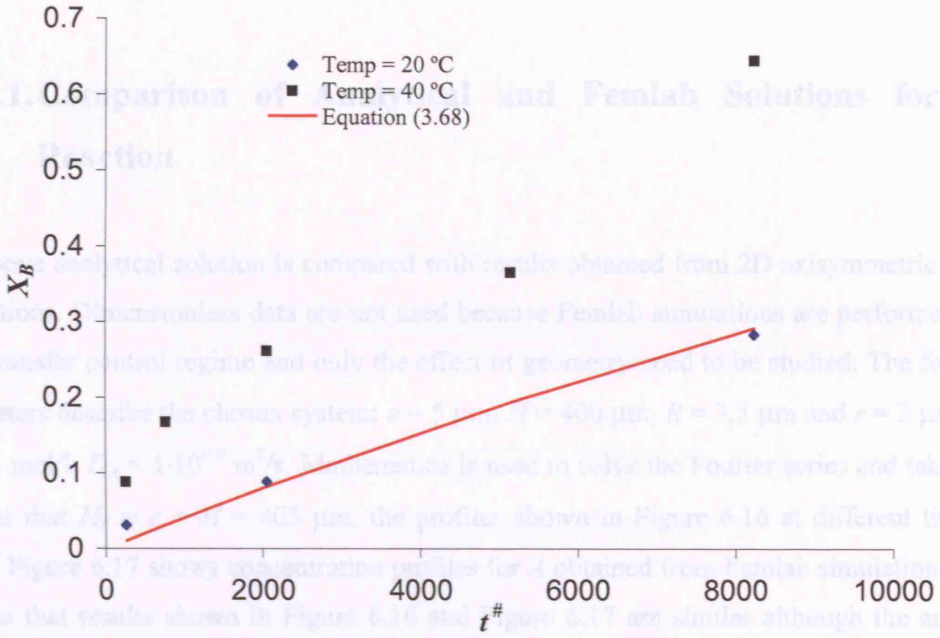

Figure 6.15. (X_B vs $t^{\#}$) curve for the hydrolysis of FDA.

6.7. Mass Transfer Control – Fast Reaction

This section analyses the case of fast reaction when the reactor operates in the mass transfer control regime. A 1-D analytical model is developed and the results are compared with the 2D axisymmetric Femlab simulations to assess the validity of this approximation.

6.7.1. No Diffusion of Gaseous Component into Liquid Phase ($D_B << D_A$ or $b > a$)

The previously analysed system is considered assuming that the component B does not penetrate into the liquid Phase 2. This happens when the reaction is fast and $D_B << D_A$ or $b > a$ (i.e. larger consumption of B than A). The final solution for the concentration profile of A is given by Eq. (6.63) (see Appendix 6A). This equation can be directly deduced from a more general solution given by Carslaw and Jaeger (1986). Although the solution is an infinite series on n, it usually gives close results to the solution at $n \rightarrow \infty$ when n is small.

$$c_A(y,t) = \frac{2}{H_T} \cdot c_{A0} \cdot \sum_{n=0}^{n=\infty} \left[\sin\left(\frac{(2n+1)\pi y}{2H_T} \right) \cdot e^{-D_A \left(\frac{(2n+1)\pi}{2H_T} \right)^2 t} \cdot \frac{2H_T}{(2n+1)\pi} \right] \qquad (6.63)$$

6.7.1.1. Comparison of Analytical and Femlab Solutions for Fast Reaction

The above analytical solution is compared with results obtained from 2D axisymmetric Femlab simulations. Dimensionless data are not used because Femlab simulations are performed in the mass transfer control regime and only the effect of geometry need to be studied. The following parameters describe the chosen system: e = 5 μm, H = 400 μm, R = 3.5 μm and r = 2 μm, c_{A0} = 0.2401 mol/l, $D_A = 1 \cdot 10^{-10}$ m^2/s. Mathematica is used to solve the Fourier series and taking into account that $H_T = e + H$ = 405 μm, the profiles shown in Figure 6.16 at different times are found. Figure 6.17 shows concentration profiles for A obtained from Femlab simulations. It can be seen that results shown in Figure 6.16 and Figure 6.17 are similar although the analytical solution does not consider the geometry of the pore and the fact that B penetrates some microns into the liquid phase.

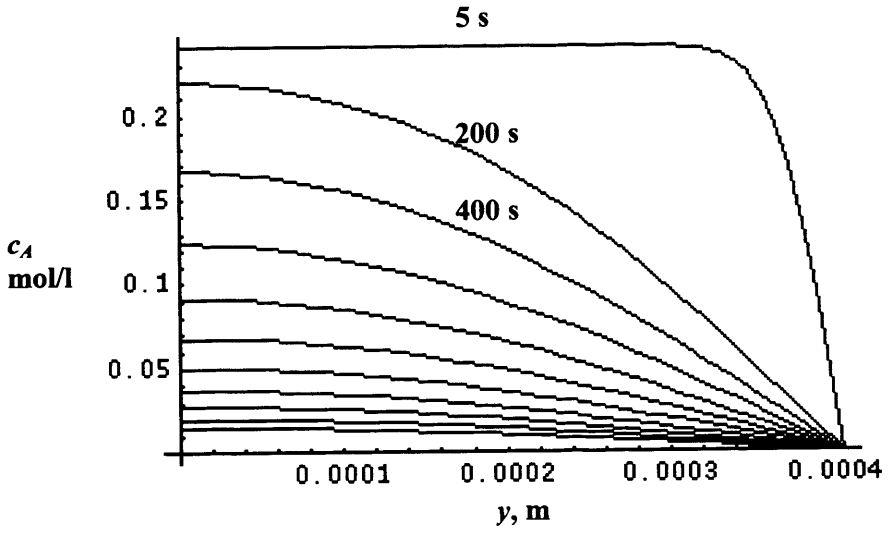

Figure 6.16. Concentration profile of A obtained by analytical solution (Eq. (6.63)). t_f = 2000 s, Δt = 200 s. System properties e = 5 μm, H = 400 μm, R = 3.5 μm and r = 2 μm, c_{A0} = 0.2401 mol/l and $D_A = 1 \cdot 10^{-10}$ m^2/s.

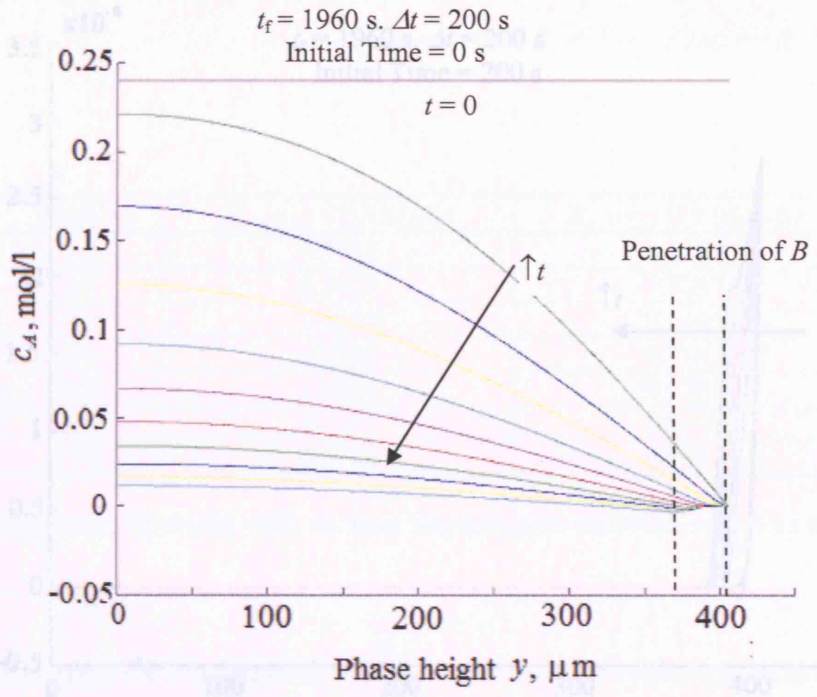

Figure 6.17. Concentration profile of A obtained from Femlab. t_f = 1960 s, Δt = 200 s. System properties e = 5 µm, H = 400 µm, R = 3.5 µm and r = 2 µm, c_{A0} = 0.2401 mol/l and $D_A = 1 \cdot 10^{-10}$ m^2/s.

The time for 90 % conversion of A is calculated by integrating the concentration profile to obtain 1390 s and 1306 s for the analytical and femlab solutions respectively. Substance B penetrates into the liquid phase ~25 µm where substance A is not present (reaction is instantaneous) as it can be seen in Figure 6.17 and Figure 6.18. If the analytical solution is applied to a length of 380 µm (total diffusion distance minus the distance that B has penetrated into the liquid phase), the time required for 90 % conversion of A is t = 1222 s. As the penetration of B is gradual, an average value of the two analytical solutions gives a closer result (and in this case the same) to the Femlab simulation.

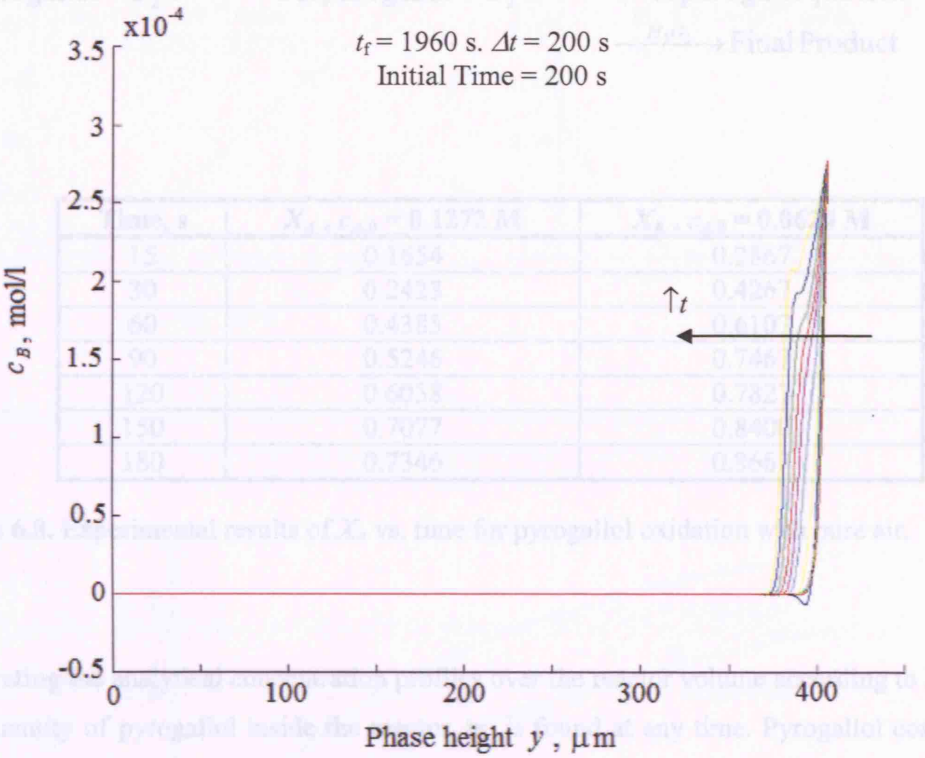

Figure 6.18. Concentration profile of *B*. Final time 1960 s, interval 200 s.

As the mesh thickness increases, the difference between the 1D analytical solution and the Femlab results increases. For a mesh thickness of e = 40 μm, channel height of H = 400 μm and penetration distance for *B* of 25 μm, the time for 90 % conversion of *B* is 1765 s and 1548 s ((1636+1460)/2) for the Femlab and analytical solutions respectively. In general, the analytical 1D solution is a good approximation for large open areas ($G_r \rightarrow 1$ and small mesh thickness ($G_h \rightarrow 1$). The solution is improved by considering the penetration of *B* into the liquid phase.

6.7.1.2. Fitting of Diffusivity to Experimental Data of *X* vs. *t*

Pyrogallol oxidation (see Eq. (6.64)) is assumed to be a fast reaction. Central Research Laboratories has carried out this reaction in a mesh microreactor with e = 5 μm, H = 100 μm, R = 3.5 μm and r = 2 μm. The gas phase was pure air (21 % oxygen in gaseous phase) and was flowing on top of the mesh. The phase underneath the mesh was filled with the liquid phase in a batch mode. Table 6.8 shows the conversion of pyrogallol (Component *A*) versus time for two different initial concentrations of pyrogallol c_{A0}.

$$\text{Pyrogallol} + O_2 \xleftarrow{OH^-} \text{Purpurogallin} + O_2 \xleftarrow{OH^-} \textit{Purpurogalloquinone} \xrightarrow{H_2O_2} \text{Final Product} \qquad (6.64)$$

Time, s	X_A, $c_{A,0}$ = 0.1272 M	X_A, $c_{A,0}$ = 0.0624 M
15	0.1654	0.2867
30	0.2423	0.4267
60	0.4385	0.6107
90	0.5246	0.7467
120	0.6038	0.7827
150	0.7077	0.8400
180	0.7346	0.8667

Table 6.8. Experimental results of X_A vs. time for pyrogallol oxidation with pure air.

Integrating the analytical concentration profiles over the reactor volume according to Eq. (6.18), the quantity of pyrogallol inside the reactor, *m*, is found at any time. Pyrogallol conversion is then calculated from Eq. (6.19). The sample variance between experimental and theoretical conversions given by Eq. (6.65) is used as an objective function to minimise so that predictions fit the experimental data. The only adjustable parameter is the pyrogallol diffusivity, which will indicate whether there is kinetic resistance. The standard deviation *S* is the square root of the sample variance S^2.

$$S^2 = \frac{1}{N} \cdot \sum_{i=1}^{N} \left(X_A^{\text{Exp}} - X_A^{\text{Th}} \right)^2 \qquad (6.65)$$

The sample variance is calculated at different diffusivities, D_A (Figure 6.19); the value of D_A at a minimum value of S^2 corresponds to the best fit between prediction and experimental data. Figure 6.20 compares the predicted and experimental conversions for the fitted diffusivity for both initial concentrations of pyrogallol.

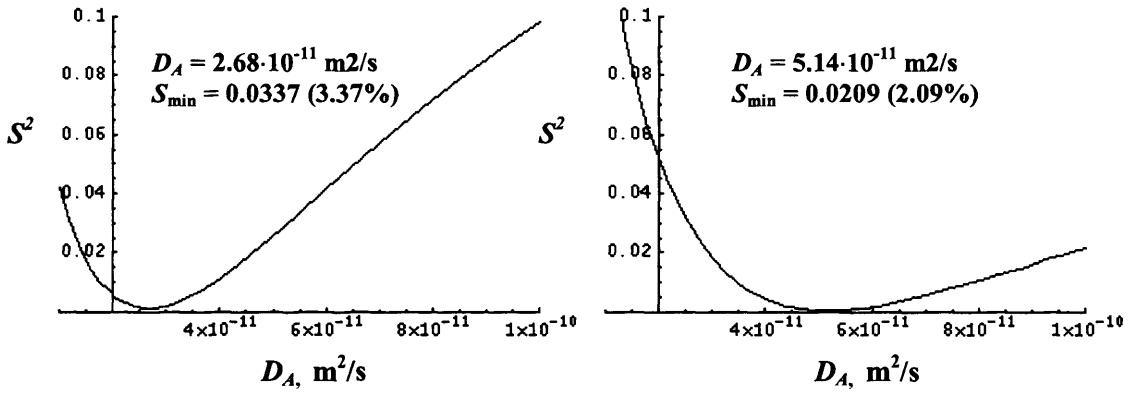

Figure 6.19. Fitting of the diffusivity to the 1D analytical solution for fast reaction.

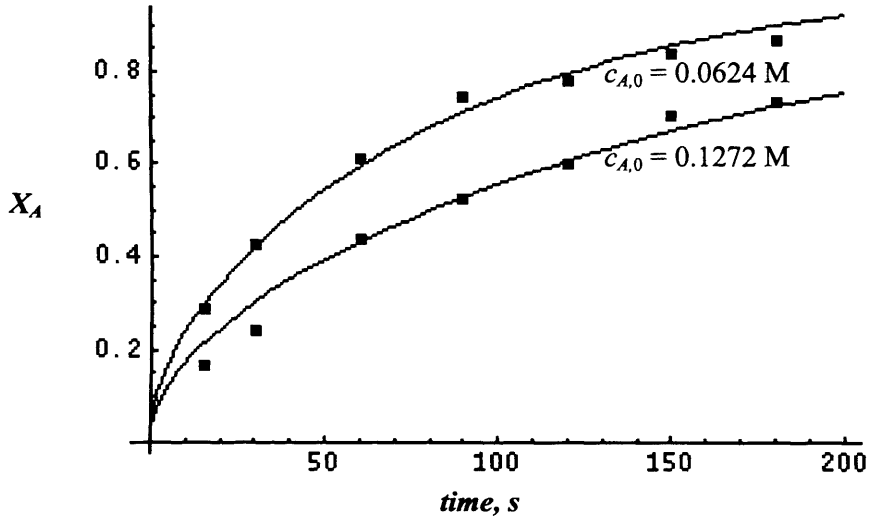

Figure 6.20. Comparison between experimental and predicted conversions (for best diffusivity fit) for the pyrogallol oxidation.

The fitted values of pyrogallol diffusivity in water are dependent on pyrogallol concentration and are smaller than those found in literature, $D_A = 7.4 \cdot 10^{-10}$ m^2/s for a diluted solution at 298 K and 1 atm, Perry and Green (1997). This indicates that there is certain kinetic resistance for this system. Thus, assuming fast reaction the analytical Eq. (6.63) can be used to calculate the change in the concentration profile of pyrogallol with time (Figure 6.21). This can be seen in Figure 6.21 for $c_{A0} = 0.1272$ mol/l and $D_A = 7.4 \cdot 10^{-10}$ m^2/s. In 200 s the reaction should be almost completed (100% conversion) if operating under mass transfer control, while Table 6.8 shows that the conversion at 180 s is only 73 %.

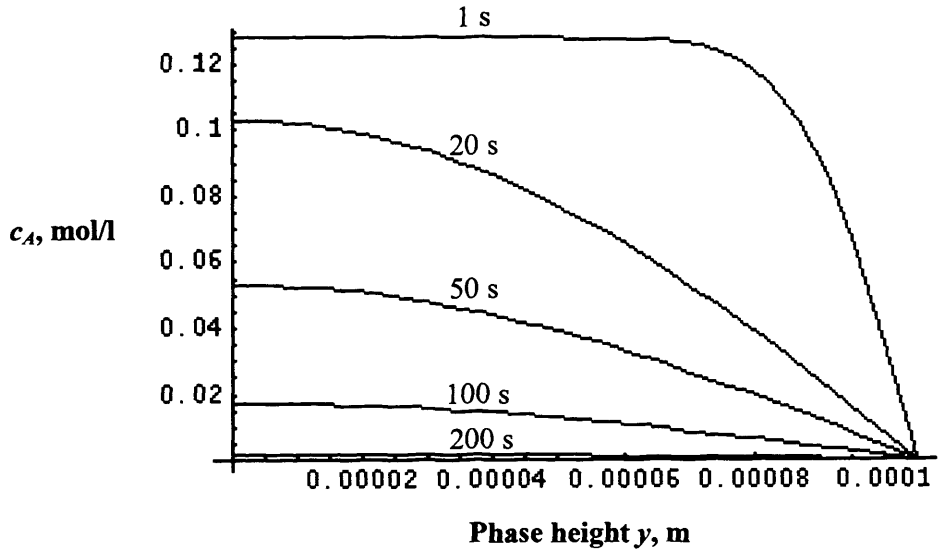

Figure 6.21. Concentration profiles of pyrogallol obtained by an analytical model for fast reaction when $c_{A0} = 0.1272$ M and $D_A = 7.4 \cdot 10^{-10}$ m^2/s.

A complex reaction mechanism given by Abrash et al. (1989) that takes into account the diffusion/reaction equation for each component was also considered. This mechanism, which that assumes 10 different substances taking part in the reaction process, is not utterly confirmed and some of the reaction rates depend on specific process conditions. Due to the mechanism complexity and experimental uncertainties in the conversion values of pyrogallol, the analysis was not possible.

The above methodology can be used to confirm whether a reaction can be considered instantaneous. When the reaction is instantaneous then the mesh microreactor can be used to estimate diffusivity of reactant *A*. If the reaction is not fast, the previously developed dimensionless parametric maps can be used to find the ratio of initial concentrations in the mesh microreactor that will bring the system to the kinetic control regime. Experiments can then be performed to extract reaction kinetics.

Considering the oxidation of Pyrogallol (*A*) in a single step with reaction orders $\alpha = 1$ and $\beta = 1$, 1.5 moles of O_2 (*B*) are required per mol of Pyrogallol (*A*) to obtain purpurogalloquinone and the final product, Abrash et al. (1989). Figure 6.22 shows conversion vs. dimensionless time at an initial concentration of Pyrogallol, $c_{A0} = 0.1272$ M, together with two different fittings to Eq. (6.24) at $Da = 0.12$ and $Da = 0.15$ (where only the first conversions were used for the curve fitting). Dimensionless time was calculated using Eq. (6.5) and $D_B = 7.4 \cdot 10^{-10}$ m^2/s. When Eq.

(6.35) is used instead of Eq. (6.24), a similar *Da* is obtained. For the CRL geometry this *Da* is already out of the limits represented in Figure 6.10 using either Eq. (6.24) or (6.35) as this reaction is fast. Therefore, *Da* must be reduced one or two orders of magnitude by using an interfacial concentration of oxygen one or two orders of magnitude smaller. The experimental value of $c_{Bint,2}$ was 267 μM but 10 μM should be used. The exact value of *Da* cannot be calculated from this new value of $c_{Bint,2}$ because the previous *Da* does not contain the real reaction constant k_A as some mass transfer resistance is present. Assuming that the new *Da* for $c_{Bint,2}$ = 10μM is 0.01, a ratio $C=c_{A0}/c_{Bint,2}$ of 3 or 11 (c_{A0} = 30 μM and c_{A0} = 110 μM) according to Figure 6.10 would be necessary to be in the kinetic control regime with differences of 2 % and 5 % respectively.

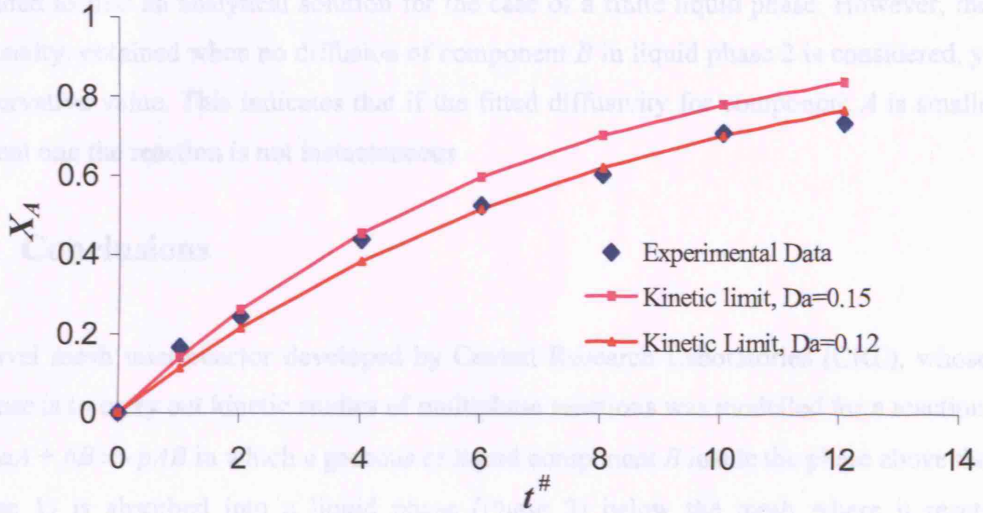

Figure 6.22. Experimental data for pyrogallol oxidation fitted to the kinetic limit given by Eq. (6.24).

For fast reactions, the pseudo-kinetic limit plays a crucial role as it allows kinetics to be retrieved at large *Da* without reducing $c_{Bint,2}$ substantially. For instance, if the previous data corresponded to a mesh microreactor with 1D geometry, 1/*Da* would be between 6 and 8, at which, according to Figure 6.7, the system can be under kinetic control (pseudo-kinetic limit), for *C* between 2 (5% tolerance) and 0.2 (1% tolerance). This means that c_{A0} could be as high as $c_{Bint,2}$ (= 267 μM) if a *C* of 1 was used.

6.7.2. Diffusion of Gaseous Component *B* into Liquid Phase 2

Although the reaction between components *A* and *B* is instantaneous, component *B* penetrates inside the liquid Phase 2 as a function of D_A/D_B as well as the reaction stoichiometry as it was observed via Femlab simulations in the previous section. Thus, there is an imaginary interface within the liquid Phase 2 that moves towards the bottom of the reactor as time proceeds, which separates a region that only contains component *B* (above this line) from the region that only contains component *A*. Therefore, the instantaneous reaction takes place at this mobile imaginary interface. Bird et al. (1964) gives the solution of the interface position as well as concentration profiles for both components with time for the case of a semi-infinite liquid phase 2, which cannot be applied to the mesh microreactor where Phase 2 is finite. If possible, it is intended to find an analytical solution for the case of a finite liquid phase. However, the fitted diffusivity, obtained when no diffusion of component *B* in liquid phase 2 is considered, yields a conservative value. This indicates that if the fitted diffusivity for component *A* is smaller than the real one the reaction is not instantaneous.

6.8. Conclusions

A novel mesh microreactor developed by Central Research Laboratories (CRL), whose main purpose is to carry out kinetic studies of multiphase reactions was modelled for a reaction of the type $aA + bB \Rightarrow pAB$ in which a gaseous or liquid component *B* inside the phase above the mesh (Phase 1) is absorbed into a liquid phase (Phase 2) below the mesh where it reacts with component *A*.

Mass‘transfer by diffusion and reaction rate equations were non-dimensionalised and solved using a finite element software (Femlab). Dimensionless parametric maps that provide the limits for kinetic control in the microreactor necessary for calculating reaction kinetics were developed for two different cases (see sections 6.4 and 6.5). In each case, the concentration of one reactive component was kept constant, the interfacial concentration of component *B* for Case 1 and the concentration of the component *A* inside phase 2 for Case 2. In Case 1 two different geometries were considered in the parametric map development, 1D and 2D axisymmetric while in Case 2 only a 2D axisymmetric geometry was analysed. For this purpose, analytical kinetic and pseudo-kinetic equations were used as limits for the Femlab simulations, which considered mass transfer together with chemical reaction. The analytical solution of the pseudo-kinetic limit, which takes into account the development of the concentration profile of component *B*, extended the applicability of the maps to considerably faster reactions. A method is suggested,

based on the parametric map, for the design of experiments needed to extract kinetics (reaction rates and orders) from experimental data. Furthermore, an analytical solution for the case of fast reactions, based on the diffusion equation, was implemented and the results were compared with 2D axisymmetric Femlab simulations.

The parametric maps as well as the fast-reaction model were used to evaluate whether experimental data from the mesh microreactor for the hydrolysis of fluorescein diacetate (FDA) and pyrogallol oxidation, can be used to determine reaction kinetics. For the hydrolysis of FDA it was found that the system was under mass transfer resistance despite the long reaction times required. In the case of the fast pyrogallol oxidation, it was shown that the reaction was mass transfer limited and concentrations of pyrogallol and oxygen were suggested, necessary to bring the system to the kinetic control regime.

Nomenclature

A, B	Reactants.
a, b, p	Stoichiometric coefficients.
c	Concentration, Kmol/m^3.
C	Ratio of initial concentration of A in phase 2 to interfacial concentration of B in phase 2.
C_B	Ratio of initial to interfacial concentration of B in Phase 2.
Co	Ratio of initial moles of A to B.
D	Diffusivity, m^2/s.
Da	Damköhler number.
e	Mesh thickness, m.
G	Geometrical Parameters.
H_T	Height of the phase plus mesh thickness, m.
H	Height of the phase, m.
k	Reaction rate constant.
P	Partition coefficient.
r	Radius of the pores, m.
R	Half pitch of the mesh, m.
t	Time, s.
T, T_B	Ratios of diffusivities.
v	Phase volume, m^3.
x, y	Spatial variables.
X	Conversion.

Greek Letters

α, β	Reaction orders.

Subscripts

A	Reactant A in Phase 2.
B	Reactant B.
C	Characteristic property.
Exp	Experimental.
F	Final.
int	Interfacial property.

K	Kinetic limit.
max	Maximum value of the variable or parameter.
min	Minimum value of the variable or parameter.
PK	Pseudo-kinetic Limit.
T	Total.
Th	Theoretical.
1	Value in Phase 1.
2	Value in Phase 2.

Superscripts

#	Dimensionless variable or parameter.

Chapter 7

Scale-Out Operation in Networks of Microreactors and Microchannels

"It is the path of least resistance that makes rivers and men crooked"

Bartlett Joshua Palmer

7.1. Introduction

The thin fluid layers present in microchannel reactors allow fast and controlled heat and mass transfer rates. For increased throughput, however, a number of such reactors operating in parallel is needed (scale-out or number-up). This type of scale up would ensure that findings from a single microchannel unit apply to the whole scaled out device, provided that the flow conditions in each channel are identical. In single-phase systems appropriate manifold structures are therefore needed to distribute the flow from a common reservoir through the microchannels to a common product reservoir in a way that maintains the same residence time in all microchannels. Mean residence time in a microchannel together with temperature and pressure determine reaction conversion and selectivity. Therefore, once a chemical reaction has been studied and a suitable residence time under certain operation conditions has been determined, it is desirable to use this residence time in all reaction micro-channels operating in parallel.

In this chapter, an analytical model based on electrical resistance networks (Golbig et al., 2002), has been developed for the study of single-phase flow distribution in manifold structures with an emphasis on two designs, namely consecutive and bifurcation. This model is used to understand the effect of manufacturing tolerances and channel blockages on flow distribution.

7.2. Background

Commenge et al. (2002) analysed flow distribution in a multichannel microreactor with a consecutive type of manifold, and optimised the reactor design for single-phase flow distribution. A resistance network method combined with an optimising function were used to

calculate the varying diameters of flow distributing and collecting channels that give almost uniform flow distribution while avoiding unrealistic channel geometries. Bejan and Errera (1997) found that a fractal tree-like network structure (observed widely in natural structures such as cracks in a dry ground, lungs, arteries or veins and urban growth) not only gave flow uniformity but also minimised flow resistance through a *volume-to-point path* in a porous medium for a single-phase fluid. Yongping and Cheng (2002) concluded that fractal tree-like microchannel networks have better heat transfer capabilities and require lower pumping power in comparison to traditional parallel channels; in this work however, additional pressure losses due to bends, which are significant at high velocities, were neglected. In contrast, in monoliths the flow expansion at the inlet cone leads to vortex formation that restricts flow uniformity in the monolith channels, Kostoglou et al. (2003); Jeong and Kim (2002).

For the design of manifold structures that ensure uniform flow distribution, the equations describing flow in each microchannel need to be known. Researchers have questioned whether flow equations from large scale systems can be used in micron size channels. In a recent review Judy et al. (2002) showed that Stokes flow theory predicted friction factors well in laminar flow while deviations were within the experimental uncertainties due to the difficulty in conducting experiments at this scale, which would explain previous discrepancies between theory and experiments. In case of gas flow inside microchannels, rarefaction phenomena may appear at Knudsen numbers ($Kn = \lambda/D_C$) larger than 0.01, which represent very small channels (e.g. Argon gas at 25 °C and atmospheric pressure has $\lambda = 0.07$ μm according to Kloc and Laudise (1998), that gives $D_C = 7$ μm).

7.3. Definition of the Problem

In the present work, flow distribution in two different manifold structures is studied using an analogy to electrical resistance networks, Golbig et al. (2002). The two most common manifold structures are a) consecutive and b) bifurcation (see Figure 7.1). The analysis is restricted to single-phase laminar flow, commonly occurring in microscale, constant density and viscosity along the whole structure and no change of moles in gaseous reactions but can be extended to include these cases. It is also assumed that the fluid behaves as a continuum and pressure drop can be calculated by the equations used in large scale flows. Initially, additional pressure losses due to entrance/exit, merging/branching and bend effect are neglected, which allows the solution to be obtained via a system of linear equations. These are added on later. Compared to the fractal tree-like structure where the channels at the last level have the smallest length and diameter, in the bifurcation structure the reaction channels (last level channels) are usually the longest ones.

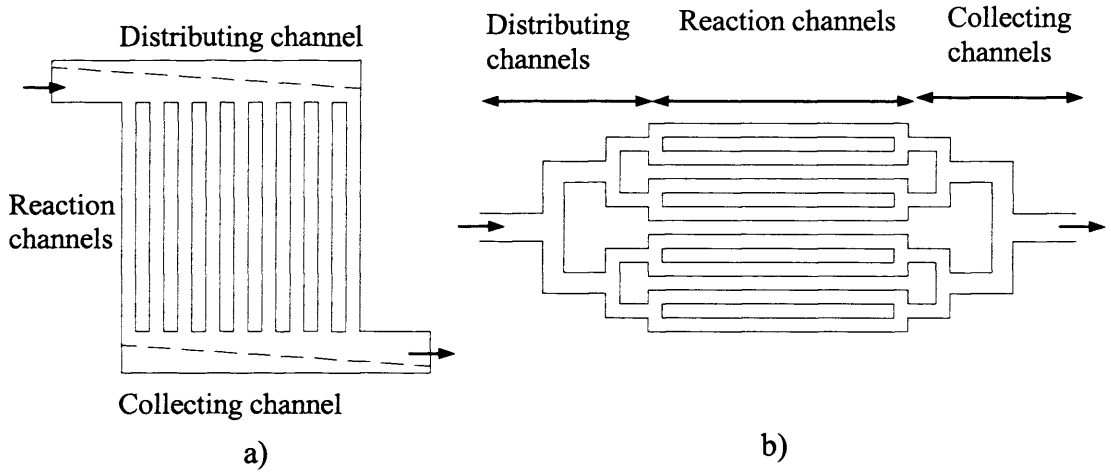

Figure 7.1. Schematic diagrams of a) consecutive and b) bifurcation manifold structures. Consecutive manifold shows two possible designs: *method 1* (——) and *method 2* (- - -).

A more complex structure with similar features to the consecutive one is analysed by a simple extension of the latter in order to prove the capability of the resistance network model (RNM). The analytical model is further developed by considering additional pressure losses due to merging/branching effects as well as bends (section 7.4.6), presenting an algorithm to solve the system of non-linear equations that is implemented for the consecutive structure, comparing the results with finite element simulations (FEMLAB ©).

7.4. Analytical Model

To study flow distribution in a manifold structure the concept of an electrical resistance network is used. This is possible under laminar flow conditions where the relationship between frictional pressure drop ΔP and flowrate Q (or velocity U) in each channel is linear and additional pressure losses at entrance, exit, bends and branching/merging of channels are generally negligible. However, in section 7.4.6 an algorithm that includes additional pressure losses in the resistance network model is presented. For laminar flow in circular channels the Hagen-Poiseuille equation can be used to estimate pressure drop for a given velocity U, Perry and Green (1999). In non-circular channels, however, the channel hydraulic diameter, D, (4 times the channel area over wetted perimeter), combined with a non-circularity factor, λ_{NC}, that depends on channel geometry need to be included in the Hagen-Poiseuille equation for pressure drop, Commenge et al. (2002). This approach is used in this work and the Hagen-Poiseuille equation becomes:

$$\Delta P = \frac{32\mu L\lambda_{NC}}{D^2}U = \frac{32\mu L\lambda_{NC}}{D^2 A}Q \tag{7.1}$$

In circular channels D is the diameter and λ_{NC}, = 1. For non-dimensionalising Eq. (7.1) the smallest dimension of the reaction channels is chosen as characteristic length, D_C (i.e. nominal diameter in circular channels and nominal depth or width in rectangular ones), while the flowrate in each reaction channel when the flow is uniformly distributed (*equipartition flowrate* for identical reaction channels) is chosen as characteristic flowrate $Q_C = Q_T /N$. The characteristic area is defined as $A_C = \pi D_C^2/4$ and $A_C = D_C^2$ for circular and rectangular channels respectively so that $A^{\#} = D^{\#2}$ for circular channels and $A^{\#} = E^{\#} W^{\#}$ for rectangular ones. For making $U^{\#} = Q^{\#}/A^{\#}$ in both geometries, the characteristic velocity is defined as $U_C = 4Q_T/(N\pi D_C^2)$ and $U_C = Q_T/(ND_C^2)$ in circular and rectangular channels respectively. The following dimensionless parameters are used: $L^{\#} = L/D_C$, $D^{\#} = D/D_C$, $W^{\#} = W/D_C$, $E^{\#} = E/D_C$, $A^{\#} = A/A_C$, $Q^{\#} = Q/Q_C$, $U^{\#} = U/U_C$, $Q^{\#}_T = N$ and dimensionless residence time and pressure are given by Eq. (7.2) and (7.3) respectively ($^{\#}$ denotes dimensionless parameter):

$$t^{\#} = tU_C / D_C = L^{\#} / U^{\#} \tag{7.2}$$

$$P^{\#} = (P - P_0)D_C /(\mu U_C) \tag{7.3}$$

where P_0 is a reference pressure. As the characteristic time t_C is D_C/U_C, it is equivalent to $t_C = ND_C^3\pi/(4Q_T)$ and $t_C = ND_C^3/Q_T$ for circular and rectangular channels respectively. From dimensional analysis Eq. (7.1) becomes Eq. (7.4) and in circular channels the dimensionless resistance is given by Eq. (7.5). In Eq. (7.4) pressure difference is equivalent to potential difference and flowrate is equivalent to current in Ohm's law:

$$\Delta P^{\#} = R^{\#} Q^{\#} \tag{7.4}$$

$$R^{\#} = 32L^{\#} / D^{\#4} \tag{7.5}$$

In non-circular channels, the non-circularity coefficient λ_{NC} can be found from the experimental values of the product fRe_{hyd} in each channel (equal to 64 in circular channels) obtained from pressure drop measurements (see Eq. (7.6)), Judy et al. (2002). However there are available equations for the most common geometries, Commenge et al. (2002); Judy et al. (2002), together with exact solutions for creeping flow at $Re_{hyd} << 1$, Happel and Brenner (1965):

$$\lambda_{NC} = \left(fRe_{hyd}\right)_{Exp} / 64 \tag{7.6}$$

In rectangular channels Eq. (7.7) is used to calculate the non-circularity coefficient λ_{NC} when $0 \leq E/W \leq 1$ while W/E is replaced by E/W when $E/W \geq 1$(Commenge et al., 2002):

$$\lambda_{NC} = \frac{3/2}{(1-0.351E/W)^2(1+E/W)^2} \qquad 0 \leq E/W \leq 1 \tag{7.7}$$

Considering the hydraulic diameter $D = 2EW/(E + W)$ and area $A = WE$, Eq. (7.1) becomes Eq. (7.4) for rectangular channels as well, where the dimensionless resistance is now defined by Eq. (7.8) or (7.9), the latter being more useful for comparisons with circular channels:

$$R^{\#} = \frac{12L^{\#}}{\min^2(E^{\#},W^{\#})\left(1-0.351\min(E^{\#}/W^{\#},W^{\#}/E^{\#})\right)^2 W^{\#}E^{\#}} \tag{7.8}$$

$$R^{\#} = \frac{128L^{\#}\lambda_{NC}}{D^{\#4}(E^{\#}/W^{\#}+W^{\#}/E^{\#}+2)} \tag{7.9}$$

Manifolds with different geometries can be compared when the corresponding reaction channels have the same cross-sectional area so that channel residence time remains constant (if the length is not modified). The smaller dimension of a rectangular channel that gives the same cross-sectional area as a circular one of diameter D is given by:

$$\min(E,W) = \left(\pi\min(E/W,W/E)\right)^{0.5} D/2 \tag{7.10}$$

The electrical networks are usually analysed by using the two Kirchhoff's rules, which are:

1. *Junction rule*: For a given junction or node in a circuit, the sum of the currents entering equals the sum of the currents leaving, which represents charge conservation. In a fluid network this is equivalent to *mass conservation*, indicating that the sum of mass entering equals the sum of mass leaving if no nuclear reactions take place. In addition, if the fluid density remains constant, the same applies for flow rates.

2. *Loop rule*: Around any closed loop in a circuit, the sum of the potential differences across all elements is zero, which represents energy conservation. In a fluid network, the same energy

balance can be applied. Bernoulli equation (Massey and Ward-Smith, 1998) is applied between points 1 and 2 in Figure 7.2 following paths A-B and C-D. The head energy losses along both paths must be identical $h_{A\text{-}B} = h_{C\text{-}D}$. These energy losses consist of viscous and inertial losses due to fluid merging/branching and channels bends. There is no gravity effect or change in velocity head for a close loop.

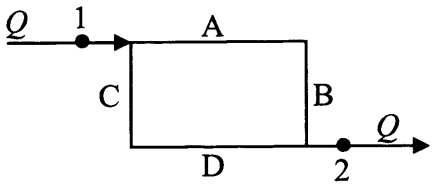

Figure 7.2. Loop rule in a fluid lop.

7.4.1. Resistance Network for Consecutive Structure

The consecutive structure depicted in Figure 7.1a is converted to the resistance network shown in Figure 7.3 that contains (N-1) loops and N reaction channels.

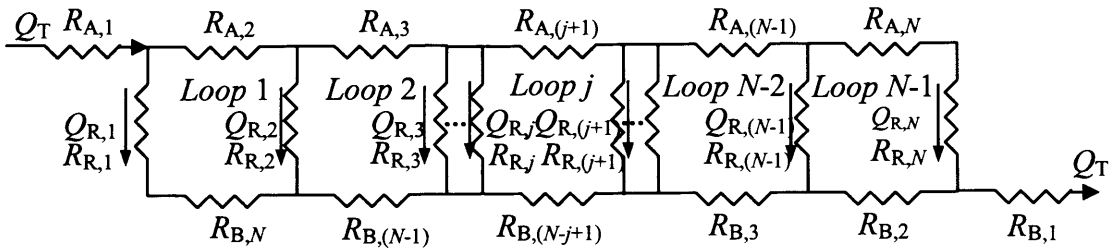

Figure 7.3. Resistance network for consecutive structure.

In this configuration the distributing and collecting channels are divided into N zones, where each zone represents the distance between two reaction channels plus the reaction channel diameter (see patterned zones in Figure 7.4). In the N-channel consecutive structure in Figure 7.3, $R_{R,j}$, $R_{A,j}$ and $R_{B,j}$ are the flow resistances at channel or zone j (j = 1 to N) for reaction, distributing and collecting channels respectively. Considering an energy balance in each loop (*loop rule*), the following (N - 1) equations are obtained:

$$Q_{A(j+1)}R_{A,(j+1)} + Q_{R,(j+1)}R_{R,(j+1)} - Q_{B,(N-j+1)}R_{B,(N-j+1)} - Q_{R,j}R_{R,j} = 0 \qquad j = 1,2,\ldots,N-1 \quad (7.11)$$

$Q_{A,(j+1)}$ and $Q_{B,(N-j+1)}$ represent flowrates in zones $(j + 1)$ and $(N - j + 1)$ of the distributing and collecting channels respectively and can be expressed as a function of the reaction channels' flowrates by applying mass balances at each junction (*junction rule*).

$$Q_{A,(j+1)} = \sum_{k=1}^{k=N} Q_{R,k} - \sum_{k=1}^{k=j} Q_{R,k} \tag{7.12}$$

$$Q_{B,(N-j+1)} = \sum_{k=1}^{k=j} Q_{R,k} \tag{7.13}$$

Substituting Eq. (7.12) and (7.13) into Eq. (7.11), non-dimensionalising and dividing throughout by $R^{\#}_{R,j}$ gives $(N - 1)$ equations represented by Eq. (7.14) for loop j. An overall mass balance produces the N^{th} expression of the linear system of N-equations, Eq. (7.15), necessary to solve the flow distribution $Q^{\#}_{R,j}$ ($j = 1$ to N):

$$-\sum_{k=j+1}^{k=N} Q^{\#}_{R,k} \frac{R^{\#}_{A,(j+1)}}{R^{\#}_{R,j}} + \sum_{k=1}^{k=j} Q^{\#}_{R,k} \frac{R^{\#}_{B,(N-j+1)}}{R^{\#}_{R,j}} - Q^{\#}_{R,(j+1)} \frac{R^{\#}_{R,(j+1)}}{R^{\#}_{R,j}} + Q^{\#}_{R,j} = 0 \qquad j = 1,2,\ldots,(N\text{-}1) \tag{7.14}$$

$$\sum_{k=1}^{k=N} Q^{\#}_{R,k} = Q^{\#}_{T} = N \tag{7.15}$$

The system represented by Eq. (7.14) and (7.15) can be expressed and solved in a matrix form, which allows for easy calculation by matrix inversion:

$$\mathbf{M} \cdot \mathbf{Q} = \mathbf{S} \tag{7.16}$$

$$\mathbf{Q} = inv(\mathbf{M}) \cdot \mathbf{S} \tag{7.17}$$

where $\mathbf{M}$ is a N x N matrix given by Eq. (7.18), $\mathbf{Q}$ is a N column vector with the N reaction channel flowrates, $Q^{\#}_{R,j}$, and the solution vector $\mathbf{S}$ is a N column vector composed of zeros and $Q^{\#}_{T}$ (equal to N) in the last position:

$$\mathbf{M}(N,N)=\begin{bmatrix} \frac{R^{\#}_{B,N}}{R^{\#}_{R,1}}+1 & -\frac{(R^{\#}_{A,2}+R^{\#}_{R,2})}{R^{\#}_{R,1}} & -\frac{R^{\#}_{A,2}}{R^{\#}_{R,1}} & -\frac{R^{\#}_{A,2}}{R^{\#}_{R,1}} & -\frac{R^{\#}_{A,2}}{R^{\#}_{R,1}} & -\frac{R^{\#}_{A,2}}{R^{\#}_{R,1}} \\ \frac{R^{\#}_{B,(N-1)}}{R^{\#}_{R,2}} & \frac{R^{\#}_{B,(N-1)}}{R^{\#}_{R,2}}+1 & -\frac{(R^{\#}_{A,3}+R^{\#}_{R,3})}{R^{\#}_{R,2}} & -\frac{R^{\#}_{A,3}}{R^{\#}_{R,2}} & -\frac{R^{\#}_{A,3}}{R^{\#}_{R,2}} & -\frac{R^{\#}_{A,3}}{R^{\#}_{R,2}} \\ \frac{R^{\#}_{B,(N-2)}}{R^{\#}_{R,3}} & \frac{R^{\#}_{B,(N-2)}}{R^{\#}_{R,3}} & \frac{R^{\#}_{B,(N-2)}}{R^{\#}_{R,3}}+1 & -\frac{(R^{\#}_{A,4}+R^{\#}_{R,4})}{R^{\#}_{R,3}} & -\frac{R^{\#}_{A,4}}{R^{\#}_{R,3}} & -\frac{R^{\#}_{A,4}}{R^{\#}_{R,3}} \\ \frac{R^{\#}_{B,2}}{R^{\#}_{R,(N-1)}} & \frac{R^{\#}_{B,2}}{R^{\#}_{R,(N-1)}} & \frac{R^{\#}_{B,2}}{R^{\#}_{R,(N-1)}} & \frac{R^{\#}_{B,2}}{R^{\#}_{R,(N-1)}} & \frac{R^{\#}_{B,2}}{R^{\#}_{R,(N-1)}}+1 & -\frac{(R^{\#}_{A,N}+R^{\#}_{R,N})}{R^{\#}_{R,(N-1)}} \\ 1 & 1 & 1 & 1 & 1 & 1 \end{bmatrix} \quad (7.18)$$

The coefficients of the matrix are calculated from the ratios of resistances $R^{\#}_{A,(j+1)}/R^{\#}_{R,j}$, $R^{\#}_{B,(N-j+1)}/R^{\#}_{R,j}$, $R^{\#}_{R,(j+1)}/R^{\#}_{R,j}$ for j = 1 to (N - 1), which together with N, the number of reaction channels, give 3(N - 1) + 1 *parameters* (*PAR*) that determine the flow distribution solution. Resistances $R^{\#}_{A,1}$ and $R^{\#}_{B,1}$ do not affect flow distribution. However if all reaction channels are identical ($R^{\#}_{R,j} = R^{\#}_{R}$), *PAR* becomes 2($N$ - 1) + 1 and if the distributing and collecting channels are also equal ($R^{\#}_{A,j} = R^{\#}_{B,j}$), *PAR* = ($N$ - 1) + 1. Moreover, when all zones in distributing and collecting channels have the same geometry ($R^{\#}_{A,j} = R^{\#}_{B,j} = R^{\#}_{A}$), *PAR* = 2, namely R_A/R_R and N. The actual ratios of channel dimensions can be extracted from these ratios of resistances according to Eq. (7.5) and (7.8) for circular and rectangular channels respectively. To calculate resistances $R^{\#}$ from Eq. (7.5) or (7.8), the length of each j-zone in the distributing and collecting channels, $L^{\#}_{A,j}$ and $L^{\#}_{B,j}$ (j = 2 to N), is defined according to Eq. (7.19) and Figure 7.4, which shows a distributing channel with constant diameter. Varying diameters for the distributing and collecting channels are also possible where the zone diameter is taken equal to the average value along its length, Commenge et al. (2002).

$$L^{\#}_{A,j} = L^{\#}_{B,j} = sep^{\#} + D^{\#}_{R,j} \qquad j = 2, 3, \ldots, N \quad (7.19)$$

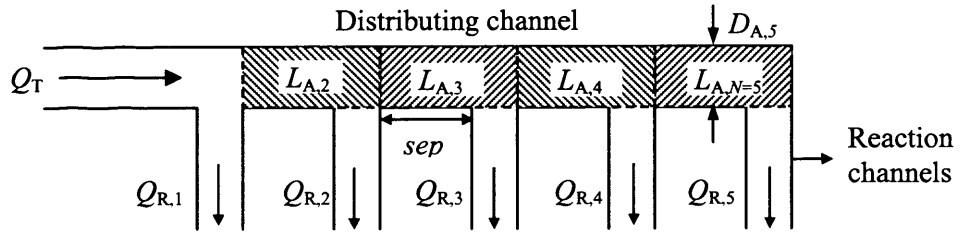

Figure 7.4. Zone length and diameter in the distributing channel.

7.4.2. Resistance Network for Bifurcation Structure

Figure 7.5 represents the resistance network for the bifurcation structure shown in Figure 7.1b, where each bifurcation generates a new bifurcation level i. The bifurcation structure produces flow equipartition when all channels at the same level have exactly the same geometrical characteristics, there is no variation in the channel diameters due to manufacturing tolerances and the length of straight channel before each bifurcation is long enough to develop a symmetrical velocity profile at the entrance of the bifurcation. This structure, however, tends to occupy larger area compared to the consecutive one. The inlet and outlet channels belong to level 0 and their resistances do not affect flow distribution but only the total pressure drop. The last bifurcation level ($i = b$) corresponds to the reaction channels. The number of reaction channels at the last level ($i = b$) is given by $N = 2^b$ and the number of channels in a lower bifurcation level i is given by $2 \cdot 2^i$, as there is the same number of channels at each side of the reaction channels. The channels at each i-level are numbered from 1 to $2 \cdot 2^i$ from top to bottom counting first the left and then the right side. If the number of a channel in the left side is j, the number of its symmetry channel in the right side is $j + 2^i$. The flow rate $Q_{i\,j}$ ($i < b$) through channel number j at level i, is the sum of the reaction channel flow rates that go from number $(j - 1) \cdot 2^{b-i} + 1$ to $j \cdot 2^{b-i}$. For instance, in a three-level structure $Q_{1,2}$ is the contribution of $Q_{3,5}$, $Q_{3,6}$, $Q_{3,7}$ and $Q_{3,8}$. The flow rate of its symmetry channel to the right side, $Q_{1,4}$ is the same. Resistance $R^{\#}_{i,j}$ (channel j at level i) is found by Eq. (7.5) or (7.8). The network can be simplified by the use of equivalent resistances for j resistances in series or in parallel respectively:

$$R^{\#}_{\mathrm{EQ}} = \sum_j R^{\#}_j \tag{7.20}$$

$$1/R^{\#}_{\mathrm{EQ}} = \sum_j 1/R^{\#}_j \tag{7.21}$$

At level i, there are 2^i equivalent resistances, which are numbered from top ($j = 1$) to bottom ($j = 2^i$). Eq. (7.22) is used to calculate equivalent resistances at level $i < b$. At level b, $R^{\#}_{\mathrm{EQ},b,j} = R^{\#}_{b,j}$. Figure 7.5 shows the area that corresponds to the equivalent resistance $R_{\mathrm{EQ},2,j}$ as a dash-dot rectangle.

$$R^{\#}_{EQ,i,j} = \frac{R^{\#}_{EQ,(i+1),j} R^{\#}_{EQ,(i+1),(j+1)}}{R^{\#}_{EQ,(i+1),j} + R^{\#}_{EQ,(i+1),(j+1)}} + R^{\#}_{i,j} + R^{\#}_{i,(j+2^i)} \qquad i = 1,2,\ldots(b\text{-}1)\,;\; j = 1,\ldots,2^i \quad (7.22)$$

Applying mechanical energy and mass balances (loop and junction rules), the following system of $N - 1 = 2^b - 1$ linear equations is found:

$$\sum_{k=S}^{k=\frac{S+V-1}{2}} Q^{\#}_{b,k} \frac{R^{\#}_{EQ,i,(2j-1)}}{R^{\#}_{EQ,i,2j}} - \sum_{k=\frac{S+V-1}{2}+1}^{k=V} Q^{\#}_{b,k} = 0 \qquad i = 1,2,\ldots,b\,; \quad j = 1,\ldots,2^i/2 \qquad (7.23)$$

where level i goes from 1 to b, and loop j goes from 1 to $2^i/2$, which is the number of close loops in each level (equations). The number of close loops or equations per level is a quarter the number of channels per level when $i < b$ and half the number of channels per level when $i = b$. S and V are given by $S = 2(j - 1)2^{b-i} + 1$ and $V = 2\,j\,2^{b-i}$. An overall mass balance similar to Eq. (7.15) with $N = 2^b$ gives the n^{th} equation of the system of N linear equations that can be expressed and solved in matrix form. The number of parameters determining the flow distribution solution for this structure is $PAR = (2^b - 1) + 1$ and is defined by the ratios $R_{EQ,i,(2j-1)}/R_{EQ,i,2j}$ (i = 1 to b and j = 1 to $2^i/2$) and the variable N. In the absence of manufacturing variations and same channel geometry at each level, flow equipartition is always achieved.

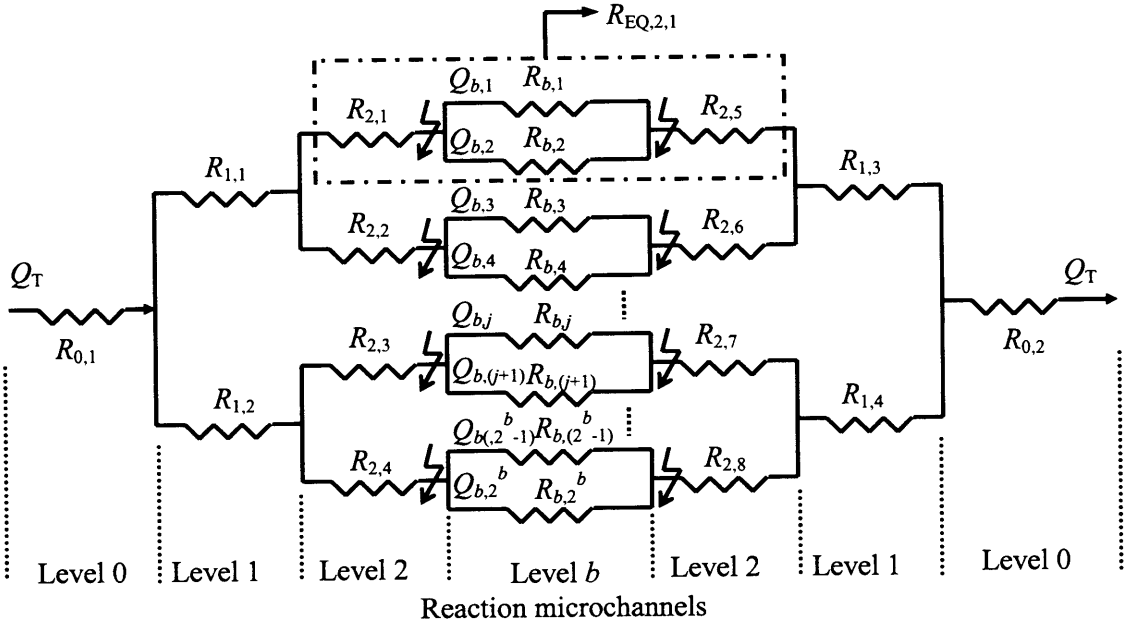

Figure 7.5. Resistance network for bifurcation structure.

As an example, a 3-level structure with 8 reaction microchannels is considered. In this case i goes from $i = 1$ to $i = b = 3$ and j (number of equation per levels) takes the values $j = 1,\ldots,2^i/2$. The equations of the system according to Eq. (7.23) are:

$i = 1, j = 1$

$$\left(Q_{3,1}^{\#} + Q_{3,2}^{\#} + Q_{3,3}^{\#} + Q_{3,4}^{\#}\right)\frac{R_{EQ,1,1}^{\#}}{R_{EQ,1,2}^{\#}} - \left(Q_{3,5}^{\#} + Q_{3,6}^{\#} + Q_{3,7}^{\#} + Q_{3,8}^{\#}\right) = 0 \tag{7.24}$$

$i = 2, j = 1$

$$\left(Q_{3,1}^{\#} + Q_{3,2}^{\#}\right)\frac{R_{EQ,2,1}^{\#}}{R_{EQ,2,2}^{\#}} - \left(Q_{3,3}^{\#} + Q_{3,4}^{\#}\right) = 0 \tag{7.25}$$

$i = 2, j = 2$

$$\left(Q_{3,5}^{\#} + Q_{3,6}^{\#}\right)\frac{R_{EQ,2,3}^{\#}}{R_{EQ,2,4}^{\#}} - \left(Q_{3,7}^{\#} + Q_{3,8}^{\#}\right) = 0 \tag{7.26}$$

$i = 3, j = 1$

$$\left(Q_{3,1}^{\#}\right)\frac{R_{EQ,3,1}^{\#}}{R_{EQ,3,2}^{\#}} - \left(Q_{3,2}^{\#}\right) = 0 \tag{7.27}$$

$i = 3, j = 2$

$$\left(Q_{3,3}^{\#}\right)\frac{R_{EQ,3,3}^{\#}}{R_{EQ,3,4}^{\#}} - \left(Q_{3,4}^{\#}\right) = 0 \tag{7.28}$$

$i = 3, j = 3$

$$\left(Q_{3,5}^{\#}\right)\frac{R_{EQ,3,5}^{\#}}{R_{EQ,3,6}^{\#}} - \left(Q_{3,6}^{\#}\right) = 0 \tag{7.29}$$

$i = 3, j = 4$

$$\left(Q_{3,7}^{\#}\right)\frac{R_{EQ,3,7}^{\#}}{R_{EQ,3,8}^{\#}} - \left(Q_{3,8}^{\#}\right) = 0 \tag{7.30}$$

$$Q_{3,1}^{\#} + Q_{3,2}^{\#} + Q_{3,3}^{\#} + Q_{3,4}^{\#} + Q_{3,5}^{\#} + Q_{3,6}^{\#} + Q_{3,7}^{\#} + Q_{3,8}^{\#} = N \tag{7.31}$$

Using Eq. (7.16) to solve the system of linear equations, the values of the matrix **M** and vectors **Q** and **S** are the following:

$$\mathbf{M}(N,N)=\left[\begin{array}{cccccccc}
\frac{R^{\#}_{\mathrm{EQ},1,1}}{R^{\#}_{\mathrm{EQ},1,2}} & \frac{R^{\#}_{\mathrm{EQ},1,1}}{R^{\#}_{\mathrm{EQ},1,2}} & \frac{R^{\#}_{\mathrm{EQ},1,1}}{R^{\#}_{\mathrm{EQ},1,2}} & \frac{R^{\#}_{\mathrm{EQ},1,1}}{R^{\#}_{\mathrm{EQ},1,2}} & -1 & -1 & -1 & -1 \\
\frac{R^{\#}_{\mathrm{EQ},2,1}}{R^{\#}_{\mathrm{EQ},2,2}} & \frac{R^{\#}_{\mathrm{EQ},2,1}}{R^{\#}_{\mathrm{EQ},2,2}} & -1 & -1 & 0 & 0 & 0 & 0 \\
0 & 0 & 0 & 0 & \frac{R^{\#}_{\mathrm{EQ},2,3}}{R^{\#}_{\mathrm{EQ},2,4}} & \frac{R^{\#}_{\mathrm{EQ},2,3}}{R^{\#}_{\mathrm{EQ},2,4}} & -1 & -1 \\
\frac{R^{\#}_{\mathrm{EQ},3,1}}{R^{\#}_{\mathrm{EQ},3,2}} & -1 & 0 & 0 & 0 & 0 & 0 & 0 \\
0 & 0 & \frac{R^{\#}_{\mathrm{EQ},3,3}}{R^{\#}_{\mathrm{EQ},3,4}} & -1 & 0 & 0 & 0 & 0 \\
0 & 0 & 0 & 0 & \frac{R^{\#}_{\mathrm{EQ},3,5}}{R^{\#}_{\mathrm{EQ},3,6}} & -1 & 0 & 0 \\
0 & 0 & 0 & 0 & 0 & 0 & \frac{R^{\#}_{\mathrm{EQ},3,7}}{R^{\#}_{\mathrm{EQ},3,8}} & -1 \\
1 & 1 & 1 & 1 & 1 & 1 & 1 & 1
\end{array}\right]\begin{array}{l} i=1 \\ \\ i=2 \\ \\ \\ i=3 \\ \\ \\ \end{array}$$

$$\mathbf{Q}(N=2^3)=\begin{bmatrix} Q^{\#}_{3,1} \\ Q^{\#}_{3,2} \\ Q^{\#}_{3,3} \\ Q^{\#}_{3,4} \\ Q^{\#}_{3,5} \\ Q^{\#}_{3,6} \\ Q^{\#}_{3,7} \\ Q^{\#}_{3,8} \end{bmatrix} \qquad \mathbf{S}(N=2^3)=\begin{bmatrix} 0 \\ 0 \\ 0 \\ 0 \\ 0 \\ 0 \\ 0 \\ N \end{bmatrix}$$

7.4.3. Overall Pressure Drop through the Microstructures

At steady state, any path on the microreactor gives the total pressure drop through the structure. Eq. (7.32) applies for the consecutive structure shown in Figure 7.3 ($Q^{\#}_{\mathrm{T}} = N$) while for the bifurcation one shown in Figure 7.5, the total resistance is calculated by Eq. (7.33) and total pressure drop via Eq. (7.34).

$$\Delta P^{\#}_{\mathrm{T,Consec}} = Q^{\#}_{\mathrm{T}}\left(R^{\#}_{\mathrm{A},1} + R^{\#}_{\mathrm{B},1}\right) + Q^{\#}_{\mathrm{R},N} R^{\#}_{\mathrm{R},N} + \sum_{j=1}^{N-1}\left(Q^{\#}_{\mathrm{T}} - \sum_{k=1}^{j} Q^{\#}_{\mathrm{R},k}\right) R^{\#}_{\mathrm{A},(j+1)} \tag{7.32}$$

$$R^{\#}_{\mathrm{T}} = R^{\#}_{0,1} + R^{\#}_{0,2} + R^{\#}_{\mathrm{EQ},1,1} \cdot R^{\#}_{\mathrm{EQ},1,2} / \left(R^{\#}_{\mathrm{EQ},1,1} + R^{\#}_{\mathrm{EQ},1,2}\right) \tag{7.33}$$

$$\Delta P^{\#}_{\mathrm{T,Bif}} = Q^{\#}_{\mathrm{T}} R^{\#}_{\mathrm{T}} \tag{7.34}$$

7.4.4. Manufacturing Tolerances and Channel Blockages

Differences in the microstructure dimensions from the nominal sizes (*tolerances*) depend on the manufacturing process and feature size and can vary with direction, IMM (2003). It is also important to take into account other phenomena as corrosion, catalyst coating and channel clogging, which produce dimensionless variations in the microchannels that affect flow distribution in a similar way as manufacturing tolerances. *Micro-electrodischarge machining* (μ-EDM) has typical manufacturing variations of 3-6 μm, IMM (2003); Benavides et al. (2001), which depend on channel length and aspect ratio. In case of parallel channels, the manufacturing variations could be minimised if the separation between two channels is greater than 200μm. *Milling* gives a maximum difference of 10-20μm between the engineering drawing and the milled channel (IMM, 2003; Madou et al., 2001). This depends on the milling machine as well as on the accuracy of the milling head. If several parallel microchannels are fabricated, the differences between them are significantly smaller (approximately 5μm). The fabrication variations using *etching* are mostly better than 20μm, and depend substantially on the wafer material, channel aspect ratio and method, IMM (2003). Together with manufacturing variations, channel narrowing due to particle deposition can also affect channel dimensions.

In order to study the effect of manufacturing tolerances on flow equipartition in manifolds, a maximum possible tolerance $\delta^{\#}_{MAX}$ (δ_{MAX}/D_C) is assumed that affects diameter ($\delta^{\#}_{D,MAX}$) in circular channels and both width ($\delta^{\#}_{W,MAX}$) and depth ($\delta^{\#}_{E,MAX}$) in rectangular ones. If $T_{i,j,}$ represents a i x j matrix with random numbers between 0 and 1, the tolerance matrix $\delta^{\#}_{i,j}$ that is applied to all channels in each structure for circular geometries is given by Eq. (7.35). Combining the tolerance matrix with that of the nominal diameter, $D^{\#}_{N,i,j,}$ (see Eq. (7.36)), gives the real channel diameters that are within $D^{\#}_{N} \pm \delta^{\#}_{D,MAX}$. This implies constant tolerance along each channel. For rectangular channels, equations similar to Eq. (7.35) and (7.36) are obtained for depth and width. If an increase in channel width also results in an increase in channel depth (same sign in all channels) not necessarily by the same amount, the same $T_{i,j,}$ matrix is used for both width and depth tolerances with $\delta^{\#}_{W,MAX}$ and $\delta^{\#}_{E,MAX}$ respectively. However, if depth and width vary independently, two different random $T_{i,j}$ matrices are used with $\delta^{\#}_{E,MAX}$ and $\delta^{\#}_{W,MAX}$ respectively. In the consecutive structure, i takes the values A for distributing, R for reaction and B for collecting channel and j refers to the channel or zone number (j = 1 to N). In the bifurcation structure i refers to the bifurcation level and j to the channel number at that level (j = 1 to $2 \cdot 2^i$ except at last level $i = b$, where j = 1 to 2^b):

$$\delta^{\#}_{i,j} = T_{i,j} \cdot 2\delta^{\#}_{MAX} - \delta^{\#}_{MAX} \tag{7.35}$$

$$D_{i,j}^{\#} = D_{\mathrm{N},i,j}^{\#} + \delta_{i,j}^{\#} \tag{7.36}$$

In the consecutive structure, the length of the reaction channels is assumed to be unaffected by tolerances while the zone lengths in the distributing and collecting channels are found from Eq. (7.37) and (7.38) for j = 1 to (N-1). In the bifurcation structure, all channel lengths are assumed to be unaffected by tolerances as they are several times the characteristic dimension D_C, and length also has a smaller effect than D_C on the pressure drop equation:

$$L_{\mathrm{A},(j+1)}^{\#} = sep^{\#} + D_{\mathrm{R},(j+1)}^{\#} + \left(D_{\mathrm{N}}^{\#} - D_{\mathrm{R,j}}^{\#}\right)/2 + \left(D_{\mathrm{N}}^{\#} - D_{\mathrm{R},(j+1)}^{\#}\right)/2 \tag{7.37}$$

$$L_{B,(N-j+1)}^{\#} = sep^{\#} + D_{\mathrm{R},(j+1)}^{\#} + \left(D_{\mathrm{N}}^{\#} - D_{\mathrm{R},j}^{\#}\right)/2 + \left(D_{\mathrm{N}}^{\#} - D_{\mathrm{R},(j+1)}^{\#}\right)/2 \tag{7.38}$$

In order to simulate channel blockage, an infinite resistance in the blocked channel is used.

7.4.5. Evaluation of Flow Distribution in Manifold Structures

In the absence of manufacturing variations and identical reaction channels, flowrate in each reaction channel is proportional to residence time and both parameters can be used to indicate how good the flow distribution is. When geometrical variations are present, however, the reaction channels do not necessarily have the same cross-sectional area and equal flowrates in each channel will not result in the same residence times. Given its importance in processes involving mass/heat transfer and reaction, residence time instead of flow rate will be used to assess flow distribution in manifold structures when variations are present. Residence time for reaction channel j = 1 to N is given by:

$$t_{\mathrm{R},j} = L_{\mathrm{R},j} / U_{\mathrm{R},j} \rightarrow t_{\mathrm{R},j}^{\#} = L_{\mathrm{R},j}^{\#} / U_{\mathrm{R};j}^{\#} \tag{7.39}$$

As different reaction channels may have different flowrates, a linear mean of the residence times may not be realistic. An average value for the structure is obtained from the ratio of the total volume in reaction channels to the total flowrate entering the structure:

$$t_{\mathrm{m}} = L\sum_{j=1}^{N} A_{\mathrm{R,j}} / Q_{\mathrm{T}} \rightarrow t_{\mathrm{m}}^{\#} = L^{\#}\sum_{j=1}^{N} A_{\mathrm{R},j}^{\#} / N \tag{7.40}$$

The standard deviation $\sigma(\%)$ of the residence time distribution in the reaction channels, which provides a measure of the uniformity of flow distribution, is given by:

$$\sigma(\%) = 100\sqrt{\frac{1}{N}\sum_{j=1}^{N}(t_{R,j}^{\#} / t_{m}^{\#} - 1)^2} \tag{7.41}$$

7.4.6. Consideration of Additional/Inertial Pressure Losses

Apart from frictional viscous energy losses, the consecutive structure can have additional energy losses due to entrance and exit effects that influence the total pressure drop and due to bends and branching/merging effects that influence directly the flow distribution. In the bifurcation structure, in addition to the entrance and exit effects, there are additional pressure losses due to stream splitting and joining before and after the reaction microchannels respectively. All these additional pressure losses can be expressed in a general way using a coefficient K (number of velocity heads) that multiplies the kinetic energy of the fluid:

$$\Delta P = K\rho\frac{U^2}{2} \tag{7.42}$$

where ΔP is the additional pressure loss, ρ is the density of the fluid and U is the velocity of the fluid in the channel where the additional pressure loss is considered. The value of the coefficient K depends on different parameters as a function of the geometry analysed. Furthermore, when additional pressure losses are considered the relationship between pressure drop and flow rate (or velocity) is not linear anymore and the equation used previously to calculate resistances is also dependent on the flow rate (or velocity):

$$\frac{\Delta P}{Q} = R = \frac{K\rho Q}{2A^2} \tag{7.43}$$

where Q is the flow rate in the channel. Therefore, the system of equations for consecutive and bifurcation structures is not linear and cannot simply be solved by inverting the matrix of the system. Non-dimensionalising, Eq. (7.43) becomes Eq. (7.44) where Re is given by Eq. (7.45), where D_C and U_C are the characteristic diameter and velocity respectively.

$$\frac{\Delta P^{\#}}{Q^{\#}} = R^{\#} = \frac{KQ^{\#}}{2A^{\#2}}Re \tag{7.44}$$

$$Re = \frac{\rho D_C U_C}{\mu} \tag{7.45}$$

7.4.6.1. Algorithm for Additional Pressure Losses

A consecutive structure with N reaction microchannels, is described by Eq. (7.14) and (7.15) where now the term of the resistances that contains the additional pressure losses is also a function of the flow rates according to Eq. (7.44). Since the system is not linear, a simple iterative method has been implemented for its solution, which was found to converge quickly and under different importance of these additional pressure losses, Zienkiewicz and Morgan (1983). Eq. (7.14) and (7.15) can be expressed in a matrix form by Eq. (7.46).

$$\mathbf{M(Q)} \cdot \mathbf{Q} = \mathbf{S} \tag{7.46}$$

where $\mathbf{M(Q)}$ is the $N*N$ matrix of the system, which is similar to matrix (7.18) but contains resistances that are a function of the flow rates, $\mathbf{Q}$ is a column vector with the flow rates of the N reaction microchannels, $Q^{\#}_{R,j}$, and $\mathbf{S}$ is a column vector that contains zeros except in the last position, which is the total flow rate $Q^{\#}_{T}$ entering the structure. The iterative method solves repeatedly Eq. (7.46) with successively improved values of $\mathbf{M(Q)}$. An initial guess $\mathbf{Q} = \mathbf{Q_0}$ is necessary, although as the resistances of the most substantial pressure drop (friction along channels) is not dependent on the flow rates, the initial guess to calculate the additional pressure losses is $\mathbf{Q} = 0$. This means that the system initially is solved neglecting the effect of the additional pressure losses due to bends, entrance/exit and merging/branching effects according to Eq. (7.47).

$$\mathbf{Q_1} = [\mathbf{M(Q_0)}]^{-1} \cdot \mathbf{S} \tag{7.47}$$

Vector $\mathbf{Q_1}$ gives the values of the flow rates in all reaction microchannels (branches) when additional pressure losses are neglected. This solution is used in the second iteration to estimate the new set of resistances and so on according to Eq. (7.48), until $(\mathbf{Q_n} - \mathbf{Q_{n-1}})$ is less than certain error tolerance.

$$\mathbf{Q_n} = [\mathbf{M(Q_{n-1})}]^{-1} \cdot \mathbf{S} \tag{7.48}$$

7.4.6.2. Estimation of *K* values in the Consecutive Structure

When there are no manufacturing variations, additional pressure losses due to merging/splitting and bend geometries do not affect flow distribution in the bifurcation structure (only total pressure drop) but they do affect the flow distribution in the consecutive structure (entrance/exit effects only influence the total pressure drop).

- *Division into Flow Streams (The Wye Geometry)*

According to Fried and Idelchik (1989), a wye is characterised by a branching angle α and the ratios of the cross-sectional areas of its branches, $A_{A,j}/A_{A,(j+1)}$, $A_{A,j}/A_{R,j}$ and $A_{A,(j+1)}/A_{R,j}$ in the case of the distributing channel of the consecutive structure when using the same nomenclature aforementioned (see Figure 7.6). Furthermore, different ratios of flowrates ($Q_{A,j}/Q_{A,(j+1)}$ and $Q_{A,j}/Q_{R,j}$) and velocities ($U_{A,j}/U_{A,(j+1)}$ and $U_{A,j}/U_{R,j}$) are possible, which together with the angle α and the ratios of cross-sectional areas will define the resistance coefficients K (velocity heads).

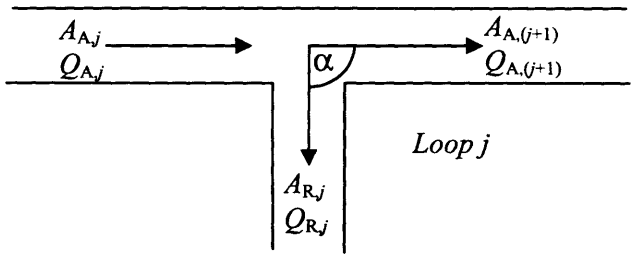

Figure 7.6. Flow stream division in the distributing channel of the consecutive structure.

In this case, the additional pressure loss is considered in the divided streams (zone j + 1 of the distributing channel and the reaction channel j). Eq. (7.49) and (7.50) for loop j = 1 to (N-1) apply when $A_{A,j} = A_{A,(j+1)}$ and $\alpha = 90°$, which is the situation in the consecutive structure designed with constant distributing/collecting (d/c) cross-section. Eq. (7.50) is only valid when d/c and reaction channels have the same height. It must be noted that if all cross-sectional areas are identical the ratio of velocities is equivalent to ratio of flow rates. The velocity between the K brackets refers to the velocity for which that value is based on and all the equations for K are expressed to be used with the fluid velocity in the channel where the pressure loss is considered in a consistent way for Eq. (7.44) to be applicable.

$$K_{A,(j+1)}(U_{A,(j+1)}) = 0.4\left(1-\frac{Q_{A,(j+1)}A_{A,j}}{Q_{A,j}A_{A,(j+1)}}\right)^2 \frac{1}{\left(Q_{A,(j+1)}A_{A,j}/Q_{A,j}A_{A,(j+1)}\right)^2} \quad ; \; j = 1,2,\ldots,N\text{-}1 \tag{7.49}$$

$$K_{R,j}(U_{R,j}) = G\left(1+0.3\left(\frac{Q_{R,j}A_{A,j}}{Q_{A,j}A_{R,j}}\right)^2\right)\frac{1}{\left(Q_{R,j}A_{A,j}/Q_{A,j}A_{R,j}\right)^2} \quad ; \; j = 1,2,\ldots,N\text{-}1 \tag{7.50}$$

In Eq. (7.50) G is equal to 1 when $A_{R,j}/A_{A,j} < 0.35$. If $A_{R,j}/A_{A,j} \geq 0.35$ and $Q_{R,j}/Q_{A,j} > 0.4$ $G = 0.55$ and if $Q_{R,j}/Q_{A,j} < 0.4$, G is given by:

$$G = 0.9\left(1-\frac{Q_{R,j}}{Q_{A,j}}\right) \tag{7.51}$$

- *Merging of Flow Streams*

For this case in the collecting channel (see Figure 7.7), the additional pressure losses account for the merging streams from the collecting channel zone (N-j+1) and reaction channel (j+1).

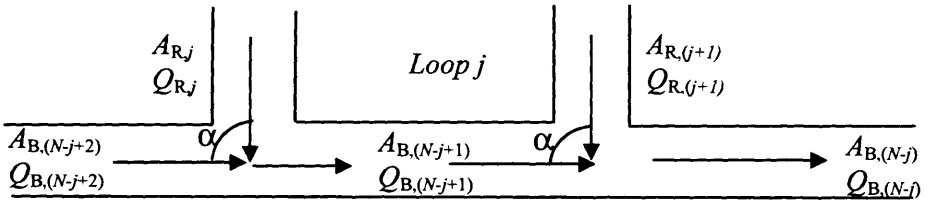

Figure 7.7. Merging of flow streams in the collecting channel of consecutive structure.

In this case, Eqs. (7.52) and (7.53) are applied, which are also for j = 1 to (N-1):

$$K_{B,(N-j+1)}(U_{B,(N-j+1)}) = \left(1.55\frac{Q_{R,(j+1)}}{Q_{B,(N-j)}} - \left(\frac{Q_{R,(j+1)}}{Q_{B,(N-j)}}\right)^2\right)\frac{1}{\left(1-Q_{R,(j+1)}/Q_{B,(N-j)}\right)^2} \tag{7.52}$$

$$K_{R,(j+1)}(U_{R,(j+1)}) = G\left(1+\left(\frac{Q_{R,(j+1)}A_{B,(N-j)}}{Q_{B,(N-j)}A_{R,(j+1)}}\right)^2 - 2\left(1-\frac{Q_{R,(j+1)}}{Q_{B,(N-j)}}\right)^2\right)\frac{1}{\left(Q_{R,(j+1)}A_{B,(N-j)}/Q_{B,(N-j)}A_{R,(j+1)}\right)^2} \tag{7.53}$$

Eq. (7.53) can be expressed as a function of index j instead of $(j+1)$ as Eq. (7.54) shows, which is used for $j = 2$ to N. In this way, contributions to the additional pressure losses in the reaction channels from Eq. (7.50) and (7.54) can be added together for reaction channel $j = 2$ to $(N\text{-}1)$. For reaction channel $j = 1$, the only contribution is Eq. (7.50) and for reaction channel $j = N$, Eq. (7.54) is the only contribution.

$$K_{R,j}(U_{R,j}) = G\left(1+\left(\frac{Q_{R,j}A_{B,(N-j+1)}}{Q_{B,(N-j+1)}A_{R,j}}\right)^2 - 2\left(1-\frac{Q_{R,j}}{Q_{B,(N-j+1)}}\right)^2\right)\frac{1}{\left(Q_{R,j}A_{B,(N-j+1)}/Q_{B,(N-j+1)}A_{R,j}\right)^2} \quad (7.54)$$

In Eq. (7.54) G is equal to 1 when $A_{R,j}/A_{B,(N-j+1)} < 0.35$. If $A_{R,j}/A_{B,(N-j+1)} \geq 0.35$ and $Q_{R,j}/Q_{B,(N-j+1)} > 0.4$, $G = 0.55$ and if $Q_{R,j}/Q_{B,(N-j+1)} < 0.4$, G is given by:

$$G = 0.9\left(1-\frac{Q_{R,j}}{Q_{B,(N-j+1)}}\right) \quad (7.55)$$

Flowrates and areas in Eq. (7.49) to (7.53) can also be dimensionless as they only appear in ratios.

7.5. Full Mathematical Model (FEM Simulations)

Some simulations are compared with 3D Femlab simulations for validation of the analytical method. The software is based on the Finite Element method and solves the continuity and Navier-Stokes equations, which are given in dimensionless form by Eq. (7.56) and (7.57) for an incompressible liquid of constant density and viscosity. Velocity and coordinates are made dimensionless with the equipartition flowrate and characteristic length respectively and the dimensionless pressure is given by Eq. (7.3). The velocity vector $\mathbf{U}^{\#}$ has the components $(U^{\#}_x, U^{\#}_y, U^{\#}_z)$.

$$\nabla^{\#} \cdot \mathbf{U}^{\#} = 0 \quad (7.56)$$

$$Re\mathbf{U}^{\#} \cdot \nabla\mathbf{U}^{\#} = -\nabla^{\#}P^{\#} + \nabla^{\#2}\mathbf{U}^{\#} + \frac{Re}{Fr}\frac{\mathbf{g}}{g} \quad (7.57)$$

The Reynolds number, Re, defined by Eq. (7.45) together with the Froude number, Fr, given by Eq. (7.58) define the system. However, the quantity $1/Fr$ is negligible at microscale. In order to

compare FEM simulations with results from the analytical model presented above, D_C and U_C have the same definition: D_C is the smallest dimension of the reaction channels and U_C is given by the equiparition flowrate Q_{EQ} divided by the characteristic area ($A_C = \pi D_C^2/4$ and $A_C = D_C^2$ for circular and rectangular channels respectively). Because a characteristic flowrate was chosen instead of a characteristic velocity, the definition of this system Reynolds number is only equivalent to the nominal Reynolds number in the reaction channels when the aspect ratio of the reaction channels is 1, that is $Re = Re_n/\min(E_R/W_R, W_R/E_R)$ where $Re_n = \rho D_C U_{Av}/\mu$.

$$Fr = \frac{U_C^2}{gD_C} \tag{7.58}$$

These simulations will help to check if the assumptions made in the RNM are correct. In this case the simulations at low Re, where additional pressure losses are negligible should be close to the results from the resistance network methodology. 3D simulations have been accomplished using square channels rather than circular ones in order to reduce the number of mesh elements while maintaining a good mesh quality.

7.6. Experimental Work

Local measurement of flowrate or velocity in microchannel is not a simple matter and generally requires expensive equipment, laser techniques being the most common: a two laser technique where a chemical is uncaged using a Nd:YAG laser and then excited using a Nd:YVO4 laser (Paul et al., 1998), one-laser techniques (Taylor et al., 1993), micro-PIV (Tseng et al. 2002). The output of these techniques is the velocity profile while the validation of the RNM only requires the average flowrate per channel. The Doppler effect technique, generally used for measuring blood flowrates, requires probes around elastic channels, which in this case is not feasible.

The device depicted in Figure 7.8 and Figure 7.9 was built in order to check different features of the analytical RNM. This device enables to measure flow distribution at different total flowrates in a way that the effect of additional pressure losses can also be analysed as a function of Reynolds number. Ethanol ($\rho_{ethanol}$ = 789 kg/m^3, γ= 0.02149 N/m) is the fluid used because of a low surface tension.

Figure 7.8. Set up of the manifold device for measuring liquid flow distribution.

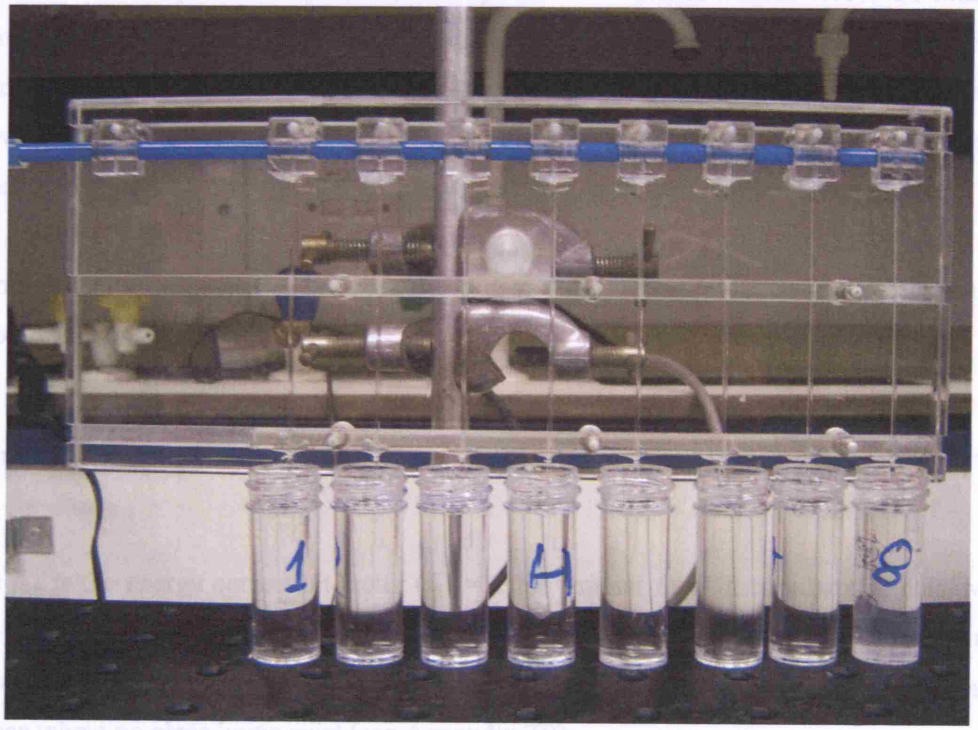

Figure 7.9. Close up of the experimental manifold device.

The distributing channel (blue channel in Figure 7.9) consists of a rigid butyrate tube (i.d = 2.2 mm, o.d.= 4.8 mm) while the branches are 50-µl precision bore capillaries (± 1% volume, 794 µm i.d., 1092 µm o.d.). The dimensions of the manifold are the following:

- Reaction microchannels (N = 8): $D^{\#}_{R,j}$ = 1, $L^{\#}_{R,j}$ = 125.9.
- Distributing channel: $D^{\#}_{A,j}$ = 2.771 (j = 1 to N), $Sep^{\#}$ = 27.71, $D^{\#}_{A,1}$ = 100.8.

The separation between microcapillaries is large enough (sep = 22 mm) for direct collection of the liquid in small plastic cylinders (see Figure 7.9). For the start-up, all branches apart from the first one are blocked until no bubbles flow through. Then, channel 1 is blocked and channel 2 is unblocked until no bubbles are observed. This process is repeated with the 8 channels until liquid free of bubbles flows through all of them. When the capillaries tips are facing the air, small diameter variations in the capillary tips result in unequal surface tension forces to be overcome, which lead to blockage of certain channels at low total flowrates Q_T. This problem can be avoided by filling the cylinders with the same flowing liquid up to the middle and immersing the capillary tips inside the liquid. However, this results in different pressures at the exit of the capillaries, which affects flow distribution. Thus, the capillaries are placed in an angle so that their tips touch the wall of the cylinder and surface tension forces are minimised (the meniscus is broken by the wall and a continuous flow of liquid is achieved). The cylinders are weighted before and after the fluid flow during certain time and the mass rates are converted to flow rates using the density of the fluid. Evaporation rates, which depend on cylinder cross section are the same in all cylinders and they were measured and found to be negligible.

If Bernoulli equation is applied between the inlet to the structure (point 1) and any two capillary tips (points 2a and 2b),

$$\rho g\left(h_{1\to 2a}-h_{1\to 2b}\right)+f_{KE}\frac{1}{2}\rho\left(U_{2a}^{2}-U_{2b}^{2}\right)+\rho g\left(z_{2a}-z_{2b}\right)+\left(P_{2a}-P_{2b}\right)=0 \qquad (7.59)$$

where f_{KE} is the energy correction factor (f_{KE} = 2 for laminar flow in circular channels; Massey and Ward-Smith, 1998). For the experimental device, the capillary tip heights and pressures are the same in all branches and only energy losses and changes in kinetic energy are considered for this case where no close loops exist (see Appendix 7B).

7.7. Results and Discussion

7.7.1. Designs and Criteria for Uniform Flow Distribution in the Absence of Manufacturing Variations

When there are no manufacturing variations, uniform flow distribution is always achieved in the bifurcation structure where the channels at each level have the same size. In the consecutive structure, however, a proper design of the distributing and collecting (d/c) channels is required for flow equipartition and two different methods are analysed below. To characterise consecutive structure designs that do not result in equipartition, a divergence parameter *FD (Flow Distribution)* is used, defined by Eq. (7.60). In the absence of manufacturing variations, where all reaction channels have the same length and area, *FD* also determines the maximum residence time divergence from the desired residence time in the reaction channels (e.g. 5.26 % when *FD* = 5 %). Therefore, *FD* is used as a design parameter when tolerances are not present.

$$FD(\%) = \max_{j=1}^{N}\left[100\frac{\left|\dot{Q}_{EQ} - \dot{Q}_{R,j}\right|}{\dot{Q}_{EQ}}\right] = \max_{j=1}^{N}\left[100\left|1 - \dot{Q}_{R,j}^{\#}\right|\right] \tag{7.60}$$

7.7.1.1. Method 1: Uniform Flow Distribution via Reduction of Pressure Drop in Distributing/Collecting (d/c) Channels

In this approach pressure drop through the d/c channels is reduced compared to that in the reaction channels. In circular channels, this can be achieved if the d/c channels have a constant diameter, D_A, larger than the reaction channels' diameter, D_R, by a factor that depends on channel geometry, number and required degree of divergence from flow equipartition, *FD*. For zero divergence, zero pressure drop in the d/c channels is required. Therefore, considering the same geometry for the d/c zones (*PAR* = 2) Eq. (7.14) and (7.15) are solved iteratively for different numbers of reaction channels *N* and different ratios of resistances R_R/R_A (equal to R_R/R_B) until the flowrate in each reaction channel diverges less than a certain % *FD*. Figure 7.10 shows results for four different *FD*: 1 %, 2 %, 5 % and 10 %. These results are valid for any channel geometry and it can be seen that a large ratio of resistances (or cross-sectional areas) is required for uniform flow distribution, especially for 1 % divergence, which increases with the number of channels.

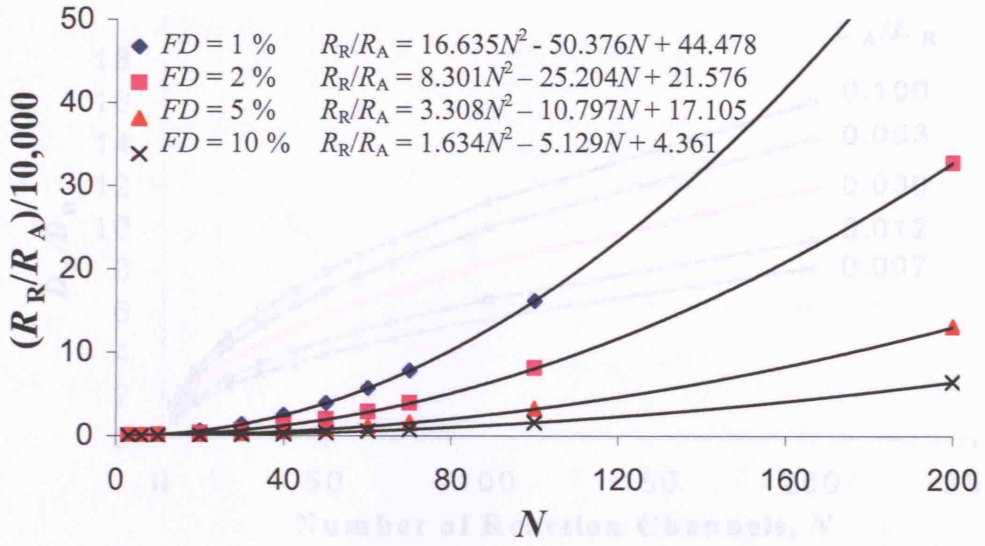

Figure 7.10. Ratio R_R/R_A required for uniform flow distribution in the consecutive structure as a function of the number of reaction channels N and the divergence from flow equipartition FD.

From the above results for resistance ratios, the actual channel diameter and length ratios can be obtained for circular geometries from Eq. (7.5). The ratios of d/c to reaction channel diameters D_A/D_R ($D^{\#}_A$ for circular channels) are shown in Figure 7.11 for 1 % divergence from flow equipartition as a function of the ratio of zone length in d/c channels to reaction channel length L_A/L_R and number of reaction channels N. These results also apply to rectangular geometries when all channels in the structure have the same or inverse aspect ratio (*see* Eq. (7.7) and (7.9)). This is feasible when different microchannel depths can be manufactured in the same substrate (i.e. anisotropic etching in silicon wafer, Powell and Harrison (2001). However, when all channels have the same depth, Figure 7.11 can be used if the width to depth ratio of the d/c channels is made equal to the depth to width ratio of the reaction channels. This is achieved using an intermediate depth between the reaction channel and the d/c channel widths. If the depth is equal to or smaller than the reaction channel width, the width of the d/c channels needs to be very large to obtain the required ratio R_R/R_A for flow equipartition (since the hydraulic diameter cannot be larger than double the minimum dimension). For any rectangular geometry (still $PAR = 2$), a similar graph to Figure 7.11 can be obtained from Figure 7.10 together with Eq. (7.8) where flow distribution would depend on 5 geometrical variables rather than 3: (L_A/L_R, E_R/W_R, E_A/W_A, W_A/W_R and N).

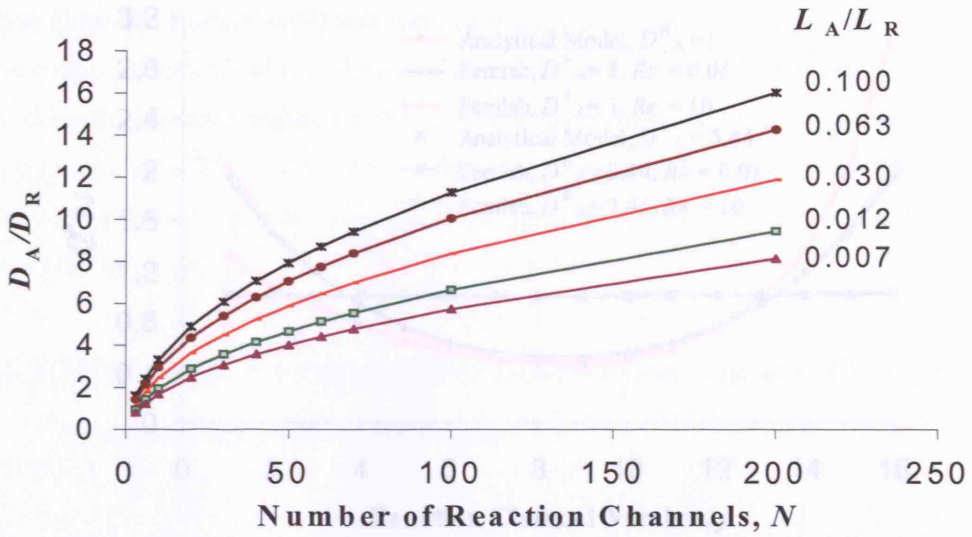

Figure 7.11. Ratio D_A/D_R of circular channels required for uniform flow distribution (FD = 1%) in the consecutive structure as a function of the number of reaction channels, N, and the length ratio L_A/L_R.

Figure 7.12 shows the flow distribution in the reaction channels for two different hydraulic diameter ratios $D^{\#}_A = 1$ (FD = 101.6%) and $D^{\#}_A = 3.44$ (FD = 1%) for a 16-channel structure with length ratio $L_A/L_R = 0.04$ and square channels (the distribution solution is the same one as for circular channels). Comparisons are also carried out with the commercial software Femlab that simulates fluid flow in the 3D microchannels. Two different Reynolds numbers, Re = 0.01 and Re = 10 are used. According to the analytical model, the structure with $D^{\#}_A = 1$ shows a 101.6 % divergence from flow equipartition while the one with $D^{\#}_A = 3.44$ shows a divergence of 1 %. The results from FEMLAB are very similar to those of the analytical model at low Re. Some discrepancies at higher Re and FD are due to the effect of additional pressure losses that are neglected in the analytical model in this case. For this structure, a 5 % divergence would reduce the required ratio $D^{\#}_A$ to 2.30.

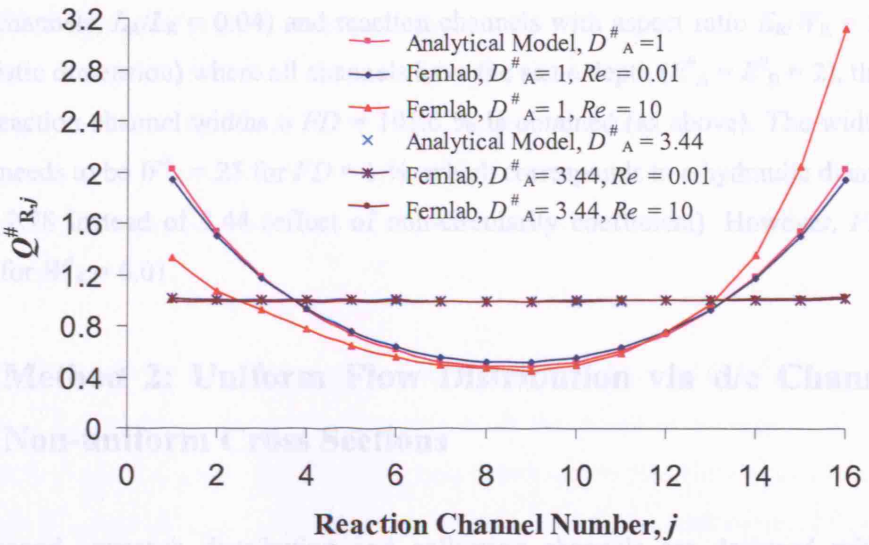

Figure 7.12. Flow distribution in square channels from analytical and Femlab models.

The implementation of the 16-channel consecutive structure with square distributing/collecting and reaction channels in Femlab software is explained in Appendix 7C for the case $D^{\#}_A = 1$. The dimensions to consider are: $W^{\#}_R = 1$, $Sep^{\#} = 1$, $L^{\#}_A/L^{\#}_R = L^{\#}_B/L^{\#}_R = 0.04 \rightarrow L^{\#}_R = 50$, $L^{\#}_{A,1} = L^{\#}_{B,1} = 10$ and $Re = 0.01$ (to minimise the additional pressure losses). Figure 7.13 shows the geometry and solution for the aforementioned structure. Both the analytical and full mathematical models produce a symmetrical velocity distribution in the reaction channels (at low Re).

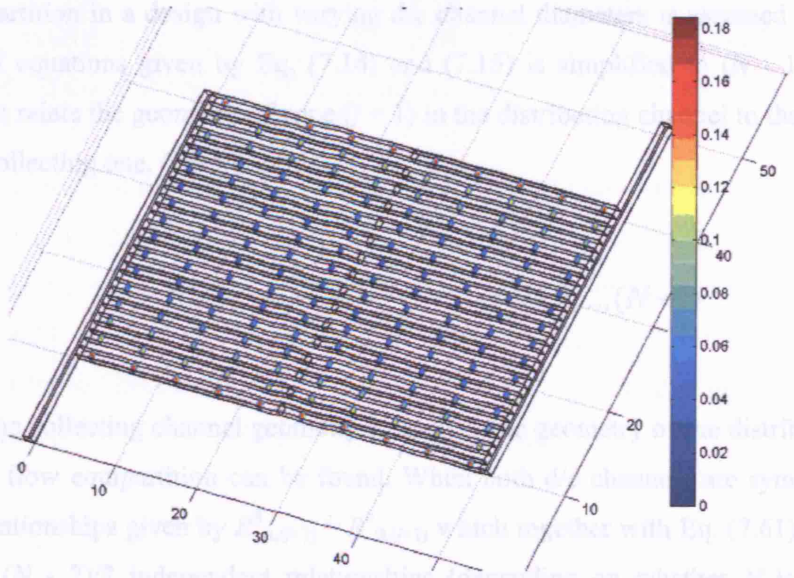

Figure 7.13. Femlab geometry and velocity field in a 16-channel structure with square channels and properties: $W^{\#}_R = 1$, $Sep^{\#} = 1$, $L^{\#}_A/L^{\#}_R = 0.04$, $L^{\#}_R = 50$, $L^{\#}_{A,1} = L^{\#}_{B,1} = 10$ and $Re = 0.01$.

If a rectangular channel structure is used with the same specifications as the one above (16 reaction channels, L_A/L_R = 0.04) and reaction channels with aspect ratio E_R/W_R = 2 (W_R is the characteristic dimension) where all channels have the same depth ($E^{\#}_A = E^{\#}_B = 2$), then for equal d/c and reaction channel widths a FD = 101.6 % is obtained (as above). The width of the d/c channels needs to be $W^{\#}_A = 25$ for FD = 1 %, which corresponds to a hydraulic diameter ratio of D_A/D_R = 2.78 instead of 3.44 (effect of non-circularity coefficient). However, FD = 5 % is achieved for $W^{\#}_A = 6.01$.

7.7.1.2. Method 2: Uniform Flow Distribution via d/c Channels with Non-uniform Cross Sections

In the second approach distributing and collecting channels are designed with gradually decreasing and increasing cross section area respectively, not necessarily linearly, in the flow direction. There is no size restriction for the d/c channel dimensions for flow equipartition but the actual size will define the total pressure drop and the effect of manufacturing tolerances. This approach is the most suitable when the manifold area needs to be minimised and all channels must have the same depth, which in turn is similar to or smaller than the reaction channels' width. Commenge et al. (2002) suggested an optimised design with non-linear d/c channels to limit the infinite solutions available for flow equipartition since some of them can give non-realistic geometries and flow recirculation patterns. Optimum linear d/c channels were also considered, which produce solutions close to flow equipartition in most cases.

If flow equipartition in a design with varying d/c channel diameters is assumed ($Q_{R,j} = Q_T/N$), the system of equations given by Eq. (7.14) and (7.15) is simplified to (N - 1) independent equations, that relate the geometry of zone (j + 1) in the distributing channel to that of zone ($N - j + 1$) in the collecting one, (see Eq. (7.61)).

$$R^{\#}_{A(j+1)} = \frac{R^{\#}_{B,(N-j+1)}}{(N/j-1)} \qquad j = 1,2,...,(N-1) \tag{7.61}$$

If therefore, the collecting channel geometry is known, the geometry of the distributing channel that produces flow equipartition can be found. When both d/c channels are symmetrical there are (N - 1) relationships given by $R^{\#}_{A,(j+1)} = R^{\#}_{B,(j+1)}$ which together with Eq. (7.61) only produce (N - 1)/2 or (N - 2)/2 independent relationships (depending on whether N is odd or even respectively), since Eq. (7.61) is the same for both $j = j$ and $j = (N - j)$. Therefore, for (N - 1)

zones there are $(N - 1)/2$ or $N/2$ degrees of freedom (either odd or even N respectively) that produce infinite geometries for flow equipartition.

A simple method is suggested below for finding the exact geometry for perfect flow equipartition in such a structure with symmetrical d/c channels that occupy small area and have close to linear diameter (or width) variation when the value of $D^{\#}_{B,N}$ (or $W^{\#}_{B,N}$ for rectangular channels) is given.

A. Initially, the *optimum linear d/c channels* are obtained by calculating $D^{\#}_{B,2}$ that together with the given $D^{\#}_{B,N}$ produces linear d/c channels with the smallest divergence FD from flow equipartition. An initial guess for $D^{\#}_{B,2}$ is found assuming perfect flow equipartition from Eq. (7.61) when $R^{\#}_{A,(j+1)} = R^{\#}_{B,(j+1)}$ ($D^{\#}_{B,1}$ does not influence the flow distribution). $D^{\#}_{B,2}$ needs to be readjusted until FD is minimised.

B. Either the collecting or distributing channel, e.g. collecting channel, is then assumed to have linear geometry defined by points $(D^{\#}_{B,2}, 2)$ and $(D^{\#}_{B,N}, N)$: $D^{\#}_{B,(j+1)} = D^{\#}_{B,2} - (j - 1)(D^{\#}_{B,2} - D^{\#}_{B,N})/(N - 2)$. The geometry of the distributing channel is found by Eq. (7.61) for flow equipartition. This does not result in identical d/c channels but very similar, one linear (see Figure 7.14) and the other slightly curved.

C. An intermediate geometry between the linear and the curved one, $D^{\#}_{B,(j+1)} = (D^{\#}_{A,(j+1)} + D^{\#}_{B,(j+1)})/2$, is used as a new geometry for the collecting channel, while from Eq. (7.61) the distributing channel geometry is recalculated, which in circular channels is the same as that of the collecting channel (see Figure 7.14). This geometry is already the final one for circular channels, in which the final value of $D^{\#}_{B,N}$ is not exactly the initial one but very close to it.

A similar procedure (but iterative in the last stage) can be applied to rectangular channels using channel widths rather than diameters. This simple method produces feasible geometries that are close to the optimum linear geometry, in just a few steps. Both the exact and optimum linear d/c channel geometries for a 16 reaction channel structure with $L_A/L_R = 0.04$ are shown in Figure 7.14 for two different initial values $D^{\#}_{B,16} = 1$ and $D^{\#}_{B,16} = 0.5$, which for the case of linear channels produce $FD = 1.90$ % and $FD = 16.8$ % respectively.

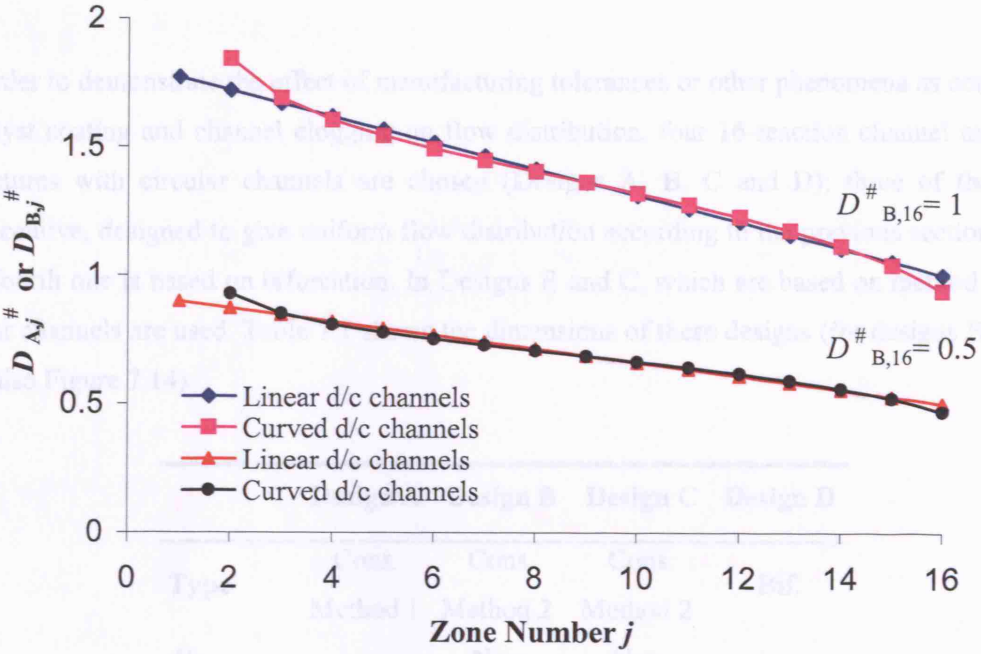

Figure 7.14. Optimum linear and curved (perfect flow equipartition) d/c channels in the consecutive structure for uniform flow distribution when initial $D^{\#}_{B,16} = 1$ and $D^{\#}_{B,16} = 0.5$.

When using optimum linear d/c channels, the divergence from flow equipartition *FD* depends on the number of reaction channels, ratio of lengths $L_A/L_R = L_B/L_R$, aspect ratio in d/c zones and reaction channels and $D^{\#}_{B,N}$ (or $W^{\#}_{B,N}$ in rectangular channels). For a specific structure, *FD* can be improved by modifying the value of $D^{\#}_{B,N}$. For example, in a consecutive circular channel geometry with optimum linear d/c channels, length ratio $L_A/L_R = 0.04$, and diameter in the first collecting channel zone equal to that of the reaction channels ($D^{\#}_{B,N} = 1$), the divergence from flow equipartition is *FD* = 1.90 % and *FD* = 19.19 % for 16-channel and 64-channel structures respectively ($D^{\#}_{B,2}$ is 1.72 and 1.95). In the 64-channel structure $D^{\#}_{B,N} = 2.4$ ($D^{\#}_{B,2} = 4.45$) is required to reduce *FD* to 1 %. In a rectangular channel structure, where all channels have the same depth, which in turn is similar to or smaller than the reaction channel width, the flow divergence for optimum linear d/c channels is much smaller. For instance, a 64-reaction channel structure with rectangular channels, optimum symmetrical d/c channels and constant depth ($E^{\#}_{i,j} = 1$) with: $L_A/L_R = 0.04$, $E_R/W_R = 1$ and $W^{\#}_{B,64} = 1$ produces *FD* = 0.33 %, although larger widths are required for the d/c channels (i.e. $W^{\#}_{B,2} = 24.1$).

7.7.2. Effect of Manufacturing Tolerances on Flow Distribution

In order to demonstrate the effect of manufacturing tolerances or other phenomena as corrosion, catalyst coating and channel clogging on flow distribution, four 16-reaction channel manifold structures with circular channels are chosen (Designs A, B, C and D); three of them are consecutive, designed to give uniform flow distribution according to the previous section while the fourth one is based on bifurcation. In Designs B and C, which are based on method 2 non-linear channels are used. Table 7.1 shows the dimensions of these designs (for designs B and C see also Figure 7.14).

	Design A	**Design B**	**Design C**	**Design D**
Type	Cons. Method 1	Cons. Method 2	Cons. Method 2	Bif.
d/c channels	Uniform	Non-linear	Non-linear	Uniform
FD, %	1	0	0	0
$D^{\#}_{A=B,j}$	3.44	----	----	----
$D^{\#}_{A=B,16}$	----	0.471	0.937	----
$D^{\#}_{i,j}$	----	----	----	1
$L^{\#}_{R,j}$	50	50	50	50
$L^{\#}_{A=B,1}$	10	10	10	----
$L^{\#}_{i,j}$ $(i < b)$	----	----	----	10
$L_{A=B}/L_R$	0.04	0.04	0.04	----

Table 7.1. Dimensions for Designs A, B, C and D, which are 16-channel structures with circular channels (see also Figure 7.14 for designs B and C). Cons. = Consecutive; Bif. = Bifurcation.

In Figure 7.15 the distribution of standard deviations of residence times, σ (%), and its mean value, σ_m (%), obtained after 10000 runs, are shown for the four designs when $\delta^{\#}_{D,MAX} = 0.05$. The residence time variation in the reaction channels for the maximum standard deviation (worst case out of 10000 runs) in each structure is shown in Figure 7.16.

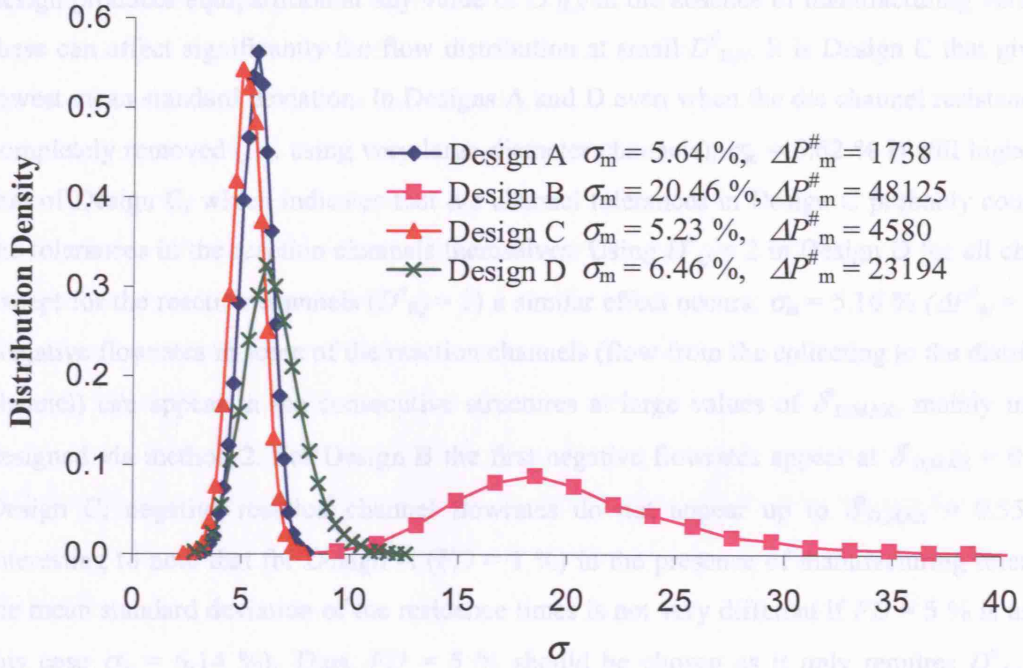

Figure 7.15. Distribution of standard deviations of residence times in the reaction channels after 10000 runs for designs A, B, C and D.

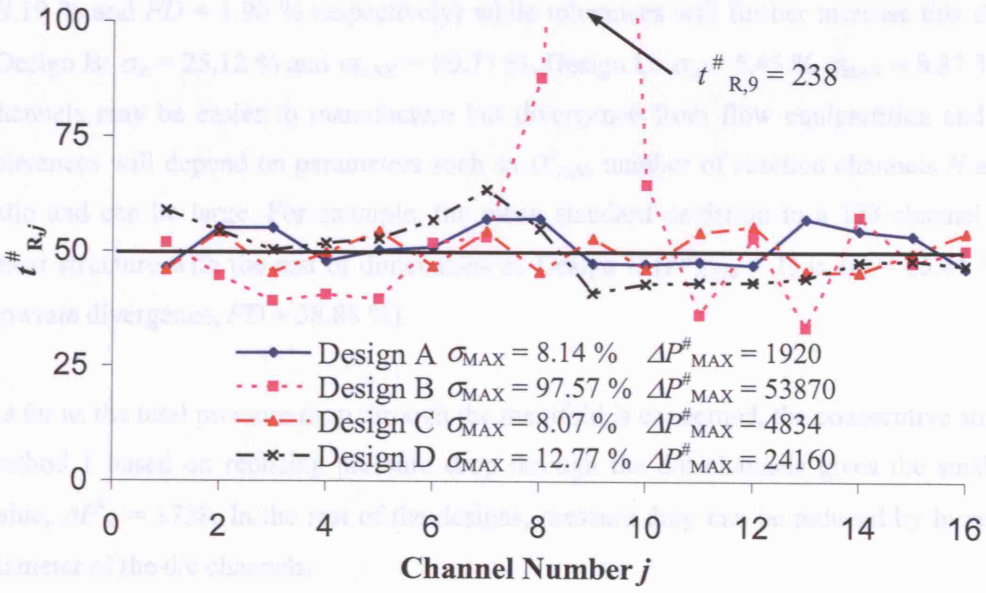

Figure 7.16. Residence times in the reaction channels of designs A, B, C and D for the worst scenario out of 10000 runs.

Design B appears to have the largest mean standard deviation, which shows that although this design produces equipartition at any value of $D^{\#}_{B,N}$ in the absence of manufacturing variations, these can affect significantly the flow distribution at small $D^{\#}_{B,N}$. It is Design C that gives the lowest mean standard deviation. In Designs A and D even when the d/c channel resistances are completely removed (i.e. using very large diameter channels), σ_m = 5.62 % is still higher than that of Design C, which indicates that d/c channel tolerances in Design C probably counteract the tolerances in the reaction channels themselves. Using $D^{\#}_{i,j}$ = 2 in Design D for all channels except for the reaction channels ($D^{\#}_{R,j}$ = 1) a similar effect occurs, σ_m = 5.16 % ($\Delta P^{\#}_m$ = 2863). Negative flowrates in some of the reaction channels (flow from the collecting to the distribution channel) can appear in the consecutive structures at large values of $\delta^{\#}_{D,MAX}$, mainly in those designed via method 2. For Design B the first negative flowrates appear at $\delta^{\#}_{D,MAX}$ = 0.10. In Design C, negative reaction channel flowrates do not appear up to $\delta^{\#}_{D,MAX}$ = 0.55. It is interesting to note that for Design A (*FD* = 1 %) in the presence of manufacturing tolerances, the mean standard deviation of the residence times is not very different if *FD* = 5 % is used (in this case σ_m = 6.14 %). Thus, *FD* = 5 % should be chosen as it only requires $D^{\#}_{A,j}$ = 2.3 compared to $D^{\#}_{A,j}$ = 3.44 for *FD* = 1%.

In the above Designs B and C, non-linear collecting and distributing channels were used. If only linear d/c channels are possible, flowrates will diverge from the equipartition flowrate (*FD* = 19.19 % and *FD* = 1.90 % respectively) while tolerances will further increase this divergence (Design B: σ_m = 25.12 % and σ_{MAX} = 90.77 %, Design C: σ_m = 5.43 % σ_{MAX} = 8.37 %). Linear channels may be easier to manufacture but divergence from flow equipartition and effect of tolerances will depend on parameters such as $D^{\#}_{B,N}$, number of reaction channels *N* and length ratio and can be large. For example, the mean standard deviation in a 128-channel optimum linear structure with the rest of dimensions as Design C ($D^{\#}_{B,128}$ = 1) is σ_m = 65.44 % (design flowrate divergence, *FD* = 38.88 %).

As far as the total pressure drop through the manifold is concerned, the consecutive structure by method 1 based on reducing pressure drop through the d/c channels gives the smaller mean value, $\Delta P^{\#}_m$ = 1738. In the rest of the designs, pressure drop can be reduced by increasing the diameter of the d/c channels.

In order to compare residence times in manifold structures with rectangular channels, these must have the same cross-sectional area (see Eq. (7.10)). If all channels are square, $\delta_{E,MAX}$ and $\delta_{W,MAX}$ are the same (or similar) and depth and width tolerances are positively proportional, i.e. a positive width tolerance produces a positive depth tolerance in each channel (e.g. KOH etching),

the results will be similar to those shown in the circular channel analysis above. However, when d/c channels have a different aspect ratio from the reaction channels, there is a reaction channel aspect ratio that minimises the effect of tolerances for each $\delta_{E,MAX}/\delta_{W,MAX}$ ratio. Finally, when the depth and width tolerances in each channel are not related (e.g. milling), they have a counteracting overall effect and there is a reaction channel aspect ratio that minimises the effect of manufacturing variations as well. As an example of the last case, Figure 7.17 shows distributions of the standard deviation of the residence times after 10000 runs for 3 different 16-channel consecutive structures (Designs E, F and G) designed by method 2 with optimum linear d/c channels where depth and width tolerances are not related, $\delta_{W,MAX} = \delta_{D,MAX}$ (value used for the circular channel case). Table 7.2 shows the dimensions of these designs. The absolute tolerances as well as lengths are the same in all designs although the dimensionless values are different. However channel separation, *sep*, is slightly modified in order to keep the ratio L_A/L_R = 0.04. Design G with a reaction channel aspect ratio of 1.4 gives the smallest mean standard deviation.

	Design E	**Design F**	**Design G**
Type	Cons. Method 2	Cons. Method 2	Cons. Method 2
d/c channels	Linear	Linear	Linear
***FD*, %**	0.14	0.032	0.069
$E^{\#}_{i,j}$	1	1	1
$W^{\#}_{R,j}$	1	2	1.4
$W^{\#}_{B=A,16}$	1	2	1.4
$W^{\#}_{B=A,2}$	6.6	20.8	12.2
$L^{\#}_{R,j}$	56.42	79.79	66.76
$L_{A=B}/L_R$	0.04	0.04	0.04
$\delta_{W,MAX}/\delta_{E,MAX}$	2	2	2
$\delta^{\#}_{W,MAX}$	0.0564	0.0798	0.0668

Table 7.2. Dimensions for Designs E, F and G, which are 16-channel consecutive structures with rectangular channels designed by method 2 with optimum linear d/c channels and same depth in all channels $E^{\#} = 1$.

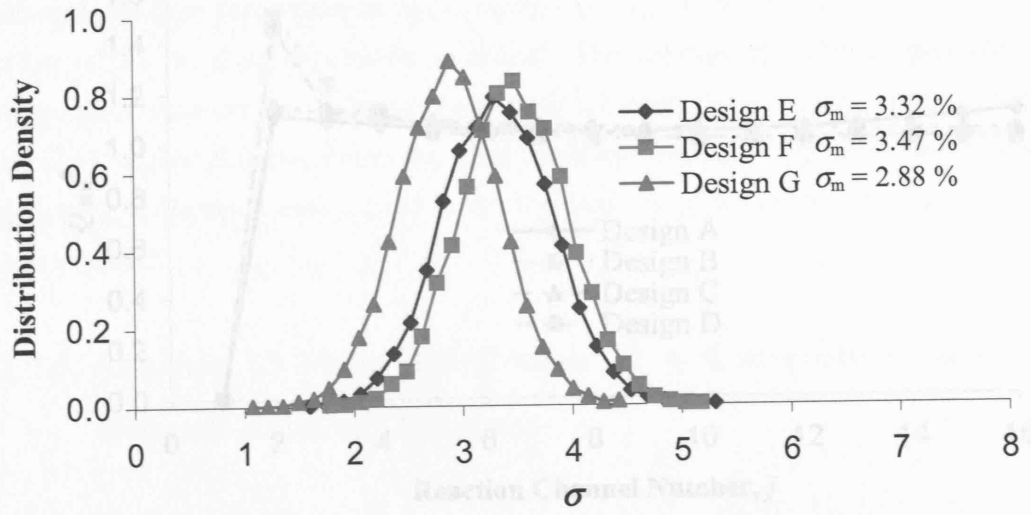

Figure 7.17. Distribution of standard deviations of residence times in the reaction channels after 10000 runs for designs E, F and G.

7.7.3. Effect of Channel Blockages on Flow Distribution

Manufacturing defects, clogging processes due to particle deposition and bubbles trapped inside the channels can give rise to channel blockages. The response of manifold Designs A, B, C and D, used in the previous section, is now studied when one reaction channel (channel 1) is blocked. Figure 7.18 shows the flowrate distribution in the reaction channels for each design. It can be seen that Design A reaches a new flow equipartition state with the flowrate of channel 1 equally distributed among the other channels. In the consecutive structures with varying diameters in the d/c channels (Designs B and C), flow equipartition is reached when the diameter of the d/c channels is sufficiently large. As a result flow distribution improves significantly when $D^{\#}_{A,16}$ increases from 0.471 (Design B) to 0.937 (Design C). A similar situation is reached in design D if the diameter of the d/c channels is sufficiently large.

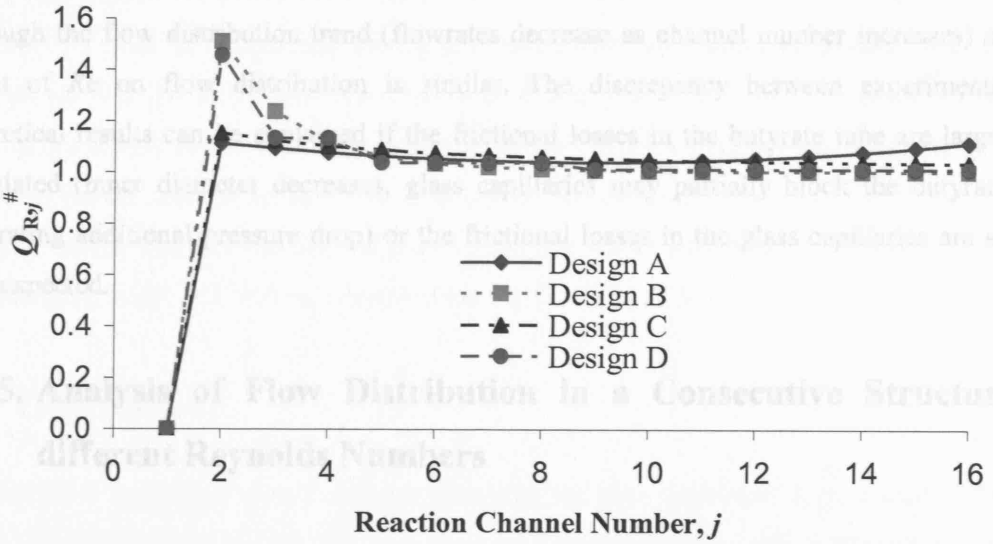

Figure 7.18. Flow distribution in reaction channels of designs A, B, C and D when channel 1 is blocked.

7.7.4. Comparison with Experimental Results

This design should give a flow equipartition of FD = 6.46 % according to the RNM of the consecutive structure. In this case there is no collecting channel and $R^{\#}_{B,j} = 0$ in the Matlab program (Appendix 7B). Figure 7.19 compares the experimental results obtained in the scale-out device shown in Figure 7.8 for three different flowrates Q_T or Re with those obtained from the RNM.

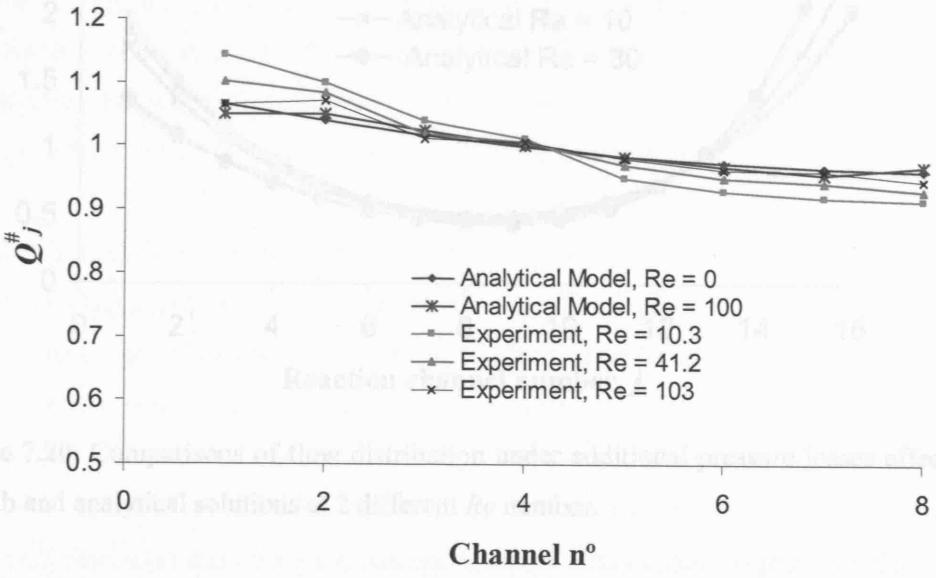

Figure 7.19. Flow distribution comparison between experimental and theoretical results.

The experimental results show a larger *FD* than results from the resistance network models although the flow distribution trend (flowrates decrease as channel number increases) and the effect of *Re* on flow distribution is similar. The discrepancy between experimental and theoretical results can be explained if the frictional losses in the butyrate tube are larger than calculated (inner diameter decreases, glass capillaries may partially block the butyrate tube generating additional pressure drop) or the frictional losses in the glass capillaries are smaller than expected.

7.7.5. Analysis of Flow Distribution in a Consecutive Structure at different Reynolds Numbers

The effect of additional pressure losses on flow distribution in manifold structures (detailed in Section 7.4.7) is demonstrated in this section. Figure 7.20 shows flow distribution in the reaction channels for a distributing/collecting channel depth and width identical to the reaction channels, $W^{\#}_{A} = E^{\#}_{A} = 1$ in a 16-channel structure with length ratio $L_A/L_R = 0.04$ and square channels (rather than circular ones in order to have faster Femlab simulations). Comparisons are also carried out with the commercial software Femlab.

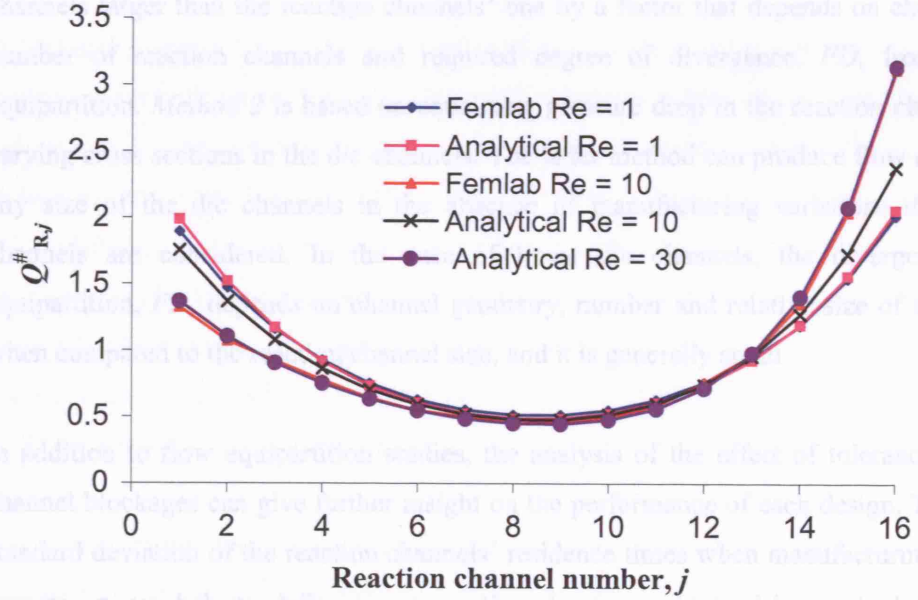

Figure 7.20. Comparisons of flow distribution under additional pressure losses effect between Femlab and analytical solutions at 2 different *Re* number.

At low Reynolds numbers ($Re \leq 1$) the agreement between analytical and full models is good. At $Re = 10$ both flow distributions do not match very well although results from Femlab simulations and the analytical model show a similar trend. In order to get the same flow distribution results in the analytical model as in the Femlab simulations at $Re = 10$, Re in the analytical model must be set up to 30. This can be due to several reasons such as: use of many channels in the Femlab simulations which does not allow sufficient mesh refinement or an underestimation of the K values calculated via Eq. (7.49) to (7.54).

7.8. Conclusions

An analytical model based on resistance networks has been developed for the study of single-phase flow distribution in manifold structures with an emphasis on two particular designs, i.e. consecutive and bifurcation, with different channel geometries. An extension of this type of approach for two-phase systems is presented in Chapter 9. The model allows manufacturing variations to be generated randomly within specified tolerances as well as blockages at any part of the structure. In the absence of manufacturing variations the bifurcation structure always produces flow equipartition. Two methods were considered for the design of the consecutive structure in order to achieve uniform flow distribution. *Method 1* is based on reducing pressure drop in the distributing/collecting (d/c) channels by using a uniform cross section in the d/c channels larger than the reaction channels' one by a factor that depends on channel geometry, number of reaction channels and required degree of divergence, *FD*, from perfect flow equipartition. *Method 2* is based on equalising pressure drop in the reaction channels by using varying cross sections in the d/c channels. The latter method can produce flow equipartition for any size of the d/c channels in the absence of manufacturing variations if non-linear d/c channels are considered. In the case of linear d/c channels, the divergence from flow equipartition, *FD*, depends on channel geometry, number and relative size of the d/c channels when compared to the reaction channel size, and it is generally small.

In addition to flow equipartition studies, the analysis of the effect of tolerances and reaction channel blockages can give further insight on the performance of each design. The value of the standard deviation of the reaction channels' residence times when manufacturing variations are present, σ, can help to define in consecutive structures obtained by *method 1* (with uniform cross section d/c channels) the optimum design value of the divergence from flow equipartition, *FD,* (i.e. 1 %, 2%, 5 % or 10 %). In structures obtained by *method 2* (with non-uniform cross section d/c channels) σ and reaction channel blockage effect define, together with the acceptable pressure drop, the minimum value of $D^{\#}_{B,N}$ (or $W^{\#}_{B,N}$ in rectangular channels) for improved flow distribution and the suitability of non-linear against linear d/c channels. It was also shown that

careful design of the d/c channels improves flow distribution and reduces total pressure drop in the bifurcation structure when there are manufacturing variations and reaction channel blockages. Moreover, in rectangular channel structures there is a reaction channel aspect ratio that minimises the effect of manufacturing variations on flow distribution.

Regarding the suitability of each manifold structure the following can be concluded. The consecutive structure obtained by *method 1* is easy to design and fabricate (Figure 7.10 applies to all designs irrespective of channel geometry and aspect ratio). This design is suitable when tolerances are large or uncertain, channel blockages are expected, different channel depths are possible, and the reaction channel depth is not limited by mass or heat transfer considerations. The consecutive structure obtained by *method 2* is suitable when the manifold area needs to be minimised and tolerances are small or well-defined. It is also preferable in cases where *method 1* is unfeasible or gives large d/c channel widths as when all channels are etched with the same depth and the reaction channel depth is similar to or smaller than the reaction channel width. The designs obtained by *method 2* are simplified using linear d/c channels, which in general produce a small divergence from flow equipartition. The bifurcation structure is generally a good design but has two disadvantages: large area occupied by the d/c channels and many splits within each flow path, which can increase pressure losses due to bends and splits (particularly important at higher flow rates) and can result in larger manufacturing variations at these points.

Additional pressure losses due to merging/splitting effects were also implemented within the resistance network model for the consecutive structure. In this case an iterative method for the calculation of the resistances, which are dependent upon flowrates (non-linear system of equations) was used. Results of the analytical model accounting for additional pressure losses showed similar trends as Femlab simulations although in the latter the effect of additional losses on flow distribution was larger. One possible reason is the underestimation of the K values (velocity heads) is the branching geometries since experimental equations for laminar flow in macrosystems were used, which have generally been obtained for large Re (< 2000) compared to those relevant to microchannels ($Re < 100$).

Flow distribution was experimentally measured in a manifold with 8 open channels as a function of the Reynolds number Re. The experimental flow distribution values FD measured are slightly larger than those obtained from the resistance network model although they follow the same trend (higher flowrates in the first branches). As Re increases, flow distribution among all branches improves in this case with open channels, effect that is also captured by the resistance network model.

Nomenclature

A	Channel cross-sectional area, m^2.
b	Maximum bifurcation level.
d/c	Distributing and collecting.
D	Hydraulic nominal diameter, m.
D_C	Characteristic length. The smallest dimension of the reaction channels (nominal diameter in circular channels and nominal depth or width in rectangular ones), m.
E	Channel depth, m.
f_{KE}	Energy correction factor for Bernoulli equation.
FD	Divergence from flow equipartition, %.
Fr	Froude number.
g	Acceleration due to gravitational force, m/s^2.
h	Head energy loss, m.
G	Parameter that is a function of the area and flowrate ratios.
W	Channel width, m.
K	Coefficient for additional pressure losses (velocity heads).
Kn	Knudsen number.
L	Channel length, m.
N	Number of reaction channels.
P	Pressure, Pa.
P_0	Reference Pressure, Pa.
PAR	Parameters determining the flow distribution solution.
Q	Flow rate, m^3/s.
R	Frictional channel resistance, Pas/m^3.
Re	Reynolds number of the structure.
Re_{hyd}	Reynolds number of channel based on the hydraulic diameter.
S, V	$S = 2(j - 1)2^{b-i} + 1$, $V = 2j2^{b-i}$. First and last reaction channel in the bifurcation manifold that contributes to the close loop j ($j = 1,\ldots,2^i/2$) of level i.
Sep	Nominal separation between reaction channels, m.
t	Mean residence time in a channel, s.
U	Fluid velocity, m/s.

Greek Letters

ρ	Density, kg/m^3.
δ	Construction tolerance, m.
λ	Molecular mean free path, m.
λ_{NC}	Non-circularity coefficient.
μ	Viscosity, kg/(ms).
σ	Sample standard deviation, %.
ΔP	Pressure drop, Pa.

Subscripts

A	Distributing channel.
B	Collecting channel.
C	Characteristic dimension.
EQ	Equivalent for resistances and equipartition for flowrates.
m	Mean value for the property distribution in the reaction channels.
MAX	Maximum value.
n	Nominal value.
R	Reaction channel.
T	Total quantity of property entering the structure.

Superscripts

#	Dimensionless variable.

Chapter 8

Effect of Gas/Liquid Inlet Conditions on the Effect of Taylor Flow Formation: Bubble and Liquid Slug Length

"First, say to yourself what you would be; and then do what you have to do"

Epictetus

8.1. Introduction

This chapter focuses on understanding bubble formation mechanism during Taylor flow. Taylor flow consists of long bubbles that fill the whole diameter of the channel (< 1mm) and flow co-currently within a liquid stream. The bubble formation mechanism depends on the mixing inlet geometry and defines bubble and liquid slug lengths. These are important parameters that influence pressure drop and fluctuations during Taylor flow in microchannels. The final objective is to combine the gained knowledge in interfacial phenomena as well as single-phase flow distribution and understand Taylor flow distribution in manifolds (see Chapter 9), which is the key issue for successfully scaling up disperse-phase microsystems.

The formation of Taylor bubbles and resulting bubble lengths were studied in small circular and rectangular cross section channels for air-water and air-octane systems. Two different types of contacting configurations were used, T- and Y-shaped respectively.

8.2. Background

8.2.1. Bubble Flow Hydrodynamics

Different two-phase flow patterns in microchannels have been reported by several investigators. Damianides and Westwater (1988) identify bubbly, plug, slug, dispersed and annular flow patterns in a water-air system using a 1 mm i.d. glass tube. Experiments carried out by Triplett

et al. (1999a and 1999b) using horizontal circular (d = 1.1 mm) and semi-triangular (d_h = 1.1 mm and 1.49 mm) microchannels observed five major patterns in both geometries: bubbly, slug (bubble train), churn, slug-annular and annular (see Figure 8.1). Although not in a linear way, these patterns are consecutively reached by both increasing the gas flow rate and decreasing the liquid flow rate. In micro-channels with an inner diameter less than 1 mm stratified flow has not been observed, due to dominance of surface tension and inertial forces over gravity forces as reported by several authors (Triplett et al., 1999a; Damianides and Westwater, 1998; Fukano and Kariyasaki, 1993).

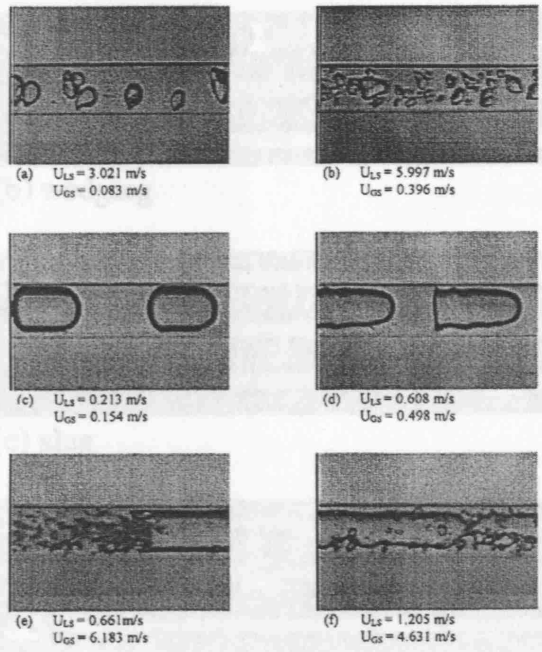

(a), (b) Bubbly, (c) and (d) slug/bubble train/Taylor flow, (e), (f) churn.

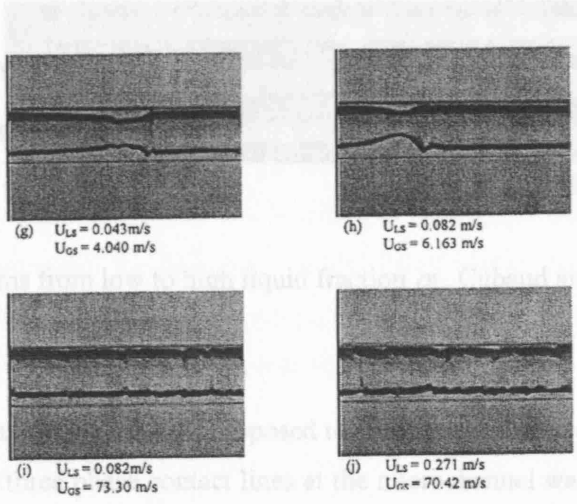

(g), (h) slug-annular, (i), (j) annular.

Figure 8.1. Pattern flows in a 1.097 mm diameter circular capillary. Triplett et al. (1999a).

Cubaud and Ho (2004) distinguish 5 flow patterns in glass and silicon square microchannels (d_h = 200 μm and 525 μm): bubbly, wedging, slug, annular and dry flow (see Figure 8.2).

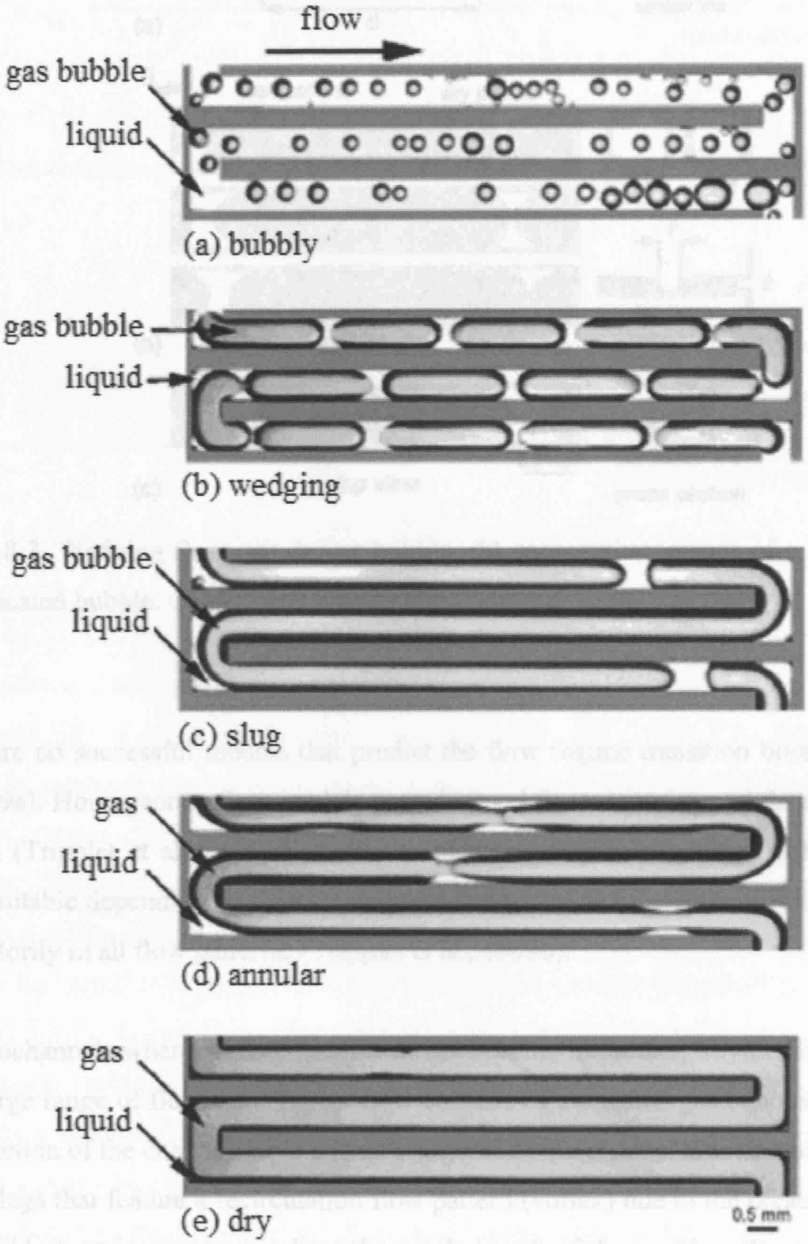

Figure 8.2. Flow patterns from low to high liquid fraction α_L. Cubaud and Ho (2004).

Wedging flow (see Figure 8.3 for detail), opposed to slug/Taylor flow, refers to the flow pattern in which bubbles form three phase contact lines at the microchannel wall and liquid only flows at the corners. Similarly, dry flow resembles annular flow in that the liquid at the microchannel walls has dried out and only remains at the corners.

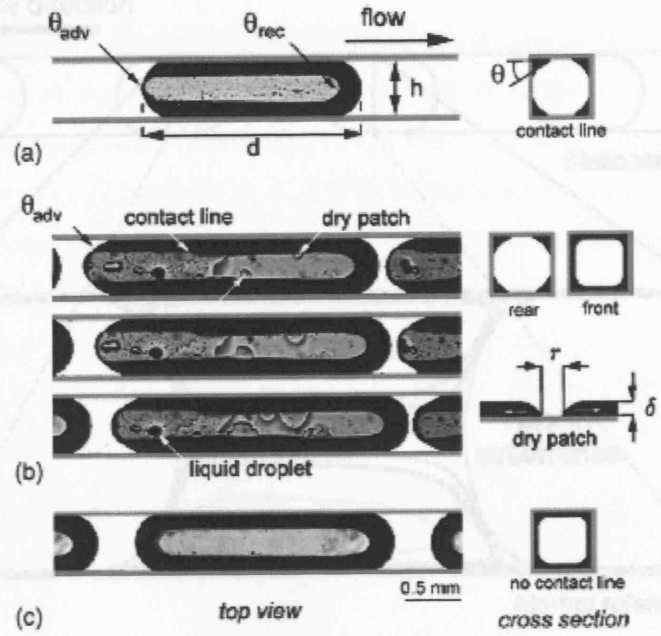

Figure 8.3. Wedging flow; (a) drying bubble, (b) consecutive images of a hybrid bubble, and (c) lubricated bubble. Cubaud and Ho (2004).

There are no successful models that predict the flow regime transition boundaries (Tripplet et al., 1999a). Homogenous flow models provide good fit to experimental data in relation to void fraction (Tripplet et al., 1999b). As far as pressure drop is concerned different models were found suitable depending on the flow patterns but no model was found to predict pressure drop satisfactorily in all flow patterns, (Tripplet et al., 1999b).

In microchannels where surface tension forces become important, Taylor flow pattern is found for a large range of flowrates. Taylor flow consists of elongated gas bubbles that fill the entire cross section of the channel, have a length larger than the channel diameter and are separated by liquid slugs that feature a recirculation flow pattern (vortex) due to the presence of the bubbles. The liquid phase is continuous along the whole length of the capillary due to the existence of a thin liquid film surrounding the bubbles, which flows under the pull of gravity (for vertical/inclined capillaries) and capillary pressure drop across a bubble and is continuously renewed by the mixing inside the liquid slug (see Figure 8.4).

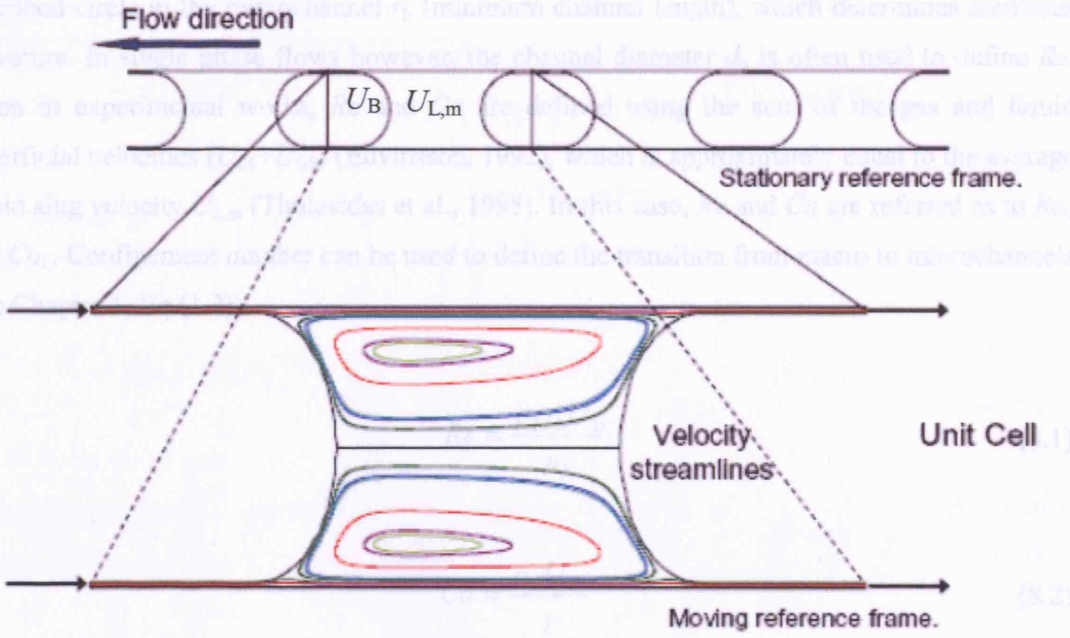

Figure 8.4. Taylor Flow in a circular capillary (Salman, 2005).

Some authors distinguish Taylor flow as a special case of slug flow where the liquid slugs are completely free of small bubbles (Irandoust and Andersson, 1989). This type of flow pattern is present in some common systems, namely, blood flow in arteries (Fung and Zweifach, 1971), polymer blow moulding, flow of foams through porous media or three-phase monolith systems (Kreutzer, 2003). Taylor flow has great potential in many industrial applications due to the fact that it is a stable pattern for a broad range of flowrates, reduces axial dispersion in the liquid because the liquid is interrupted by the bubbles and the film surrounding the bubbles is thin (Salman, 2005). Taylor flow also enhances radial mass/heat transfer as a consequence of the recirculation pattern inside the liquid slugs (Burns et al., 2001). This internal recirculation generates a concentration gradient in the radial direction that enhances mass transfer between the flow at the wall and that along the axis of the capillary as well as increases the contact time and area between these two regions. Reproducible and controllable liquid slug and bubble sizes enable accurate control of the interfacial area for mass/heat transfer between phases. Bubble and liquid slug sizes are mainly a function of superficial velocities and gas/liquid inlet configuration (Amador et al., 2004).

8.2.2. Taylor Flow Hydrodynamic Parameters

In two-phase Taylor flow, the dimensionless numbers *Re*, *Ca* and *Bo* given by Eq. (8.1)-(8.3) are generally defined as a function of the bubble velocity U_B and the radius of the largest

inscribed circle in the microchannel r_h (minimum channel length), which determines meniscus curvature. In single phase flows however, the channel diameter d_h is often used to define *Re*. Often in experimental works, *Re* and *Ca* are defined using the sum of the gas and liquid superficial velocities (U_{LS}+U_{GS}) (Edvinsson, 1992), which is approximately equal to the average liquid slug velocity $U_{L,m}$ (Thulasidas et al., 1995). In this case, *Re* and *Ca* are referred as to Re_L and Ca_L. Confinement number can be used to define the transition from macro to microchannels (see Chapter 1, Eq.(1.2)).

$$Re = \frac{\rho_L r_h U_B}{\mu_L} \tag{8.1}$$

$$Ca = \frac{\mu_L U_B}{\gamma} \tag{8.2}$$

$$Bo = \frac{(\rho_L - \rho_G) g r_h^2}{\gamma} \tag{8.3}$$

Hydrodynamic parameters have a strong influence on transport properties, determining the contact area and time between phases and the diffusion distances. In Taylor flow, these parameters are: thickness of liquid film surrounding the bubble, $\delta = (r\text{-}r_B)$, which determines diffusion distance from film to vortex and dispersion (Salman, 2005), relative velocity of bubbles with respect to liquid slugs (*W*), which determines the contact time between phases, velocity profile and streamlines in the liquid slug that determine, in addition to the contact time between phases, axial and radial dispersion in the liquid, and bubble shape, length and separation that defines the interfacial contact area between phases.

Film Thickness, δ The thickness of this film is a function of the Capillary number and length of the bubbles for small *Ca* values (Schwartz 1986).Theoretical analysis involves the solution of the Navier-Stokes and normal stress interface condition equations. In low viscosity liquids in microchannels it is typically 1-20 μm thick. Ratulowski and Chang (1990) suggested that the dependence of film thickness on bubble length is due to Marangoni effects. Film thickness can be measured by spectrometric methods, relative velocity of the gas bubble, dispersion, direct observation through a microscope and conductimetric methods (Irandoust and Andersson, 1989). Table 8.1 outlines some of the correlations available in literature for the prediction of film thickness.

Dimensionless Film thickness, δ/r	Validity	Method	Author
$\frac{\delta}{r} = 0.5Ca^{1/2}$	Circular, horizontal $7.5\cdot10^{-5} < Ca < 0.014$	Conductimetry	Fairbrother (1935)
$\frac{\delta}{r} = -0.05(cm/s)^{1/2}\cdot\left(\frac{\mu_L}{\gamma}\right)^{1/2} + 0.89\cdot Ca_L^{1/2}$	Circular channels $7\cdot10^{-6} < Ca < 2\cdot10^{-4}$	Conductimetry	Marchessault and Mason (1960)
$\frac{\delta}{r} = 0.643\cdot(3\cdot Ca)^{2/3}$	Circular channels $0 < Ca < 5\cdot10^{-3}$ $Err < 10\%$	Theory	Bretherton (1961)
$Bo - 0.842 = 1.10\cdot\left(\frac{\delta}{r}\right)^{2/3} + 1.85\cdot\left(\frac{\delta}{r}\right) = 1.25\cdot Ca^{2/9} + 2.24\cdot Ca^{1/3}$	Circular, vertical channels, Stagnant liquid	Theory	Bretherton (1961)
$\frac{\delta}{r} = 0.5Ca^{1/2}$ $\frac{\delta}{r} = 0.643\cdot(3\cdot Ca)^{2/3}$	Circular, horizontal $5\cdot10^{-5} < Ca < 3\cdot10^{-4}$ $2\cdot10^{-4} < Ca < 2\cdot10^{-3}$	Conductimetry	Chen (1986)
$f(Ca)$ Numerical method $\frac{Ca}{Bo} = \frac{1-4\delta^2+3\delta^4-4\cdot\delta^4\log\delta}{8\delta^2}$	Circular, horizontal $1\cdot10^{-4} < Ca < 1\cdot10^{-1}$	Theory	Reinelt (1987)
$\frac{\delta}{r} = 0.36\left(1-\exp(3.08Ca_L^{0.54})\right)$	Circular, horizontal	Photometric technique	Irandoust and Andersson, (1989)
Film evolution equation + Young-Laplace equation	Square channels	Theory	Kolb and Cerro (1993b)

Table 8.1. Correlations for prediction of film thickness.

Marchessault and Mason (1960) used a conductimetric technique to measure film thickness inside circular capillaries. Bretherton (1961) considered a system of inviscid bubbles with spherical caps, creeping flow and applied perturbation theory to obtain the equation on Table 8.1. The relationship was obtained in the limit of $Ca \rightarrow 0$. Bretherton (1961) also obtained an equation for film thickness in vertical capillaries with stagnant liquid, in which Bo, film thickness and Ca are related at $Ca \rightarrow 0$. Chen (1986) carried out experiments to measure film thickness in both air bubble and oil drop systems, and found that the film thickness agrees well with expressions obtained by Fairbrother (1935) and Bretherton (1961) depending on the Ca

number (see Table 8.1) and reaches an equilibrium value for very small *Ca* values. Reinelt (1987) applied a numerical method to calculate the film thickness at *Ca* in a wider range, i.e. $1 \cdot 10^{-4} < Ca < 1 \cdot 10^{-1}$. Reinelt's results agree well with Bretherton's at very small values of *Ca*, where Bretherton's approach is valid.

In square capillaries, Kolb and Cerro (1993b) developed a film evolution equation that, when combined with the Young-Laplace equation, forms a set of composite equations which completely describe the interface profile (and therefore film thickness) as a function of *Ca* and *Bo* numbers. Cubaud and Ho (2004) have experimentally observed that the thin film surrounding the bubbles in a partially wetting system in square capillaries dries out as a function of bubble velocity and capillary size with liquid flow remaining only at the corners.

Surface wettability plays an important role in Taylor flow and especially in film formation. Figure 8.5 represents the process for film formation in Taylor flow in circular capillaries as indicated by Jensen (2002): (a) when the bubble in at rest the static contact angles form; (b) as a small pressure gradient is applied, the bubble is compressed until receding and advancing contact angles are reached, when the bubble commences to move; (c) as the pressure gradient (flow) increases dynamic contact angles must be considered which are a function of velocity (see Chapter 4); (d) at certain pressure gradient (a function of capillary size and wetting properties) the film surrounding the bubble is developed leading to different average velocities for bubble and liquid slug and the bubble is no longer in contact with the capillary wall. In this case, an apparent contact angle can be introduced. Serizawa et al. (2001) carried out Taylor flow experiments in very small capillaries where no film was observed under chosen flow conditions. The lower the surface tension and contact angle of a system is, the smaller the required flowrates for the bubble to develop a thin film.

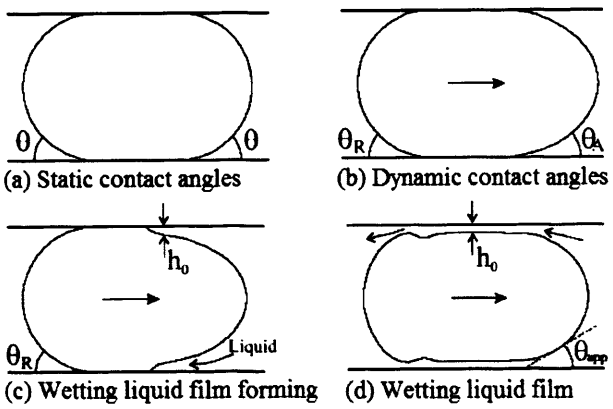

Figure 8.5. Film formation for Taylor flow in circular capillaries at increasing capillary numbers. Jensen (2002).

Relative velocity of the bubbles, *W*. The surrounding film makes bubbles flow faster than liquid. Considering an inclined capillary, a mass balance to a portion of a bubble and a portion of the liquid slug leads to Eqs. (8.4) and (8.5) as shown by Thulasidas et al. (1995).

$$A_B \cdot U_B = A \cdot U_{L,m} + q_{lf} \tag{8.4}$$

$$W = \frac{U_B - U_{L,m}}{U_B} = 1 - \left(\frac{A_B}{A}\right) \pm \frac{q_{lf}}{A \cdot U_B} \tag{8.5}$$

where A is the capillary cross section area, A_B is the bubble cross section area and q_{lf} is the liquid flowrate in the surrounding film, which is driven by the pressure gradient across the bubble. The pressure drop across a bubble is composed of a hydrostatic term (in inclined channels) and a capillary term that is a function of meniscus curvature at the back and front of the bubble and varies with $Ca^{2/3}$ for circular (Bretherton, 1961) and polygonal channels (Wong et al., 1992c). For thin films q_{lf} can be considered to be only a function of gravity (Edvinsson, 1994) and in this case the sign + in Eq. (8.5) applies to upward flow while the sign – applies to downward flow. In polygonal microchannels, the fluid flow along the corners driven by the pressure difference across the bubble becomes substantial even in horizontal channels (Wong, 1992). Therefore, the larger the film thickness the larger the relative velocity of the bubbles W, which explains why short bubbles which have not developed a constant film thickness travel faster than long bubbles and may result in bubble coalescence in Taylor flow (see experimental section). Eq. (8.5) allows to estimate the dimensionless relative velocity of the bubbles W with respect to the average velocity of the liquid slug $U_{L,m}$ by knowing the film thickness,

Considering the approximation $(A\text{-}A_B) = 2\pi r\delta$ and $q_{lf} = 0$ in horizontal channels, Eq. (8.5) for horizontal channels results in $W = 2(\delta/r)$ and equations given in Table 8.1 can directly be used to predict W. Eqs. (8.6) and (8.7) are examples of the analysis carried out by Fairbrother (1935) and Bretherton (1961) respectively. For vertical channels, Bretherton (1961) obtained Eq. (8.8) to calculate W.

Fairbrother (1935) $\quad W = 1.0 \cdot Ca^{1/2} \qquad 7.5 \cdot 10^{-5} < Ca < 0.014$ (8.6)

$$W = 1.29(3Ca)^{2/3} \qquad Ca \to 0$$

Bretherthon (1961) $\qquad$ Horizontal tubes (8.7)

Error less than 10 % for $Ca < 5 \cdot 10^{-3}$

Bretherthon (1961)

$$W = 1.29(3Ca)^{2/3}\left(1 \pm 2/3Bo + f(Bo^2)\right) \quad Ca \to 0 \qquad (8.8)$$

Vertical tubes, for rising (+) and descending (-) bubbles

Wong (1992) analysed bubble flow in horizontal polygonal channels and obtained Eq. (8.9) for W, which considers the flow at the corners q_{lf} driven by the capillary pressure difference across the bubble. Constants C_1 and C_2 are a function of the channel geometry, being $C_1 = 0.9397$ and $C_2 = 6.415 \cdot 10^{-4}$ in a square microchannel. The value of $C_1 = 0.9397$ corresponds to A_B/A in static conditions while the term $C_2/(L_B Ca^{1/3})$ accounts for liquid flow along the microchannels corners.

$$W = 1 - \left(C_1 + \frac{C_2}{L_B Ca^{1/3}} \right) \qquad (8.9)$$

According to Bretherton (1961) there is no bubble rise inside a circular capillary for Bond numbers $Bo < 0.842$. Thus, in small diameter circular capillaries (small Bo), bubbles begin to slow down and eventually a discontinuity in the liquid phase appears when capillary forces overcome buoyancy forces. Bi and Zhao (2001) reported that capillary geometry also influences bubble rise in a vertical capillary with stagnant liquid. They suggested that in channels with corners (square, rectangular and triangular), bubbles always rise independently of channel diameter since liquid exists at the corners and discontinuity is not allowed. This agrees with the Concus-Finn condition only for contact angles $\theta < 90° - \beta$, when there is no solution for an interface at the corners (Concus and Finn, 1969, 1974).

Taylor (1960) carried out similar experiments to those by Fairbrother (1935) for a wider range of Ca values, $0 < Ca < 2$. High viscosity fluids instead of high bubble velocities were used in order to produce high Ca. It was concluded that Eq. (8.6) by Fairbrother was a good approximation in the range $0 < Ca < 0.09$, instead of the range $0 < Ca < 0.014$ where Fairbrother carried out experiments. Taylor (1960) found that W reaches an asymptotic limit of $W \approx 0.56$ for large values of Ca where the stresses due to viscosity are more important that those due to surface tension. Subsequently, Kolb and Cerro (1991) measured an asymptotic limit of $W = 0.60$ and $W = 0.64$ for circular and square capillaries respectively.

For a low viscosity fluid in a large round tube, Eq. (8.10) by Wallis (1969) can be used to calculate the drift velocity of gas slugs, where r is the inner diameter of the channel and Fr is the Froude number (ratio of inertial to buoyancy forces).

$$Fr = \frac{U_B}{\sqrt{gr}} = 0.495 \tag{8.10}$$

In the case of small tubes, Tung and Parlange (1976) modified the previous equation, taking into account surface tension forces.

$$Fr^2 = 0.544 - \frac{0.236 \cdot \gamma}{\rho g r^2} = 0.544 - \frac{0.236}{Eo} \tag{8.11}$$

Eotvos number *Eo* is defined as the ratio of buoyancy to surface tension forces.

Streamline patterns inside the liquid slug: Particle Image Velocimetry (PIV) can be used to determine velocity distribution inside liquid slugs (Bugg, 2002). This technique consists of seeding the liquid with neutrally buoyant solid particles and then illuminating it with a laser sheet while different photographs are taken in very small time intervals. The video images are analysed frame by frame and flow velocity field is built by measuring the displacement of the seed particles. The velocity distribution has a strong influence in the overall mass transfer and liquid-phase residence time distribution inside the capillary (Thulasidas, 1997). Taylor (1961) was the first to suggest three different patterns of streamlines as shown below.

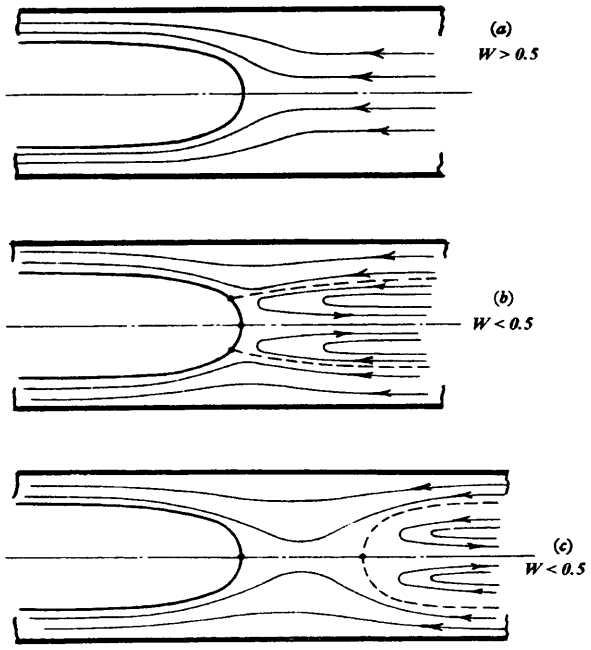

Figure 8.6. Possible streamlines in slug flow. Direction of streamlines relative to bubble. Taylor (1961).

At $W = 0.5$, $U_B = 2 \cdot U_{L,m}$, and assuming fully developed parabolic flow in the liquid at a cross section further away from the bubble ends, Eq. (8.12) defines the liquid slug velocity profile, where r_x is a radial position. The maximum liquid velocity $U_{L,max}$ is reached at the axis of the capillary and is related to the area-averaged liquid velocity by Eq. (8.13). Thus, $U_B = 2 \cdot U_{L,m} = U_{L,max}$ at $W = 0.5$.

$$U_L(r_x) = \frac{(P_0 - P_L)r}{4\mu_L L}\left[1 - \left(\frac{r_x}{r}\right)^2\right] = U_{L,max}\left[1 - \left(\frac{r_x}{r}\right)^2\right] \tag{8.12}$$

$$U_{L,max} = 2U_{L,m} \tag{8.13}$$

Consequently, in circular capillaries at high Ca when $W > 0.5$, $U_B > U_{L,max}$ and the liquid at any location inside the slug is moving towards the rear bubble meniscus relative to the bubble position as represented by Figure 8.6a (complete bypass). In systems where $W < 0.5$, $U_B < U_{L,max}$ and the liquid in the capillary centre moves away from the bubble producing a vortex formation with two potential flow patterns as shown in Figure 8.6b and c. The first pattern represented in Figure 8.6b features one stagnation point on the bubble vertex together with a stagnation ring on the bubble surface where streamlines separate. The second pattern shown in Figure 8.6c features two stagnation points on the bubble axis. The surface formed by connecting the stagnation ring at the rear of one bubble with the stagnation ring at the head of the preceding bubble separates the vortex from the rest of the liquid in the vicinity of the wall (liquid film). The vortex contains recirculating liquid whose regeneration is only possible by diffusion from the film at the wall but not by convection. The radius of the stagnation ring increases by decreasing the relative bubble velocity W, i.e. resulting in reduction of film thickness. Thus the existence of a stagnation ring implies the formation of a counter rotating toroidal vortex.

Cox (1964) observed the streamline patterns shown in Figure 8.6a and b experimentally. The flow pattern in Figure 8.6c has not been observed experimentally although Giavedoni and Saita (1997) have observed it in their numerical study of the front of a semi-infinite Taylor bubble. In square capillaries where there is no symmetry axis, streamline patterns are still similar to those observed in circular capillaries. For square capillaries, Kolb and Cerro (1991) measured the transition to complete bypass at $W = 0.54$, $Ca = 0.60$. The theoretical value $W = 0.50$ for complete bypass in circular capillaries considers fully developed flow inside the liquid slug, which does not always apply near the bubble ends and consequently for small liquid slug length. Thulasidas et al. (1997) applied PIV to obtain streamline patterns experimentally both in circular and square capillaries.

Figure 8.7 shows three different situations in a circular capillary: (a) toroidal vortex flow at low velocity with $Ca = 0.015$ and long liquid slug, (b) complete bypass pattern for $Ca = 0.52$ and (c) toroidal vortex flow at $Ca = 0.15$ and short liquid slug where the close proximity of the bubble ends results in non-straight streamlines.

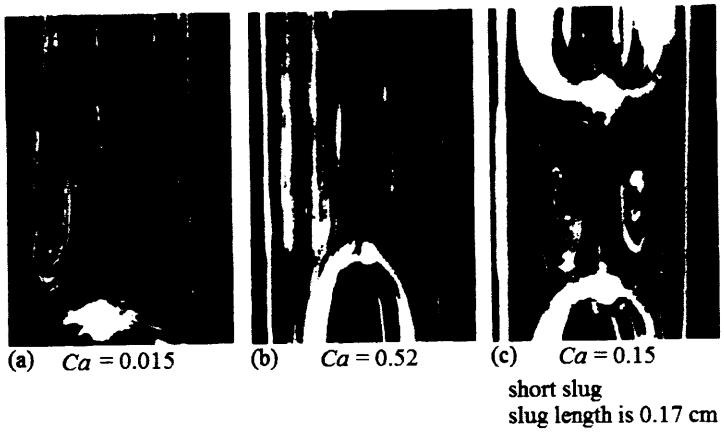

Figure 8.7. Streamlines inside a liquid slug in a circular capillary (Thulasidas et al., 1997).

Figure 8.8 shows different streamline patterns for different *Ca* inside a square capillary.

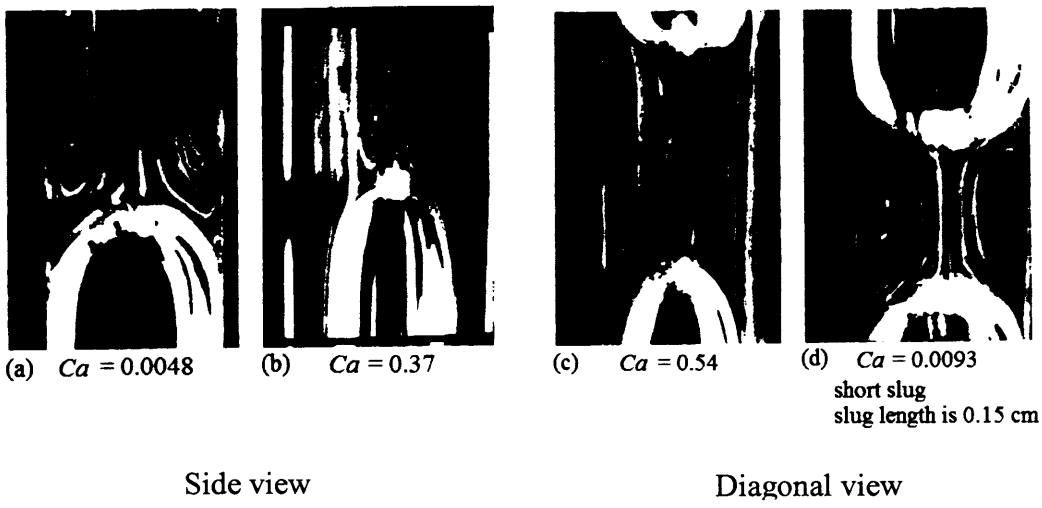

Figure 8.8. Streamlines inside a liquid slug in a square capillary (Thulasidas et al., 1997).

The complexity of Taylor flow in square capillaries increases at capillary numbers $Ca < 0.10$ when the bubble becomes not axisymmetric. Diffusion distances (film thickness) and streamlines on the axial and diagonal planes are different and a 3D analysis is required. Kolb

and Cerro (1993a) calculated the liquid flow rate in the surrounding film around an axisymmetric bubble in a square capillary by an infinite series of harmonic polynomials.

Liquid slug and bubble length: Liquid slug length is an important factor in mass transfer (Salman, 2005) and pressure drop (Kreutzer, 2003). In large slugs, axial diffusion length increases, thus diminishing mass transfer rates. Gas and liquid flow rates and gas/liquid inlet configuration are the most determining factors for liquid slug length (see section 8.4) although other variables such as stream composition, surface tension or contact angle must also be considered.

Bubble Shape: A similar approach to that presented in Chapter 5 to calculate meniscus shape and breakthrough pressure under flow conditions has been previously applied to obtain bubble shapes and liquid slug flow patterns in Taylor Flow (Shen and Udell, 1985; Edvinsson, 1994; Giavedoni and Saita, 1997 and 1999). Bubble shape is a function of *Ca* and *Re* (Edvinsson, 1994). At $Ca < 0.01$ the assumption of bubbles with hemispherical caps inside a circular capillary is valid. As *Ca* increases, the convexity of the rear meniscus decreases until it becomes inverted (concave). For very viscous liquids, the rear meniscus can penetrate all the way through the bubble resulting in stalactite flow. When inertial forces become important, the film near the rear meniscus develops a multiple wavelet, whose amplitude increases as *Re* increases.

Recirculation Time: Inside vortices, streamlines are closed and the recirculation time is defined as the time for the liquid to move from one end to the other (Thulasidas et al, 1997):

$$\tau = \frac{\text{(Half vortex volume)}}{\text{(Vortex flow rate)x(Slug time)}} \tag{8.14}$$

Recirculation time is an important parameter that influences mass and heat transfer between the vortex and the thin film close to the capillary wall. In Taylor flow, slug length and liquid slug/bubble velocities determine recirculation time. Recirculation time is often made dimensionless with respect to the time that takes a full slug length travelling with the bubble velocity ($t_S = L_S/U_B$) to cross a stationary plane fixed to the capillary:

8.2.3. Models for Taylor Flow Hydrodynamics

Thulasidas et al. (1995, 1997) developed a simple hydrodynamic model for Taylor bubble flow in circular and square capillaries. It can be used to predict bubble velocity, liquid film thickness

and volume fraction of liquid and gas. The analysis considers a bubble with hemispherical caps of diameter d_B and cylindrical body, which is a good approximation for circular capillaries and square capillaries at large *Ca*, where the bubble is axisymmetric. The assumptions for this model are:

1. The flow rate q_{lf} of the surrounding film is defined with respect to a stationary co-ordinate system and is only a consequence of gravity and a function of the film thickness, tube angle and liquid properties.
2. The pressure change inside the bubble due to the height is negligible.
3. A cylindrical bubble implies no pressure drop along its cylindrical body. A non-uniform bubble shape would result on pressure gradients modifying the film flow rate q_{lf}.
4. Shear stresses in the bubble surface are assumed to be zero (no Marangoni effects).
5. The bubble caps are hemispheres of diameter d_B.
6. The unit cell for the analysis is one bubble together with one liquid slug as in Figure 8.9. A co-ordinate system moving with the bubble U_B velocity is chosen.

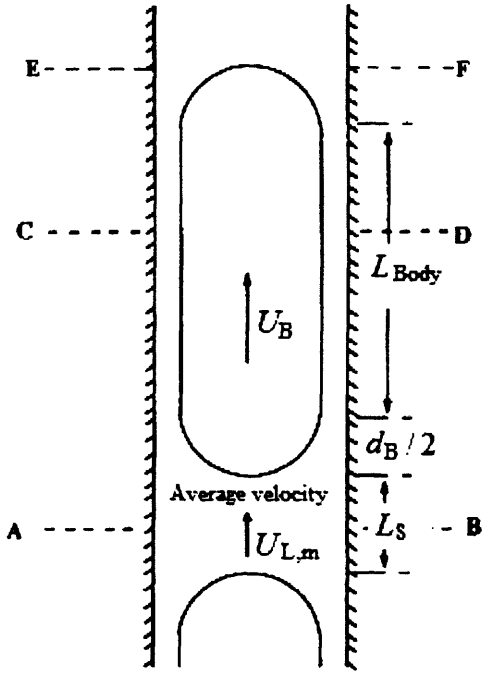

Figure 8.9. Unit cell with one slug and one bubble inside the capillary

The length of the unit cell is expressed as

$$L_C = L_{Body} + d_B + L_S \tag{8.15}$$

Applying the continuity equation to the moving system in Figure 8.9, Eq. (8.5) that relates bubble velocity and average liquid velocity is obtained. Although $U_{L,m} < U_B$, the properties inside the unit cell do not change with time.

Taking into account the time that takes one unit cell (t_C) and one bubble (t_B) to cross a stationary plane AB and assuming a cylindrical bubble with hemispherical caps, the gas superficial velocity U_{GS} is can be calculated by Eq. (8.17).

$$t_C = \frac{L_C}{U_B};\ t_B = \frac{L_{Body} + d_B}{U_B} \tag{8.16}$$

$$U_{GS} = \frac{A_B U_B}{A L_C}\left(L_{Body} + \frac{2}{3} d_B\right) \tag{8.17}$$

Similarly, considering the time that takes the liquid slug ($t_S = L_S/U_B$) and the liquid around the bubble (t_B) (same as the bubble to cross a stationary plane EF), the mass balance to the cell defined by Eq. (8.5) and the variable liquid cross sectional area, which is a function of the bubble shape, Eq. (8.18) defines the liquid superficial velocity

$$U_{LS} = \frac{U_B}{A L_C} \cdot \left(A U_{L,m} \frac{L_S}{U_B} - q_{lf} \frac{L_{Body} + d_B}{U_B} + \pi \frac{d_B^3}{12}\right) \tag{8.18}$$

Interestingly, the sum of gas and liquid superficial velocities given by Eqs. (8.17) and (8.18) is equal to the liquid slug average velocity. Eq. (8.5) is used to obtain a value for q_{lf}.

$$J = U_{LS} + U_{GS} = U_{L,m} \tag{8.19}$$

From this correlation the bubble velocity can be found by substituting Eq. (8.19) into Eq. (8.5) if estimates for A_B and q_{lf} are available. The film flow rate q_{lf} is obtained from a momentum balance to a differential cylinder inside the film with thickness $r+\Delta r$, in which gravity generates the flow. No slip condition applies at the wall while $dU/dr = 0$ on the bubble surface. The resulting velocity profile (see Figure 8.10) is given in Eq. (8.20) obtaining the film flowrate via Eq. (8.21):

$$U_{lf}(r_x) = \frac{\rho_L g r^2}{4\mu_L}\left[1-\left(\frac{r_x}{r}\right)^2 + 2\left(\frac{r_B}{r}\right)^2 \ln\left(\frac{r_x}{r}\right)\right] \tag{8.20}$$

$$q_{lf} = \int_0^{2\cdot\pi}\int_{r_B}^{r} U_{lf}(r_x) r_x dr_x d\theta$$

$$q_{lf} = \frac{\pi\rho_l g r^4}{8\mu_L}\left[1+4\left(\frac{r_B}{r}\right)^4\left[\frac{3}{4}-\ln\left(\frac{r_B}{r}\right)-\left(\frac{r_B}{r}\right)^{-2}\right]\right] \tag{8.21}$$

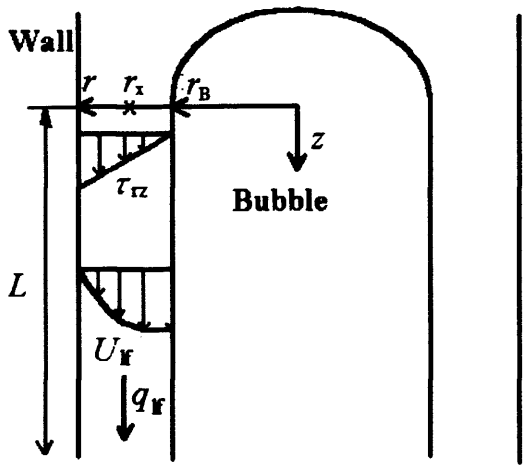

Figure 8.10. Velocity and shear stress profile inside the film.

In square capillaries with axisymmetric bubbles (Figure 8.11), the surrounding film flow rate has been computed by Kolb and Cerro (1993a) via an infinite series of harmonic polynomials and refined by Thulasidas and Cerro (1995) who obtained Eq. (8.22).

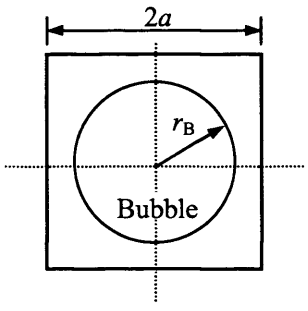

Figure 8.11. Axisymmetric bubble in square capillaries, $Ca > 0.04$.

$$q_{lf} = \frac{\rho_L g r_h^4}{8\mu_L}\left[4.499 + 0.09528R_B - 16.21R_B^2 + 9.216R_B^3 + 8.566R_B^4 - 6.09R_B^5\right] \qquad (8.22)$$

In Eq. (8.22), r_h is half-width of the square capillary and $R_B = r_B/r_h$ is the dimensionless bubble radius. For the case of a non-axisymmetric bubble with constant curvature at the part of the body near the corners, $1/r_{ccor}$ (Figure 8.12), the film flow rate consists of two flow rates. First, the flow rate at the corners calculated via Eq. (8.22) with $R_B = r_{s(B\text{-}B)}/r_h$ and second, the flow rate at the sides calculated via Eq.(8.23) for a flat film surface (Bird, 1964). Kolb and Cerro (1993a) indicate that the flow at the corners of the capillary at low Ca is more than 95% of the total. Therefore, there is a substantial difference in the relative bubble velocity W for upward and downward flows in square capillaries at low Ca. They measured a transition from non-axisymmetric to axisymmetric bubbles at $Ca \sim 0.04$.

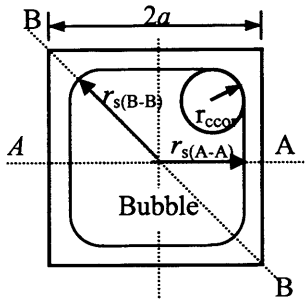

Figure 8.12. Non-axisymmetric bubble in square capillaries, $Ca < 0.04$.

$$q_{lf} = \frac{2\rho_L g\left(r_{s(A-A)} - r_{ccor}\right)\left(r_h - r_{s(A-A)}\right)^3}{3 \cdot \mu_L} \qquad (8.23)$$

The bubble velocity W is calculated via Eq. (8.5) with q_{lf} and A_B, which is a function of the capillary number as previously discussed. Thulasidas et al. (1995) reported different values of bubble diameters for the case of upward, downward and horizontal flows, above all in the lower Ca range, both in circular and square capillaries.

Eq. (8.24) gives the volume fraction of the gas inside the capillary, where U_{GS} is given by Eq. (8.17), leading to Eq. (8.25) that allows the estimation of bubble ($L_{Body}+d_B$) to unit cell (L_C) length ratio, β.

$$\alpha_G = \frac{U_{GS}}{U_B} \tag{8.24}$$

$$\beta = \alpha_G \cdot \frac{A}{A_B} + \frac{d_B}{3 \cdot L_C} \tag{8.25}$$

The model presented by Thulasidas et al. (1995) is useful to estimate liquid slug velocity, bubble velocity (estimating film thickness from Table 8.1), volume fraction α_G and bubble to unit cell length ratio β. This model agrees well with experimental data.

Thulasidas et al. (1997) developed simple analytical expressions to predict the position of the stagnation surface that separates the vortex from the film r^1, the vortex centre r^0 at which $U_{L,m} = U_B$, flow rates of circulating vortices and circulation times (see Figure 8.13). These parameters are very important in a mass/heat transfer analysis.

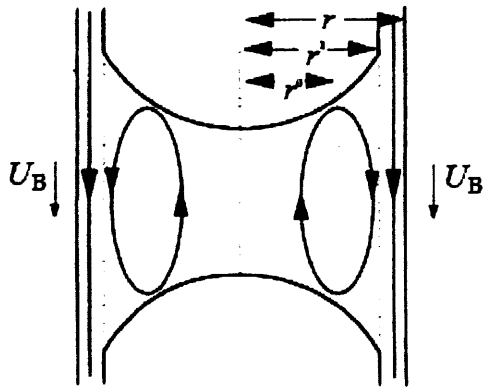

Figure 8.13. Recirculation pattern inside the liquid slug.

The dimensionless bubble velocity ψ is a unique function of Ca, both for circular and square capillaries since $U_{L,m} \approx U_{LS} + U_{GS}$:

$$\psi = \frac{U_B}{J} \approx \frac{U_B}{U_{L,m}} = \frac{1}{1-W} = f(Ca) \tag{8.26}$$

For circular capillaries, ψ ranges from $\psi = 1$ at low Ca ($W = 0$) to $\psi = 2.5$, at large Ca (asymptotic value $W = 0.6$). However, in square capillaries, the lower limit of ψ has been measured $\psi = 1.5$ since there is always some flow through the corners. A moving co-ordinate system at the bubble velocity in a circular capillary is considered. Assuming a parabolic profile

within the liquid slug and using velocities relative to the bubble velocity, the velocity profile in a cross section away from the bubble ends is:

$$U_{L,rel}(r_x) = 2 \cdot U_{L,m} \cdot \left[1 - \left(\frac{r_x}{r}\right)^2\right] - U_B = \frac{2 \cdot U_B}{\psi} \cdot \left[1 - \left(\frac{r_x}{r}\right)^2\right] - U_B \tag{8.27}$$

The radial position r^0, which defines the surface where the axial component of the relative liquid velocity is 0, is obtained at $U_{L,,rel}(r_x) = 0$ and defines the centre of the vortex:

$$r^0 = \frac{r}{\sqrt{2}} \cdot \sqrt{2 - \psi} \tag{8.28}$$

The position of the stagnation surface that separates the vortex from the film is obtained by knowing that the liquid flow rate inside the slug from the stagnation surface to the wall corresponds to the liquid flowrate that passes to the next liquid slug ($(A\text{-}A_B)U_B+q_{lf}$). For a moving system at U_B, analysis yields:

$$2 \cdot \pi \cdot \int_{r^1}^{r} U_{ls}(r_x) \cdot r_x \cdot dr_x = (A - A_B) \cdot U_B + q_{lf}$$
$$r^1 = r \cdot \sqrt{2 - \Psi} \tag{8.29}$$

where r^0 and r^1 are only a function of ψ, which is a function of Ca. When the relative velocity of the bubbles W is equal to or greater than the maximum slug liquid velocity, i.e. $W \geq 0.5$ or $\psi \geq 2$, complete bypass exists and r^0 and r^1 become zero.

Thulasidas et al. (1997) applied the same procedure to square capillaries considering that the velocity profile for fully developed flow is given by an infinite series (Eq. (8.30)), and found the vortex centre position (x^0,y^0) and the stagnation surface position (x^1,y^1) numerically:

$$U(x,y) = \frac{\Delta P \cdot r_h^2}{2 \cdot \mu_L} \cdot \left[1 - Y^2 + \sum_{n=0}^{n=\infty} \frac{32 \cdot (-1)^{n+1} \cdot \cosh(C_n \cdot X) \cdot \cos(C_n \cdot Y)}{[(2 \cdot n + 1) \cdot \pi]^3 \cdot \cosh(C_n)}\right] \tag{8.30}$$

where ΔP is the pressure gradient, r_h is half-size of the square tube, X and Y are the dimensionless co-ordinate positions with respect to r_h and C_n =[(2·n + 1)·π/2]. Taking into account the average and maximum velocities obtained by Eq. (8.30) and the definition of ψ, it is

possible to express the relative liquid velocity with respect to the bubble velocity by Eq. (8.31). This equation indicates a complete bypass at $\psi = 2.096$ versus $\psi = 2.0$ in the case of circular capillaries:

$$U_{\mathrm{Rel}}(x,y) = \frac{3.5568 \cdot U_{\mathrm{B}}}{\psi} \cdot \left[1 - Y^2 + \sum_{n=0}^{n=\infty} \frac{32 \cdot (-1)^{n+1} \cdot \cosh(C_n \cdot X) \cdot \cos(C_n \cdot Y)}{[(2 \cdot n + 1) \cdot \pi]^3 \cdot \cosh(C_n)} \right] \tag{8.31}$$

Taking into account the definition of recirculation time in Eq. (8.14), the dimensionless recirculation time in circular capillaries can be expressed as,

$$\tau_{cir} = \frac{\pi \cdot (r^0)^2 \cdot l_{\mathrm{S}}}{\int_0^{r^0} 2 \cdot \pi \cdot r_{\mathrm{x}} \cdot U_{\mathrm{L}}(r_{\mathrm{x}}) \cdot dr_{\mathrm{x}} \cdot \frac{l_{\mathrm{S}}}{U_{\mathrm{B}}}} = \frac{l_{\mathrm{S}} \cdot (r^0)^2}{2 \cdot \frac{l_{\mathrm{S}}}{U_{\mathrm{B}}} \cdot \int_0^{r^0} U_{\mathrm{L}}(r_{\mathrm{x}}) \cdot r_{\mathrm{x}} \cdot dr_{\mathrm{x}}} \tag{8.32}$$

8.2.4. Marangoni Effects

Marangoni effects refer to surface tension gradients over the bubble surface, which generate tangential stresses that must be balanced for the free surface to be in equilibrium. This change on bubble boundary conditions affects Taylor flow hydrodynamic parameters such as bubble shape and velocity. Surface tension gradients are coupled to the fluid field, bubble shape and contaminant advection-diffusion equations on the surface and can be mathematically considered (see Eq. (5.8) in Chapter 5). However, they are generally uncontrollable as a result of gradients in temperature, solvent concentration and electric potential (Brennen, 2005). The analysis of contaminants transport on a surface involves an adsorption/desorption and convective flow process onto the surface as presented by Stone (1990), who uses a convection-diffusion equation. The following dimensionless numbers are common in this analysis: Surface Peclet Number Pe_{S} that relates surface convection rates to surface diffusion rates; the adsorption Stanton number St_{a} that is the ratio of surface adsorption to surface convection rates, the desorption Stanton number St_{d} that is the ratio of surface desorption to surface convection rates; elasticity number *El* that indicates the ability of the contaminant to modify surface tension and the Marangoni number *Ma* that defines the ratio of Marangoni to viscous stresses (Ghadiali and Gaver III, 2003).

8.2.5. Effect of Gas/Liquid Inlet Conditions on Taylor Flow Formation in Circular/Square Channels: Liquid Slug/Bubble Length

Pressure drop in channels during Taylor flows is a crucial factor when designing manifold structures for multiphase flow distribution and is dependent on the bubble number as well as on the amount of wall perimeter wetted by the liquid slugs (Kreutzer, 2003). It is important therefore to be able to predict the bubble and slug lengths under different fluid properties, channel design and operational parameters. Although the bubble to slug length ratio can be estimated from the inlet gas and liquid flowrates (Eq. (8.25), Thulasidas et., al.1995), their absolute values will depend on the dynamics of the two-phase contacting at the inlet as little change due to bubble break-up/coalescence is expected within the microchannel. Yet despite its importance, there is no systematic investigation on Taylor bubble formation in small channels. Existing literature covers larger systems and mainly small, non Taylor bubbles (bubble diameter smaller than channel diameter).

Most of the work on bubble formation relates to non-confined systems in which gas is injected into a stagnant liquid via a small orifice from which bubbles detach due to buoyancy (Kumar and Kuloor, 1970; Clift, 1978). *Single-stage* and *multiple-stage* models have been proposed to understand bubble growth and detachment at low to intermediate gas flow rates. In the *single-stage* model, the bubble grows smoothly until buoyancy exceeds opposed forces resulting in the bubble detachment. In a *multiple-stage* model the bubble growth mechanism is not linear; the standard approach is to consider a first stage where a neckless bubble forms at the orifice and a second "lift-off" stage at which the bubble develops a neck that connects the bubble to the orifice (Clift, 1978). Two additional mechanisms known as *bubble pairing* (bubble coalescence at the orifice) and *jetting* (bubble forming via jet break-up) may occur at high gas flow rates (Clift, 1978).

In the microscale or under microgravity conditions other forces (liquid/gas inertial and static/dynamic surface tension forces) in addition to buoyancy may control bubble detachment as indicated by Kim et al. (1994) and Nahra and Kamatoni (2003) that analysed bubble formation under liquid flow. Rayner and Trägårdh, 2002 modelled bubble formation in membrane emulsification in cross-flow operation carrying out a force balance that defines bubble detachment when buoyancy and liquid drag forces overcome those due to surface tension. Liquid and gas inertia forces (Bhumia et al., 2000) and dynamic surface tension force (Rayner and Trägårdh, 2002) may also play role in bubble detachment as a function of system geometry and properties.

The present work is undertaken because of the lack of knowledge to predict bubble and liquid slug lengths for Taylor flow in capillaries as a function of inlet configuration. Bubble/liquid slug length affects pressure drop and fluctuations during Taylor flow, which greatly influence flow distribution in manifolds. Two standard types of contacting configurations, such as T- and Y-mixers are analysed.

8.3. Experimental Section

8.3.1. Experimental Set-Up

Two liquids with different surface tension were chosen, n-octane (Fluka n° 74823, purum > 95 %, GC) and deionised water with properties given in Table 8.2 Zero grade air (ρ = 1.19 kg/m^3) is used for the gas phase.

Property	N-octane	Water
Density ρ	703 kg/m^3	998 kg/m^3
Surface tension to air, γ	0.0205 N/m	0.072 N/m
Dynamic viscosity, μ	0.00052 Pa·s	0.00095 Pa·s

Table 8.2. Liquid properties at the reference temperature of 25°C.

The experiments on Taylor flow formation in microchannels were carried out in the set up shown in Figure 8.14. The liquids were introduced into the different test sections using a 4-piston MilliGat pump (0-6 ml/min), which is designed to deliver pulseless flow. The air flow rate was supplied from a gas cylinder and was regulated with a Bronkhorst EL-FLOW F-110C mass flow controller for flows between 0.01-1 ml/min gas and a Chell Mk4607 mass flow controller for flows between 1-20 ml/min. Rigid plastic tubing was used for the fluidic connections in order to reduce any effects caused by flexible tube expansions and vibrations.

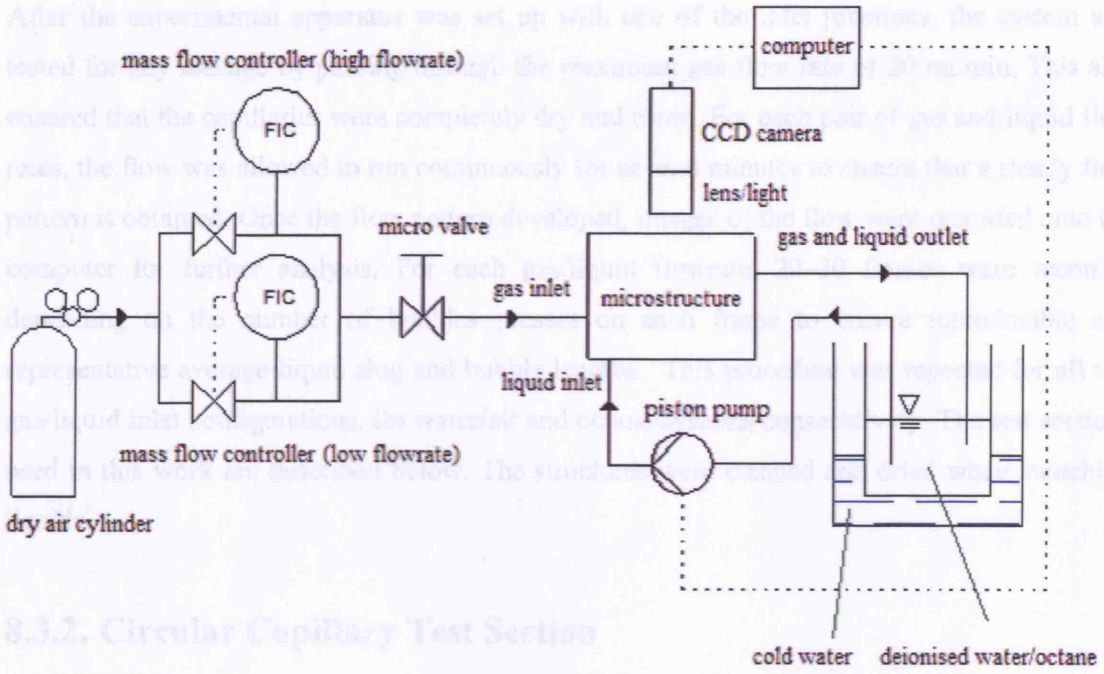

Figure 8.14. Diagram of the experimental set-up to analyse bubble formation.

A large pressure drop just before the gas inlet was effected by the use of a micrometering valve to limit any pressure fluctuation from further disturbing the flow in the test section. The micrometering valve is placed as close as possible to the bubble formation point so that pressure fluctuations during bubble formation affect only the small volume of air between the micrometering valve and the bubble formation point. This procedure allows generation of stable and reproducible Taylor bubbles at any gas/liquid flowrate (i.e. 0.1 ml/min of gas and liquid). It was found that placing the exit of the test channel aligned with the liquid surface of the collecting beaker helped remove some of the pressure fluctuations associated with bubble exiting.

For the observation of the Taylor bubble formation at the inlet of each test section a high-speed camera Kodak Ektapro HS 4540, which can record images up to 4,500 frames per second with full resolution of 256x256, was used. Bubble and slug sizes within the test sections were recorded with a high-resolution (1008x1018) video camera Kodak ES 1.0 mounted on a Prior Scientific Micrososcope with a 2X lense. Aequitas IA Lite software was used initially and later substituted by an in-house developed Matlab code (see Appendix 8A) for the automatic analysis of the bubble/slug lengths after calibration of the camera pixels with a micrometer plate.

After the experimental apparatus was set up with one of the inlet junctions, the system was tested for any leakage by passing through the maximum gas flow rate of 20 ml/min. This also ensured that the capillaries were completely dry and clean. For each pair of gas and liquid flow rates, the flow was allowed to run continuously for several minutes to ensure that a steady flow pattern is obtained. Once the flow pattern developed, images of the flow were recorded onto the computer for further analysis. For each gas/liquid flowrate, 20–30 frames were recorded depending on the number of bubbles present on each frame to ensure reproducible and representative average liquid slug and bubble lengths. This procedure was repeated for all test gas/liquid inlet configurations, for water/air and octane/systems consecutively. The test sections used in this work are described below. The structures were cleaned and dried when switching liquids.

8.3.2. Circular Capillary Test Section

The gas and liquid inlets and the test channel are glass capillaries, which are brought together at acrylic inlet junctions shown in Figure 8.15. The channels in these structures were drilled in such a way that their diameters at the point of contact of the gas and liquid matched the internal diameters of the gas and liquid capillary inlets and of the test channel. Two different internal diameters were used for the gas and liquid inlets and the test channel, namely 0.35 mm and 0.76 mm. The test channel was 10 cm long with an inner diameter of 0.794 mm. As can be seen in Figure 8.15, in the Y configuration the gas and liquid inlet capillaries join at 90°. The flow arrangements in the structures are noted with a suffix to the structure name. The structure (TS-2) can be setup with the gas (TS-2a) or liquid (TS-2b) flowing in the inlet perpendicular to the main channel. Structure TS-2 can also be used as a tee junction with the gas and liquid joining at 180° (TS-2c).

In this setup, a 8.5 mm inner diameter cylindrical glass box filled with glycerol is fitted around the test channel through which the bubble and slug lengths are viewed. Because the refractive indexes of glass and glycerol match, the refraction of light at the outer wall of the glass capillary is avoided (Thulasidas et al., 1995). To ensure that a clear image is obtained without refraction, the viewing cell was fitted with two *flat* glass windows, approximately 24 mm long on opposite sides of the cell.

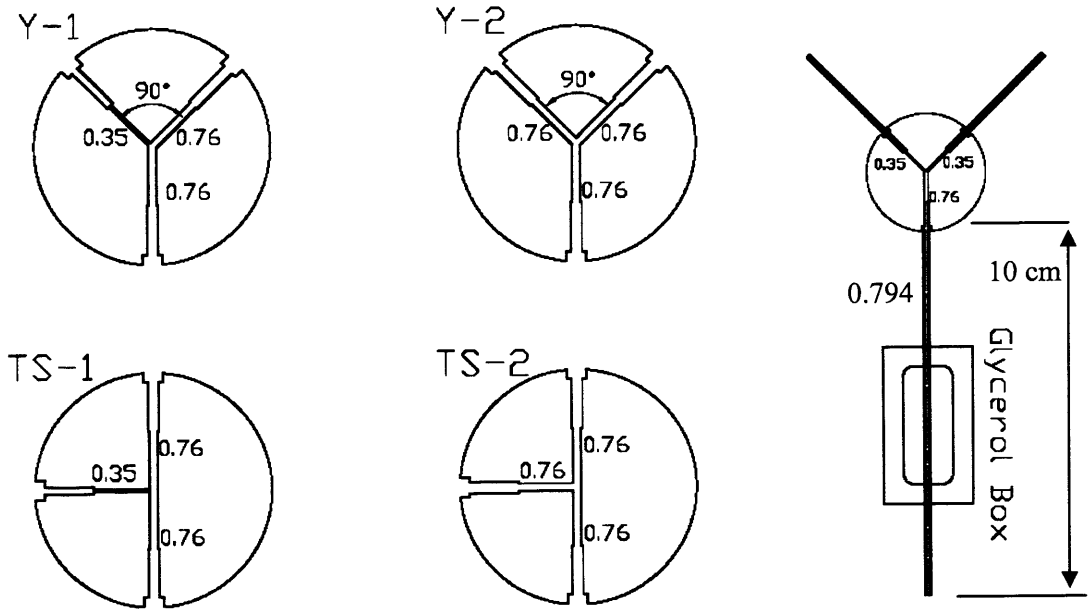

Figure 8.15. Different acrylic inlet configurations used in the study. Dimensions are channel diameters in mm.

8.3.3. Square Capillary Test Section

In this case, the wafers are made of acrylic and feature square channels produced by micro-milling. An acrylic wafer is milled with the required depth of the channel and a second one is thermally bonded on top of the first wafer to generate a closed channel. The wafer is fixed within an aluminium case composed of two plates that has threads for the inlet and the outlet ports (1/4-inch 28) suitable for 1/16-inch outer diameter tubes. The aluminium plates feature a window that allows flow pattern observation (see Figure 8.16).

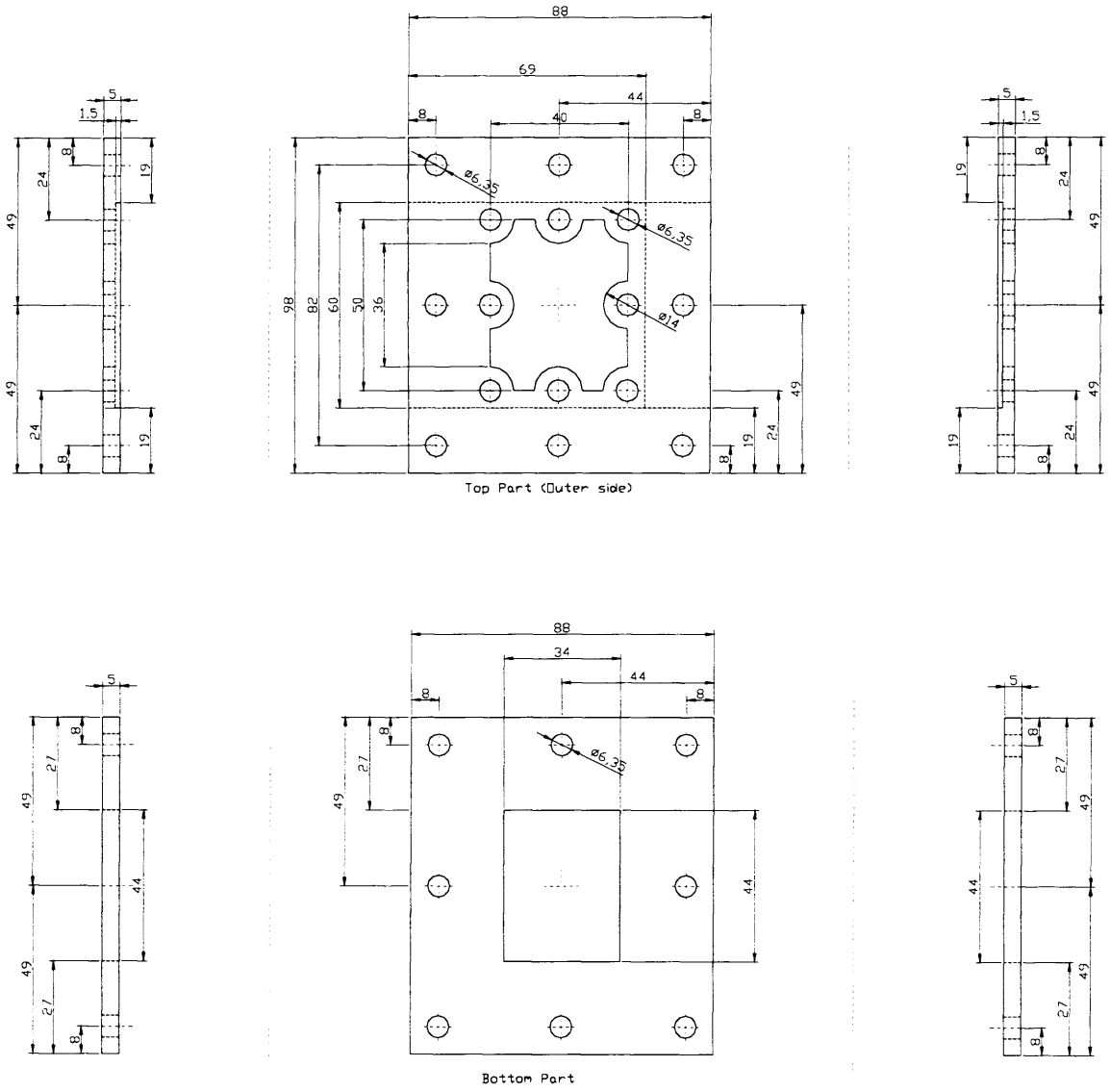

Figure 8.16. Aluminium case for support and connection of the acrylic wafers.

Based on results from circular cross section systems, two inlet structures were chosen, namely T-2 (Figure 8.17) that has a side entrance of smaller cross section that the main channel and T-3 (Figure 8.18), whose side entrance has the same diameter as the main channel. In structure T-2, the liquid inlet channel has a width of 240 μm and a depth of 625 μm. The square main channel has a width and depth of $w = e = 625$ μm. The liquid flows through a zigzag channel that generates substantial pressure drop to improve stability of Taylor bubbles and finally is mixed with the gas at the junction. This structure is only used with the liquid at the side entrance (small cross section channel).

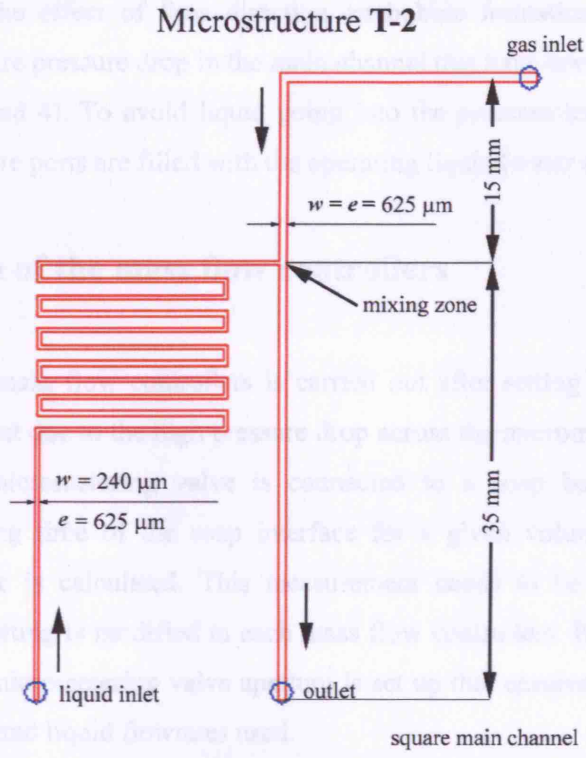

Figure 8.17. Drawing of the microstructure T-2

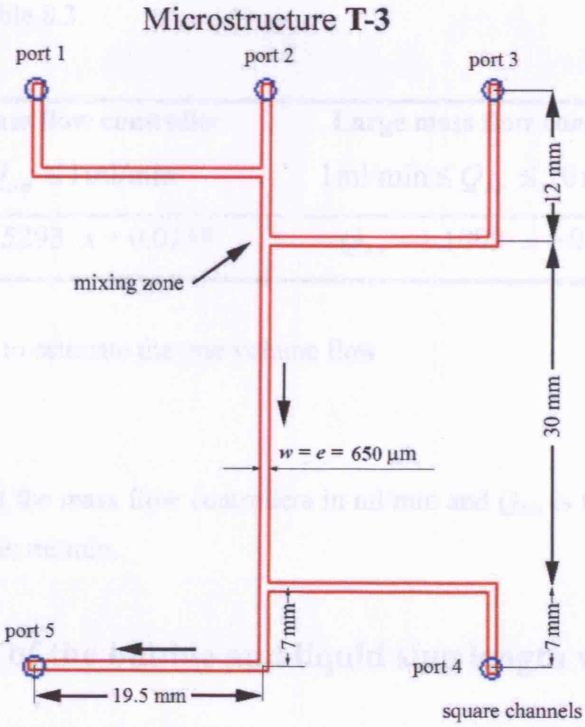

Figure 8.18. Drawing of the microstructure T-3.

In structure T-3 all channel are square with $w = e = 650$ μm. The gas and liquid inlets can be swapped, to analyse the effect of flow direction on bubble formation. There are also two pressure ports to measure pressure drop in the main channel that have been blocked during these experiments (ports 3 and 4). To avoid liquid going into the pressure transducer, the channels connected to the pressure ports are filled with the operating liquid (water or octane).

8.3.4. Calibration of the mass flow controllers

Calibration of the air mass flow controllers is carried out after setting up the micrometering valve before the gas inlet due to the high pressure drop across the micrometering valve. The gas inlet containing the micrometering valve is connected to a soap bubble flow meter. By measuring the travelling time of the soap interface for a given volume of the pipette, the volumetric air flowrate is calculated. This measurement needs to be done every time the micrometering valve setting is modified in each mass flow controllers. Before carrying out the calibration, a suitable micrometering valve aperture is set up that ensures stable Taylor flow in the whole range of gas and liquid flowrates used.

Two correlations are estimated for each new experiment to calculate the actual volumetric air flowrate from the reading value of the mass flow controllers. Two of these correlations are shown exemplary in Table 8.3.

Small mass flow controller	**Large mass flow controller**
$0 \le Q_{Air} \le 1\,\text{ml/min}$	$1\,\text{ml/min} \le Q_{Air} \le 20\,\text{ml/min}$
$Q_{Air} = 1.5293 \cdot x + 0.0139$	$Q_{Air} = 1.1009 \cdot x + 0.0769$

Table 8.3. Correlations to estimate the true volume flow

x is the reading value at the mass flow controllers in ml/min and Q_{Air} is the actual value of the volumetric air flowrate in ml/min.

8.3.5. Calculation of the bubble and liquid slug length with MATLAB

Because of the large number of digital images and bubbles to be analysed, the measurement of the liquid slug and bubble lengths was automated via a MATLAB script (Appendix 8A) that

also calculates the average values. Figure 8.19 shows a grey scale image that contains three bubbles and three liquid slugs and is used to illustrate how the MATLAB program works.

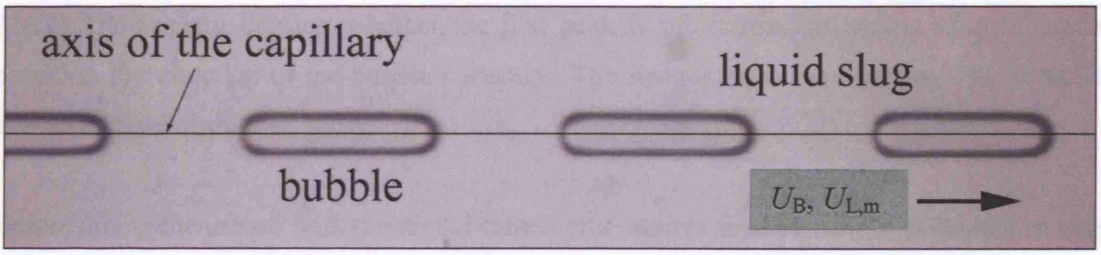

Figure 8.19. Image of three complete bubbles and three complete liquid slugs

The thick black bubble shape is a result of the small light reflection due to the bubble curvature. Along the capillary axis, MATLAB analyses the greyscale intensity as a function of pixel number. Figure 8.20 gives a MATLAB plot showing the results of the analysis of Figure 8.19.

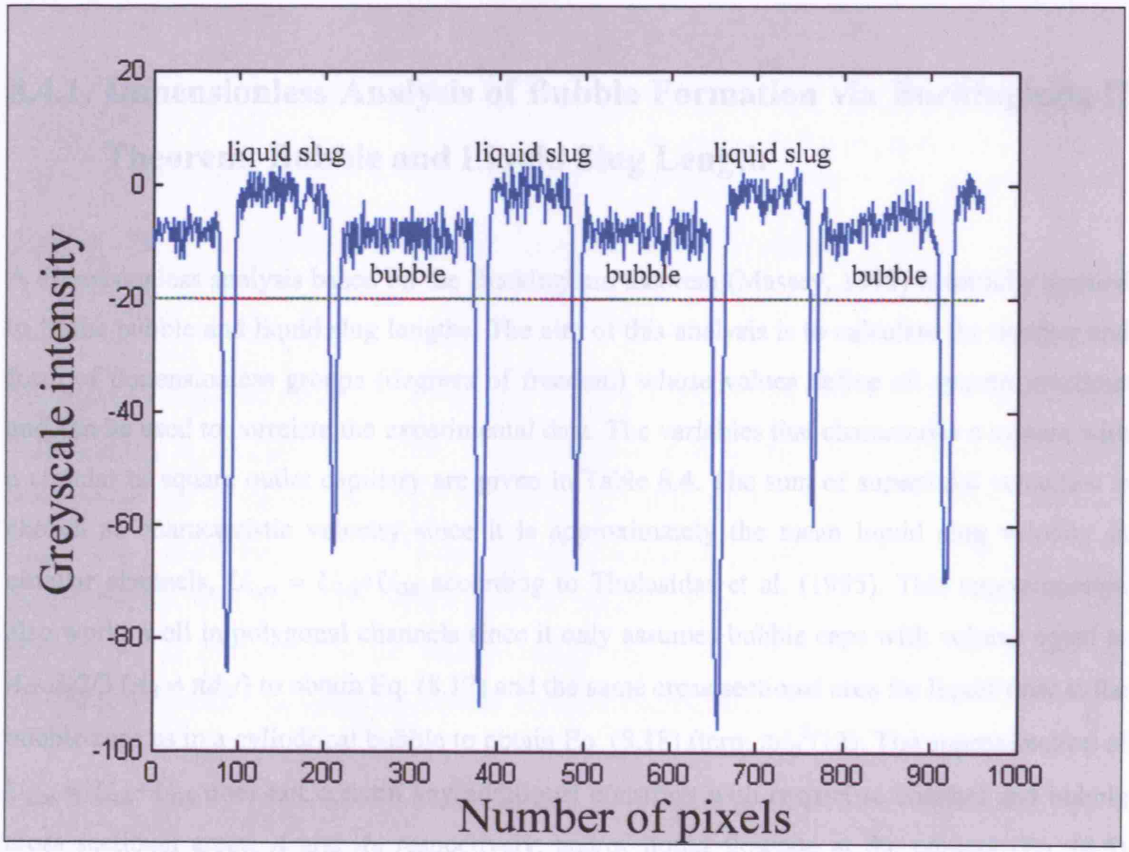

Figure 8.20. Matlab analysis of pixel intensity from Figure 8.19.

Comparing Figure 8.19 and Figure 8.20, it can be seen that the peaks in Figure 8.20 correspond to the bubble beginning and end. For greyscale intensity equal to -20, the bubble and liquid slug lengths are estimated by calculating the distance between two peaks. A function in the MATLAB program decides, whether the first peak is the starting or ending of a bubble by checking the direction of the bubble curvature. The images must show at least one complete bubble and liquid slug.

Before taking the images with the digital camera, the camera field of view is calibrated in order to calculate the pixel size. A calibrated scale was photographed using the same magnification as that used in the experiment measuring a pixel size of 12.73 μm. Therefore, this is the maximum accuracy when measuring the bubble and liquid slug length with the current magnification. A minimum of 30 bubbles and liquid slugs are analyzed to in order to obtain statistically significant average values. The span of the bubble and liquid slugs distributions is generally very narrow (see Appendix 8A).

8.4. Results and Discussion

8.4.1. Dimensionless Analysis of Bubble Formation via Buckingham Π Theorem: Bubble and Liquid Slug Length

A dimensionless analysis based on the Buckingham theorem (Massey, 1998) is initially applied to fit the bubble and liquid slug lengths. The aim of this analysis is to calculate the number and form of dimensionless groups (degrees of freedom) whose values define all system solutions and can be used to correlate the experimental data. The variables that characterise a system with a circular or square outlet capillary are given in Table 8.4. The sum of superficial velocities is chosen as characteristic velocity since it is approximately the mean liquid slug velocity in circular channels, $U_{L,m} \approx U_{LS}+U_{GS}$ according to Thulasidas et al. (1995). This approximation also works well in polygonal channels since it only assumes bubble caps with volume equal to $A_B \cdot d_B 2/3$ ($A_B \neq \pi d_B/$) to obtain Eq. (8.17) and the same cross sectional area for liquid flow at the bubble caps as in a cylindrical bubble to obtain Eq. (8.18) (term $\pi d_B^3/12$). The approximation of $U_{L,m} \approx U_{LS}+U_{GS}$ does not contain any additional constrain with respect to channel and bubble cross sectional areas, A and A_B respectively, and/or liquid flowrate at the corners (Eq. (8.5) applies for any channel and bubble geometry).

Symbol	Variables of the system
ρ_L, ρ_G	Liquid and gas density
μ_L, μ_G	Liquid and gas dynamic viscosity
L_B or L_S	Bubble and liquid slug length
γ	Surface tension
r_h	Radius of largest inscribed circle inside the outlet microchannel (radius in circular channels) and the smallest dimension in rectangular channels. (Characteristic length)
$r_{h,L}$, a_L	Radius of largest inscribed circle inside the liquid inlet channel and aspect ratio
$r_{h,G}$, a_G	Radius of largest inscribed circle inside the Gas inlet channel and aspect ratio
ω_{LG}	Angle formed by the liquid and gas channels
ω_{LO}	Angle formed by the liquid and outlet channels
$(U_{GS}+U_{LS}) \approx U_{L,m}$	Sum of superficial velocities $\approx U_{L,m}$ (Characteristic velocity)
U_{LS} (bubble) or U_{GS} (liquid slugs)	Liquid or gas superficial velocity in outlet channel
g	Acceleration due to gravity

Table 8.4. System variables that represent the bubble formation system.

There are 16 variables although the influence of the gas density and viscosity are neglected. The variables $r_{h,L}$, a_L, $r_{h,G}$, a_G, ω_{LG} and ω_{LO} are not required if analysing a given geometry remaining 8 variables. All of the variables (mechanical) given in Table 8.4 can be expressed with three fundamental units: length in [m], mass in [kg] and time in [s] and in this case the rank of a matrix formed with rows that represent the exponents of mass, length and time for all these variables is 3. According to the Buckingham-Theorem the number of variables minus the dimensional matrix rank yields the number of dimensionless groups.

In this case, 8-3 = 5 independent dimensionless groups define all solutions of the system and one of them Π_1 (dimensionless bubble or liquid slug length) can be written as a function of the others. Table 8.5 gives the dimensionless groups for the proposed case. We_L, Re_L, and Bo_L are defined based on the sum of the superficial velocities (or liquid slug average velocity $U_{L,m}$). The Ca_L number is linearly dependent on We_L and Re_L, $Ca_L = We_L/Re_L$.

Definition	Name and explanation
$L_B^{\#} = \frac{L_B}{r_h}, L_S^{\#} = \frac{L_S}{r_h}$	Relative bubble and liquid slug length with respect to the characteristic length
$U_{LS}^{\#} = \frac{U_{LS}}{U_{LS}+U_{GS}}$ or $U_{GS}^{\#} = \frac{U_{GS}}{U_{LS}+U_{GS}}$	Ratio of liquid (or gas) superficial velocity to sum of superficial velocities ($U_{L,m}$)
$We_L = \frac{\rho_L r_h (U_{LS}+U_{GS})^2}{\gamma}$	Weber number: ratio of inertial to surface tension forces
$Re_L = \frac{\rho_L r_h (U_{LS}+U_{GS})}{\mu_L}$	Reynolds number: ratio of inertial to viscous forces
$Bo_L = \frac{\rho_L g r_h^2}{\gamma}$	Bond number: ratio of gravitational to surface tension forces

Table 8.5. Dimensionless numbers to calculate the bubble and liquid slug length.

This analysis gives no information about the relationship that correlates the different dimensionless numbers. The "Nonlinear Fit" function of software Mathematica is used to fit the experimental data of bubble length to the general expression given by Eqs. (8.33).

$$\frac{L_B}{r_h} = a \cdot \left(\frac{U_{LS}+U_{GS}}{U_{LS}}\right)^{\alpha} We_L^{\beta} \cdot Re_L^{\gamma} \cdot Bo^{\delta} \tag{8.33}$$

where a, α, β, γ and δ are real numbers. The values of L_S/r_h can be fitted to a similar expression using the variable $(U_{LS}+U_{GS})/U_{GS}$ instead of $(U_{LS}+U_{GS})/U_{LS}$. However, the best estimation of L_S/r_h is obtained based on bubble length from Eq. (8.25), which has no adjustable parameters.

8.4.2. Circular Cross-Section Microchannels

8.4.2.1. Bubble Formation

A Taylor bubble has a length larger than the channel diameter for a constant film thickness to develop and is considered to be "formed" when its length is not further modified within the channel after the inlet. Formation of bubbles followed two different steps,

A. Bubble formation at the gas inlet resulting in Taylor or non Taylor bubbles.

B. Modification of bubble size once it is formed through bubble coalescence or pairing along the microchannel.

A – Bubble Formation at the Gas Inlet

Mechanism 1, shown in Figure 8.21 is characterized by the formation of a gas chamber that contacts the tube walls in one or more areas. Bubbles break at the tip of this gas chamber following a snap-off mechanism as a result of a Rayleigh instability (Rayleigh, 1879). The rate of bubble formation once this mechanism is initiated is very stable and the bubble movement is very smooth with small pressure fluctuations associated with the bubble break-up from the inlet. The initiation of such a mechanism and the gas chamber length, however, are not easily reproducible and depend on wetting conditions. The chamber formation is more likely to happen in systems with a large liquid phase contact angle. In the present study, this mechanism is only observed in the water-air-acrylic system ($\theta \approx 70°$) and occurs with both liquid and gas on the side entrance. The influence of wettability on this mechanism is clearly manifested at high gas/liquid flowrates in the Y and TS structures (see Figure 8.15) at which the gas chamber just fills the entire acrylic section and bubbles are formed at the glass section (small θ). This mechanism has also been reported in a concentric configuration (Amador et al., 2005).

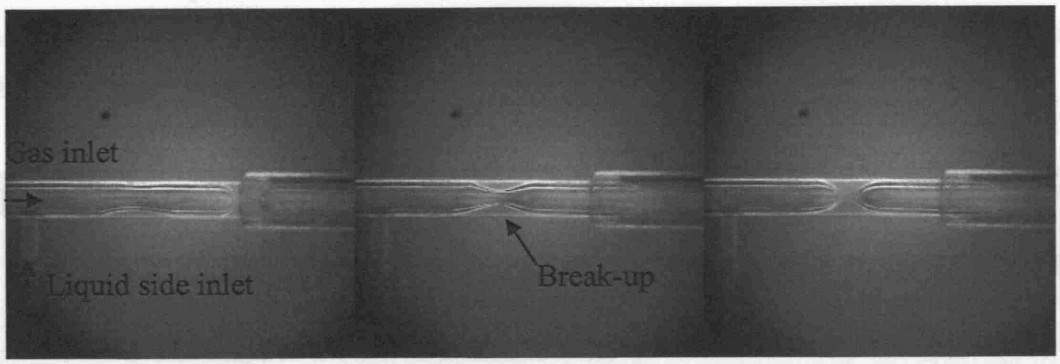

Figure 8.21. Bubble formation in structure TS-1b for system water/air/acrylic. U_{LS} = 0.0110 m/s, U_{GS} = 0.0473 m/s.

Mechanism 2 is the most common bubble formation mechanism (Bhunia et al., 1998). It consists of two stages; during the first stage bubble growth takes place at the gas inlet while in the second stage the bubble "lifts-off" developing a neck. Break-up of the neck occurs when the detachment forces overcome surface tension forces (Figure 8.22). Longer necks are observed in the water-air system.

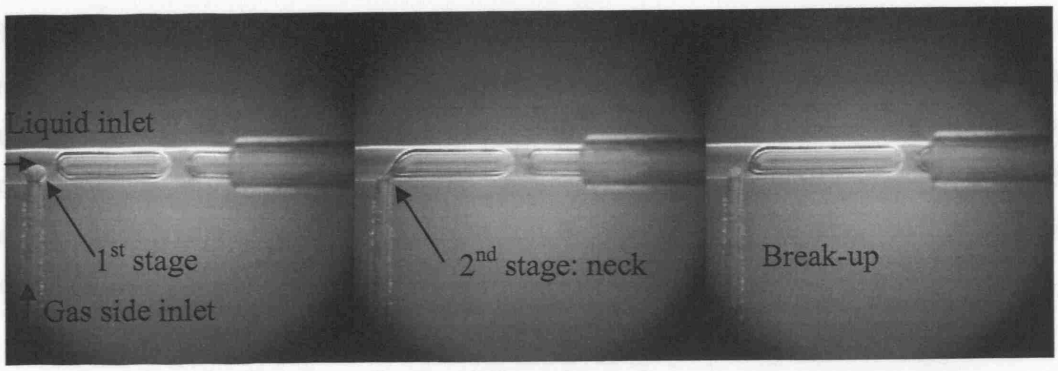

Figure 8.22. Bubble formation in structure TS-1a for system water/air/acrylic. U_{LS} = 0.03287 m/s, U_{GS} = 0.1989 m/s.

Mechanism 3, seen in Figure 8.23 is observed for the case of a wetting liquid phase and a gas inlet channel of the same size or larger than the liquid channel that is in the same direction as the test section channel. The forming bubble advances until the gas/liquid interface around the liquid inlet becomes unstable resulting in break-up and bubble formation. Bubble/liquid slug lengths are very reproducible for low to moderate liquid inlet velocities. The location of the interface break-up is almost coincident with the liquid inlet independently of gas/liquid flowrates. This differs from *mechanism 1* in which the break-up location depends on the three-phase contact points of the gas chamber.

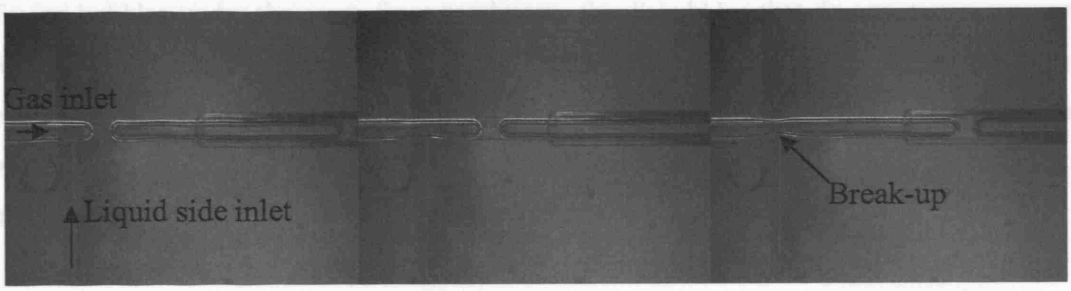

Figure 8.23. Bubble formation in structure TS-1b for system octane/air/acrylic. U_{LS} = 0.0110 m/s, U_{GS} = 0.1231 m/s.

For structure TS-1b, *Mechanism 2* produced uniform bubble sizes apart from high liquid flow rates where the high inertia of the liquid jet disrupts the bubble formation (see Figure 8.26). The bubble formation mechanism that the water-air system follows often switches from *mechanism 1* to *mechanism 2* (or *mechanism 3* as a function of gas/liquid inlet geometry), which results in

different bubble/liquid slug lengths. For instance, structure TS-1a produces small bubbles (small gas inlet) via *mechanism 2* for the octane-air system and for the air-water system under certain conditions. In the latter system, *mechanism 2* often switches to *mechanism 1* under the same flow conditions so that bubbles become longer. This is an important consideration when analysing gas/liquid manifold structures, in which bubble/liquid slug lengths obtained in parallel microchannels having even gas/liquid distribution can be different (see Chapter 9).

B. Change of Bubble Size along the Test Microchannel.

Bubble pairing (Clift, 1978) at the gas inlet was observed at low liquid flowrates and high gas flowrates in small gas inlets (e.g. structure TS1-a). The number of paired bubbles that form the final Taylor bubble depends on flowrate and inlet geometry conditions. As the forming bubble coalesces with the preceding one, a larger bubble is formed which quickly necks and detaches. This is repeated with the next bubble forming at the gas inlet until the large bubble moves away from the gas inlet and a new pairing process begins. This phenomenon has also been reported by Amador et al. (2005) in a concentric gas/liquid inlet.

Bubble coalescence along the test channel occurs when bubbles have different velocities. This is expected when bubbles have different diameters according to Eq. (8.5). Since bubble diameter (or film thickness) in Taylor flow is only dependent on *Ca*, bubble coalescence can only take place when small non-Taylor bubbles are formed together with Taylor bubbles. Non-Taylor bubbles have not developed a cylindrical body and they have a higher velocity compared to Taylor bubbles under the same flow conditions. Small bubbles that do not pair are generally formed when using small gas inlets and high liquid flow rates. Figure 8.24 shows a non-Taylor bubble coalescing with a Taylor bubble forming a larger Taylor bubble. Taylor bubbles formed by this mechanism tend to have a distribution of lengths since coalescence appears to happen randomly.

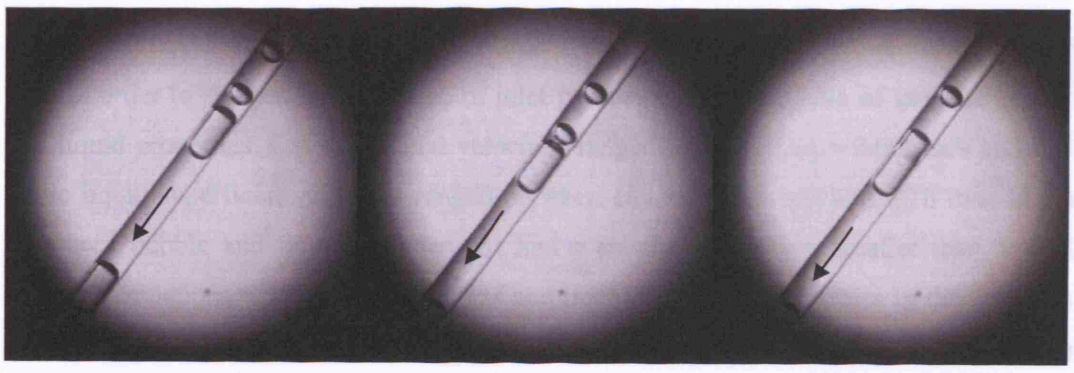

Figure 8.24. Bubble coalescence of a small bubble (Non-Taylor) into a long bubble (Taylor).

Bubble pairing was observed with octane in structures TS-1a and Y-1a (see Figure 8.25 for a bubble formation mechanism map in TS-1a and gas/liquid superficial velocities 0-0.06 m/s). No pairing was seen with water. Coalescence appeared especially with structures TS-1a and Y-1a, caused by the small size of the gas inlet, which favours formation of smaller gas bubbles. Sometimes even short Taylor bubbles were observed to coalesce with each other and this was especially evident at higher liquid flow rates.

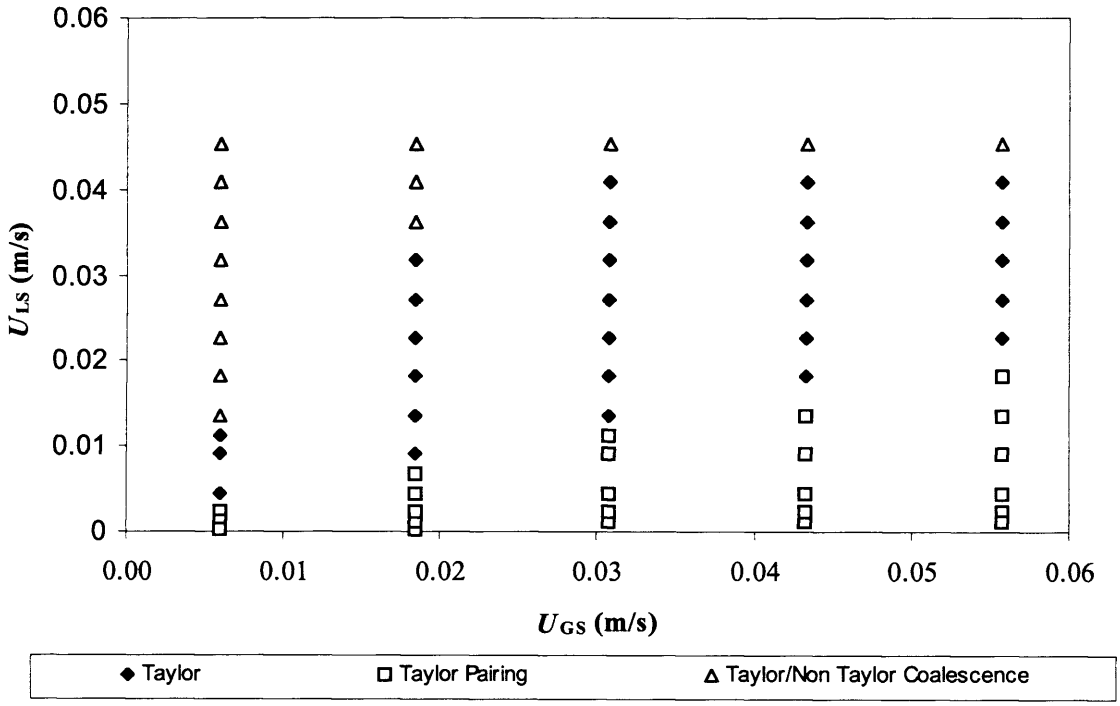

Figure 8.25. Conditions that lead to formation of Taylor bubbles either at inlet or as a result of pairing and coalescence in the octane/air system for structure TS-1a.

8.4.2.2. Bubble Length

Bubble and liquid slug lengths were measured in the different acrylic structures shown in Figure 8.15 in order to analyse the influence of inlet geometry, diameter ratio of gas and liquid inlets and liquid properties. Gas superficial velocities ranged between U_{GS} = 0.006 m/s and 0.58 m/s while liquid superficial velocities ranged between U_{LS} = 0.0005 m/s and 0.16 m/s. In general, measured bubble and liquid slug lengths had a standard deviation smaller than 5 %. Large standard deviations were found at low gas and liquid superficial velocities in the system water-air, which has a high surface tension where pressure fluctuations during bubble formation and exit became substantial. Also in some cases the bubble sizes formed were not uniform, i.e.

structure TS-1b for octane at high liquid flowrates. In this case the high liquid velocity at the side entrance and the small surface tension of the octane-air system results in irregular bubble formation (Figure 8.26).

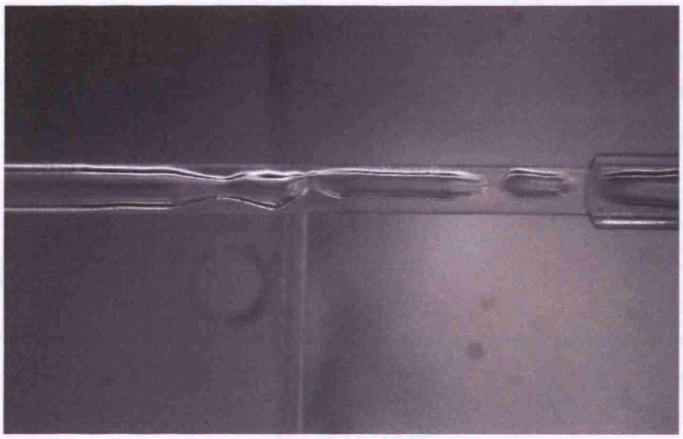

Figure 8.26. Irregular bubble formation in structure TS-1b at high liquid flowrates.

Considering a given geometry, no gravity and gas inertial effects $L_B/r_h = f((U_{GS}+U_{LS})/U_{LS}, Ca_L, Re_L)$ (see Table 8.5). To quantify the effect of the We_L and Re_L numbers, the dimensionless bubble length (L_B/r) is plotted against the ratio $(U_{GS}+U_{LS})/U_{LS}$. Figure 8.27 and Figure 8.28 show results for TS-2b (liquid at side entrance) and TS-2c (tee junction) operating with octane-air. With these systems bubbles were mainly formed via *Mechanism 3* and *2* respectively. Both graphs show that the ratio $(U_{GS}+U_{LS})/U_{LS}$ is the parameter that bubble length is most sensitive to. However, in structure TS-2c there is also a variation of bubble length with gas superficial velocity, U_{GS} at each ratio $(U_{GS}+U_{LS})/U_{LS}$, which does not appear in structure TS-2b. This may indicate that when the two fluids join at $\omega_{LG} = 180°$ there is greater influence of inertial forces (We_L and Re_L) on the bubble length compared to 90° contact. Results from structure Y-2 for the octane-air system, where *Mechanism 2* is dominant, show variation with gas velocity for each ratio $(U_{GS}+U_{LS})/U_{LS}$ in between those from TS-2c and TS-2b structures. Furthermore, the bubble lengths produced by these three configurations are very similar at low superficial gas velocities ($U_{GS} < 0.1231$ m/s) and begin to differ as the gas velocity increases, indicating that the effect of the inlet geometry (angles of liquid, gas and outlet channels) on bubble length becomes more important as the gas superficial velocity U_{GS} increases at each ratio $(U_{GS}+U_{LS})/U_{LS}$ (increase of inertial forces).

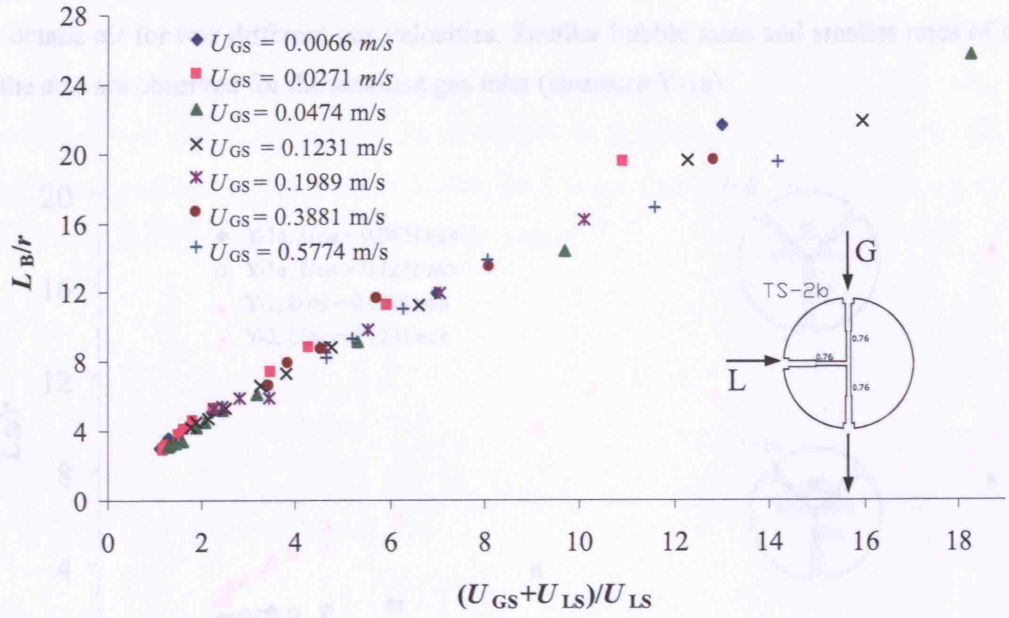

Figure 8.27. Dimensionless bubble length for different $(U_{GS}+U_{LS})/U_{LS}$ ratios in structure TS-2b with octane/air, $6.5\times10^{-4} \le We_L \le 7.0$, $3.8 \le Re_L \le 395$.

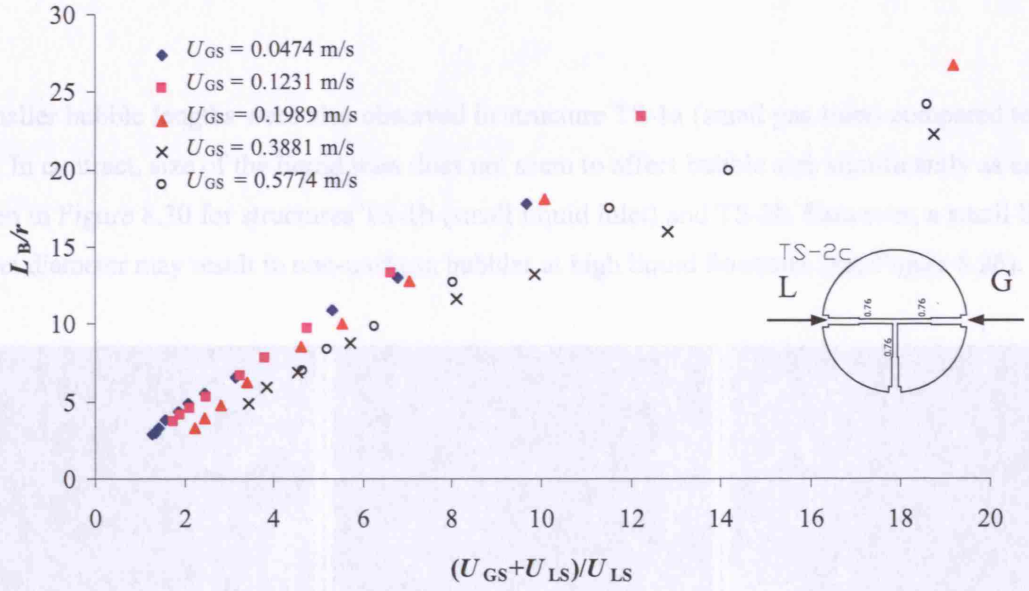

Figure 8.28. Dimensionless bubble length for different $(U_{GS}+U_{LS})/U_{LS}$ ratios in structure TS-2c with octane/air. $0.036 \le We_L \le 7.0$, $28 \le Re_L \le 395$.

Figure 8.29 shows the effect of gas inlet diameter on bubble lengths in structures Y-1a and Y-2 for octane-air for two different gas velocities. Smaller bubble sizes and smaller rates of change of the size are observed for the smallest gas inlet (structure Y-1a).

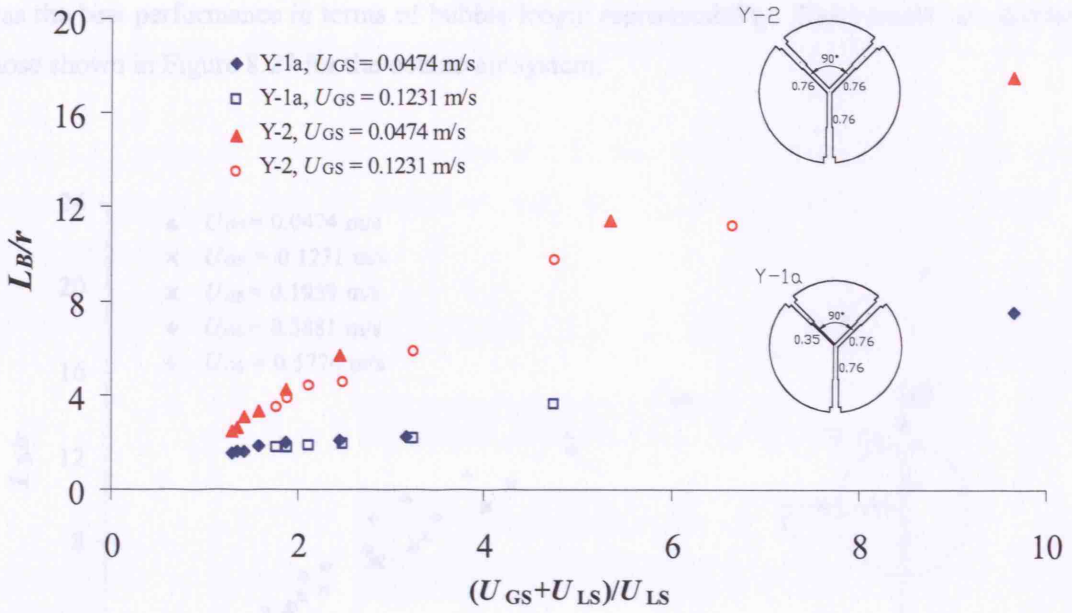

Figure 8.29 .Comparison of dimensionless bubble lengths in structures Y-1a and Y-2 with octane/air.

Smaller bubble lengths were also observed in structure TS-1a (small gas inlet) compared to TS-2a. In contract, size of the liquid inlet does not seem to affect bubble size significantly as can be seen in Figure 8.30 for structures TS-1b (small liquid inlet) and TS-2b. However, a small liquid inlet diameter may result in non-uniform bubbles at high liquid flowrates (see Figure 8.26).

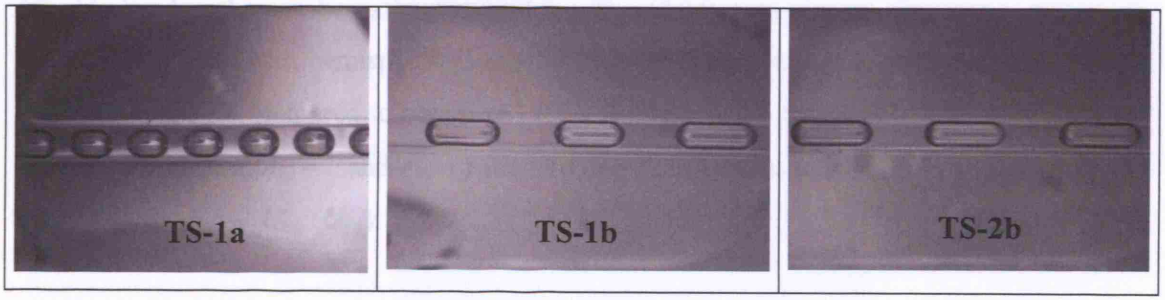

Figure 8.30. Bubble and slug lengths in structures TS-1a, TS-1b and TS-2b for the system octane-air at U_{LG} = 0.03287 m/s and U_{GS} = 0.0474 m/s.

Results on bubble length for the water-air system were similar to those for the octane-air system (small dependence of bubble length on We_L and Re_L), although they showed a smaller variation of the bubble length with increasing gas superficial velocity for each ratio $(U_{GS}+U_{LS})/U_{LS}$ in structures TS-2c and Y-2. Figure 8.31 shows bubble length results for structure TS-2b, which was the best performance in terms of bubble length reproducibility. These results are similar to those shown in Figure 8.27 for the octane-air system.

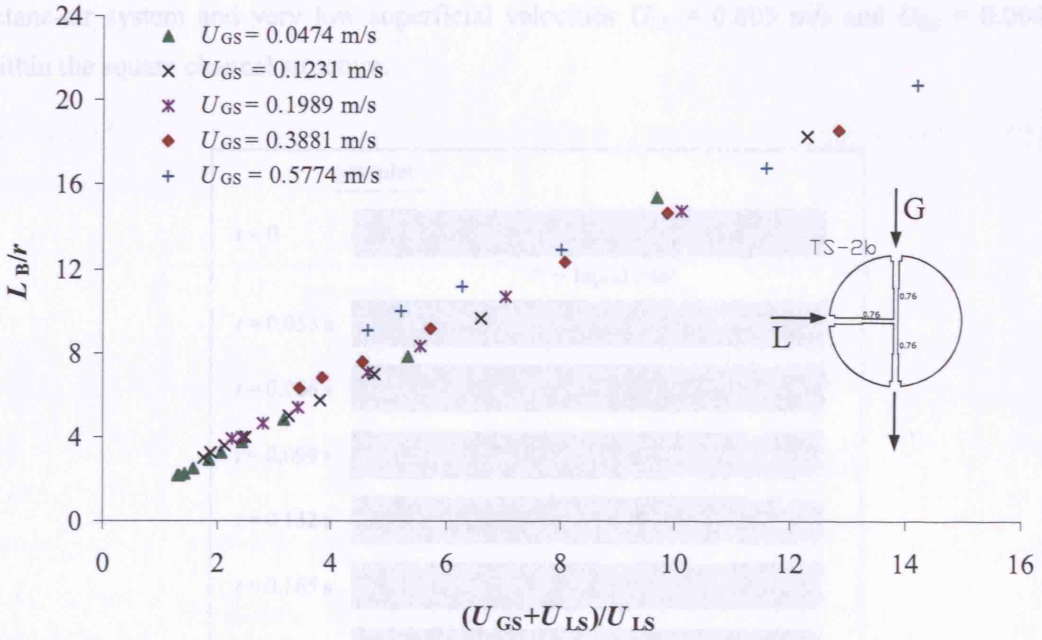

Figure 8.31. Dimensionless bubble length for different U_{GS}/U_{LS} ratios in structure TS-2b with water, $0.015 \leq We_L \leq 2.98$, $22 \leq Re_L \leq 308$.

Liquid slug lengths can be estimated applying Eq. (8.34) from Eq. (8.25), which assumes a cylindrical bubble with hemispherical caps, where the bubble radius r_B, cross section A_B and bubble velocity U_B (required to obtain α_G) are a function of Ca (see Table 8.1). At low Ca for circular channels, $A/A_B \approx 1$ and $r^{\#}_B \approx 1$, simplifying Eq. (8.34) to $L^{\#}_S = (L^{\#}_B (1-\alpha_G)-2/3)/\alpha_G$ and $\alpha_G = U_{GS}/U_B \approx U_{GS}/(U_{GS}+U_{LS})$.

$$L^{\#}_S = \frac{L^{\#}_B(1-\alpha_G A/A_B)-2r^{\#}_B/3}{\alpha_G A/A_B} \tag{8.34}$$

8.4.3. Square Cross Section Microchannels

8.4.3.1. Bubble Formation in Microstructures T-2 and T-3

A) Mechanism of Bubble Formation for N-Octane/Air System in Microstructure T-2

Figure 8.32 shows the temporary evolution of a forming bubble at the gas/liquid inlet for the octane-air system and very low superficial velocities U_{LS} = 0.003 m/s and U_{GS} = 0.004 m/s within the square channel structure.

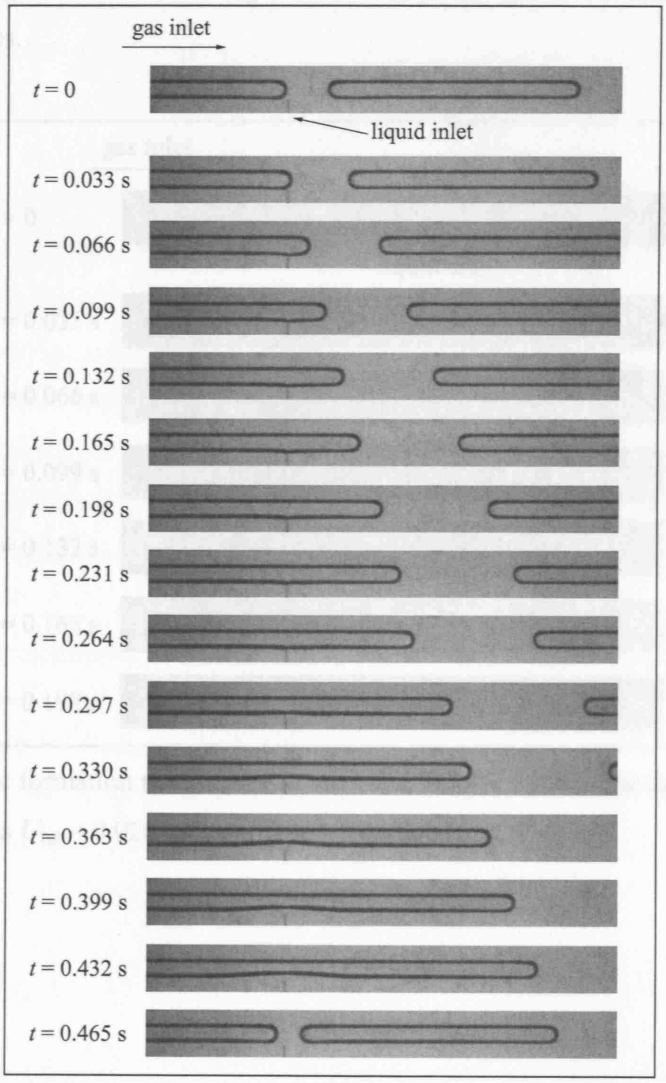

Figure 8.32. Bubble formation mechanism in structure T-2 for n-octane at the side entrance and low superficial velocities U_{LS} = 0.003 m/s and U_{GS} = 0.004 m/s.

The time scale starts immediately after one bubble has been formed. The time interval between the images is $\Delta t = 0.033$ s. The bubble forms via *mechanism 3* and the liquid flowing around the forming bubble increases the liquid slug length between the forming and the preceding bubbles. Because of the liquid flow in the corners of the rectangular channel, it is easier for the liquid phase to bypass the forming bubble compared to circular channels, which results in longer liquid slugs, and therefore bubbles, under the same superficial velocities. After $t \approx 0.3$ s, a bubble neck starts forming. This necking process is related to instabilities in the bubble surface and to the momentum of the inflowing liquid. The neck continuous growing until the bubble forms and detaches.

Figure 8.33 and Figure 8.34 show images of bubble formation in the same system at higher superficial velocities.

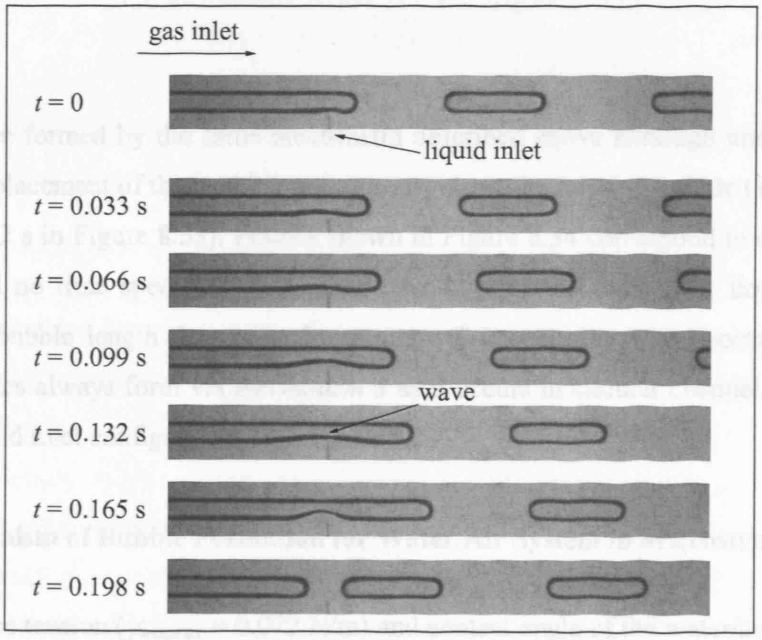

Figure 8.33. Bubble formation mechanism in structure T-2 for n-octane at the side entrance and superficial velocities $U_{LS} = 0.026$ m/s and $U_{GS} = 0.02$ m/s.

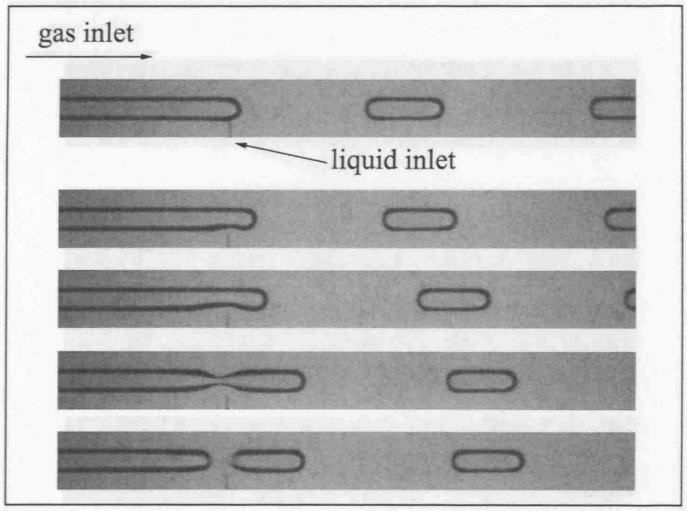

Figure 8.34. Bubble formation mechanism in structure T-2 for n-octane at the side entrance and superficial velocities U_{LS} = 0.052 m/s and U_{GS} = 0.02 m/s.

The bubbles are formed by the same mechanism described above although under certain flow conditions, displacement of the necking point occurs along the forming bubble (see frames at t = 0.099 s to 0.132 s in Figure 8.33). Frames shown in Figure 8.34 correspond to different bubble formations and no time specification is given. As U_{LS} for the same U_{GS}, liquid slug length increases and bubble length decreases. In structure T-2 operating with n-octane on the side entrance, bubbles always form via *mechanism 3* as it occurs in circular channel structures with similar gas/liquid inlet configuration (see Figure 8.23).

B) Mechanism of Bubble Formation for Water/Air System in Microstructure T-2

The high surface tension ($\gamma_{water/air}$ = 0.072 N/m) and contact angle of the water/air system results in bubble formation via *mechanism 1* with the necking region away from the gas/liquid inlet. Figure 8.35 shows the bubble formation mechanism for water/air at superficial velocities U_{LS} = 0.011 m/s and U_{GS} = 0.02 m/s.

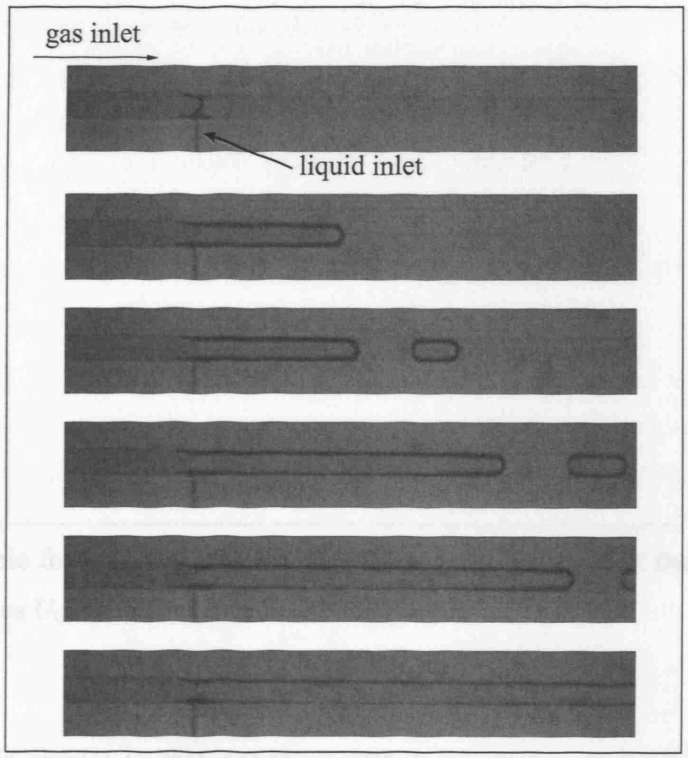

Figure 8.35. Bubble formation mechanism in structure T-2 for water at the side entrance and superficial velocities U_{LS} = 0.011 m/s and U_{GS} = 0.02 m/s.

In this case, the bubble formation mechanism is unstable and the necking position changes with time. An air/water interface, which can be seen in the first image in Figure 8.35, is formed above the liquid inlet. Then, this interface advances creating an expanding air chamber while small bubbles detach. After a while, the air chamber detaches and a new gas/liquid interface forms above the inlet. Sometimes, the air chamber reaches the outlet by forming contact points at the channel walls that stabilise it and the bubbles are formed outside the micro channel in the external plastic tube, which the water wets better and a regular bubble slug flow is then observed there. This mechanism occurs for low liquid superficial velocities at all gas superficial velocities. It is not possible to measure the bubble and the liquid slug lengths due to the unstable nature of the flow.

Figure 8.36 shows the bubble formation process in the water/air system in structure T-2 at superficial velocities of U_{LS} = 0.014 m/s and U_{GS} = 0.066 m/s.

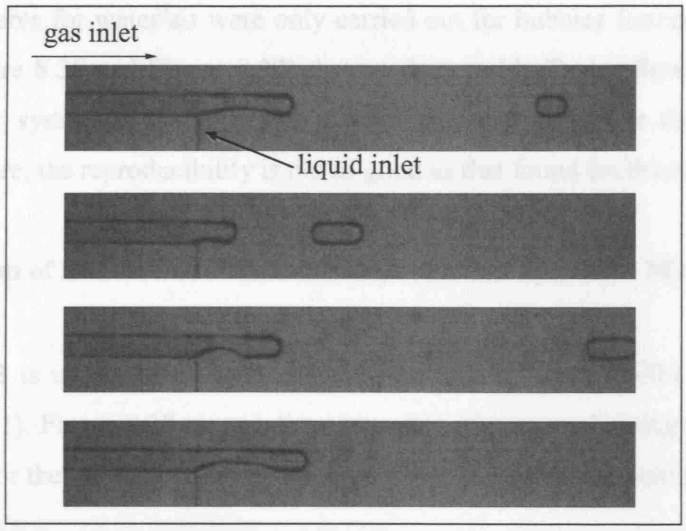

Figure 8.36. Bubble formation mechanism in structure T-2 for water at the side entrance and superficial velocities U_{LS} = 0.014 m/s and U_{GS} = 0.066 m/s.

This mechanism is similar to that occurring with n-octane/air, *mechanism 3*, although the necking position is slightly displaced downstream and there is a meniscus contact point with the wall as seen in *mechanism 1*. The position of the neck can change for different values of the superficial velocity as shown in Figure 8.36 and Figure 8.37 while sometimes the position of the neck appears even outside this image.

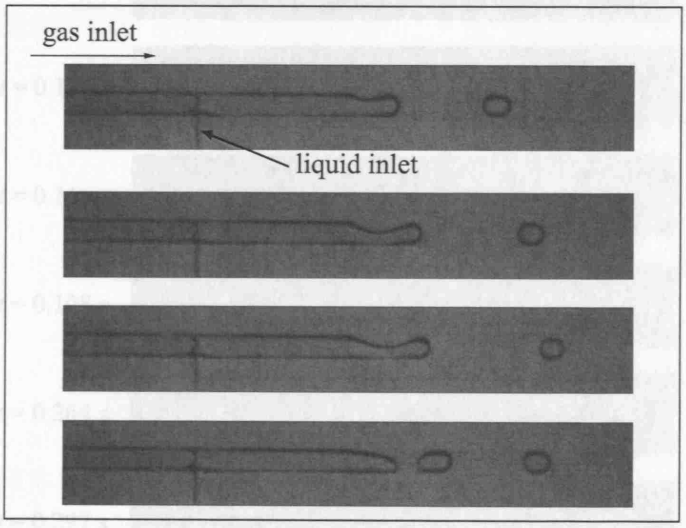

Figure 8.37. Bubble formation mechanism in structure T-2 for water at the side entrance and superficial velocities U_{LS} = 0.028 m/s and U_{GS} = 0.144 m/s.

Length measurements for water/air were only carried out for bubbles formed with the last two mechanisms (Figure 8.36 and Figure 8.37) that produce stable Taylor flow. Another problem with the water/air system is that different mechanisms can occur for the same superficial velocities. Therefore, the reproducibility is not as good as that found for the octane/air system.

C) Mechanism of Bubble Formation for N-Octane/Air System in Microstructure T-3

Microstructure T-3 is used with either the gas (T-3a) or the liquid (T-3b) phase on the side entrance (via port 1). Figure 8.38 gives a time sequence of images showing the gas/liquid inlet in structure T-3a for the n-octane/air system for very low superficial velocities, U_{LS} = 0.002 m/s and U_{GS} = 0.003 m/s.

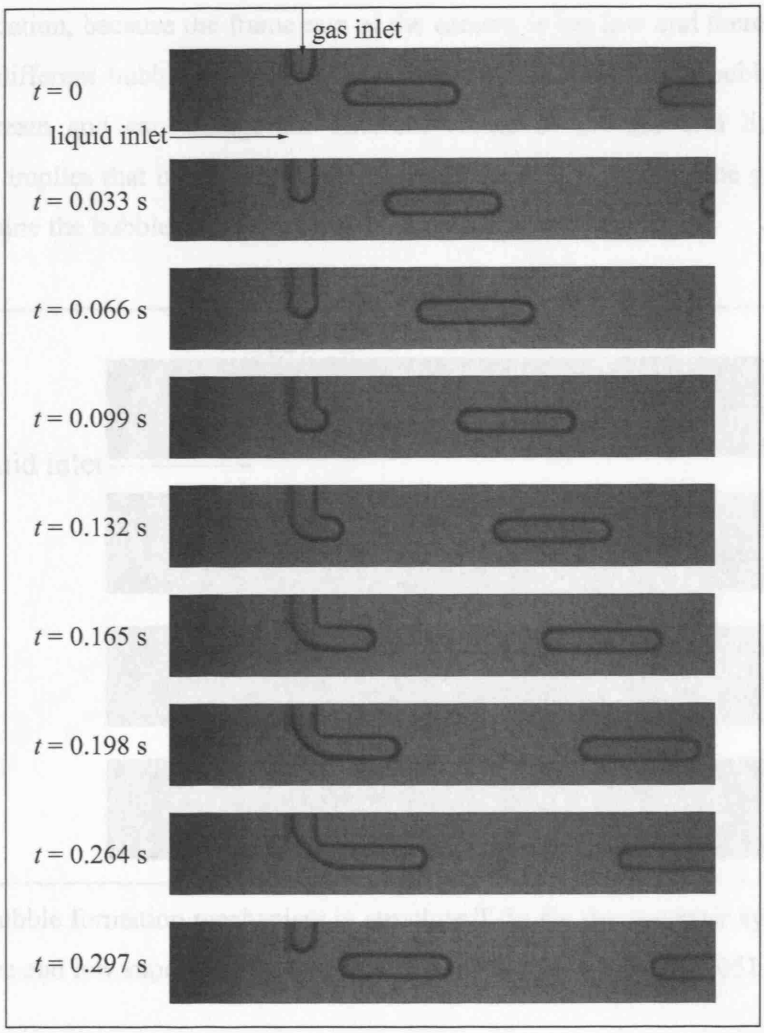

Figure 8.38. Bubble formation mechanism in structure T-3a for n-octane/air system with air at the side entrance and low superficial velocities U_{LS} = 0.002 m/s and U_{GS} = 0.003 m/s.

Bubble formation follows *mechanism 2*. The momentum of the liquid deforms the gas downstream and the length of the liquid slug increases. After t = 0.198 s a neck with an angle nearly 45 ° at the gas inlet is developed. During this stage, the neck may not be pinned at the gas inlet mouth but inside the gas channel. The same mechanism is observed for different gas and liquid superficial velocities. In structure T-3b (liquid at the side inlet) the bubble formation mechanism is very similar to that mentioned above for the n-octane/air system in the microstructure T-2, *mechanism 3* (Figure 8.32-Figure 8.34).

D) Mechanism of Bubble Formation for System Water/Air in Microstructure T-3

Figure 8.39 shows the bubble formation mechanism for the water/air system in structure T-3a for superficial velocities U_{LS} = 0.008 m/s and U_{GS} = 0.051 m/s. In this series of images, there is no time specification, because the frame rate of the camera is too low and therefore the images correspond to different bubble formations. The neck position where the bubble is formed is displaced upstream and can change for different values of the gas and liquid superficial velocities. This implies that in the case of the water-air system the size of the gas inlet channel does not determine the bubble size as much as in the n-octane/air system.

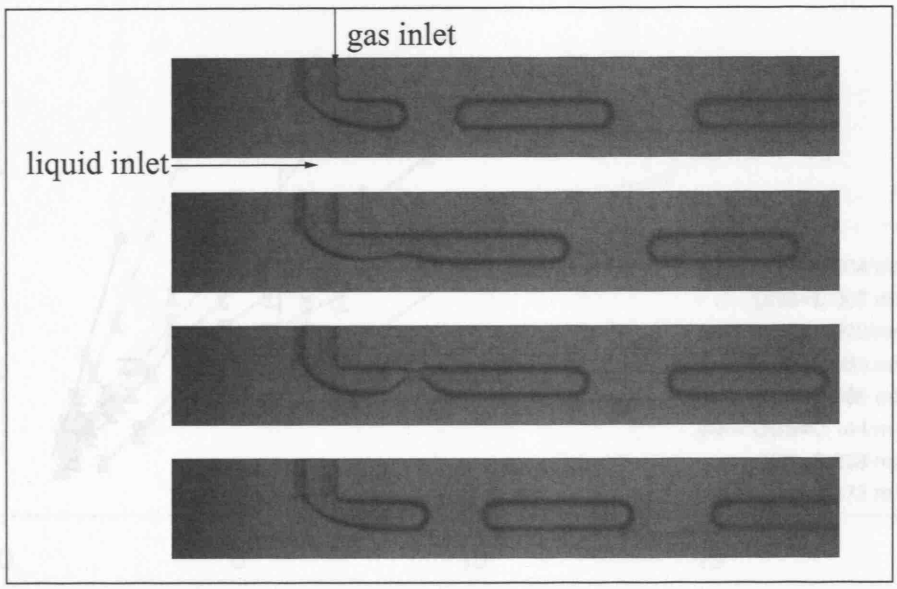

Figure 8.39. Bubble formation mechanism in structure T-3a for the water/air system with air at the side entrance and low superficial velocities U_{LS} = 0.008 m/s and U_{GS} = 0.051 m/s.

The bubble formation mechanism where the liquid is introduced at the side entrance, T-3b is very similar to that occurring in structure T-2 already described in Figure 8.36 and Figure 8.37.

8.4.3.2. Bubble and Liquid Slug Lengths in Structures T-2 and T-3

Bubble and liquid slug lengths were measured for gas superficial velocities between U_{GS} = 0.004 m/s and 0.473 m/s and liquid superficial velocities between U_{LS} = 0.003 m/s and 0.25 m/s. Images were taken for different pairs of gas and liquid superficial velocities although some conditions resulted in bubble and/or liquid slugs longer than the field of view of the camera. The bubble and liquid slug lengths were measured using a MATLAB script described in section 8.3.5 and explained in Appendix 8A. The values in Figure 8.40-Figure 8.53 are average values for at least 30 bubbles with errors bars calculated as plus/minus one standard deviation σ_v. Therefore, they represent the span of the size distribution plus measurement error, which is ±12.7 μm.

A) Bubble and Liquid Slug Length in Microstructure T-2

The microstructure T-2 was used with both n-octane/air and water/air systems. Figure 8.40 shows the dimensionless bubble length L_B/r_h for n-octane/air as a function of the ratio $(U_{GS}+U_{LS})/U_{LS}$ for different values of the gas superficial velocity U_{GS}.

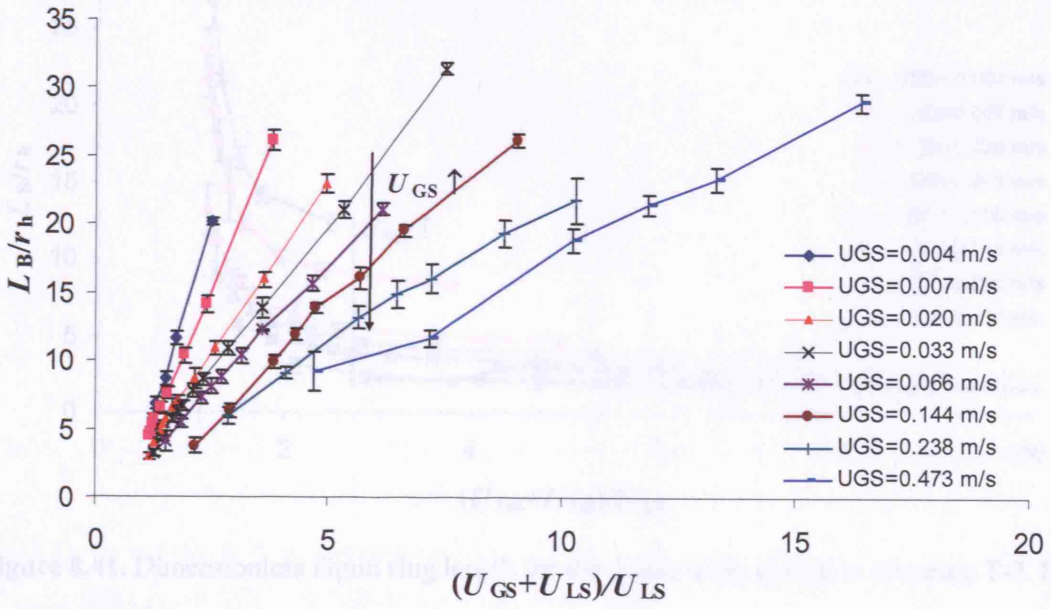

Figure 8.40. Dimensionless bubble length for the n-octane/air system in structure T-2. Error bars calculated as ± σ_v.

The dimensionless bubble length L_B/r_h increases as $1/U^{\#}_{LS} = (U_{GS}+U_{LS})/U_{LS}$ increases following a nearly linear trend for each gas superficial velocity. This is a general trend that applies to all

gas/liquid inlet configurations and liquid/gas systems. The slope of these straight lines decreases as the gas superficial velocity increases resulting in smaller bubble lengths for the same $(U_{GS}+U_{LS})/U_{LS}$ at higher gas superficial velocities. This is a consequence of an increase in liquid and gas inertial forces that lead to earlier bubble break-up resulting in smaller bubbles/liquid slugs for the same gas volume fraction.

Figure 8.41 shows the dimensionless liquid slug length also as a function of $(U_{GS}+U_{LS})/U_{LS}$ for the system n-octane/air. Contrary to bubble length, the dimensionless liquid slug length decreases as $(U_{GS}+U_{LS})/U_{LS}$ increases and does not follow a linear trend for $(U_{GS}+U_{LS})/U_{LS} < 2$ ($U_{LS} > U_{GS}$). A linear trend of Ls/r_h is obtained versus $(U_{GS}+U_{LS})/U_{GS}$, and this is a preferable choice to fit the experimental data. As the superficial gas velocity increases while $(U_{GS}+U_{LS})/U_{LS}$ is kept constant, the dimensionless liquid slug length decreases by a similar factor to the dimensionless bubble length. This factor should be the same is W is kept constant but W changes as a function of liquid flow at the corners and film thickness according to Eq. (8.5).

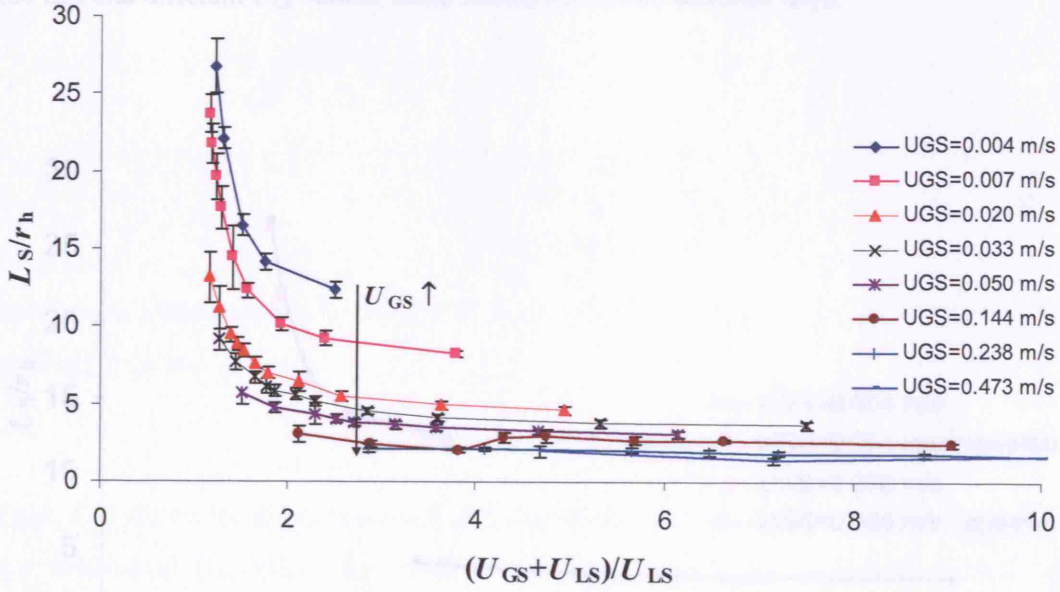

Figure 8.41. Dimensionless liquid slug length for the n-octane/air system in structure T-2. Error bars calculated as ± σ_v.

Reproducibility of bubble and liquid slug lengths at experiments carried out in different days is good in all systems where the bubble formation mechanism is stable. The measurements of bubble and liquid slug length for the n-octane/air system in structure T-2 are reproducible with a

repeatability of ± 2%. Figure 8.42 and Figure 8.43 show results of dimensionless bubble and liquid slug lengths in structure T-2 for the system n-octane/air carried out in different days.

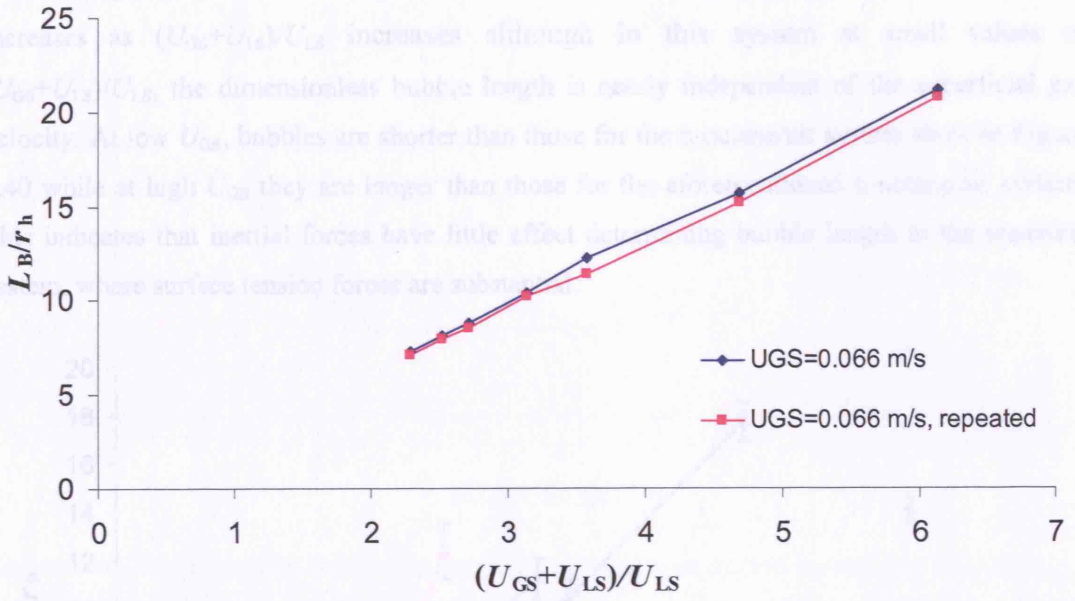

Figure 8.42. Dimensionless bubble length for the n-octane/air system in structure T-2 at U_{GS} = 0.06 m/s and different U_{LS} values. Runs carried out in two different days.

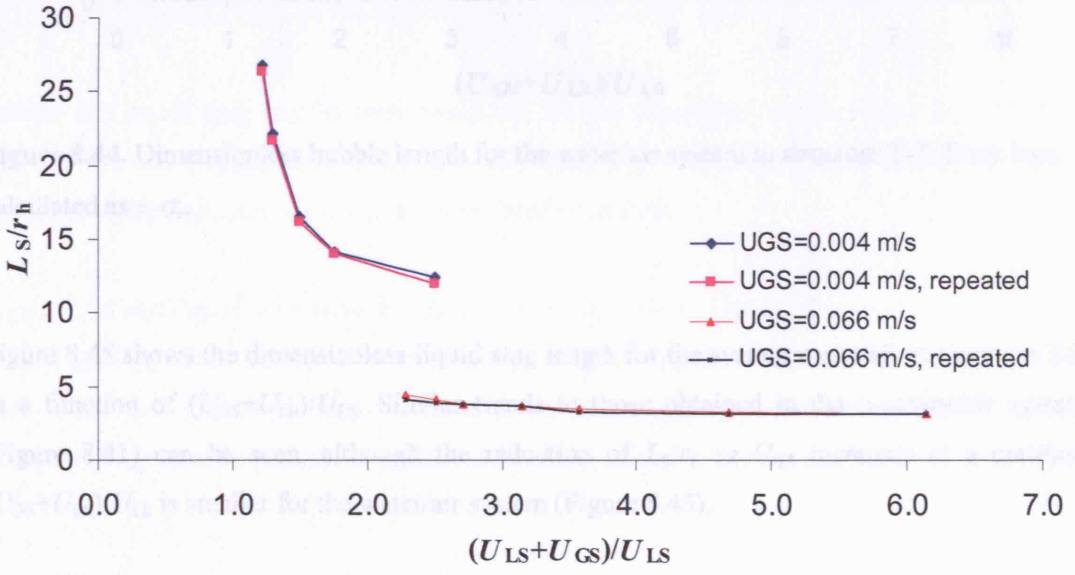

Figure 8.43. Dimensionless liquid slug length for the n-octane/air system in structure T-2 at U_{GS} = 0.0004 and 0.066 m/s and different U_{LS} values. Runs carried out in two different days.

The available data for the system water/air in structure T-2 is less than that for the n-octane/air system because of unstable flow at very low flowrates. Figure 8.44 shows the dimensionless bubble length for the water/air system as a function of $(U_{GS}+U_{LS})/U_{LS}$. Bubble length also increases as $(U_{GS}+U_{LS})/U_{LS}$ increases although in this system at small values of $(U_{GS}+U_{LS})/U_{LS}$, the dimensionless bubble length is nearly independent of the superficial gas velocity. At low U_{GS}, bubbles are shorter than those for the n-octane/air system show in Figure 8.40 while at high U_{GS} they are longer than those for the aforementioned n-octane/air system. This indicates that inertial forces have little effect determining bubble length in the water/air system, where surface tension forces are substantial.

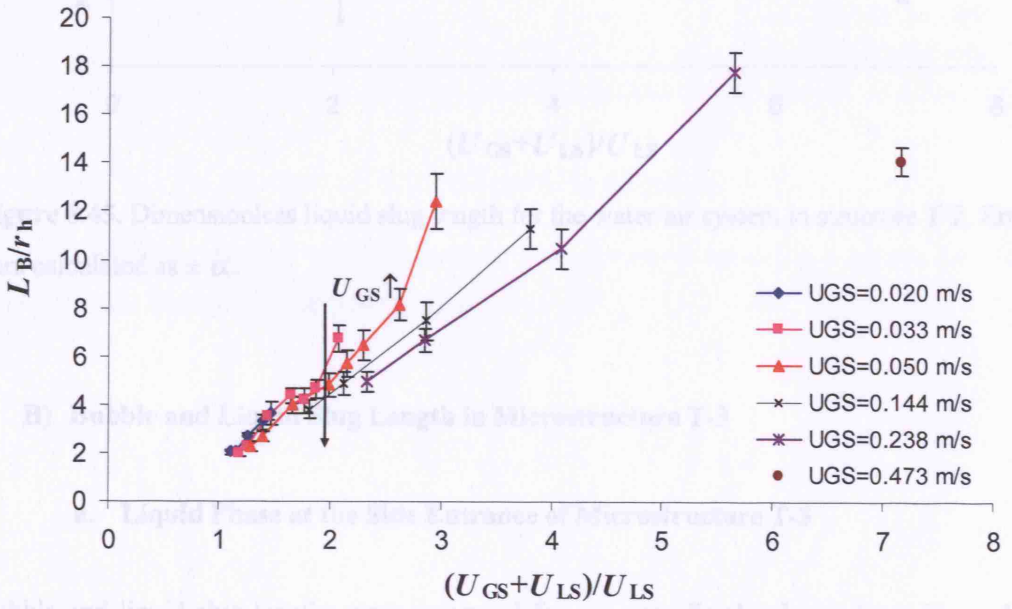

Figure 8.44. Dimensionless bubble length for the water/air system in structure T-2. Error bars calculated as $\pm \sigma_v$.

Figure 8.45 shows the dimensionless liquid slug length for the system water/air in structure T-2 as a function of $(U_{GS}+U_{LS})/U_{LS}$. Similar trends to those obtained in the n-octane/air system (Figure 8.41) can be seen, although the reduction of L_S/r_h as U_{GS} increases at a constant $(U_{GS}+U_{LS})/U_{LS}$ is smaller for the water/air system (Figure 8.45).

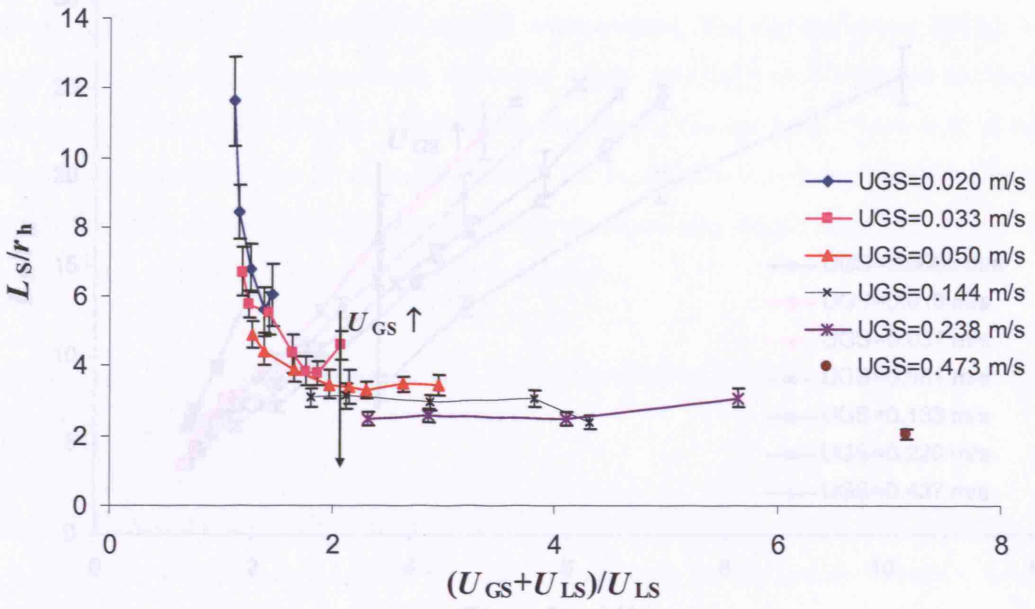

Figure 8.45. Dimensionless liquid slug length for the water/air system in structure T-2. Error bars calculated as ± σ_v.

B) Bubble and Liquid Slug Length in Microstructure T-3

a. Liquid Phase at the Side Entrance of Microstructure T-3

Bubble and liquid slug lengths were measured for gas superficial velocity from U_{GS} = 0.0066 m/s to 0.473 m/s and liquid superficial velocity from U_{LS} = 0.002 m/s to 0.25 m/s. Images were taken for different combinations of the superficial velocities.

Figure 8.46 and Figure 8.47 show the dimensionless bubble and liquid slug lengths versus ratios $(U_{GS}+U_{LS})/U_{LS}$ when the liquid is connected to the side entrance for the n-octane/air system. This is the same gas/liquid inlet configuration as the one set up in structure T-2. However, in structure T-3 gas and liquid inlets as well as the outlet channel have the same cross section.

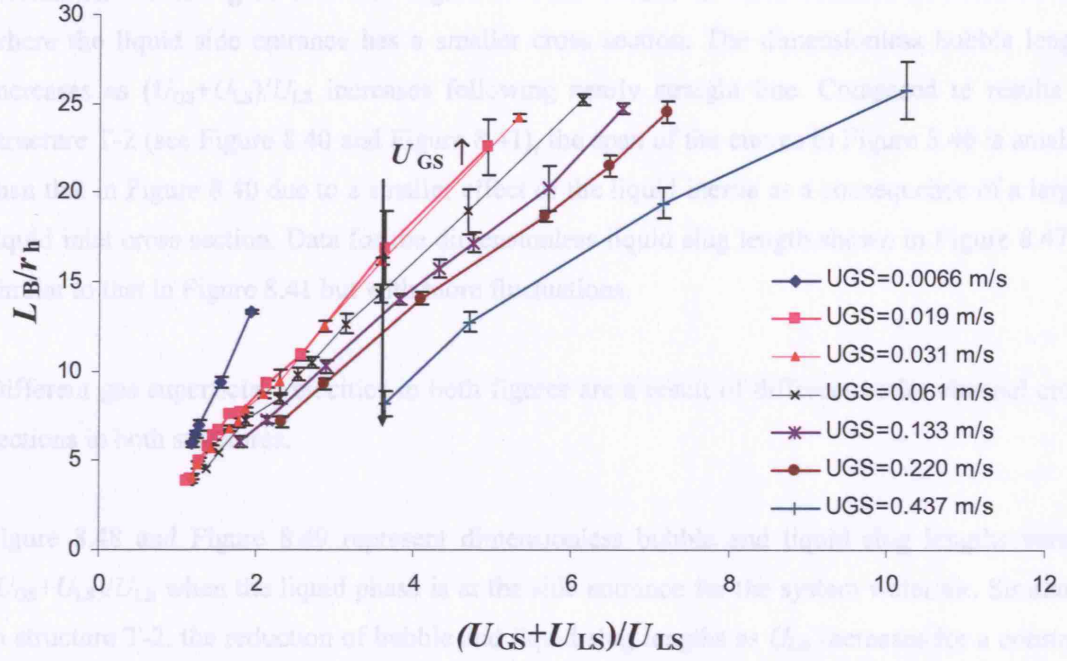

Figure 8.46. Dimensionless bubble Length for the n-octane/air system in structure T-3, liquid at side Entrance. Error bars calculated as ± σ_v.

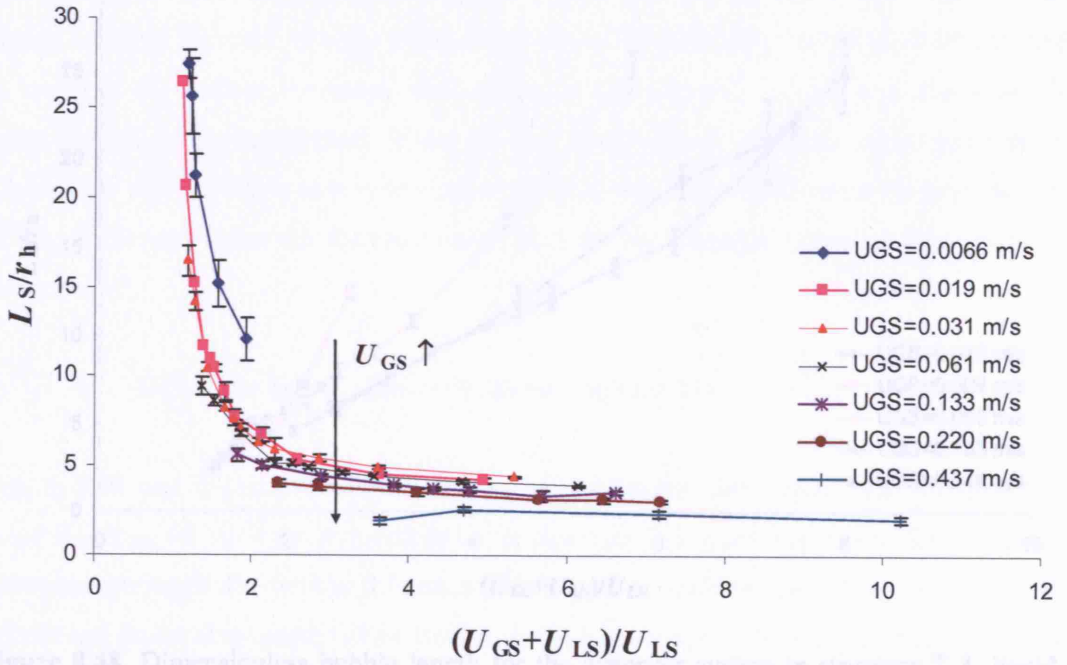

Figure 8.47. Dimensionless liquid slug length for the n-octane/air system in structure T-3, liquid at side entrance. Error bars calculated as ± σ_v.

Results shown in Figure 8.46 and Figure 8.47 are similar to those obtained in structure T-2 where the liquid side entrance has a smaller cross section. The dimensionless bubble length increases as $(U_{GS}+U_{LS})/U_{LS}$ increases following nearly straight line. Compared to results in structure T-2 (see Figure 8.40 and Figure 8.41), the span of the curves in Figure 8.46 is smaller than that in Figure 8.40 due to a smaller effect of the liquid inertia as a consequence of a larger liquid inlet cross section. Data for the dimensionless liquid slug length shown in Figure 8.47 is similar to that in Figure 8.41 but with more fluctuations.

Different gas superficial velocities in both figures are a result of different outlet channel cross sections in both structures.

Figure 8.48 and Figure 8.49 represent dimensionless bubble and liquid slug lengths versus $(U_{GS}+U_{LS})/U_{LS}$ when the liquid phase is at the side entrance for the system water/air. Similarly to structure T-2, the reduction of bubble and liquid slug lengths as U_{GS} increases for a constant ratio $(U_{GS}+U_{LS})/U_{LS}$ is less important than for the octane-air system due to a less significant effect of inertial forces over surface tension forces.

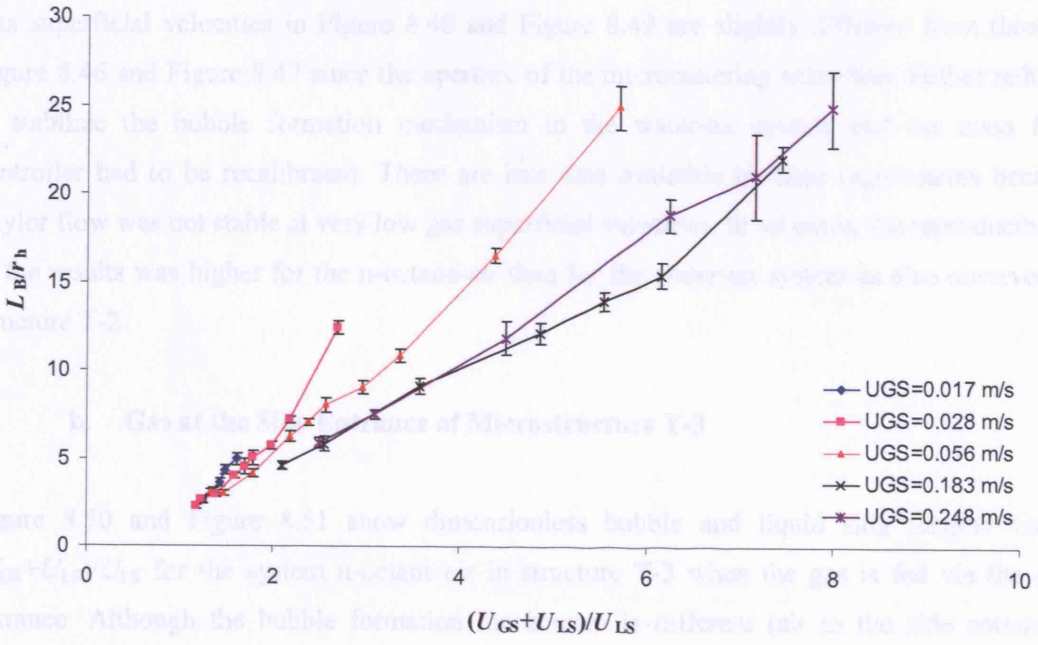

Figure 8.48. Dimensionless bubble length for the water/air system in structure T-3, liquid at side entrance. Error bars calculated as ± σ_v.

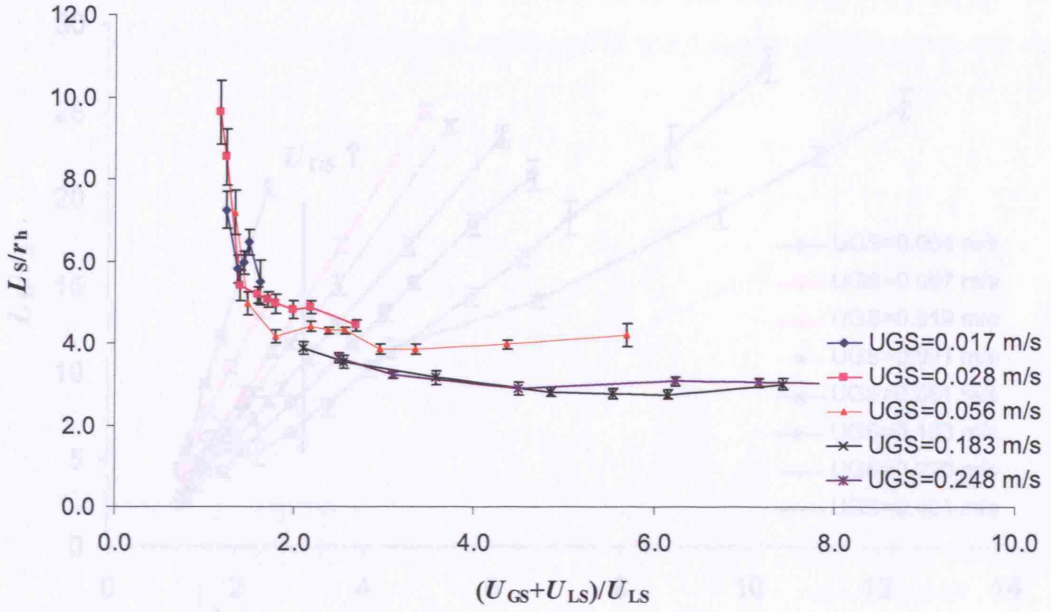

Figure 8.49. Dimensionless liquid slug length for the water/air system in structure T-3, liquid at side entrance. Error bars calculated as ± σ_r.

Gas superficial velocities in Figure 8.48 and Figure 8.49 are slightly different from those in Figure 8.46 and Figure 8.47 since the aperture of the micrometering valve was further reduced to stabilize the bubble formation mechanism in the water-air system and the mass flow controller had to be recalibrated. There are less data available in these experiments because Taylor flow was not stable at very low gas superficial velocities. In all cases, the reproducibility of the results was higher for the n-octane-air than for the water-air system as also observed in structure T-2.

b. Gas at the Side Entrance of Microstructure T-3

Figure 8.50 and Figure 8.51 show dimensionless bubble and liquid slug lengths versus $(U_{GS}+U_{LS})/U_{LS}$ for the system n-octane/air in structure T-3 when the gas is fed via the side entrance. Although the bubble formation mechanism is different (air in the side entrance), bubble and liquid slug lengths show similar trends and values to those in structure T-2 (Figure 8.40 and Figure 8.41) and in structure T-3 (Figure 8.46 and Figure 8.47) when the liquid is at the side entrance.

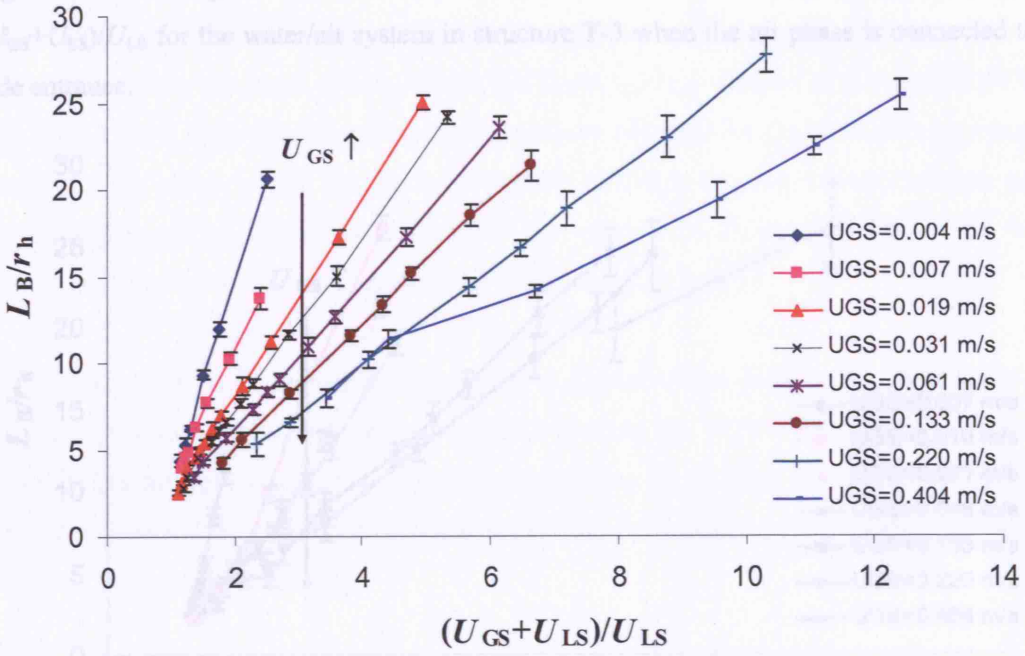

Figure 8.50. Dimensionless bubble length for the n-octane/air system in structure T-3, gas at side entrance. Error bars calculated as ± σ_v.

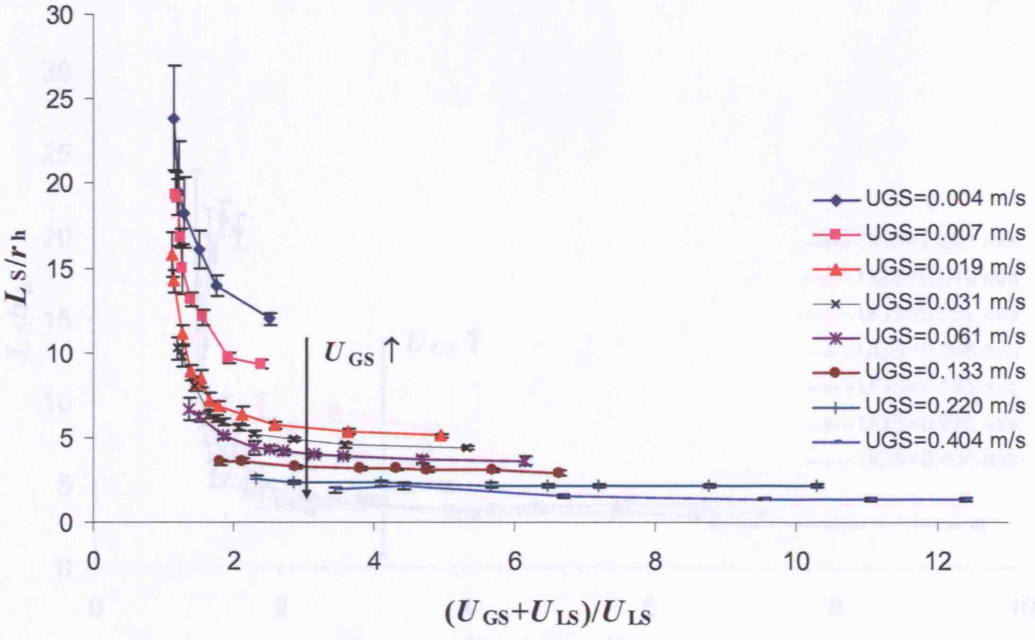

Figure 8.51. Dimensionless liquid slug length for the n-octane/air system in structure T-3, gas at side entrance. Error bars calculated as ± σ_v.

Figure 8.52 and Figure 8.53 show the dimensionless bubble and liquid slug length versus $(U_{GS}+U_{LS})/U_{LS}$ for the water/air system in structure T-3 when the air phase is connected to the side entrance.

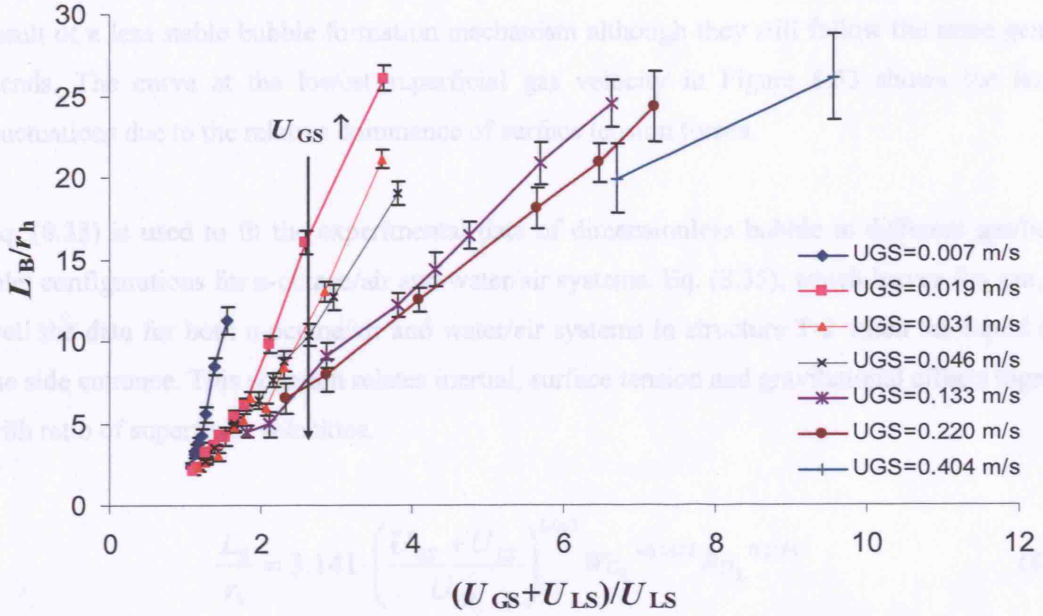

Figure 8.52. Dimensionless bubble length for the water/air system in structure T-3, gas at side entrance. Error bars calculated as ± σ_v.

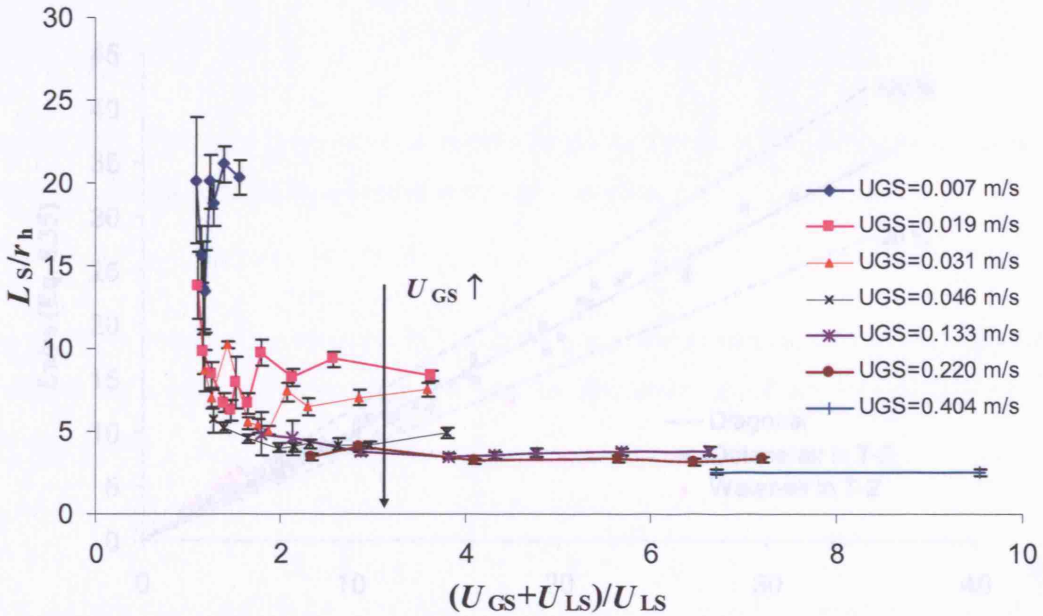

Figure 8.53. Dimensionless liquid slug length for the water/air system in structure T-3, gas at side entrance. Error bars calculated as ± σ_v.

Similarly to the water/air system in the other gas/liquid inlet configurations, the dependence of the dimensionless bubble length to superficial gas velocity is not as important as in the n-octane/air system, above all at low values of $(U_{GS}+U_{LS})/U_{LS}$. Results of dimensionless liquid slug length show large fluctuations compared to those obtained for the n-octane/air system as a result of a less stable bubble formation mechanism although they still follow the same general trends. The curve at the lowest superficial gas velocity in Figure 8.53 shows the largest fluctuations due to the relative dominance of surface tension forces.

Eq. (8.33) is used to fit the experimental data of dimensionless bubble in different gas/liquid inlet configurations for n-octane/air and water/air systems. Eq. (8.35), which leaves Re_L out, fits well the data for both n-octane/air and water/air systems in structure T-2 when the liquid is at the side entrance. This equation relates inertial, surface tension and gravitational effects together with ratio of superficial velocities.

$$\frac{L_B}{r_h} = 3.141 \cdot \left(\frac{U_{GS} + U_{LS}}{U_{LS}} \right)^{1.013} We_L^{-0.1622} Bo_L^{0.1164} \tag{8.35}$$

Figure 8.54 sows the dimensionless bubble length versus the predicted value from Eq. (8.35).

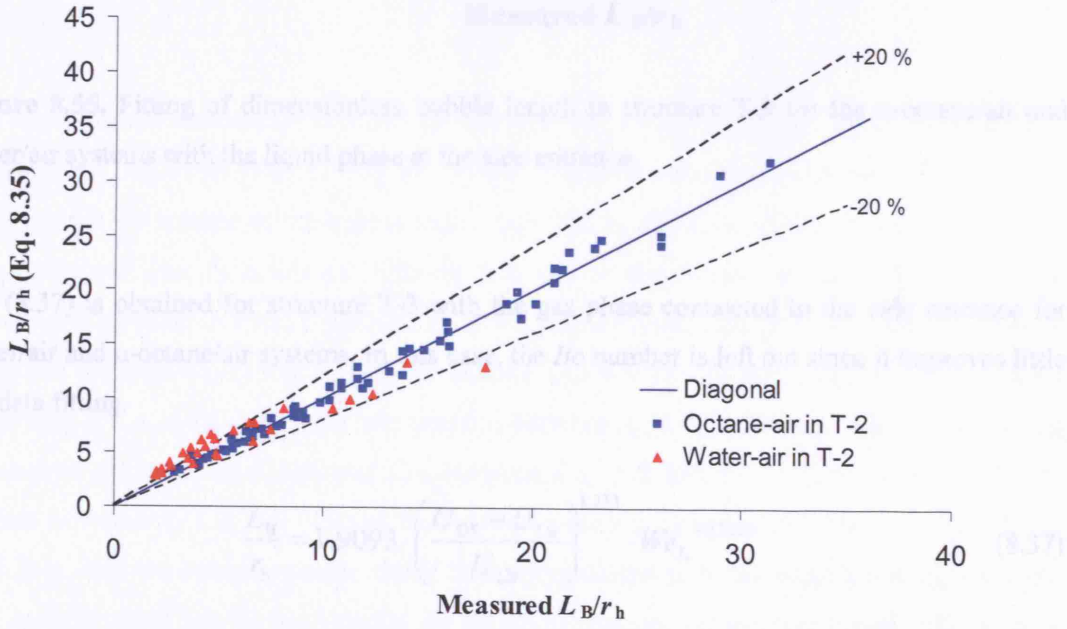

Figure 8.54. Fitting of dimensionless bubble length in structure T-2 for the n-octane/air and water/air systems with the liquid phase at the side entrance.

Eq. (8.36) is obtained for structure T-3 with the liquid phase connected to the side entrance for water/air and n-octane/air systems. Figure 8.55 shows the dimensionless measured bubble length versus the calculated value by Eq. (8.36).

$$\frac{L_B}{r_h} = 6.66 \cdot \left(\frac{U_{GS} + U_{LS}}{U_{LS}} \right)^{1.043} \cdot We_L^{-0.10} \cdot Bo_L^{0.252} \tag{8.36}$$

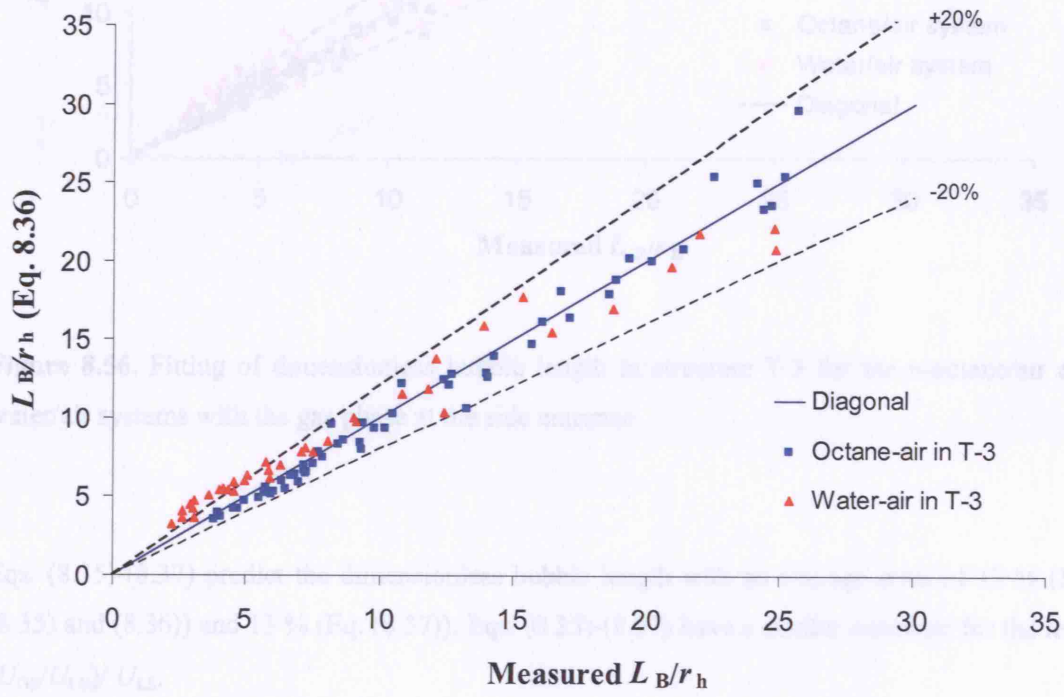

Figure 8.55. Fitting of dimensionless bubble length in structure T-3 for the n-octane/air and water/air systems with the liquid phase at the side entrance.

Eq. (8.37) is obtained for structure T-3 with the gas phase connected to the side entrance for water/air and n-octane/air systems. In this case, the *Bo* number is left out since it improves little the data fitting.

$$\frac{L_B}{r_h} = 1.9093 \cdot \left(\frac{U_{GS} + U_{LS}}{U_{LS}} \right)^{1.133} \cdot We_L^{-0.1666} \tag{8.37}$$

Figure 8.56 shows the dimensionless bubble length versus the value calculated by Eq. (8.37).

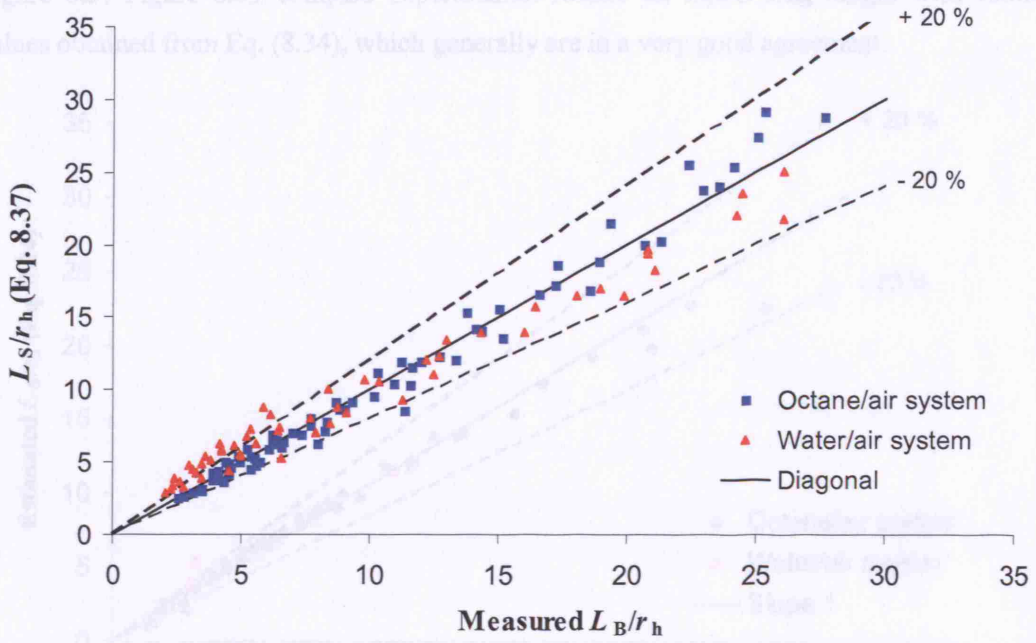

Figure 8.56. Fitting of dimensionless bubble length in structure T-3 for the n-octane/air and water/air systems with the gas phase at the side entrance.

Eqs. (8.35)-(8.37) predict the dimensionless bubble length with an average error of 12 % (Eq. (8.35) and (8.36)) and 13 % (Eq. (8.37)). Eqs. (8.35)-(8.37) have a similar exponent for the term $(U_{GS}/U_{LS})/\ U_{LS}$.

The experimental dimensionless liquid slug length can be fully predicted by Eq. (8.34) initially obtained by Thulasidas et al. (1995) for circular capillaries. In square capillaries this equation assumes that the volume of the bubble caps is equal to $A_B \cdot d_B 2/3$. In square channels, the bubble cross sectional area A_B is always different than that of the channel A due to the fluid at the corners and its value in static conditions is $A_B = 0.9397A$ (Wong, 1992). Kolb and Cerro (1993a) measured the transition to axisymmetric bubbles ($A_B = 0.7854$A assuming $d_B = d$) in square capillaries at $Ca_L = 0.04$. A linear interpolation between $A_B/A = 0.9397$ and $A_B/A = 0.785$ could be used to estimate A_B at different Ca_L between $Ca_L = 0$ and $Ca_L = 0.04$. However, in the present experiments $Ca_L < 0.015$ and the bubble velocity is estimated via Wong's Eq. (8.9) for low Ca so that the bubble cross sectional area is approximated to the static value $A_B = 0.9397$. The calculation of the bubble velocity by Eq. (8.9) requires the average liquid slug velocity, which is considered to be $U_{L,m} = U_{LS}+U_{GS}$.

Figure 8.57-Figure 8.59 compare experimental results on liquid slug length with estimated values obtained from Eq. (8.34), which generally are in a very good agreement.

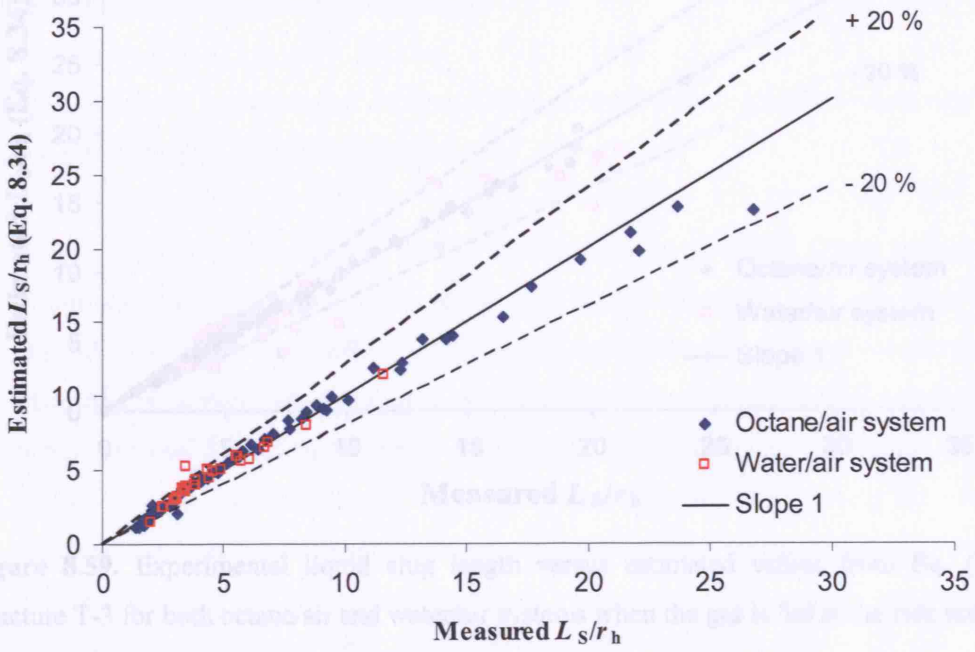

Figure 8.57. Experimental liquid slug length versus estimated values from Eq. (8.34) in structure T-2 for both octane/air and water/air systems.

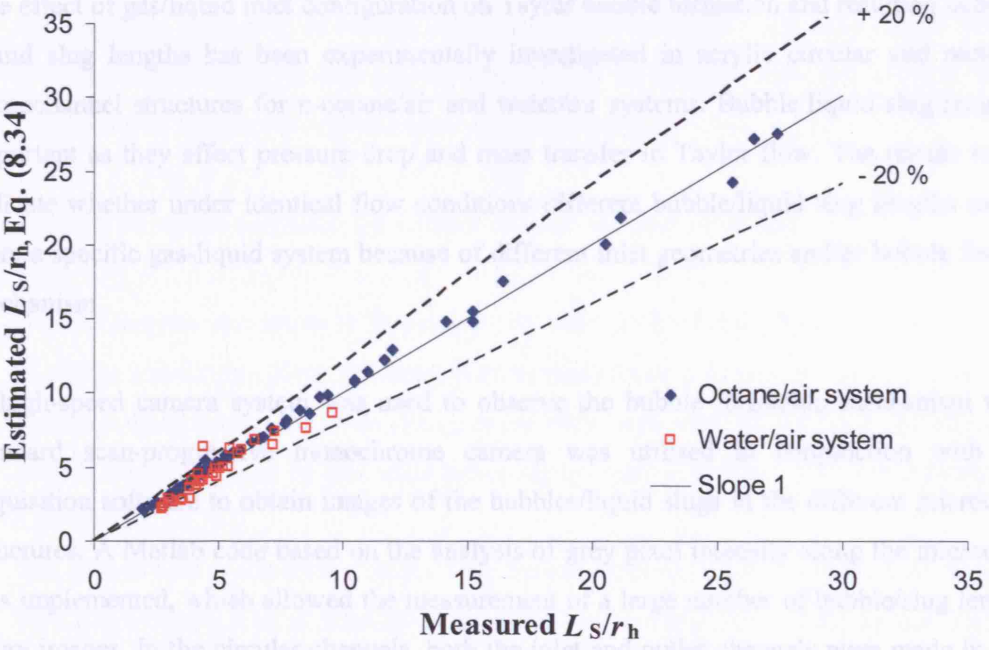

Figure 8.58. Experimental liquid slug length versus estimated values from Eq. (8.34) in structure T-3 for both octane/air and water/air systems when the liquid is fed at the side entrance.

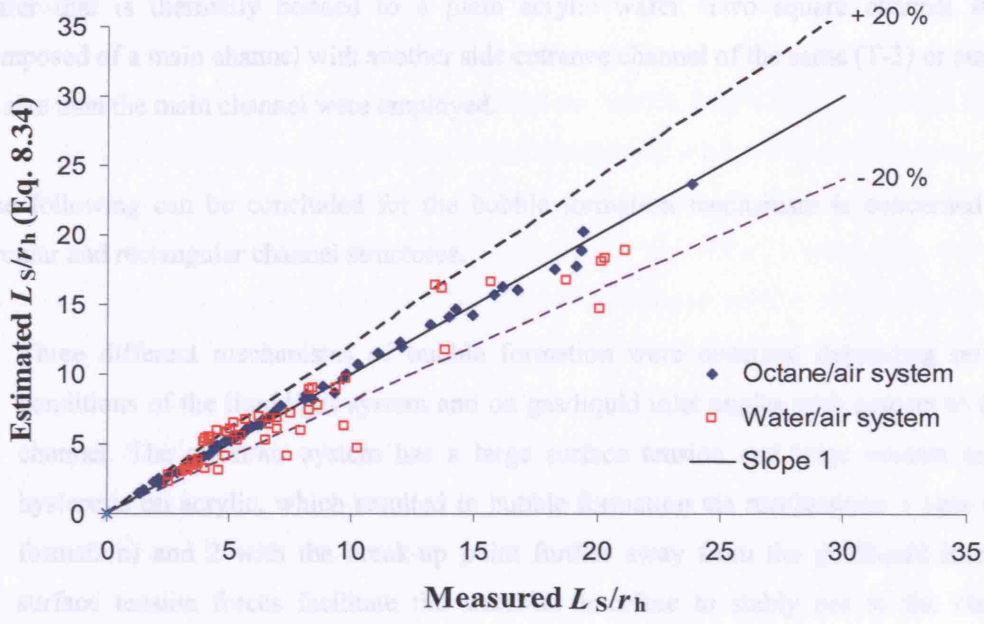

Figure 8.59. Experimental liquid slug length versus estimated values from Eq. (8.34) in structure T-3 for both octane/air and water/air systems when the gas is fed at the side entrance.

8.5. Conclusions

The effect of gas/liquid inlet configuration on Taylor bubble formation and resulting bubble and liquid slug lengths has been experimentally investigated in acrylic circular and rectangular microchannel structures for n-octane/air and water/air systems. Bubble/liquid slug lengths are important as they affect pressure drop and mass transfer in Taylor flow. The results will also indicate whether under identical flow conditions different bubble/liquid slug lengths can form from a specific gas-liquid system because of different inlet geometries and/or bubble formation mechanism.

A high-speed camera system was used to observe the bubble formation mechanism while a standard scan-progressive monochrome camera was utilised in conjunction with image acquisition software to obtain images of the bubbles/liquid slugs in the different microchannel structures. A Matlab code based on the analysis of grey pixel intensity along the microchannel was implemented, which allowed the measurement of a large number of bubble/slug lengths in many images. In the circular channels, both the inlet and outlet channels were made in acrylic pieces at the gas/liquid contacting region by precisely drilling holes in T and Y configurations while glass capillaries were mounted to the outlets of the pieces. In the square channels, both the inlet and the main channels were made in acrylic by micro-milling channels on a rectangular

wafer that is thermally bonded to a plain acrylic wafer. Two square channel structures composed of a main channel with another side entrance channel of the same (T-3) or smaller (T-2) size than the main channel were employed.

The following can be concluded for the bubble formation mechanism is concerned in both circular and rectangular channel structures.

1. Three different mechanisms of bubble formation were observed depending on wetting conditions of the liquid/gas system and on gas/liquid inlet angles with respect to the main channel. The water/air system has a large surface tension and large contact angle and hysteresis on acrylic, which resulted in bubble formation via mechanisms 1 (gas chamber formation) and 2 with the break-up point further away from the gas/liquid inlet. Large surface tension forces facilitate the water/air interface to stably pin to the channel at different locations. The n-octane/air system formed bubbles via mechanisms 2 and 3 with the break-up point just at the gas/liquid inlet. In the majority of cases uniform bubble sizes were produced.
2. Bubble pairing and coalescence were present in some cases and considerably modified the sizes of the already formed bubbles. For cases where coalescence was present, a wide distribution of bubble sizes was obtained.
3. Surface properties can affect the type of mechanism present and when the contact angle of the system is large (e.g. water/air) different contact points in *mechanism 1* just before the break-up region appear which are not reproducible on different runs and result on different bubble/liquid slug sizes under the same flow conditions.

The analysis of bubble lengths in the circular channel structures indicated,

1. Bubble lengths are strongly dependent on the ratio of superficial velocities, $(U_{GS} + U_{LS})/U_{LS}$, and for any given geometry they increase linearly as $(U_{GS} + U_{LS})/U_{LS}$ increases. In most configurations, $(U_{GS} + U_{LS})/U_{LS}$ is the only parameter determining the bubble size. Liquid slug length can be estimated assuming cylindrical bubbles with hemispherical caps applying Eq. (8.16).
2. Gas inlet diameter affects the sizes of the formed bubbles while liquid inlet diameter has a very small effect. This is because gas channel size defines the surface tension forces that have to be overcome for the bubble to detach.
3. There are no main differences on results obtained for n-octane/air and water/air systems as far as bubble length is concerned.

The analysis carried out in the rectangular channel structures indicated,

1. Similar to circular channels, the dimensionless bubble length L_B/r_h increases as $(U_{GS} + U_{LS})/U_{LS}$ increases in an almost linear way for both n-octane and water/air systems.
2. However, the dimensionless bubble length L_B/r_h decreases as U_{GS} increases while $(U_{GS} + U_{LS})/U_{LS}$ is kept constant (gas/liquid inertial effects). This effect is more pronounced in the n-octane/air system than in the water/air system where large surface tension forces are more important determining sizes than inertial forces. This is the main difference with respect to circular channel structures. In circular channels the inertia of the incoming liquid over a forming bubble is greater than that in rectangular channels due to larger liquid velocities in the film surrounding the bubble (corners in square channels increase the area for liquid flow). Wong (1992) indicates that pressure drop across one bubble inside a circular microchannel is 2.8 times smaller than that in a square channel. Thus, circular channels of the analysed size produce similar bubble sizes in both octane/air and water/air systems, which are significantly smaller that those in square channels at low superficial velocities but become comparable as inertial forces in the square channel structure increase (compare results in Figure 8.27 and Figure 8.31 to those in Figure 8.40 or Figure 8.46 for similar values of $(U_{GS} + U_{LS})/U_{LS}$ and U_{GS}).
3. The dimensionless liquid slug length L_S/r_h decreases as $(U_{GS} + U_{LS})/U_{LS}$ increases. For a constant $(U_{GS} + U_{LS})/U_{LS}$ ratio, L_S/r_h decreases as U_{GS} increases similar to bubble lengths in order to maintain the volume fraction. The dimensionless liquid slug length decreases marginally for larger values of gas superficial velocity.
4. In general, the dimensionless bubble and liquid slug lengths of the water/air system are smaller than those for the n-octane/air system.
5. The system water/air shows higher fluctuations in the bubble and liquid slug length results compared to the n-octane/air system. This is because the Taylor flow is less reproducible as a consequence of poor wetting conditions on the acrylic material and large pressure fluctuations during bubble formation (high surface tension).
6. The experimental data on bubble length in both octane/air and water/air systems can be fitted to correlations based on ratio $(U_{GS} + U_{LS})/U_{LS}$, We_L and Bo_L with an average error of 12-13 %.
7. The dimensionless liquid slug length L_S/r_h can accurately be predicted based on theory (Eq. (8.34)) from bubble length data.

In general, it can be said that one of the most important factors determining bubble and liquid slug length, apart from the gas/liquid inlet configuration, is the channel geometry. Behaviour in different channel geometries may be extrapolated from the available area for liquid flow and

compared to results in circular and rectangular channel structures in which the areas for liquid flow around the bubbles can be estimated.

Nomenclature

a	Aspect ratio.
A_B	Cross sectional area of the bubble, m^2.
A	Cross sectional area of the capillary, m^2.
Bo	Bond number, $Bo = (\rho_L-\rho_G)gr_h^2/\gamma$.
Bo_L	Bond number, $Bo = \rho_L gr_h^2/\gamma$.
C_1	Constant in Eq. (8.9).
C_2	Constant in Eq. (8.9).
C_n	Parameter $[(2n+1)\pi]^3$.
Ca	Capillary number based on the bubble velocity U_B.
Ca_L	Capillary number based on the liquid slug average velocity $U_{L,m} \approx U_{LS}+U_{GS}$.
d	Capillary diameter, m.
d_h	Diameter of the largest inscribed circle to the channel, m.
e	Channel depth, m.
E_i	Bessel-function of first kind of order zero
El	Elasticity number.
f	Friction factor
g	Acceleration due to gravity, m/s^2.
J	Sum of the gas and liquid superficial velocity, m/s.
L	Length of the capillary, m.
L_S	Liquid slug length, m.
L_B	Bubble length, m.
n	Index of the summation.
P	Pressure, Pa.
Pe	Peclet number.
$q_{l,f}$	Flow rate of the surrounding film, m^3/s.
Q	Volumetric flowrate, m^3/s.
r	Capillary radius, m.
r_B	Bubble radius, m.
r_h	Radius of the largest inscribed circle to the channel used as characteristic length, m.
r_x	Radial axis coordinate, m.
r^0	Radius of the vortex centre, m.
r^1	Radius of the dividing streamline, m.
$r_{s(A-A)}$	Dimensionless radius of the flat side of the non-axisymmetric bubble.

$r_{s(B-B)}$	Dimensionless radius to the bubble corner of the non-axisymmetric bubble.
r_{Roor}	Dimensionless radius of the bubble corner of the non-axisymmetric bubble.
R_B	Dimensionless bubble diameter.
Re	Reynolds number based on the bubble velocity U_B.
Re_L	Reynolds number based on the liquid slug average velocity $U_{L,m} \approx U_{LS}+U_{GS}$.
St_d	Stanton number.
t	Time, s.
t_m	Mean residence time, s.
U_B	Bubble velocity, m/s.
U_{GS}	Gas superficial velocity, m/s.
U_{LS}	Liquid superficial velocity, m/s.
$U_{L,m}$	Mean liquid slug velocity, which is approximated by ($U_{GS}+U_{LS}$), m/s.
$U_{l,f}$	Velocity of the surrounding film, m/s.
$U_{L,m,rel}$	Mean liquid velocity relative to the bubble velocity, m/s.
w	Width, m.
W	Relative velocity of the bubbles.
We	Weber-number based on the bubble velocity U_B.
We_L	Weber-number based on the liquid slug average velocity $U_{L,m} \approx U_{LS}+U_{GS}$.
x	Axial axis coordinate, m.
y	Lateral axis coordinate, m.
X	Dimensionless axial axis coordinate, m.
Y	Dimensionless lateral axis coordinate.

Greek Letters

α	Parameter.
α_G	Volume fraction of the gas phase.
β	Parameter and bubble to unit length ratio.
γ	Surface tension, N/m.
δ	Film thickness, m.
Δ	Difference
μ	Dynamic viscosity, Pa·s.
ρ	Density, kg/m^3.
σ_v	Standard deviation.
Ψ	Dimensionless bubble velocity.
ω_{LG}	Angle formed by the liquid and gas inlet channels.

ω_{LO}	Angle formed by the liquid and outlet channels.

Subscripts

B	Bubble.
Body	Body of the bubble without accounting for the bubble ends.
C	Cell, which is composed by a bubble and a liquid slug.
G	Gas.
L	Liquid.
m	mean.
max	maximum.
rel	Relative to the bubble velocity.
S	Slug.

Superscripts

#	Dimensionless variable.

Chapter 9

Pressure Drop and Fluctuations during Taylor Flow in Square Capillaries: Manifold Flow Distribution

"There are two possible outcomes: If the result confirms the hypothesis, then you've made a measurement. If the result is contrary to the hypothesis, then you've made a discovery."

Enrico Fermi

9.1. Introduction

Pressure drop and fluctuations are key factors to understand flow distribution of gas and liquid phases in a flow manifold. A similar analysis to that carried out in Chapter 7 for single phase flow distribution is applied to a 2-channel manifold for Taylor flow taking into account that a) pressure drop in Taylor flow is different from that of single-phase flow and dependent not only on gas/liquid superficial velocities but bubble and liquid slug lengths and b) pressure fluctuations occur during bubble formation in both the liquid phase (the bubble constrains the liquid passage) and the gas phase (pressure difference to overcome surface tension forces to form a bubble). The model is used to calculate the required external resistances to be placed in the gas and liquid distributing channels in order to avoid backflow or channel "cross-talk" and ensure equal flow distribution in each channel of the manifold.

9.2. Background

Flow distribution of two-phase flows in parallel microchanels is influenced by several phenomena: location of the gas phase introduction point either before the liquid distributing channel or after it (in each branch of the manifold), pressure drop of gas and liquid single-phase flows in the distributing channels, pressure drop of Taylor flow in the parallel manifold channels and pressure fluctuations during bubble formation and exiting.

9.2.1. Gas/Liquid Flow Distribution and Location of Gas Phase Injection

There has been very limited research carried out on gas and liquid flow distribution in manifolds in small/micro channels. Most of this work is related to distribution of already formed gas/liquid dispersions (Stark and Manga, 2000; Matsui et al. 2003) or to boiling phenomena where bubbles are generated at nucleating sites in the parallel microchanels filled with the liquid, causing large pressure drop fluctuations (Zhang et al., 2002; Qu and Mudawar, 2003; Hetsroni et al., 2005; Mukherjee and Kandlikar, 2005; Kandlikar et al., 2005).

Matsui et al (2003) investigated flow distribution of nitrogen-water isothermal mixtures in a consecutive manifold of five 6-mm width parallel channels and a 10-mm width distributing channel for different channel cross section heights that range between 0.2-2 mm. The results show liquid and gas maldistribution under all conditions since the distributing channel is only 1.67 times larger than the branches. As the channel cross section height reduces to 0.2 mm, frictional losses become more important resulting in decreasing liquid flowrates from the first to the fifth branch. As channel cross section height increases, inertial forces become substantial and the largest liquid flowrate is found at the last branch. These findings agree well with results obtained with the resistance network model for single-phase flow in the consecutive structure presented in Chapter 7. In general the flow distribution of the gas phase follows an opposite trend to that of the liquid phase and improves at large gas flowrates. Stark and Manga (2000) studied the motion of long bubbles in a network of tubes using a resistance network model to simulate porous media as a function of *Ca* number and bubble volume fraction. Bubble presence increases the resistance to flow and residence time distribution of the bubbles to go through the network increases as the gas volume fraction increases. Their results indicate that at low volume fractions most of the bubbles follow a limited number of high-flow pathways in the network.

In manifold microstructures where boiling is carried out, single-phase flow is distributed among the parallel channel where the gas phase is generated. The random generation of bubbles in time and space gives rise to different pressure fluctuations and pressure drop in each of the parallel channels that leads to maldistribution of the single-phase fluid and even reverse flow (Mukherjee and Kandlikar, 2005; Qu and Mudawar, 2003). Kandlikar et al. (2005) has experimentally analysed the use of channel constrictions to generate extra pressure drop in the liquid phase at the liquid inlets together with fabricated nucleation sites to stabilize and balance the gas/liquid flowrates in all branches.

There is scarce research on generation and distribution of two-phase Taylor/bubble flow where bubbles are formed at the inlet of each parallel channel. Institut für Mikrotechnik (IMM) has developed the micro bubble column (MBC), which consists of multiple parallel channels where liquid and gas are mixed. Jähnisch et al. (2000) investigated the performance of the micro bubble column for direct fluorination of toluene using elemental fluorine. Liquid and gas are distributed separately and the distributing channels are of considerable smaller diameter than the main reaction channels. Gas is injected into the liquid parallel microchannels via a small orifice. Pictures of the MBC show non-uniform Taylor flow within the parallel channels while even simultaneous Taylor and annular flow in different parallel channels was reported under certain flow conditions. Losey et al. (2002) use a similar approach to distribute gas and liquid phases into 10 parallel reaction channels that contain 50-μm microstructured silicon supports to improve gas/liquid contact. Flow pictures at relatively high gas flowrates show uneven distribution of the phases with large difference in bubble size across the parallel channels. They comment on the need to overcome surface tension forces to generate fluid flow in microchannels but there is no reference to the effect of surface tension forces on gas/liquid flow distribution.

De Mas et al. (2003; 2005) specifically address the issue of gas and liquid flow distribution in a microfabricated multiphase reactor for direct flourination reactions. The microreactor consists of either two or three stacked reaction layers, each of which has 20 parallel reaction microchannels of triangular cross section. Gas and liquid are introduced from separate inlet ports and flows out of the device via a single outlet port. They are able to operate the microreactor under even gas and liquid distribution among the parallel channels in each wafer and among the wafers by having gas and liquid distributing channels that generate a large pressure drop with respect to the pressure drop in the main reaction channel (25 and 50 times in the liquid and gas distributors respectively). The large pressure drop in the distributing channels effected by cross section reduction, prevents "cross-talk" between reaction channels. Uniform flow regime is observed and comparable slug frequencies and velocities, measured via wave-guided optical multiphase sensors, are obtained. However, no systematic analysis is presented, on the relation of required pressure drop with gas/liquid flowrates and pressure fluctuations due to surface tension during bubble formation. De Mas et al. apply a resistance network model for the distribution of the single phases based on frictional losses similar to that presented in Chapter 7. Since the model does not introduce pressure fluctuations due to bubble formation it does not predict the required external resistances to avoid gas or liquid reverse flow in some of the parallel channels. For design, they suggest gas and liquid distributing channels that generate a pressure drop at least one order of magnitude larger than that in the reaction channels.

9.2.2. Pressure Drop in Taylor Flow

Standard models used to predict pressure drop in two-phase flows in pipes (Friedel, 1978) generally do not agree well with experimental results in capillaries (Triplett et al., 1999b). A reason is that the contribution of surface tension forces to pressure drop becomes substantial in small capillaries, specifically at the front and back of the bubbles (Bretherton, 1961). Grolman (1996) developed a pressure drop model for monolith reactors considering hydrostatic and viscous pressure drop inside the liquid slug but neglected the effect of capillary forces (front and back of bubbles). The model included an empirical term proportional to the velocity of the bubbles, which they relate to entrance/exit effects. Woehl and Cerro (2001) developed a pressure drop model for Taylor flow that considers the pressure drop at the back and front of the bubbles due to surface tension in addition to hydrostatic and viscous contributions in the liquid slug (inertial effects are neglected). They estimate the pressure drop due to the difference in shape between the front and back ends of the bubbles by applying Bretherton's results from a circular capillary in the limit of $Ca \rightarrow 0$. Equations of the model are not given in their work.

Bretherton (1961) obtained the pressure drop along a single bubble in a circular capillary in the limit $Ca \rightarrow 0$ by applying lubrication theory and a matched asymptotic expansion method,

$$P_{\text{Back}} - P_{\text{front}} = 9.40 Ca^{2/3} \left(\frac{\gamma}{r_h} \right) \tag{9.1}$$

Wong (1992) applied a different method based on the existence of a contact-line drag that arises from the motion of the bubble contact line and obtained expressions for the pressure drop along a bubble in different microchannel geometries when $Ca \rightarrow 0$. An integral force balance was applied to determine the pressure drop along the bubble that balances the drag force, which originates predominantly at the thin film around the bubble ends (not affected by capillary corners). In the case of a square channel the pressure drop along a bubble is,

$$\begin{aligned} P_{\text{Back}} - P_{Front} &= 3.553 Ca^{2/3} \left(\frac{\gamma}{r_h} \right) \qquad L_B << Ca^{-1} \\ P_{\text{Back}} - P_{Front} &= 3.559 Ca^{2/3} \left(\frac{\gamma}{r_h} \right) \qquad L_B = Ca^{-1} \end{aligned} \tag{9.2}$$

$$P_{\text{Back}} - P_{Front} = 5.380Ca^{2/3}\left(\frac{\gamma}{r_h}\right) \qquad L_B = Ca^{-5/3}$$

Eq. (9.2) indicates that pressure drop in Taylor flow in square capillaries is expected to be smaller than that in circular capillaries contrary to the results obtained by Ratulowski and Chang (1989) who predicted higher pressure drop over a bubble inside a square tube than inside a circular channel with the same hydraulic diameter. Hazel and Heil (2002) applied a finite element method to calculate the pressure drop along the front of a bubble in a rectangular channel for $Re << 1$ and any Ca. They found that Eq. (9.2) predicts pressure drop accurately at low $Ca < 10^{-3}$ but under predict the pressure drop at higher Ca (at $Ca = 0.01$ the error is 5 %), contrary to the analysis in circular channels at Ca, where pressure drop along a bubble is over predicted at large Ca. According to Wong (1992), the reduced contact between bubble and capillary wall in polygonal capillaries compared to circular capillaries reduces the drag force and therefore reduces the pressure drop across the bubble tip.

Frictional and hydrostatic pressure drop during Taylor flow occurs in the liquid slug as a result of viscous forces as a consequence of wall friction (no slip). In laminar flow conditions ($2Re_L << 2300$), frictional pressure losses ΔP_L can be calculated by means of a modified Hagen-Poiseuille equation for any channel geometry (Commenge et al., 2002).

$$\Delta P_L = \frac{L\beta_L 32\mu U_{L,m}}{d_{hyd}^2}\lambda_{NC} \pm \rho_L gL\sin\varphi = f\beta_L \frac{L}{d_{hyd}}\frac{1}{2}\rho_L U_{L,m}^2 \pm \rho_L gL\sin\varphi \qquad (9.3)$$

where L is the capillary length, β_L is the fraction of liquid slug length given by Eq. (9.4), μ is the dynamic viscosity of the fluid, $U_{L,m}$ is the mean velocity in the liquid slug ($U_{L,m} \approx U_{LS}+U_{GS}$), d_{hyd} is the hydraulic diameter of the capillary, ρ_L is the liquid density, g is the acceleration due to gravity, φ is the inclination angle with respect to the horizontal, λ_{NC} is the non-circularity factor and f is the friction factor. β_L is not included in the gravity term if a thin liquid film surrounding the bubbles is considered. The friction factor f is given by Eq. (9.5) (Re_L is defined using the radius of an inscribed circle to the channel, r_h).

$$\beta_L = \frac{L_S}{L_S + L_B} \qquad (9.4)$$

$$f = \frac{1}{d^{\#}_{hyd}} \frac{64}{Re_L} \lambda_{NC} \tag{9.5}$$

The non-circularity factor λ_{NC} for rectangular channels is given by Eq. (7.7). In the case of square channels, used in the present chapter, the hydraulic diameter is equal to $2r_h$ and $d^{\#}_{hyd} = d_{hyd}/r_h = 2$, $\lambda_{NC} = 0.890$ and $f = 56.96/(2Re_L)$.

Stark and Manga (2000) simulated the motion of long bubbles in a network of circular cross section tubes, calculating the volumetric flowrate via Eq. (9.6), which considers frictional losses and the pressure drop due to the bubble presence (ΔP_B),

$$Q = \frac{\pi r_h^{\,2}}{8 \mu_L \beta_L L} \left[\Delta P - \sum_{N_B} \Delta P_B(Q) \right] \tag{9.6}$$

where ΔP is the total pressure drop (external pressure difference required) and N_B is the number of bubbles in the tube length L. They calculated ΔP_B from Bretherton (1961). Kreuzter (2003) analysed pressure drop during Taylor flow in circular channels for three different systems, water/air, decane/air and tetradecane/air. He fitted experimental data to an equation similar to Eq. (9.3) with $\varphi = 0$, where the friction factor f accounted for frictional and capillary pressure drop. By plotting fRe_L, versus the dimensionless slug length, $L^{\#}_S$, Kreutzer (2003) concluded that for each system the friction factor is only a function of slug length and there is no effect of the mean liquid velocity. The variation of f with system properties was modelled by using the ratio Re_L/Ca_L, which is independent of mean liquid velocity $U_{L,m}$ (see Eq. (9.8)). The component of the friction factor f due to the bubbles is expressed by Eq. (9.7) with two adjustable parameters fitted to $a = 0.43$ and $b = 0.33$.

$$\xi = a \left(\frac{1}{L^{\#}_S} \left(\frac{Re_L}{Ca_L} \right)^b \right) \tag{9.7}$$

$$f = \frac{64}{2Re_L} \left[1 + 0.17 \frac{2}{L^{\#}_S} \left(\frac{2Re_L}{Ca_L} \right)^{0.33} \right] = \frac{64}{2Re_L} \left[1 + 0.43 \frac{1}{L^{\#}_S} \left(\frac{Re_L}{Ca_L} \right)^{0.33} \right] \tag{9.8}$$

Combination of Eq. (9.3) and Eq. (9.8) for circular channels results in an equation that clearly shows the contribution of the number of bubbles to the total pressure drop,

$$\Delta P = \underbrace{\left(\frac{64}{2Re_L}\right)\beta_L \frac{L}{d_{hyd}}\frac{1}{2}\rho_L U_{L,m}^2}_{\text{Frictional } \Delta P} + \underbrace{N_B}_{\text{N° Bubbles}}\underbrace{\left(0.43\frac{64}{2Re_L}\left(\frac{Re_L}{Ca_L}\right)^{0.33}\right)\frac{1}{d_{hyd}}\frac{1}{2}\rho_L U_{L,m}^2}_{\Delta P \text{ per bubble}} \quad (9.9)$$

Experimental pressure drop was substantially larger than that predicted via computational fluid dynamics, which fitted better the experimental results when $a = 0.16$ and $b = 0.33$. This increase in pressure drop was attributed to Marangoni effects. A similar expression to estimate pressure drop in square capillaries has not been tested yet. In order to obtain the value of the adjustable parameters, the overall friction factor f is measured experimentally from Eq. (9.10),

$$f_{exp} = \frac{\Delta P - \rho_L g L \sin\varphi}{\beta_L \frac{L}{d_{hyd}}\frac{1}{2}\rho_L U_{L,m}^2} \quad (9.10)$$

9.2.3. Pressure Fluctuations in Taylor Flow

Pressure fluctuations during bubble formation in Taylor flow can be caused by a) pressure drop variation due to void fraction variation within a channel, especially in short channels containing few bubbles and b) pressure fluctuations during bubble formation at the inlet, which also translate into pressure drop variations that result in oscillating bubble and liquid average velocities. These pressure drop fluctuations along the parallel channels in a manifold can be of different magnitude depending on gas/liquid flowrates, number of bubbles and gas channel diameter. Furthermore, they take place at different times in the different parallel channels influencing gas/liquid flow distribution, which leads to different flow patterns and even reverse flow (Kandlikar et al., 2005). As the diameter of the gas channel decreases, pressure fluctuations due to bubble formation become more substantial, while those due to void fraction variation remain constant.

Most of the available work that analyses pressure fluctuations in microchannels has been carried out for boiling where pressure fluctuations are a consequence of vapour generation within the microchannels. Qu and Mudawar (2002) distinguish two different types of dynamics instabilities in a microchannel manifold used for boiling, namely, pressure drop oscillation caused by an oscillation of the boiling boundary between inlet and outlet and parallel channel instability. They measured pressure fluctuations between the distributing and collecting channels but not in each parallel microchannel and found that the first pressure

instability is substantially more important that the latter and introduces large pressure and temperature fluctuations.

However, no systematic analysis on pressure fluctuations during Taylor bubble formation has been carried out that relates magnitude of the pressure fluctuations with surface tension forces, channel diameters and gas/liquid superficial velocities. The maximum pressure difference during bubble formation is generally approximated to $\Delta P = 4\gamma/d$ (Di Marco et al., 2003; Rayner and Trägårdh, 2002). The analysis carried out in Chapter 5 on breakthrough pressure of gas into liquid separated by a pore under flow conditions indicated that this breakthrough pressure decreases with an increase of the liquid flowrate. This is the result of an intrinsic pressure reduction over the bubble surface, which is not measured further away from the bubble formation point (not detected using a probe in the liquid phase). A similar effect is expected here, resulting in smaller breakthrough pressure and therefore pressure fluctuation in the gas phase as liquid flowrate increases.

In order to estimate the pressure fluctuation in the gas phase, the minimum pressure difference across the interface after a bubble is formed also needs to be estimated. If a spherical meniscus is assumed during the bubble formation and the apparent contact angle of the meniscus after a bubble is formed is $\theta_{Initial}$ (capillary pressure of $\Delta P_{initial}$), Eq. (9.11) can be used to estimate the pressure fluctuation. Under static conditions $\cos\theta_{Breakthrough} = \max[\cos(\theta_R - 90°), \cos 0°]$ and as a first approximation $\cos\theta_{Initial} \approx \cos 90° = 0$ obtaining Eq. (9.12).

$$\Delta P_{Fl} = \Delta P_{B,G} - \Delta P_{Initial} = \gamma f_{Laplace} \frac{\cos\theta_{Breakthrough} - \cos\theta_{initial}}{r_h} \tag{9.11}$$

$$\Delta P_{Fl} = \Delta P_{B,G} - \Delta P_{Flat} = \gamma f_{Laplace} \frac{\max[\cos(\theta_R - 90°), \cos 0]}{r_h} \tag{9.12}$$

where $f_{Laplace}$ = 2 for circular channels but is contact angle dependent and of smaller magnitude in polygonal channels (see Chapter 3).

Pressure fluctuations in the liquid channels have two components: a) pressure fluctuations in the gas phase during bubble formation due to surface tension forces that need to be overcome, which are translated into pressure drop fluctuations in the liquid phase and b) additional pressure drop in the liquid phase due to partial channel blockage as the forming bubble grows.

9.3. Taylor Flow Distribution in a 2-channel Manifold: Resistance Network Model

A 2-channel manifold as that shown in Figure 9.1 is considered for the analysis of the effect of pressure fluctuations on the gas and liquid flow distribution. Pressure fluctuations in the gas and liquid inlets are the result of overcoming surface tension forces during bubble formation. The channel diameter where bubbles form (gas or liquid channel depending on bubble formation mechanism), system properties and flow conditions determine the amplitude of the pressure fluctuations. Thus, the use of small channels at the gas/liquid inlet results in large pressure fluctuations that are more likely to unbalance the liquid and gas flow in a manifold.

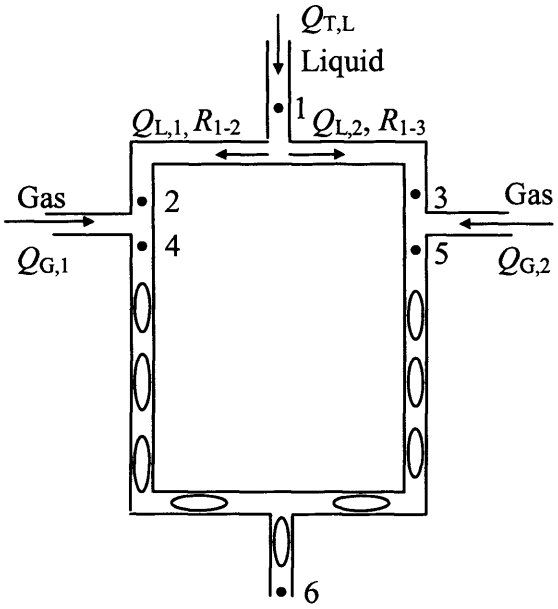

Figure 9.1. Diagram of a two channel structure for Taylor flow.

Neglecting pressure drop due to inertial effects at bends and bifurcations/junctions, a pressure balance to the close loop shown in Figure 9.1 results in Eq. (9.13).

$$\Delta P_{1-2} + \Delta P_{2-4} + \Delta P_{4-6} = \Delta P_{1-3} + \Delta P_{3-5} + \Delta P_{5-6} \tag{9.13}$$

In this case, pressure drop between points 2 and 4 and between 3 and 5 is only due to the process of bubble formation that produces temporary pressure fluctuations. The situation at a specific time is considered. The most severe case for flow distribution corresponds to the situation when the pressure drop between points 2 and 4 is equal to the magnitude of the

pressure fluctuations due to surface tension forces $\Delta P_{2\text{-}4} = \Delta P_{FI}$ (peak of pressure fluctuation in first channel) and pressure drop between 3 and 5 is minimum $\Delta P_{3\text{-}5} = 0$ (valley of pressure fluctuation in second channel). Thus, Eq. (9.13) is reduced to Eq. (9.14). These pressure fluctuations introduce gas and liquid fluctuating flow distributions although the average liquid and gas distributions are not affected provided that no back flow occurs (cross-talk between channels). The real situation is different since small channel tolerances have a substantial impact on pressure fluctuations due to surface tension forces and bubble formation (bubble formation mechanism, bubble frequency, bubble and liquid lengths) may vary among the parallel channels.

$$\Delta P_{1-2} + \Delta P_{FI} + \Delta P_{4-6} = \Delta P_{1-3} + \Delta P_{5-6} \tag{9.14}$$

9.3.1. A Simple Model for Conservative Design of Multiphase Manifolds

The magnitude of the pressure fluctuations ΔP_{FI} depends on surface tension, channel geometry and flow conditions as shown in the Results section although the maximum average value is used for design purposes. Single phase pressure drops $\Delta P_{1\text{-}2}$ and $\Delta P_{1\text{-}3}$ depend on liquid flowrate and channel geometry while pressure drops $\Delta P_{4\text{-}6}$ and $\Delta P_{5\text{-}6}$ depend on gas flowrate and gas and liquid slug lengths in addition to channel geometry and liquid flowrate. If the manifold is designed for even flow distribution, $\Delta P_{4\text{-}6} \approx \Delta P_{5\text{-}6}$, obtaining,

$$\Delta P_{1-2} - \Delta P_{1-3} = -\Delta P_{FI} \tag{9.15}$$

In this case, uniform gas distribution is considered to avoid coupling of both phases although a similar approach can be applied to the design of the gas inlet channels to produce even flow distribution. Considering that the pressure drop across a single channel is $\Delta P = RQ$ (see Chapter 7), $Q_{T,L} = 2Q_{EQ,L} = Q_{L,1}+Q_{L,2}$ and resistances $R_{1\text{-}2}$ and $R_{1\text{-}3}$ are identical, Eq. (9.15) results in Eq. (9.17). The total liquid flowrate $Q_{T,L}$ is assumed to be constant independently of the pressure fluctuations. $Q_{EQ,L}$ is the equipartition flowrate for the liquid phase.

$$R_{1-2}Q_{L,1} - R_{1-3}Q_{L,2} = -\Delta P_{FI} \tag{9.16}$$

$$\frac{Q_{L,1}}{Q_{EQ,L}} = 1 - \frac{\Delta P_{Fl}}{Q_{T,L} R_{1-2}}$$

$$R_{1-2} = \frac{\Delta P_{Fl}}{Q_{T,L}\left(1 - \frac{Q_{L,1}}{Q_{EQ,L}}\right)} \tag{9.17}$$

Eq. (9.17) can be used to estimate the external resistance, R_{1-2} required to achieve a flowrate $Q_{L,1}$ that fluctuates within a given percentage of the equipartition flowrate for a total flowrate $Q_{T,L}$. The required resistance R_{1-2} to achieve certain $Q_{L,1}/Q_{EQ,L}$ increases as $Q_{T,L}$ decreases and $Q_{L,1}/Q_{EQ,L}$ approaches 1 (equidistribution). The required resistance R_{1-2} to avoid backflow from channel 1 into channel 2 as a result of pressure fluctuations due to bubble formation is obtained when $Q_{L,1}/Q_{EQ,L} = 0$. The required channel length L_{1-2} and/or channel width/depth is then obtained from the definition of R_{1-2},

$$R_{1-2} = \frac{32 \mu L_{1-2} \lambda_{NC}}{d_{hyd,1-2}^{\ 2} A} \tag{9.18}$$

where λ_{NC} is the non-circularity coefficient given by Eq. (7.7). Considering even gas flow distribution, this is likely to be a conservative calculation since as $Q_{L,1}$ becomes significantly smaller than $Q_{L,2}$, the Taylor pressure drop in channel 1 is likely to be smaller than that in channel 2 ($\Delta P_{4-6} < \Delta P_{5-6}$, see Figure 9.7 and Figure 9.8). Thus, $Q_{L,1}$ must increase in order to balance pressure drop in both branches and the system is stabilised again. Flow distribution issues are more important at low flowrates when ΔP_{Fl} is the largest and $\Delta P_{Fl} >> \Delta P_{4-6}$, $\Delta P_{Fl} >> \Delta P_{5-6}$.

9.3.2. Consideration of Taylor Pressure Drop in Model

A more accurate model can be obtained by considering that $\Delta P_{4-6} \neq \Delta P_{5-6}$ and applying Eq. (9.14) where $\Delta P_{4-6} = R_{4-6} Q_{L,1}$ and $\Delta P_{5-6} = R_{5-6} Q_{L,2}$ (resistances still are a function of liquid and gas flowrates although the liquid flowrates are used to define the resistances) to obtain Eq. (9.19a). This equation is used to calculate the required resistance $R_{1-2} = R_{1-3}$ for a given flowrate ratio $Q_{L,1}/Q_{EQ,L}$ ($Q_{L,1}/Q_{EQ,L} = 0$ to calculate R_{1-2} to avoid reverse flow) according to Eq. (9.19b).

$$\frac{Q_{L,1}}{Q_{EQ}} = \frac{2R_{1-2} + 2R_{5-6} - \Delta P_{Fl}/Q_{EQ,L}}{2R_{1-2} + R_{4-6} + R_{5-6}} \tag{9.19a}$$

$$R_{1-2} = \frac{Q_{L,1}/Q_{EQ,L}\left(R_{4-6}+R_{5-6}\right)+\Delta P_{FI}/Q_{EQ,L}-2R_{5-6}}{2\left(1-Q_{L,1}/Q_{EQ,L}\right)} \tag{9.19b}$$

Resistances $R_{4-6} = \Delta P_{4-6}/Q_{L,1}$ and $R_{5-6} = \Delta P_{5-6}/Q_{L,2}$ are a function of liquid and gas flowrates apart from channel geometry. The values of ΔP_{4-6} and ΔP_{5-6} for square channels can be calculated via Eq. (9.28) (see below) as a function of gas and liquid flowrates obtained via Eq. (9.19a). In the present case, the gas phase is assumed to flow evenly among all channels ($Q_{G,1} = Q_{G,2} = Q_{EQ,G}$) although an equation similar to Eqs. (9.19a) and (9.19b) can be applied for the gas phase. Therefore, this model can be applied in two different ways,

1. For certain variation $Q_{L,1}/Q_{EQ,L}$ at the fluctuation peak, the required distribution channel size can be directly obtained from Eq. (9.19b) (resistance R_{1-2}).
2. For a manifold geometry, $Q_{L,1}/Q_{EQ,L}$ is calculated from Eq. (9.19a) (iterative procedure).

However, the necessary values of the bubble and liquid slug lengths L_B and L_S obtained via Eqs. (8.37)-(8.39) and (8.36) and applied in Eq. (9.28) to calculate ΔP_{4-6} and ΔP_{5-6} require the use of the average liquid and gas flowrates instead of the peak values obtained via Eq. (9.19a). The resistance network models presented in Chapter 7 can be utilised to obtain these average gas and liquid flowrates. Calculation of $Q_{L,1}/Q_{EQ,L}$ for a specific system requires an iterative process while the required R_{1-2} is directly obtained for a given $Q_{L,1}/Q_{EQ,L}$ from Eq. (9.19b).

This same model can be applied to design the required resistances in the gas inlet channels to avoid backflow of the gas phase. Furthermore, gas and liquid distribution can be easily coupled solving gas and liquid peak flowrates via an iterative procedure, which can be implemented for any number of parallel channels.

9.4. Experimental Work

Experimental work to measure pressure drop and pressure fluctuations in Taylor flow and visualise gas/liquid flow distribution in a 2-channel structure has been carried out.

9.4.1. Microstructures

Structure T-3 shown in Figure 9.2 is used to measure pressure drop in Taylor flow and pressure fluctuations during bubble formation. The structure features square cross section channels of

identical dimensions ($e = w = 650$ µm) and consists of an acrylic wafer on which channels are milled, thermally bonded to another acrylic wafer.

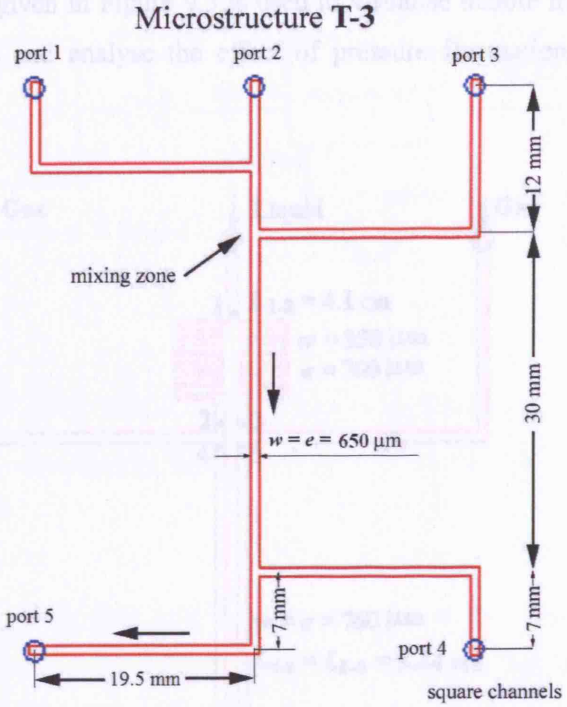

Figure 9.2. Drawing of microstructure "T-3".

There are five ports integrated in the microstructure. These ports are used differently depending on the type of measurement carried out as shown in Table 9.1.

N°	Measurement	Port 1	Port 2	Port 3	Port 4	Port 5
1	ΔP between port 3 and 5	Gas inlet	Liquid inlet	Pressure measurement port	Blocked	Outlet
2	ΔP between port 3 and 4	Gas inlet	Liquid inlet	Pressure measurement port	Pressure Port	Outlet
3	Pressure fluctuations in liquid inlet	Pressure port	Liquid inlet	Gas inlet	Blocked	Outlet
4	Pressure fluctuations in Gas inlet*	Blocked	Liquid inlet	Gas inlet	Blocked	Outlet

* A micro-tee junction in the gas tube outside the wafer is used as the pressure measurement port.

Table 9.1. Port connections for pressure drop and pressure fluctuations measurements in microstructure T-3.

The pressure fluctuations in the gas inlet are measured via a micro-tee junction in the gas tube, connected between the micrometering valve and the gas inlet port in the microstructure (port 3).

The 2-channel manifold given in Figure 9.3 is used to visualise bubble frequency and velocity in two parallel channels and analyse the effect of pressure fluctuations on gas/liquid flow distribution.

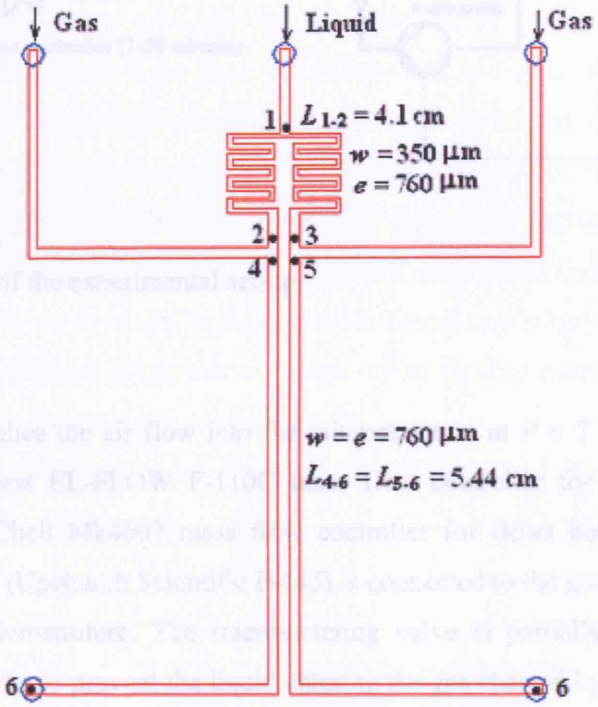

Figure 9.3. 2-channel manifold to analyse gas/liquid flow distribution during Taylor flow.

Both acrylic structures are fitted into an aluminium case represented in Figure 8.16. The inlet and outlet PEEK™ tubing is connected to the acrylic structure via Upchurch Scientific pressure threaded ports (1/4“ 28), which have a ferrule type seal (model P-200) and take tubes of 1/16“ outer diameter.

9.4.2. Experimental Set-Up

The two systems analysed are water/air and n-octane/air. Properties of the liquid phases at 25 °C are given in Table 8.2. Figure 9.4 shows the experimental set-up.

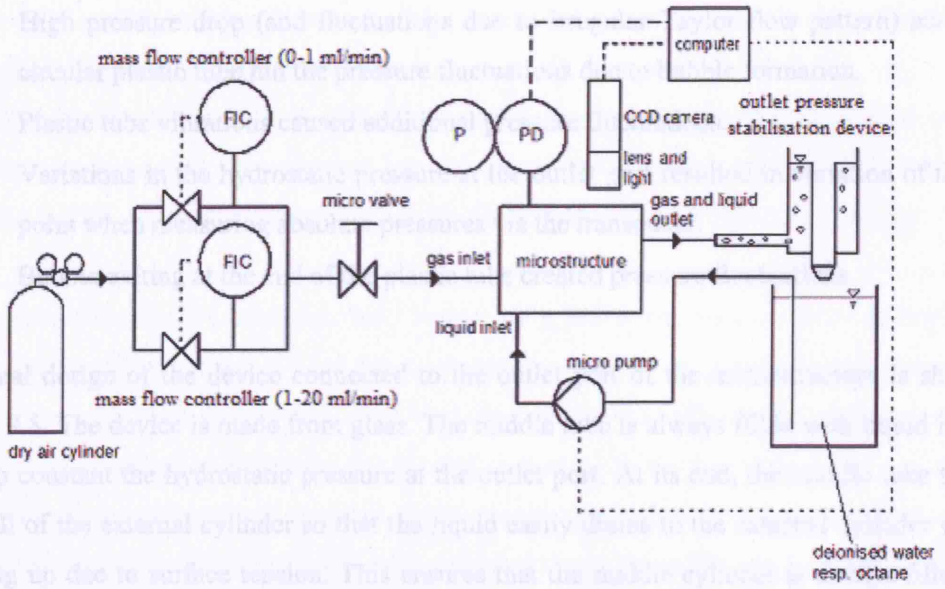

Figure 9.4. Scheme of the experimental set-up.

An air cylinder supplies the air flow into the microstructure at P = 7 bar via two mass flow controllers, Bronkhorst EL-FLOW F-110C mass flow controller for flows between 0.01-1 ml/min gas and a Chell Mk4607 mass flow controller for flows between 1-20 ml/min. A micrometering valve (Upchurch Scientific P-445) is connected to the gas tubing close to the gas inlet port of the microstruture. The micrometering valve is partially closed and generates sufficient pressure drop to prevent the liquid entering the gas channel by compression (only the gas between the valve and the junction inlet port is compressed). Since the gas volume between the micrometering valve and the gas inlet port is very small, pressure fluctuations during bubble formation do not result on the liquid phase entering the gas channel.

The liquid phase, either water or n-octane, is fed to the microstructure by a 4-piston MilliGat pump (0-6 ml/min), operated via a computer. The gas/liquid mixture is collected in a beaker, which in the case of the n-octane is also the reservoir (closed loop). It was observed that the design of the outlet tubing influenced greatly the quality of the results in relation to measurement of pressure fluctuations and pressure drop. Initially, a long plastic tube was connected at the channel outlet and transferred the mixture at the bottom of a beaker. This resulted in poor and noisy pressure signals because:

- The temporary change of the liquid level in the beaker modified the hydrostatic pressure at the outlet port. This could be avoided by controlling the liquid level in the beaker.
- Poor liquid wetting in the plastic tube and observed bubble coalescence.

- High pressure drop (and fluctuations due to irregular Taylor flow pattern) across the circular plastic tube hid the pressure fluctuations due to bubble formation.
- Plastic tube vibrations caused additional pressure fluctuations.
- Variations in the hydrostatic pressure at the outlet port resulted in variation of the zero point when measuring absolute pressures via the transducer.
- Bubble exiting at the end of the plastic tube created pressure fluctuations.

The final design of the device connected to the outlet port of the microstructure is shown in Figure 9.5. The device is made from glass. The middle tube is always filled with liquid in order to keep constant the hydrostatic pressure at the outlet port. At its end, the middle tube touches the wall of the external cylinder so that the liquid easily drains to the external cylinder without building up due to surface tension. This ensures that the middle cylinder is always filled with liquid at a constant height and the hydrostatic pressure at the outlet port remains constant. The diameter of this tube is substantially larger than the bubble diameters so that bubbles do not clog the tube and the liquid phase is continuous. There are no flexible connections and the bubbles exit the microstructure directly from the middle tube.

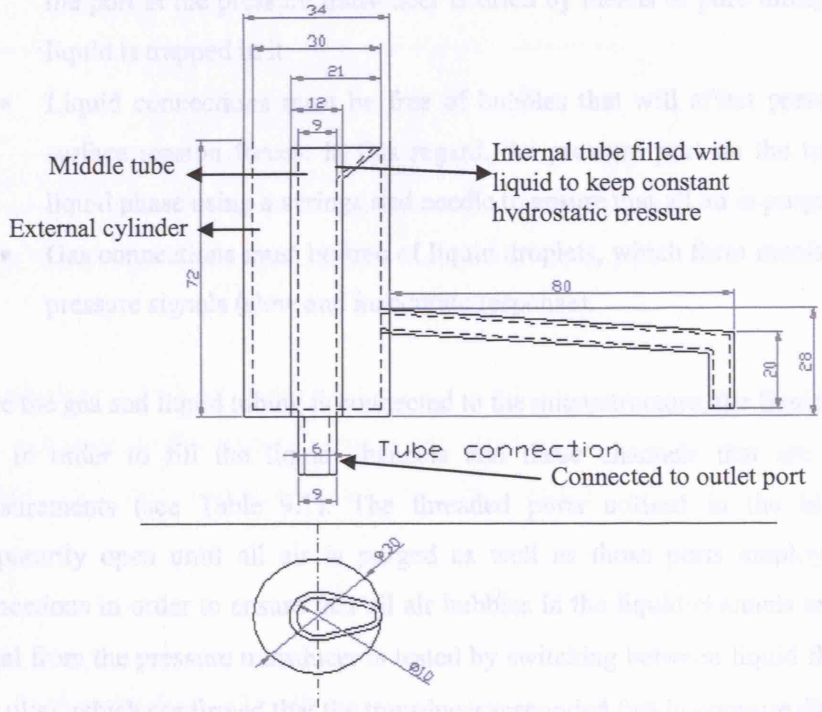

Figure 9.5. Final outlet construction.

A ring light system and a microscope (Prior scientific) are utilised to visualise the flow and obtain homogeneously illuminated pictures via a CCD-camera (Kodak ES 1.0 Megaplus 1008X1018) connected to the top of the microscope. The exposure time is controlled to obtain sharp images. Pictures are downloaded into the computer via a frame grabber (Data translation) and analysed via a Matlab code (see Appendix 8A) to obtain bubble/liquid slug lengths.

A pressure transducer (AutoTran Inc., series 860) based on piezoresistive technology is connected to the pressure ports of the microstructure and used to obtain measurements of absolute pressure (one port of the transducer open to the atmosphere; eg. liquid/gas pressure fluctuations) or pressure difference (both ports connected to the microstructure; e.g. pressure drop). The pressure transducer sends an electric signal to a i/o board that is connected to a data acquisition card (Data Translation DT-340), operated via Measure Foundry software (from Data Translation). The pressure transducer can operate at 4 different pressure ranges: 0-0.5 psi, 0-1 psi, 0-2 psi and 0-4 psi. When connecting the liquid or gas channels to the transducer pressure ports the following must be considered:

- When a transducer port is left open to the atmosphere or is connected to a gas channel the port at the pressure transducer is dried by means of pure nitrogen to ensure that no liquid is trapped in it.
- Liquid connections must be free of bubbles that will affect pressure readings due to surface tension forces. In this regard, the pressure port on the transducer is filled of liquid phase using a syringe and needle to ensure that all air is purged.
- Gas connections must be free of liquid droplets, which form menisci and result in poor pressure signals (slow and inaccurate response).

Once the gas and liquid tubing is connected to the microstructure, the liquid flow is started at 20 μl/s in order to fill the liquid channels and those channels that are blocked during the measurements (see Table 9.1). The threaded ports utilised in the blocked channels are temporarily open until all air is purged as well as those ports employed for liquid phase connections in order to ensure that all air bubbles in the liquid channels are removed. Pressure signal from the pressure transducer is tested by switching between liquid flowrates (e.g. 19 μl/s to 1 μl/s), which confirmed that the transducer responded fast in pressure differences.

Before and after each run the zero point of the pressure signal is checked to ensure proper function of the pressure transducer and ports (e.g. no trapped bubbles) for which the gas flow is stopped between two runs and the liquid flow is decreased to 0.1 μl/s (very low flow). During

this check, the gas ports are temporally and partially open to prevent any gas from clogging the main channel, which would affect the pressure reading. If the zero point during a run changes more than 0.05 V (18 Pa) pressure connections to the transducer are checked and the run is repeated.

9.4.3. Calibration of Mass Flow Controllers/ Pressure Transducer

The micrometering valve is partially closed until a steady and reproducible Taylor flow pattern is obtained at all gas/liquid flow conditions analysed for both water/air and octane/air systems. The pressure drop across the micrometering valve should be large enough to avoid the liquid going into the gas channel but it should allow the desirable maximum gas flowrate. Next, the mass flow controllers are calibrated using a bubble flowmeter, which is connected after the micrometering valve. The bubble flowmeter measures volumetric flowrates at atmospheric pressure, which are converted into mass flowrates. Calibration is carried out after the micrometering valve is set up since the flowrate delivered by the mass flow controller can be affected by the pressure at its outlet. Table 9.2 shows the equations to calculate the gas flowrates as a function of mass flow controller readings.

Low mass flow controller	High mass flow controller
$0 \leq Q_G \leq 1$ ml/min	$1 < Q_G \leq 20$ ml/min
Q_G (ml/min)= 1.4848 · reading + 0.00013	Q_G (ml/min)= 1.0763 · reading

Table 9.2. Volumetric flowrate across the mass flow controllers as a function of reading.

The pressure transducer is operated at the lowest pressure range (0-3500 Pa) since the pressure drop and pressure fluctuations measured were always smaller than 3500 Pa. A water manometer is used to calibrate the pressure transducer obtaining Eq. (9.20).

$$P(\text{Pa}) = 372.806 \cdot \text{reading(volts)} \tag{9.20}$$

9.4.4. Analysis of Pressure Drop, Pressure Fluctuations and Bubble/Slug Lengths

Measurements of pressure drop, pressure fluctuations and bubble/liquid slug lengths are taken for microstructure T-3. The pressure signal is acquired as a voltage signal with a sampling

frequency of 500 s^{-1}. An Excel (Microsoft) macro enables the pressure versus time data transfer from Data Translation Measure Foundry to an excel file.

Bubble and slug lengths are obtained as in Chapter 8. For each gas and liquid flowrates, a Kodak E.S. 1.0 Megaplus camera mounted on a Prior Scientific microscope takes 30 pictures of the bubble flow that are downloaded to the computer via the framegrabber. Sampling rate varied depending on flowrate to ensure that each frame contained different bubbles. These pictures are stored as TIF-files on the hard disc and analysed by a MATLAB script (Appendix 8A) that returns the number of bubbles and bubble and liquid slug lengths to a text file. The averaged values of bubble and liquid slug lengths at each flow condition are used in the calculations.

Bubble frequency was also measured with an infrared emitter/sensor, which measures bubble frequency based on light diffraction at the bubble surface when a bubble passes in front of sensor. An IR emitting diode with peak at 940 nm (Vishay Telefunken, model TSAL4400) and an IR detector (Farnell, model TSL261), which combines an optical sensor, a transimpedance amplifier and a filter to cut out visible light, are used.

9.5. Results And Discussion

Results on average pressure drop, pressure fluctuations and liquid/gas flow distribution during Taylor flow in square channels are analysed as a function of gas and liquid flow rates and system properties. Table 9.3 shows the combinations of liquid and gas flowrates utilised in the experiments to generate Taylor flow with different bubble and liquid slug lengths.

	Q_G						
Q_L	$[10^{-9}m^3/s]$	*1*	*5*	*10*	*20*	*40*	*80*
	2.477	X	X	X	X		
	7.426	X	X	X	X	X	X
	12.375	X	X	X	X	X	X
	17.938		X	X	X	X	X
	53.814			X	X	X	X
	89.690				X	X	X
	179.381				X	X	X

Table 9.3. Gas and liquid flow rates investigated during Taylor flow experiments.

9.5.1. Pressure Drop during Taylor Flow in Square Channels

9.5.1.1. Pressure Drop in the Presence of a Channel Bend

To analyse the effect of a channel bend on pressure drop during Taylor flow, two different measurements were conducted. The pressure drop for the system water/air during Taylor flow was measured both between ports 3 and 5 and ports 3 and 4 (cases 1 and 2 in Table 9.1, see Figure 9.2). The section between ports 3 and 5 contains a 90° bend. The major advantage of measuring pressure drop between ports 3 and 5 is that this section is nearly double the length of the section between ports 3 and 4, and would result in more accurate values of pressure drop.

The comparison between the values of pressure drop for both measurements is shown in Figure 9.6, representing the dimensionless liquid slug length $L^{\#}_S$ versus fRe_L (Eq. (9.10)). Both trends are similar indicating that for these gas/liquid flowrates, the effect of the bend on pressure drop is not important. Thus, the influence of the bend in the channel is neglected in the following studies and results from both measurements are combined. As the liquid slug length increases, the value of fRe_L approaches the value of single phase in square channels, $fRe_L = 28.5$ for square channels (see Eq. (9.5)). It must be noted that Re_L is based on capillary radius r_h. Kreutzer (2003) shows similar graphs in circular channels using $fRe_{L,d}/4$ where $Re_{L,d}$ is the Reynolds number using the average liquid slug velocity and the channel diameter, which in circular channels is $fRe_{L,d}/4 = 16$ ($fRe_{L,d}/4 = 14.25$ in square channels).

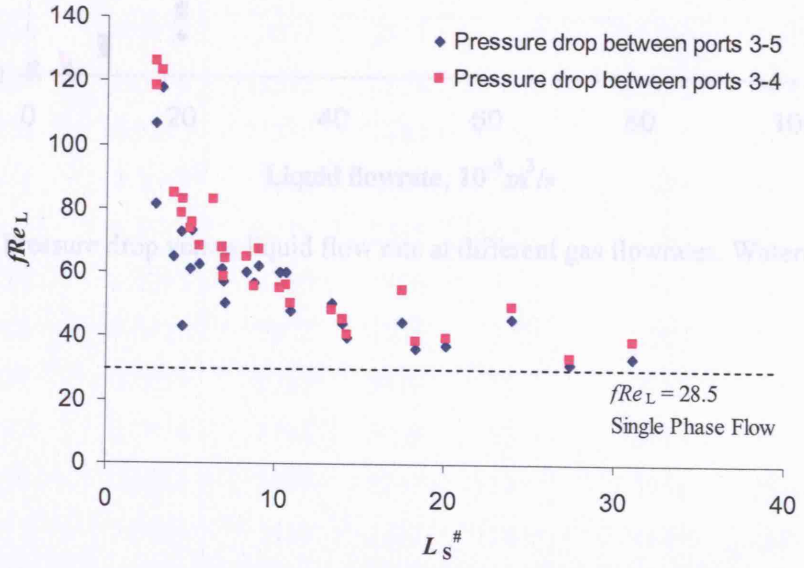

Figure 9.6. Product fRe_L versus dimensionless slug length $L^{\#}_S$ for water/air Taylor flow and two different ways of measuring pressure drop.

9.5.1.2. Effect of System Properties and Gas/Liquid Flowrates on Pressure Drop during Taylor Flow in Square Microchannels

Pressure drop during Taylor flow in a microchannel was studied initially. A correlation similar to that given by Kreutzer (2003) for pressure drop in circular channels during Taylor flow (see Eq. (9.3) and (9.8)) is developed that allows for direct comparison between different channel geometries. This equation relates an overall friction factor, f, with Reynolds number Re_L, Capillary number Ca_L and the dimensionless liquid slug length, $L^{\#}_S$.

The measured values of pressure drop between ports 3 and 5 as a function of the liquid flow rates at constant gas flow rates are shown in Figure 9.7 and Figure 9.8 for water/air and octane/air respectively.

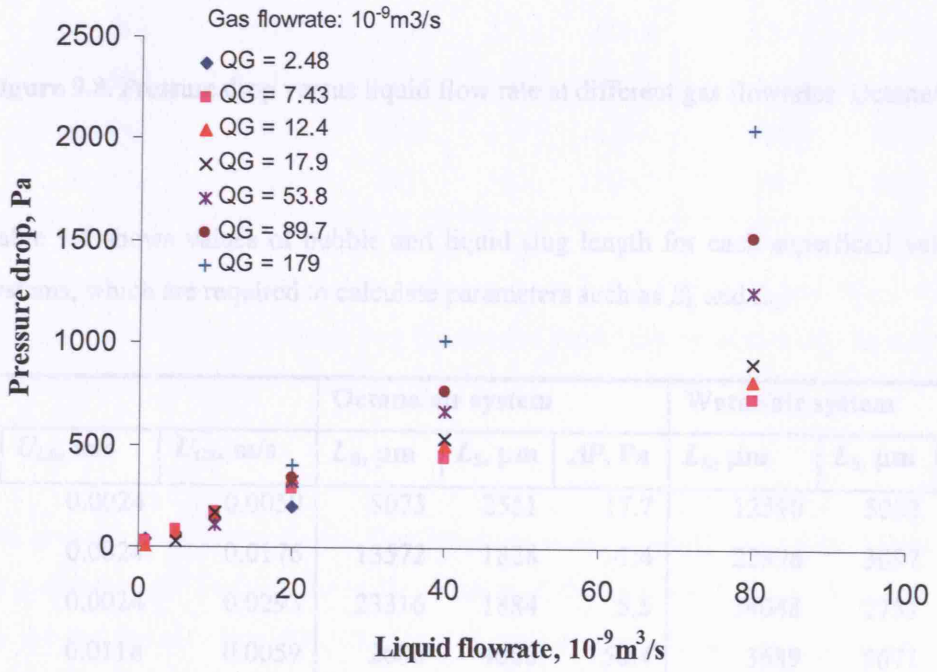

Figure 9.7. Pressure drop versus liquid flow rate at different gas flowrates. Water/air system.

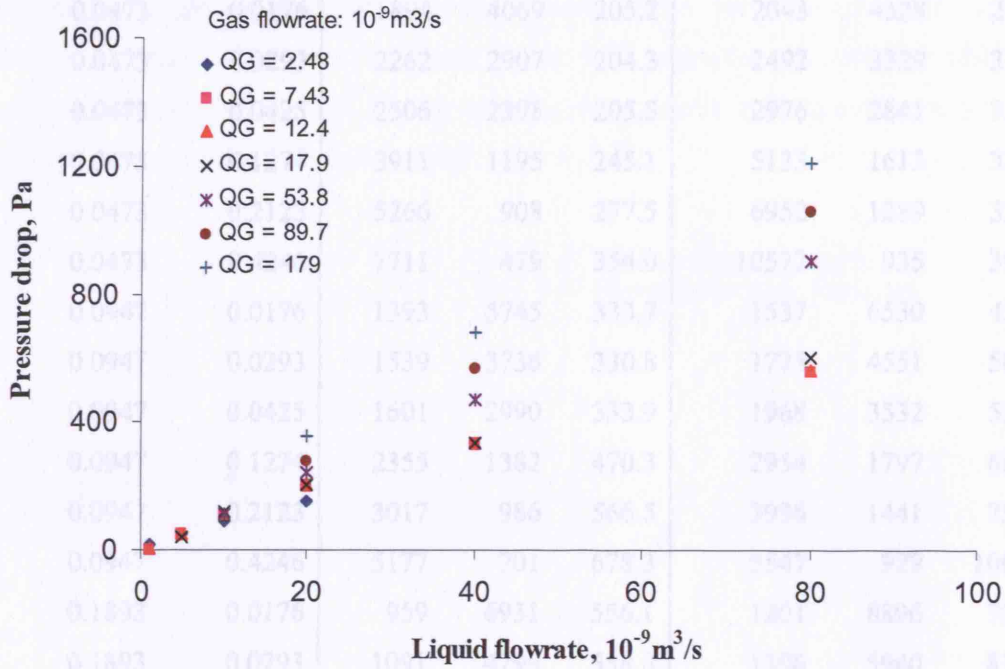

Figure 9.8. Pressure drop versus liquid flow rate at different gas flowrates. Octane/air system.

Table 9.4 shows values of bubble and liquid slug length for each superficial velocity in both systems, which are required to calculate parameters such as β_L and L_C.

		Octane/air system			Water/air system		
U_{LS}, m/s	U_{GS}, m/s	L_B, μm	L_S, μm	ΔP, Pa	L_B, μm	L_S, μm	ΔP, Pa
0.0024	0.0059	8073	2551	17.7	12590	5083	36.2
0.0024	0.0176	13572	1828	-1.4	22996	3097	27.0
0.0024	0.0293	23316	1884	5.5	34048	2751	3.4
0.0118	0.0059	2606	4066	50.4	3689	5671	60.8
0.0118	0.0176	4114	2245	52.4	5207	2930	83.5
0.0118	0.0293	5780	1896	51.3	6515	2286	68.3
0.0118	0.0425	7022	1720	37.9	8097	2059	29.5
0.0237	0.0059	1782	5470	89.9	2355	7782	130.7
0.0237	0.0176	2785	3039	105.4	3139	3455	164.7
0.0237	0.0293	3489	2242	113.5	3951	2696	163.5
0.0237	0.0425	3838	1897	116.9	4480	2224	170.5
0.0237	0.1274	7501	1156	111.8	9645	1477	109.3
0.0473	0.0059	1426	8460	150.4	1599	10103	194.4

0.0473	0.0176	1894	4069	205.2	2043	4328	282.2
0.0473	0.0293	2262	2907	204.3	2492	3329	334.3
0.0473	0.0425	2506	2398	205.5	2976	2841	316.5
0.0473	0.1274	3911	1195	245.1	5133	1613	323.4
0.0473	0.2123	5266	908	277.5	6952	1289	335.5
0.0473	0.4246	7711	479	354.0	10572	935	396.4
0.0947	0.0176	1393	5745	333.7	1537	6530	430.5
0.0947	0.0293	1539	3736	330.8	1775	4551	500.2
0.0947	0.0425	1601	2990	333.9	1968	3532	534.2
0.0947	0.1274	2355	1382	470.3	2954	1797	668.9
0.0947	0.2123	3017	986	566.5	3936	1441	759.7
0.0947	0.4246	5177	701	678.3	5547	929	1009.8
0.1893	0.0176	959	6931	556.1	1201	8896	729.6
0.1893	0.0293	1091	4799	558.3	1396	5940	818.8
0.1893	0.0425	1093	3713	600.6	1369	4616	900.2
0.1893	0.1274	1473	1489	898.3	1863	2250	1253.9
0.1893	0.2123	1921	1147	1053.5	2405	1649	1512.9
0.1893	0.4246	3911	1021	1205.7	3703	1063	2046.9

Table 9.4. Average pressure drop (between ports 3 and 5), bubble and liquid slug lengths for octane/air and water/air systems as a function of superficial velocities in a square microchannel of diameter d = 650 μm.

The pressure drop during Taylor flow increases almost linearly as the liquid flowrate increases for a constant gas flowrate due to the increase of the frictional pressure drop in the liquid slug. As the gas flowrate increases, the slope of pressure drop versus liquid flowrate increases as a result of an increase of the liquid slug average velocity ($U_{L,m} \approx U_{LS}+U_{GS}$) as well as an increase in bubble frequency that results in larger pressure drop across the gas phase. The frictional pressure drop due to gas phase flow is negligible. The main difference between pressure drop values of water/air and octane/air systems is mainly caused by different values of viscosity, 0.00095 Pa·s and 0.00052 Pa·s respectively (see Table 8.2) and different bubble/liquid slug properties for the same flow rates. The water has a higher viscosity than octane resulting in larger liquid frictional pressure drop but lower bubble frequency for identical gas/liquid flowrates that counteracts the difference in pressure drop due to a smaller bubble pressure drop contribution.

The friction factor is calculated from experimental values via Eq. (9.10) with sin $\varphi = 0$ (horizontal channels). Figure 9.9 and Figure 9.10 represent the product fRe_L versus dimensionless liquid slug length, $L^{\#}_S$, for water/air and octane/air systems respectively following the methodology given by Kreutzer (2003).

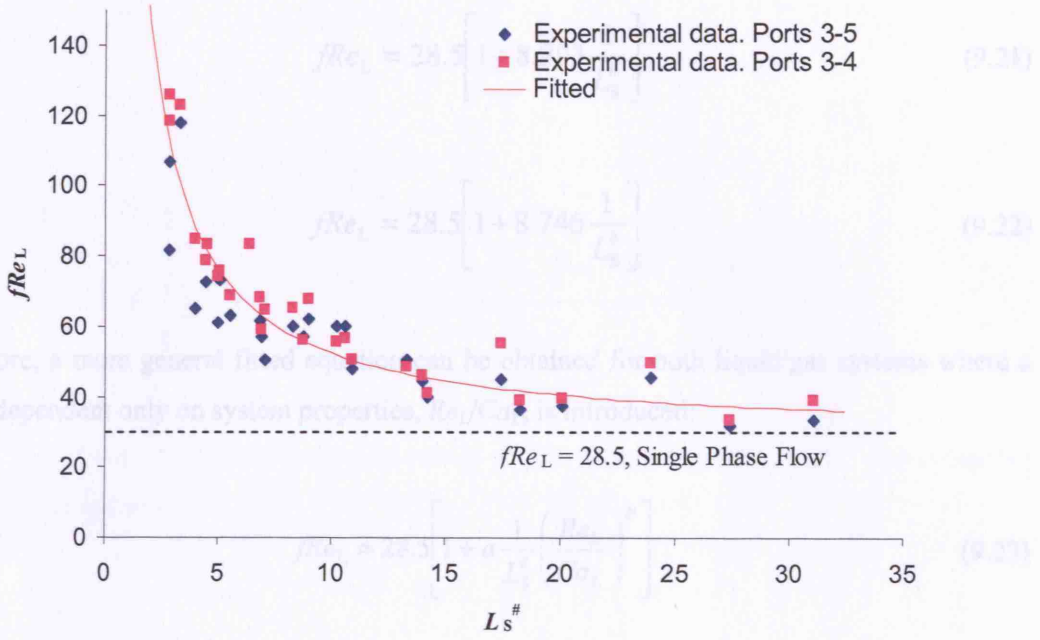

Figure 9.9. Non-linear fit of measured values of fRe_L versus dimensionless liquid slug length $L^{\#}_S$ for water/air system.

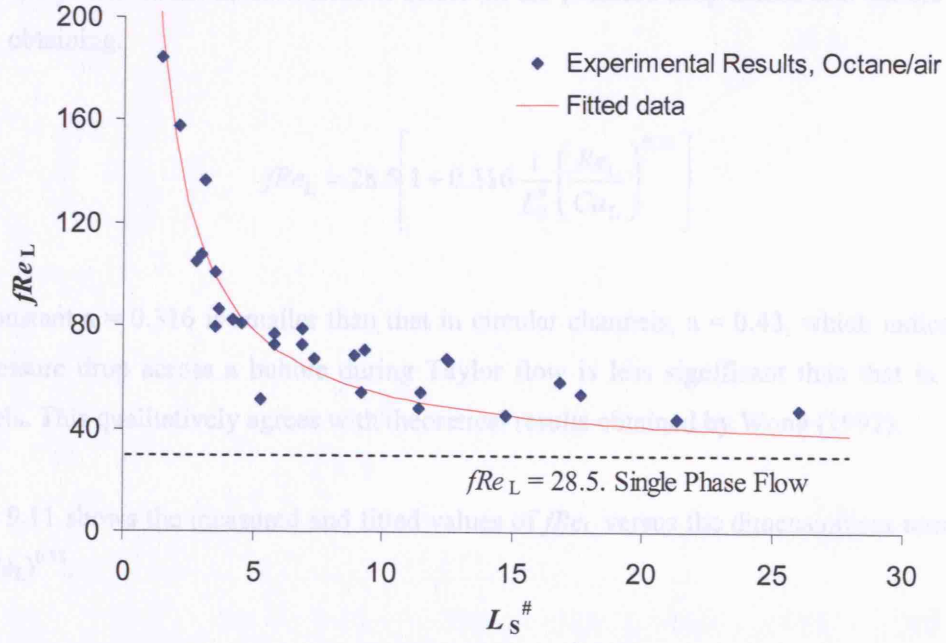

Figure 9.10. Non-linear fit of measured values of fRe_L versus dimensionless liquid slug length $L^{\#}_S$ for octane/air system. Pressure drop measured between ports 3 and 5.

The fitted values shown in Figure 9.9 and Figure 9.10 correspond to Eqs. (9.21) and (9.22) for water/air and octane/air systems respectively where the power of $L^{\#}_S$ is taken as 1 to obtain the number of bubbles when the friction factor is substituted in Eq. (9.3). The fit indicates that slug length is the only parameter determining the friction factor for each liquid/gas system:

$$fRe_L = 28.5\left[1+8.293\frac{1}{L^{\#}_S}\right] \tag{9.21}$$

$$fRe_L = 28.5\left[1+8.746\frac{1}{L^{\#}_S}\right] \tag{9.22}$$

Therefore, a more general fitted equation can be obtained for both liquid/gas systems where a factor dependent only on system properties, Re_L/Ca_L, is introduced:

$$fRe_L = 28.5\left[1+a\frac{1}{L^{\#}_S}\left(\frac{Re_L}{Ca_L}\right)^b\right] \tag{9.23}$$

The best fitting was obtained for a = 31.488 and b = -0.133. In order to compare experimental results obtained by Kreutzer (2003) for circular channels (see Eq. (9.8)) with those obtained in the present work for rectangular channels, b is set to b = 0.33, which corresponds to the theoretical power of the surface tension effect on the pressure drop across one bubble (Wong, 1992), obtaining:

$$fRe_L = 28.5\left[1+0.316\frac{1}{L^{\#}_S}\left(\frac{Re_L}{Ca_L}\right)^{0.33}\right] \tag{9.24}$$

The constant a = 0.316 is smaller than that in circular channels, a = 0.43, which indicates that the pressure drop across a bubble during Taylor flow is less significant than that in circular channels. This qualitatively agrees with theoretical results obtained by Wong (1992).

Figure 9.11 shows the measured and fitted values of fRe_L versus the dimensionless number $L^{\#}_S$ $(Ca_L/Re_L)^{0.33}$.

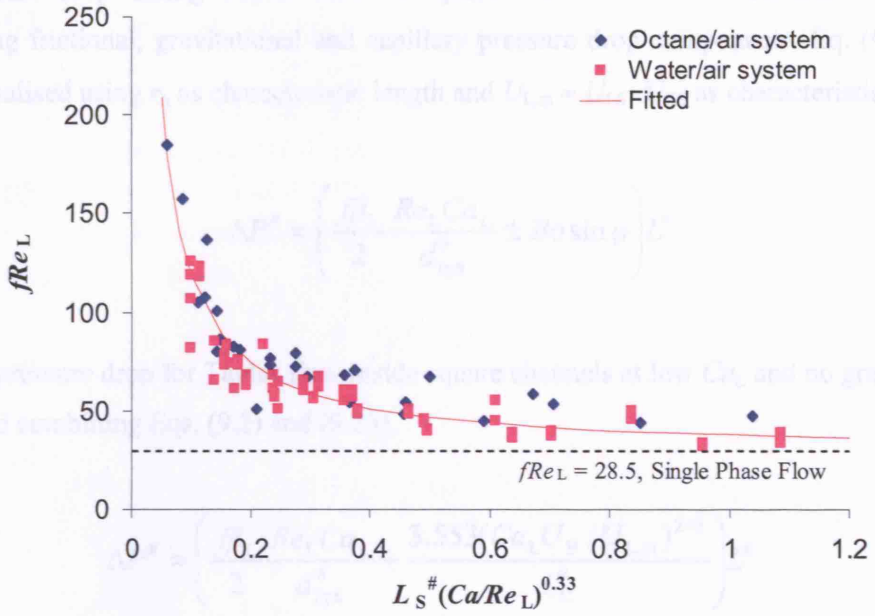

Figure 9.11. Non-linear fit of measured values of fRe_L versus $L^{\#}_S$ $(Ca_L/Re_L)^{0.33}$ for octane/air and water/air systems.

Results for octane/air and water/air systems fall on the same line represented by Eq. (9.24). As the number $L^{\#}_S$ $(Ca_L/Re_L)^{0.33}$ increases for increasing liquid slug length, the value of fRe_L approaches the limit for single phase flow fRe_L = 28.5. Figure 9.12 compares measured and fitted values of fRe_L for octane/air and water/air systems.

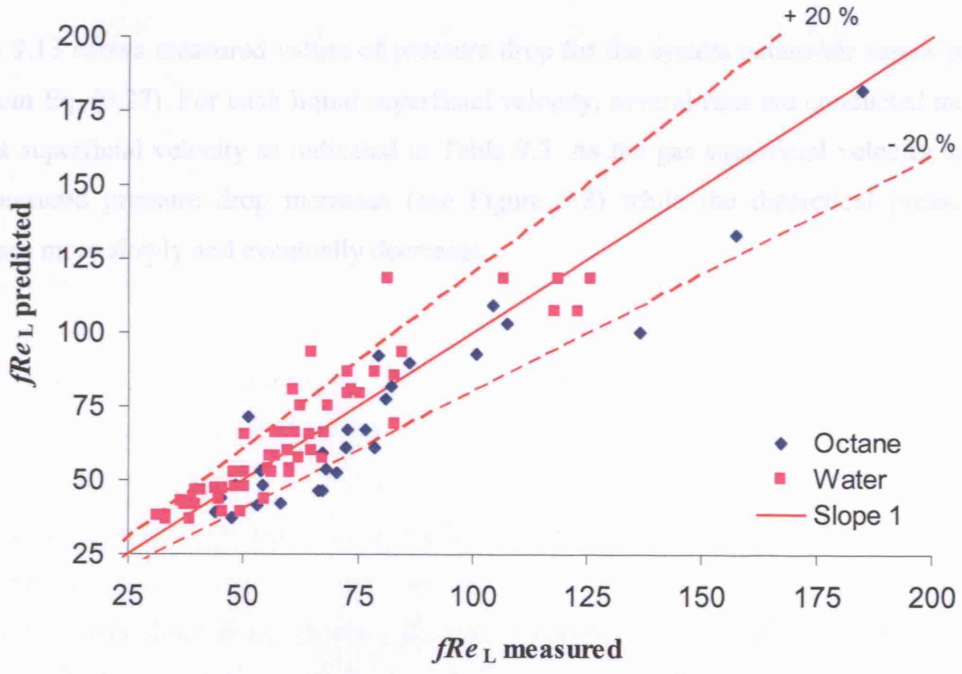

Figure 9.12. Comparison between measured and fitted (Eq. (9.24)) values of fRe_L.

The pressure drop during Taylor flow in square channels can be estimated from theory considering frictional, gravitational and capillary pressure drop components. Eq. (9.3) is non-dimensionalised using r_h as characteristic length and $U_{L,m} \approx U_{LS}+U_{GS}$ as characteristic velocity,

$$\Delta P^{\#} = \left(\frac{f\beta_L}{2} \frac{Re_L Ca_L}{d^{\#}_{hyd}} \pm Bo \sin\varphi \right) L^{\#} \tag{9.25}$$

The total pressure drop for Taylor flow inside square channels at low Ca_L and no gravity effects is obtained combining Eqs. (9.2) and (9.25),

$$\Delta P^{\#} = \left(\frac{f\beta_L}{2} \frac{Re_L Ca_L}{d^{\#}_{hyd}} + \frac{3.553(Ca_L U_B / U_{L,m})^{2/3}}{L^{\#}_C} \right) L^{\#} \tag{9.26}$$

where $f = 28.5/Re_L$ (see Eq. (9.5)) and $d^{\#}_{hyd} = 2$ for square channels,

$$\Delta P^{\#} = \left(\underbrace{7.13\beta_L Ca_L}_{\text{Due to friction In liquid slug}} + \underbrace{\frac{3.553(Ca_L U_B / U_{L,m})^{2/3}}{L^{\#}_C}}_{\text{Due to capillary forces}} \right) L^{\#} \tag{9.27}$$

Figure 9.13 shows measured values of pressure drop for the system octane/air versus predicted one from Eq. (9.27). For each liquid superficial velocity, several runs are conducted modifying the gas superficial velocity as indicated in Table 9.3. As the gas superficial velocity increases, the measured pressure drop increases (see Figure 9.8) while the theoretical pressure drop increases more slowly and eventually decreases.

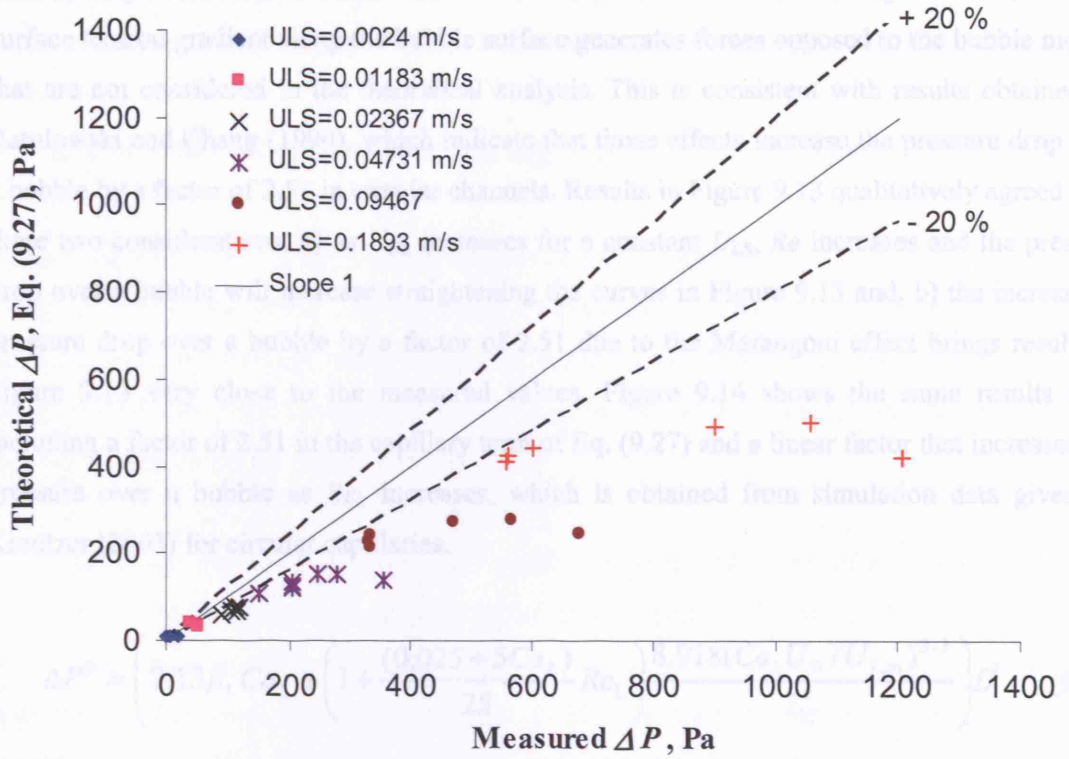

Figure 9.13. Theoretical values of Taylor pressure drop versus measured values for the octane/air system.

As U_{GS} increases for a given U_{LS}, the average liquid slug velocity $U_{L,m}$ and therefore Ca_L increase but the fraction of liquid slug β_L and $1/L^{\#}_C$ decrease as a result of longer bubbles. Longer bubbles reduce liquid length for frictional losses and also the capillary pressure losses as a consequence of a smaller number of bubbles per unit length. This produces a maximum local pressure drop for each U_{LS} according to the theory represented in Eq. (9.27), which is based on Wong's results (Wong, 1992). Wong's results based on a singular perturbation method are only valid for $Ca \rightarrow 0$ and no inertial effects $Re = 0$. Hazel and Heil (2002), who applied a finite element method for $Re \ll 1$ and any Ca, indicate that Wong's results of pressure drop along a bubble are valid up to $Ca = 0.001$ with an error of 5% at $Ca = 0.01$. Ca_L varies from 0.00021 to 0.015 for the results shown in Figure 9.13 and this small error cannot explain the discrepancy between experimental and theoretical values. The inertial effect on pressure drop along one bubble as Re_L varies from 3 to 270 may become substantial. Kreutzer (2003) shows that the pressure drop along a bubble during Taylor flow in circular channels doubles when $Re_{L,d}$ increases from 1 to 500 at constant $Ca_L = 0.01$. Experimental results for pressure drop in circular channels obtained by Kreutzer (2003) are also substantially larger than those obtained via finite element simulations, which consider actual values of Ca_L and Re_L. The discrepancy

between experimental and theoretical values is associated with the Marangoni effect, where a surface tension gradient along the bubble surface generates forces opposed to the bubble motion that are not considered in the theoretical analysis. This is consistent with results obtained by Ratulowski and Chang (1990), which indicate that those effects increase the pressure drop over a bubble by a factor of 2.51 in circular channels. Results in Figure 9.13 qualitatively agreed with these two considerations: a) as U_{GS} increases for a constant U_{LS}, Re increases and the pressure drop over a bubble will increase straightening the curves in Figure 9.13 and, b) the increase of pressure drop over a bubble by a factor of 2.51 due to the Marangoni effect brings results in Figure 9.13 very close to the measured values. Figure 9.14 shows the same results after including a factor of 2.51 in the capillary term of Eq. (9.27) and a linear factor that increases the pressure over a bubble as Re_L increases, which is obtained from simulation data given by Kreutzer (2003) for circular capillaries.

$$\Delta P^{\#} = \left(7.13\beta_L Ca_L + \left(1 + \frac{(0.025 + 5Ca_L)}{25} Re_L \right) \frac{8.918 (Ca_L U_B / U_{L,m})^{2/3}}{L_C^{\#}} \right) L^{\#} \qquad (9.28)$$

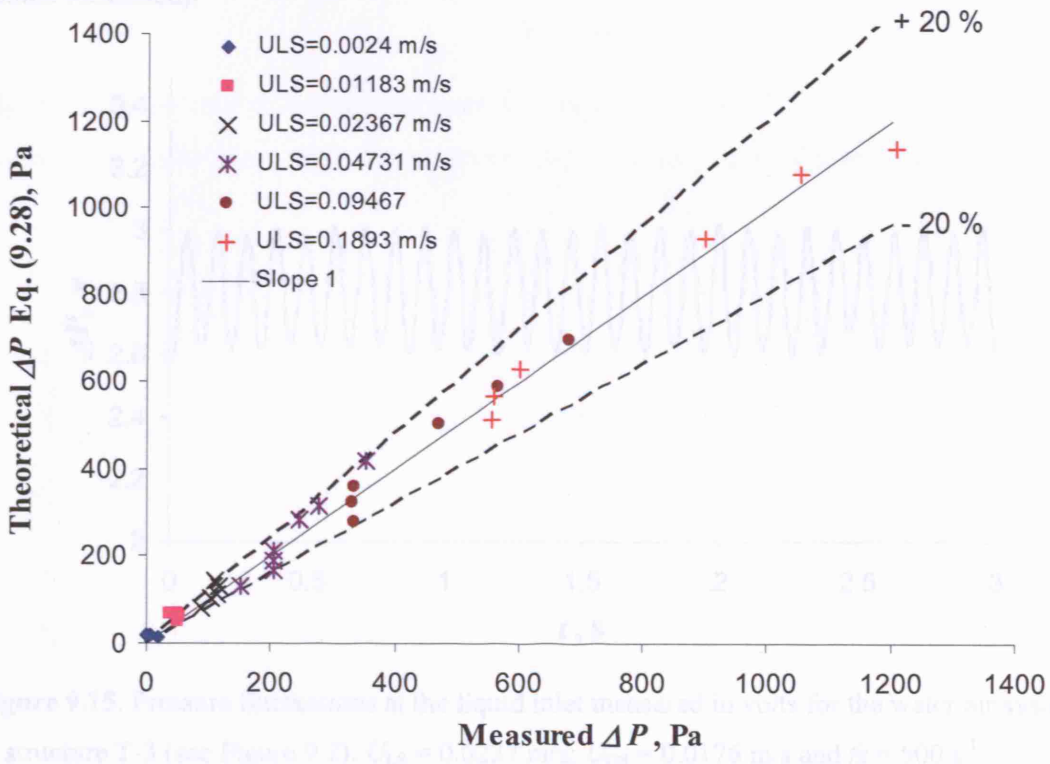

Figure 9.14. Modified theoretical values of pressure drop during Taylor flow (Eq. (9.28)) versus measured values for the octane/air system.

As can be seen in Figure 9.14, theoretical results predicted by Eq. (9.28) fit the pressure drop measured values well (better than Eq. (9.24)), with an average error of ~ 8 % at $\Delta P > 100$ Pa.

9.5.2. Pressure Fluctuations during Taylor Flow in Square Channels

Further work was carried out to study the pressure fluctuations in the liquid and gas phases as a result of bubble formation and the effect of flow rates, liquid/gas properties and capillary diameter on them. Average pressure fluctuations in the liquid and gas phases are measured for the gas/liquid flow rates shown in Table 9.3 using the pressure transducer connected to the ports as described in Table 9.1 (cases 3 and 4).

The final set-up described in section 9.4 enabled clear measurement of pressure fluctuations. Figure 9.15 shows the voltage signal collected by the pressure transducer during measurement of pressure fluctuations in the liquid inlet for the water/air system. The voltage reading is converted into pressure signal (Pa) using Eq. (9.20). The frequency of the pressure fluctuations is compared to bubble formation frequency and were found to match (i.e. fluctuations due to bubble formation).

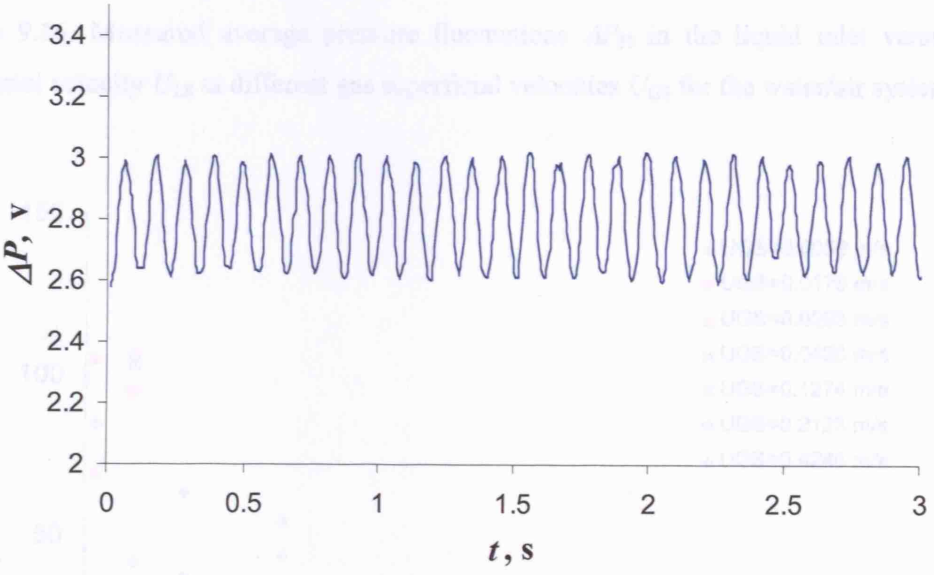

Figure 9.15. Pressure fluctuations at the liquid inlet measured in volts for the water/air system in structure T-3 (see Figure 9.2). $U_{LS} = 0.0237$ m/s; $U_{GS} = 0.0176$ m/s and $fz = 500$ s^{-1}.

Figure 9.16 and Figure 9.17 show measured average amplitude of pressure fluctuations in the *liquid inlet* during bubble formation as a function of liquid and gas superficial velocities, U_{LS}

and U_{GS}, for water/air and octane/air systems respectively. Pressure fluctuations decrease as U_{LS} increases in both systems for all U_{GS}. This is the result of increasing inertial forces in the liquid phase versus surface tension forces, which causes a pressure reduction over the bubble surface (see Chapter 5). There is no clear trend on the variation of the pressure fluctuation magnitude as U_{GS} decreases for a constant U_{LS}.

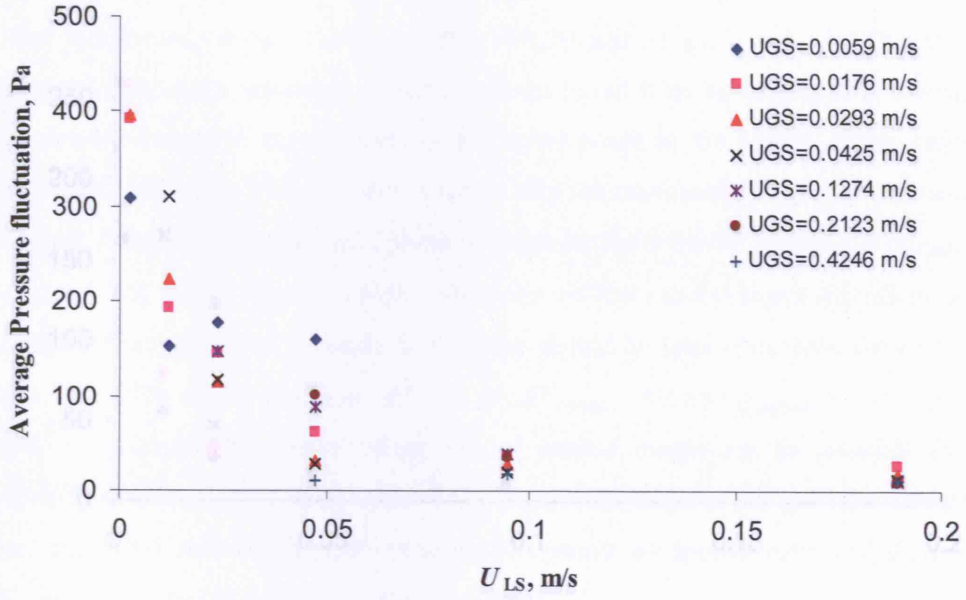

Figure 9.16. Measured average pressure fluctuations ΔP_{Fl} in the liquid inlet versus liquid superficial velocity U_{LS} at different gas superficial velocities U_{GS} for the water/air system.

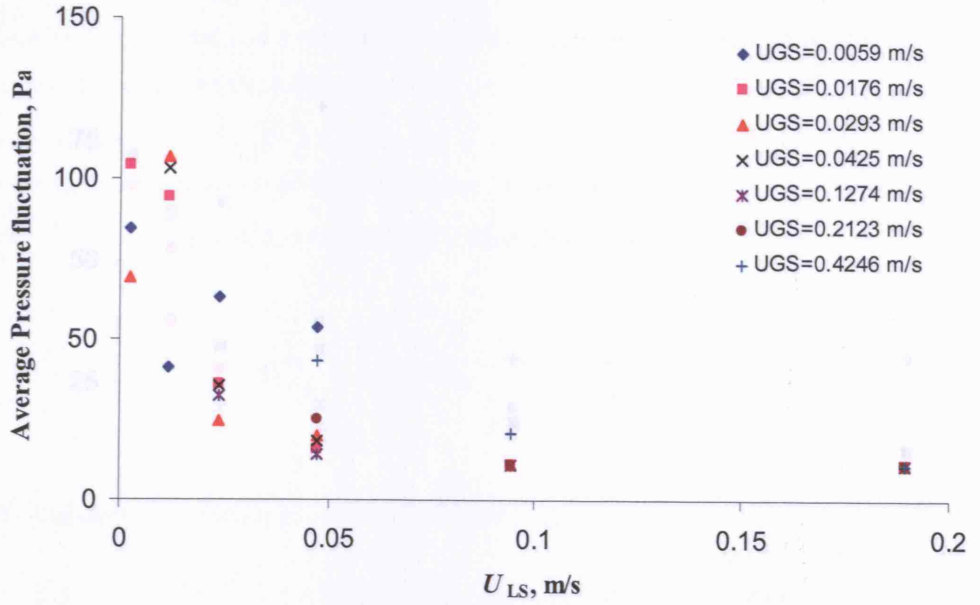

Figure 9.17. Measured average pressure fluctuations ΔP_{Fl} in the liquid inlet versus liquid superficial velocity U_{LS} at different gas superficial velocities U_{GS} for the octane/air system.

Figure 9.18 and Figure 9.19 show measured average amplitude of pressure fluctuations in the *gas inlet* during bubble formation as a function of liquid and gas superficial velocities, U_{LS} and U_{GS}, for water/air and octane/air systems respectively. Pressure fluctuations in the gas inlet also decrease as U_{LS} increases in both systems for all U_{GS} while they increase as U_{GS} increases.

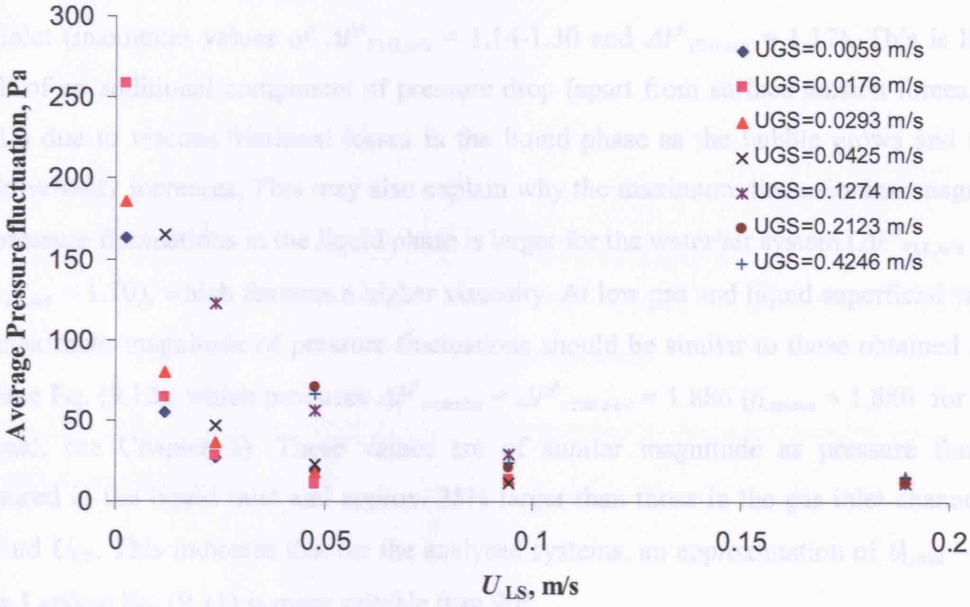

Figure 9.18. Measured average pressure fluctuations ΔP_{FI} in the gas inlet versus liquid superficial velocity U_{LS} at different gas superficial velocities U_{GS} for the water/air system.

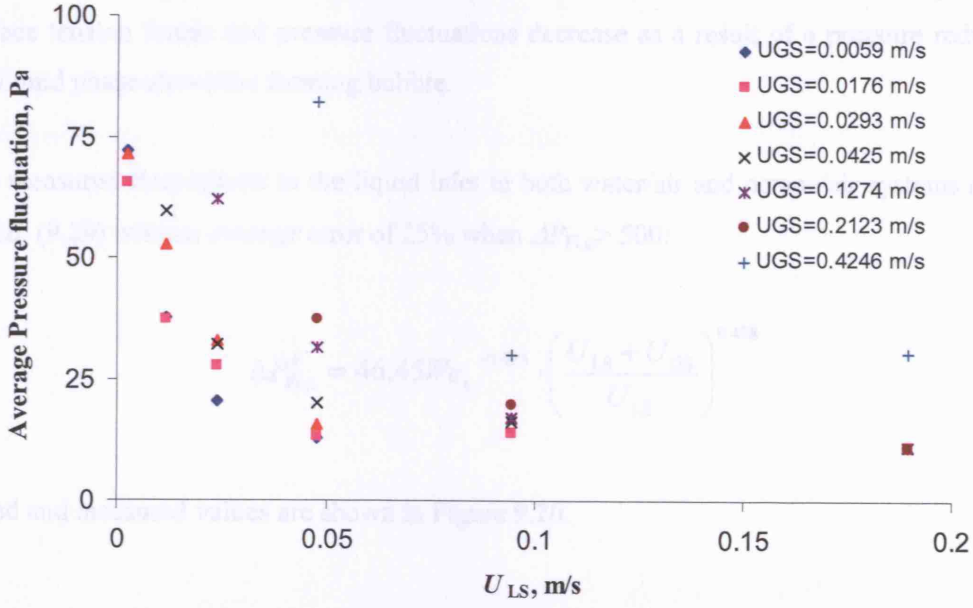

Figure 9.19. Measured average pressure fluctuations ΔP_{FI} in the gas inlet versus liquid superficial velocity U_{LS} at different gas superficial velocities U_{GS} for the octane/air system.

Pressure fluctuations in the liquid and gas phases depend on bubble formation as a consequence of overcoming surface tension forces. As the superficial liquid velocity U_{LS} increases, inertial forces in the liquid phase increase and the pressure over the bubble surface reduces. This causes a reduction in the magnitude of the pressure fluctuations (see Chapter 5). This effect is seen in both gas and liquid channels. The magnitude of the pressure fluctuations in the liquid inlet (maximum values of $\Delta P^{\#}_{Fl,L,w/a} = 1.79$ and $\Delta P^{\#}_{Fl,L,o/a} = 1.70$) are larger than those measured in the gas inlet (maximum values of $\Delta P^{\#}_{Fl,G,w/a} = 1.14\text{-}1.30$ and $\Delta P^{\#}_{Fl,G,o/a} = 1.17$). This is likely the result of an additional component of pressure drop (apart from surface tension forces, see Eq. (9.11)) due to viscous/frictional losses in the liquid phase as the bubble grows and the local liquid velocity increases. This may also explain why the maximum dimensionless magnitude of the pressure fluctuations in the liquid phase is larger for the water/air system ($\Delta P^{\#}_{Fl,L,w/a} = 1.79 > \Delta P^{\#}_{Fl,L,o/a} = 1.70$), which features a higher viscosity. At low gas and liquid superficial velocities, the maximum magnitude of pressure fluctuations should be similar to those obtained from the Laplace Eq. (9.12), which produces $\Delta P^{\#}_{water/air} = \Delta P^{\#}_{octane/air} = 1.886$ ($f_{Laplace} = 1.886$ for a square channel, see Chapter 3). These values are of similar magnitude as pressure fluctuations measured in the liquid inlet and approx. 35% larger than those in the gas inlet channel at low U_{LS} and U_{GS}. This indicates that for the analysed systems, an approximation of $\theta_{Initial} \sim 67°\text{-}70°$ in the Laplace Eq. (9.11) is more suitable than 90°.

Pressure fluctuations measured in the liquid and gas inlets for both water/air and octane/air systems are fitted to equations as a function of the Weber number We_{LS} and the ratio of flowrates $(U_{LS}+U_{GS})/U_{LS}$. As We_L number increases, inertial forces become more important than surface tension forces and pressure fluctuations decrease as a result of a pressure reduction in the liquid phase above the forming bubble.

The measured fluctuations in the liquid inlet in both water/air and octane/air systems are fitted by Eq. (9.29) with an average error of 25% when $\Delta P_{Fl,\mu} > 500$:

$$\Delta P^{\#}_{Fl,\mu} = 46.45 We_L^{-0.625} \cdot \left(\frac{U_{LS} + U_{GS}}{U_{LS}} \right)^{0.438} \tag{9.29}$$

Fitted and measured values are shown in Figure 9.20.

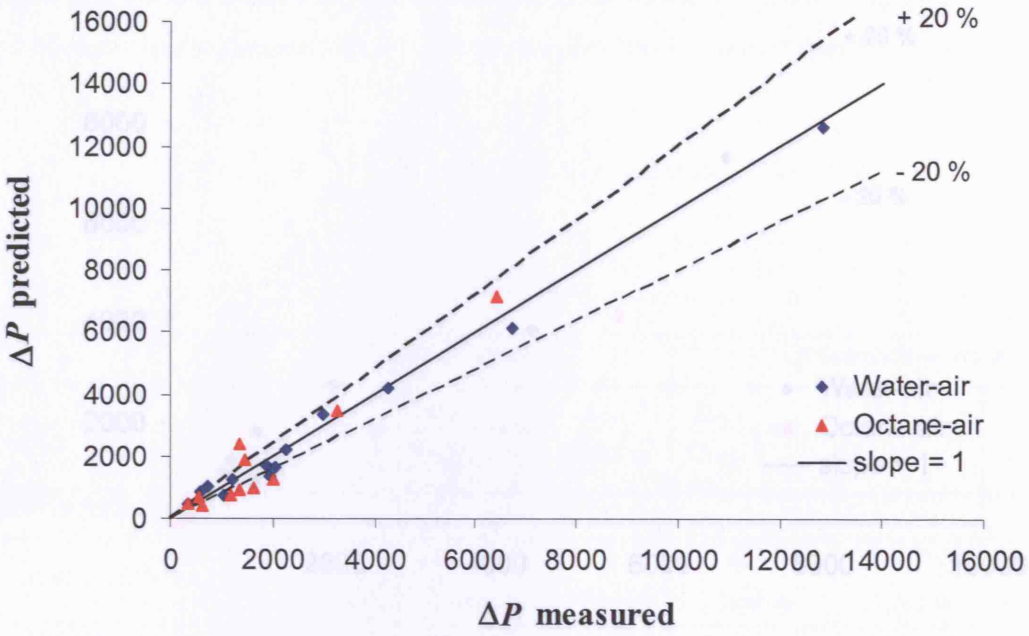

Figure 9.20. Measured and predicted pressure fluctuations in the liquid inlet for both water/air and octane/air systems.

The pressure fluctuations in the gas inlet in both water/air and octane/air systems are fitted by Eq. (9.30) with an average error of 26% when $\Delta P_{Fl,\mu} > 250$.:

$$\Delta P^{\#}_{Fl,\mu} = 24.83 We_L^{-0.622} \cdot \left(\frac{U_{LS} + U_{GS}}{U_{LS}} \right)^{0.518} \tag{9.30}$$

Fitted and measured values of the pressure fluctuations are shown in Figure 9.21.

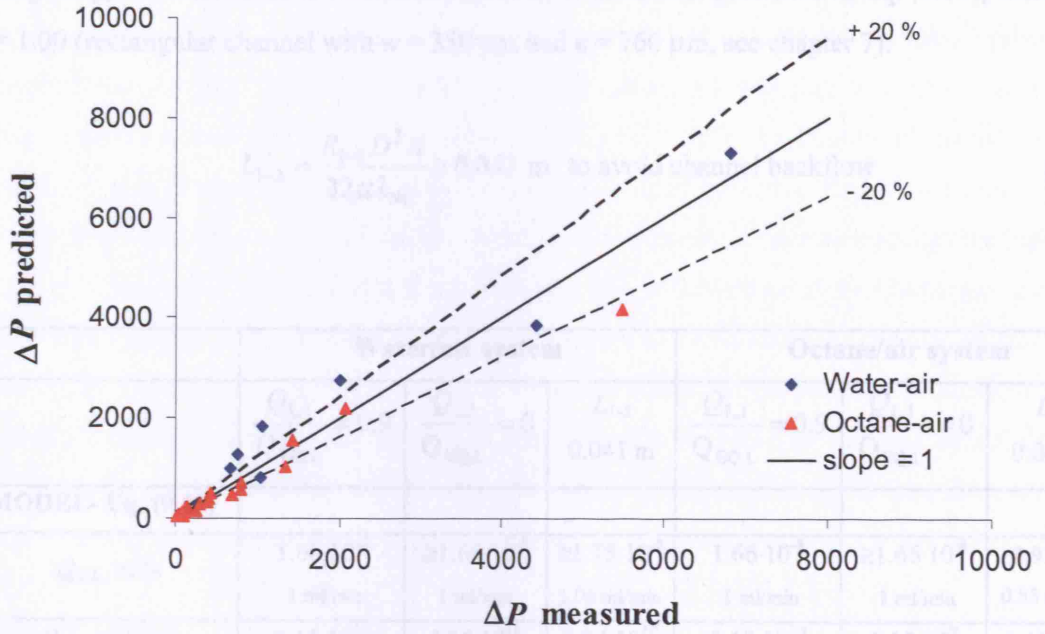

Figure 9.21. Measured and predicted pressure fluctuations in the gas inlet for both water/air and octane/air systems.

Eqs. (9.29) and (9.30) were obtained via the "nonlinearfit" function of Mathematica software. The maximum pressure fluctuation noise caused by the liquid pump is approximately $\Delta P \approx 0.03$ v (11 Pa) at the highest liquid flowrates analysed ($U_{LS} > 0.095$ m/s) and this explains the larger relative scatter between fitted and measured values at low pressure fluctuations (high liquid flowrates).

9.5.3. Flow Distribution during Taylor Flow in a 2-Channel Manifold

The 2-channel manifold shown in Figure 9.3 has rectangular channels of dimensions $e_{1\text{-}2} = w_{1\text{-}2} = 760$ μm and liquid inlet channels of dimensions $e_{1\text{-}2} = 350$ μm and $w_{1\text{-}2} = 760$ μm. Pressure fluctuations due to bubble formation are estimated via Eq. (9.12) to obtain $\Delta P_{Fl,w\text{-}a} = 357.4$ Pa and $\Delta P_{Fl,o\text{-}a} = 101.7$ Pa and the microstructure should operate stably in the range 1-10 ml/min of gas and liquid flowrates. Table 9.5 shows resistances and channel lengths for water/air and octane/air using both models described by Eqs. (9.17) and (9.19). Two cases are considered, $Q_{L,1}/Q_{EQ,L} = 0.9$ and $Q_{L,1}/Q_{EQ,L} = 0$ (to avoid back flow). The resistances $R_{1\text{-}2}$ for $Q_{L,1}/Q_{EQ,L} = 0.9$ and $Q_{L,1}/Q_{EQ,L} = 0$ are calculated using the two methods aforementioned, which are then used to calculate the required channel lengths $L_{1\text{-}2}$, e.g. Eq. (9.31) shows the required channel

length $L_{1\text{-}2}$ to avoid channel backflow according to the model presented in Eq. (9.17), where λ_{NC} = 1.00 (rectangular channel with w = 350 μm and e = 760 μm, see chapter 7):

$$L_{1\text{-}2} = \frac{R_{1\text{-}2} D^2 A}{32 \mu \lambda_{NC}} \geq 0.043 \text{ m} \quad \text{to avoid channel backflow} \tag{9.31}$$

	Water/air system			**Octane/air system**		
	$\frac{Q_{L,1}}{Q_{EQ,L}} = 0.9$	$\frac{Q_{L,1}}{Q_{EQ,L}} = 0$	$L_{1\text{-}2}$ 0.041 m	$\frac{Q_{L,1}}{Q_{EQ,L}} = 0.9$	$\frac{Q_{L,1}}{Q_{EQ,L}} = 0$	$L_{1\text{-}2}$ 0.041 m
MODEL- Eq. (9.17)						
$Q_{T,L}$, m^3/s	$1.66 \cdot 10^{-8}$ 1 ml/min	$\geq 1.66 \cdot 10^{-8}$ 1 ml/min	$\geq 1.75 \cdot 10^{-8}$ 1.06 ml/min	$1.66 \cdot 10^{-8}$ 1 ml/min	$\geq 1.66 \cdot 10^{-8}$ 1 ml/min	$\geq 0.911 \cdot 10^{-8}$ 0.55 ml/min
$R_{1\text{-}2}$, pa·s/m^3	$2.15 \cdot 10^{11}$	$2.15 \cdot 10^{10}$	$2.04 \cdot 10^{10}$	$6.13 \cdot 10^{10}$	$6.13 \cdot 10^{9}$	$1.12 \cdot 10^{10}$
$L_{1\text{-}2}$, m	0.4325	0.0432	0.0410	0.2250	0.0225	0.0410
MODEL- Eq. (9.19)						
$Q_{L,1}$, m^3/s (low flow)	$7.47 \cdot 10^{-9}$	0	0	$7.47 \cdot 10^{-9}$	0	0
$Q_{L,2}$, m^3/s (peak flow)	$9.13 \cdot 10^{-9}$	$1.66 \cdot 10^{-8}$	$1.42 \cdot 10^{-8}$	$9.13 \cdot 10^{-9}$	$1.66 \cdot 10^{-8}$	$7.80 \cdot 10^{-9}$
$L_{B,4\text{-}6} = L_{B,5\text{-}6}$, μm (Eq. (8.37))	3937[1]	3937[1]	4419[1]	3385	3385	6225
$L_{S,4\text{-}6} = L_{S,5\text{-}6}$, μm (Eq. (8.34))	3423[1]	3423[1]	3310[1]	2873	2873	2549
$\Delta P_{4\text{-}6}$, Pa	99.1	60.3[2]	56.9[2]	52.2	31.6	21.8
$R_{4\text{-}6}$, pa·s/m^3	$1.33 \cdot 10^{10}$	$\rightarrow \infty$	$\rightarrow \infty$	$6.98 \cdot 10^{9}$	$\rightarrow \infty$	$\rightarrow \infty$
$\Delta P_{5\text{-}6}$, Pa	107.2	142.2	123.6	56.5	75.2	36.4
$R_{5\text{-}6}$, Pa·s/m^3	$1.17 \cdot 10^{10}$	$8.57 \cdot 10^{9}$	$8.69 \cdot 10^{9}$	$6.19 \cdot 10^{9}$	$4.53 \cdot 10^{9}$	$4.66 \cdot 10^{9}$
$Q_{T,L}$, m^3/s	$1.66 \cdot 10^{-8}$	$\geq 1.66 \cdot 10^{-8}$	$\geq 1.42 \cdot 10^{-8}$ 0.86 ml/min	$1.66 \cdot 10^{-8}$	$\geq 1.66 \cdot 10^{-8}$	$\geq 7.80 \cdot 10^{-9}$ 0.47 ml/min
$R_{1\text{-}2}$, Pa·s/m^3	$2.10 \cdot 10^{11}$	$1.66 \cdot 10^{10}$	$2.04 \cdot 10^{10}$	$5.87 \cdot 10^{10}$	$3.51 \cdot 10^{9}$	$1.12 \cdot 10^{10}$
$L_{1\text{-}2}$, m	0.4227	0.0333	0.0410	0.2154	0.0129	0.0410

[1] Minimum air flowrate of 1 ml/min is considered to calculate U_{GS} and average values of $Q_{L,1}$ and $Q_{L,2}$.

[2] It should be noted that $Q_{L,1}$ = 0 does not yield $\Delta P_{4\text{-}6}$ = 0 since the average liquid slug velocity is $U_{L,m} = U_{LS} + U_{GS}$ and air equipartition is considered.

Table 9.5. Calculation of required resistances (distributing channel length) for certain peak $Q_{L,1}/Q_{EQ,L}$ and minimum operable liquid flowrate to avoid backflow in a given 2-channel manifold geometry.

Results from the simplified model (Eq. (9.17)) are always conservative. The column for $L_{1\text{-}2}$ = 4.1 cm indicates that the designed 2-channel manifold prevents backflow when operating at liquid flowrates $Q_{T,L}$> 1.06 ml/min and $Q_{T,L}$> 0.55 ml/min for water/air and octane/air systems respectively according to the simple model given by Eq. (9.17). Application of the model given by Eq. (9.19) produces slightly lower minimum flowrates for the 2-channel manifold, $Q_{T,L}$ > 0.86 ml/min and $Q_{T,L}$ > 0.47 ml/min for water/air and octane/air systems respectively (based on $Q_{T,G}$ = 1 ml/min). For the actual channel length $L_{1\text{-}2}$ = 0.0410 m of the 2-channel manifold shown in Figure 9.3, the minimum total liquid flowrate to avoid backflow can also be calculated via Eq. (9.17) to obtain $Q_{T,L}$ = 1.06 ml/min. It must be noted that the pressure fluctuations due to bubble formation decrease as liquid and gas flowrates increase so that the actual limiting flowrates to prevent backflow in the 2-channel manifold will be even lower than those obtained when calculating fluctuations via Eq. (9.12) ($\Delta P_{Fl,w\text{-}a}$ = 357.4 Pa and $\Delta P_{Fl,o\text{-}a}$ = 101.7 Pa).

A more accurate approach would be to couple gas and liquid flow distribution using the same model for the gas phase and iterating the liquid and gas flowrates. In the experiments conducted in the 2-channel manifold the gas was distributed using an external tee-junction connected to circular gas inlet rigid tube made of Teflon of d = 100 μm and $L_{1\text{-}2,\,G}$ = 10 cm. These channels result in $Q_{G,I}/Q_{EQ,G}$ > 0.947 when $Q_{T,G}$ = 1 ml/min and no backflow for flowrates $Q_{T,G}$ > 0.053 ml/min for the water/air system according to the model given in Eq. (9.17).

Equal liquid flowrates were measured in both parallel channels for zero gas flow after checking for leaks at the inlet ports. Liquid and gas flowrates shown in Table 9.3 ($Q_{T,L}$ > 0.06 ml/min and $Q_{T,G}$ > 0.149 ml/min) were tried. The 2-channel manifold generally delivered even flow distribution for both water/air and octane/air systems. Figure 9.22 to Figure 9.25 show sequences of Taylor flow and bubble formation in the two channel structure for both water/air and octane/air systems at two different gas and liquid flowrates. It was found that when liquid flowrates were larger than $Q_{T,L}$ = 0.6 ml/min and $Q_{T,L}$ = 0.3 ml/min in water/air and octane/air systems respectively no backflow was observed. These values are slightly smaller than the theoretical ones presented in Table 9.5 ($Q_{T,L}$ = 0.87 ml/min and $Q_{T,L}$ = 0.3 ml/min for water/air and octane/air systems respectively), which are for $Q_{G,T}$ = 1 ml/min and also maximum pressure fluctuations.

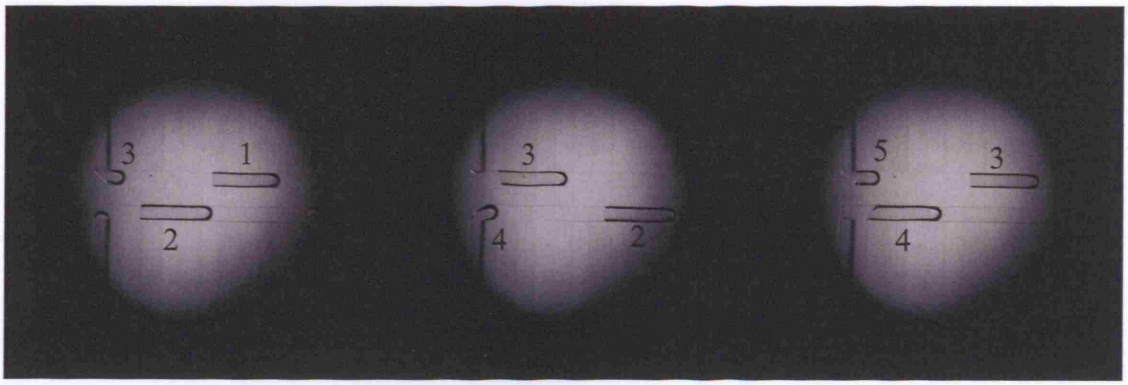

Figure 9.22. Liquid and gas distribution in the 2-channel manifold shown in Figure 9.3 for the water/air system when $Q_{T,G}$ = 1.03 ml/min, $Q_{T,L}$ = 1.8 ml/min. Frame separation of 0.12 s. Same bubble velocity and frequency in channels 1 and 2, $fz_{B,1} = fz_{B,2}$ = 4.8 bubbles/s.

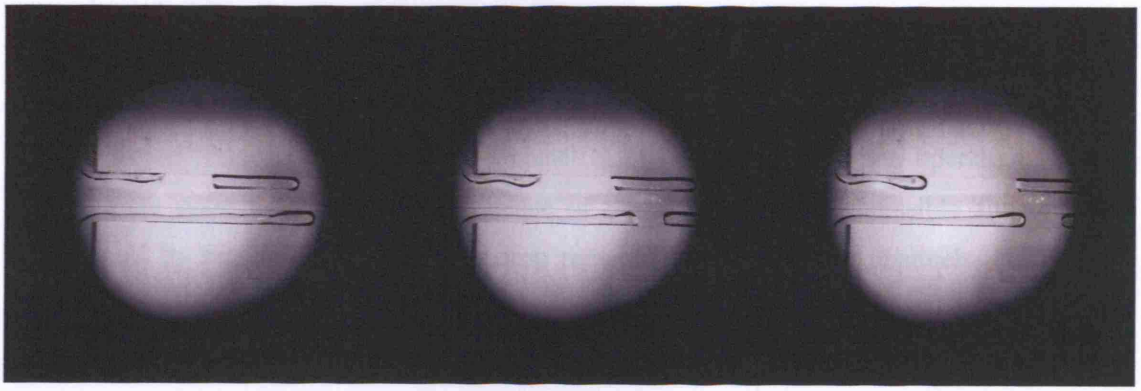

Figure 9.23. Liquid and gas distribution in the 2-channel manifold shown in Figure 9.3 for the water/air system when $Q_{T,G}$ = 5.46 ml/min, $Q_{T,L}$ = 4.8 ml/min. Frame separation of 0.008 s. Different bubble formation mechanism results in slightly different bubble frequency, length and velocity in channels 1 and 2, $fz_{B,1}$ = 23.1 bubbles/s, $fz_{B,2}$ = 27.3 bubbles/s.

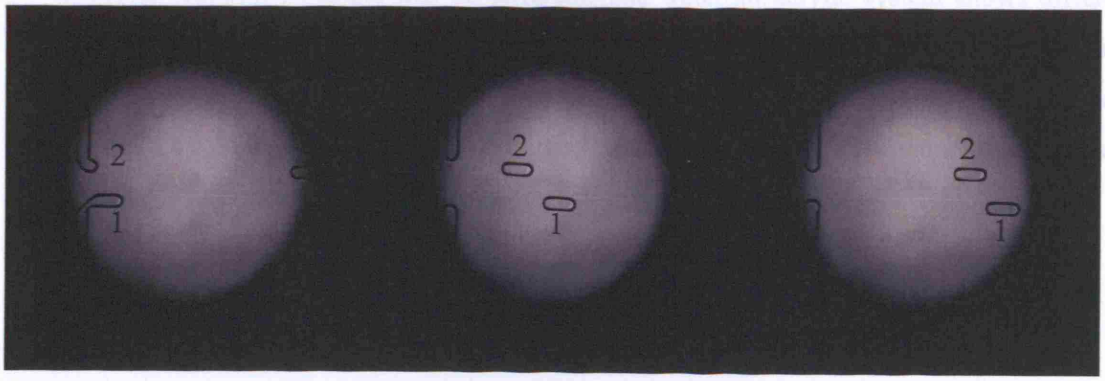

Figure 9.24. Liquid and gas distribution in the 2-channel manifold shown in Figure 9.3 for the octane/air system when $Q_{T,G}$ = 0.167 ml/min, $Q_{T,L}$ = 0.60 ml/min. Frame separation of 0.20 s. Same bubble frequency in channels 1 and 2, $fz_{B,1} = fz_{B,2}$ = 2.7 bubbles/s.

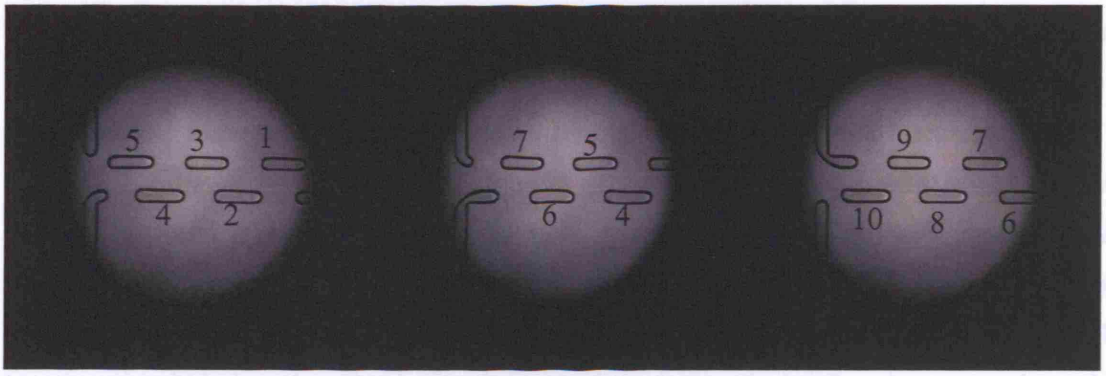

Figure 9.25. Liquid and gas distribution in the 2-channel manifold shown in Figure 9.3 for the octane/air system when $Q_{T,G}$ = 1.03 ml/min, $Q_{T,L}$ = 1.8 ml/min. Frame separation of 0.03 s. Same bubble frequency in channels 1 and 2, fz_B = 45.0 bubbles/s.

Additional issues encountered during the experimental work are,

- The liquid phase goes into the air channel at $Q_{T,G}$ < 1 ml/min when operating with the water/air system. This is a consequence of the air being a compressible fluid. This is avoided by setting up the pressure drop required in the gas inlet channels, close to the gas/liquid junction where bubbles form.
- Systems with large surface tension and high contact angle present wetting issues and can lead to different bubble formation mechanisms. This will result in different average pressure fluctuations in each manifold as well as different bubble/liquid slug lengths, leading to different pressure drop and therefore uneven average liquid/gas flow distribution. Even if the external resistance is sufficiently large as to produce even average liquid/gas flow distribution, the available surface area, hydrodynamics and bubble frequency in each of the manifold reaction channels will be different. The water/air/acrylic system shows different bubble formation mechanisms when operating at high gas/liquid flowrates as seen in Figure 9.23. In the top channel, a necking process appears with a long neck while in the bottom channel an air chamber forms with different contact points along the channel that results in different bubble frequency and size compared to the top channel.

9.6. Conclusions

Pressure drop during Taylor flow in square channels as well as pressure fluctuations during bubble formation have been investigated. These are two key elements to understand gas and liquid flow distribution in manifolds operating in the Taylor flow regime.

Average pressure drop during Taylor flow is measured in an acrylic structure with square microchannels for both octane/air and water/air systems. Results are correlated to a semiempirical expression as that implemented by Kreutzer (2003) for circular channels. A theoretical expression for pressure drop in square channels (Eq. (9.28)) that fits well experimental data is deduced, which is based on frictional losses in the liquid phase, capillary pressure drop across a bubble and inertial and Marangoni effects. The dimensionless pressure drop depends on the Reynolds and Capillary numbers as well as dimensionless liquid slug length and bubble length and velocity. Pressure drop during Taylor flow in square channels is found to be lower than that in circular channels as suggested by Wong (1992).

An investigation on the pressure fluctuations in the gas and the liquid channels due to bubble formation is conducted in an acrylic structure with square microchannels for both octane/air and water/air systems. Pressure fluctuations are found to be dependent on liquid/gas flowrates and inertial forces apart from channel geometry and surface tension forces. Experimental pressure fluctuation magnitudes in the gas and liquid inlets are fitted to two equations as a function of the Weber number and the ratio of superficial velocities $(U_{LS}+U_{GS})/U_{GS}$. Pressure fluctuations in both channels decrease as liquid flowrate increases, which qualitatively agrees with the reduction of gas breakthrough pressure analysed in Chapter 5 as a result of decreased liquid pressure over the gas-liquid interface with increasing liquid velocity. Application of the Laplace pressure Eq. (9.11) with a contact angle for the meniscus breakthrough position of 0° and a contact angle after bubble detachment of $\theta_{initial} = 90°$ yields smaller pressure fluctuations in the gas inlet that those measured for water/air and octane/air systems as liquid and gas flowrates tend to zero. Pressure fluctuations in the liquid inlet were found to be larger than those measured in the gas inlet, which is explained by an additional viscous/frictional pressure drop component in the liquid phase as the bubble grows and partially blocks the channel.

A resistance network model is implemented for a 2-channel manifold that is used to analyse flow distribution during Taylor flow. The model has no adjustable parameters and relates pressure drop of the single and Taylor phases (including models to predict liquid slug and bubble lengths) and pressure fluctuations in gas and liquid channels with the required external resistances to avoid backflow of either phase. The model provides quantitative information for the design of manifolds to achieve uniform flow distribution in Taylor flow. According to the model, as total liquid and gas flowrates decrease, ΔP across the resistances of the single phase distributing channels ($R_{1\text{-}2}$ for the liquid phase in Figure 9.1) decreases while pressure fluctuations increase. Thus, there is a minimum value of the total gas and liquid flowrates, $Q_{T,L}$ and $Q_{T,G}$, below which backflow between parallel channels occurs.

For design purposes, the maximum pressure fluctuations expected and found for zero gas/liquid flowrates are employed. Although the model was only applied in this study to the gas or liquid phase independently, it can easily be used for both phases to take into account their interaction. The same concept can be applied to manifolds of any number of channels such as the consecutive and bifurcation structures presented in Chapter 7. In this case, the resistance of each *reaction channel* is split in three components: resistance of the single phase flow, resistance of the pressure fluctuation due to bubble formation and resistance of the Taylor flow region. A non-linear system of equations is thus obtained that can be solved iteratively.

The model is applied to the design of a 2-channel manifold that is successfully operated with octane/air and water/air systems using air flowrates in the range of 0.15-5 ml/min and liquid flowrates in the range 0.6-5 ml/min. For the system water/air, air flowrates lower than 1 ml/min resulted in the liquid phase going into the gas channel due to the compressibility of the air phase. This issue is solved placing the external resistance of the gas channel for even flow distribution very close to (but not at) the gas-liquid contacting region, so that there is little air volume to be compressed. Even flow distribution is more difficult with non-wetting or partially wetting systems because different bubble formation mechanisms in the different channels may appear, which produce different liquid slug/bubble lengths and pressure fluctuations.

Nomenclature

A	Cross sectional area of the channel, m^2.
Bo	Bond number, $\rho_L g r_h^2/\gamma$.
Ca	Capillary number based on bubble velocity, $Ca = \mu U_{L,m}/\gamma$.
Ca_L	Capillary number based on liquid slug average velocity, $Ca = \mu U_B/\gamma$.
d	Capillary diameter, m.
d_h	Diameter of the largest inscribed circle to the channel, m.
d_{hyd}	Hydraulic channel diameter, m.
e	Channel depth, m.
f	Friction factor.
$f_{Laplace}$	Constant in the Laplace pressure equation.
fz	Sampling frequency, s^{-1}.
g	Acceleration due to gravity, m/s^2.
L	Channel length, m.
L_B	Bubble length, m.
L_C	Cell length composed of one bubble plus one liquid slug, m.
L_S	Slug length, m.
N_B	Number of bubbles.
P	Pressure, Pa.
Q	Flow rate, m^3/s.
r_h	Radius of the largest inscribed circle to the channel (characteristic length), m.
R	Flow resistance, $Pa \cdot s/m^3$.
Re	Reynolds number, $Re = \rho_L r_h U_B/\mu_L$.
Re_L	Reynolds number based on the liquid slug average velocity, $Re_L = \rho_L r_h U_{L,m}/\mu_L$.
$Re_{L,d}$	Reynolds number based on channel hydraulic diameter, $Re_{L,d} = \rho_L d_{hyd} U_{L,m}/\mu_L$.
t	Time, s.
U_B	Bubble velocity, m/s.
U_{GS}	Gas superficial velocity, m/s.
U_L	Local liquid velocity, m/s.
$U_{L,m}$	average liquid slug velocity, m/s.
U_{LS}	Liquid superficial velocity, m/s.
V	Volume, m^3.
w	Channel width, m.
We	Weber number based on bubble velocity, $We = \rho_L r_h U_B^2/\gamma$.
We_L	Weber number based on liquid slug average velocity, $We_L = \rho_L r_h U_{L,m}^2/\gamma$.

Greek letters

β_L	Ratio of the liquid slug length to the cell length, $\beta_L = L_S/(L_S+L_B)$.
ΔP	Pressure drop or fluctuation, Pa.
$\Delta P^{\#}$	Dimensionless pressure drop in the capillary scale, $\Delta P r_h/\gamma$.
$\Delta P^{\#}_{\mu}$	Dimensionless pressure drop in the viscous scale, $\Delta P r_h/(\mu_L U_{L,m})$.
ϕ	Solid wall inclination at the point of contact of the three-phase contact line.
γ	Surface tension, N/m.
λ_{NC}	Non-circularity factor.
μ	Dynamic viscosity, Pa·s/m^2.
θ	Contact angle.
ρ	Density, kg/m^3.
ξ	Component of the pressure drop friction factor due to the bubbles.

Subscripts

B	Bubble
C	Cell (one bubble plus one liquid slug).
EQ	Equipartition.
Fl	Fluctuations.
Flat	Flat meniscus.
G	Gas.
hyd	Hydraulic.
Initial	Initial meniscus position after a bubble is formed.
L	Liquid.
o/a	Octane/air system.
R	Receding.
S	Liquid slug.
T	Total.
w/a	Water/air system.

Superscripts

#	Dimensionless variable.

Chapter 10

Conclusions and Future Work

"If one does not know to which port one is sailing, no wind is favourable"

Seneca

10.1. Introduction

In the present work, two different types of two-phase flow microreactors have been investigated, namely, the mesh microreactor (continuous-phase microreactor) and Taylor flow microreactor (disperse-phase microreactor). The first part of the thesis (chapters 2 to 6) investigates hydrodynamics, mass transfer and chemical reaction in the mesh microreactor as pertinent to the intended use for sequential screening of fluid-liquid reactions in both batch and flow-through modes. The second part of the thesis focuses on the scale out of single-phase (chapter 7) and two-phase (chapters 8 and 9) flow microreactors, addressing key current issues such as the effect of channel manufacturing tolerances and blockages on single-phase flow distribution and the effect of pressure fluctuations during bubble formation on liquid and gas flow distribution in manifolds that operate in Taylor flow regime. The knowledge gained on surface tension forces in the analysis of breakthrough and critical entry pressures in chapters 3-5 is applied.

10.2. Mesh Microreactor for Sequential Catalyst Screening

10.2.1. Geometry Optimisation for Even Flow Distribution and Minimum Sample Dispersion

In chapter 2, flow distribution in the mesh microreactor is investigated in order to obtain an optimised geometry that delivers the same mean residence time in all reaction paths as well as a narrow overall residence time distribution (RTD) (from inlet to outlet of microreactor). Similar mean residence times in the reaction plate improve reaction selectivity and efficiency when the reactor operates in flow-through mode. A narrow overall RTD minimises sample dispersion in

both batch (during filling/emptying stages) and flow-through modes and therefore enables an increase in the capacity for sequential kinetic screening. Main contributions in this study consist of 1) implementation of an analytical resistance network model (RNM) for a plate-type microreactor subject to assumptions that are validated via Computational Fluid Dynamics (CFD) and experimental observation. The model is successfully used to optimise the geometry of the mesh microreactor. The assumption of straight streamlines in the reaction plate used in the RNM is proved to be accurate when the plate geometry is designed for flow equipartition; 2) an easy methodology for retrieving accurate RTD curves from particle tracking data, based on implementation of proper boundary conditions for the particle release.

10.2.2. Modelling of Phase Stability in the Mesh Microreactor

Chapters 3 to 5 deal with phase stability in the mesh microreactor. This is a key aspect for the operation of the mesh microreactor where a mesh with openings separates the phases and allows interfacial mass transfer by diffusion through the openings. A mesh with straight openings enables a large open area that results in higher interfacial mass transfer than in traditional membranes. Furthermore it is easy to control which phase fills the openings of the mesh.

Chapter 3 presents a systematic methodology for determining the meniscus position, shape (area) and stability range within circular or polygonal pores having constant or tapered cross section in thin solid layers (meshes) that separate two fluid phases. Meniscus position and shape affect interfacial mass transfer. The model for a single pore is based on the variation of the system contact angle due to hysteresis and on apparent contact angle change at the pore ends (pore mouths), which significantly increase the range of pressure difference between the phases that the interfacial meniscus can withstand without breakthrough of one phase into the other (stability range). This has often been overlooked in analyses for membranes, which refer to breakthrough and critical entry to the pore pressure indistinguishably. The effect of line tension on contact angle in the context of breakthrough pressures in microscale is brought to attention for the first time. The effect of line tension on contact angle increases as the meniscus three-phase contact line contorts at the pore ends (edge effect), which results in an increase or decrease of the available range of pressure differences depending on its sign, positive or negative respectively. An analysis that indicates the wetting conditions for maximum meniscus stability is carried out in tapered circular cross section pores, which can be used to select the mesh material or coating for stability improvement as well as the mesh side on which the wetting phase should be placed for maximum stability. An equation to calculate the corner angle in a tapered polygonal pore is presented, which highlights the fact that the pore tapering angle

also affects the critical contact angle at which arc menisci develop according to the Concus-Finn condition (Concus and Finn, 1969). A generalised expression is obtained that is used to calculate the Laplace capillary pressure for systems with contact angle hysteresis in polygonal pores when arc menisci are present. This expression reduces to that presented by Mason and Morrow (1984) when the contact angle of the arc menisci and main terminal meniscus is the same. Experimental work carried out in single cylindrical and square capillaries confirmed the effect of solid wall inclination change at the pore ends on available range of pressure difference. For capillary diameters $d > 200$ μm theory predictions agree well with experimental results while for capillary diameters $d < 100$ μm the stability range of pressure difference measured experimentally is smaller than that predicted from theory, This, however, can be explained by an effect of negative line tension on contact angle. Since contact angle hysteresis is affected by surface roughness, additional experiments characterising the smoothness of the capillary corners could give further insight on whether the advancing and receding contact angles can be used at the pore ends in order to calculate breakthrough pressures.

Chapter 4 focuses on the analysis of breakthrough pressure in meshes with different design, material and opening size and shape. Experimental work was undertaken in order to detect deviations from the single pore model presented in chapter 3 and model them. These include the effect of fluid flow pressure drop along the mesh, effect of supports/foreign particles, defective pores produced during the mesh manufacture and priming operation on reduction of the meniscus stability range. A model to estimate the effective reduction of the available range of pressure difference due to fluid flow pressure drop is presented which accounts for factors such as phase heights, fluid velocity, wafer inclination, flow directions and fluids properties. In general, the single pore methodology presented in chapter 3 estimates breakthrough pressure accurately when operating with large opening meshes. The effect of supports/foreign particles on breakthrough pressure reduction was a striking discovery taking into account that mesh contamination with dust particles is very common. In those meshes with openings of comparable size to dust particles, the breakthrough pressure reduction of the wetting phase can be more than one order of magnitude. The meniscus breakthrough process that takes place when foreign particles or supports are present was considered to happen either at the pore or during the spreading. These two processes were modelled and experimentally validated using glass ballotini particles as well as meshes with built-in supports. These insights have been applied to design a mesh with improved phase stability performance. Additional breakthrough experiments, similar to those carried out with ballotini particles should be conducted with dust particles to confirm the reduction on breakthrough pressure observed in those meshes with openings of comparable size to standard dust particles (1-20 μm). Characterization of dust

particles in relation to wettability, particle geometry and size would help to better understand the limiting achievable breakthrough pressures when working in standard atmosphere.

Chapter 5 analyses the effect of fluid flow over the meniscus on breakthrough pressure for the case when the pores are filled with a gas phase. A rigorous numerical analysis is conducted that consists of solving the Navier-Stokes equations for the flow field around the meniscus, which coupled with the normal stress condition on the meniscus interface produce the meniscus shape, pressure and viscous stresses. At low *Re* and *Ca*, surface tension forces dominate and the Laplace equation for static conditions can be applied to calculate breakthrough pressure. At low *Re* and high *Ca* (*We* << *Ca*) viscous forces become dominant which may increase the breakthrough pressure by pushing the meniscus inside the pore as it grows. Under these conditions the meniscus is highly deformable. At high Weber numbers (*We* >> *Ca*) and high Reynolds numbers *Re,* inertial forces become dominant, resulting in a reduction of the breakthrough pressure due to the pressure reduction that takes place in the liquid phase above the meniscus as this grows. In this regime, the meniscus features a symmetric shape with higher curvature at the centre of the opening than at the sides. A simplified analytical solution is developed that can be applied in the inertial regime to obtain meniscus shape and breakthrough pressure under flow conditions. Results from the numerical model are validated using a test device that contains one single 2D opening (slit). Additional modelling and experimental work is required to better understand flow effect on meniscus shape and breakthrough pressure in 3D systems such as the real mesh. In this case, additional parameters such as separation between openings in both directions of the plane need to be considered. The analytical model implemented can be modified to quickly assess 3D systems.

10.2.3. Mass Transfer/Chemical Reaction in the Mesh Microreactor

Chapter 6 deals with coupled mass transfer between phases and chemical reaction for a mesh microreactor operating in batch mode with homogeneous catalyst. A model is presented that is used to obtain dimensionless parametric maps for different stoichiometry and reaction orders that determine under which conditions mass transfer resistance is negligible and chemical kinetics can be directly retrieved from conversion vs. time experimental data. If the reaction is under mass transfer control regime, new reaction conditions (initial reactant concentration ratio, phase height or solvent) that bring the system into the kinetic control regime can be obtained from these maps via an iterative procedure. These maps are created by comparing the full numerical solution to kinetic (no mass transfer resistance) and pseudokinetic limits. The pseudokinetic limit refers to a situation where there is an initial mass transfer resistance by the

excess reactant while its concentration profile is developed but the chemical reaction does not influence the way this concentration profile develops. In this case, an analytical solution to calculate the reactant's conversion versus time has been developed which allows system kinetics to be retrieved with *Da* several orders of magnitude larger than applying just the kinetic limit. The application of these parametric maps is demonstrated for two chemical reactions carried out in the mesh microreactor. More complex reactions can be analysed with the same parametric maps by considering the slowest reaction step.

The analytical solution for the pseudokinetic limit is only available for 1D geometries while a 2D axisymmetric geometry defines better the real system. For a complete characterisation of the mesh microreactor for kinetic sequential screening, additional work is required to develop dimensionless parametric maps when the reactor operates in flow-through mode or when heterogeneous catalyses are investigated. In the case of heterogeneous catalysis, the thickness of the solid catalyst coating on the mesh in addition to pore geometry and phase height determines the fastest reaction rate that can be studied in the mesh microcontactor.

10.3. Single-Phase Flow Distribution in Manifolds

The simple concept of scaling up microreactors via parallelisation (scale out) is one of the main advantages of microreaction technology, ensuring that the research carried out in a single microchannel can still be applied to the large scale device. Even flow distribution among the parallel channels and microreactor units is required to ensure that all parallel channels operate under the same conditions. Commenge et al. (2002) analysed flow distribution in a microchannel reactor but Chapter 7 presents additional contributions to the field: two different methods for designing the distributing and collecting channels, consideration of bifurcation structure, effect of manufacturing tolerances and channel blockages on flow distribution and effect of additional pressure losses on flow distribution.

Chapter 7 investigates flow distribution in the parallel channels of a manifold by implementing an analytical resistance network model that is validated via Computational Fluid Dynamics simulations and experimental work. The model can deal with circular and rectangular cross section channels of any channel aspect ratio. The model is used to optimise the geometry of two different manifold structures (consecutive and bifurcation structures) in order to achieve even flow distribution. In the consecutive structure two different approaches for even flow distribution are investigated, 1) sufficiently large distributing/collecting channels that produce a negligible pressure drop and 2) distributing/collecting channels with varying cross section. The

model allows the effect of channel variations due to manufacturing tolerances as well as channel blockages on flow distribution to be considered, which give further insight on which manifold designs perform better and are the most robust. In summary, the consecutive structure by method **1)** is suitable when manufacturing tolerances are large or uncertain, channel blockages are expected and different channel depths are possible. The consecutive structure by method **2)** is suitable when manufacturing tolerances are small and well-defined, the manifold area needs to be minimised or when a single channel depth is possible which in turn is smaller than the reaction channel width. The bifurcation structure is generally a good design but has two disadvantages: it has a large footprint area and it features many splits within each flow path, which can produce high pressure losses due to bends and splits (particularly important at higher flow rates) and can result in larger manufacturing variations at these points.

The resistance network model was further developed to deal with additional/inertial pressure losses and therefore allows flow distribution to be analysed as a function of the Reynolds number *Re*. Flow distribution results at different *Re* were compared to Femlab simulations. Inertial effects had the same trend in both cases although they were more significant in the Femlab simulations, perhaps because of the use of experimental velocity head coefficients *K* obtained for macrosystems. Flow distribution was experimentally analysed in a manifold with 8 open channels, resulting in slightly larger flow variability than that obtained from the resistance network model. However, the overall flowrate profile across the branches and the direction of the *Re* effect on flow distribution was the same as that obtained from the model.

Additional work for microreactor scale out is required for even heat flux distribution to ensure that temperatures are the same in all parallel channels and microreaction units.

10.4. Two-phase Flow Distribution in Manifolds

The knowledge gained on interfacial phenomena and single-phase flow distribution is applied to the investigation of liquid and gas flow distribution in microchannel manifolds operating in the Taylor flow regime. Even flow distribution in Taylor flow manifolds is the key issue when scaling out channels operating in this flow regime. Irreproducible bubble formation mechanism as well as pressure fluctuations during bubble formation lead to uneven liquid and gas flow distribution and bubble/liquid slug lengths.

Chapter 8 deals with bubble formation mechanisms for Taylor bubbles and the effect of different liquid/gas inlet geometries on bubble/liquid slug lengths in octane/air and water/air

systems. Two different types of liquid/gas contacting configurations were used in both circular and rectangular cross-section microchannels, namely T- and Y-shaped. All bubble formation mechanisms are classified into three different types: gas chamber formation, 2-stage bubble formation mechanism with necking process and 1-stage bubble formation mechanism without necking process. Taylor bubbles may either form at the gas inlet, or as a result of bubble pairing or/and coalescence in the main channel. Coalescence was only observed when small non-Taylor bubbles (bubble length < channel diameter) were formed, which had higher velocity than long Taylor bubbles. A Matlab script was implemented, which allowed bubble and liquid slug lengths to be measured automatically by analysing pixel intensity. In general, uniform bubble sizes were achieved except when coalescence was present. Bubble and liquid slug lengths were found to be strongly dependent on the ratio of gas to liquid superficial velocities, above all in the structures with circular channels. The structures with rectangular channels, showed a substantial dependence on gas/liquid inertial forces (increase of liquid and gas superficial velocities for a constant ratio). This is because in rectangular channels the inertial force of the incoming liquid over the bubble is smaller than in circular channels due to the flow at the corners and high liquid/gas flowrates are required to overcome surface tension forces. Surface tension and wall wetting properties can affect the type of mechanism, which was found to be less reproducible for the water/air system (higher contact angle and surface tension). It was found that the diameter of the gas inlet greatly affected the sizes of the formed bubbles while the liquid inlet diameter had a very small effect. Experimental bubble lengths are fitted to an equation that considers three dimensionless numbers, ratio of superficial velocities, *We* and *Bo* numbers. The equation deduced by Thulasidas et al. (1995) to calculate the bubble to liquid slug length ratio in circular microchannels is applied to accurately estimate liquid slug length from bubble length in square microchannels under assumptions that are experimentally proved to be valid. These results are used below to fully predict pressure drop in Taylor flow. They are also used in a resistance network model to predict liquid/gas flow distribution in a manifold during Taylor flow.

Pressure drop during Taylor flow and pressure fluctuations during bubble formation in both the liquid and the gas channels were investigated in a square channel microstructure and results are presented in chapter 9. An equation for average pressure drop in Taylor flow in square cross section capillaries is obtained from the experimental data following the methodology by Kreutzer (2003) for circular capillaries, which accounts for frictional losses of the liquid slugs and capillary pressure losses along the bubbles. An equation (Eq. 9.28) that is fully based on theoretical considerations about pressure drop across single bubbles, frictional losses in the liquid phase, inertial and Marangoni effects, is developed that predicts accurately experimental results on pressure drop. Pressure fluctuations in the liquid and gas channels during bubble

formation are experimentally measured at different gas and liquid superficial velocities and fitted as a function of We and ratio of gas to liquid superficial velocities. Pressure fluctuations in both liquid and gas channels decrease as the liquid superficial velocity increases as expected according to the modelling conducted in chapter 5 to predict bubble breakthrough pressure under flow conditions. Results at low gas and liquid flowrates are found to be of similar magnitude to those obtained when applying the Laplace equation for static conditions. Pressure fluctuations in the liquid inlet were found to be larger than those measured in the gas inlet. This is likely to be the result of additional pressure losses due to partial channel blockage as bubble forms.

A model for assessing flow distribution in manifolds operating under Taylor flow regime was implemented. Equations for pressure fluctuations obtained in chapter 9 and Eq. (9.28), which fully predicts pressure drop in Taylor flow using the equations obtained in chapter 8 for bubble/liquid slug length, are inputs to the model. This model is able to predict the required external resistances to avoid channel backflow (channel "crosstalk") or the minimum liquid and gas flowrates at which a microchannel manifold geometry can be operated without backflow as a function of pressure fluctuations during bubble formation and single-phase and two-phase flow pressure losses. This is the first available model able to predict channel backflow as a function of pressure fluctuations during bubble formation. An important conclusion from this model is that using a bifurcation structure, assuming no channel dimension variations and identical bubble formation mechanism in both channels, the average liquid and gas flowrates should be identical in both parallel microchannels at any liquid/gas flowrates provided that the backflow point is not reached. This highlights the importance of having reproducible bubble formation mechanism under identical liquid/gas flowrate conditions, which is not always the case for non-wetting liquids as observed in the water/air system. Different bubble formation mechanisms for identical liquid/gas flowrates result in different bubble/liquid slug lengths that will generate different pressure drops and will therefore unbalance the liquid/gas distribution.

Further analysis on pressure fluctuations during bubble formation is required to understand the exact difference between the pressures in the gas and liquid ports at each point of the fluctuations. This can be investigated by measuring the differential pressure between the gas and liquid inlets during bubble formation, ensuring that the pressure connections to the pressure transducer allow a fast response in both lines. The flow distribution model for Taylor flow presented in chapter 9 can be extended to consider different manifold geometries and multiple parallel reaction channels. In this case, a Monte Carlo approach could be applied to deal with different bubble formation stages at each parallel channel.

Appendix

Appendix 2A

Matlab Program for Flow Distribution in the Reaction Plate of the Mesh Microreactor

```
% Consecutive structure. Implementation of the resistance network model.
% Analysis of flow distribution in Plate of Mesh Microreactor.
% DIA does reference to the width of the channel and DEPTH to the other dimension.

clear CHAN;
clear M;
clear Q;
clear S;
clear R;
clear d;
clear dep;
clear DIA;
clear DEPTH;
clear LEN;
clear equi;
clear Rm;
clear VEL;
clear AREA;
clear tresid;

% INPUT DATA.

% Mode 1 is to work with resistances.
% Mode 0 is to work only with ratios of resistances.
mode = 1;
mode_2 = 1; % This mode always is set up at 1.

% Number of fluid paths in parallel reaction plate.
n=200;
CHAN=[1:n]';
omega = pi/(4*n);  % Radians per fluid path considering 45 degrees quadrant.

 % Length of the reaction fluid paths for quadrant shape, mm.
lm = 32;
l0 = 1; % Approximate.
% Extra length of the distributing and collecting channels, mm.
lexd=pi*(lm/1000)/(4*n);
lexc=pi*(lm/1000)/(4*n);

 % Desired diameters for distributing (1), reaction(2) and collecting (3) microchannels, microns.
d(1)=1000;
d(2)=omega*lm*1000;
d(3)=1000;
% Desire depth for distributing (1), reaction (2) and collecting (3) microchannels, microns.
dep(1)=150;
```

```
dep(2)=100;
dep(3)=150;
% The quadrant shape is the initial shape even when designing for same residence times.

 % Total flow rate to distribute in half the quadrant, ml/hr.
qt = 60;
% Equipartition flow.
Qeq = qt/n;
QEQ = zeros(n);
QEQ(:)=Qeq;
% Liquid viscosity = vis[=]kg/(ms). S.I
vis=0.001;

% Calculation of width, depth and lengths

% Length of the reaction channels.
LEN=zeros(3,n);
LEN_R = zeros (1,n);  % Vector with the recalculated values of path lengths.
LEN_R(:)=lm;

 for i=1:3
   for j=1:n
      DIA(i,j) = d(i);
      DEPTH(i,j)=dep(i);  % Tolerances not considered in depths.
   end
end

% When flowrates are solved for a fixed geometry, the loop while-end is not required.
while abs(LEN(2,n)-LEN_R(n))>0.001

% Lengths calculated in mm.
LEN(1,1)=lexd;
LEN(2,1)= LEN_R(1);
LEN(3,1)=lexc;
LEN(1,:)=0;

for j=2:n
   LEN(2,j) = LEN_R(j);
end

for j=1:(n-1)
   LEN(3,n-j+1) = sqrt((LEN(2,j+1)*sin(omega))^2+(LEN(2,j+1)*cos(omega)-LEN(2,j))^2);
end


% Calculation of the resistances.

% Nomenclature of the resistances RAi=R(1,j), Rmi=R(2,i) and RBi=R(3,j).

for i =1:3  % 1 (distributing), 2(reaction), 3(collecting).
   for j=1:n   % R(1,1) and R(3,1) are for the elongation of the dist. and coll. channels.
      % Calculation of the resistances: Hagen Poiseuille, kg/s*m4.

    if i ==1
      R(i,j) = 0;
```

```
    else
      if i == 2
        R(i,j)= 12*vis*(log(lm/1000)-log(l0/1000))/((DEPTH(i,j)*10^(-6))^3*omega); % S.I.
      else
        R(i,j)=resistance(vis,LEN(i,j), DEPTH(i,j),DIA(i,j)); % S.I.
      end
    end

    end
end

% Resolution of the linear system of equations.
for  i=1:(n-1)
   for j=1:n

      if j<i
         M(i,j)=R(3,n-i+1);
      elseif j==i
         M(i,j)=R(3,n-i+1)+R(2,i);
      elseif j==i+1
         M(i,j)=-(R(1,i+1)+R(2,i+1));
      elseif j>i+1
         M(i,j)=-R(1,i+1);
      end
   end

   S(i)=0;

end
% Last row of the matrix and the solution.
M(n,:)=1;
S(n)=qt;

Q=inv(M)*S';

for i=1:n
   % equi is the FD parameter.
   equi(i)=100*abs(1-abs(Q(i)-Qeq)/Qeq);
end

equi_min=min(equi);

% Calculation of the residence times in reaction microchannels.
%This is the effective diameter of the fluid paths considering that this depends on the length of
% the path in mm as LEN.
DIA(2,:)=omega*(LEN(2,:)+l0)/2;
AREA = DIA(2,:).*DEPTH(2,:).*10^(-9)    % Area, m2.
VEL=(Q./AREA').*10^(-6)./3600;          % Velocity, m/s.
% Average cross section of paths in initial quadrant shape, m2.
section_average=dep(2)*10^(-6)*omega*(lm+l0)*0.001/2;
% Desired residence time, s.
tr_desired=(lm-l0)*0.001/(Qeq*10^(-6)/3600/section_average);
LEN_R=l0 + (tr_desired.*Q./(DIA(2,:)'*dep(2))./3600.*10^6)';   % mm.

end
```

```
tresid=((LEN_R'-l0)./VEL)/1000          % Residence time, s.

% Statistic analysis of the data.
tmean = mean(tresid);              % Mean of the residence times.
s_2 = (1/n)*sum((tresid-tmean).^2);    % Sample variance.
s = sqrt(s_2);                 % Sample standard deviation.

% Calculation of the total pressure drop.
ap=0   % Initialization
for i=1:(n-1)
   ap=ap + 2.777777*10^(-10)*((qt-Q(i))*R(1,i+1));
end
ap=ap + (qt*(R(1,1)+R(3,1)) + Q(n)*R(2,n))*2.777777*10^(-10);

% Results.
 results = [CHAN Q tresid]
Qeq
tmean, s_2, s, ap
[xm_2,im]=max(tresid);
[xm_3,im]=min(tresid);
ends=[xm_2,xm_3]
equi_min
ratio=(R(1,2)./R(2,1))

% Graphic representation.
[xm_1,im]=max(Q);
subplot(2,1,1), plot(CHAN,Q);
hold on;
plot(CHAN,QEQ);
xlabel('Fluid Path Number');
ylabel('Flow rate');
axis([1,n,0,(xm_1)*1.1]);
hold off;

subplot(2,1,2), plot(CHAN,tresid);
hold on
TMEAN=zeros(n); % To represent the mean residence time.
TMEAN(:)=tmean;
plot(CHAN,TMEAN);
xlabel('Fluid Path Number');
ylabel('Residence time, s');
hold off;
```

Appendix 2B

Matlab Program for Plate Geometry under Flow Equipartition

```
% This program calculates the geometry of the mesh microreactor by a simplified Resistance
Network Method (RNM).
% Model considers flow equipartition.
% S.I units if not specified otherwise.

format long e;
quadrant = pi/4;
N = 200; % N is the number of fluid paths + 1.

sector_rad = quadrant/(N-1);
vis = 0.001;    % Fluid viscosity.
width = 0.0008; % Width of the collecting channel.
depth = 0.001 ; % Depth of the collecting channel.
heightsi = 0.00005; % This is half the phase height.
Wb = zeros (1,N); % Widths of the collecting subregions.
Db = zeros (1,N); % Depths of the collecting sublenghts.
Lb = zeros (1,N); % Sublengths of the collecting channel.
Lr = zeros(1,N); % Lengths of the reaction paths.
Lr(N) = 0.03325; % Length of the first segment.
PHI = zeros (1,N); % Angle in radians for all the points.
PHI(N) = 0;
LANDA = zeros (1,N);  % Matrix of the non-circularity coefficients.
LANDA(1,:) = (3/2)/((1-0.351*width/depth)^2*(1+width/depth)^2);
Wb(1,:) = width;
Db(1,:) = depth;

for j=(N-1):-1:1
   PHI(j) = PHI(j+1)+sector_rad;
   options = optimset('Largescale','off');
   x = fzero('f',Lr(j+1),options,j,vis,Lr(j+1),PHI(j+1),PHI(j),LANDA(N-j+1),Db(N-j+1),Wb(N-
    j+1),heightsi,sector_rad);
   Lr(j) = x;
   Lb(N-j+1) = sqrt((Lr(j+1)*sin(PHI(j+1))-Lr(j)*sin(PHI(j)))^2+(Lr(j+1)*cos(PHI(j+1))-
Lr(j)*cos(PHI(j)))^2);
end
```

Function f.m

```
function y = f(x,j,vis,L,PHIj1,PHIj,LANDAf,Dbf,Wbf,height,sector_rad)

y =(j*32*vis*(sqrt((-L*sin(PHIj1)+x*sin(PHIj))^2+(L*cos(PHIj1)-x*cos(PHIj))^2))*LANDAf
*(Dbf+Wbf)^2)/(4*Dbf^3*Wbf^3)-3*vis/(2*height^3*sector_rad)*(log(L)-log(x));
```

Appendix 2C

Solution of Fluid Flow in Mesh Microreactor via Femlab ®

Draw mode: The 3D geometry is drawn by using 2D *work planes* added in the draw menu. For the mesh microreactor geometry, three *x-y* planes are defined. The first work plane is defined at $z = 0$ and contains a 45-degree sector of a circle of radius $L^{\#} = L/H = 330$ (see Figure 2C.1a); the second work plane is defined at $z = 13$ and is another 45-degree sector of a circle of radius of $L^{\#} = 320$ and without the region that corresponds to the inlet (see Figure 2C.1b); the third work plane is defined at $z = 13$ and it is only the part that represents the collecting channel without the region of the outlet (dash region in Figure 2C.1c).

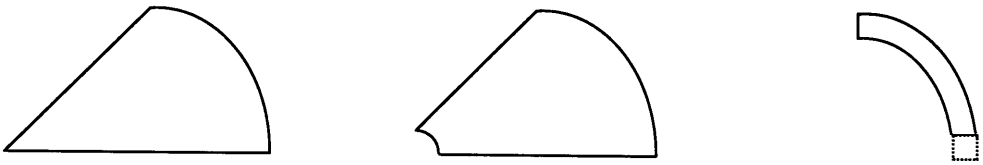

a) b) c)

Figure 2C.1. 2D *work plane* geometries utilised to construct the final 3D geometry for the mesh microreactor: a) *work plane 1*, b) *work plane 2* and c) *work plane 3*.

Work plane 1 is extruded 13 units from z = 0 to z = 13, *work plane 2* is extruded 12 units from $z = 13$ to $z = 1$ and *work plane 3* is extruded 5 units from z = 13 to z = 8 (for a collecting channel of $E^{\#}_{B} = 7$) resulting in three solids EXT1, EXT2 and EXT3. The following operations are conducted to obtain the final 3D solid: EXT1-EXT2 = CO1 and CO1-EXT3 = Final_Solid.

Mesh Mode: FEMLAB 3.0a generates meshes of isotropic tetrahedrons in size. Isotropic meshing results in a very large number of elements considering that the geometry features a large aspect ratio x and y ($L^{\#} = 330$) to z ($H^{\#} = 1$) and at least 2 elements are used in the z direction of the thin plate. This leads to memory problems when solving the Navier-Stokes equations with four dependent variables U_x, U_y, U_z and P. The number of tetrahedral elements is reduced to avoid memory issues by scaling the geometry in the z direction by a factor 5 to 10 to

produce *non-isotropic* second order Lagrange p2-p1. Meshing functions are used to limit the element size along certain edges and faces.

The memory usage depends upon number of nodes, number of dependent and independent variables, numerical method and sparsity of system matrices which is governed by the shape of the geometry and mesh (spheres and cubes increase the memory requirement). The following considerations help memory management: a) reduce original size of geometry by making use of symmetry planes, b) avoid small objects and singular geometries and c) keep a high mesh quality, which reduces memory requirement when using an iterative solver).

Boundary Mode: The Hagen Poiseuille parabolic velocity profile given by Eq. (2C.1)is used as boundary condition in the inlet channel of radius $r^{\#} = 5$ (see Figure 2C.2). The average and also characteristic velocity is $U_0 = Q_T/(\pi r^2)$ so that $U^{\#}_0 = 1$.

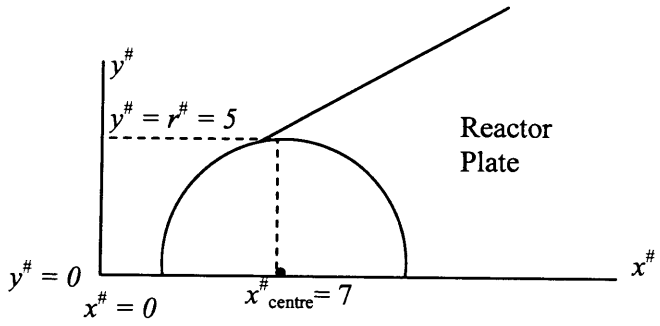

Figure 2C.2. Inlet channel to the reaction plate of the mesh microreactor.

$$U_z^{\#} = 2U_0^{\#}(1-((x^{\#} - x^{\#}_{centre})^2 + (y^{\#} - y^{\#}_{centre})^2)/r^{\#2}) \qquad (2C.1)$$

The rest of boundary conditions consider: straight out flow, $P = 0$ for the outlet, slip/symmetry boundary for the symmetry boundary and no-slip condition for all walls.

Subdomain Mode: The properties of the fluid in the fluid volume are defined in Subdomain→ Subdomain Settings. Comparing the coefficients of the dimensionless form of the Navier-Stokes equation with that available in FEMLAB, ρ is equivalent to Re and μ is equivalent to 1 while gravity force is not considered.

Solve Mode: The iterative solver GMRES (less memory demanding) is utilised with incomplete LU preconditioning, non-linear tolerance of 1E-7 and drop tolerance = 0.0007 (damping factor close to 1 and nito close to 4.8 to ensure convergence).

Appendix 2D

Interpolation of Geometry Obtained via Resistance Network Model into Femlab

```
% This file interpolates (x,y) data in order to plot a 2D profile which can then be used to
% generate a solid plane in Femlab.
% Some Femlab functions such as geomspline only work with Femlab running under Matlab.
% Page 28 on the Matlab interface Guide.

% Open data files to retrieve the x and y values of the profile.

[file_1,error_op_1] = fopen('X_DATA2.txt')
[file_2,error_op_2] = fopen('Y_DATA2.txt')
[Xdata,COUNT_1]=fscanf(file_1,'%lf',[1,inf]);
[Ydata,COUNT_2]=fscanf(file_2,'%lf',[1,inf]);

 % Close the data files.
error_cl_1 = fclose(file_1);
error_cl_2 = fclose(file_2);

% Change units.
xvalue = 10.*Xdata;
yvalue =10.*Ydata;

X = [xvalue;yvalue];
plot(X(1,:),X(2,:), 'ro');
c = geomspline(X,'splinemethod','uniform','closed','off');
hold on;
geomplot(c,'pointmode','off')
axis equal

% c is a open curve and it is closed by connecting the first and last points.
c2 = curve2([X(1,1) X(1,end)],[X(2,1) X(2,end)]);

% This geometry can now be converted into a 2D solid (surface) and imported to Femlab ->
% Import -> Geometry objects-> s
s = geomcoerce('solid',{c,c2}); % The interpolated curve and the curve c2 (line) are joined
% together forming a solid.
hold on
geomplot(s)
axis equal

% This solid can also be directly stored into the fem structure in either the draw field or the
% geom field (analysed geometry).
```

Appendix 2E

Residence Time Distribution in 2D Laminar Flow

For validation of the particle tracking approach considered in the analysis of the mesh microreactor a 2D simple case is analysed. Fluid flow between parallel sheets as shown in Figure 2E.1 features straight streamlines and an analytical solution for the residence time distribution of the fluid elements.

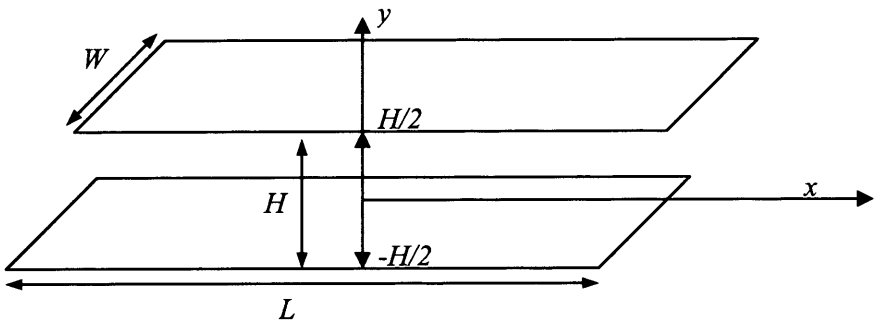

Figure 2E.1. Flow between parallel sheets.

Eq. (2E.1) is the velocity profile for flow between parallel sheets. The reactor space time $\tau = V/Q_0 = V/(U_{x,mean}WL)$ is always coincident with the mean time of the RTD.

$$U_x = \frac{\Delta P \cdot H^2}{8\mu}\left[1-\left(\frac{y}{H/2}\right)^2\right] = \frac{3}{2}U_{x,mean}\left[1-\left(\frac{x}{H/2}\right)^2\right] = \frac{3Q_0}{2WH}\left[1-\left(\frac{y}{H/2}\right)^2\right] \qquad (2E.1)$$

The time of passage of an element of fluid at a distance y (or $-y$) is given by Eq. (2E.2) since the fluid elements have a constant velocity along the reactor, U_x, as a function of their y position.

$$t(\pm y) = \frac{L}{U_x(y)} = \frac{2WHL}{3Q_0}\left(\frac{1}{\left[1-(y/(H/2))^2\right]}\right) = \frac{2\tau}{3}\frac{1}{\left[1-(y/(H/2))^2\right]} \qquad (2E.2)$$

The fraction of total fluid passing between y and $(y + dy)$ and $-y$ and $(-y\text{-}dy)$ is expressed by Eq. (2E.3). The factor 2 indicates that there are two differentials with the same velocity at $U_x(y) = U_x(-y)$. To evaluate the integral the limits would be from $y = 0$ to $y = H/2$.

$$\frac{dQ}{Q_0} = \frac{U_x(y)W2dy}{Q_0} = \frac{U_x(y)W2dy}{U_{x,\text{mean}}WH} = \frac{U_x(y)2dy}{U_{x,\text{mean}}H} \tag{2E.3}$$

A time differential is written as,

$$dt = \frac{16y\tau}{3H^2(1-(y/(H/2))^2)^2}dy \tag{2E.4}$$

$$dt = \frac{12t^2 ydy}{\tau H^2} \tag{2E.5}$$

The fluid fraction is related to the fraction of the fluid with residence time between t and (t + dt).

$$\frac{dQ}{Q_0} = \frac{L}{t(y)}\frac{W2dy}{Q_0} = \frac{LW}{tQ_0}\frac{\tau H^2}{12t^2 y}2dt \tag{2E.6}$$

$$\frac{dQ}{Q_0} = \frac{2\tau^2 H}{6t^3\left(H^2(3t-2\tau)/(3t)\right)^{0.5}} = \frac{2\tau^2}{6t^3\left((3t-2\tau)/(3t)\right)^{0.5}}dt \tag{2E.7}$$

By definition, $\mathbf{E}(t)$ is given by

$$\mathbf{E}(t) = \frac{2\tau^2}{6t^3\left((3t-2\tau)/(3t)\right)^{0.5}} \tag{2E.8}$$

The function $\mathbf{E}(t)$ is made dimensionless by use of the dimensionless time, t/τ, to obtain Eq. (2E.9).

$$\mathbf{E}(t/\tau) = \frac{2}{6(t/\tau)^3\left((3t/\tau-2)/(3t/\tau)\right)^{0.5}} \tag{2E.9}$$

The function $\mathbf{E}$ tends to infinity as t/τ approaches 0.6667 (see Figure 2.9).

Appendix 2F

Particle Tracking in 2D Laminar Flow

```
% Calculation of the Residence Time Distribution via particle tracking for 2D laminar flow.
clear particles
ydivisions = 100000;
len=1;
Umax = 1;
tmean=len/(Umax*2/3);
Rad = 0.50;
ri=-0.50;
rf=0.50;
step = (rf-ri)/ydivisions;
r=[ri+step:step:rf-step];
U=Umax*(1-(r./Rad).^2);
T=len./U; % Vector that contains the residence time for each initial position.
T=T./tmean;
times=3;
tmax=times*len/(Umax/1.5)/tmean;
tmin=min(T);
intervalos = 1000; % Discrete intervals for E function.
intervaltime = (tmax-tmin)/intervalos;

media = 0;
ratio = ones(1,ydivisions-1);
particles = 0;
stdev = 0;
stdev2=0;
for i = 1:ydivisions-1
  if i ==1
       ratio(1) = 1; % The number of particles released at the location with lowest velocity is
       normalised to 1 (close to the wall).
  else
    % Variable ratio(i) gives the number of particles at position i with respect to position 1.
    ratio (i) = U(i)/U(1);
  end
    media = media +ratio(i)*T(i); % Particles from same position have the same res. time.
    stdev =stdev + ratio(i)*T(i)^2;
    particles=particles+ratio(i); % Total number of particles N.
end
%This mean is correct because the time for all particles is known.
media = media/particles;
% The standard deviation can be calculated in both ways.
stdev = sqrt(stdev/particles - media^2);

% Density function.
density=zeros(intervalos,1);
for i=1:ydivisions-1
% position(i) stores the position of the time interval that corresponds to particles in location i.
  position = 1+round((T(i)-tmin)/(intervaltime));
```

```
  if position>intervalos

  else
    % Density contains the number of particles within the time interval numbered position.
    density(position)=density(position)+1*ratio(i);
  end

end

% Now, the density function E is normalised so that the area under the curve is 1.
for i=1:intervalos
  density(i) = density(i)/(intervaltime*particles);
end

Tfinal=[tmin:intervaltime:tmax-intervaltime]';

plot(Tfinal,density);
xlabel('standard deviation');
ylabel('density');
results=[Tfinal density];
media1=0;
area = 0;
for i=1:intervalos
  media1=media1+density(i)*Tfinal(i)*intervaltime;
  area = area+density(i)*intervaltime;
end

plot(Tfinal,density);
axis([0 5 0 5]);
xlabel('Dimensionless time');
ylabel('E');

% Comparison with analytical expression for E(t).

den=2*1^2./((6.*Tfinal.^3).*((3.*Tfinal-2*1)./(3.*Tfinal)).^0.5);

den;
hold on
plot(Tfinal,den,'r')

mediabuena=0;
divisor=0;
for i=1:intervalos % First interval with infinite density is removed
  mediabuena=mediabuena+den(i)*Tfinal(i)*intervaltime;
  divisor=divisor + den(i)*intervaltime;
end
```

Appendix 2G

Initial Conditions for Particle Tracking - Femlab

```
% This program sets up the initial distribution of particles, run the postpart function to retrieve
the residence time of each particle that reaches the collecting channel.

clear CO
clear T
ti=0;
tf=3500;

% Positions of released particles.
 % The released particles are in the same radial position (start of active region).

radius=55.6;
num=201;
phi=linspace(0,0.78539,num); % Generates num points between 0 and 0.78539 rad (included).
phi(length(phi))=[]; %This eliminates the particles at the wall that have zero velocity.
x=radius.*cos(phi);
y=radius*sin(phi);
COxy=[x;y]
zlocations = 15;  % Layers in the phase height of H = 100 microns.
zmin = 12;    % z at the bottom of reaction plate.
zmax = 13.0;    % z at the top of reaction plate.
delta = (zmax-zmin)/(zlocations+1);
z=linspace(zmin+delta,zmax-delta,zlocations);

for i=1:length(z)
   zvector=z(i).*ones(1,length(COxy));
   COintermediate=[COxy;zvector];
   if i==1
      CO = COintermediate;
   else
      CO=[CO,COintermediate];
   end
end

% Number of positions where particles are released ((num-1)*zlocations).
Ilocations = length(CO);


% Small time step to resolve most of the particles (step = 1/500*tmean or smaller).

step=2;
time1=[ti:step:tf];
% Different time steps at different times can be used in those regions with high velocity
% gradient in order to improve accuracy.
%time2=[tf:step2:tf2];
%time3=[tf2:step3:tf3];
%time3=[tf3:step4:tf4];
%time4=[t4:step5:tf5];
```

```
time=[time1];
intervals = length(time)

% M is a 3D matrix with positions of all particles at different time steps: 3 rows that are x, y and
% z coordinates.
% Columns for each particle and 3rd dimension for diff. time steps.
% Scheme 3 corresponds to 2nd order Runge-Kutta.
M = postpart(fem,'t',time,'scheme',3,'partscoord',CO, 'anim','off');

% When 'anim' is on, the next two lines must be active to record videos.
% movie(gcf,M)
% movie2avi(M,'IMRET_video_0-1_quadrant')
```

Appendix 2H

Residence Time Distribution in Mesh Microreactor

```
% This program calculates the Residence Time Distribution in the mesh Microreactor from the
matrix that contains residence time of each of the released particles (obtained from postpart.m).

clear density

% Ilocations is the number of locations where particles are released.
% Ilocations1 is the number of locations from which particles arrived.
% particles is the number of particles that arrived accounting for velocity correction.
% particles_released is the number of particles released accounting for velocity correction.

% Retrieval of the velocity components for all initial positions from Femlab.
Ux=real(postinterp(fem,'u',CO,'ext',1));
Uy=real(postinterp(fem,'v',CO,'ext',1));
Uz=real(postinterp(fem,'w',CO,'ext',1));

% (CO(1,:)./modulus)i + (CO(2,:)./modulus)j is the unit perpedicular vector to inlet plane
modulus = sqrt(CO(1,:).^2+CO(2,:).^2);

% U is a vector with the initial velocities perpendicular to the inlet plane of all the particles.
U= Ux.*CO(1,:)./modulus+Uy.*CO(2,:)./modulus;

% The time for each particle to cross a specific boundary.
radius = 320;
T = zeros (1,Ilocations);
for i =1:Ilocations
  for j = 1:intervals
    if M(1,i,j)>200
      y_channel = sqrt(radius^2-M(1,i,j)^2); % For quadrant shape it is the equation of a circle.
      % (-0.00030615*M(1,i,j)^2+0.038283*M(1,i,j)+26.621709)*10; % Specific geometry.
      if M(2,i,j)>y_channel %Particle has reached the collecting channel
        T(i) = step*j;
        break
      else
        T(i)=0;
      end

    end
  end
end

tmean=1016.27;

[m,n]=min(U)
particles_released=0;
ratio = ones(1,Ilocations);
for i=1:Ilocations
  ratio (i) = U(i)/U(n);
```

```
   particles_released=particles_released+ratio(i);
end

Tfind=find(T(:)==0);
Ilocations1=Ilocations-length(Tfind);
T(Tfind)=[]; % Removal of those particle that did not reach the collecting channel.
U(Tfind)=[]; % Removal of those particle that did not reach the collecting channel.
ratio(Tfind)=[];
trial=length(T);

% Residence time is made dimensionless with respect to the space time tau = V/Q.
T=T./tmean;
% The maximum time considered is this number of times more than the mean residence time.
times=5.0;
tmax=times;
tmin=min(T);
intervalos = 100; % Discretised intervals for E function.
intervaltime = (tmax-tmin)/intervalos;
media = 0;
particles = 0;
stdev=0;
stdev2=0;
for i = 1:Ilocations1
      media = media +ratio(i)*T(i);
      particles=particles+ratio(i);
end

media = media/particles_released; % The mean is not 1 because not all the particles arrive.

density=zeros(intervalos,1);
suma=0;
for i=1:Ilocations1
  position = 1+fix((T(i)-tmin)/(intervaltime)); % fix function instead of round
  if position>intervalos

  else
     % ratio contains the particles released from each Ilocation.
     density(position)=density(position)+1*ratio(i);
  end

end

 % Area under the curve from t=0 to t=inf is 1.
for i=1:intervalos
  density(i) = density(i)/(intervaltime*particles_released);
end

Tfinal=[tmin:intervaltime:tmax-intervaltime]';

% Plotting the data.
plot(Tfinal,density);
xlabel('standard deviation');
ylabel('density');
results=[Tfinal density];
media1=0;
```

```
area = 0;
for i=1:intervalos
  media1=media1+density(i)*Tfinal(i)*intervaltime;
  area = area+density(i)*intervaltime;
end
media, media1

plot(Tfinal,density);
axis([0 3.5 0 6]);
xlabel('Dimensionless time');
ylabel('E');


% Analytical expression of E(t) for 2D laminar flow.
den=2*1^2./((6.*Tfinal.^3).*((3.*Tfinal-2*1)./(3.*Tfinal)).^0.5);

hold on
plot(Tfinal,den,'r')

mediabuena=0;
divisor=0;
for i=2:intervalos
  mediabuena=mediabuena+den(i)*Tfinal(i)*intervaltime;
  divisor=divisor + den(i)*intervaltime;
end
```

Appendix 3A

Meniscus Shape in Circular Cross Section and Tapered Pores under Gravity

In cylindrical or circular tapered pores, the meniscus is axisymmetric, which means that the 3D shape is generated by rotation of a 2D $y(x)$ profile around the y-axis. According to Figure 3A.1, R_1 is the radius of curvature of the profile at the point in question, P, on the paper plane. R_2 is chosen on the plane perpendicular to that of the paper and, for axisymmetric figures, it is given by extending the normal to the profile until it cuts the axis of revolution (y-axis).

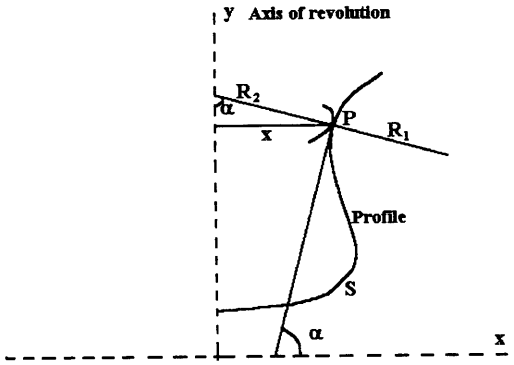

Figure 3A.1. Radii of curvature for a 2D axisymmetrical surface.

The definition of radius of curvature R_1 at the point P is given by Eq.(3A.1), where α is the angle of the tangent to the profile in point P with the x-axis and S is the arc length, as given by Bronshtein and Semendyayev (1997).

$$\frac{1}{R_1} = \frac{\partial \alpha}{\partial S} \tag{3A.1}$$

For an axisymmetric shape, the second radius of curvature, R_2, can simply be written as a function of the co-ordinate x and angle α according to Figure 3A.1, obtaining Eq.(3A.2).

$$\frac{1}{R_2} = \frac{\sin \alpha}{x} \tag{3A.2}$$

Substituting Eqs. (3.14), (3A.1) and (3A.2) into Eq. (3.6), taking ΔP_0 by Eq. (3.15) and applying a dimensionless analysis with the radius at the lower part of the pore r_{lower} as the characteristic length, Eq. (3A.3) is obtained. Eqs. (3A.4) and (3A.5) complete the set of three ordinary differential equations giving the relationship between x, y and α with S. The Bond number, Bo, which represents the ratio of gravitational to surface tension forces, is given by Eq. (3.21).

$$\frac{d\alpha}{dS^{\#}} = Bo\left(h^{\#}_{0,\text{rise}} + y^{\#}\right) - \frac{\sin\alpha}{x^{\#}} \tag{3A.3}$$

$$\frac{dx^{\#}}{dS^{\#}} = \cos\alpha \tag{3A.4}$$

$$\frac{dy^{\#}}{dS^{\#}} = \sin\alpha \tag{3A.5}$$

This system of ODEs is subjected to the initial conditions ($S = 0$, apex of meniscus): $x = 0, y = 0$ and $\alpha = 0$, (Aguilera and López, 2003). In tapered pores/capillaries, the stable configuration shown in Figure 4b is considered. The angle α at the pore wall ($x = r = r_s + h\tan|\phi_{Int}|$) is given by $\alpha = 90°\text{-}\theta_{App} = 90°\text{-}(\theta + |\phi_{Int}|)$, where θ is the contact angle of the wetting phase with the solid wall. The solution of the parametric system of Eqs. (3A.3)-(3A.5) gives simultaneously the meniscus profile $y^{\#}(x^{\#})$ together with the capillary rise $h^{\#}_{0,\text{rise}}$ (pressure difference at the meniscus apex expressed as length from a flat interface to the meniscus apex). For tapered pores, if line tension effects are important (at micro/nano scale or substantial surface roughness and heterogeneity) the actual contact angle θ is dependent on capillary radius r (see Eq. (3.9)) that depends on the three-phase contact line height h (see Eq. (3.20)), given by Eq.(3A.6). It is important to note that $h^{\#}_0$ is the actual height of the meniscus apex from the small pore opening and it is only equal to $h^{\#}_{0,\text{rise}}$ (pressure difference at the meniscus apex expressed as height) for the capillary rise experiment. In the case of a mesh pore, they are related by Eq. (3A.7).

$$h^{\#} = h^{\#}_0 + y^{\#}_{\max} \tag{3A.6}$$

$$h^{\#}_0 = h^{\#}_{0,\text{rise}} - \frac{\Delta P^{\#}_{C,NW}}{Bo} \tag{3A.7}$$

In order to find the meniscus profile and position the following iterative procedure is used: a value of $h^{\#}$ in equilibrium is assumed, $x^{\#} = 1 + h^{\#}\tan\phi_{Int}$ is now fixed, θ is calculated (if

necessary) via Eq. (3.9) if θ_Y, γ and σ are known, the boundary condition $\alpha(x^{\#} = r^{\#})$ is determined, meniscus profile and $h^{\#}_{0,rise}$ are solved simultaneously via Eqs. (3A.3)-(3A.5) and the assumed value of h is checked via Eq (3A.6). This new value of h can be used in the next iteration the required tolerance is achieved. Asekomhe et al. (2003) solved the meniscus rise in conic capillaries under gravity in order to estimate the line tension using experimental data from the capillary rise for which by minimizing an objective function defined as the error between the calculated endpoint values of the hypothesized interface and the measured ones.

The matlab code below solves the system of Eqs. (3A.3)-(3A.5).

File PrMen2DIM

```
% PrMen.m File contains the model of the meniscus profile.
% Dimensionless equations.
% Definition of the function
function Vpoint=PrMen2DIM(S,V);
% Bond Number
Bo=0.02475946;
% Dimensionless meniscus height in the apex with respect to the pore
radius
h=78.776978;
% Differential equation system
Vpoint=zeros(3,1);
Vpoint(1)=sin(V(3));
Vpoint(2)=cos(V(3));
Vpoint(3)=Bo*(h+V(1))-sin(V(3))/V(2);
```

File PrMen2IBDIM.m

```
% Simulation conditions.
% Beginning of the simulation. Dimensionless Arc lenght (S) with
% respect to pore radius.
So=0
% End of simulation.
Sf=1.41
% Initial Conditions of y, x and alfa respectively.
Vo=[0 0.000001 0]
% Function used to solve the differential equation.
% y#=V(1), x#=V(2), alfa#=V(3).
[S,V]=ode45('PrMen2DIM',[So,Sf],Vo)
% Graphic representation.
figure;
plot((V(:,2)-0.000001),V(:,1),'r'), grid;
xlabel('x#');
ylabel('y#');
```

Appendix 3B

Critical Filling/Breakthrough Pressures in Axisymmetric Pores with Round Ends

If the corners of the pores are geometrically round and of comparable radius R_{Cor} to the capillary radius r, a similar analysis to that by Purcell (1949) for doughnut-shaped pores can be applied to calculate the pressure difference at which breakthrough of each phase takes place. For the case represented in Figure 3B.1 the radius of the meniscus at the point of contact of the three-phase contact line is given by $r = r(\phi=0) + R_{Cor}(1-\cos\phi)$ that substituted in Eq. (3.22) yields Eq. (3B.1) that can be used to calculate the pressure difference P_{NW}-P_W at the small or large pore openings considering that the value of $r(\phi=0)$ is different in both cases, $r_s(\phi=0)$ and $r_l(\phi=0)$.

$$\Delta P_{NW} = P_{NW} - P_W = \frac{2\gamma\cos(\theta+\phi)}{r(\phi=0) + R_{Cor}(1-\cos\phi)} \tag{3B.1}$$

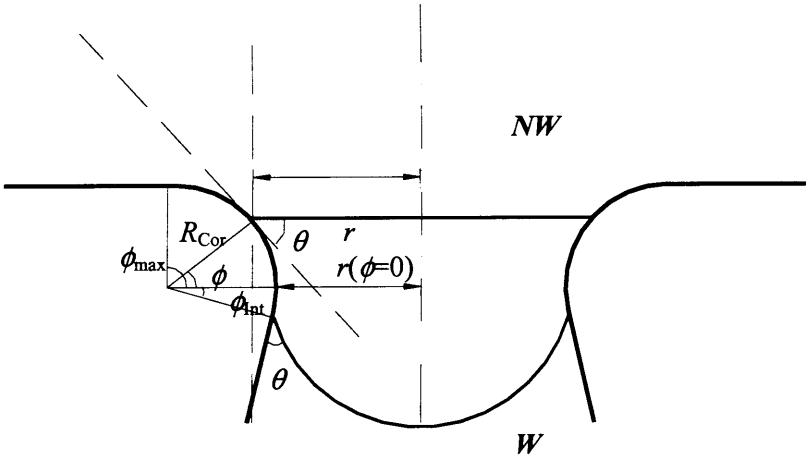

Figure 3B.1. Change of the apparent contact angle at the pore ends due to the solid wall inclination change ϕ.

The value of ϕ at which the maximum and minimum value of $\Delta P_{NW} = P_{NW}$-P_W is reached ($(\Delta P_{B,W} = -(\Delta P_{NW})_{min}$, $(\Delta P_{B,NW} = (\Delta P_{NW})_{max})$ is found by $d\Delta P_{NW}/d\phi = 0$ that yields $\sin(\theta+\phi)=\sin\theta/(1+r/R)$, which reduces to Eqs. (3B.2) and (3B.3).

$$\phi(\Delta P_{B,NW}) = \arcsin\left[\frac{\sin\theta_R}{1+r_W(\phi=0)/R}\right]-\theta_R \quad \text{At } W \text{ pore end (Receding Meniscus)} \tag{3B.2}$$

$$\phi(\Delta P_{B,W}) = 180°-\arcsin\left[\frac{\sin\theta_A}{1+r_{NW}(\phi=0)/R}\right]-\theta_A \quad \text{At } NW \text{ pore end(Advancing Meniscus)} \tag{3B.3}$$

To calculate the value of ϕ for breakthrough of the W phase the meniscus is advancing and θ_A is used for the contact angle while for breakthrough of the NW phase θ_R is used instead. The radii r_W and r_{NW} are the pore radii at the wetting and non-wetting pore ends respectively, r_1 or r_s depending on the placement of the phases. $\Delta P_{B,W}$ at the non-wetting pore end and $\Delta P_{B,NW}$ at the wetting pore end may take place before the maximum or minimum apparent contact angle is reached respectively. Critical filling pressures can be also found following the same approach although for ϕ_{Int} close to zero, Table 3.2 can be used within a small error.

Purcell analysis can be applied to any axisymmetrical pore to calculate breakthrough or critical filling pressures. Non-axisymmetrical pores are generally modelled using the Mayer and Stowe and Princen Method (Mayer and Stowe, 1965; Princen (1969)), which gives exact solutions in the absence of gravity for uniform cross-section non-axisymmetric pores. Mason and Morrow (1994) combined both analyses into a method to estimate the effect of contact angle on interface drainage curvatures in converging-diverging pore throats formed by adjacent spheres. Several authors have still applied the Mayer and Stowe method to calculate an approximation of the meniscus curvature inside of non-uniform cross section pores (Legait, 1983; Man and Jin (1999, 2001)). This works well for zero contact angle systems in which the narrowest section of the pore defines the maximum capillary pressure for drainage. However, as the contact angle increases, the effect of the solid wall inclination change becomes more important that the difference in capillary pressure due to a non-circular cross section and the maximum capillary pressure is not reach at the narrowest part of the pore (Mason and Morrow, 1994).

Appendix 3C

Formation of Arc Menisci in Tapered Pores

Figure 3C.1 represents a tapered capillary with a regular polygonal cross section (square in this case). The angle required for the Concus-Finn condition (Concus and Finn, 1968) is half the internal angle that two of the faces of the tapered capillary make.

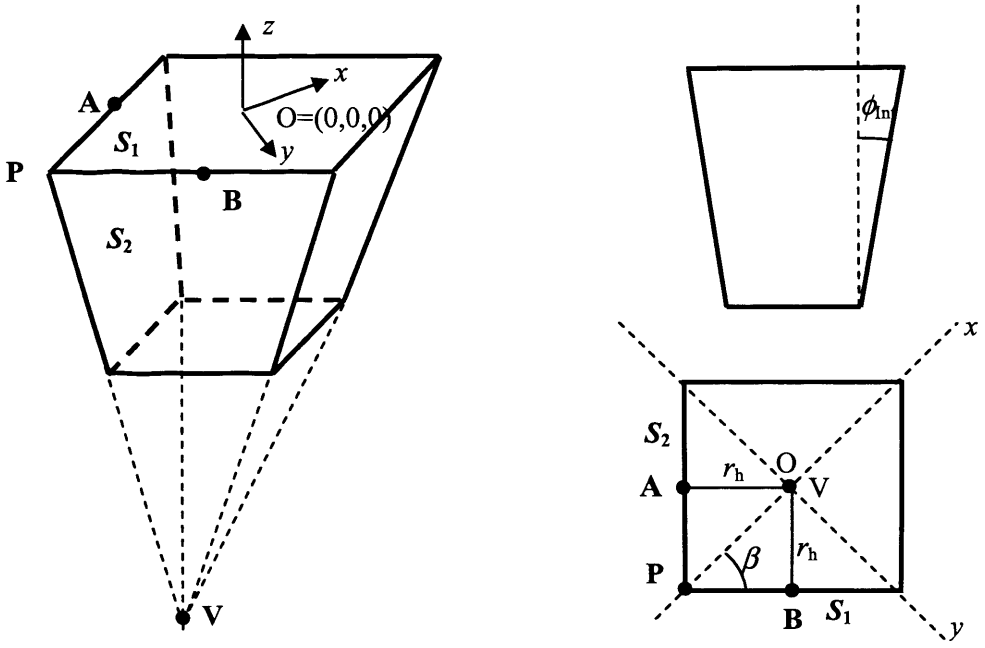

Figure 3C.1. Geometry of a tapered capillary with a regular polygonal cross section.

Therefore, two vectors, **a** and **b**, normal to surfaces S_1 and S_2 are required in order to find the angle according to Eq. (3C.1).

$$\cos(2\beta_{Corner}) = \frac{\mathbf{a} \bullet \mathbf{b}}{|\mathbf{a}| \cdot |\mathbf{b}|} \tag{3C.1}$$

Four characteristic points chosen are,

$$\begin{aligned} &O = (0,0,0) \quad P = (-r_h / \sin\beta, 0, 0) \quad V = (0,0,-r_h/\tan\phi_{Int}) \\ &A = (-r_h \sin\beta, r_h \cos\beta, 0) \quad B = (-r_h \sin\beta, -r_h \cos\beta, 0) \end{aligned} \tag{3C.2}$$

The cross product of vectors AV and PV gives the vector **a** and the cross product of vectors PV and BV gives the vector **b**.

$$\mathrm{PV} = \frac{r_h}{\sin\beta}\mathbf{i} + 0\mathbf{j} - \frac{r_h}{\tan\phi_{Int}}\mathbf{k} \tag{3C.3}$$

$$\mathrm{AV} = r_h \sin\beta\mathbf{i} - r_h \cos\beta\mathbf{j} - \frac{r_h}{\tan\phi_{Int}}\mathbf{k} \tag{3C.4}$$

$$\mathrm{BV} = r_h \sin\beta\mathbf{i} + r_h \cos\beta\mathbf{j} - \frac{r_h}{\tan\phi_{Int}}\mathbf{k} \tag{3C.5}$$

$$\mathbf{a} = \mathrm{AVxPV} = \begin{pmatrix} \mathbf{i} & \mathbf{j} & \mathbf{k} \\ r_h \sin\beta & -r_h \cos\beta & -\frac{r_h}{\tan\phi_{Int}} \\ \frac{r_h}{\sin\beta} & 0 & -\frac{r_h}{\tan\phi_{Int}} \end{pmatrix} = \frac{r_h^2 \cos\beta}{\tan\phi_{Int}}\mathbf{i} - \left(\frac{r_h^2}{\sin\beta\tan\phi_{Int}} - \frac{r_h^2 \sin\beta}{\tan\phi_{Int}}\right)\mathbf{j} + \frac{r_h^2}{\tan\beta}\mathbf{k} \tag{3C.6}$$

$$\mathbf{b} = \mathrm{BVxPV} = \begin{pmatrix} \mathbf{i} & \mathbf{j} & \mathbf{k} \\ r_h \sin\beta & +r_h \cos\beta & -\frac{r_h}{\tan\phi_{Int}} \\ \frac{r_h}{\sin\beta} & 0 & -\frac{r_h}{\tan\phi_{Int}} \end{pmatrix} = -\frac{r_h^2 \cos\beta}{\tan\phi_{Int}}\mathbf{i} - \left(\frac{r_h^2}{\sin\beta\tan\phi_{Int}} - \frac{r_h^2 \sin\beta}{\tan\phi_{Int}}\right)\mathbf{j} - \frac{r_h^2}{\tan\beta}\mathbf{k} \tag{3C.7}$$

The dot product of **a** and **b** and their modules, |**a**| and |**b**| are substituted into Eq. (3C.1) to obtain β_{corner}.

$$\beta_{corner} = \frac{1}{2}\arccos\left[(\cos\beta)^2 \cos(2\phi_{Int}) - (\sin\beta)^2\right] \tag{3C.8}$$

It can be shown that $\theta < 90^o\text{-}\beta_{corner}$ is equivalent to Eq. (3C.9) for tapered pores of regular polygonal cross section.

$$\theta < \arccos\left[\cos\phi_{Int}\sqrt{\sin^2\beta + \tan^2\phi_{Int}}\right] \tag{3C.9}$$

Appendix 3D

Formation of Arc Menisci in Tapered Pores II

Since the meniscus of constant curvature inside pores when arc menisci are not present is spherical, the conditions under which a solution for a spherical meniscus can span over the whole cross section are analysed. The interface shape of a spherical meniscus is given by Eq. (3D.1) being the centre of the sphere at the point $(x,y,z) = (0,0,0)$.

$$z = \pm\sqrt{R^2 - x^2 - y^2} \tag{3D.1}$$

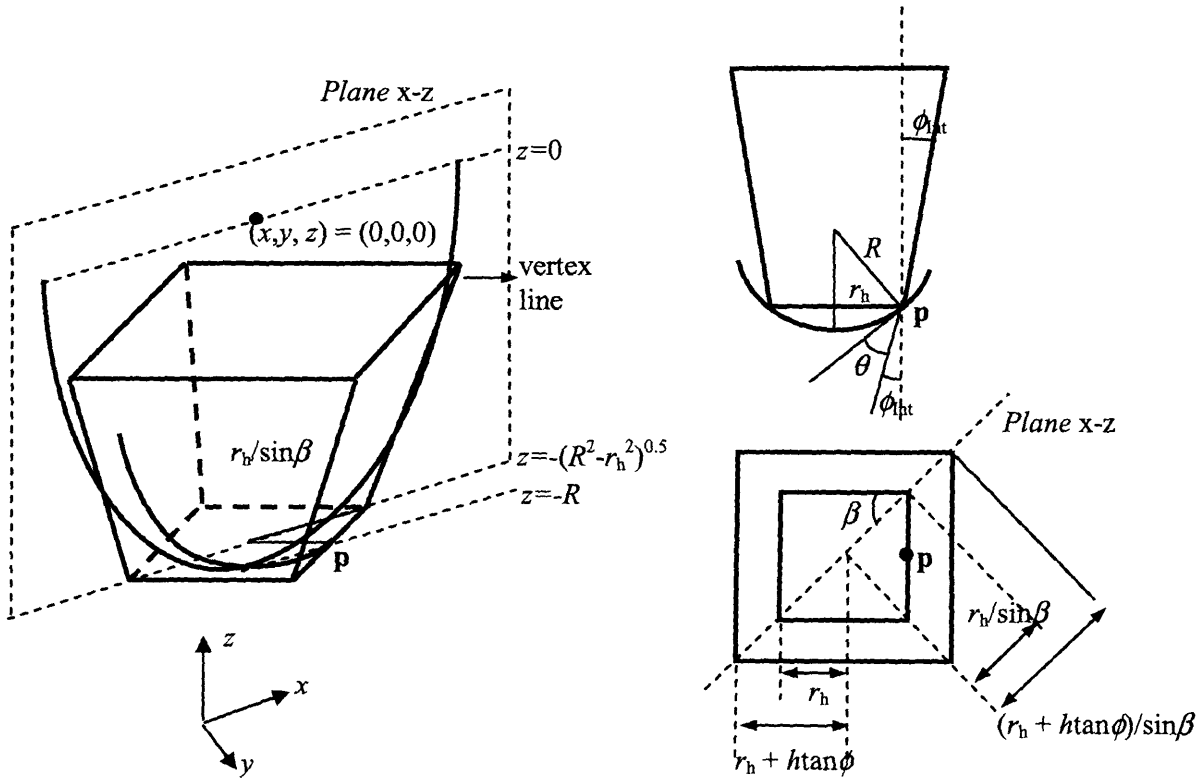

Figure 3D.1. Polygonal cross section tapered capillary.

The radius of curvature of the spherical meniscus can be written as a function of the contact angle θ, solid wall inclination in the interior of the pore at the lowest point of the three-phase contact line ϕ_{Int} and the radius of the inscribed circle to the polygon r_h (see point **p** in Figure 3D.1),

$$R = \frac{r_h}{\cos(\theta + \phi_{Int})} \tag{3D.2}$$

It is important to note that this does not apply to the rest of points of the contact line, $R \neq r /\cos(\theta + \phi_{Int})$, being r the radius from the centre of the inscribed circle to the point along the contact line.

A solution for a spherical meniscus, defined by Eq. (3D.1), that fills the cross section of a tapered capillary for a given contact angle θ and solid wall inclination ϕ_{Int} is reduced to the solution of the vertex line (furthest point from the centre of the sphere) and the intersection of the sphere with the place x-z. The equation of the circle contained in the plane x-z is,

$$z = \pm\sqrt{\frac{r_h^2}{\cos^2(\theta + \phi_{Int})} - x^2} \tag{3D.3}$$

The line $z = ax + b$ that defines the vertex line of the polygonal pore that falls in the plane x-z passes through the point,

$$\text{at } x = \frac{r_h}{\sin\beta} \quad z = -\sqrt{\left(\frac{r_h}{\cos(\theta + \phi_{Int})}\right)^2 - r_h^2} \tag{3D.4}$$

and has the slope,

$$a = \frac{\sin\beta}{\tan\phi_{Int}} \tag{3D.5}$$

The final equation of the line is,

$$\begin{aligned} z &= \frac{\sin\beta}{\tan\phi_{Int}} x - \frac{r_h}{\cos(\theta + \phi_{Int})}\left[\sqrt{1 - \cos(\theta + \phi_{Int})^2} + \frac{\cos(\theta + \phi_{Int})}{\tan\phi_{Int}}\right] \\ z &= \frac{\sin\beta}{\tan\phi_{Int}} x - \frac{r_h}{\cos(\theta + \phi_{Int})}\left[\sin(\theta + \phi_{Int}) + \frac{\cos(\theta + \phi_{Int})}{\tan\phi_{Int}}\right] \end{aligned} \tag{3D.6}$$

Eqs. (3D.3) and (3D.4) are squared and equated in their z^2 term to obtain the following quadratic equation $c_1x^2+c_2x+c_3 = 0$,

$$\left[\left(\frac{\sin\beta}{\tan\phi_{Int}}\right)^2+1\right]x^2+2\frac{\sin\beta}{\tan\phi_{Int}}\frac{r_h}{\cos(\theta+\phi_{Int})}\left[\sin(\theta+\phi_{Int})+\frac{\cos(\theta+\phi_{Int})}{\tan\phi_{Int}}\right]x+$$
$$\frac{r_h^2}{\cos(\theta+\phi_{Int})^2}\left[\left(\sin(\theta+\phi_{Int})+\frac{\cos(\theta+\phi_{Int})}{\tan\phi_{Int}}\right)^2-1\right]=0 \qquad (3D.7)$$

This equation has no real solution when $(c_2^2 - 4c_1c_3) < 0$ leading to the following condition for existence of arc menisci,

$$\left(\frac{\sin\beta}{\tan\phi_{Int}}\right)^2+1<\left(\sin(\theta+\phi_{Int})+\frac{\cos(\theta+\phi_{Int})}{\tan\phi_{Int}}\right)^2 \qquad (3D.8)$$

$$\sqrt{\frac{\sin^2\beta+\tan^2\phi_{Int}}{\tan^2\phi_{Int}}}<\sin(\theta+\phi_{Int})+\frac{\cos(\theta+\phi_{Int})}{\tan\phi_{Int}}=\frac{\cos\theta}{\sin\phi_{Int}} \qquad (3D.9)$$

$$\theta<\arccos\left[\cos\phi_{Int}\sqrt{\sin^2\beta+\tan^2\phi_{Int}}\right] \qquad (3D.10)$$

Condition by Eq. (3D.10) reduces to $\theta < (90°-\beta)$ when $\phi_{Int} = 0°$ (non-tapered pores).

The angle ϕ_{Int} is the one measured with respect to the walls at the point where r_h is computed. This is the reason that the slope of the vertex line contains the term $\sin\beta$. Non polygonal cross sections are evaluated in the same way as shown in Figure 3D.2.

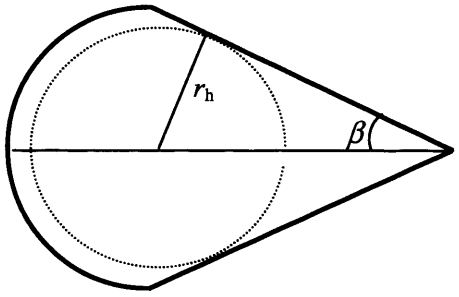

Figure 3D.2. Analysis of pores with irregular cross section.

Consider a system with $\theta = 40°$ inside a square uniform cross section pore ($\beta = 45°$, $\phi_{Int} = 0$). A spherical meniscus is not possible since $\theta < (90°-\beta)$ (see Figure 3D.3 for $\phi_{Int} = 0°$). However, the

same system within a tapered pore is allowed to have an equilibrium spherical meniscus as shown in Figure 3D.3 for $\phi_{Int} = 25°$ and $\phi_{Int} = 40°$, in which the vertex line intersect the circle on plane *x*-*z*.

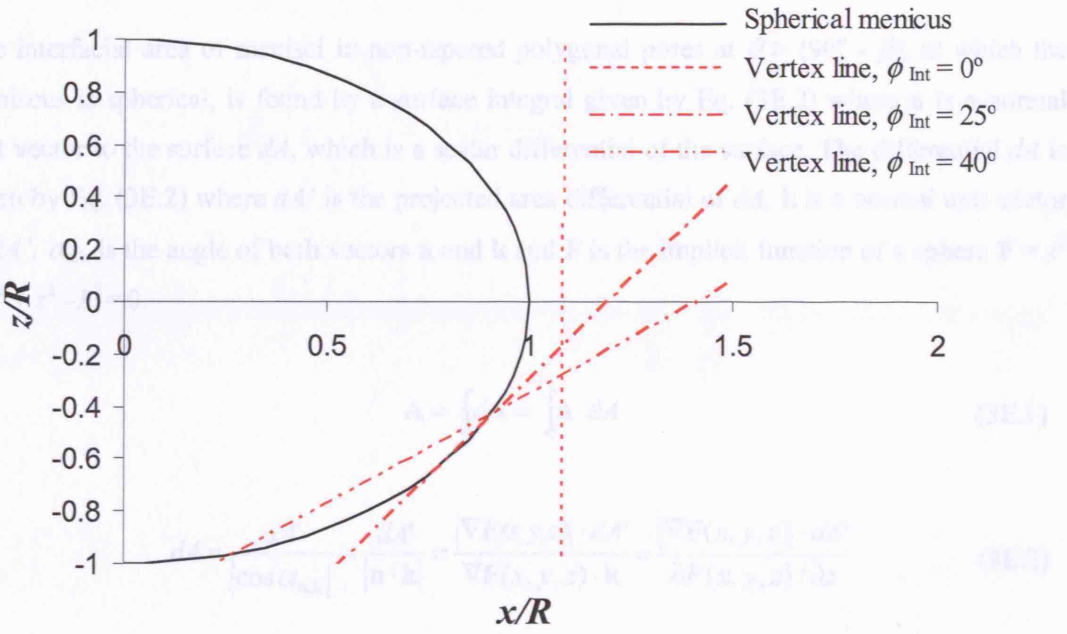

Figure 3D.3. Existence of an equilibrium spherical meniscus for a system with $\theta = 40°$ within three different square cross section ($\beta = 45°$) pores with $\phi_{Int} = 0°$, $\phi_{Int} = 25°$ and $\phi_{Int} = 40°$. In order to avoid drawing three different circles, the results shown in Figure 3D.3 are obtained using R as the characteristic dimension and therefore r_h has a different value in the three cases.

The solution for $\beta = 45°$, $\phi_{Int} = 25°$ is almost a tangent line to the circle, since the critical contact angle according to condition by Eq. (3D.10) is 39.9°. It is important to note that the solid wall inclination of the vertex line is not ϕ_{Int}.

Appendix 3E

Meniscus Area in Polygonal Pores at $\theta > (90°-\beta)$

The interfacial area of menisci in non-tapered polygonal pores at $\theta > (90° - \beta)$, at which the meniscus is spherical, is found by a surface integral given by Eq. (3E.2) where **n** is a normal unit vector to the surface dA, which is a scalar differential of the surface. The differential dA is given by Eq. (3E.2) where dA' is the projected area differential of dA, **k** is a normal unit vector to dA', $\alpha_{\mathbf{n},\mathbf{k}}$ is the angle of both vectors **n** and **k** and **F** is the implicit function of a sphere $\mathbf{F} = x^2 + y^2 + z^2 - R^2 = 0$.

$$\mathbf{A} = \int_S d\mathbf{A} = \int_S \mathbf{n} \cdot dA \tag{3E.1}$$

$$dA = \frac{dA'}{\left|\cos \alpha_{\mathbf{n},\mathbf{k}}\right|} = \frac{dA'}{\left|\mathbf{n} \cdot \mathbf{k}\right|} = \frac{\left|\nabla \mathbf{F}(x,y,z)\right| \cdot dA'}{\nabla \mathbf{F}(x,y,z) \cdot \mathbf{k}} = \frac{\left|\nabla \mathbf{F}(x,y,z)\right| \cdot dA'}{\partial F(x,y,z)/\partial z} \tag{3E.2}$$

As the domain is polygonal, Cartesian co-ordinates are more suitable, and an expression for the meniscus area in any polygonal pore with $\theta > (90° - \beta)$ is found by substituting Eq.(3E.2) into Eq. (3E.1), and using $z = (R^2 - x^2 - y^2)^{0.5}$, resulting in Eq. (3.47) shown above.

For instance, the hexagonal domain shown in Figure 3E.1 is divided into simple subdomains (triangles and squares) where the surface integral given by Eq. (3.47) is solved in subdomains Ω_1 and Ω_2, being the total area 4 times those values as given by Eq. (3E.3). It is important to realise that in the subdomain Ω_1 x ranges from $(y/(3)^{1/2} - L)$ to $-L/2$ instead of from $-L$ to $(y/(3)^{1/2} - L)$ in order to not get the dashed-domain shown in Figure 3E.1.

$$A = 4\left(A_{\Omega 1} + A_{\Omega 2}\right) = 4\left(\int_0^{L\sqrt{3}/2} \int_{y/\sqrt{3}-L}^{-L/2} \frac{R}{\sqrt{R^2 - y^2 - x^2}} dxdy + \int_0^{L\sqrt{3}/2} \int_{-L/2}^{0} \frac{R}{\sqrt{R^2 - y^2 - x^2}} dxdy \right) \tag{3E.3}$$

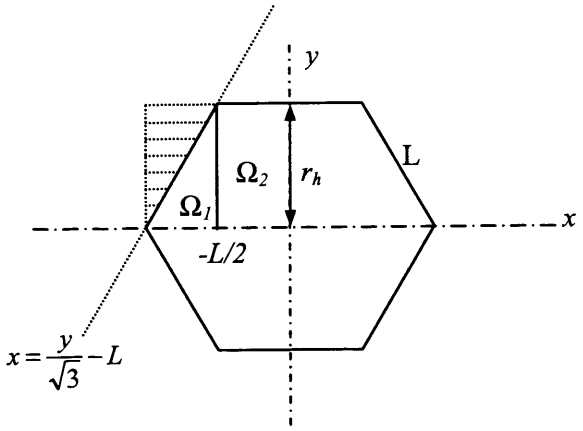

Figure 3E.1. Hexagonal domain used to calculate the meniscus area in a hexagonal pore when $\theta > (90° - \beta)$

Appendix 3F

Meniscus Shape in a Hexagonal Pore

The augmented Young-Laplace Eq. (3.48) is given by Eq. (3F.1) for a three dimensional system in cylindrical co-ordinates. It is solved in a sector of angle $\phi = \pi/n$ that corresponds to half angle of the corner (equal to 30° for hexagonal pores), where n is the number of sides of the polygonal pore. The meniscus surface is defined by its radial position $R^{\#}(z^{\#}, \phi)$, which is a function of the height from the meniscus apex, $z^{\#}$ and the angle co-ordinate ϕ. In the pressure isotherm $\Pi^{\#}(h^{\#})$, $h^{\#} = 1\text{-}R^{\#}\cos\phi$. At $z^{\#} \to \infty$, when the meniscus becomes two dimensional (AM fully developed), Figure 3F.1 represents its profile for the sector of angle $0 < \phi < \pi/n$.

$$\frac{2R^{\#}\cdot\frac{\partial R^{\#}}{\partial\phi}\cdot\frac{\partial R^{\#}}{\partial z^{\#}}\cdot\frac{\partial R^{\#}}{\partial\phi\partial z^{\#}}-R^{\#}\cdot\left[1+\left(\frac{\partial R^{\#}}{\partial z^{\#}}\right)^2\right]\cdot\frac{\partial^2 R^{\#}}{\partial\phi^2}-R^{\#}\cdot\left[R^{\#2}+\left(\frac{\partial R^{\#}}{\partial\phi}\right)^2\right]\cdot\frac{\partial^2 R^{\#}}{\partial z^{\#2}}+\left(\frac{\partial R^{\#}}{\partial\phi}\right)^2}{\left[R^{\#2}+\left(\frac{\partial R^{\#}}{\partial\phi}\right)^2+R^{\#2}\cdot\left(\frac{\partial R^{\#}}{\partial z^{\#}}\right)^2\right]^{3/2}}+$$

$$+\left[R^{\#2}+\left(\frac{\partial R^{\#}}{\partial\phi}\right)^2+R^{\#2}\cdot\left(\frac{\partial R^{\#}}{\partial z^{\#}}\right)^2\right]^{-1/2}+\frac{\varepsilon^{\#}}{\left(1-R^{\#}\cdot\cos\phi\right)^3}-M^{\#}\cdot\mathrm{sech}^2\left(\frac{1-R^{\#}\cdot\cos\phi}{w^{\#}}-2\right)=\kappa^{\#} \quad (3F.1)$$

Where $\varepsilon^{\#}$, $w^{\#}$ and $M^{\#}$ are three parameters of the pressure isotherm $\Pi^{\#}$ (spike function).

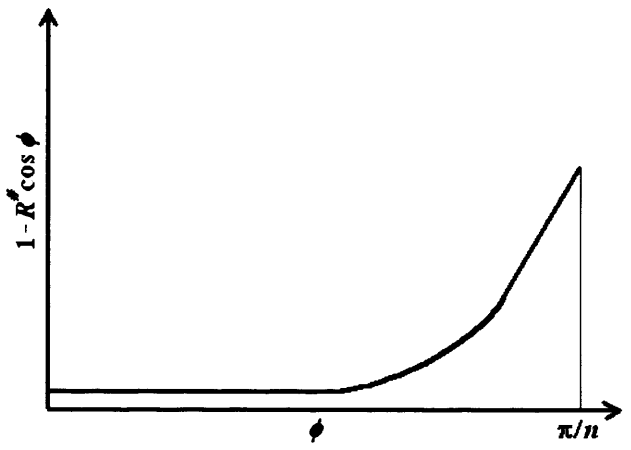

Figure 3F.1. Meniscus profile in a polygonal tube at $z^{\#} \to \infty$.

The boundary conditions for Eq. (3F.1) are (Wong, 1992),

$$R^{\#}\left(\phi, z^{\#}=0\right)=0 \tag{3F.2}$$

$$\frac{\partial R^{\#}}{\partial z^{\#}}\left(\phi, z^{\#} \to \infty\right)=0 \tag{3F.3}$$

$$\frac{\partial R^{\#}}{\partial \phi}\left(\phi=0, z^{\#}\right)=0 \tag{3F.4}$$

$$\frac{\partial R^{\#}}{\partial \phi}\left(\phi=\frac{\pi}{N}, z^{\#}\right)=0 \tag{3F.5}$$

$z^{\#}$ can be considered infinite (AM fully developed) in the range from 1.3 to 4.5 depending on the value of $w^{\#}M^{\#}$, wetting properties and geometry of the polygonal pore (Wong et al., 1992b). At $z^{\#} = 0$ there is a singularity and, the z-coordinate is stretched as shown in Eq. (3F.6) in order to avoid this singularity.

$$z^{\#}=\frac{\Psi^{\#2}}{2} \tag{3F.6}$$

Although the exact value of $\kappa^{\#}$ can be calculated using the MS-P method, Wong et al. (1992c), found that their numerical mixed Picard-Newton method does not converge when a fixed known value of $\kappa^{\#}$ is used. Therefore, $\kappa^{\#}$ is found as part of the solution, which means that another boundary condition is necessary. This boundary condition rises from applying L'Hospital's rule to Eq. (3F.1) with the z-coordinate stretched.

$$At\ \phi=0 \qquad \frac{\partial}{\Psi^{\#}}\left(\frac{\partial^2 R^{\#}}{\partial \phi^2}\right)-2\cdot\frac{\partial R^{\#}}{\partial \Psi^{\#}}=\left(\varepsilon^{\#}-\kappa^{\#}\right)\cdot\left(\frac{\partial R^{\#}}{\partial \Psi^{\#}}\right)^3 \tag{3F.7}$$

Applying Equations (3F.1) to (3F.7) together, $R^{\#}(\phi, z^{\#})$ and $\kappa^{\#}$ are solved. The final value of $\kappa^{\#}$ matches well with the exact value calculated by analytical methods as that given by Mason and Morrow (1984). Applying Wong's method, the meniscus shape in a hexagonal pore when $\theta = 0°$ is solved. The program gives the function radius $R^{\#}(\phi, z^{\#})$ in the range from $\phi = 0°$ to $\phi = \beta/2°$ as a solution. The input data that the Fortran code needs are: number of grid points for ϕ and $z^{\#}$

directions, m_ϕ and m_z respectively, domain boundary of $z^\#$, $z^\#_{max}$, maximum number of iterations, contact angle (from 0 to 90-β) and the parameters $\varepsilon^\#$, $M^\#$ and $w^\#$ for the spike function. The output data is analysed by a Matlab code to generate the final meniscus shape presented in Figure 3.17 using the symmetry planes in a regular polygon and transforming the cylindrical co-ordinates into cartesian ones. In addition, the grid points in the z-direction are equally spaced according to the stretching coordinate but not with respect to the z coordinate. The parameters used to obtain Figure 3.17 and Figure 3F.2 are the following: $n = 6$, $m_\phi = 50$, $m_z = 100$, $z^\#_{max} = 2$, contact angle, $\theta = 0°$, $\varepsilon^\# = 1 \cdot 10^{-12}$, $D^\# = 0.5762$ and $w^\# = 0.0002$. AM are fully developed at $z^\# \approx 1.25$, which implies that the deviation from a spherical meniscus is small.

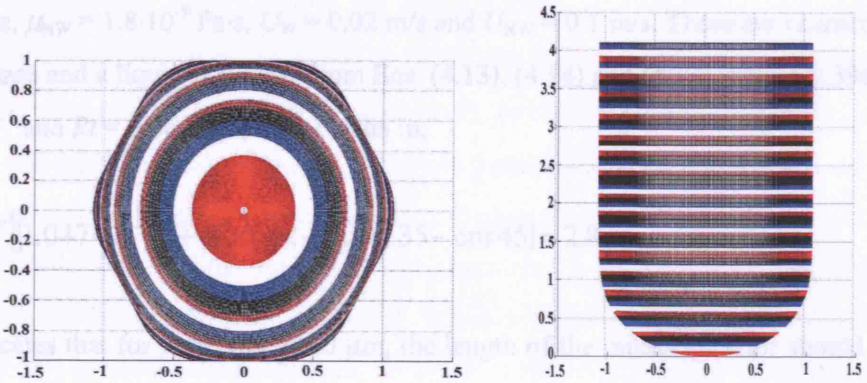

Figure 3F.2. Hexagonal meniscus, $\theta = 0°$, top and side views.

Appendix 4A

Effect of Fluid Pressure Drop on the Available Range of Pressure Difference

For illustration consider a system with circular non-tapered pores (ϕ_{Int} = 0°, $r^{\#}$ = 1) and horizontal plates, operating in counter-current flow with $H_W = H_{NW} = 2d$, d = 100 μm. The properties of the phases are, γ= 0.0215 N/m, θ= 45°, ρ_W = 800 kg/m^3, ρ_{NW} = 1.2 kg/m^3, μ_W = 0.0015 Pa·s, $\mu_{NW} = 1.8 \cdot 10^{-5}$ Pa·s, U_W = 0.02 m/s and U_{NW} = 0.1 m/s. These are characteristic of a gas *NW* phase and a liquid *W* phase. From Eqs. (4.13), (4.14) and (4.17), $Ca_W = 1.396 \cdot 10^{-3}$, $Bo_W = 0.913 \cdot 10^{-3}$ and Rt = 0.06. Eq. (4.19) results in,

$$L^{\#}\left[\left(1.047 \cdot 10^{-3}(1+0.06)\right)\right] < -2(\cos 135 - \cos 45) = 2.83 \qquad \boldsymbol{L^{\#} < 2550} \qquad (4A.1)$$

which indicates that for pores of r = 50 μm, the length of the microcontactor should be shorter than 12.8 cm. If the non-wetting phase is another liquid with the same properties to those of the wetting phase instead of gas, the pressure drop effect is more significant, and $L^{\#} < 1352$. In the first case, if the microcontactor must be 15 cm long, positioning it at an angle can solve the problem since the static pressure change in the liquid and gas are very different. As can be seen from Eq. (4.19) the minimum required inclination in this case is α= -10.5°:

$$\begin{gathered} 3000\left[1.047 \cdot 10^{-3}(1+0.06) + 0.9125 \cdot 10^{-3}(0.9985)\sin\alpha\right] < 2.83 \\ \sin\alpha < -0.183 \rightarrow \boldsymbol{\alpha < -10.5^{\circ}} \end{gathered} \qquad (4A.2)$$

However, when two liquids with similar densities are used, gravity does not play an important role in this case (see Eq. (4.19)) and a reduction of the pore size is necessary in order to operate with L = 15 cm. If the phase height and length are kept to H = 200 μm and L = 15 cm, $U_W = U_{NW}$ and $\mu_W = \mu_{NW}$ (Rt = 1), the maximum pore radius that can be used is,

$$\frac{L^{\#}}{H_W^{\#2}} < \frac{2.83}{2 \cdot 12 \cdot Ca_W} = 84.5 \qquad r < 84.5 \cdot \frac{H_W^2}{L} \rightarrow \boldsymbol{r < 22.5\,\mu m} \qquad (4A.3)$$

Appendix 4B

Meniscus Breakthrough at the Pore Stage for a Non-Wetting Phase

A mesh with cylindrical pores ($\phi_{Int} = 0$), $\phi_{S,Int} = 0, \theta = \theta_S = 130°$ (built-in supports), $d_S/r = 2$ and support height $y_S/r = 1.5$ is considered. The curve ΔP vs. y for $y_S = y$ uses the maximum apparent contact angle at point 1, $\theta_{App} = \theta + \phi_{max} - \varphi$, for $\varphi \geq 40°$ according to Eq. (4.35) and $\theta_{App} = 180°$ for $\varphi < 40°$ (Eq. (4.37)). Eq. (4.34) indicates that $y_{\Delta Pmax}/r = 0.933$, with corresponding pressure difference $\Delta Pr/\gamma = 0.821$ (point **b**), while the pressure difference when the meniscus breaks at the pore mouth is $\Delta Pr/\gamma = 0.80$ (point **d**). In this case, $y_{\Delta Pmax} < y_S < y_{\phi max}$ (case 3 in Table 4.2) and the pressure difference at $y_{\Delta Pmax}$ is a global maximum. Figure 4B.1 shows that for supports with $y_S/r > 1.39$ ($y_S/r = 1.5$ in this case), the maximum pressure difference is reached at $y_{\Delta Pmax}/r = 0.933$. Thus, for the support height considered ($y_S/r = 1.5$) the maximum pressure difference during this stage occurs at point **b**. When the meniscus is moving it is possible that this maximum may be overcome even at lower pressure difference due to inertia in a similar way as a meniscus oscillates around the equilibrium position during a capillary rise experiment (Duarte et al., 1996). As the contact angle $\theta = \theta_S$ approaches 180°, the effect of supports vanishes (corresponding curves are not shown).

C

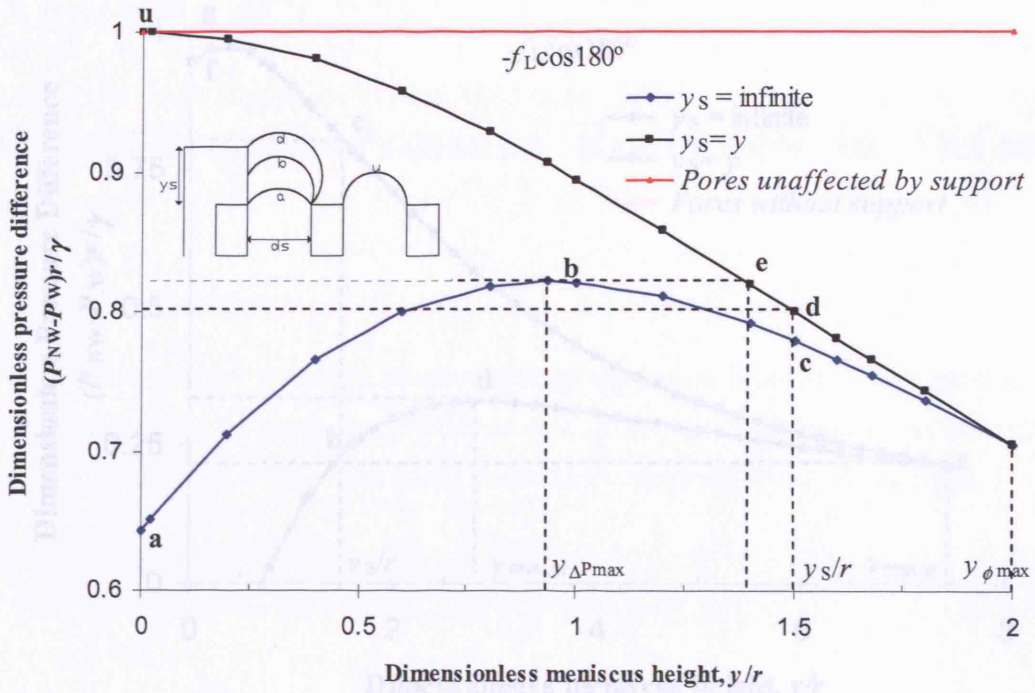

Figure 4B.1. Dimensionless pressure difference $(P_{NW}-P_W)r/\gamma$ as a function of the dimensionless meniscus height y/r, during the *meniscus breakthrough at the pore* stage. Cylindrical pores ($\phi_{Int} = 0$), $\phi_{S,Int} = 0, \theta = \theta_S = 130°$ and $d_S/r = 2$.

A system with the same properties as the previous example is considered apart from different contact angles at the pore and the support, $\theta = 130°$ and $\theta_S = 70°$. The two characteristic points of the ΔP vs. y curve for $y_S = \infty$ are $y_{\Delta Pmax}/r = 2.86$ (point **d**) and $y_{\phi max}/r = 7.42$ (point **e**). For the ΔP vs. y curve for $y_S = y$, at $\varphi_S < 30°$ breakthrough takes place at the support top and at $\varphi_S > 30°$ breakthrough takes place first at the pore mouth. However, for $20° < \varphi_S \leq 40°$, $\theta_{App,max} = 180°$ (see Eq. (4.37)). Therefore, the values of the maximum apparent contact angle are: $\theta_{App,max} = \theta_S + \phi_{S,max} + \varphi_S$ when $0° < \varphi_S < 20°$, $\theta_{App,max} = 180°$ when $20° < \varphi_S < 40°$ and $\theta_{App,max} = \theta + \phi_{max} - \varphi_S$ when $\varphi_S > 40°$. For the case of a support height of $y_S/r = 1.5$, the meniscus follows the path **b-c** with a breakthrough pressure of $\Delta Pr/\gamma = 0.80$.

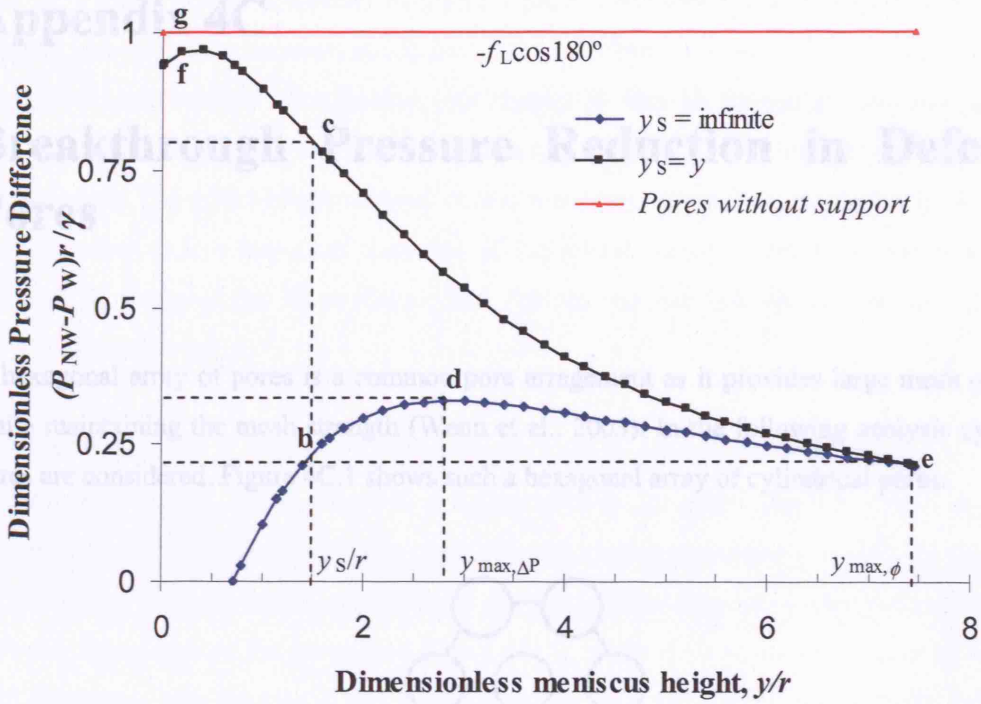

Figure 4B.2. Maximum pressure difference $(P_{NW}-P_W)r/\gamma$ as a function of the dimensionless meniscus height y/r, during the *meniscus breakthrough at the pore* stage. Cylindrical pores ($\phi_{Int} = 0$), $\phi_{S,Int} = 0$, $\theta = 130°$, $\theta_S = 70°$ and $d_S/r = 2$.

This example demonstrates that for $y_S = 0$, the maximum achievable pressure difference (point **f**) is smaller than that in pores unaffected by supports (point **g**). The smaller contact angle at the support compared to that at the pores results in a smaller maximum apparent contact angle, $\theta_{App,max} = 70+90° = 160°$ compared to $\theta_{App,max} = 180°$ at the pore mouth. Therefore, parts of the mesh in which the contact angle is smaller due to surface heterogeneities, impurities or surface roughness can also give rise to a decrease of the maximum pressure difference. Supports and particles of different properties (θ_S and $\phi_{S,Int}$) than the mesh pores will also affect the critical filling pressure of a phase in the pore, although this may not affect the microcontactor performance significantly, as only a few pores, those affected by the supports will be filled with a different phase than the rest of the pores.

Appendix 4C

Breakthrough Pressure Reduction in Defective Pores

A hexagonal array of pores is a common pore arragement as it provides large mesh open area while maintaining the mesh strength (Wenn et al., 2003). In the following analysis cylindrical pores are considered. Figure 4C.1 shows such a hexagonal array of cylindrical pores.

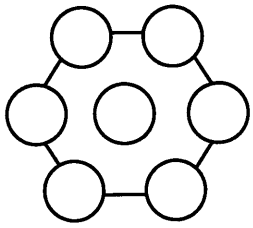

Figure 4C.1. Hexagonal array of cylindrical pores.

Different types of defects resulting from joined pores are shown in Figure 4C.2, where p is the distance between the centres of two adjacent pores and d is the pore diameter. Two, three, four and seven standard pores have joined respectively forming a larger opening.

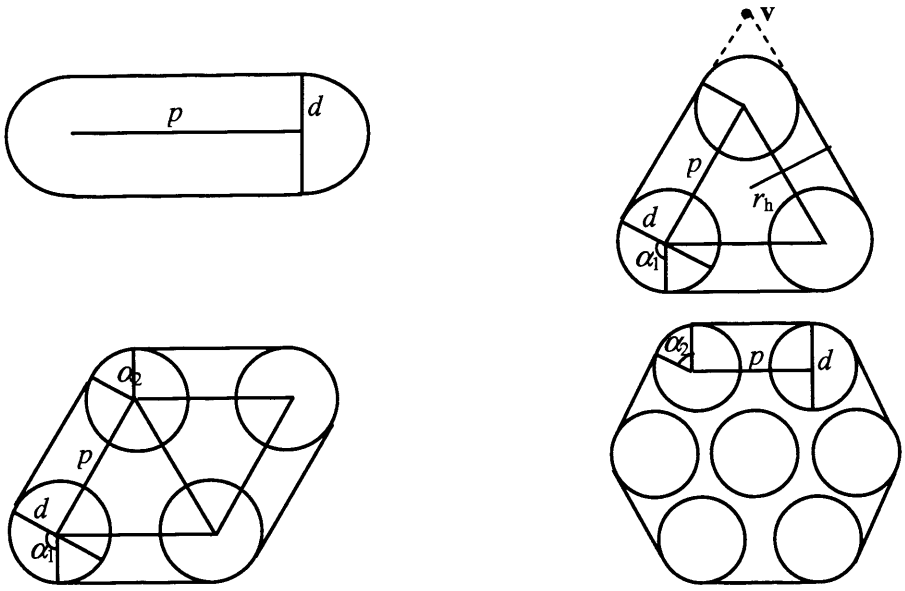

Figure 4C.2. Analysed defects in a hexagonal array: 2, 3, 4 and 7 pores joined.

The defective openings composed of 3 and 7 pores, correspond to a triangular and hexagonal (larger) pore with round corners and radius of the inscribed circle $r_{h,3} = d/2+p/(2\tan 60)$ and $r_{h,7} = p\sin 60°+d/2$ respectively. Arc menisci (see chapter 3) may be formed at the round corners of these openings, depending on the contact angle and the ratio $f = d/p$, apart from the case of two joined pores. The effect of arc menisci on the meniscus curvature is neglected in the analysis below since it is less important than that of the joined pores. However, it can be taken into account by applying the Mayer-Stowe and Princen method (Mason and Morrow, 1984, for regular polygonal pores).

The Gauss Eq. (4C.1) is used to calculate the meniscus mean curvature in the joined pores (Mason and Morrow, 1984), where $\kappa^{\#}$ is the normalised curvature, θ is the contact angle, p', is the perimeter of the defective opening and A' is the meniscus projected area. In the two joined-pore case, p', is equal to the perimeter of one circle with diameter d plus twice the distance between the centres of the pores (see Figure 4C.2), while A' is equal to the area of one circle with diameter d plus the area of the rectangle with sides d and p, (see Figure 4C.2). In a similar way p' and A' are calculated for the other geometries, taking into account that $\alpha_1 = 120°$ and $\alpha_2 = 60$.

$$\kappa^{\#} = r\frac{p'}{A'}\cos\theta \tag{4C.1}$$

Table 4C.1 shows the equations for p', A' and $\kappa^{\#}$ for the different defective openings.

Joined pores	p'	A'	$\kappa^{\#}$
2	$2p+\pi d$	$pd+\pi\left(\frac{d}{2}\right)^2$	$\frac{2f+\pi f^2}{2f+(\pi/2)f^2}\cos\theta$
3	$3p+\pi d$	$\frac{\sqrt{3}}{4}p^2+3p\frac{d}{2}+\pi\left(\frac{d}{2}\right)^2$	$\frac{3f+\pi f^2}{\sqrt{3}/2+3f+(\pi/2)f^2}\cos\theta$
4	$4p+\pi d$	$\frac{\sqrt{3}}{2}p^2+4p\frac{d}{2}+\pi\left(\frac{d}{2}\right)^2$	$\frac{4f+\pi f^2}{\sqrt{3}+4f+(\pi/2)f^2}\cos\theta$
7	$6p+\pi d$	$3\frac{\sqrt{3}}{2}p^2+6p\frac{d}{2}+\pi\left(\frac{d}{2}\right)^2$	$\frac{6f+\pi f^2}{3\sqrt{3}+6f+(\pi/2)f^2}\cos\theta$

Table 4C.1. Values of p', A' and $\kappa^{\#}$ for different joined-pore defects.

As can be seen the dimensionless curvature is expressed as a function of two parameters, the ratio of pore diameter to distance between centres of adjacent pores ($f = d/p$) and the contact angle θ. The curvature of the 3-pore defect can be normalised with respect to r_h instead of ($d/2$), by multiplying $\kappa^{\#}$ by $r_h/(d/2)$.

$$\kappa^{\#} = \frac{2\cos\theta}{3\left(\frac{f}{3f+\sqrt{3}} + \frac{1}{3+\pi f}\right)} \tag{4C.2}$$

When $f \to 0$, the 3-pore opening is a perfect triangular pore and Eq. (4C.2) reduces to $\kappa^{\#} = 2\cos\theta$, that is the dimensionless curvature of a spherical meniscus in a triangular (or any polygonal) pore for contact angles where arc menisci do not form, $\theta > 60°$. At $\theta < 60°$ the solution by Mason and Morrow (1984) for meniscus curvature can be used. For the other limiting case, $f \to \infty$, that represents a cylindrical pore with radius r_h, again $\kappa^{\#} = 2\cos\theta$.

For all intermediate cases the dimensionless curvature is smaller than $2\cos\theta$, reaching a minimum at $f = 0.7425$ where $\kappa^{\#} = 1.7776\cos\theta$. Interestingly 1.7776 is the same as the Laplace factor f_L when arc menisci are present in a triangular pore at contact angle 0° since at zero contact angle, the arc menisci formed have diameter equal to d. As a result, in a three-pore defective opening with $f \geq 0.7425$ arc menisci will not form at any contact angle since as the contact angle increases the arc menisci would approach the projected vertex (see point **v** in three-pore defect in Figure 4C.2), until they vanish at $\theta = 90° - \beta = 60°$, β being half the angle of the polygon corner. Therefore, the round corners have a similar effect on the reduction of the meniscus curvature as the arc menisci while they reduce the contact angle range for which arc menisci are present. A similar analysis can be applied to the 7-pore defective opening.

Since $\Delta P^{\#} = \Delta P r/\gamma = \kappa^{\#}$ the percentage of pressure difference decrease, D_{Defect}, resulting from defective pores in a mesh at a specific contact angle is calculated via Eq. (4C.3).

$$D_{Defect}(\%) = 100\frac{\left(\kappa^{\#}\right)_{1\,pore} - \left(\kappa^{\#}\right)_{Defect}}{\left(\kappa^{\#}\right)_{1\,pore}} \tag{4C.3}$$

As can be seen this decrease percentage is not dependent on the contact angle (neglecting arc menisci formation).

As an example the following case is considered: a mesh with $f = 0.571$, $\theta_A = 30°$ and $\theta_R = 10°$. The following percentage decrease in pressure difference with respect to a single cylindrical pore ($\kappa^{\#}_{1Pore} = 2\cdot\cos\theta$) is obtained for any contact angle if arc menisci are neglected: 2 pores, 34.5 %, 3 pores, 55.7 %, 4 pores, 63.5 % and 7 pores, 75.6 %. The variation in pressure difference range with apparent contact angle for different defective pores is shown in Figure 4C.3. Three zones separated by dashed lines can be identified: meniscus at the wetting end (*W*), meniscus pinned at any part of the pore (Pinned) and meniscus at the non-wetting end (*NW*). A non-defective mesh with these dimensions can operate with a dimensionless pressure difference between 2 and -1, but the same mesh with a two-joined-pore defect has an operation range between 1.310 and -0.655 (reduction of 34.5 %). To avoid breakthrough in the mesh only apparent contact angles between 50° and 110° are allowed. This leads to smaller interfacial areas compared to non-defective meshes where apparent contact angles 0° and 180° that produce hemispherical menisci of maximum interfacial area at the *W* and *NW* pore ends respectively are allowed. The percentage pressure difference reduction is the same as the reduction in the whole stability range (sum of breakthrough pressures in both pore ends). These problems are magnified when the number of pores joined increases to 3, 4 or 7 as shown in Figure 4C.3.

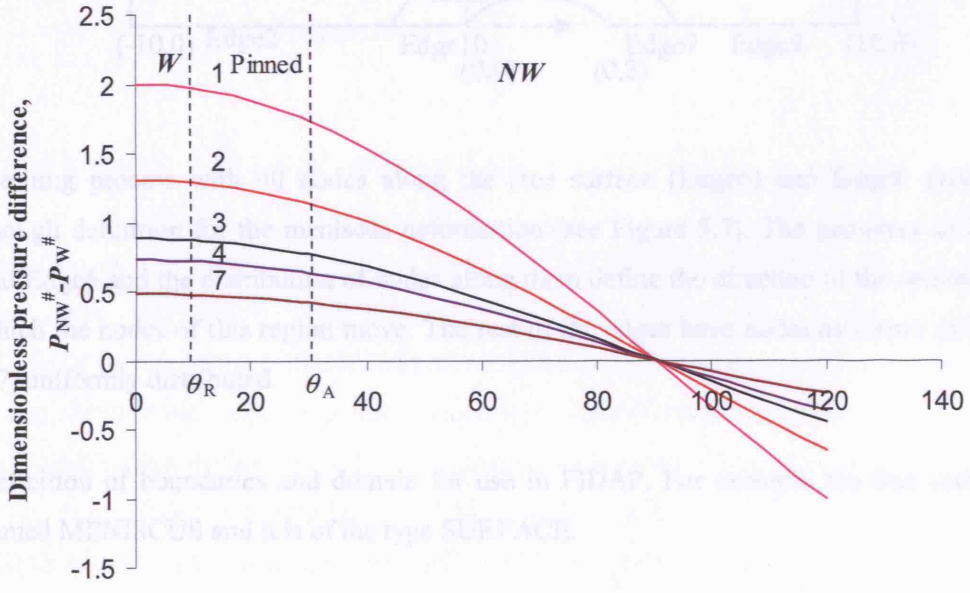

Figure 4C.3. Pressure difference across phases $\Delta P^{\#}$ vs θ_{App} for 1, 2, 3, 4 and 7 pores joined.

A similar analysis can be applied to any pore geometry. Kuiper et al. (2002) shows ceramic microsieves with slit-shaped perforations that are similar to the 2 joined pore opening above.

Appendix 5A

FIDAP Implementation of Gas Breakthrough under Liquid Flow Conditions

The implementation of FIDAP is shown for the following case: $H^{\#} = 2$, $Ca = 0.01$, $Re_{Stan} = 1$, $P^{\#}_{G,0} = \cos45°/(0.01) + (P_L - \tau_{nn})_{mean} = 98.1$ and $l^{\#} = 10$ (see Figure 5.7).

Geometry and mesh implementation in Gambit 2.1

- Geometry definition of the boundaries and regions that will contain moving nodes and fixed nodes. Selecting a first case with $\theta_{App} = 45°$, $R^{\#} = 1/\cos45 = 1.414$.

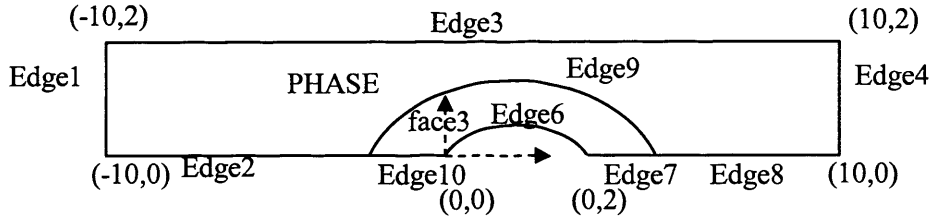

- Meshing process with 40 nodes along the free surface (Edge6) and Edge9, producing enough definition for the meniscus deformation (see Figure 5.7). The geometry of Edge9 and Edge6 and the distribution of nodes along them define the direction of the spines along which the nodes of this region move. The rest of the edges have nodes as shown in Figure 5.7, uniformly distributed.

- Definition of boundaries and domain for use in FIDAP. For example the free surface is named MENISCUS and it is of the type SURFACE.

Initial and boundary conditions and main equations in the liquid domain (FIDAP)

- Import geometry and mesh from GAMBIT. Visualise the geometry and make note of the node numbers n_1 and n_2 in Figure 5.7.

- The liquid domain and the meniscus, inlet, outlet and walls are defined as entities. The meniscus is defined as a Surface entity with SURFACE TENSION MODEL = MSURF = 1,

FREE SURFACE DEPTH = 15 (moving elements from the free surface), SPINE GENERATION = SPINES, SURFACE DEFORMATION = STRAIGHT AND CURVED SURFACE = CURVED.

- Definition of the system properties: DENSITY = $Re = Re_{stan}/h^{\#} = 0.5$, SURFACE TENSION = $1/Ca = 100$, SURFACE PRESSURE = $P^{\#}_{G} = 27.39+\cos 45°/(0.01 \cdot 1) = 98.1$ (see Eq. (5.45)), VSICOSITY = 1 (dimensionless viscosity is always 1).

- Implementation of boundary conditions. Nodes n_1 and n_2 are defined as fixed nodes via DEGREE OF FREEDOM = SURFACE, REGION SELECTED = NODES = n_1 (or n_2), VALUE = 0, X/ZC COMPONENT = X = 0, Y/RC COMPONENT = Y = 0 and Z/THETA COMPONENT = Z = 0. The inlet boundary condition defined by Eq. (5.47) is introduced making $U_x = 0 - 1.5y^2+3y$ and $U_y = 0$ is introduced as a second order polynomial, POLYNOMIAL = 2, command line: 0 3 0 1 0 -1.5 0 2 0, which expresses the velocity polynomial coefficients $VAL\ \alpha_1 p^{1,1} p^{2,1} p^{3,1}\ \alpha_2 p^{1,2} p^{2,2} p^{3,2}$ according to,

$$Polynomial = VAL + \sum_{i=1}^{n} \alpha_i x^{p1,i} y^{p2,i} z^{p3,i} \tag{5.1}$$

The rest of boundary conditions are set according to Eqs.(5.49)-(5.52).

- Definition of the simulation features, such as PRECISION = DOUBLE, mixed pressure formulation (MIXED = 1e-9), SURFACE TYPE = FREE, 2D, INCOMPRESSIBLE, STEADY (or TRANSIENT), NON-LINEAR (This is important to consider the inertial term in the Navier-Stokes equations that contain *Re*), NEWTONIAN and ISOTHERMAL. The Newton-Rhapson method is used with 30 maximum number of iterations METHOD = N.R. = 30, SOLUTION TOLERANCE = VELCONV = 1e-5, RESIDUAL TOLERANCE = RESCONV = 1e-5 and RELAXATION FACTOR = ACCF = 0.1 (it can be modified to improve convergence).

Appendix 5B

Mathematica Script for Analytical Solution of Gas Breakthrough under Liquid Flow

Mathematic script for Eq. (5.60). The script is for the example Re = 100, Ca = 0.01, $H^{\#}$ = 2 and $\Delta P^{\#}$ = 28.7.

Input:

DP = 28.7

Re = 100

Ca = 0.01

H = 2

$$\text{sol} = \text{NDSolve}\left[\left\{\text{DP} - 1.86 * \frac{\text{Re}}{2} * \left(1 - \left(\frac{\text{H}}{\text{H} - \text{y[x]}}\right)^2\right) == -\frac{1}{\text{Ca}} * \frac{\text{y''[x]}}{\left(1 + \text{y'[x]}^2\right)^{3/2}}, \text{y[0]} == 0, \text{y'[0]} == 0.75\right\},\right.$$

$$\left.\text{y}, \{\text{x}, 0, 2\}, \text{MaxSteps} \to 2000000, \text{InterpolationPrecision} \to 30, \text{StartingStepSize} \to 0.01, \text{MaxStepSize} \to 0.01\right]$$

Output:

{{y→InterpolatingFunction[{{0.,2.}},<>]}}

Input:

Plot[y[x]/.sol,{x, 0.0001, 2}, PlotRange→All]

Output:

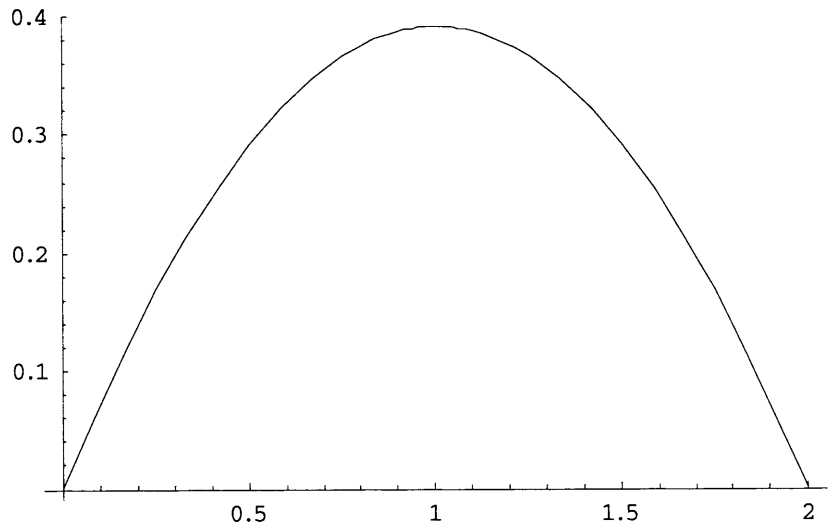

Appendix 6A

Fast Reaction of *A* and *B* at the Interface

Figure 6A.1 represents the system analysed. The spatial variable considered is y and the height of the micro-reactor is $H_T = H + e$, where H is the height of the channel in phase 1 and e is the mesh thickness. The co-ordinate origin for y is in the gas-liquid interface ($y = 0$).

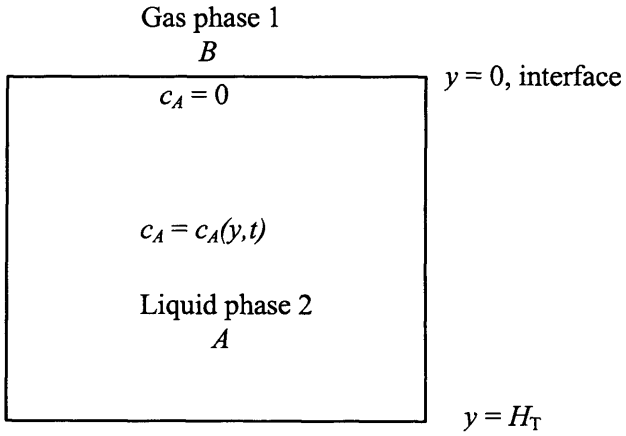

Figure 6A.1. Sketch of the model for fast reaction at the interface.

Eq. (6A.1) for mass transfer by diffusion describes mass transfer under fast reaction. Fick's law applies at low concentrations of reactants and products in the solvent.

$$\frac{\partial c_A}{\partial t} = D_A \cdot \frac{\partial^2 c_A}{\partial y^2} \tag{6A.1}$$

with the following initial and boundary conditions for $c_A(y,t)$,

1. $$c_A(y,0) = c_{A0} \tag{6A.2}$$

2. $$c_A(0,t) = 0 \tag{6A.3}$$

3. $$\frac{\partial c_A(H_T,t)}{\partial z} = 0 \tag{6A.4}$$

The last boundary condition implies that there is no flux of A at the bottom of the reactor. First, a general solution of the diffusion equation when c_A tends to zero as $t \to \infty$ for all y is calculated by using the method of separation of variables. The solution given by Eq. (6A.5) is assumed.

$$c_A(y,t) = Y(y) \cdot T(t) \tag{6A.5}$$

Substituting this solution in the diffusion equation, the following expression is obtained.

$$Y \cdot \frac{\partial T}{\partial t} = D_A \cdot T \cdot \frac{\partial^2 Y}{\partial y^2} \tag{6A.6}$$

Separating variables and using T' and Y'' to denote first and second derivatives of T (with respect to t) and Y (with respect to y) respectively, Eq. (6A.7) is obtained,

$$\frac{Y''}{Y} = \frac{T'}{D_A \cdot T} = -\lambda^2 \tag{6A.7}$$

where $-\lambda^2$ is a constant since each side of the equation is only dependent on one variable. Taking λ as a real number, the value of the constant $-\lambda^2$ is chosen for the imposed boundary condition $c_A(y,\infty) = 0$. Eq. (6A.7) is equivalent to two ordinary differential equations (ODEs), given by Eqs. (6A.8) and (6A.9),

$$Y'' + \lambda^2 Y = 0 \tag{6A.8}$$

$$T' + \lambda^2 D_A T = 0 \tag{6A.9}$$

which can be easily integrated. For the first one, a solution $Y(y) = C e^{jy}$ is tried and two different values of j are found.

$$C \cdot j^2 \cdot e^{jy} + C \cdot \lambda^2 \cdot e^{jy} = 0 \tag{6A.10}$$

$$j = \pm\sqrt{-\lambda^2} = \pm i\lambda \tag{6A.11}$$

Once the values for j are known, the solution of $Y(y)$ is given by Eq. (6A.12) or Eq. (6A.13), as applying Macclaruin series the expression e^{iu} is equivalent to $\cos(u) + i \cdot \sin(u)$.

$$Y(y) = A_1 \cdot e^{i\lambda y} + B_1 \cdot e^{-i\lambda y} \tag{6A.12}$$

$$Y(y) = A_2 \cdot \cos(\lambda y) + B_2 \cdot \sin(\lambda y) \tag{6A.13}$$

The second ODE produces Eq. (6A.14).

$$T(t) = C \cdot e^{-D_A \lambda^2 t} \tag{6A.14}$$

The final solution for the concentration function according to Eq. (6A.5) is,

$$c_A(y,t) = \left(A \cdot \cos(\lambda y) + B \cdot \sin(\lambda y)\right) \cdot e^{-D_A \lambda^2 t} \tag{6A.15}$$

where the constant C is absorbed into the two other constants. In order to satisfy the boundary condition $c_A(0,t) = 0$, A must be zero. In addition to this, applying the other boundary condition $\partial c_A(H_T, t)/\partial y = 0$ (see Eq. (6A.17)), the available values for λ are given by Eq. (6A.18).

$$\frac{\partial c_A}{\partial y} = B \cdot e^{-D_A \lambda^2 t} \cdot \lambda \cdot \cos(\lambda y) \tag{6A.16}$$

$$\frac{\partial c_A(H_T,t)}{\partial y} = B \cdot e^{-D_A \lambda^2 t} \cdot \lambda \cdot \cos(\lambda H_T) = 0 \tag{6A.17}$$

$$\cos(\lambda H_T) = 0 \rightarrow \lambda = \frac{(2n+1)\pi}{2H_T} \quad n = 0,1,2,3... \tag{6A.18}$$

Therefore, the function $c_A(y,t)$ can be represented for the Fourier series given by Eq. (6A.19),

$$c_A(y,t) = \sum_{n=0}^{n=\infty} B_r \cdot \sin\left(\frac{(2n+1)\pi y}{2H_T}\right) \cdot e^{-D_A\left(\frac{(2n+1)\pi}{2H_T}\right)^2 t} \tag{6A.19}$$

In order to calculate the Fourier coefficients B_r, the initial condition is applied, $c_A(y,0) = c_{A0}$.

$$c_A(y,0) = \sum_{n=0}^{n=\infty} B_r \cdot \sin\left(\frac{(2n+1)\pi y}{2H_T}\right) = c_{A0} \tag{6A.20}$$

As the value of $c_A(y,0)$ is known, it is only necessary to apply the definition of the Fourier coefficient B_r,

$$B_r = \frac{2}{H_T} \cdot \int_{y_0}^{y_0+H_T} c_{A0} \cdot \sin\left(\frac{(2n+1)\pi y}{2H_T}\right) dy = c_{A0} \frac{2H_T}{(2n+1)\pi} \tag{6A.21}$$

where y_0 is arbitrary and it will be 0.

Appendix 7A

Flow Distribution in a Complex Manifold Structure – Multiple Feeds

Figure 7A.1 shows a more complex structure designed for reaction purposes. Basically it is composed of two overlapping consecutive structures with a common collecting channel that is now the reaction channel, which is also fed with raw material at a flowrate $Q^{\#}_{T,B}$.

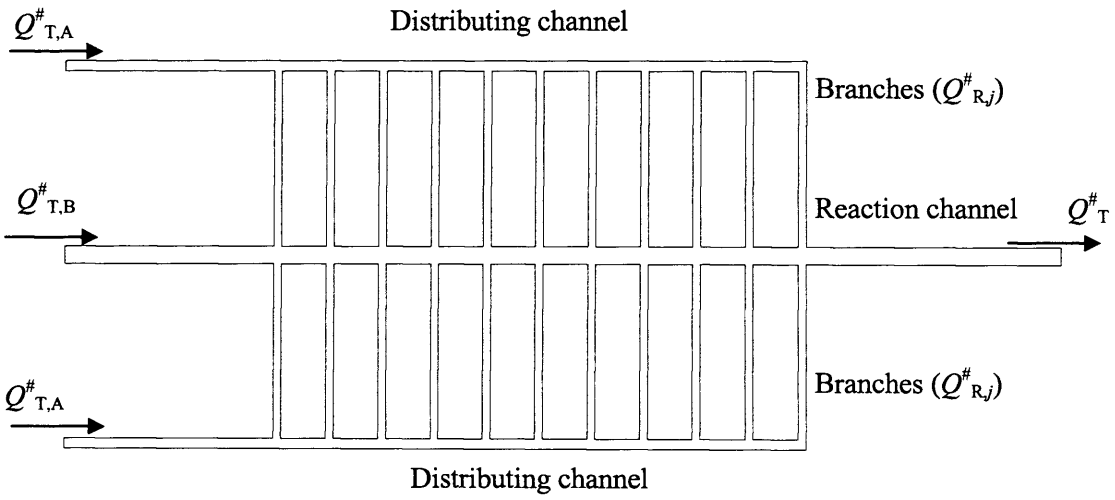

Figure 7A.1. Sketch of a more complex reaction manifold that is solved by the resistance network method.

A reaction aA + bB ⇔ cC +dD is considered in the structure depicted in Figure 7A.1 where all streams are gaseous. Reactant A is introduced through the two distributing channels at the same flow rate, $Q^{\#}_{T,A}$. Reactant B is introduced through the common reaction channel, which is the collecting channel in a simple consecutive structure (Figure 7.3) with a flow rate $Q^{\#}_{T,B}$. The same nomenclature for the subscripts applies: A for distributing, B for collecting (now reaction channel) and R for the branches. Flows in all channels are laminar at this scale, and for this reason small channel width and depth that define the diffusion distances are necessary. The catalyst is placed in the reaction microchannel either as a packed bed or coated at the channel bottom. For a packed bed, the equation used to calculate pressure drop through this channel is different.

The structure represented in Figure 7A.1 can be simplified to the resistance network shown in Figure 7A.2. Due to the symmetry in both distributing channels (same number of branches and same flow distribution when manufacturing tolerances are not considered), the equations of the model are similar to those used in the consecutive structure, taking into account that now the reaction channel (previously collecting channel) is fed with a flow rate of raw material $Q^{\#}_{T,B}$ and the flow rates from the branches are double.

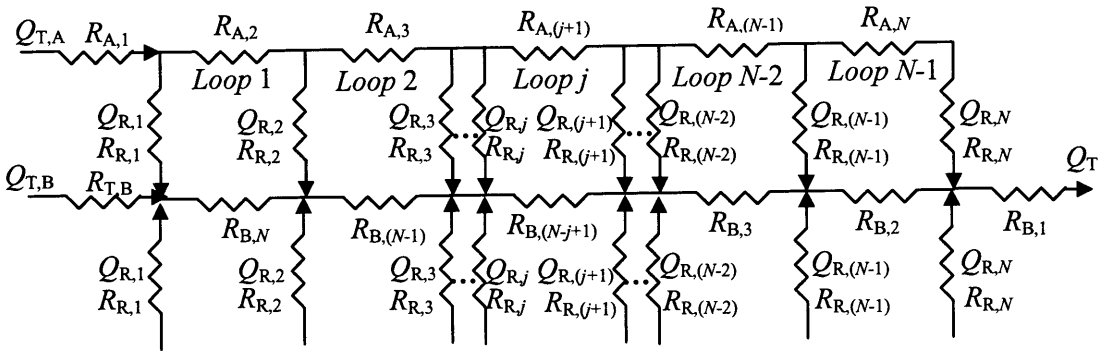

Figure 7A.2. Resistance network for the reactor shown in Figure 7A.1.

As in the consecutive structure, N equations are necessary to solve the N flow rates in the different branches. According to the *loop rule* that corresponds to energy balances in all loops and the nomenclature stated in Figure 7A.2, Eq. (7.11) also applies in this manifold for each loop j (j = 1,2,...,N-1). Applying the *junction rule* the flowrates of the distributing zones, $Q_{A,(j+1)}$, are solved in the same way as in the consecutive structure by Eq. (7.12) and Eq. (7A.1) is used to solve the flowrates in the collecting channel zones, $Q_{B,(N-j+1)}$ (now reaction channel zones).

$$Q_{B,(N-j+1)} = Q_{T,B} + 2 \cdot \sum_{k=1}^{k=j} Q_{R,k} \tag{7A.1}$$

Substituting Eq. (7.12) and (7A.1) into Eq. (7.11), non-dimensionalising according to the aforementioned characteristic dimensions and dividing throughout by $R^{\#}_{R,j}$ gives (N - 1) equations represented by Eq. (7A.2) for loop j. A mass balance to the flowrate distributed among the branches produces the n^{th} expression of the linear system of N-equations, Eq. (7A.3), necessary to solve the flow distribution $Q^{\#}_{R,j}$ (j = 1 to N).

$$-\sum_{k=j+1}^{k=N} Q^{\#}_{R,k}\cdot\frac{R^{\#}_{A,(j+1)}}{R^{\#}_{R,j}}+2\cdot\sum_{k=1}^{k=j} Q^{\#}_{R,k}\cdot\frac{R^{\#}_{B,(N-j+1)}}{R^{\#}_{R,j}}-Q^{\#}_{R,(j+1)}\cdot\frac{R^{\#}_{R,(j+1)}}{R^{\#}_{R,j}}+Q^{\#}_{R,j}=-Q^{\#}_{T,B}\cdot\frac{R^{\#}_{B,(N-j+1)}}{R^{\#}_{R,j}}\quad j=1,2,\ldots,N-1 \tag{7A.2}$$

$$n^{th}\quad equation\qquad Q^{\#}_{T,A}=\sum_{k=1}^{k=N} Q^{\#}_{R,k}=N \tag{7A.3}$$

As previously, these N equations can be expressed and solved in a matrix form via Eqs. (7.16) and (7.17) where now M is a N x N matrix given by Eq. (7A.4), Q is a N column vector with the N reaction channel flowrates, $Q^{\#}_{R,j}$ and the solution vector S is a N column vector formed by $Q^{\#}_{T,B}R^{\#}_{B,(N-j+1)}/R^{\#}_{R,j}$ for j = 1, 2,...,N-1 and $Q^{\#}_{T,A}$ = N in the last position j = N. Under these assumptions this system has the same *PAR* as the consecutive structure previously analysed and the same number of ratios of resistances defining the distribution solution: $PAR = 3(N\text{-}1) + 1$.

$$\mathbf{M}(N,N)=\begin{bmatrix}
2\frac{R^{\#}_{B,N}}{R^{\#}_{R,1}}+1 & -\frac{(R^{\#}_{A,2}+R^{\#}_{R,2})}{R^{\#}_{R,1}} & -\frac{R^{\#}_{A,2}}{R^{\#}_{R,1}} & -\frac{R^{\#}_{A,2}}{R^{\#}_{R,1}} & -\frac{R^{\#}_{A,2}}{R^{\#}_{R,1}} & -\frac{R^{\#}_{A,2}}{R^{\#}_{R,1}} \\
2\frac{R^{\#}_{B,(N-1)}}{R^{\#}_{R,2}} & 2\frac{R^{\#}_{B,(N-1)}}{R^{\#}_{R,2}}+1 & -\frac{(R^{\#}_{A,3}+R^{\#}_{R,3})}{R^{\#}_{R,2}} & -\frac{R^{\#}_{A,3}}{R^{\#}_{R,2}} & -\frac{R^{\#}_{A,3}}{R^{\#}_{R,2}} & -\frac{R^{\#}_{A,3}}{R^{\#}_{R,2}} \\
2\frac{R^{\#}_{B,(N-2)}}{R^{\#}_{R,3}} & 2\frac{R^{\#}_{B,(N-2)}}{R^{\#}_{R,3}} & 2\frac{R^{\#}_{B,(N-2)}}{R^{\#}_{R,3}}+1 & -\frac{(R^{\#}_{A,4}+R^{\#}_{R,4})}{R^{\#}_{R,3}} & -\frac{R^{\#}_{A,4}}{R^{\#}_{R,3}} & -\frac{R^{\#}_{A,4}}{R^{\#}_{R,3}} \\
2\frac{R^{\#}_{B,2}}{R^{\#}_{R,(N-1)}} & 2\frac{R^{\#}_{B,2}}{R^{\#}_{R,(N-1)}} & 2\frac{R^{\#}_{B,2}}{R^{\#}_{R,(N-1)}} & 2\frac{R^{\#}_{B,2}}{R^{\#}_{R,(N-1)}} & 2\frac{R^{\#}_{B,2}}{R^{\#}_{R,(N-1)}}+1 & -\frac{(R^{\#}_{A,N}+R^{\#}_{R,N})}{R^{\#}_{R,(N-1)}} \\
1 & 1 & 1 & 1 & 1 & 1
\end{bmatrix} \tag{7A.4}$$

When the number of moles changes as the reaction proceeds (conversion increase), the flow rate in the reaction channel will change with time. If the number of moles decreases due to the reaction, the design accomplished for the entering flow rate is conservative but if the number of moles decreases along the reaction a better design is achieved by using the flowrate in the reaction channel at the final conversion.

Case Study: Methanol Oxidation

The design shown in Figure 7A.1 has been applied to a real case based on the methanol oxidation given by Eq. (7A.5). Although the number of moles changes as the reaction advances, since a large part of the total flowrate accounts for the inert gas Helium, constant flow rate in the reaction channel is considered. Another issue is the use of substances with different

viscosities whose mixing along the reaction channel produces different intermediate viscosities and there will be different viscosities in each part of the manifold structure. As Helium viscosity is between the viscosity of Oxygen and Methanol and the difference is not large, the effect has been neglected. While different substances are present at different points of the structure if conversion does not affect viscosity in the reaction channel, an iterative solution (based on kinetics) is not necessary. Circular channels are considered for simplification.

$$CH_3OH + \tfrac{1}{2}O_2 \Rightarrow CH_2O + H_2O \qquad (7A.5)$$

The total flowrate entering the structure, $Q_T = 2Q_{T,A}+Q_{T,B}$, is in the range 10-25 ml/min although $Q_{T,B}$ will account for 75-90 % of the total flow rate. The suitable residence time for the methanol oxidation in the reaction channel is 5 – 10 ms as a function of Q_T.

Maximum Dimensions:

- Branches and distributing channels: These must be solved in order to get equal flow distribution in the branches. The minimum size for the diameter of the branches would be $D_{R,j}$ = 50-60 μm.

Therefore, the input data for the Matlab program that solves the structures is:

- Q_T = 600 ml/hr = 10 ml/min
- $Q_{T,A}$ = 50 ml/hr = 0.8333 ml/min.
- $Q_{T,B}$ = (83.33% of the total flow rate).
- Uniform viscosity, $\mu_{Gas} = 3.89 \cdot 10^{-5}$ Pas.
- Separation between branches *sep* = 482 μm.
- From *Sep* and $D_{R,j}$ the reaction channel length is 2 cm.
- Number of branches N = 40.
- Branch length $L_{R,j}$ = 1 cm.
- Minimum branch diameter $D_{R,j}$ = 54.5 μm
- Extra length between reaction channel and inlet/outlet = 0.5 cm.

The solution obtained for the case of branch flowrates 2% within the equipartition flow rate (*FD* = 2%, Q_{EQ} = 0.0208 ml/min) is:

Ratio D = Diameter ratio of distribution channel to branches = 4.364 $\Rightarrow D_{A,j}$ = 237.8 μm

Ratio R = Diameter ratio of reaction channel to branches = 9.451 $\Rightarrow D_{A,j}$ = 515.08 μm

In this case there are two different ratios as there are three different channels with different flowrates, namely reaction and distributing channels and branches. This final result is obtained by applying an iterative process where *Ratio D* and *Ratio R* are increased until good equipartition is achieved. Next, *Ratio R* is adjusted until the flow distribution in all branches is perfectly symmetrical, which gives the best flow equipartition for that *Ratio D* (smaller *FD*).

- Average velocity (for Q_{Av} = 550 ml/hr = $1.528 \cdot 10^{-7}$ m^3/s)= $U_{B,,av}$ = 0.7333 m/s
- Average residence time (length = 2.5 cm) = $t_{B,,av}$ = 0.034 s = 34 ms.

This time is larger than 10 ms so that if the residence time must be between 5 and 10 ms, the width and depth of the reaction channel should be around 247.2·247.2 μm in order to get a residence time of 7.85 ms. If the design data related to number, diameter and length of the branches and length of the reaction channel cannot be changed the only option to reduce the *Ratio D* and *Ratio R* is increasing *FD* (%). Residence time 7.85 ms is found when *Ratio D* = 2.13 and *Ratio R* = 4.62 for which *FD* = 32 %. This means that all the flow rates are 32 % within the equipartition flow rate, which does not indicate a good distribution. However changing some design data to the following, a better design is obtained:

- Separation between reaction channels *sep* = 1021 μm (reaction channel 2 cm long).
- Decreased number of branches N = 20.
- Increased branch length $L_{R,j}$ = 2 cm.
- Minimum branch diameter $D_{R,j}$ = 53.5 μm

The solution under these conditions improves the flow distribution to *FD* = 8 %.

Ratio D = 2.135 $\Rightarrow D_{A,j}$ = 114.2 μm.
Ratio R = 4.621 $\Rightarrow D_{B,j}$ = 247.2 μm

Better flow distribution can still be achieved by additional increase of the branch length and decrease of the number of branches. Another option is to reduce the length of the reaction channel so that a larger reaction channel can be used keeping the same residence time. In this structure a modification on the fresh flowrates that are entering the system will affect the flow distribution (change in *FD*) even if additional pressure losses are not taken into account. Figure 7A.3 shows the flow distribution for the previous design (*FD* = 8% and $Q_{T,B}/Q_T$ = 0.833) and for

C

the same design with a ratio $Q_{T,B}/Q_T$ = 0.5, where *FD* goes from 8 % to 24 % due to the asymmetrical flow distribution.

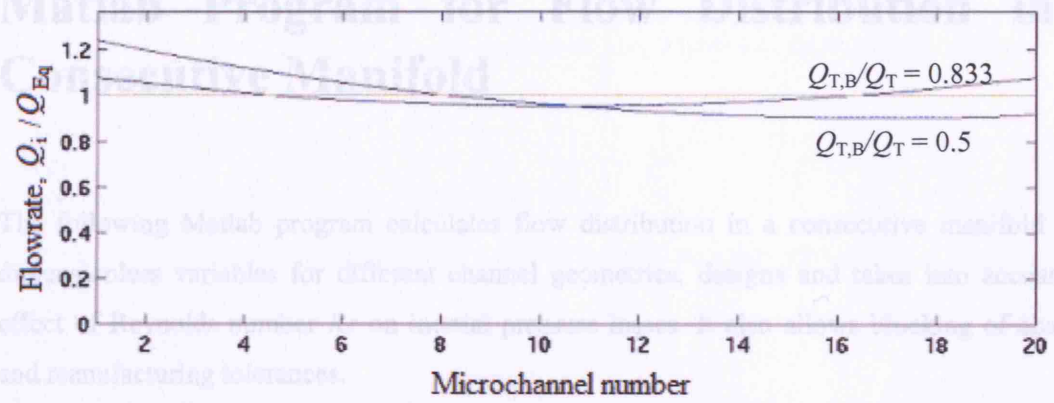

Figure 7A.3. Influence of the flowrate ratio $Q_{T,B}/Q_T$ in flow distribution for the structure.

A test case for the design of a methanol oxidation reactor with multiple inlets was studied with the resistance network model, in order to achieve equal flow distribution in the multiple inlets. The structure can be considered as an overlap of two consecutive structures along the collecting channel, which is used as a reaction channel. Flow is introduced in the reaction channel, $Q^{\#}_{T,B}$, as well as in both distributing channels, $Q^{\#}_{T,A}$, according to Figure 7A.1. It is found that flow distribution in the multiple inlets depends on the ratio of these two flowrates as well as all the geometry of the system. For each specific geometry, there is a ratio of flowrates $Q^{\#}_{T,B}/ Q^{\#}_{T,A}$ that produces a symmetrical flow distribution (neglecting additional pressure losses), which correspond to the smallest value of *FD* (%) (optimum solution).

Appendix 7B

Matlab Program for Flow Distribution in a Consecutive Manifold

The following Matlab program calculates flow distribution in a consecutive manifold using dimensionless variables for different channel geometries, designs and takes into account the effect of Reynolds number *Re* on inertial pressure losses. It also allows blocking of channels and manufacturing tolerances.

File main.c

```
% Consecutive structure. Implementation of resistance network method.
% Program contains all possible solutions for consecutive structure.
% Study of resistance ratios, tolerances and blockages.
% Program allows to take into account additional pressure losses at
high Re.
% All values are dimensionless (characteristic length = channel
smallest dimension)


clear TRESIDENCIA
cont=1; % 1 if no stochastic approach is used.
dist=zeros(cont,1)

for o=1:cont

clear CHAN;
clear M;
clear K;
clear Q;
clear Qn;
clear S;
clear R;
clear Radd;
clear DIA;
clear DEPTH;
clear LEN;
clear equi;
clear Rm;
clear VEL;
clear AREA;
clear tresid;

% INPUT DATA.
% Modes
% Mode_1=0 is to work only with ratios of resistances.
mode_1 = 1;
% Two possible channel geometries: circular, rectangular
```

```
shape='rectangular';
% Three possible designs Constant, nonlinear and linear d/c channels.
distColl='constant'

ro =0; % Reynolds number for additional pressure losses.
fke = 2; % Energy correction factor in laminar flow
% Tolerances: tol and tolD, tolerances in channel width and depth
resp.
tol=0; %0.05; %0.0643275; % This is the dimensionless
tolerance.(tol/Dc)
tolD=0; %0.05; %0.032164;
% Length of the reaction microchannels.
lm = 50; %64.3275;
% Extra length of the distributing and collecting channels.
lexd=10;
lexc=10;
LEN(1,1)=lexd;
LEN(2,1)= lm;
LEN(3,1)=lexc;
% Number of microchannels (or microreactors) in parallel.
n=16;
CHAN=[1:n]';
% Separation between reaction microchannes.
sep = 1;
% Total flow rate to distribute.
qt = n;
% Equipartition flow
Qeq = qt/n;
QEQ = zeros(n);
QEQ(:)=Qeq;

% Next, the nominal values of the hydraulic diameters are defined.
% Diameter of circular channel or width in rectangular channel.
DIA=zeros(3,n);

% Generation of the random matrix with values between 0 and 1.
% 3 rows: 1 for distributing, 2 for reaction, 3 for collecting
channel.
B=rand(3,n);     % Matrix for tolerance in width (diameter in circular
channels).
BD=rand(3,n);    % Matrix for tolerances in channel depth.
B=B.*(2*tol)-tol;      % Tolerance of + - %*2.
BD=BD.*(2*tolD)-tolD;

switch lower(shape)
  case 'circular' % Circular channels
    d(3)=3.5; % This is the width of last zone if design is varying
              d/c channels.
    d(2)=1;   % Characteristic length.
    d(1)=3.5;
    DIA=VARYINGCIR(n,distColl,d);
    for i=1:3
        for j=1:n
            DIA(i,j)=DIA(i,j)+B(i,j);
        end
    end

  case 'rectangular'
    d(3)=1; % Nominal widths. Width of last zone.
    d(2)=1;
```

```
    d(1)=1;
    de(3)=1; % Nominal depths.
    de(2)=1;
    de(1)=1;
    DEPTH=zeros(3,n);
    for i=1:3
        DEPTH(i,:)=de(i);
    end
    % Thus, function VARYINGREC only returns the channel widths.
    DIA=VARYINGREC(n,distColl,d,de);

    for i=1:3
        for j=1:n
            % Different tolerances for depth and width are possible.
            DIA(i,j)=DIA(i,j)+B(i,j);
            DEPTH(i,j)=DEPTH(i,j)+BD(i,j);
        end
    end

  otherwise
    disp('Shape undefined');
end


% Calculation of lengths
% Generation of the random matrix with values between 0 and 1.
% It has 3 rows: 1 for distributing, 2 for reaction, 3 for collecting.

for i=1:3
    for j=1:(n-1)
        if i==1
            % Diameters of reaction microchannels affect sublengths.
            LEN(i,j+1)=LENGTHCON(sep,d(2),DIA(2,j+1),DIA(2,j));
        elseif i==2
            LEN(i,j+1) = lm;
        else
            LEN(i,j+1)=LENGTHCON(sep,d(2),DIA(2,n-j+1),DIA(2,n-j));
        end
    end
end


% Area of all channels
switch lower(shape)
    case 'circular'
        for i=1:3
            for j=1:n
                 AREA(i,j) = (DIA(i,j)).^2; % Dimensionless area
            end
        end
    case 'rectangular'
        for i=1:3
            for j=1:n
                 % Dimensionless area
                 AREA(i,j) = (4/pi)*DIA(i,j).*DEPTH(i,j);
            end
        end
    otherwise
        disp('Shape undefined')
        pause
```

```
end
Q = zeros(n,1);
Qa=zeros(n,1);
Qb=zeros(n,1);
Qa(1)=qt;
Qb(1)=qt;
Qn = ones(n,1);
Radd=zeros(3,n);

while abs(Qn-Q)>0.0001
% In iteration 1, Q = 0 and additional losses are not considered.
Qn=Q;

% Calculation of the resistances after geometry and tolerances
% Nomenclature: RAj=R(1,j), Rmj=R(2,j) and RBj=R(3,j).
switch lower(shape)
    case 'circular'
        for i =1:3  % 1 (distributing), 2(reaction), 3(collecting).
            for j=1:n
                R(i,j)=(32*LEN(i,j))/(DIA(i,j)^4) + Radd(i,j);
            end
        end
    case 'rectangular'
        for i=1:3
            for j=1:n
                % Characteristic area as in circular channels.
                % Ac=(PI*Dc^2)/4, Uc = Qc*4/(pi*Dc^2)
                if (DEPTH(i,j)/DIA(i,j))<=1
                    R(i,j)=(3*pi*LEN(i,j))/(DIA(i,j)*DEPTH(i,j)^3*(1-
                    0.351*DEPTH(i,j)/DIA(i,j))^2) + Radd(i,j);
                else
                    R(i,j)=(3*pi*LEN(i,j))/(DEPTH(i,j)*DIA(i,j)^3*(1-
                    0.351*DIA(i,j)/DEPTH(i,j))^2) + Radd(i,j);
                end
            end
        end
    otherwise
        disp('Shape undefined')
        pause
end


% Removal of collecting channels.
% For collection of fluid directly in different reservoirs.
%R(3,:)=0

if mode_1==0 % When working with resistances.
    ratio=0.0000015259;
    R(2,:)=1;
    R(1,:)=ratio;
    R(3,:)=R(1,:);
end

% Blockage of reaction channels.

%R(2,8)=10^10*R(2,6);
%R(2,1)=10^10*R(2,6);
%R(2,15)=10^10*R(2,6);
```

```
% Solution of the linear system of equations.
for  i=1:(n-1)
    for j=1:n
        if j<i
            M(i,j)=R(3,n-i+1);
        elseif j==i
            M(i,j)=R(3,n-i+1)+R(2,i);
        elseif j==i+1
            M(i,j)=-(R(1,i+1)+R(2,i+1));
        elseif j>i+1
            M(i,j)=-R(1,i+1);
        end
    end

    S(i)=0;

end
% Last row of the matrix and final solution.
M(n,:)=1;
S(n)=qt;

Q=inv(M)*S';

%Flowrates in distributing (Qa) and collecting (Qb) zones.
    for j=1:(n-1)
        Qa(j+1)=qt;
        Qb(n-j+1)=0;
        for k=1:j
            Qa(j+1)=Qa(j+1)-Q(k);
            Qb(n-j+1)=Qb(n-j+1)+Q(k);
        end
    end

% Additional resistances due to merging/branching and inertial effects
% All K refer to the velocity of the channel.
    for i =1:3  % 1 (distributing), 2(reaction), 3(collecting).
        for j=1:n   % Radd(1,1) and Radd(3,1) for d/c channel inlets.
            if i == 2
               % For reaction channels there are two extra additional
               % losses due to the merging and branching.
               % For j = 1 and j = n there is only one contribution
               % plus bends.
               if (AREA(2,j)/AREA(1,j))<0.35
                   gi1=1;
               else
                   if (Q(j)/Qa(j))<0.4
                       gi1=0.9*(1-Q(j)/Qa(j));
                   else
                       gi1=0.55;
                   end
               end
               if (AREA(2,j)/AREA(3,n-j+1))<0.35
                   gi2=1;
               else
                   if (Q(j)/Qb(n-j+1))<0.4
                       gi2=0.9*(1-Q(j)/Qb(n-j+1));
                   else
                       gi2=0.55;
                   end
               end
```

```
            if j==1
                K(i,j)= fke*(1-(Qa(j)*AREA(2,j)/(Q(j)*AREA(1,j)))
                ^2);
                Kuno(i,j)=gi1*1/((Q(j)*AREA(1,j)/(Qa(j)*AREA(2,j)))
                ^2)*(1+0.3*((Q(j)*AREA(1,j)/(Qa(j)*AREA(2,j)))^2));
            elseif j==n
                K(i,j)= -fke*(1-(Qb(n-j+1)*AREA(2,j)/(Q(j)*
                AREA(3,n-j+1)))^2);
                Kuno(i,j)=gi2*1/((Q(j)*AREA(3,n-j+1)/(Qb(n-
                j+1)*AREA(2,j)))^2)*(1+(Q(j)*AREA(3,n-j+1)/(Qb(n-
                j+1)*AREA(2,j)))^2-2*(1-Q(j)/Qb(n-j+1))^2);
            else
                K(i,j)= fke*(1-(Qa(j)*AREA(2,j)/(Q(j)*
                AREA(1,j)))^2)-fke*(1-(Qb(n-j+1)
                *AREA(2,j)/(Q(j)*AREA(3,n-j+1)))^2);

                Kuno(i,j)=gi1*1/((Q(j)*AREA(1,j)/(Qa(j)*AREA(2,j)))
                ^2)*(1+0.3*((Q(j)*AREA(1,j)/(Qa(j)*AREA(2,j)))^2))+
                gi2*1/((Q(j)*AREA(3,n-j+1)/(Qb(n-j+1)*
                AREA(2,j)))^2)*(1+(Q(j)*AREA(3,n-j+1)/(Qb(n-j+1)
                *AREA(2,j)))^2-2*(1-Q(j)/Qb(n-j+1))^2);
            end
             Radd(i,j)=K(i,j)*ro*Q(j)/(2*(AREA(i,j)^2));
        elseif i ==1
            if j==1
                K(i,j)=0;
                Kuno(i,j)=0;
            else
                K(i,j)= fke*(1-(Qa(j-1)*AREA(1,j)/(Qa(j)*AREA(1,j-
                1)))^2);
                Kuno(i,j)=0.4*((1-Qa(j)*AREA(1,j-1)/(Qa(j-
                1)*AREA(1,j)))^2)*1/((Qa(j)*AREA(1,j-1)/(Qa(j-
                1)*AREA(1,j)))^2);
            end
            Radd(i,j)=K(i,j)*ro*Qa(j)/(2*(AREA(i,j)^2));

        else
            if j==n
                K(i,n-j+1)=0;
                Kuno(i,n-j+1)=0;
            else
                K(i,n-j+1)= -fke*(1-(Qb(n-j)*AREA(3,n-j+1)/(Qb(n-
                j+1)*AREA(3,n-j)))^2);
                Kuno(i,n-j+1)= (1.55*Q(j+1)/Qb(n-j)-(Q(j+1)/Qb(n-
                j))^2)*1/((1-Q(j+1)/Qb(n-j))^2);
            end
            Radd(i,n-j+1)=K(i,n-j+1)*ro*Qb(n-j+1)/(2*(AREA(i,n-
            j+1)^2));
        end

    end
end
% End of calculation of additional resistances.

end

for i=1:n
    % equi is the percentage of equipartition achieved.
    % It only depends on the ratio R(1,:)=R(3,:)/R(2,:).
```

```
    equi(i)=100*abs(1-abs(Q(i)-Qeq)/Qeq);
end

equi_min=min(equi);

% Calculation of residence times in reaction microchannels(2).
% Two ways of calculating the mean residence time.
tmean=0;
tmean2=0;
switch lower(shape)
    case 'circular'
        AREA = (DIA(2,:)).^2;    % Dimensionless area
    case 'rectangular'
        AREA = (4/pi)*DIA(2,:).*DEPTH(2,:);
    otherwise
        disp('Shape undefined')
        pause
end

VEL=(Q./AREA'); % Dimensionless Velocity.
tresid=(LEN(2,:)'./VEL); % Dimensionless Residence time.
for i=1:n
    tmean=tmean+Q(i)*tresid(i);
    tmean2=tmean2+LEN(2,i)*AREA(i);
end
tmean=tmean/qt;
tmean2=tmean2/qt;

% Statistical analysis of the data.

s_2 = (1/n)*sum((tresid-tmean).^2); % Sample variance.
s = 100*(sqrt(s_2)/tmean);          % Sample standard deviation in %.
ss_2=(1/n)*sum((Q-Qeq).^2);
ss=100*(sqrt(ss_2)/Qeq);            % Sample st. dev. for flow rates.

% Calculation of total pressure drop
ap=0;   % Initialization
qAB=qt;
for j=1:(n-1)
    qAB=qAB-Q(j); % Flowrates in the zones of the d/c channels.
    ap=ap + qAB*R(1,j+1);
end

ap=ap + (qt*(R(1,1)+R(3,1)) + Q(n)*R(2,n));

% Results
Qeq;
%tmean,tmean2, s_2, s,ss_2,ss, ap
[xm_2,im]=max(tresid);
[xm_3,im]=min(tresid);
ends=[xm_2,xm_3];
equi_min
ratio=(R(1,2)./R(2,1));



% This is only for the case of running the program cont times.
% dist stores the standard deviations of all runs.
% TRESIDENCIA stores all the residence times.
```

```
% Doing [value posi]=max(dist) the values and position of the maximum
% standard deviation is retrieved and doing TRESIDENCE(:,position)  we
% get the residence time distribution for the worst scenario
dist(o,1)=s;
TRESIDENCIA(:,o)=tresid;
totalPDrop(o,1)=ap;
end

% Graphical Representation.
[xm_1,im]=max(Q);
subplot(2,1,1), plot(CHAN,Q);
hold on;
plot(CHAN,QEQ);
xlabel('Microchannel number');
ylabel('Flow rate');
axis([1,n,0,(xm_1)*1.1]);
hold off;

subplot(2,1,2), plot(CHAN,tresid);
hold on
TMEAN=zeros(n);
TMEAN(:)=tmean;
plot(CHAN,TMEAN);
xlabel('Microchannel number');
ylabel('Dimensionless Residence time');
axis([1,n,0,(xm_2)*1.1]);
hold off;
```

File LENGTHCON.m

```
% This function calculates the length of the d/c and reaction channels
% in a consecutive structure.
function length=LENGTHCON(sep,wn,wj1,wj)

    length=(sep + wj1+(wn-wj)/2 + (wn-wj1)/2);
```

File VARYINGCIR.m

```
% This function solves d/c channels with "varying" diameters

% Function VARYINGCIR redefine the matrix DIA for 3 different cases.
% (1) constant diameter d/c channels, (2) curved d/c channels and (3)
% linear d/c channels.
% W is a vector with the 3 diameters.
function vary=VARYINGCIR(number,mode,W)
global dif

vary=zeros(3,number);
vary(2,:)=W(2);
switch lower(mode)
    case 'constant'
        vary(1,:)=W(1);
        vary(3,:)=W(3);
    case {'nonlinear','linear'}
```

```
        vary(3,number)=W(3);
        vary(3,2)=(number/1-1)^0.25*vary(3,number);
        vary(3,2)=2;  % to modify Db,2 once Db,N is fixed.
        for j=1:number
            vary(3,j)=vary(3,2)-((vary(3,2)-vary(3,number))/(number-
            2))*(j-2);
        end
        % This is to use the same curved geometry d/c channels.
        % vary(3,:)=dif;
        vary(1,1)=vary(3,1);
        for j=1:(number-1)
            vary(1,j+1)=(number/j-1)^0.25*vary(3,(number-j+1));
        end
        % For use of same curved geometry in d/c channels.
        % dif=(vary(1,:)+vary(3,:))/2;

        % Compare strings mode and 'linear'.
        % Returns 1 if they are the same, executing the sentence.
        if strcmpi(mode,'linear')
            vary(1,:)=vary(3,:);   % This is to do linear chambers.
        end

    otherwise
        disp('d/c channel geometry unknown');
        pause
end
```

File VARYINGREC.m

```
% This function solves d/c channels with "varying" diameters.
% W = Nominal width vector and DE is the nominal depth vector.
function vary=VARYINGREC(number,mode, W,DE)
vary=zeros(3,number);
vary(2,:)=W(2);
switch lower(mode)
    case 'constant'
        vary(1,:)=W(1);
        vary(3,:)=W(3);
    case {'nonlinear','linear'}
        % Width of last zone in collecting channel.
        vary(3,number)=W(3);
        if (DE(3)/W(3))<=1
            ResN=1/((number/1-1)*DE(3)^3*W(3)*(1-0.351*DE(3)/W(3))^2);
        else
            ResN=1/((number/1-1)*W(3)^3*DE(3)*(1-0.351*W(3)/DE(3))^2);
        end
        % Initially WIDTH(3,2)=DEPTH(3,2) is assumed.
        % vary(3,2)=DE(3)
        % This equation is only for depth/width<=1. For the contrary
        % the polynomial is 5 order instead of second order.
        points=roots([ResN*DE(3)^3 -(2*0.351*DE(3)^4*ResN+1) DE(3)^5
        *ResN*0.351^2]);
        vary(3,2)=max(points);
        vary(3,2)=6.6; % Result modified by hand to improve it.
        for j=1:number
```

```
            vary(3,j)=vary(3,2)-((vary(3,2)-vary(3,number))/(number-
            2))*(j-2);
        end
        vary(1,1)=vary(3,1);
        % Only for linear chamber so far.
        % Compare strings mode and 'linear'.
        % Returns 1 if they are the same, executing the sentence.
        if strcmpi(mode,'linear')
            vary(1,:)=vary(3,:);   % This is to do linear chambers.
        End

    otherwise
        disp('d/c channel geometry unknown');
        pause
end
```

Appendix 7C

Implementation of 16 Channel Manifold in Femlab

The dimensions of the channels are: $D^{\#}_{A} = 1$, $W^{\#}_{R} = 1$, $Sep^{\#} = 1$, $L^{\#}_{A}/L^{\#}_{R} = L^{\#}_{B}/L^{\#}_{R} = 0.04 \rightarrow L^{\#}_{R} = 50$, $L^{\#}_{A,1} = L^{\#}_{B,1} = 10$ and $Re = 0.01$ (to minimise the additional pressure losses). The small reaction channel separation makes the assumption of fully developed flow in the distributing/collecting channels less accurate; this may be reason for the small discrepancy between the Femlab and the analytical solutions even at $Re = 0.01$. The implementation in Femlab follows:

A. 3D incompressible Navier-Stokes mode with 4 dependent variables ($U^{\#}_{x}$, $U^{\#}_{y}$, $U^{\#}_{z}$ and $P^{\#}$). Lagrange-Quadratic element and non-linear stationary solver type.

B. The gravity effect of Froude number is considered to be negligible.

C. To draw the manifold structure, 3 different y-z work planes are used: 1) at $x = 0$ containing the face of the distributing channel, which is extruded -1 units in the x-direction in order to create the distributing channel, 2) at $x = 25$ where places cross sections in the middle of each reaction channel are drawn in order to integrate the velocity profile over the cross section obtaining the flowrate in each channel. Furthermore, this cross sections are first embedded into the 3D drawing and then extruded -25 and 25 units in the x directions, generating the reaction channels and 3) at $x = 50$ containing the face of the collecting channel, which is extruded 1 unit in the x-direction generating the collecting channel (see Figure 13).

D. Subdomain settings: Femlab implements the Navier-Stokes equation in the form given by Eq. (7C.1). Thus, $\rho = Re$, $\mu = 1$ and F = 0 are the values typed in Femlab in order to solve the dimensionless incompressible Navier-Stokes given by Eq. (7.57). Using these definitions the value of $P^{\#}$ from femlab is the same defined by Eq. (7.3).

$$\rho\mathbf{U}\cdot\nabla\mathbf{U} + \nabla P - \nabla(\mu(\nabla\mathbf{U} + (\nabla\mathbf{U})^{\mathrm{T}}) = \mathbf{F} \qquad (7C.1)$$

E. Boundary settings: In order to have the same definition of Re in both the analytical model and the FEM simulations, D_C and U_C must be the same. For this reason, the width and depth

of the reaction channels is 1 in the square channels and the flowrate $Q^{\#}_{T}$ entering the structure must be equal to N. If this flowrate is not equal to N, the definition of Re between the analytical model and the Femlab simulations will be different and the equiparition flowrate and the Re used for the Femlab simulations must be readjusted to the one defined with the equiparition flowrate. At the exit "straight out flow" is chosen ($P^{\#} = 0$ and at the rest of walls, "no-slip" condition is defined.

F. Mesh generation: Fine mesh setting are used to generate the mesh with the constraint of maximum edge size (general) equal to 1. The mesh, composed of 7868 nodes and 21168 elements, has a high quality (0.791) and the solution conserves the mass flow.

In order to reduce the memory usage due to the large number of elements, the next functions are selected: an iterative solver (GMRES) rather than a non-iterative one that is more memory demanding, element type Lagrange p2-p1, sparse null space function and an incomplete LU preconditioning tuning the drop tolerance. If more than 16 channels are used, memory problems come appear if the same number of elements per volume is kept.

Appendix 8A

Matlab Program for Measurement of Bubble and Liquid Slug Lengths

```
% This program is used to measure bubble and liquid slug length.
% Illumination during experiments is very important although a
reference light outside the capillary is considered.
% The image is load into a matrix
clear limita;
clear limitb;
clear length;

% Two files are created and open. One for results and another to log
errors
[file_1,error_op_1] = fopen('RESULTS_BUBBLES_G5II.txt','a');
[file_2,error_op_2] = fopen('RESULTS_SLUGS_G5II.txt','a');
[file_3,error_op_3] = fopen('LOGS_G5II.txt','a');
fprintf(file_1,'**************************************************
**********************************************');
fprintf(file_1, '\n%s: Bubble Lengths, microns\n \n', datestr(now));
fprintf(file_2,'**************************************************
**********************************************');
fprintf(file_2, '\n%s: Liquid Slug Lenghts, microns\n \n',
datestr(now));
fprintf(file_3,'**************************************************
**********************************************');
fprintf(file_3,'\n%s: Tracking of the Analysis \n\nFilename \t\tType
\tBubbles nº \tSlugs nº \tDescription\n\n',datestr(now));

% Number of pictures to analyse.
file_end =10;
file_start = 0; %0 if the first photo analysed is 001.
path('E:\g=100_1=5\',path)
bodystring = 'image000';

for i = 1:1:(file_end-file_start+1)

% Each time that the file does not exist, we move on to the next file.
error= 'no';
FileName = strcat(bodystring, char('0'*((file_start+i-
1)<100)),char('0'*((file_start+i-1)<10)),int2str((i+file_start-
1)),'.tif');

try
    Picture = imread(FileName);
catch
    error = 'si';
    fprintf(file_3,'%s\n',lasterr);
end
if error =='no'
[rows, columns]=size(Picture);
magnification = 12.73;% Number of microns per pixel in the image.
diameter = 710; % This is the dimension of the inner diameter.
pixels_diam = diameter/magnification;
```

```
%This is the row that is scanned and analysed.
rowi=348;
rowii=rowi+diameter/(1.5*magnification);

Imagei = double(Picture(rowi, :));
Imageii = double(Picture(round(rowii),:));
Image = zeros(1,columns);
Image = Imagei - Imageii;

% This is the threshold of intensity.
l_inten = -40;

% Plot of the intensity along the main axis.
plot_yes =1;
if plot_yes ==1
    pixels = [1:1:columns];
    plot(pixels,Image);
    xlabel('pixel');
    ylabel('intensity');
    hold on;
    plot(pixels, l_inten);
end


% Margin of intensity and blurred effect.
margin = 80;
% This is the margin to select the points. The largest the better.
More points captured in Limits.
blurred = 20; % We consider a blurred effect of 20 pixels.


Limits=find(Image<l_inten & Image >(l_inten-margin));
Limits=[Limits,2000];
[n,m]=size(Limits);
la=zeros(1,m); %Maximum number of Limits (always less than m).
lb=zeros(1,m);
length = zeros(1,m);
cont_a=1;
cont_b = 1;
cont2_a = 0;
cont2_b = 0;
limit = 0.8*double(Image(Limits(1))); % The factor 0.8 is adjusted.
rowcheck=round(pixels_diam/4);
int_upper = Picture(rowi-rowcheck,Limits(1));

% I can improve the detection, scanning a vertical line 20 or 30
pixels(the blurred factor) far away from Limits(1).

if double(int_upper)-double(Imageii(Limits(1)))<limit
    % Initially only one point is considered as criterion.
    edge_a=0; % It means it is the end of a bubble.
else
   edge_a=1; % It means it is the beginning of a bubble.
End

% It specifies if it is the beginning or end of a bubble.
first_edge = edge_a;
for i = 2:1:m
   if (Limits(i)-Limits(i-1))<blurred
```

```
        if edge_a == 1;
            % Algorithm to take the firt number of all of them.
            cont_a=cont_a+1;

        else
            cont_b=cont_b+1;
            % Algorithm to take the last number of all of them.
        end
    else
        if edge_a ==1
            cont2_a=cont2_a+1;
            la(cont2_a)=Limits(i-cont_a);

            % Counter of subpoints within a limit a is set to 1 again.
            cont_a = 1;
            if i == m
                last_edge = edge_a;
            end
            edge_a = 0;
        else
            cont2_b=cont2_b+1;
            % In this case, it is not i-cont_b but i-1, which is the
            last value of the point in boundary b.
            lb(cont2_b)=Limits(i-1);

            cont_b=1; % The counter of subpoints within a limit b is
            set to 1 again.
            if i ==m
                last_edge = edge_a;
            end
            edge_a=1; % Next boundary is a edge a.
        end
    end
end
laa=find(la~=0); % Only values different from zero are kept.
lbb=find(lb~=0);
la = [la(1:1:max(laa))];
lb=[lb(1:1:max(lbb))];
if first_edge==1
    if last_edge ==1
        type = 'a';
        % First and last boundaries detected are starting boundaries
        of bubbles.ONE BUBBLE CUT AT THE END.
    else
        type = 'b';
        % First is starting bubble and last is ending bubbles. NO
        BUBBLES CUT.
    end
else
    if last_edge ==1
        type = 'c';
        % First is ending bubble and last is starting bubble. ONE
        BUBBLE CUT AT THE BEGINNING and ANOTHER AT THE END.
    else
        type = 'd';
        % First is ending bubble and last is ending bubble. ONE BUBBLE
        CUT AT THE BEGINNING.
    end
end

switch lower(type)
```

```
    case 'a'
        explanation = 'One bubble cut at the end of the image';
        [k, l]=size(lb);
        bubbles = l;
        slugs = bubbles;
        % Vector with the length of all the bubbles;
        bubble_l = zeros(1,bubbles);
        slug_l = zeros (1,bubbles);
        for i = 1:1:bubbles
            bubble_l(i) = magnification*(lb(i)-la(i));
            slug_l(i) = magnification*(la(i+1)-lb(i));
        end
    case 'b'
         explanation = 'No bubbles cut in the image';
        [k, l]=size(la);
        bubbles = l;
        slugs = bubbles-1;
        bubble_l = zeros(1,bubbles);
        slug_l = zeros (1,bubbles-1);
        for i = 1:1:bubbles
            bubble_l(i) = magnification*(lb(i)-la(i));
        end
        for i = 1:1:(bubbles-1)
            slug_l(i) = magnification*(la(i+1)-lb(i));
        end
    case 'c'
        explanation = 'bubbles cut at the beggining and at the end';
        [k, l]=size(la);
        bubbles = l-1;
        slugs = bubbles+1;
        bubble_l = zeros(1,bubbles);
        slug_l = zeros (1,bubbles+1);
        for i = 1:1:bubbles
            bubble_l(i) = magnification*(lb(i+1)-la(i));
        end
        for i = 1:1:(bubbles+1)
            slug_l(i) = magnification*(la(i)-lb(i));
        end
    case 'd'
        explanation = 'One bubble cut at the beggining of the image';
        [k, l]=size(la);
        bubbles = l;
        slugs = bubbles;
        bubble_l = zeros(1,bubbles);
        slug_l = zeros (1,bubbles);
        for i = 1:1:bubbles
            bubble_l(i) = magnification*(lb(i+1)-la(i));
            slug_l(i) = magnification*(la(i)-lb(i));
        end

end

for i =1:bubbles
    COUNT_1 = fprintf(file_1, '%f\t %s\n', bubble_l(i),FileName);
end
for i = 1:slugs
    COUNT_2 = fprintf(file_2, '%f\t %s\n',slug_l(i), FileName);
end

COUNT_3 = fprintf(file_3,'%s \t %s \t   %i \t\t   %i
\t\t%s\n',FileName,type, bubbles, slugs,explanation );
```

```
end % End of the if error.

end
fprintf(file_1,'**************************************************
**************************************************\n');
fprintf(file_2,'**************************************************
**************************************************\n');
fprintf(file_3,'**************************************************
**************************************************\n');
% Close the data files.
error_cl_1 = fclose(file_1);
error_cl_2 = fclose(file_2);
error_cl_3 = fclose(file_3);

disp('END OF THE PROGRAM')
```

The program returns three files

RESULTS_SLUGS_G3.txt

```
06-May-2004 22:39:25: Liquid Slug Lengths, microns

763.800000   G3L17_001.tif
687.420000   G3L17_001.tif
623.770000   G3L17_001.tif
814.720000   G3L17_003.tif
763.800000   G3L17_003.tif
801.990000   G3L17_004.tif
751.070000   G3L17_004.tif
661.960000   G3L17_004.tif
789.260000   G3L17_006.tif
751.070000   G3L17_006.tif
636.500000   G3L17_006.tif
840.180000   G3L17_007.tif
738.340000   G3L17_007.tif
687.420000   G3L17_007.tif
...
```

File RESULTS_BUBBLES_G3.txt

```
06-May-2004 22:39:25: Bubble Lengths, microns

3386.180000  G3L17_001.tif
3271.610000  G3L17_001.tif
3449.830000  G3L17_003.tif
3144.310000  G3L17_003.tif
3589.860000  G3L17_004.tif
3538.940000  G3L17_004.tif
3297.070000  G3L17_006.tif
3093.390000  G3L17_006.tif
3411.640000  G3L17_007.tif
3424.370000  G3L17_007.tif
...
```

File LOGS_G3.txt

```
06-May-2004 22:39:25: Tracking of the Analysis

Filename          Type  Bubbles nº  Slugs nº    Description

G3L17_001.tif      c       2           3        Bubbles cut at the
beginning and at the end
Error using ==> imread
File "G3L17_002.tif" does not exist.
G3L17_003.tif      d       2           2        One bubble cut at the
beginning of the image
G3L17_004.tif      c       2           3        Bubbles cut at the
beginning and at the end
Error using ==> imread
File "G3L17_005.tif" does not exist.
G3L17_006.tif      c       2           3        Bubbles cut at the
beginning and at the end
G3L17_007.tif      c       2           3        Bubbles cut at the
beginning and at the end
...
```

Bibliography

Abdallah R., Meille V., Shaw J., Wenn D. and de Bellefon C., *Gas-liquid and Gas-liquid-solid Catalysis in a Mesh Microreactor*, Chem. Commun., **4**, 372-373 (2004).

Abraham M.H., Ibrahim A., Zissimos A.M., Zhao Y.H., Comer J. and Reynolds D.P., *Application of Hydrogen Bonding Calculations in Property Based Drug Design,* Drug Discovery Today, **7(20),** 1056-1063 (2002).

Abrash H. I., Shih D., Elias W. and Malekmehr F., *A Kinetic Study of the Air Oxidation of Pyrogallol and Purpurogallin*, Int. J. Chem. Kinet., **21**, 465-476 (1989).

Adam N.K., *Principles of Penetration of Liquids into Solids*, Discuss. Faraday Soc., **3**, 5-11 (1948).

Adamson A.W. and Gast A.P., *Physical Chemistry of Surfaces: Chapter II – Capillarity*, 6th Ed., John Wiley & Sons, Inc. (1997).

Aguilera M. and López A., *Fenómenos de Transporte I (TF-1221),* Lecture notes, Universidad Simón y Bolivar (2003).

Amador C., Angeli P. and Gavriilidis A., *Flow Distribution in Microreactor Scale-out Geometries and the Effect of Manufacturing Tolerances and Channel Blocking*, Chem. Eng. J., **101**, 379-390 (2004).

Amador C., Angeli P., Gavriilidis A., Shaw J. and Wenn D., *Analysis of Mass transfer and Chemical Reaction in a Mesh Microreactor*, Proc. 1st Int. Symposium on Process Intensification and Miniaturisation (PIM-1), 18-21 August (2003), Newcastle (UK).

Amador C., Salman W., Sanguanpiyapan S., Gavriilidis A. and Angeli P., *Effect of Gas-Liquid Inlet Conditions on the Mechanism of Taylor Flow Formation*, 5th Internacional Conference on Multiphase Flow, ICMF'04. Yokohama, Japan, paper No. 515.

Arkilic E.B., Martín A.S. and Breuer K., *Gaseous Slip Flow in Long Microchannels*, J. Microelectromech. Syst., **6(2)**, 167-178 (1997).

Asekomhe S.O. and Elliott J.A.W., *The Effect of Interface Deformation due to Gravity on Line Tension Measurement by the Capillary Rise in a Conical Tube*, Colloids and Surfaces A: Physicochem. and Eng. Aspects, **220**, 271-278 (2003).

Ashgriz N., *Free Surface Flows*, http://www.mie.utoronto.ca/labs/mfl/HFM2.htm.

Bejan A. and Errera M.R., *Deterministic Tree Networks for Fluid Flow: Geometry for Minimal Flow Resistance Between a Volume and One Point*, Fractals, **5,** 685-695 (1997).

Benavides G.L., Adams D.P. and Yang P., *Meso-Machining Capabilities*, Sandia Report SAND2001-1708, June (2001).

Bhumia A., Kamotani Y. and Nahra K., *Bubble Formation on a Wall in Cross-Flowing Liquid and Surrounding Fluid Motion, with and without Heating*, NASA/CP, 1500-1509 (2000).

Bi Q. C. and Zhao T.S., *Taylor Bubbles in Miniaturized Circular and Noncircular Channels*, Int. J. Multiphase Flow, **27**, 561-570 (2001).

Bibby I.P., Harper M.J. and Shaw J., *Design and Optimization of MicroFluidic Reactor through CFD and Analytical Modeling*, Proc. 2nd Int. Conf. on Microreaction Technology, 335-339 (1998).

Bico J. and Quéré D., *Rise of Liquids and Bubbles in Angular Capillary Tubes*J. Colloid Interface Sci., **247**, 162-166 (2002).

Bird R.B., Stewart W.E. and Lightfoot E.N., *Transport Phenomena*, John Wiley and Sons, New York (2002).

Blokhuis E.M., *Comments on Effect of Gravity on Contact Angle: A Theoretical Investigation*, J. Chem. Phys., **109**, 3651 (1998)], Letters to the editor, **112(12)**, 5511-5512 (2000).

Boruvka L. and Neumann A.W., *Generalization of the Classical Theory of Capillarity*, J. Chem. Phys., **66(12)**, 5464-5476 (1977).

Brennen C.E., *Fundamentals of Multiphase Flow*, Cambridge University Press (2005).

Bretherton F. P., *The Motion of Long Bubbles in Tubes,* J. Fluid Mech., **10**, 166-188 (1961).

Bronshtein I.N. and Semendyayev B., *Handbook of Mathematics*, 3rd Ed., Springer-Verlag, New York (1997).

Bugg J.D. and Saad G.A., *The Velocity Field around a Taylor Bubble Rising in a Stagnant Viscous Fluid: Numerical and Experimental Results,* Int. J. of Multiphase Flow, **28,** 791-803 (2002).

Burns J. R. and Ramshaw C., *The Intensification of Rapid Reactions in Multiphase Systems using Slug Flow in Capillaries,* Lab on a Chip, **1**, 10-15 (2001).

Byoung-sik K. and Harriott P., *Critical Entry Pressure for Liquids in Hydrophobic Membranes,* J. Colloid Interface Sci., **115(1)**, 1-8 (1984).

Carslaw H.S. and Jaeger J.C, *Conduction of Heat in Solids,* 2nd Ed., Oxford (1986).

Cassie A.B.D. and Baxter S., *Wettability of Porous Surfaces*, Trans. Faraday Soc., **40,** 546-551 (1944).

Chebbi R., *Deformation of Advancing Gas-Liquid Interfaces in Capillary Tubes*, J. Colloid Interface Sci., **265**, 166-173 (2003).

Checco A. and Guenoun P., *Non-linear Dependence of the Contact Angle of Nanodroplets on Contact Line Curvature*, Physical Review Letters, **91(18),** 186101 (2003).

Chen J.D., *Measuring the Film Thickness Surrounding a Bubble inside a Capillary*, J. Colloid Interface Sci., **109(2)**, 341-349 (1986).

Clift, R., Grace J.R. and Weber M.E., *Bubbles, Drops and Particles*, Academic Press, New York (1978).

Commenge J.M., Falk L., Corriou J.P. and Matlosz M., *Optimal Design for Flow Uniformity in Microchannel Reactors*, AIChE J., **48,** 345-358 (2002).

Concus P. and Finn R., *On the Behavior of a Capillary Surface in a Wedge*, Proc. Natl. Acad. Sci., U.S.A., **63(2)**, 292-299 (1969).

Concus P. and Finn R., *On the Capillary Free Surfaces in the Absence of Gravity*, Acta Math, **132**, 177-198 (1974).

Concus P., Finn R. and Weislogel M., *Measurement of Critical Contact Angle in a Microgravity Space Experiment*, Experiments in Fluids, **28(3)**, 197-205 (2000).

Concus P. and Finn R., *Capillary Wedges Revisited*, SIAM J. Math. Anal., **27**, 56-69 (1996).

Crank J., *Mathematics of Diffusion*, 2nd Ed., Clarendon Press, Oxford (1975).

Crisp D.J. and Thorpe W.H., *The Water-Protecting Properties of Insect Hairs*, Disc. Faraday Soc., **3**, 210-220 (1948).

Cubaud T. and Fermigier M., *Advancing Contact Lines on Chemically Patterned Surfaces*, J. Colloid Interface Sci.,**269**, 171-177 (2004).

Cubaud T. and Ho C-M., *Transport of Bubble in Square Microchannels*, Phys. Fluids., **16(12)**, 4575-4585 (2004).

Cypes S.H. and Engstrom J.R., *Construction, Analysis and Evaluation of a Microfabricated Stripping Column*, Proc. 7th Int. Conf. on Microreaction Technology, 35-37 (2003).

Damianides, C.A. and Westwater, J.W., *Two-phase Flow Patterns in a Compact Heat Exchanger and in Small Tubes*. In: Proc. 2nd UK National Conf. on Heat Transfer, Glasgow, 14-16 September. Mechanical Engineering Publications, London, pp. 1257-1268 (1988).

Danckwerts P. V., *Absorption by Simultaneous Diffusion and Chemical Reaction into Particles of Various Shapes and into Falling Drops*, Trans. Faraday Soc., **47**, 1014-1023 (1951)

De Bellefon C., Abdallah R., Lamouille T., Pestre N., Caravieilhes S. and Grenouillet P., *High Throughput Screening of Molecular Catalysts Using Automated Liquid Handling, Injection and Microdevices,* Chimia, **56(11)**, 621-626 (2002)

De Mas N., Günther A., Schmidt M.A. and Jensen K.F., *Scalable Microfabricated Multiphase Reactors for Direct Flourination Reactions*, Proc. 12th Int. Conf. on Solid-State Sensors, Actuators and Microsystems, 655-658 (2003).

De Mas N., Günther A., Kraus T., Schmidt M.A. and Jensen K.F., *Scaled-Out Multilayer Gas-Liquid Microreactors with Integrated Velocimetry Sensors*, Ind. Eng. Chem. Res., **44**, 8997-9013 (2005).

Di Marco P., Grassi W., Memoli G., Takamasa T., Tomiyama A. and Hosokawa S., *Influence of Electric Field on Single Gas-Bubble Growth and Detachment in Microgravity*, Int. J. Multiphase Flow, **29**, 559-578 (2003).

Dong M. and Chatzis I., *The Imbibition and Flow of a Wetting Liquid along the Corners of a Square Capillary Tube*, J. Colloid Interface Sci., **172**, 278-288 (1995).

Duarte A.A., Strier D.E. and Zanette D.H., *The Rise of a Liquid in a Capillary Tube Revisited: A Hydrodynamical Approach*, Am. J. Phys., **64(4)**, 413-418 (1996).

Duncan D., Li D., Gaydos J. and Neumann A.W., *Correlation of Line Tension and Solid-Liquid Interfacial Tension from the Measurement of Drop Size Dependence of Contact Angle*, J. Colloid Interface Sci., **169**, 256-261 (1995).

Edvinsson, R., *Monolith Reactors in Three-Phase Processes*, Thesis, University of Technology Göteborg, 1994

Ehrfeld W., *Promising Prospects for Microreaction Technology,* Proc. 7th Int. Conf. on Microreaction Technology, 13-15 (2003).

Ehrfeld W., Hessel V. and Löwe H., *Microreactors - New Technology for Modern Chemistry*, Wiley-Vch, Weinheim (2000).

Engler M., Kockmann N., Kiefer T. and Woias P., *Numerical and Experimental Investigation on Liquid Mixing in Static Micro Mixers*, Proc. 7th Int. Conf. on Microreaction Technology, 88-90 (2003).

Farin G., *From Conics to NURBS: A Tutorial and Survey*, IEEE Computer Graphics & Applications, 78-86, September 1992.

FEMLAB Reference Manual (2002).

Feng Z. and Serizawa A., *Two-Phase Flow Patterns in Ultra-Small-Channels,* 2nd Japanese-European Two-Phase Flow Group Meeting, Tsukuba - Japan, 25-29 September (2000).

Finn R., *Capillary Surface Interfaces*, Notices of the AMS, **46(7)**, 770-781 (1999).

Fogler H.S., *Elements of Chemical Reaction Engineering*, 4th Ed., Prentice-Hall, New Jersey (2005).

Freíd E. and Idelchik I.E., *Flow Resistance: A Design Guide for Engineers*, Hemisphere, New York (1989).

Friedel, L. *Pressure Drop during Gas/Vapor-Liquid Flow in Pipes*, Chemie-Ingenieur-Technik, **50**, 167-180 (1978).

Fukano, T., Kariyasaki, A., *Characteristics of Gas-Liquid Two-Phase Flow in a Capillary*, Nucl. Eng. Des., **141**, 59-68 (1993).

Fung Y.C. and Zweifach B.W., *Microcirculation: Mechanics of Blood Flow in Capillaries*, Annu. Rev. Fluid Mech., **3**, 189-210 (1971).

FIDAP 8.7.0 Manual, 2002.

Gaydos J. and Neumann A.W., *The Dependence of Contact Angles on Drop Size and Line Tension*, J. Colloid Interface Sci., **120(1)**, 76-86 (1987).

Gavriilidis A., Angeli P., Cao E., Yeong K.K. and Wan Y.S.S., *Technology and Applications of Microengineered Reactors,* Trans IchemE, **80(A),** 3-30 (2002).

Ghadiali S.N and Gaver III D.P, *The Influence of Non-Equilibrium Surfactant Dynamics on the Flow of a Semi-Infinite Bubble in a Rigid Cylindrical Capillary Tube*, J. Fluid Mech., **478**, 165-196 (2003).

Giavedoni M.D. and Saita F.A., *The Axisymmetrical and Plane Cases of Gas Phase Steadily Displacing a Newtonian Liquid – A Simultaneous Solution of the Governing Equation*, Phys. Fluids., **9(8)**, 2420-2428 (1997).

Giavedoni M.D. and Saita F.A., *The Rear Meniscus of a Long Bubble Steadily Displacing a Newtonian Liquid in a Capillary Tube*, Phys. Fluids., **11(4),** 786-794 (1999).

Gibbs J.W., *The Scientific Papers* – Vol. I, Dover, New York (1961).

Gobby D., Angeli P. and Gavriilidis A., *Mixing Characteristics of T-type Microfluidic Mixers*, J. Micromech. Microeng., **11**, 126-132 (2001).

Golbig K., Taghavi-Moghadam S. and Born P., *CYTOS™ Technology – Microreaction Technology in Practical Sense*, Proc. 6th Int. Conf. on Microreaction Technology, 131-134 (2002).

Grolman E., Edvinsson R., Stankiewicz A. and Moulijn J., *Hydrodynamics Instabilities in Gas-Liquid Monolithic Reactors*, Proc. ASME Heat Transfer Div. **3**, 171-178 (1996).

Gu Y., Li D. and Cheng P., *Determination of Line Tension from the Shape of Axisymmetric Liquid-Vapour interfaces around a Conic Cylinder*, J. Colloid Interface Sci., **180**, 212-217 (1996).

Hapgood K., Litster J.D., Biggs S.R. and Howes T., *Drop Penetration into Porous Powder Beds*, J. Colloid Interface Sci., **253**, 353-366 (2002).

Happel J. and Brenner H., *Low Reynolds Number Hydrodynamics: With Special Applications to Particulate Media,* Chapter 2, Prentice-Hall International, Englewood Cliffs, New Jersey (1965).

Harkins W.D., *Linear or Edge Energy and Tension as Related to the Energy of Surface Formation and of Vaporization*, J. Chem. Phys., **5**, 135-140 (1937).

Hazel A.L. and Heil M., *The Steady Propagation of a Semi-infinite Bubble into a Tube of Elliptical or Rectangular Cross-section*, J. Fluid Mech., **470**, 91-114 (2002).

He B., Lee J. and Patankar N.A., *Contact Angle Hysteresis on Rough Hydrophobic Surfaces*, Colloids and Surfaces A: Physicochem. Eng. Aspects, **248**, 101-104 (2004).

Hessel V., Hard S. and Löwe H., *Chemical Micro Process Engineering: Fundamentals, Modelling and Reactions*, Wiley, Weinheim (2005).

Hessel V., Ehrfeld W., Golbig K., Haverkamp V. and Löwe H., *Gas/Liquid Dispersion Process in Micromixers: The Hexagon Flow,* Proc. 2nd Int. Conf. on Microreaction Technology, 259-266 (1998).

Hetsroni G., Mosyak A., Pogrebnyak E. and Segal Z., *Explosive Boiling of Water in Parallel Microchannels*, Int. J. Multiphase Flow, **31**, 371-392 (2005).

Hetsroni G., Mosyak A., Segal Z. and Pogrebnyak E., *Two-phase Flow Patterns in Parallel Micro-channels,* Int. J. Multiphase Flow, **29**, 341-360 (2003).

Ho C. and Tai Y., *Micro-electro-mechanical Systems (MEMS) and Fluid Flows,* Annu. Rev. Fluid. Mech., **30,** 579-612 (1998).

Holowach M.J., Hochreiter L.E. and Cheung F.B., *A model for Droplet Entrainment in Heated Annular Flow*, Int. J. Heat Fluid Flow, **23**, 807-822 (2002).

Iguchi M, Terauchi Y. and Yokoya S-I, *Effect of Cross-Flow on the Frequency of Bubble Formation from a Single Hole Nozzle*, Metall. Mater. Trans. B, **29B**, 1219-1225 (1998).

Institut fuer Mikrotechnik Mainz (IMM), Germany, Private communication (2003).

Irandoust S. and Andersson B., *Liquid Film in Taylor Flow through a Capillary*, Ind. Eng. Chem. Res., **28**, 1684-1688 (1989).

Jähnisch K., Baerns M., Hessel V., Ehrfeld W., Haverkamp V., Löwe H., Wille Ch. and Guber A., *Direct Flourination of Toluene using Elemental Fluorine in Gas/Liquid Microreactors*, J. Fluorine Chem., **105**, 117-128 (2000).

Jensen K.F., *Microreaction Engineering- Is Small Better?*, Chem. Eng. Sci., **56**, 293-303 (2001).

Jensen, M. J., *Bubbles in Microchannels*, Thesis, Technical University of Denmark (2002).

Jensen M.J., Goranovic G. and Bruus H. *The Clogging Pressure of Bubbles in Hydrophilic Microchannels Contractions*, J. Micromech. Microng., **14**, 876-883 (2004).

Jensen W.C., Li D., *Determination of Line Tensions from the Capillary Rise in a Conical Tube,* Colloids and surfaces A: Physicochemical and Engineering Aspects, **156**, 519-524 (1999).

Jeong S. and Kim W., *A Study on the Optimal Monolith Combination for Improving Flow Uniformity and Warm-up Performance of an Auto-Catalyst*, Chem. Eng. Process., in Press, 1-17 (2002).

Johnson K.E, Private Communication (2004).

Judy J., Maynes D. and Webb B.W., *Characterization of Frictional Pressure drop for Liquid Flows through Microchannels,* Int. J. Heat Mass Transfer, **45**, 3477-3489 (2002).

Kasagi N., Shikazono N., Suzuki Y. and Oku T., *Assessment of High-Performance Compact Micro Bare-tube heat Exchanger for Electronic Equipment Cooling,* Proc. 1st Int. Symposium on Process Intensification and Miniaturisation, 17 (2003).

Kandlikar S.G., Kuan W.K., Willistein D.A. and Borrelli J., *Stabilization of Flow Boiling in Microchannels using Pressure Drop Elements and Fabricated Nucleation Sites*, J. Heat Transfer, **128(4)**, 389-396 (2006).

Kew P.A. and Cornwell K., Correlations for the Prediction of Boiling Heat Transfer in Small-Diameter Channels, Appl. Thermal Eng., **17**, 705–715 (1997).

Kim B. and Harriott P., *Critical Entry Pressure for liquids in Hydrophobic Membranes* J. Colloid Interface Sci., **115(1)**, 1-8 (1987).

Kim I.H., Kamotani Y. and Ostrach S., *Modeling Bubble and Drop Formation in Flowing Liquids in Microgravity*, AIChE, **40(1)**, 19-28 (1994).

Kloc Ch. and Laudise R.A., *Vapour Pressures of Organic Semiconductors: α-hexathiophene and α-quaterthiophene,* J. Cryst. Growth, **193**, 563-571(1998).

Kolb W.B. and Cerro R.L., *Film Flow in the Space between a Circular Bubble and Square Tube,* J. Colloid Interface Sci., **159**, 302-311 (1993a).

Kolb W.B. and Cerro R.L., *The Motion on Long Bubbles in Tubes of Square Cross Section,* Phys. Fluids A, **5(7)**, 1549-1557 (1993b).

Kostoglou M., Housiada P. and Konstandopoulos G., *Multi-channel Simulation of Regeneration in Honeycomb Monolithic Diesel Particulate Filters,* Chem. Eng. Sci., **58,** 3273-3283 (2003).

Kreutzer, M., *Hydrodynamics of Taylor Flow in Capillaries and Monolith Reactors*, Thesis, University of Technology, Delft (2003).

Kuiper S., Brink R., Nijdam W., Krijnen G.J.M. and Elwenspoek M.C., *Ceramic Microsieves: Influence of Perforation Shape and Distribution on Flow Resistance and Membrane Strength*, J. Membr. Sci., **196**, 149-157 (2002).

Kumar, R., Kuloor N.R., *The Formation of Bubbles and Drops*, Vol. 8, Academic Press, New York (1990).

Lago M. and Araujo M., *Capillary Rise in Porous Media*, J. Colloid Interface Sci., **234**, 35-43 (2001).

Langbein D., *Fluid Statics and Dynamics in Microgravity*, J. Phys.: Condens. Matter **2**, SA491-SA498 (1990).

Leal L.G., *Laminar Flow and Convective Transport Processes: Scaling Principles and Asymptotic Analysis*, Butterworth-Heinemann, 197-206 (1992).

Legait B., *Laminar Flow of Two Phases through a Capillary Tube with Variable Square Cross-Section*, J. Colloid Interface Sci., **96(1)**, 28-38 (1983).

Levenspiel, O., *Chemical Reaction Engineering,* Chapter 9, Wiley, New York (1972).

Li D., *Drop Size Dependence of Contact Angles and Line Tensions of Solid-Liquid Systems, Colloids and Surfaces A*: Physicochemical and Engineering Aspects, **116**, 1-23 (1996).

Li D. and Steigmann D.J., *Positive Line Tension as a Requirement of Stable Equilibrium, Colloids and Surfaces A*: Physicochemical and Engineering Aspects, **116**, 25-30 (1996).

Lide D.R., *Characteristics of Particles and Particle Dispersoids* In *CRC Handbook of Chemistry and Physics*, 75th Ed., CRC Press, Florida, 15-38 (1995).

Lin F.Y.H., Li D. and Neumann A.W., *Effects of Surface Roughness on the Dependence of Contact Angles on Drop Size,* J. Colloid Interface Sci., **159,** 86-95 (1993).

Lin F.Y.H. and Li D., *The Effect of Surface Heterogeneity on the Drop Size Dependence of Contact Angles*, Chem. Eng. Sci., **50**, 2633-2639 (1995).

Lin, F.Y.H. and Li D., *The Influence of Inclination of a solid Surface on Contact Angles Due to the Effect of Line Tension*, Colloids and Surfaces A: Physicochemical and Engineering Aspects, **87(2)**, 93-100 (1994).

Losey M.W., Jackman R.J., Firebaugh S.L., Schmidt M.A. and Jensen K.F., *Design and Fabrication of Microfluidic Devices for Multiphase Mixing and Reaction*, J. Microelectromech. Syst., **11(6)**, 709-717 (2002).

Madou M., *Fundamentals of Microfabrication* , CRC Press, New York (1997).

Madou M.J., Lee L.J., Koelling K.W., Daunert S., Lai S., Koh C.G., Juang Y., Yu L. and Lu Y., *Design and Fabrication of Polymer Microfluidic Platforms for Biomedical Applications*, Annu. Tech. Conf.-Soc. Plast. Eng., 59th, **3,** 2534-2538 (2001).

Man H.N. and Jing X.D., *Network Modeling of Wettability and Pore Geometry Effects on Electrical Resistivity and Capillary Pressures*, J. Petroleum Sci. Eng., **24**, 255-267 (1999).

Man H.N. and Jing X.D., *Network Modeling of Strong and Intermediate Wettability on Electrical Resistivity and Capillary Pressure*, Adv. Water Resources, **24,** 345-363 (2001).

Marmur A., *Line Tension and the Intrinsic Contact Angle in Solid-Liquid-Fluid Systems*, J. Colloid Interface Sci., **186**, 462-466 (1997).

Marmur A., *Line Tension Effect on Contact Angles: Axisymmetric and Cylindrical Systems with Rough or Heterogeneous Solid Surfaces,* Colloids and Surfaces A: Physicochemical and Engineering Aspects, **136**, 81-88 (1998).

Maruyama T., Kaji T., Ohkawa T., Sotowa K., Matsushita H., Kubota F., Kamiya N., Kusakabe K. and Goto M., *Intermittent Partition Walls Promote Solvent Extraction of Metal ions in a Microfluidic Device*, Analyst, **129**, 1008-1013 (2004).

Massey B. and Ward-Smith J., *Mechanics of Fluids*, 7th Ed., Spon Press (1998).

Mason G. and Morrow N.R., *Meniscus Curvatures in Capillaries of Uniform Cross-Section,* J. Chem. Soc., Faraday Trans., **80**, 2375-2393 (1984).

Mason G. and Morrow N.R., *Effect of Contact Angle on Capillary Displacement Curvatures in Pore Throats formed by Spheres*, J. Colloid Interface Sci., **168**, 130-141 (1994).

Mason G. and Morrow N.R., *Meniscus Curvatures in Capillaries of Uniform Cross-Section,* J. Chem. Soc., Faraday Trans., **80**, 2375-2393 (1984).

Matijevic E., *Surface and Colloid Science*, Vol. II, Wiley-Interscience, New York (1969).

Matsui H., Masafumi H., Hiroshi N. and Fujita H., *Two-Phase Flow Distribution in Multipass Compact Channels*, Proc. UK-Japan Two-phase Flow Seminar (2003).

Mayer, R.P. and Stowe R.A., *Mercury Porosimetry – Breakthrough Pressure for Penetration Between Packed Spheres*, J. Colloid Interface Sci., **20**, 893 (1965).

Mayer, R.P. and Stowe R.A., *Mercury Porosimetry: Filling of Toroidal Void Volume Following Breakthrough between Packed Spheres*, J. Phys. Chem., **70**, 3867 (1966).

Mayer R.P. and Stowe R.A., *Nodoids and Toroids: Comparison of two Geometries for the Meniscus Profile of a Wetting Liquid between two Touching Isolated Spheres and Extensions to the Model of a Collection of Packed Spheres*, J. Colloid Interface Sci., in Print (2005).

Mies M.J.M., Rebrov E.V., de Croon M.H.J.M and Schouten J.C., *A Novel High-Throughput Microreactor for Screening of Catalyst Coatings for highly Exothermic Reactions*, Proc. 7th Int. Conf. on Microreaction Technology, 25-27 (2003).

Nahra H.K. and Kamotani Y., *Prediction of Bubble Diameter at Detachment from a Wall Orifice in liquid Cross-Flow under Reduced and Normal Gravity Conditions*, Chem. Eng. Sci., **58**, 55-69 (2003).

New Jersey Centre for Microchemical Systems, *Partners and Sponsors*, http://www.njcmcs.org/partners_sponsors.htm.

O'Brien W. J. and Ryge G., *Wettability of poly(methyl methacrylate) treated with silicon tetrachloride.* J. Prosthet. Dent.,**15(2)**, 304-308, 1965.

Orr F. M., Brown R. A. and Scriven L.E., *Three-Dimensional Menisci: Numerical Simulation by Finite Elements*, J. Colloid Interface Sci., **60(1)**, 137-147 (1977).

Qu W. and Mudawar I., *Transport Phenomena in Two-Phase Micro-Channel Heat Sinks*, Proc. IMECE, November 17-22 (2002).

Qu W. and Mudawar I., *Measurement and Prediction of Pressure Drop in Two-Phase Micro-Channel Heat Sinks*, Int. J. Heat Mass Transfer, **46**, 2737-2753 (2003).

Papanastasiou T.C., Georgiou G.C. and Alexandrou A.N., *Viscous Fluid Flow*, CRC Press (2000).

Patzek T. W., *Verification of a Complete Pore Network Simulator of Drainage and Imbibition*, SPE/DOE Improved Oil Recovery Symposium, Oklahoma, 3-5 April 2000.

Paul P.H., Gasguillo M.G., and Rakestraw D.J., *Imaging of Pressure-and Electrokinetically Driven Flows through Open Capillaries,* Anal. Chem., **70**, 2459-2465 (1998).

Pellicer J., Manzanares J. A. And Mafé S., *The Physical description of Elementary Surface Phenomena: Thermodynamics versus Mechan*ics, Am. J. Phys., **63(6)**, 542-547 (1995).

Perry R.H., Green D.W., *Perry's Chemical Engineers' Handbook*, 7th Ed., McGraw-Hill (1997).

Philip, J.R., *Unitary Approach to Capillary Condensation and Adsorption.* J. Chem. Phys., **66**, 5069-5075 (1977).

Piegl L. and Tiller W., *The NURBS Book*, 2nd Ed., Springer, Berlin (1997).

Pompe, T. and Herminghaus G., *Three-Phase Contact Line Energetics from Nanoscale Liquid Surface Topographies*, S. Phys. Rev. Lett., **85**, 1930-1933 (2000).

Powell O. and Harrison B., *Anisotropic Etching of {100} and {110} planes in (100) Silicon*, J. Micromech. Microeng., **11**, 217-220 (2001).

Prasad R., Khare S., Sengupta A. and Sirkar K.K., *Novel Liquid-in-Pore Configurations in Membrane Solvent Extraction*, AIChE, **36(10),** 1592-1596 (1990).

Prasad R. and Sirkar K.K., *Solvent Extraction with Microporous Hydrophilic and Composite Membranes*, AIChE, **33(7)**, 1057-1066 (1987).

Princen H.M., *Capillary Phenomena in Assemblies of Parallel Cylinders I. Capillary Rise between Two Cylinders*, J. Colloid Interface Sci., **30(1)**, 69-75 (1968).

Princen H.M., *Capillary Pressure Behaviour in Pores with Curved Triangular Cross-Section: Effect of Wettability and Pore Size Distribution*, Colloids Surf., **65**, 221-230 (1992).

Princen H.M., *Capillary Rise in Systems with more than Two Cylinders*, J. Colloid Interface Sci., **30(3)**, 359-371 (1969).

Purcell, W.R., *Capillary Pressures - Their Measurement Using Mercury and the Calculation of Permeability*, Trans. AIME., **186**, 39-48 (1949).

Ratulowski J. and Chang H.C., *Marangoni Effects of Trace Impurities on the Motion of Long Gas Bubbles in Capillaries*, J. Fluid Mech., **210**, 303-328 (1990).

Ratulowski J. and Chang H.C., *Transport of Gas Bubbles in Capillaries*, Phys, Fluids., A1, **10**, 1642-1655 (1989).

Rayleigh L., *On the Instability of Jets*, Proc. London Math. Soc., **10(4)** (1879).

Rayner M and Trägårdh G., *Membrane Emulsification Modelling: How Can We Get from Characterisation to Design?*, Desalination, **145**, 165-172 (2002).

Reed B.W., Semmens M.J. and Cussler E.L., *Membrane Contactors,* In: Noble R.D. and Stern S.A (Ed.), *Membrane Separation Technology. Principles and Applications*, 467-498, Elsevier Science (1995).

Reid R.C., Prausnitz J.M and Poling B.E., *The Properties of Gases and Liquids*, 4th Ed., McGraw Hill, New York (1987).

Reinelt D. A., *The Rate at which a Long Bubble Rises in a Vertical Tube*, J. Fluid Mech., **175**, 557-565 (1987).

Riley K. F., Hobson M.P. and Bence S.J., *Mathematical Methods for Physics and Engineering*, 2nd Ed., Cambridge University Press, Cambridge (2002).

Roberge D.M., *Microreactor Technology: A Revolution for the Fine Chemical and Pharmaceutical Industries?,* Chem. Eng. Technol., **28(3)**, 318-323 (2005).

Robins I., Shaw J., Miller B., Turner C. and Harper M., *Solute Transfer by Liquid/Liquid Exchange without Mixing in Micro-Contactor Devices*, Proc. 1st Int. Conf. on Microreaction Technology, 35-46 (1997).

Rogers D.F. and Adams J.A., *Mathematical Elements for Computer Graphics*, 2nd Ed., McGraw Hill, New York (1990).

Rose W. and Heins R.W., *Moving Interfaces and Contact Angle Rate-Dependency*, J. Colloid Interface Sci., **17**, 39-48 (1962).

Roura P. and Fort J., *Local Thermodynamic Derivation of Young's Equation*, J. Colloid Interface Sci., **272**, 420-429 (2004).

Rowlinson J.S. and Widom B., *Molecular Theory of Capillarity*, Oxford Science Publications, New York, 1984.

Rusanov A.I., *Classification of Line Tension,* Colloids and Surfaces A: Physicochemical and Engineering Aspects, **156**, 315-322 (1999).

Salman W., *Characterisation and Modelling of Taylor Flow in Small Circular Channels for the Purpose of Sequential Screening*, Thesis Doctoral, University College London (2005).

Salman, W., Gavriilidis A. and Angeli P., *A Model for Predicting Axial Mixing During Gas-Liquid Taylor Flow in Microchannels at Low Bodenstein Numbers*, Chem. Eng. J., **101**, 391-396 (2004).

Serizawa A. and Kawara Z. *Two-Phase Flow in Micro-Channels*, 39th European Two-Phase Flow Group Meeting, Aveiro - Portugal, 17-20 June (2001).

Shouxiang M., Geoffrey M. and Norman R. M., *Effect of Contact Angle on Drainage and Imbibition in Regular Polygonal Tubes*, Colloids Surf., **A 117**, 273-291 (1996).

Shaw J., Simpson I., Turner C., *Measurement and Modelling of Liquid Flows in Micro-Engineered Structures,* DECHEMA Monographs, **132**, 235-242 (1996a).

Shaw J., Miller B., Turner C., Harper M. and Graham, S., *Mass Transfer of Species in Micro-Contactor: CFD Modelling and Experimental Validation*, μTAS96 (1996b).

Shaw J., Turner C., Miller B., Robins I., Kingston J., Harper M., *Characterisation of Micro-Contactor for Solute Transfer between Immiscible Liquids and Development of Arrays for High Throughput*, Proc. 2nd Int. Conf. on Microreaction Technology, 267-271 (1998).

Shaw J., Nudd R., Naik B., Turner C., Rudge D., Benson M. and Garman A., *Liquid/Liquid Extraction Systems using Micro-Contactors Arrays*, μTAS (2000).

Shen E. I. and Udell K.S., A *Finite Element Study of Low Reynolds Number Two-Phase Flow in Cylindrical Tubes*, J. Appl. Mech., **52,** 253-256 (1985).

Shouxiang M., Geoffrey M. and Norman R.M., *Effect of Contact Angle on Drainage and Imbibition in Regular Polygonal Tubes*, Colloids Surf., **A 117**, 273-291 (1996).

Sinnott R.K., *Chemical Engineering Design - Coulson & Richardson's Chemical Engineering vol. 6*, 2nd Edition, Pergamon Press, Oxford (1993).

Solomentsev Y. and White L.R., *Microscopic Drop Profiles and the Origins of Line Tension*, J. Colloid Interface Sci., **218**, 122-136 (1999).

Sotowa K-I. and Kusakabe K., *Design of Microchannels for Use in Distillation Devices,* Proc. 7th Int. Conf. on Microreaction Technology, 156-157 (2003).

Stark J. and Manga M., *The Motion of Long Bubbles in a Network of Tubes*, Transport in Porous Media, **40**, 201-218 (2000).

Steigmann D.J. and Li D., *Energy Minimizing States of Capillary Systems with Bulk, Surface and Line Phases*, IMA J. Appl. Math., **55**, 1-17, 1995.

Stone H.A., *A Simple Derivation of the Time-Dependent Convection-Diffusion Equation for Surfactant Transport along a Deforming Interface*, Phys. Fluids., **2**, 111-112 (1990).

Swain P. S. and Lipowsky R., *Contact Angle on Heterogeneous Surfaces: A New Look at Cassie's and Wenzel's Laws*, Langmuir, **14**, 6772-6780 (1998).

TeGrotenhuis W.E., Cameron R., Butcher M.G., Martin P.M., and Wegeng R.S., *Micro Channel Devices for Efficient Contacting of Liquids in Solvent Extraction*, Separation Science and Technology, PNNL-SA-28743 (1998).

Taylor G.I., *Deposition of a Viscous Fluid on the Wall of a Tube,* J. Fluid Mech., **10**, 161-165 (1961).

Taylor J.A. and Yeung E.S., *Imaging of Hydrodynamic and Electrokinetic Flow Profiles in Capillaries,* Anal. Chem., **65**, 2928-2932 (1993).

Thulasidas T.C., Abraham M.A. and Cerro R.L., *Bubble-Train Flow in Capillaries of Circular and Square Cross Section*, Chem. Eng. Sci., **50,** 183-199 (1995).

Thulasidas T.C., Abraham M.A. and Cerro R.L., *Flow Patterns in Liquid Slugs during Bubble-Train Flow inside Capillaries*, Chem. Eng. Sci., **52**, 2947-2962 (1997).

Thulasidas T.C., Abraham M.A. and Cerro R.L., *Dispersion during Bubble-Train Flow in Capillaries*, Chem. Eng. Sci., **54**, 61-76 (1999).

Tice J.D., Lyon A.D. and Ismagilov R.F., *Effects of Viscosity on Droplet Formation and Mixing in Microfluidic Channels*, Anal. Chim. Acta, **507**, 73-77 (2004).

Tompkins C.J., Michaels A.S. and Peretti S.W., *Removal of p-nitrophenol from Aqueous Solution by Membrane-Supported Solvent Extraction*, J. Membr. Sci., **75**, 277-292 (1992).

Triplett K. A., Ghiaasiaan S. M., Abdel -Khalik S.I. and Sadowski D.L., *Gas-Liquid Two-Phase Flow in Microchannels, Part I: Two-Phase Flow Patterns*, Int. J. Multiphase Flow, **25**, 377-394 (1999a).

Triplett K. A., Ghiaasiaan S. M., Abdel -Khalik S.I. and Sadowski D.L., *Gas-Liquid Two-Phase Flow in Microchannels, Part II: Void Fraction and Pressure Drop,* Int. J. Multiphase Flow, **25**, 399-410 (1999b).

Tseng F.G., Yang I.D. and et al., *Fluid Filling into Micro-Fabricated Reservoirs*, Sensors and Actuators, **97-98**, 131-138 (2002).

Turner C., Shaw J., Miller B. and Bains V., *Solvent Extraction using Micro-Mesh Reactors*, 4th Int. Conf. on Microreaction Tehcnology, Poster Session 1, Atlanta (2000).

Turner C., Shaw J., Miller B. and Bains V., *Solvent Extraction using Micro-Mesh Reactors*, Proc. 4th Int. Conf. on Microreaction Technology, 334-340 (2000).

Vaidya A.M, Bell G. and Halling P.J, *Aqueous-organic Membrane Bioreactors. Part I. A Guide to Membrane Selection*, J. Membr. Sci., **71**, 139-149 (1994a).

Vaidya A.M, Bell G. and Halling P.J, *Aqueous-organic Membrane Bioreactors. Part II. Breakthrough Pressure Measurement*, J. Membr. Sci., **97**, 13-26 (1994b).

Volpe C.D., Maniglio D., Morra M. and Siboni S., *The Determination of a 'Stable Equilibrium' Contact Angle on Heterogeneous and Rough Surfaces*, Colloids Surf., A, **206**, 47-67 (2002).

Wang R., Cong L. and Kido M., *Evaluation of the Wettability of Metal Surfaces by Micro-Pure Water by means of Atomic Microscopy*, Appl. Surf. Sci., **191**, 74-84 (2002).

Wapner P.G. and Hoffman W.P., *Partial Wetting Phenomena on Nonplanar Surfaces and in Shaped Microchannels*, Langmuir, **18(4)**, 1225-1230 (2002).

Ward C.A. and Sasges M.R., *Effect of Gravity on Contact Angle: A Theoretical Investigation*, J. Chem. Phys., **109(9)**, 3651-3660 (1998a).

Ward C.A. and Sasges M.R., *Effect of Gravity on Contact Angle: A Experimental Investigation*, J. Chem. Phys., **109(9)**, 3661-3670 (1998b).

Ward C.A., Rahimi P., Sasges M.R. and Stanga D., *Contact Angle Hysteresis Generated by the Residual Gravitational Field of the Space Shuttle*, J. Chem. Phys., **112**, 7195-7202 (2000).

Weislogel M.M. and Lichter S., *Capillary Flow in an Interior Corner*, J. Fluid Mech., **373**, 349-378 (1998).

Wenn D.A., Shaw J.E.A and Mackenzie B., *A Mesh Microreactor for Two-phase Reactions*, Lab Chip, **3,** 180-186 (2003).

Wenzel R.N., *Resistance of Solid Surfaces to Wetting by Water,* Ind. Eng. Chem., **28(8),** 988-994 (1936).

Widom B., *Line Tension and the Shape of a Sessile Drop*, J. Phys. Chem., **99**, 2803 (1995).

Wiesler F., *Membrane Contactors: An Introduction to the Technology*, Ultrapure Water, May/June, 27-31 (1996).

Wiesler F., *Membrane Contactors: Reduce Chemical Use and Blow-downs*, WWI. October (2003).

Woehl P. and Cerro R.L., *Pressure Drop in Monolith Reactors*, Catal. Today, **69**, 171-174 (2001).

Wong H., *The Motion of a Long Bubble in Polygonal Capillaries at Low Capillary Numbers*, Dissertation at University of California-Berkeley (1992)

Wong H., Morris S., and Radke J., *Two-Dimensional Menisci in Non-axisymmetric Capillaries*, J. Colloid Interface Sci., **148(2)**, 284-287 (1992a).

Wong H., Morris S., and Radke J., *Three Dimensional Menisci in Polygonal Capillaries*, J. Colloid Interface Sci., **148(2)**, 317-336 (1992b).

Wong H., Morris S., and Radke J., *The Motion of a Long Bubble in Polygonal Capillaries at Low Capillary Numbers,* Thesis, University of California, Berkeley (1992c).

Yang J.M., Yang X., Ho C.-M. and Tai Y.-C., *Prediction of the Pressure Drop Through Micromachined Particle Filters,* Proc. of Int. Conf. on Modeling and Simulation of Microsystems (MSM'99), San Juan, Puerto Rico, 546-549 (1999). Microfabricated meshes.

Yang M. and Cussler E.L., *Designing Hollow-Fiber Contactors*, AlChE J., **32(11)**, 1-5 (1986).

Yongping C. and Cheng P., *Heat Transfer and Pressure Drop in Fractal Tree-Like Microchannel Nets,* Int. J. Heat Mass Transfer, **45,** 2643-2648 (2002).

Yoshida J-I., Nagaki A. and Suga. S., *Highly Selective Reactions using Microstructured Reactors*, Proc. 7th Int. Conf. on Microreaction Technology, 1-2 (2003).

Yost F.G., Michael J.R. and Eisemann E.T., *Extensive Wetting Due to Roughness,* Acta Mater., **43 (1)**, 299-305 (1995).

Zhang L., Koo J-M., Jiang L., Asheghi M., Goodson K., Santiago J.G. and Kenny T.W., *Measurements and Modeling of Two-Phase Flow in Microchannels with Nearly Constant Heat Flux Boundary Conditions*, J. Microelectromech. Syst., **11(1)**, 12-19 (2002).

Zienkiewicz O.C. and Morgan K., *Finite Elements and Approximation*, Wiley-Interscience, John Wiley & Sons, New York (1983).

Zitny R., Private Communication (2004).